60th International Conference for Students of Physics and Natural Sciences

Open Readings 2017

March 14-17, 2017

Vilnius, LITHUANIA

Programme and Abstracts

CONFERENCE CHAIRS

Vytautas Butkus, *Faculty of Physics, Vilnius University & Light Conversion Ltd.*
Jonas Berzinš, *TNO Delft & Friedrich-Schiller-University Jena*

ORGANIZING COMMITTEE

Sonata Adomavičiūtė, *Faculty of Physics, Vilnius University*
Jogundas Armaitis, *Institute of Theoretical Physics and Astronomy, Vilnius University*
Danas Buožius, *Faculty of Physics, Vilnius University*
Vilius Karsokas, *Faculty of Physics, Vilnius University*
Tomas Kontrimas, *Center for Physical Sciences and Technology & Faculty of Physics, Vilnius University*
Rasa Krikstaponyte, *Vilnius Gediminas Technical University*
Gintarė Kuksėnaitė, *Faculty of Physics, Vilnius University*
Dovilė Lengvinaitė, *Department of General Physics and Spectroscopy, Faculty of Physics, Vilnius University*
Mažena Mackoit, *Center for Physical Sciences and Technology & EPS YM Vilnius*
Giedrius Pakalka, *Faculty of Physics, Vilnius University*
Povilas Račkauskas, *Faculty of Physics, Vilnius University*
Edvinas Skliutas, *Faculty of Physics, Vilnius University & SPIE Chapter of Vilnius University*
Kamilė Skorupskaitė, *Faculty of Physics, Vilnius University*
Inga Songailienė, *Institute of Biotechnology, Vilnius University*
Jurgita Strakšytė, *Faculty of Physics, Vilnius University*
Laura Šerkšnytė, *Faculty of Physics, Vilnius University & OSA Chapter of Vilnius University*
Andrius Vaitkūnas, *Center for Physical Sciences and Technology & Faculty of Physics, Vilnius University*

PROGRAMME COMMITTEE:

Ramūnas Aleksiejūnas, *Semiconductor Physics Department, Faculty of Physics, Vilnius University*
Jogundas Armaitis, *Institute of Theoretical Physics and Astronomy, Vilnius University*
Jevgenij Chmeliov, *Department of Theoretical Physics, Faculty of Physics, Vilnius University*
Justinas Čeponkus, *Department of General Physics and Spectroscopy, Faculty of Physics, Vilnius University*
Audrius Gegeckas, *Institute of Biotechnology, Vilnius University*
Vilmantas Gėgžna, *Institute of Applied Research, Vilnius University*
Mindaugas Karaliūnas, *Department of Optoelectronics, CPST & Baltic Institute of Advanced Technologies*
Mangirdas Malinauskas, *Laser Research Center, Vilnius University*
Rasa Pauliukaitė, *Department of NanoEngineering, Center for Physical Sciences and Technology*
Tomas Serevičius, *Institute of Applied Research, Vilnius University*
Kastytis Zubovas, *Fundamental Research Department, Center for Physical Sciences and Technology*

Faculty of Physics
Vilnius University
Saulėtekio Ave. 9-III, LT-10222 Vilnius
LITHUANIA

www.ff.vu.lt
www.openreadings.eu

ISSN 2029-4425

Contents

Contents 3
Conference programme 4
List of poster presentations 8
Invited speakers 21
Oral session 1 31
Astrophysics and Astronomy
Oral session 2 37
Theoretical Physics
Oral session 3 45
Chemistry and Chemical Physics
Oral session 4 53
Spectroscopy, Methods and Devices for Physical Diagnostics
Oral session 5 59
Laser Physics and Optical Technologies
Oral session 6 67
Material Science and Modern Technologies
Oral session 7 75
Functional Materials and Derivatives
Oral session 8 81
Semiconductor and Condensed Matter Physics
Oral session 9 89
Nanomaterials and Nanotechnology
Oral session 10 97
Biochemistry, Biophysics and Biotechnology
Oral session 11 103
Biology, Genetics and Biomedical Sciences
Poster session 1 111
Poster session 2 183
Poster session 3 255
Poster session 4 329
Author index 400

Conference programme

14 March, TUESDAY

09:00	**John Ellis**, King's College London, UK; CERN **BRIEF INTRODUCTION TO EVERYTHING**		**22**
	ORAL SESSION O1		
10:00	Eimantas Ledinauskas, Kastytis Zubovas **EFFECTS OF STOCHASTICITY IN THE EVOLUTION OF ISOLATED DWARF GALAXIES**	O1-1	**32**
10:15	Alexander Gorbatsievich, Stanislav Komarov, Alexander Tarasenko **TIME DELAY OF RADIATION FROM PULSAR IN A BINARY SYSTEM THAT MOVES IN FIELD OF SCHWARZSCHILD BLACK HOLE**	O1-2	**33**
10:30	Aidas Sadauskas, Kastytis Zubovas **ANALYSIS OF HYDRODYNAMIC MODEL OF ACTIVE GALACTIC NUCLEUS - INDUCED OUTFLOW**	O1-3	**34**
10:45	Azem Hysa, Marsida Klemo **INVARIANT MANIFOLDS AND SPACE MISSION DESIGN**	O1-4	**35**
11:00	COFFEE BREAK		
	ORAL SESSION O2		
11:15	Maciej Lewicki **STRONG INTERACTIONS INVESTIGATION METHODS AT NA61/SHINE EXPERIMENT**	O2-1	**38**
11:30	Michał Naskręt **SIGNALS OF THE ONSET OF DECONFINEMENT @ CERN**	O2-2	**39**
11:45	Kiryl Piasotski **SUPERSYMMETRY BASED ALGEBRAIC APPROACH TO THE SCHRODINGER EIGENVALUE PROBLEM**	O2-3	**40**
12:00	Rytis Kazakevičius, Julius Ruseckas **DIFFUSION IN HETEROGENEOUS MEDIA**	O2-4	**41**
12:15	Karolina Borek, Piotr Deuar **STATIONARY SOLUTIONS OF STOCHASTIC EQUATIONS WITH QUANTUM FLUCTUATIONS FOR ULTRACLOLD GASES**.	O2-5	**42**
12:30	Laima Busaite, Marcis Auzinsh, Andris Berzins, Ruvin Ferber, Florian Gahbauer, Reinis Lazda **OPTICALLY DETECTABLE MAGNETIC RESONANCE SIGNALS IN NITROGEN - VACANCY CENTRES IN DIAMOND NEAR GROUND STATE LEVEL CROSSING**	O2-6	**43**
12:45	BREAK		
13:15-15:00	**POSTER SESSION P1**		**111**
15:00	**Ben Feringa**, University of Groningen, Netherlands **MOLECULAR MOTORS AND SWITCHES**		**23**
16:00	COFFEE BREAK		
	ORAL SESSION O3		
16:15	Eglė Bašinskaitė, David Paleček, Petra Edlund, Emil Gustavsson, Sebastian Westenhoff, Donatas Zigmantas **CHARGE SEPARATION AND BAND SHIFT PHENOMENA IN REACTION CENTERS OF PURPLE BACTERIA**	O3-1	**46**
16:30	Sabina Brazevic, Michel Sliwa, Yoichi Kobayashi, Jiro Abe, Gotard Burdzinski **IMPACT OF ARYL-SUBSTITUENTS IN 3H-NAPHTHOPYRANS ON THE RATES OF PHOTOCHROMIC REACTION**	O3-2	**47**
16:45	Artiom Magomedov, Paul Gratia, Michael Saliba, Tadas Malinauskas, Maryte Daskeviciene, M. Khaja Nazeeruddin, Vytautas Getautis **NOVEL BRANCHED HOLE TRANSPORTING MATERIALS FOR PEROVSKITE SOLAR CELLS: SYNTHESIS AND PERFORMANCE**	O3-3	**48**
17:00	Krzysztof Żukowski, Joanna Kosman, Bernard Juskowiak **MODIFIED PEROXIDASE-MIMMICKING DNAZYMES AND THEIR POTENCIAL USE AS BIOSENSORS**	O3-4	**49**
17:15	Marina Roshchina, Andrei Ivanets, Vladimir Prozorovich, Elena Petrova, Vladimir Pankov **SORPTION PERFOMANCES OF MgFe2O4 SPINEL TOWARDS Mn2+, Cu2+, Co2+, Ni2+ IONS**	O3-5	**50**
17:30	Andrius Merkys, Antanas Vaitkus, Saulius Gražulis **SPOTTING THE UNUSUAL GEOMETRY IN CRYSTAL STRUCTURES**	O3-6	**51**
17:45	BREAK		
18:00	**OSA WELCOME EVENING** **"Career in Science" Discussion** with Special Guests		

15 March, WEDNESDAY

09:00	**Philip Russell**, Max Planck Institute of Light, Germany **LIGHT-MATTER INTERACTIONS IN PHOTONIC CRYSTAL FIBRES**		**24**
	ORAL SESSION O4		
10:00	Marcin Witkowski, Agata Królikowska, Janusz Cukras, Jacek Szczytko, Jolanta Bukowska **HEAVY METAL IONS SENSING BY SURFACE-ENHANCED RAMAN SCATTERING SPECTROSCOPY USING HYBRID MAGNETIC Fe3O4/Ag NANOPARTICLES**	O4-1	**54**
10:15	Raminta Mazėtytė, Urtė Bubnienė, Arūnas Ramanavičius, Renata Karpič **pH INFLUENCE ON SPECTROSCOPIC PROPERTIES OF GLUCOSE OXIDASE**	O4-2	**55**
10:30	Nikodem Stolarczyk, Piotr Wcisło **SHAPES OF MOLECULAR OPTICAL RESONANCES – TOWARDS A GLOBAL SOLUTION OF THE TRANSPORT-RELAXATION EQUATION**	O4-3	**56**
10:45	Sandeep Gawali, Luca Leggio, Miguel Sanchez, Sergio Rodriguez, Daniel Gallego, Horacio Lamela **BEAM COMBINATION OF DIODE LASERS FOR OPTO-ACOUSTIC APPLICATIONS**	O4-4	**57**
11:00	COFFEE BREAK		
	ORAL SESSION O5		
11:15	Natalia Kokareva, Kirill Safronov, Dmitrii Gulkin, Ksenia Abrashitova, Vladimir Bessonov, Andrey Fedyanin **FABRICATION OF PLANAR OPTICAL WAVEGUIDES BY TWO-PHOTON LITHOGRAPHY TO CONTROL BLOCH SURFACE WAVES IN PHOTONIC CRYSTALS**	O5-1	**60**
11:30	Iaroslav Gnilitskyi, Alexandr S. Fedotov, Alexandr K. Fedotov, Leonardo Orazi **SUPERHYDROPHILIC PROPERTIES OF SILICON DRIVEN BY FEMTOSECOND PULSES**	O5-2	**61**
11:45	Sergey Nazarov, Alexandra Trofimova, Elen Tolstik, Rainer Heintzmann, Uladzimir Mahilny, Alexei Tolstik **VOLUME HOLOGRAPHIC ELEMENTS ON THE BASIS OF PHENANTHRENEQUINONE – POLYMETHYLMETHACRYLATE COMPOSITE FOR MICROSCOPICAL APPLICATIONS**	O5-3	**62**
12:00	Karolis Adomavičius, Ernestas Žeimys, Benas Makauskas **PROPERTIES OF TERAHERTZ RADIATION GENERATED IN AIR BY TUNABLE FEMTOSECOND LASER PULSES**	O5-4	**63**
12:15	Tomas Kontrimas, Sergejus Orlovas **FOCAL LINE ENGINEERING OF VECTOR OPTICAL BEAMS WITH PARABOLIC SYMMETRY CROSS-SECTION**	O5-5	**64**
12:30	Vitalis Vosylius, Sergejus Orlovas **"OPTICAL KNIVES" ENGINEERING USING VECTOR MATHIEU BEAMS**	O5-6	**65**
12:45	BREAK		
13:15-15:00	**POSTER SESSION P2**		**183**
15:00	**Xi-Cheng Zhang**, University of Rochester, USA **THz: IMAGING BEYOND LIGHT**		**25**
16:00	COFFEE BREAK		
	ORAL SESSION O6		
16:15	Vytautas Jakštas, Ignas Grigelionis, Vytautas Janonis, Irmantas Kašalynas **TERAHERTZ EMISSION FROM AlGaN/GaN STRUCTURES WITH GRATING-TYPE ELECTRODES**	O6-1	**68**
16:30	Augustas Vaitkevičius, Etiennette Auffray, Mikhail Korjik, Marco Lucchini, Saulius Nargelas, Oleg Sidletskiy, Yevgeny Tretsiak, Gintautas Tamulaitis **FREE CARRIER ABSORPTION FOR CHARACTERIZATION OF FAST CARRIER DYNAMICS IN SCINTILLATORS**	O6-2	**69**
16:45	Mihirsinh Chauhan, Jaishree Vyas, Vishwa Bhatt, Manoj Kumar, Khushdeep Kaur, Vaibhav Rao, Brijesh Tripathi **ROLE OF DOPED AND UNDOPED ELECTRON TRANSPORT LAYER IN VERTICALLY STACKED PHOSPHORESCENT MULTILAYER ORGANIC LIGHT EMITTING TRANSISTOR**	O6-3	**70**
17:00	Žygimantas Vosylius, Algirdas Novičkovas, Vincas Tamošiūnas **NOVEL DESIGN OF SOLAR SIMULATOR EMPLOYING HIGH POWER LIGHT EMITTING DIODES**	O6-4	**71**
17:15	Henrikas Dapkus, Akvilė Zabiliūtė-Karaliūnė, Pranciškus Vitta **DEVELOPMENT AND CHARACTERIZATION OF PHOSPHOR CONVERTED LED LAMPS FOR NICHE APPLICATIONS**	O6-5	**72**
17:30	Gleb Gribovskii **THREE-DIMENSIONAL STRESS-STRAIN STATE AND VOLUMETRIC DAMAGEABILITY OF TIRE–ASPHALT CONTACT PAIR**	O6-6	**73**
19:00	Special Breakthrough Lecture on **GRAVITATIONAL WAVES** live with **Eugenio Coccia** Gran Sasso Science Institute, Italy		**26**

16 March, THURSDAY

09:00	**Michael Grätzel**, École Polytechnique Fédérale de Lausanne, Switzerland **ENERGY BEYOND OIL**		**27**
	ORAL SESSION O7		
10:00	Kasparas Rakstys, Sanghyun Paek, Peng Gao, Tomasz Marszalek, Kristijonas Genevicius, Vygintas Jankauskas, Wojciech Pisula, Mohammad Khaja Nazeeruddin **FACE-ON ORIENTED DOPANT-FREE HOLE TRANSPORTING MATERIAL FOR 19% PEROVSKITE SOLAR CELLS**	O7-1	**76**
10:15	Paulina E. Kruk, Tomasz K. Pietrzak, Jerzy E. Garbarczyk **NANOCRYSTALLIZATION OF Na3V2(PO4)2F3 GLASS**	O7-2	**77**
10:30	Julija Grigorjevaitė, Arturas Katelnikovas **HIGHLY EFFICIENT RARE-EARTH DOPPED RED-EMITTING PHOSPHORS**	O7-3	**78**
10:45	Paulius Baronas, Gediminas Kreiza, Patrik Scajev, Vladislavas Čerkasovas, Edvinas Radiūnas, Povilas Adomėnas, Ona Adomėnienė, Karolis Kazlauskas, Jean-Charles Ribierre, Chihaya Adachi, Saulius Juršėnas **BIFLUORENE SINGLE CRYSTALS FOR ORGANIC LASERS**	O7-4	**79**
11:00	COFFEE BREAK		
	ORAL SESSION O8		
11:15	Mantas Dmukauskas, Arūnas Kadys, Tadas Malinauskas, Tomas Grinys, Ignas Reklaitis, Kazimieras Badokas, Martynas Skapas, Roland Tomašiūnas, Darius Dobrovolskas, Sandra Stanionytė, Ines Pietzonka, Martin Strassburg, Hans-Jürgen Lugauer **INFLUENCE OF METALORGANIC PRECURSORS FLOW INTERRUPTION TIMING ON GREEN InGaN MULTIPLE QUANTUM WELLS**	O8-1	**82**
11:30	Evelina Pozingytė, Renata Butkutė, Bronislovas Čechavičius, Martynas Skapas, Algirdas Selskis, Gediminas Niaura, Arūnas Krotkus **TEMPERATURE-DEPENDENT PHOTOLUMINESCENCE STUDY OF THERMALLY ANNEALED GaAsBi/AlAs QUANTUM WELLS**	O8-2	**83**
11:45	Ieva Beleckaitė, Ramūnas Adomavičius **DETERMINATION OF TERAHERTZ RADIATING ELECTRIC DIPOLE ORIENTATION BY TERAHERTZ EMISSION MEASUREMENTS**	O8-3	**84**
12:00	Jakub Polaczynski, Andrzej Witowski, Michal Szot, Monika Zieba, Tomasz Story **OPTICAL PROPERTIES OF EPITAXIAL Sn(1-x)Mn(x)Te LAYERS STUDIED BY FOURIERTRANSFORM INFRARED SPECTROSCOPY**	O8-4	**85**
12:15	Alexander Fedotov, Sergey Perevoznikov, Aliaksei Pashkevich **THE EVALUATION OF THE CHARGE CARRIERS PARAMETERS AND FERMI LEVEL IN MULTICARRIER BI-BASED ALLOYS**	O8-5	**86**
12:30	Bartłomiej Seredyński, Piotr Starzyk, Wojciech Pacuski **TOWARDS TRANSMISSION STUDIES OF POLARITONS: II-VI SEMICONDUCTOR MICROCAVITIES LIFT-OFF**	O8-6	**87**
12:45	BREAK		
13:15-15:00	**POSTER SESSION P3**		**255**
15:00	**Naomi Halas**, Rice University, USA **LIGHT-HARVESTING NANOPARTICLES, CANCER THERAPY AND SOLAR STEAM GENERATION**		**28**
16:00	COFFEE BREAK		
	ORAL SESSION O9		
16:15	Anna Matsukovich, Elena Shabunya-Klyachkovskaya, Olga Kulakovich, Mikhail Smirnov, Aleksey Perepelitsa, Sergey Gaponenko **THE RAMAN SCATTERING ENHANCEMENT OF CdS QUANTUM DOTS**	O9-1	**90**
16:30	Jelena Kosmaca, Liga Jasulaneca, Raimonds Meija, Jana Andzane, Donats Erts **CHARACTERIZATION OF Bi2Se3 NANORIBBONS BY IN-SITU SCANNING ELECTRON MICROSCOPY**	O9-2	**91**
16:45	Gleb Gorokhov, Darya Meisak, Dzmitry Bychanok, Silvia Bistarelli, Stefano Bellucci **RANDOM CIRCUIT METHOD FOR MWCNT-NH2 COMPOSITES MODELING**	O9-3	**92**
17:00	Grzegorz Kolodziej, Michal M. Wojcik **TEMPERATURE TUNING OF LOCALISED SURFACE PLASMON RESONANCE IN GOLD NANOPARTICLES BASED ON ANTI-GALVANIC REDUCTION**	O9-4	**93**
17:15	Nikolai Mitetelo, Sergey Svyakhovskiy, Alexandra Gartman, Anton Maydykovskiy **OPTICAL RESPONSE OF COMPOSITE PLASMONIC STRUCTURES**	O9-5	**94**
17:30	Paulina Grzaczkowska, Jakub Mikulski, Przemyslaw Kowalik, Tomasz Wojciechowski, Krzysztof Fronc, Rafal Rudniewski, Roman Minikayev, Mariusz Lapinski, Jaroslaw Rybusinski, Anita Gardias, Jacek Szczytko, Danek Elbaum, Bozena Sikora **PREPARATION OF MAGNETIC Fe3O4 NANOPARTICLES WITH POTENTIAL APPLICATION IN BIOMEDICINE**	O9-6	**95**
17:45	BREAK		
18:00	**VTEX Workshop on Scientific Publishing**, powered by SPIE		

17 March, FRIDAY

09:00	**Robin Lovell Badge**, Francis Crick Institute, UK **GENE EDITING: NEW BRAVE WORLD**		**29**
	ORAL SESSION O10		
10:00	Monika Glemžaitė, Sandra Baronaitė, Aistė Zentelytė, Jūratė Savickienė, Natalija Krasovskaja, Audronė Arlauskienė, Rūta Navakauskienė **HUMAN AMNIOTIC FLUID-DERIVED MESENCHYMAL STEM CELLS: FEATURES AND DIFFERENTIATION POTENTIAL**	O10-1	**98**
10:15	Tatiana Kochetkova, Yuliya Kunitskaya, Elizaveta Kavalenka, Elena Golubeva, Pavel Bulai **THE EFFECT OF LONG-TERM ELECTRICAL STIMULATION ON MEMBRANE POTENTIAL OF C6 RAT GLIOMA CELLS**	O10-2	**99**
10:30	Asta Luciunaite, Indre Dalgediene, Aurelija Zvirbliene **ACTIVATION OF MACROPHAGES WITH VARIOUS STRUCTURE OLIGOMERS AND THEIR IMMUNE COMPLEXES**	O10-3	**100**
10:45	Irmantas Mogila, Miglė Kazlauskienė, Gintautas Tamulaitis, Virginijus Šikšnys **DELETION ANALYSIS OF MULTISUBUNIT CRISPR-CAS EFFECTOR COMPLEX**	O10-4	**101**
11:00	COFFEE BREAK		
	ORAL SESSION O11		
11:15	Eglė Maksimovaitė, Daniel Herring, Marc Goodfellow **MODELLING RESPONSES TO VISUAL STIMULI IN ALZHEIMER'S DISEASE**	O11-1	**104**
11:30	Vytautas Žėkas, Reda Matuzevičienė, Dovilė Karčiauskaitė, Asta Mažeikienė, Neringa Burokienė, Mantas Radzevičius, Aušra Janulionienė, Zita Aušrelė Kučinskienė **ATHEROSCLEROSIS RISK FACTORS INFLUENCE ENDOTHELIAL MICROVESICLE COUNT IN PERIPHERAL BLOOD**	O11-2	**105**
11:45	Ilya Yakavets, Igor Yankovsky, Henri-Pierre Lassalle, Lina Bezdetnaya, Vladimir Zorin **mTHPC NANODELIVERY SYSTEM BASED ON CYCLODEXTRINS**	O11-3	**106**
12:00	Evelina Voronovič, Greta Jarockytė, Artiom Skripka, Vitalijus Karabanovas, Ričardas Rotomskis **TOXICITY AND ACCUMULATION OF UPCONVERTING NANOPARTICLES IN CANCER CELLS**	O11-4	**107**
12:15	Nadzeya Nazarova, Yuri Avlasevich, Stanislav Baluschev, Katharina Landfester **ANNIHILATION UPCONVERSION AS AN ALL-OPTICAL TEMPERATURE SENSING TOOL FOR LIFE-SCIENCE**	O11-5	**108**
12:30	Jekaterina Latynis, Vitaly Kocherbitov, Justas Barauskas, Gediminas Niaura **HYDRATION OF CYTOCHROME C STUDIED BY VIBRATIONAL SPECTROSCOPY AND CALORIMETRY**	O11-6	**109**
12:45	BREAK		
13:15-15:00	**POSTER SESSION P4**		**329**
15:00	**Frederik Claeyssens**, University of Sheffield, UK **LIGHT-BASED BIOMATERIALS STRUCTURING FOR TISSUE ENGINEERING**		**30**
19:00	**CONFERENCE PARTY and AWARD CEREMONY** powered by SPIE		

List of poster presentations

14 March, TUESDAY

13:15-15:00 **POSTER SESSION P1**

Monika Stangret, Anna Bartkiewicz **PROPER MOTION STUDIES IN G23.657-0.127**	P1-01	112
Mateusz Narożnik **THE MODEL OF ORBITAL MOTION AROUND SPHERICAL AND NON-SPHERICAL BODIES**	P1-02	113
Volha Siliuk, Leonid Katkovsky **CROSS-CALIBRATION OF MULTISPECTRAL IMAGES OF BELARUSSIAN SATELLITE AND OTHERS AEROSPACE SYSTEM WITH ATMOSPHERIC CORRECTION**	P1-03	114
Vytautas Dūdėnas, Thomas Gajdosik **USING TECHNIQUES OF ALGEBRAIC RENORMALIZATION FOR THE TWO HIGGS DOUBLET MODEL WITH ONE HEAVY NEUTRINO**	P1-04	115
Anton Kuncinas, Thomas Gajdosik **ANALYSIS OF THE TWO HIGGS DOUBLET MODEL: IN SEARCH OF THE VALID CP-CONSERVING POTENTIAL**	P1-05	116
Augustinas Stepšys, Saulius Mickevičius, Darius Germanas, Ramutis Kazys Kalinauskas **CONSTRUCTION OF ANTISYMMETRIC BASIS STATES FOR SIX BODY SYSTEMS IN TRANSLATIONALLY INVARIANT BASIS**	P1-06	117
Mantas Račiūnas, Egidijus Anisimovas, Christoph Sträter, André Eckardt, Ian B. Spielman, Gediminas Juzeliūnas **SEMI-SYNTHETIC ZIGZAG OPTICAL LATTICE FOR ULTRACOLD ATOMS**	P1-07	118
Ulada Vysotskaya, Irina Shapochkina **DIFFUSION OF A BROWNIAN PARTICLE IN A PERIODIC POTENTIAL WITH A FINITE LIFE-TIME**	P1-08	119
Pok Man Lo, Michał Marczenko, Krzysztof Redlich, Chihiro Sasaki **ADDITIONAL STRANGE RESONANCES FROM LATTICE QCD**	P1-09	120
Piotr Gładysz, Karolina Słowik **ASYMMETRIC QUANTUM SYSTEMS IN STRONG ELECTROMAGNETIC FIELDS AS TERAHERTZ RADIATION SOURCES**	P1-10	121
Mažena Mackoit, Audrius Alkauskas **OPTICAL PROPERTIES OF BORON VACANCIES AND BORON VACANCY COMPLEXES IN HEXAGONAL BORON NITRIDE**	P1-11	122
Gintaras Kerevičius **IDENTIFICATION OF THE ENERGY SPECTRUM OF AUTOIONIZING STATES OF STRONTIUM EXCITED BY ELECTRON IMPACT**	P1-12	123
Gleb Bogomol, Janek Laanearu **WAVE MODELING USING SMOOTHED PARTICLE HYDRODYNAMICS**	P1-13	124
Vytautas Bubilaitis, Olga Rancova, Darius Abramavičius **DICHOTOMOUS MODEL FOR SYSTEM-ENVIRONMENT INTERACTION IN PHOTOSYNTHETIC COMPLEX**	P1-14	125
Dovilė Lengvinaite, Sonja Grubisic, Kęstutis Aidas, Ilija Cvijetic, Aatto Laaksonen, Francesca Mocci **QM/MM PROTOCOL FOR STUDYING INTERACTIONS IN IONIC LIQUIDS: CHARGES OPTIMIZATION**	P1-15	126
Monika Kubek, Karolina Slowik **NANOANTENNAS FOR INDUCED CIRCULAR DICHROISM**	P1-16	127
Yaroslav Zubritsky, Alex Malevich, Elena Shalamberidze, George Pitsevich, Valdas Sablinskas **THEORETICAL STUDY OF THE ROVIBRATIONAL SPECTRUM OF WATER MOLECULE TRAPPED IN ARGON MATRIX IN THE AND SPECTRAL REGIONS**	P1-17	128
Artem Sosnovsky, George Pitsevich, Ekaterina Kozlovskaya, Valdas Sablinskas **ANHARMONIC CALCULATIONS OF THE STRUCTURE AND IR SPECTRA OF THE WATER CLUSTERS IN THE VACUUM, ARGON AND WATER MEDIUM**	P1-18	129
Anton Paltsev, Alex Malevich, George Pitsevich, Ekaterina Kozlovskaya, Vitas Balevicius **DFT STUDY OF THE IR SPECTRA AND STRUCTURE OF THE H+5O2+X COMPLEXIS (X=Ar,Ne,He) IN HARMONIC AND ANHARMONIC APPROXIMATIONS**	P1-19	130
Darya Meniailava, Maksim Shundalau **POTENTIAL ENERGY SURFACE OF THE GROUND TRIPLET STATE OF UO3 MOLECULE**	P1-20	131
Sonata Kvedaravičiūtė, Andrés Cedillo, Kęstutis Aidas **QUANTUM CHEMICAL MODELING OF AQUEOUS ACIDITIES FOR 2-, 3- AND 4-PHENACYLPYRIDINES**	P1-21	132
Alex Kozhanovsky, George Pitsevich, Ekaterina Kozlovskaya, Vitas Balevicius **THE ANHARMONIC COUPLINGS OF THE SHARED PROTON STRETCHING VIBRATION IN THE PROTONATED WATER DIMER: MP4 STUDY**	P1-22	133
Milda Koreivaitė, Greta Majauskaitė, Kęstutis Aidas **QUANTUM CHEMICAL PREDICTIONS OF AQUEOUS ACIDITIES FOR SECONDARY BENZENESULFONAMIDES**	P1-23	134
Ivan Reznikov **THE APPLICATION OF NEURAL NETWORKS FOR ACTIVATED CARBON SYNTHESIS**	P1-24	135

Antanas Vaitkus, Andrius Merkys, Saulius Gražulis **AUTOMATING THE DERIVATION OF CHEMICAL INFORMATION FROM CRYSTALLOGRAPHIC DATA**	P1-25	136
Marta Pakiet, Iwona Kowalczyk, Bogumił Brycki **AGGREGATION AND SPECTROSCOPIC PROPERTIES OF GEMINI SURFACTANTS WITH ESTER GROUPS**	P1-26	137
Maksim Kutuzau, Dzmitry Kotsikau, Vladimir Pankov **LOW-TEMPERATURE SYNTHESIS AND MAGNETIC PROPERTIS OF NANOSIZED Mn-FERRITES**	P1-27	138
Róża Hamera-Fałdyga, Małgorzata Celeda, Grzegorz Mlostoń **UNEXPECTED COURSE OF REACTIONS OF HETARYL AND FERROCENYL SUBSTITUTED SECONDARY METHANOLS WITH LAWESSON'S REAGENT (L.R.)**	P1-28	139
Gábor Zoltán Elek, Victor Borovkov, Margus Lopp, Dzmitry Kananovich **ENANTIOSELECTIVE SYNTHESIS OF EPOXYKETONES VIA AEROBIC OXIDATION OF CYCLOPROPANOLS**	P1-29	140
Robert Ambroziak **MAGNETIC NANOPARTICLES FOR SHINERS MEASUREMENTS**	P1-30	141
Austėja Bukauskytė, Alytis Gruodis, Renata Karpič **FLUORESCENCE QUANTUM YIELD OF PERYLENEDIIMIDE COMPOUNDS**	P1-31	142
Tadas Cepulis, Eigirdas Skuodis, Dalius Gudeika **SYNTHESIS AND PROPERTIES OF PHENOTHIAZINE-BASED DERIVATIVES**	P1-32	143
Giedrė Gaidamavičienė, Artūras Žalga, Edvardas Kazakevičius **AQUEOUS SOL–GEL SYNTHESIS AND THERMOANALYTICAL STUDY OF La1.9Ca0.1Mo2O8.95**	P1-33	144
Paulina Grzelak, Grzegorz Mlostoń **THIA-DIELS-ALDER REACTIONS OF DIHETARYL THIOKETONES WITH 2,4-HEXADIENE; A RARE CASE OF STEPWISE, DIRADICAL [4+2]-CYCLOADDITIONS**	P1-34	145
Dainora Jankunaite, Dalius Gudeika **SYNTHESIS AND PROPERTIES OF DONOR-ACCEPTOR CARBAZOLE-BASED DERIVATIVES**	P1-35	146
Vytenis Jočys, Valdemaras Aleksa, Jonas Kausteklis **RAMAN STUDY OF WATER STRUCTURES IN 1-BUTYL-3-METHYLIMIDAZOLIUM BROMIDE AND NITRATE AND WATER MIXTURES**	P1-36	147
Mantas Jonušis, Indrė Misiūnaitė, Girius Kisielius, Inga Čikotienė **SYNTHESIS OF 3,5-DIARYL-2-SUBSTITUTED-THIOPHENES**	P1-37	148
Karolis Karpavičius, Jonas Bucevičius, Maris Turks, Tadas Bucevičius, Paulius Baronas, Saulius Juršėnas, Sigitas Tumkevičius **SYNTHESIS AND PHOTOPHYSICAL PROPERTIES OF (1,2,3-TRIAZOL-4-YL)-7-DEAZAPURINES AND PURINES**	P1-38	149
Urszula Kiełczewska, Agnieszka Wojtkielewicz, Paulina Uścinowicz, Leszek Siergiejczyk, Artur Radkiewicz, Jacek W. Morzycki **SYNTHESIS OF NEW STEROIDAL PYRIMIDOBENZIMIDAZOLE DERIVATIVES**	P1-39	150
Monika Kirsnyte, Arunas Stirke, Algimantas Janarauskas, Roxana-Mihaela Apetrei **COMPARISON OF BIOGENIC AND BY MICROEMULSION POLYMERIZED POLYPYRROLE MICROSPHERES**	P1-40	151
Ramūnas Levinas, Natalija Tsyntsaru, Henrikas Cesiulis **ELECTRODEPOSITION AND STUDY OF MOLYBDENUM SULFIDE FILMS**	P1-41	152
Oleksandra Yu. Mariichak, Vyacheslav N. Baumer, Georgii M. Rozantsev, Serhii V. Radio **LN-CONTAINING HETEROPOLY TUNGSTATES WITH PEACOCK–WEAKLEY ANION: SYNTHESIS AND CRYSTAL STRUCTURE OF ISOSTRUCTURAL SALTS Na9[Ln(W5O18)2]·35H2O (Ln=Gd, Er)**	P1-42	153
Lyubov Makarova, Yuliya Sergienko, Yuliya Ivanova, Iosyp Opeida, Svitlana Zhiltsova **OXIDATIVE DESTRUCTION OF METHYL VIOLET AND METHYLENE BLUE DYES BY FENTON REACTION**	P1-43	154
Oleksandra Yu. Mariichak, Tetiana O. Arzamastseva, Illia V. Kapitanov, Yevgen Karpichev, Georgii M. Rozantsev, Serhii V. Radio **CE-CONTAINING POLYOXOTUNGSTATES: SYNTHESIS, FTIR SPECTROSCOPY, AND SURFACE MICROMORPHOLOGY**	P1-44	155
Iwona Misztalewska-Turkowicz, Agnieszka Z. Wilczewska **SYNTHESIS AND COMPLEXING ACTIVITY OF NEW POLYMERIZABLE N-HETEROCYCLIC CARBENE PRECURSORS**	P1-45	156
Karolis Norvaisa, Dalius Gudeika **SYNTHESIS AND INVESTIGATION OF PHENYL CARBAZOLEDERIVATIVES CONTAINING INDOLE UNITS**	P1-46	157
Edvinas Orentas, Algirdas Neniškis, Dovilė Anderson, Tomas Javorskis **HYDROGEN-BONDED SUPRAMOLECULAR NANOTUBES FROM SMALL BUILDING BLOCKS**	P1-47	158
Lina Pavasarytė, Vytautas Klimavičius, Vytautas Balevičius, Aivaras Kareiva **INVESTIGATION OF STRUCTURAL PROPERTIES OF Eu3+-DOPED Y3-xSmxAl3O12 GARNETS**	P1-48	159
Karolis Petrauskas, Svajus Asadauskas **RECYCLING OF RUBBER BY SUPPRESSION OF MOLECULAR SELF-HEALING PROCESS**	P1-49	160
Jurate Petroniene, Inga Morkvenaite-Vilkonciene, Almira Ramanaviciene, Ausra Valiuniene, Arunas Ramanavicius **SCANNING ELECTROCHEMICAL MICROSCOPY COMBINED WITH FAST FOURIER TRANSFORM IMPEDANCE SPECTROMETER FOR LOCAL ELECTROCHEMICAL IMPEDANCE MEASUREMENTS**	P1-50	161
Arūnas Pulmanas, Filipas Ambrulevičius **DRAG FORCE AND QUARTZ RESONATOR ADMITTANCE STUDY OF AQUEOUS SOLUTION LAYER PROPERTIES AT POLYMER COATED ELECTRODE SURFACE**	P1-51	162
Eva Raudonyte-Svirbutaviciene, Alexandra Neagu, Cheuk-Wai Tai, Arturas Katelnikovas **LIGHT DRIVEN SYNTHESIS OF NANOSTRUCTURES**	P1-52	163

Barbara Seroka, Jacek W. Morzycki, Rafał R. Siciński, Zenon Łotowski **SYNTHESIS OF STEROID VIC-DIAMINO LIGANDS USING STRECKER REACTION**	P1-53	164
Alina Slepets, Tetiana Voitenko, Sergiy A. Nedilko, Sergiy G. Nedilko **SYNTHESIS AND PROPERTIES OF THE Ca1-2xCe2xMo1-xGexO4 (0 ≤ x≤ 0.2) CRYSTALS**	P1-54	165
Solomakha Tatsiana, Tratsiak Yauhen **THE SYNTHESIS CONDITIONS EFFECT ON LUMINESCENT PROPERTIES OF BaI2:Eu2+,3+ FINE POWDERS**	P1-55	166
Joanna Stocka **FTIR MATRIX ISOLATION AND CPMD METHODS IN CONFORMATIONAL ANALYSIS OF THF MOLECULE**	P1-56	167
Marija Špandyreva, Ieva Matulaitienė, Ilja Ignatjev, Zenonas Kuodis, Gediminas Niaura **ELECTROCHEMICAL SERS STUDY OF PHENYL-TERMINATED SELF-ASSEMBLED MONOLAYERS WITH AMIDE GROUP**	P1-57	168
Justina Šulgaitė, Rytis Vincentas Urbonas, Inga Čikotienė **DIRECTED HIGH-THROUGHPUT SCREENING OF AQUEOUS-PHASE SONOGASHIRA COUPLING REACTION FOR SYNTHESIS OF BIOTIN-11-dNTPs**	P1-58	169
Nikita Tsimbrovsky, George Pitsevich, Ekaterina Kozlovskaya, Vitas Balevicius **DETERMINATION OF THE DEGREE OF PES ANHARMONICITY**	P1-59	170
Aurelija Urbanaitė, Inga Čikotienė **SYNTHESIS OF POLYSUBSTITUTED PYRROLES VIA TANDEM 1,3-ADDITION-5-ENDO-DIG CYCLIZATION OF 1-(1-ALKYNYL)CYCLOPROPYL IMINES**	P1-60	171
Modestas Vainoris, Henrikas Cesiulis, Natalia Tsyntsaru **ELECTRODEPOSITED COBALT FOAMS AS CATALYSTS FOR WATER ELECTROLYSIS**	P1-61	172
Adrián Vicent Claramunt, Algimantas Paškevičius, Jurgita Švedienė, Eglė Gudeliūnaitė, Silvija Kiverytė, Roberta Petrauskaitė, Laimonas Griškevičius, Audrius Zolumskis, Evaldas Naujalis **THERMAL DESORPTION METHODOLOGY FOR VOLATILE ORGANIC COMPOUNDS (VOC'S) IDENTIFICATION: POSSIBLE APLICATION IN INVASIVE FUNGAL INFECTIONS**	P1-62	173
Audrius Zolumskis, Audrius Sadaunykas, Audrius Markevičius **STAINLESS STEEL CAPILLARY COLUMNS FOR GAS CHROMATOGRAPHY. PREPARATION AND USAGE**	P1-63	174
Gediminas Braziulis, Giedrė Gaidamavičienė, Artūras Žalga **SOL–GEL SYNTHESIS, CRYSTAL STRUCTURE, SURFACE MORPHOLOGY, AND FT-IR SPECTROSCOPICAL INVESTIGATION OF ALKALINE-EARTH METAL MOLYBDATES**	P1-64	175
Hamid Reza Hamedi, Gediminas Juzeliunas **PULSE PROPAGATION FOR CLOSED LOOP QUANTUM SYSTEMS**	P1-65	176
Pavel Labatsevich **SPONTANEOUS EMISSION FACTOR INFLUENCE ON OUTPUT PARAMETERS OF THE VERTICAL-CAVITY SURFACE-EMITTING LASERS**	P1-66	177
Vitali Ghoghoberidze, David Kakulia, Akaki Lomia, Avto Tavkhelidze **DENSITY OF QUANTUM STATES IN PERIODICAL STRUCTURES**	P1-67	178
Klaidas Grigaravicius, Tomas Vaitkunas, Audrius Jutas **ON THE QUESTION OF POISSON'S RATIO IN MULTI-SCALE MODELLING OF BCC LATTICES**	P1-68	179
Linas Petkevičius, Romas Baronas **MODELLING MICRO-REACTOR WITH AN NERNST LAYER**	P1-69	180
Krystsina Usheva, Semen Kuten, Arkadiy Khruschinsky, Leonid Babichev **FEATURES OF XS GENERATION FOR RADIAL REFLECTOR OF THE VVER REACTOR IN SERPENT MONTE CARLO CODE**	P1-70	181
Elena Levchuk, Yury Shkliaryk, Olga Lavrova **EFFECT OF CONTROLLING GATE GEOMETRY ON DONOR QUBITSFUNCTIONALITY**	P1-71	182

15 March, WEDNESDAY

13:15-15:00 **POSTER SESSION P2**

Dainius Kučinskas, Rimantas Budriūnas, Arūnas Varanavičius **HIGH-ENERGY CONTINUUM GENERATION IN AN ARRAY OF THIN PLATES PUMPED BY TUNABLE FEMTOSECOND IR PULSES**	P2-01	184
Miglė Kuliešaitė, Julius Vengelis **INVESTIGATION OF SUPERCONTINUUM GENERATION IN PHOTONIC CRYSTAL FIBER USING CHIRPED FEMTOSECOND PULSES**	P2-02	185
Julius Lukošiūnas, Rosvaldas Šuminas, Nail Garejev, Gintaras Tamošauskas, Audrius Dubietis **MULTI-OCTAVE SPANNING NONLINEAR INTERACTIONS INDUCED BY FEMTOSECOND FILAMENTATION IN POLYCRYSTALLINE ZNSE**	P2-03	186
Augustinas Petrulenas, Nortautas Ulevicius, Aleksej M. Rodin **SIXTH HARMONIC GENERATION IN BBO CRYSTAL AT 224 NM WITH HIGH REPETITION RATE PICOSECOND LASER**	P2-04	187
Laurynas Veselis, Tadas Bartulevičius, Aleksej Rodin, Nerijus Rusteika **COMPACT Yb:YAG CPA SYSTEM WITH ALL-IN-FIBER SEED SOURCE**	P2-05	188
Eimantas Zopelis, Aleksej M. Rodin **HIGH GAIN Yb:YAG CHIRPED PULSE AMPLIFIER PUMPED WITH HIGH BRIGHTNESS LASER DIODES**	P2-06	189
Justas Girskis **RESEARCH OF CERAMIC Yb:YAG LASER GENERATION AND SPECIFICATIONS**	P2-07	190
Sergey Grigoryev **RADIATION DYNAMICS OF SPACE-DISTRIBUTED MODEL SOLID-STATE LASER WITH HIGH DEFINITION**	P2-08	191
Domas Kudarauskas **OPTICAL PARAMETRIC AMPLIFICATION EXITED BY SPATIALLY INCOHERENT CONICAL RADIATION**	P2-09	192
Saulius Frankinas, Tadas Bartulevičius, Andrejus Michailovas, Nerijus Rusteika **INVESTIGATION OF PASSIVELY MODE-LOCKED FIBER YB DOPED FEMTOSECOND OSCILLATOR FOR GENERATION OF PARABOLIC PULSES IN FIBER AMPLIFIER**	P2-10	193
Tadas Bartulevičius, Andrejus Michailovas, Nerijus Rusteika **PULSE SHAPING IN Yb DOPED FIBER CHIRPED PULSE AMPLIFICATION SYSTEM USING FIBER BRAGG GRATING FILTER**	P2-11	194
Yuriy Pilgun **PLANE-WAVE EXPANSION MODELLING OF LASER BEAM PROPAGATION IN GYROTROPIC MEDIUM**	P2-12	195
Alfonsas Juršėnas, Sergejus Orlovas **OPTICAL FOCAL LINE ENGINEERING METHODS USING VECTOR BESSEL BEAMS**	P2-13	196
Sergej Orlov, Paulius Slevas, Valerijus Smilgevicius **CONVERSION OF ORBITAL-TO-SPIN ANGULAR MOMENTUM OF LIGHT UNDER FOCUSING: THEORETICAL ANALYSIS AND EXPERIMENTAL VERIFICATION**	P2-14	197
Ada Gajauskaite, Sergejus Orlovas **ANALYSIS OF PULSED VECTOR BESSEL BEAMS**	P2-15	198
Pavel Gotovski, Sergejus Orlovas **BESSEL BEAMS AND FOCAL LINE ENGINEERING FOR LARGE SCALE PHOTONIC THRUSTERS**	P2-16	199
Karolina Liebert, Martyna Rachon, Jaroslaw Suszek, Artur Sobczyk, Jaroslaw Bomba, Maciej Sypek **PROPERTIES AND APPLICATION OF SPIRAL STRUCTURE IN THz RANGE**	P2-17	200
Martyna Rachon, Karolina Liebert, Jaroslaw Suszek, Maciej Sypek **SUB-WAVELENGTH CODING TECHNIQUE FOR THz DIFFRACTIVE LENS**	P2-18	201
Mindaugas Juodėnas, Tomas Tamulevičius, Linas Šimatonis, Sigitas Tamulevičius **INVESTIGATION OF FEMTOSECOND LASER INDUCED CHEMICAL ETCHING OF FUSED SILICA**	P2-19	202
Linas Simatonis, Arturas Grabusovas, Tomas Tamulevicius **FORMATION OF PERIODIC GRATINGS IN STAINLESS STEEL USING FEMTOSECOND LASER INTERFERENCE ABLATION**	P2-20	203
Jonas Berzins **SUB-WAVELENGHT PERIODIC STRUCTURES AND THEIR FORMATION BY DIRECT LASER INTERFERENCE PATTERNING**	P2-21	204
Anastasia Tabolich, Mustafo Asimov **BIOMEDICAL APPLICATION THE PHENOMENON OF LASER-INDUCED OXYHEMOGLOBIN PHOTODISSOCIATION**	P2-22	205
Giedrė Grigalevičiūtė, Evaldas Balčiūnas, Linas Jonušauskas, Sima Rekštytė, Daiva Baltriukienė, Virginija Bukelskienė, Mangirdas Malinauskas **FABRICATION OF FLEXIBLE MICROPOROUS 3D SCAFFOLDS VIA STEREOLITHOGRAPHY**	P2-23	206
Simonas Varapnickas, Linas Jonušauskas, Mangirdas Malinauskas **FUNCTIONALIZATION OF POLY(ETHYLENE GLYCOL) DIACRYLATE FOR PLASMONICALLY ENHANCED 3D LASER LITHOGRAPHY AND TEMPERATURE SENSING APPLICATIONS**	P2-24	207
Laurynas Petronis, Tomas Tolenis, Lina Grinevičiūtė **NOVEL METHOD FOR NORMAL INCIDENCE POLARIZERS WITH SCULPTURED THIN FILMS**	P2-25	208

Laura Šerkšnytė, Mikas Vengris **MEASUREMENTS OF PHASE CHARACTERISTICS IN OPTICAL COATINGS BY RESONANCE SCANNING INTERFEROMETER**	P2-26	209
Giedrius Abromavicius, Tomas Juodagalvis, Ramutis Drazdys **OPTICAL AND MECHANICAL PROPERTIES OF Al2O3 THIN FILMS PREPARED BY ION BEAM SPUTTERING**	P2-27	210
Tatiana Kornienko, Alexei Tolstik **PHOTOELECTRIC RESPONSE IN NONCENTROSYMMETRIC PHOTOREFRACTIVE CRYSTALS UNDER PULSE EXCITATION**	P2-28	211
Inga Brice, Antons Pribitoks, Janis Alnis **TOWARDS WGM RESONATOR STABILISED ON Rb 5S-5P TRANSITION LINES**	P2-29	212
Alok Anand Yadav, Aurimas Baškevičius, Simas Butkus, Ona Balachninaitė, Valdas Sirutkaitis **MULTIPLE PULSE FEMTOSECOND LASER-INDUCED BREAKDOWNSPECTROSCOPY IN MONITORING OF MICROMACHINING PROCESSOF MATERIALS IMMERSED IN WATER**	P2-30	213
Yauheniya Korza, Liudmila Trotsiuk, Anna Matsukovich, Olga Kulakovich, Elena Shabunya-Klyachkovskaya **SERS IDENTIFICATION OF ICON PAINTS USING AU NANOPARTICLES IN CHLOROFORM**	P2-31	214
Sopfy Kavalenka, Bobkova Maryia **VISIBLE RANGE SPECTROMETER FOR BIOLOGICAL APPLICATION IN SITU**	P2-32	215
Edvinas Radiunas, Karolis Kazlauskas, Saulius Juršėnas **CORRECT EVALUATION OF FLUORESCENCE QUANTUM YIELD IN ORGANIC FILMS**	P2-33	216
Miglė Radžvilaitė, Martynas Velička, Valdas Šablinskas **LOW TEMPERATURE STUDY OF EXTRACELLULAR FLUID OF KIDNEY TISSUE BY MEANS OF SURFACE-ENHANCED RAMAN SCATTERING SPECTROSCOPY**	P2-34	217
Yuliya Mindarava, Anna Matsukovich, Maksim Shundalau **SPECTROSCOPIC (FTIR, RAMAN, UV/VIS) AND THEORETICAL (DFT, MRPT, BIOLOGICAL ACTIVITY) STUDIES OF ADAMANTANE-CONTAINING COMPOUNDS, PROMISING FOR THE DEVELOPMENT OF ANTIBACTERIAL DRUGS**	P2-35	218
Liudmila Trotsiuk, Anna Matsukovich, O. Kulakovich, E. Shabunya-Klyachkovskaya **EFFECT OF THE METAL-ANALYTE ARRANGEMENT ON THE EFFICIENCY OF SURFACE ENHANCED RAMAN SCATTERING**	P2-36	219
Laimonas Deveikis, Tomas Ceponis, Eugenijus Gaubas **CHARACTERISATION OF NON-IRRADIATED AND NEUTRON IRRADIATED GALLIUM NITRIDE BY ESR SPECTROSCOPY**	P2-37	220
Anton Martenov, Leanid Katkouski, Valeriy Stanchick **HIGH RESOLUTION SOLAR SPECTROPOLARIMETER SSP-600 FOR DETERMINATION OF RADIATION PARAMETERS**	P2-38	221
Algirdas Pabedinskas, Žilvinas Ežerinskis, Justina Šapolaitė, Matas Pocevičius, Laurynas Butkus, Laurynas Bučinskas, Rūta Druteikienė, Andrius Garbaras, Vidmantas Remeikis **14C MEASUREMENT IN THE TREE RING OF PINUS SILVESTRIS BY SINGLE STAGE ACCELERATOR MASS SPECTROMETER**	P2-39	222
Vladimir Abdulajev, Andrius Garbaras1, Elena Lagzdina, Danielius Lingis, Jevgenij Garankin, Artūras Plukis, Rita Plukienė, Vidmantas Remeikis, Arūnas Gudelis **PECULIARITIES OF BURNING THE GRAPHITE SAMPLES**	P2-40	223
Ausrine Jurkeviciute, Linas Simatonis, Serghej L. Prischepa, Tomas Tamulevicius **INVESTIGATION OF GRAPHENE LASER ABLATION PARAMETERS EMPLOYING RAMAN SPECTROSCOPY**	P2-41	224
Artūras Grabusovas, Tomas Klinavičius, Linas Šimatonis, Tomas Tamulevičius, Sigitas Tamulevičius **FABRICATION OF PERIODIC MICRO-STRUCTURES USING MULTIPLE BEAM HOLOGRAPHIC LITHOGRAPHY AND MODELLING OF 3D BEAM INTERFERENCE**	P2-42	225
Elena Daugnoraitė, Evaldas Stankevičius, Gediminas Račiukaitis **EXAMINATION OF PHOTOPOLYMERIZATION PROCESS IN CASE OF NANOSECOND AND PICOSECOND LASER PULSES**	P2-43	226
Mantas Garliauskas, Evaldas Stankevičius **GENERATION OF GOLD NANOPARTICLES BY NANOSECOND LASER PULSE IRRADIATION OF THIN GOLD FILMS**	P2-44	227
Edvinas Skliutas, Sigita Kašėtaitė, Linas Jonušauskas, Sima Rekštytė, Jolita Ostrauskaitė, Mangirdas Malinauskas **BIORESISTS FROM RENEWABLE RESOURCES AS SUSTAINABLEPHOTORESINS FOR 3D LASER MICROLITHOGRAPHY: MATERIALSYNTHESIS, CROSS-LINKING RATE AND CHARACTERIZATION OFTHE STRUCTURES**	P2-45	228
Vytautas Janonis, Vytautas Jakštas, Irmantas Kašalynas, Pawel Prystawko **INVESTIGATION OF REFLECTIVITY OF PLASMON–PHONON MODES IN GRATING-COUPLED AlGaN/GaN HETEROSTRUCTURES GROWN ON SiC AND GaN SUBSTRATES**	P2-46	229
Domas Jokubauskis, Linas Minkevičius, Rimvydas Venckevičius, Dalius Seliuta, Gintaras Valušis **DETECTION OF LOW DENSITY HIDDEN OBJECTS USING TERAHERTZ RADIATION**	P2-47	230
Evaldas Bilotas, Paulius Ragulis, Žilvinas Kancleris **TRANSMISSION OF ELECTROMAGNETIC RADIATION THROUGH MODERN WINDOW PANES IN WIFI FREQUENCY RANGE**	P2-48	231
Vladislovas Čižas, Pranciškus Vitta **INVESTIGATION AND OPTIMIZATION OF THE SOLID-STATE LUMINAIRES FOR STREET LIGHTING**	P2-49	232
Miglius Budriūnas, Pranciškus Vitta **DEVELOPMENT OF THE ZigBee RF4CE BASED SMART LIGHTING CONTROL SYSTEM PROTOTYPE**	P2-50	233

Vishwa Bhatt, Mihirsinh Chauhan, Khushdeep Kaur, Vaibhav Rao, Pankaj Yadav, Brijesh Tripathi, U. K. Dwivedi, Manoj Kumar **INVESTIGATION OF RECOMBINATION MECHANISM IN GREEN OLET INCORPORATING TPBI AS ELECTRON TRANSPORT LAYER**	P2-51	234
Taisuke Matsui, Ieva Petrikyte, Tadas Malinauskas, Konrad Domanski, Maryte Daskeviciene, Matas Steponaitis, Paul Gratia, Wolfgang Tress, Juan-Pablo Correa-Baena, Antonio Abate, Anders Hagfeldt, Michael Graetzel, Mohammad Khaja Nazeeruddin, Vytautas Getauti **ADDITIVE-FREE POLYMERIC TRIARYLAMINE DERIVATIVE AS HOLE TRANSPORTING MATERIALS FOR STABLE PEROVSKITE SOLAR CELLS**	P2-52	235
Edita Vernickaitė, Pavel Globa, Henrikas Cesiulis, Natalia Tsyntsaru **ELECTROCHEMICAL BARRIER LAYER THINNING OF ANODIC ALUMINUM OXIDE**	P2-53	236
Zeel Purohit, Manoj Kumar, Brijesh Tripathi **INFLUENCE OF HIGH VOLTAGE STRESS ON THE EFFICIENCY OF C-Si SOLAR CELLS**	P2-54	237
Rokas Jasiūnas, Vidmantas Gulbinas **EXCITON AND CHARGE CARRIER DYNAMICS IN ALL-POLYMER TQ1:N2200 SOLAR CELL**	P2-55	238
Monica Fernandez Barcia, Volker Hoffmann, Steffen Oswald, Ulrike Wolff, Margitta Uhlemann, Annett Gebert **ELECTRODEPOSITION OF MANGANESE LAYERS FROM AQUEOUS ELECTROLYTES**	P2-56	239
Tomas Drunga, Tomas Grinys **FABRICATION OF STRUCTURES IN Er2O3 FILMS USING PHOTOLITOGRAPHY AND WET ETCHING**	P2-57	240
Denisa Dosenovicova, Jelena Maricheva, Alex Neumüller, Oleg Sergeev, Olga Volobujeva, Albert Nasibulin, Julia Kois, Andres Öpik, Sergei Bereznev **SELECTIVE PHOTOELECTROCHEMICAL DEPOSITION OF PPY ONTO HYDROGENATED a-Si FOR OPTOELECTRONIC APPLICATIONS**	P2-58	241
Kravchenko Aleksandra, Guschik Dmitriy, Yurkova Aleksandra **STRUCTURE AND PHASE COMPOSITION OF POWDERED QUASICRYSTALLINE Al-Fe-Cr ALLOY AFTER CONSOLIDATION BY QUASI-HYDROSTATIC COMPRESSION**	P2-59	242
Aistė Lisauskaitė, Virginija Jankauskaitė, Mindaugas Liaudanskas, Akvilė Andziukevičiūtė-Jankūnienė **POLYDIMETHYLSILOXANE - CELLULOSE AND PLANT MATERIAL COMPOSITES THEIR PROPERTY AND ANTIMICROBIAL ACTIVITY**	P2-60	243
Alexander Malashevich, Nikolai Cherenda, Valentin Astashinski, Anton Kuzmitski **STRUCTURE AND PHASE COMPOSITION CHANGES IN CARBON STEEL (U9) AFTER COMPRESSION PLASMA FLOW TREATMENT**	P2-61	244
Gerda Mikalauskaite, Virginija Daukantiene **INVESTIGATION OF THE TEXTILE BONDS STRENGTH UNDER SPECIFIED AGEING CONDITIONS**	P2-62	245
Antonio Mulone, Uta Klement, Aliona Nicoleno **STRUCTURE AND THERMAL RESISTANCE ANALYSIS OF Fe-W COATINGS ELECTRODEPOSITED FROM GLYCOLATE-CITRATE PLATING BATH**	P2-63	246
Augustas Nekrošius **PHOTOELECTRIC PROPERTIES OF a-SI:H WITH V2O5-X WINDOW LAYER**	P2-64	247
Aliona Nicolenco, Volker Hoffmann, NataliaTsyntsaru, Eva Pellicer, Jordina Fornell, Jordi Sort, Henrikas Cesiulis **MAGNETIC AND MECHANICAL PROPERTIES OF ELECTODEPOSITED Fe-W ALLOYS**	P2-65	248
Pavel Orsich, Vitaly Mechinski, Mikhail Korjik, Valera Dormenev, Hans-Georg Zaunick **CRYSTALLINE MATERIALS FOR HADRONIC CALORIMETRY DETECTING MODULES AT HIGH LUMINOSITY COLLIDER EXPERIMENTS.**	P2-66	249
Pranas Usinskas, Zivile Stankeviciute, Aivaras Kareiva **CALCIUM HYDROXYAPATITE THIN FILMS ON NOVEL SILICON NITRIDE SUBSTRATE**	P2-67	250
Michele Zanatta, Naida El Habra, Francesca Visentin, Gianluca Pozza, Alessandro Zambon, Nicola Elvassore, Monica Giomo, Giovanna Brusatin **INVESTIGATION ON PH GRADIENT FORMATION AT MICROSTRUCTURED ELECTRODES USING SICM**	P2-68	251
Liudmila Shemet, Sergei Sherbakov, Aleh Nasan **THE SIMULATION OF CRACK-LIKE DAMAGE**	P2-69	252
Sergei Sherbakov, Aleh Nasan, Liudmila Shemet **CALCULATION OF WHEEL-RAIL SYSTEM IN TRIBO-FATIGUE STATEMENT**	P2-70	253

16 March, THURSDAY

13:15-15:00 **POSTER SESSION P3**

Danielė Anilionytė, Dalius Gudeika, Juozas V. Gražulevičius, Arūnas Miasojedovas **THE INVESTIGATION OF TRIPLET STATES IN 1.8-NAPHTHALIMIDE DERIVATIVES**	P3-01	256
Sergejus Balčiūnas, Maksim Ivanov, Jūras Banys, Satoshi Wada **DIELECTRIC PROPERTIES OF BaTiO3-KNbO3 COMPOSITES**	P3-02	257
Piotr Baranowski, Tomasz Pietrzak, Jerzy Garbarczyk **OPTIMIZATION OF NANOCRYSTALLIZATION OF Li3xNa3(1-x)V2(PO4)3 GLASSES**	P3-03	258
Greta Bučytė, Steponas Raišys, Povilas Adomėnas, Karolis Kazlauskas, Saulius Juršėnas **OPTIMIZATION OF MODIFIED ANTHRACENE COMPOUNDS FOR LIGHT UPCONVERSION**	P3-04	259
Tadas Buciunas, Paulius Baronas, Tomas Matulaitis, Juozas Vidas Grazulevicius, Saulius Antanas Jursenas **HIGHLY EFFICIENT THERMALLY ACTIVATED DELAYED FLUORESCENCE IN TRIAZINE-CARBAZOLE DERIVATIVES**	P3-05	260
Lesya Demchenko, Anatoliy Titenko, Yaroslav Titenko, Eduard Udovenko **THE EFFECT OF THERMOMAGNETIC TREATMENT ON STRUCTURE AND PROPERTIES OF Cu-Al-Mn SHAPE MEMORY ALLOYS**	P3-06	261
Jędrzej Doliński, Przemysław Piotr Michalski, Tomasz Karol Pietrzak, Jerzy Edward Garbarczyk **THERMAL AND ELECTRICAL CHARACTERIZATION OF LIVBO3F GLASSES AND NANOMATERIALS**	P3-07	262
Justyna Frąckiewicz, Tomasz Pietrzak, Jerzy Garbarczyk **SYNTHESIS AND CHARACTERIZATION OF LiFe0.44Mn0.44V0.08PO4 GLASS AND NANOMATERIALS**	P3-08	263
Agata Gołębiewska, Przemysław Piotr Michalski, Tomasz Karol Pietrzak, Jerzy Edward Garbarczyk **INVESTIGATION OF STRUCTURAL PROPERTIES OF LITHIUM MANGANESE BORATE**	P3-09	264
Paulius Imbrasas, Karolis Kazlauskas, Tomas Matulaitis, Juozas V. Gražulevičius, Saulius Juršėnas **OLEDS BASED ON TRIAZINE DERIVATIVES FEATURING THERMALLY ACTIVATED DELAYED FLUORESCENCE**	P3-10	265
Justina Jovaišaitė, Erika Bizdena, Maris Turks, Saulius Juršėnas **CONTROL OF OPTICAL PROPERTIES AND SENSING APPLICATION OF PURINE DERIVATIVE**	P3-11	266
Rasa Keruckiene, Viktorija Mimaite, Jonas Keruckas, Dmytro Volyniuk, Juozas Vidas Grazulevicius **DERIVATIVES OF INDOLE AND BENZO[b]CARBAZOLE AS ELECTROACTIVE MATERIALS**	P3-12	267
Olena Ishchenko, Maksym Koliada, Viktoriia Plavan **STARCH-BASED BIODEGRADABLE FILMS BEHAVIOUR AFFECTED BY COLLAGEN DERIVATIVES INCORPORATION**	P3-13	268
Regimantas Komskis, Titas Braukyla, Nobuya Sakai, Maryte Daskeviciene, Vygintas Jankauskas, Egidijus Kamarauskas, Tadas Malinauskas, Henry J. Snaith, Saulius Jursenas, Vytautas Getautis **SYNTHESIS AND INVESTIGATION OF V-SHAPED HOLE-TRANSPORTING MATERIALS CONTAINING TRÖGER`S BASE CORE AND TPD-TYPE BRANCHES**	P3-14	269
Nadzeya A. Kukhta, Dmytro Volyniuk, Khrystyna Ivaniuk, Juozas Vidas Grazulevicius **DEVELOPMENT OF THE EFFICIENT HOST/GUEST SYSTEMS FOR DEEP-BLUE ORGANIC LIGHT-EMITTING DIODES**	P3-15	270
Iryna Olyshevets, Sergii Smola, Nataliia Kariaka, Olena Litsis, Vladimir M. Amirkhanov **LUMINESCENCE AND STRUCTURE OF EUROPIUM(III) TETRAKIS-COMPLEXES WITH SULFONYLAMIDOPHOSPHATE (SAPh) LIGANDS**	P3-16	271
Olena Litsis, Tatiana Yu. Sliva, Yu.V. Kolomzarov, I.E. Minakova, Vladimir M. Amirkhanov **EUROPIUM COORDINATION COMPOUNDS BASED NANODIMENSION THIN FILMS FOR LIGHT-EMITTING DEVICES**	P3-17	272
Justina Malakauskaitė, Gediminas Kreiza, Karolis Kazlauskas, Saulius Juršėnas **CHARACTERIZATION AND OPTIMIZATION OF FUNCTIONAL ORGANIC FILMS PREPARED BY BLADE-COATING**	P3-18	273
Karolina Maleckaitė, Dalius Gudeika, Juozas V. Gražulevičius, Arūnas Miasojedovas **THE INVESTIGATION OF PHOTOPHYSICAL PROPERTIES OF NEW NAPHTALIMIDE CORE DERIVATIVES**	P3-19	274
Tomas Matulaitis, Juozas Vidas Gražulevičius, Dmytro Volyniuk **STRUCTURE-PROPERTY RELATIONSHIP OF BIPOLAR ORGANIC SEMICONDUCTORS**	P3-20	275
Przemysław Piotr Michalski, Tomasz Karol Pietrzak, Jerzy Edward Garbarczyk **LiFeBO3 PREPARED VIA THERMAL NANOCRYSTALLIZATION OF AMORPHOUS PRECURSOR**	P3-21	276
Jessica Patel, Mihirsinh Chauhan, Chandrakanth P, Maitrayee Trivedi, Vaibhav Rao, Brijesh Tripathi, Manoj Kumar, Manoj Kumar Pandey **REGULATING THE OPTICAL, ELECTROCHEMICAL AND MORPHOLOGICAL PARAMETERS OF FLUORANTHENE AND P3HT BLEND BY N,N-DIMETHYLACETAMIDE**	P3-22	277
Yaroslav Titenko, Andriy Olefir, Anatoliy Titenko, Lesya Demchenko **THE EFFECT OF THERMOMECHANICAL TREATMENT ON STRUCTURE AND MECHANICAL PROPERTIES OF FERROMAGNETIC Fe-Ni-Co-Ti ALLOYS**	P3-23	278
Wiktoria Zajkowska, Tomasz Pietrzak, Jerzy Garbarczyk **METAL-TO-INSULATOR TRANSITION IN NANOCRYSTALLIZED 90MgV2O5 · 10P2O5 GLASSES.**	P3-24	279
Naoual Al Armouzi, Mustapha Mabrouki, Nourreeddine Kouider **PREPARATION OF CUO NANOWIRES BY THERMAL OXIDATION**	P3-25	280
Artsiom Antanovich, Anatol Prudnikau, Mikhail Artemyev **SYNTHESIS AND OPTICAL PROPERTIES OF SEMICONDUCTOR COLLOIDAL QUANTUM WELLS**	P3-26	281
Marcin Bartmanski, Marek Foltyn, Konrad Norowski, Maciej Zgirski **NANOSECOND RESOLUTION CALORIMETRY USING DAYEM NANOBRIDGES**	P3-27	282

Dovile Baziulyte-Paulaviciene, Ricardas Rotomskis, Vitalijus Karabanovas, Simas Sakirzanovas **UPCONVERTING NANOPARTICLES FOR THERANOSTIC**	P3-28	283
Arkadiusz Grempka, Mateusz Król, Michał Wójcik, Jacek Szczytko **DETERMINATION OF THE SIZE OF THE CORE OF MAGNETIC COBALT NANOPARTICLES USING THE FARADAY EFFECT**	P3-29	284
Sakshum Khanna, Gauravi Xavier **LOW TEMPERATURE RELOCATION OF ALIGNED SINGLE CRYSTAL SILICON NANOWIRES ONTO ALIEN SUBSTRATE.**	P3-30	285
Andriy Kusyak, Natalia Kusyak, Katerina Sviriduk, Petro Gorbyk **ADSORPTION OF Y3+ IONS WITH NANOCOPOSITES BASED ON SINGLE-DOMAIN Fe3O4 MODIFIED WITH TiO2**	P3-31	286
Karolina Łempicka, Konrad Norowski, Magdalena Grzeszczyk, Barbara Piętka, Jacek Szczytko **THICKNESS OF THE EXFOLIATED MoSe2 MEASURED BY REFLECTOMETRY AND RAMAN SCATTERING**	P3-32	287
Aneta Leniart, Pawel W. Majewski **MATERIALS BASED ON SELF-ASSEMBLING BLOCK COPOLYMER AND LIQUID CRYSTAL HYBRIDS**	P3-33	288
Natalya Leonova, Svetlana Zhiltsova **STRUCTURE AND PROPERTIES OF EPOXY-SILICA AND EPOXY-TITANIA COMPOSITES OF CATIONIC POLYMERIZATION**	P3-34	289
Algimantas Lukša, Gvidas Astromskas, Viktorija Nargelienė, Andrius Sakavičius, Arūnas Šetkus **INFLUENCE OF THERMAL TREATMENT ON GRAPHENE - METAL CONTACT**	P3-35	290
Tristan Mangeolle, Thomas Pons, Frédéric Marchal **MULTIMODAL NANOPROBE FOR GUIDED SURGERY OF OVARIAN PERITONEAL CARCINOMATOSIS**	P3-36	291
Valentin Natarov, Dzmitry Kotsikau, Eugenia Korobko, Anna Eroma, Zoya Novikova, Vladimir Pankov **TEMPLATE-FREE SYNTHESIS OF MAGNETITE NANORODS FOR THE IMPROVENMENT OF RHEOLOGICAL PERFORMANCE OF CARBONYL IRON OIL SUSPENSIONS**	P3-37	292
Agnė Mikalauskaitė, Renata Karpicz, Arūnas Jagminas **THE INFLUENCE OF ADDITION PURE AMINO ACIDS ON THE PROPERTIES OF LUMINESCENT GOLD CLUSTERS**	P3-38	293
Fyodor Morozko, Vladislav Popov, Andrey Novitsky **FINITE DENSITY OF STATES FOR HYPERBOLIC METAMATERIALS WITHIN OPERATOR EFFECTIVE MEDIUM APPROXIMATION**	P3-39	294
Vytautas Navikas, Martynas Gavutis, Ramūnas Valiokas **RAPID PROTOTYPING OF NANOELECTRODE AND METAMATERIAL ARRAYS BY LIPID DIP-PEN NANOLITHOGRAPHY**	P3-40	295
Piotr Antoni Orłowski, Grzegorz Kołodziej, Bartłomiej Seredyński, Adam Wincukiewicz, Jakub Polaczyński, Arkadiusz Leniart, Maria Kamińska **INVESTIGATION OF ELECTROCONDUCTIVITY ANDLUMINESCENCE IN ORGANIC POLYMER THIN-LAYERS SYSTEM**	P3-41	296
Elena Petrova, Marina Roshchina, Vladimir Pankov **NON-AGGLOMERATED MgFe2O4 NANOPARTICLES WITH INCREASED SATURATION MAGNETIZATION VALUE VIA ANNEALING IN NaCl MATRIX**	P3-42	297
Aleksandra Fedosyuk, Aliaksandra Radchanka, Artsiom Antanovich, Anatol Prudnikau, Maksim V. Kvach, Vadim Shmanai, Mikhail Artemyev **QUANTIFICATION OF AMPHIPHILIC POLYMER MOLECULES ON THE SURFACE OF HYBRID LUMINESCENT NANOCRYSTAL-POLYMER COMPOSITES FOR BIOMAGING**	P3-43	298
Simonas Ramanavičius, Arūnas Jagminas **SOLVOTHERMAL SYNTHESIS OF COBALT FERRITE NANOPARTICLES**	P3-44	299
Martynas Skapas, Renata Butkutė, Arūnas Kadys, Valentina Plaušinaitienė **ELEMENTAL AND PHASE ANALYSIS OF NANOSCALE STRUCTURES BY HRTEM**	P3-45	300
Marina Tretjak **RESISTIVITY AND LOW FREQUENCY NOISE CHARACTERISTICS OF EPOXY CARBON COMPOSITES**	P3-46	301
Vadim Chernyavsky, Margarita Kurasova, Sergii Gandzyuk, Alexandra Yurkova **STRUCTURE AND MECHANICAL PROPERTIES OF ALCUNIFECR HIGH ENTROPY ALLOY REZULTED FROM MECHANICAL ALOYING, ANNEALING AND SINTERING**	P3-47	302
Vera Vashkevich, Valery Lapanik, Krystina Volk, Anatolij Minko **INFLUENCE OF MODIFIED DETONATION NANODIAMONDS ON ELECTRO-OPTICAL PROPERTIES OF NEMATIC LIQUID CRYSTALS**	P3-48	303
Maksimas Anbinderis **TRANSFORMATION OF PHYSICAL PARAMETERS OF MICROWAVE DIODES ON THE BASE OF MODULATION DOPED SEMICONDUCTOR STRUCTURES UNDER LIGHT ILLUMINATION**	P3-49	304
Milda Budreckaitė, Kazimieras Nomeika, Ramūnas Aleksiejūnas **ANALYSIS OF InGaN STRUCTURES USING TIME-RESOLVED SPECTROSCOPIC TECHNIQUES**	P3-50	305
Vladislavas Čerkasovas, Paulius Baronas, Gediminas Kreiza, Povilas Adomėnas, Ona Adomėnienė, Karolis Kazlauskas, Saulius Juršėnas **INVESTIGATION OF EXCITON DIFFUSION AND ANNIHILATION IN BIFLUORENE SINGLE CRYSTAL**	P3-51	306
Alexander Fedotov, Sergey Perevoznikov, Uladzislau Humennik **THE FOURIER MOBILITY SPECTRUM ANALYSIS APPLICATION TO Bi-Sn SUPERDILUTED ALLOYS**	P3-52	307
Tatyana Gaydamak, Galyna Zvyagina, Konstantin Zhekov, Igor Bilich, Dmitriy Chareev **PIEZOMAGNETISM IN FeSe**	P3-53	308

Marek Kolenda, Tadas Malinauskas, Darius Dobrovolskas, Arūnas Kadys **InN GROWTH ON GaN AND SAPPHIRE BY MOVPE AND CHARACTERIZATION**	P3-54	309
Julia Kondratieva, Jury Pokotilo **HYDROGEN STATE TRANSFORMATION-DURING THE HEAT TREATMENT OF HYDROGENATED SILICON**	P3-55	310
Vaida Marčiulionytė, Augustas Vaitkevičius, Yevgeny Tratsiak, Y. Bokshits, Andrei Borisevich, Mikhail Korjik, Gintautas Tamulaitis **LUMINESCENCE IN YCAGG:Ce GLASS CERAMICS FOR WHITE LEDs**	P3-56	311
Andrei Novikau, Mikhail Lobanok, Stanislav Prokopyev, Peter Gaiduk **GROWTH OF THIN SILICON CARBIDE LAYERS ON SILICON-GERMANIUM BUFFERS**	P3-57	312
Lyudmila Omelchenko, Andrei Solovjov, Ruslan Vovk **FLUCTUATION CONDUCTIVITY AND PSEUDOGAP IN Y1-xPrxBa2Cu3O7-δ SINGLE CRYSTALS**	P3-58	313
E. V. Petrenko, A. L. Solovjov, K. Buchkov, E. Nazarova, K. Rogacki **EXCESS CONDUCTIVITY AND POSSIBLE PSEUDOGAP STATE IN FeSe0.94 IRON-BASED SUPERCONDUCTORS**	P3-59	314
Marius Pikčiūnas, Ignas Reklaitis, Domas Paipulas **HIGH ASPECT RATIO DRY ETCHING METHOD FOR GAN BASEDCAPACITOR TYPE DETECTOR FORMATION**	P3-60	315
Kornelijus Pūkas, Tomas Čeponis, Eugenijus Gaubas **STUDY OF PHOTORESPONSE CHARACTERISTICS IN NEUTRON IRRADIATED STRUCTURES OF AMMONO-THERMAL GALLIUM NITRIDE**	P3-61	316
Przemyslaw Pula, Grzegorz Luka, Elzbieta Guziewicz **ELECTRICAL AND OPTICAL PROPERTIES OF ZnO LAYERS GROWN ON SiO2/Si (111) SUBSTRATES BY ATOMIC LAYER DEPOSITION**	P3-62	317
Martynas Riauka, Kazimieras Nomeika, Saulius Nargelas, Ramūnas Aleksiejūnas **CARRIER DYNAMICS IN INN WITH DIFFERENT GROWTH PARAMETERS**	P3-63	318
Sandra Stanionytė, Vaidas Pačebutas **GROWTH OF GaInAsBi LAYERS ON InP FOR MID-INFRARED OPTICAL DEVICES**	P3-64	319
Henrikas Svidras, Luiz Galvao Tizei, Mathieu Kociak **WAVELENGTH FILTERED CORRELATION FUNCTIONS IN ELECTRON MICROSCOPY-BASEDCATHODOLUMINESCENCE FOR LIFETIME MEASUREMENTS**	P3-65	320
Vilius Vertelis **PHOTOELECTRIC PROPERTIES OF Tl1-xIn1-xIVAxSn2 ALLOYS**	P3-66	321
Martynas Vilkaitis, Nerija Žurauskienė **INVESTIGATION OF MAGNETORESISTANCE OF NANOSTRUCTURED La-Sr-Mn-O FILMS WITH MANGANESE EXCESS.**	P3-67	322
Vadim Zhivulko, Olga Borodavchenko **STRUCTURAL AND OPTICAL PROPERTIES OF Cu2ZnSnSe4 THIN FILMS FOR SOLAR CELLS**	P3-68	323
Sergey Aplesnin, Aliona Zhivulko, Olga Demidenko, Kazimir Yanushkevich **THE Mn1-xGdxSe SOLID SOLUTIONS AND THEIR STRUCTURAL CHARACTERISTICS**	P3-69	324
Justina Aglinskaitė, Akvilė Zabiliūtė-Karaliūnė, Pranciškus Vitta **LASER DIODE INDUCED PHOTOLUMINESCENCE CHARACTERIZATION OF YAG:Ce3+ CERAMICS AND POWDER PHOSPHORS**	P3-70	325
Gintarė Kuksėnaitė, Karolis Kazlauskas, Gediminas Kreiza, Arūnas Miasojedovas, Paulius Baronas, Aurimas Bieliauskas, Vytautas Getautis, Algirdas Šačkus, Saulius Juršėnas **INFLUENCE OF PERIPHERAL PHENYLS TO EXCITED STATE RELAXATION AND AGGREGATION INDUCED FLUORESCENCE IN NITRILE COMPOUNDS**	P3-71	326
Kazimieras Badokas, Tadas Malinauskas, Tomas Grinys, Rytis Dargis **GROWTH AND CHARACTERISATION OF NON-POLAR AND SEMI-POLAR GaN ON Si WITH Er2O3 INTERLAYER**	P3-72	327

17 March, FRIDAY

13:15-15:00 **POSTER SESSION P4**

Marius Dagys, Audrius Laurynėnas, Dalius Ratautas, Juozas Kulys, Regina Vidžiūnaitė, Martynas Talaikis, Gediminas Niaura, Liucija Marcinkevičienė, Rolandas Meškys, Sergey Shleev **OXYGEN ELECTROREDUCTION CATALYSED BY LACCASE WIRED TO GOLD NANOPARTICLES VIA THE TRINUCLEAR COPPER CLUSTER**	P4-01	330
Agnė Jurevičiūtė, Asta Stapulionytė **CYTOGENOTOXIC EFFECTS IN COMMON ONION (ALLIUM CEPA L.) ROOT CELLS INDUCED BY TOPSOIL CONTAMINATED WITH ANTHROPOGENIC AND BIOGENIC BYPRODUCTS**	P4-02	331
Reznikova Diana **INFLUENCE OF SIDERITIS TAURICA ON LIPID PEROXIDATION AND ANTIOXIDATIVE SYSTEMS IN ALLOXAN-INDUCED DIABETIC RATS**	P4-03	332
I. Sadauskienė, I. Stankevičienė, K. Adomaitytė, A. Liekis, R. Naginienė, V. Šimakauskienė, D. Baranauskienė **SUPEROXIDE DISMUTASES ACTIVITY IN MICE BRAIN UNDER SELENIUM AND/OR ALIUMINIUM IONS TREATMENT**	P4-04	333
Povilas Gabralevičius, Sven Clausen, Frank Schneider **INVESTIGATION OF HYBRID MONTE CARLO ALGORITHM FOR RADIATION DOSE PREDICTION OF INTRABEAM® SPHERICAL APPLICATOR**	P4-05	334
Greta Ašmenaitė, Gerda Petkutė, Milda Stankevičiūtė, Laura Butrimavičienė **GENOTOXICITY ASSESSMENT OF HEAVY METAL MODEL MIXTURE IN SWAN MUSSEL, EUROPEAN PERCH AND COMMON ROACH GILLS**	P4-06	335
Janina Greiciūnaitė, Roberta Valskienė, Laura Butrimavičienė, Janina Baršienė **ENVIRONMENTAL GENOTOXICITY STUDIES IN ERYTHROCYTES CELLS OF FISH COLLECTED IN THE EASTERN GOTLAND BASIN OF THE BALTIC SEA**	P4-07	336
Elona Jankauskaitė, Agata Kodroń, Ewa Bartnik **EFFECTS OF SEX HORMONES ON CELL DEATH IN CELLS WITH MUTATIONS RESPONSIBLE FOR LEBER'S HEREDITARY OPTIC NEUROPATHY**	P4-08	337
Gediminas Drabavičius, Arūnas Šilanskas, Tomas Šinkūnas, Giedrius Gasiūnas **PROOFREADING DOMAIN FACILITATES SPACER INTEGRATION IN CRISPR-CAS – AN ADAPTIVE PROKARYOTIC IMMUNITY**	P4-09	338
Tomas Kairys, Vėtra Markevičiūtė, Gražina Kleinotienė, Arijanda Neverauskienė **REVIEW OF PACIENTS, DIAGNOSED WITH NON HODGINS LYMPHOMA, TREATED VUL S/K CHILDRENS HOSPITAL IN YEARS 2010-2015**	P4-10	339
Nerijus Karlonas **DEVELOPMENT OF MIXED-MODE POLYMERIC SORBENT ASSAY FOR A MULTI-RESIDUE ANALYSIS OF DRUGS IN BIOLOGICAL MATRICES BY FAST GAS CHROMATOGRAPHY TECHNIQUE**	P4-11	340
J. Kelpšienė, S. Supronienė **BACTERIAL DISEASES CAUSED OF PSEUDOMONAS SPP. IDENTIFICATION IN LITHUANIAN WHEAT**	P4-12	341
Emilija Kurlytė, Skaistė Tulytė **INTRAPERITONEAL VERSUS INTRAVENOUS CHEMOTHERAPY: TREATING OVARIAN CANCER**	P4-13	342
Vėtra Markevičiūtė, Tomas Kairys, Gražina Kleinotienė, Arijanda Neverauskienė **REVIEW OF PACIENTS, DIAGNOSED WITH HODGKIN LYMPHOMA AND TREATED IN VUL S/K CHILDREN`S HOSPITAL IN 2010-2015**	P4-14	343
Gediminas Misevičius, Jolanta Patamsytė, Donatas Žvingila **USE OF DNA MARKERS IN THE DIFFERENTIATION OF RELATED PLANT SPECIES**	P4-15	344
Emil Paluch, Agata Piecuch, Ewa Obłąk, Łukasz Lamch, Kazimiera Wilk **BIOFILM PREVENTION OF PSEUDOMONAS AERUGINOSA AND STAPHYLOCOCCUS EPIDERMIDIS BY DICEPHALIC CATIONIC SURFACTANTS AND THEIR INTERACTIONS WITH DNA**	P4-16	345
Tatjana Pladere, Jurgis Skilters, Gunta Krumina **CHARACTERISTICS OF GROUPING BY SIMILARITY IN CONJUNCTION VISUAL SEARCH.**	P4-17	346
Jurgita Kelpsiene, Neringa Rasiukeviciute, Skaidre Suproniene, Grazina Kadziene **F. GRAMINEARUM PRESENCE ON NON-GRAMINACEOUS PLANTS**	P4-18	347
Karolis Sivickis, Dovile Cepukoit, Goda Norkute, Daiva Burokiene **AN IMPORTANCE OF PHYTOPHTHORA SPECIES OF OAK DECLINE IN LITHUANIA**	P4-19	348
Sonata Adomaviciute, Akvile Slektaite-Kisone, Ricardas Rotomskis **SYNTHESIS OPTIMISATION OF POLYVINYLPYRROLIDONE STABILIZED GOLD NANOPARTICLES**	P4-20	349
Agne Kunickaite, Ausra Stumbryte, Zivile Gudleviciene, Daiva Dabkeviciene, Regina Liudkeviciene, Genovefa Garmiene, Saulius Cicenas **COMBINED EFFECT OF HPV AND GENETIC POLYMORPHISMS IN TP53, MDM2, MDM4, MTHFR, CCR5 AND CASP8 IN LUNG CANCER**	P4-21	350
Elizaveta Tarakanova, Elena Kozlova **EMOTION RECOGNITION ALGORITHM BASED ON INTEL REALSENSE TECHNOLOGY**	P4-22	351
Ilona Uzieliene, Jaroslav Denkovskij, Daiva Bironaite, Saule Valiuniene, Roma Griniene, Zygmunt Mackevic, Eiva Bernotiene	P4-23	352

THE COMPARISON OF CHONDROGENIC DIFFERENTIATION POTENTIAL IN HUMAN MESENCHYMAL STEM CELLS FROM MENSTRUAL BLOOD AND BONE MARROW USING ACTIVIN A AND TGF-B3		
Laima Vasiliauskaitė, Inga Bikulčienė, Zita Aušrelė Kučinskienė, Arvydas Kaminskas, Vaiva Hendrixson **EVALUATION OF ADIPOSE TISSUE FATTY ACID COMPOSITION IN PATIENTS WITH NEPHROLITHIASIS**	P4-24	353
Lauma Busa, Kristine Zadvinska, Arta Bardule, Arturs Viksna **ACCUMULATION OF SEVERAL HEAVY METALS AND CHANGES IN STABLE CARBON AND NITROGEN ISOTOPE RATIOS IN RED-CAPPED SCABER STALK (LECCINUM AURANTIACUM)**	P4-25	354
Paulius Butkus, Gediminas Staigvila, Sonata Tolvaišienė, Vitalij Novickij **SUB-MICROSECOND PULSED ELECTRIC AND MAGNETIC FIELD GENERATION FACILITIES FOR TRANSIENT CELL MEMBRANE PERMEABILIZATION**	P4-26	355
Ana Chaleckaja, Lidija Tetianec, Juozas Kulys, Liucija Marcinkeviciene, Jonita Stankeviciute, Rolandas Meskys **BIOCONVERSION OF GLYCEROL INTO GLYCERIC ACID CATALYZED BY PQQ-DEPENDENT ALCOHOL DEHYDROGENASE**	P4-27	356
Ignas Čiplys, Vilmantas Gėgžna, Darius Varanius, Aurelija Vaitkuvienė, Gunaras Terbetas, Laura Neverauskienė, Jurgita Ušinskienė, Juozas Vidmantis Vaitkus **CORRELATION AND CLASSIFICATION ANALYSIS OF HUMAN INTERVERTEBRAL DISC AUTO-FLUORESCENCE SPECTRA**	P4-28	357
Farrakhova Dina, Yakavets Ilya, Loschenov Victor, Zorin Vladimir, Bolotine Lina **DISTRIBUTION OF CHLORIN PHOTOSENSITIZERS IN MONOLAYER AND SPHEROID CELL CULTURES**	P4-29	358
Justina Gruzauskaite, Ingrida Jurkeviciute, Lidija Tetianec, Regina Vidziunaite, Liucija Marcinkeviciene **INVESTIGATION OF LACCASE ADSORBTION ON MAGNETIC NANOPARTICLES AND KINETICS OF THE ADSORBED ENZYME**	P4-30	359
Elizaveta Kavalenka, Alena Kavalenka, Olga Hozyanin **DIFFERENT PARTICIPATION OF CYTOSKELETON ELEMENTS IN REGULATION OF MECHANICAL PROPERTIES IN HUMAN BLOOD NEUTROPHILS AND ERYTHROCYTES**	P4-31	360
Aura Kisieliūtė, Inga Morkvėnaitė-Vilkončienė, Jūratė Petronienė, Anton Popov, Almira Ramanavičienė, Aušra Valiūnienė, Roxana-Mihaela Apetrei, Geta Carac, Arūnas Ramanavičius **POLYPYRROLE-MODIFIED ASPERGILLUS NIGER CELLS FOR MICROBIAL FUEL CELL/BIOSENSOR ELECTROCHEMICAL SYSTEMS**	P4-32	361
Kristina Lupeikytė, Romualdas Rudys **OPTIMIZING THE EFFECTIVENESS OF PHOTOSENSIBILISED TUMOR THERAPY BY USING 5 – AMINOLEVULINIC ACID, ITS ESTERS AND MIXTURES CONTAINING HYALURONIC ACID**	P4-33	362
Greta Musteikyte, Vytautas Smirnovas **OPTIMIZATION OF SOD1 AGGREGATION CONDITIONS IN VITRO AND IMPACT OF ENVIRONMENTAL FACTORS TO AGGREGATION KINETICS**	P4-34	363
Marijus Plečkaitis, Vladimir Sivakov, Vitalijus Karabanovas **STUDY OF MESOPOROUS SILICA NANOWIRES AS POTENTIAL CONTRAST AGENT FOR CANCER DIAGNOSTICS**	P4-35	364
Vilmantas Pupkis, Indrė Lapeikaitė, Vilma Kisnierienė **ION CHANNEL ACTIVITY FOUND IN CYTOPLASMIC DROPLETS OF NITELLOPSIS OBTUSA USING PATCH CLAMP TECHNIQUE**	P4-36	365
Polina Shishkanova, Darya Sharshunovich, Galina Semenkova, Victor Sorokin, Oleg Shadyro **AROMATIC FUNCTIONALLY SUBSTITUTED IMINES AND HYDRAZIDES - MYELOPEROXIDASE INHIBITORS**	P4-37	366
Rokas Skaisgiris, Arūnas Miasojedovas, Alytis Gruodis, Dalius Gudeika, Juozas V. Gražulevičius, Saulius Juršėnas **ORGANIC COLORIMETRIC SENSORS FOR BIOLOGICAL APPLICATIONS BASED ON DIMETHYLAMINOBENZENE MOIETY**	P4-38	367
Mantas Stankevičius, Živilė Cibulskaitė, Nijolė Kazlauskienė, Ričardas Rotomksis **FLUORESCENCE MICROSCOPY OF QUANTUM DOTS DISTRIBUTION IN RAINBOW TROUT EMBRYOS CHORION**	P4-39	368
Karina Stumbriene, Skaidre Suproniene, Renata Gudiukaite, Roma Semaskiene **EFFICACY OF SELECTED BACILLUS SUBTILIS STRAINS AGAINST FUSARIUM HEAD BLIGHT OF WHEAT CAUSED BY ARTIFICIAL INFECTION**	P4-40	369
Povilas Simonis, Skirmantas Kersulis, Voitech Stankevich, Vytautas Kaseta, Egle Lastauskiene, Arunas Stirke **CASPASE DEPENDENT APOPTOSIS INDUCED IN YEAST CELLS BY NANOSECOND PULSED ELECTRIC FIELDS**	P4-41	370
Darius Šulskis, Vytautas Smirnovas, Ludmilla Morozova-Roche **AGGREGATION AND STABILITY OF S100A9 PROTEIN**	P4-42	371
Aivaras Vilkas, Dovile Baziulyte-Paulaviciene, Simas Sakirzanovas, Vitalijus Karabanovas, Ricardas Rotomskis **UPCONVERTING NANOPARTICLES OPTICAL PROPERTIES DEPENDENCE ON SIZE AND SHELL**	P4-43	372
Povilas Zdanis, Saulius Bagdonas **SPECTROMETRIC ANALYSIS OF PHOTOTRANSFORMATIONS OF NATURAL PIGMENTS IN EXTRA VIRGIN OLIVE OIL**	P4-44	373
Pramodkumar P Gupta, Dalius Kučiauskas, Shanker Lal Kothari, Virupaksha A. Bastikar, Mindaugas Valius **IN SILICO ANALYSIS AND MOLECULAR DOCKING STUDIES OF RH1 DRUG WITH UPREGULATED KINASES IN RH1 RESISTANCE HUMAN BREAST CANCER CELL LINE MDA-MB231.**	P4-45	374
Janina Brastovickytė-Stankevič **FLOOD FORECASTING SYSTEM UPGRADE BY ADDING ICE PHENOMENA**	P4-46	375

Austeja Juskaite, Karolis Kluonaitis, Jolita Badariene, Ruta Mameniskiene **ANXIETY AND DEPRESSION IN PEOPLE WITH EPILEPSY AND PATIENT WITH CORONARY ARTERY DISEASE: COMPARATIVE ANALYSIS**	P4-47	376
Janina Tutkuviene, Justina Katinaite, Austeja Juskaite **SELF-ESTEEM, ATTITUDE TOWARDS THE OWN BODY SIZE AND WEIGHT CONTROL OF WOMEN BEFORE AND DURING THE PREGNANCY**	P4-48	377
Laurynas Krikščikas, Steigvilė Byčenkienė, Genrik Mordas, Vidmantas Ulevičius **SOURCE APPORTIONMENT OF SECONDARY ORGANIC AEROSOL IN CONIFEROUS FOREST AREA**	P4-49	378
Yuliya Kunitskaya, Tatiana Kochetkova, Elizaveta Kavalenka, Elena Golubeva, Pavel Bulai **ENHANCEMENT OF RAT GLIOMA CELLS PROLIFERATION UNDER CHRONICAL ELECTRICAL STIMULATION AT 10 Hz**	P4-50	379
Domas Linkevičius, Aušra Saudargienė **COMBINING NEURON AND MCELL TO INVESTIGATE THE PROPERTIES OF CAV3-KV4 CHANNEL NANODOMAINS**	P4-51	380
Aleksey Lomako, Leanid Katkouski **COMBINATION ALGORITHM OF LOW RESOLUTION MULTISPECTRAL IMAGE AND HIGH RESOLUTION PANCHROMATIC IMAGE FOR THE BELARUSIAN SATELLITE DATA**	P4-52	381
Viktorija Mačiulytė, Edvinas Stonevičius **REMOTE SENSING OF VEGETATION CONDITIONS**	P4-53	382
Tatsiana Mikhailava, Dmitry Shchehrykovich **REMOVING SEASONALITY FROM FINANCIAL ASSETS (TIME SERIES) AS PART OF THE PRE-PROCESSING OF DATA.**	P4-54	383
Žygimantas Palaitis **COREALATION OF BOREHOLE HEAT EXCHANGER HEAT CONDUCTIVITY AND GEOLOGICAL CONDITIONS**	P4-55	384
Julija Pauraite, Genrik Mordas, Vidmantas Ulevicius **TEMPERATURE DEPENDING EMISSIONS OF BIOGENIC SECONDARY ORGANIC AEROSOL FROM FORESTS**	P4-56	385
Michał Mikołajczyk, David Pastor-Calle, Anna Pastuszczak, Rafał Kotyński **COMPRESSIVE PATTERN RECOGNITION USING PHASE-ONLY FILTERING**	P4-57	386
Anželika Pavlova, Giedrius Tušinskis, Feliksas Kuliešius **PREDICTION OF INTERNET TRAFFIC USING METHODS OF NONLINEAR DYNAMICS**	P4-58	387
Siarhei Sadau, Alena Kazlova **THE INFORMATION MODEL OF EMOTION FOR FACIAL EXPRESSION COMPONENTS**	P4-59	388
Zakaria Khaouch, Mustapha Zekraoui, Nourreeddine Kouider, Mustapha Mabrouki **MECHATRONIC DESIGN OF AN ELECTROMECHANICAL PITCHING SYSTEM FOR MORE REALISTIC LOAD SIMULATIONS OF WIND TURBINES BY MEANS OF THE BOND GRAPH METHODOLOGY**	P4-60	389
Sazzad Mahmood, Ondrej Hajdusek **TRANSCRIPTOME ANALYSIS OF BORRELIA AFZELII-INFECTED TICK IXODES RICINUS**	P4-61	390
Agnė Kalnaitytė, Saulius Bagdonas, Ričardas Rotomskis **PHOTOSTABILITY OF CORE AND CORE/SHELL QUANTUM DOTS IN THE PRESENCE OF ALBUMIN AND IN MOUSE FIBROBLAST CELLS**	P4-62	391
Elizaveta Kavalenka, Tatiana Kochetkova, Yuliya Kunitskaya, Elena Golubeva, Pavel Bulai **AMPLIFICATION OF HELA CELL PROLIFERATION BY PERIODIC PULSED ELECTRIC FIELD**	P4-63	392
Airina Mazėtytė, Romual Eimont, Agnė Vailionytė, Gintarė Garbenčiūtė, Vytautas Cėpla, Rūta Aldonytė, Ramūnas Valiokas **MICROFABRICATED COLLAGENOUS HYDROGELS AS SCAFFOLDS FOR 3D CELL CULTURE**	P4-64	393
Vytautas Samalavičius, Robert Mokrik **TRITIUM ACTIVITY DISTRIBUTION BY MONITORING DATA IN GROUNDWATER OF QUATERNARY AQUIFER SYSTEM, LITHUANIA**	P4-65	394
Lukas Plastinkin, Marija Matulionytė, Vilius Poderys, Ričardas Rotomskis **TEMPERATURE DEPENDENT SPECTRAL CHANGES OF PROTEIN STABILIZED GOLD NANOCLUSTERS DISPERSED IN PHOTORESIST SOLUTION.**	P4-66	395
Morta Marcinkutė, Vilius Poderys, Isabel Gessner, Sanjay Mathur, Eva Hemmer, Fiorenzo Vetrone, Ričardas Rotomskis **UPCONVERTING NANOPARTICLES OPTICAL PROPERTIES AND STABILITY DEPENDANCE ON PROTEINCOATING**	P4-67	396
Ilya Yakavets, Igor Yankovsky, Kiryl Barysau, Maksim Vorobyeu, Konstantin Jukov, Lina Bezdetnaya Lina, Vladimir Zorin **NANOSIZED INCLUSION COMPLEXES BETWEEN CYCLODEXTRINS AND PORPHYRINS**	P4-68	397
Jan Babiuch-Hall, Krzysztof Kacperski, Maciej Ustynowicz, Mgr Wojciech Adamczyk, Alexander Korneluk, Natalia Kuk, Kacper Ornat, Paweł Szczypkowski, Weronika Zdziarska, Jacek Szczytko **3D PRINTING IMAGING PHANTOMS FOR GAMMA SCINTIGRAPHY**	P4-69	398
Egle Marija Ramanauskaite **FROM STARDUST TO BLOOD STALLS: HOW INTERDISCIPLINARY CITIZEN SCIENCE IS CHANGING THE WAY WE DO RESEARCH**	P4-70	399

Invited speakers

BRIEF INTRODUCTION TO EVERYTHING

John Ellis

King‘s College London, UK; CERN

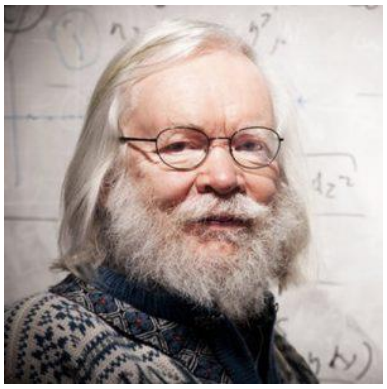

Jonathan Richard Ellis is one of the most respected scientists in modern-day physics with research interest in particle physics, astrophysics, cosmology and quantum gravity. A laureate of such prestigious accolades as the Maxwell Award and Paul Dirac Medal currently holds the Clerk Maxwell Professorship of Theoretical Physics at King’s College in London.

While a theoretical physicist at heart, most of Ellis’ research has been directly related to experiments, since it focuses on the phenomenological aspects of particle physics – the bridge between theory and experiment. Professor John Ellis has been a key contributor to the studies of physics of world-famous particle accelerators in CERN: writing the first surveys of possible LEP physics and possible beyond the Standard Model physics at LHC, leading Theory Division for a number of years.

John Ellis played an extremely important role in the discovery process of the Higgs boson. His remarkable ideas led to the discovery of the gluon and he has successfully predicted masses of both, bottom and top, quarks. In addition, his other merits include work on supersymmetric models and their relationships to the dark matter theories. And with publications on quantum gravity and string theory Ellis continues to contribute to the combined human knowledge.

As of 2016, based on INSPIRE-HEP reference system for scientific papers in particle physics and related fields, John Ellis is an author of over 1000 scientific papers with a total of 70,000 citations and an h-index of 139. Although a prolific researcher, he rarely shines away from the opportunity to share his passion with the world.

When did you decide that you would become a theoretical physicist?

I was always interested in the most fundamental things, and for me physics was the most fundamental science. For a long time I was torn between particle physics, astrophysics and cosmology, though my formal training was in particle physics. Finally, the field in which I am working now is a combination of the two.

What is the interplay between theory and experiment?

I feel there is a symbiotic relationship between theory and experiment that is a little bit like going around and around the accelerator, with the theories giving you a little kick each time, enabling experiments to understand things a bit better at higher energies.

The lecture is sponsored by EPS Young Minds.

MOLECULAR MOTORS AND SWITCHES

Ben Feringa

University of Groningen, Netherlands

Bernard Lucas "Ben" Feringa – laureate of 2016 Nobel Prize in Chemistry – synthetic chemist, specializing in molecular nanotechnology and homogeneous catalysis. Ben Feringa holds over 30 patents and has published over 750 peer reviewed research papers to date, cited more than 40 000 times and has an h-index in excess of 101. He has guided over 100 PhD students over his career.

His research performance is so exceptional that he is generally regarded as one of the world's most creative and productive chemists. He has achieved breakthroughs in various fields of chemistry, including organic synthesis, catalysis, supramolecular chemistry and nanotechnology.

His discovery in 1999 of the 'molecular motor', a light-driven rotating molecule, is widely recognized as a world-class breakthrough. The potential applications of this concept are as numerous as they are spectacular. The idea that molecular motors can transport themselves through the bloodstream, in order to deliver drugs to previously unreachable locations in the human body with a high degree of accuracy, is particularly inspiring. This work has been laying the ground-work for a key component of future molecular nanotechnology i.e. nanomachines and nanorobots powered by molecular motors.

Feringa has been awarded numerous prizes, including the 2004 Spinoza Prize, the highest Dutch prize in science. In 2011 he received the Van't Hoff medal. In May 2013 he was awarded a TOP grant for his research on molecular motors. In 2013 Feringa was awarded the Lilly European Distinguished Science Award, followed by the Marie Curie Medal. Also in 2013 he was awarded two important Japanese prizes, in 2014 followed by the prestigious Cope Scholar Award of the American Chemical Society. In 2015 he received the Chemistry for the Future Solvay Prize.

What is the secret to success in scientific publishing?

In my opinion a regular number of novel discoveries; the feeling of amazement reading a new issue of a journal and seeing remarkable findings.

What is your advice to young emerging scientists?

Not to be afraid to ask daring questions and to enter into an adventure with chemistry. The molecular world is unlimited and the molecular approach is central in tackling many of the major challenges in science and society ranging from materials and energy carriers to the drugs of the future.

LIGHT-MATTER INTERACTIONS IN PHOTONIC CRYSTAL FIBRES

Philip Russell

Max Planck Institute of Light, Germany

Philip Russell is a world renowned physicist who works as the Director at the Max-Planck Institute for the Science of Light and holds the Krupp Chair in Experimental Physics at the University of Erlangen-Nuremberg in Erlangen, Germany. With over 600 publications and a co-inventor status on 37 disclosures or patents under his name, Russell's work is considered boundary-pushing in the field of photonics.

After obtaining his PhD at the University of Oxford and subsequently working in research laboratories and universities in France, Germany and the USA he began laying out the theoretical groundwork for what would become a milestone in optical sciences – the invention of photonic crystal fibre (PCF).

This class of optical fibres is based on the properties of photonic crystals. Because of its ability to confine light in hollow cores or with confinement characteristics not possible in conventional optical fibre, PCF is now finding application in a wide range of areas, including but not limited to high-power lasers, broadband supercontinuum devices in metrology, optical-coherence tomography, spectroscopy and sensors. Russell and his team are still conducting ground-breaking research in this field.

As a prolific scientist he is a frequent awardee of various accolades some of which include: OSA's Joseph Fraunhofer Award/Robert M. Burley Prize for the invention of PCF, Royal Society/Wolfson Research Merit Award., Körber European Science Prize and many more. Philip Russell is also known of his work with optical societies, in particularly Optical Society of America, while motivating the upcoming generation.

You originally had an idea, back in 1991, for a photonic crystal fibre. Can you take me back to that period in time?

Well, back at that time I had been working on optical fibres for quite some years, I'd been at Southampton since 1986 and got involved in all sorts of things like Bragg gratings and various kinds of fibre devices. But prior to that, I'd also worked on periodic structures <…> did some experiments when I was in Germany, in that particular area of how light behaves in periodic structures. And I got sort of fascinated by it. Beautiful field.

So you're trying to sell this idea back in the early 90s of a periodic structure within the core of an optical fibre, which is going to enhance your ability to transmit light – was that the idea?

No, I was just curious – it was pure curiosity. Would it be possible to do this? And I can think of some nice things you might be able to do: you could, for example, put gas in the core and make lasers; you could maybe transmit very high power laser light because there's no solid material in the core, it wouldn't damage so easily. I didn't think of half of the possibilities.

The lecture is sponsored by OSA.

THz: IMAGING BEYOND LIGHT

Xi-Cheng Zhang

University of Rochester, USA

Xi-Cheng Zhang is a Chinese-American Physicist. His research is focused on the generation, detection, and applications of free-space THz beams with ultrafast optics. Zhang has received 29 US patents, authored and co-authored 24 books, 300 refereed papers cited more than 31 000 times (h-index above 78). He served as chairman of NATO Sensor and Electronics Technology Task Group and Chairman of NATO Exploratory Team.

Zhang is an internationally recognized scientist and leader in THz science and technology. Zhang's contribution to the development of THz time-domain spectroscopy, together with other leading researchers, has altered this scientifically important, but historically inaccessible, spectroscopic region. Research on THz waves has the potential to trigger advances, including nondestructive testing, homeland security, and biomedical applications.

His group has proved that under intense pulsed laser excitation the very air that we breathe is capable of generation and detection of THz waves. The use of air, instead of crystals or antennas, as both the emitter and the sensor, has led to the development of THz systems with unprecedented broad bandwidth and high peak electric field with application in imaging, linear and nonlinear material characterization. Moreover, using these techniques, remote generation and detection of THz waves is feasible, therefore one can envision standoff detection of threat or hazardous substances.

Zhang has been awarded numerous awards, including the National Science Foundation's CAREER award, Research Corporation's Cottrell Award, and China's Outstanding Scholar Award. He is a Fellow of IEEE, the Optical Society of America, and was elected a Fellow of the American Physics Society.

What are some future opportunities for THz science?

Some industrial THz systems can be used for homeland security and quality control applications, whereas THz communication systems offer unprecedented bandwidth for secure, ultrahigh-definition wireless video. THz sensing systems are attractive for environmental studies and space science, and THz imaging medical systems can be used for diagnosing and treating certain cancers and other diseases. THz/extreme ultraviolet table top systems can be used for dynamic imaging on the molecular level. A novel concept is combining THz photonic, electronic and plasmonic technologies.

Advice for students in learning, career, life?

I encourage students to set "blue sky" goals. Be ambitious; set your sights higher than you first think you may achieve. If you don't try, you definitely will not reach the goal, but if you give your best effort, you will make progress and you may surprise yourself with what you really can achieve.

The lecture is sponsored by OSA and Center for Physical Sciences & Technology.

GRAVITATIONAL WAVES

Eugenio Coccia

Gran Sasso Science Institute; University of Rome Tor Vergata, Italy

Eugenio Coccia is director of the Gran Sasso Science Institute (INFN Center for Advanced Studies) and professor of Physics at the University of Rome Tor Vergata. He is experimental physicist with a focus on the detection and study of gravitational waves.

Over 100 years ago, Albert Einstein predicted that gravitational waves could be detected, when he published his theory of general relativity. Einstein's theory states that large objects can alter the fabric of space and time, just as a rock causes ripples when dropped into a pool of water. Gravitational waves, or the ripples in space-time, would be created when two massive objects, such as black holes, came into contact. In the beginning of 2016, physicists detected the gravitational waves, what is believed to be one of the biggest scientific breakthroughs.

Eugenio Coccia is one of the authors of the discovery of gravitational waves, carried out by the LIGO-Virgo collaboration. He was also Director of the INFN Laboratories of the Gran Sasso and President of the Italian Society of General Relativity and Gravitational Physics. He led experiments on the Explorer gravitational wave detector at CERN and on the Nautilus detector at the INFN's laboratories. Since 2006, he has been participating in the experiments with the Virgo gravitational wave interferometer in Italy.

He is also Chair of the Gravitational Wave International Committee (GWIC) and member of the Council of the European Physical Society. He is the author of about 270 scientific articles and editor of six books in the field of astroparticle physics. For his contributions in this research, in 2012, he was awarded the "Giuseppe Occhialini" prize of the Institute of Physics and the Italian Physical Society, honored by Italian President in 2011 and received number of other national and international acknowledgments.

Thoughts on the detection of gravitational waves:

> *This is an exciting and unforgettable moment: I have spent 35 years of my life in this research. Detecting gravitational waves and proving the existence of black holes all in once is wonderful. Humanity has now a new sense: from now on we will not only see the cosmos, but also listen to its vibrations, its music.*

ENERGY BEYOND OIL

Michael Grätzel

École Polytechnique Fédérale de Lausanne, Switzerland

Michael Grätzel is one of the most renowned material scientists worldwide, who recently received the Millenium Technology Award. He is a pioneer in the area of energy and electron transfer reactions and their application on solar energy, optoelectronics, and in lithium-ion batteries. Grätzel has published more than 1300 papers, two books and holds over 50 patents. The Scientifc American ranks him among the top 50 scientists worldwide. He belongs to the top 3 most cited chemists (over 190,000 times, h-index 202!) and his name appears regularly when Nobel prizes are discussed.

Grätzel has developed a new type of photovoltaic cell, known as 'Grätzel cell', which is based on dyes and relies on the process of photosynthesis. Playing an important role in low-cost, large-scale solutions for renewable energy they have been moved to production by industry on the megawatt scale as light-weight flexible cells for powering portable electronic devices and as electricity producing glass panels for application in building integrated photovoltaics. In addition to photovoltaics, the concept of Grätzel cell can also be applied in batteries and hydrogen production, all important components of future energy needs.

Besides the mentioned applications, the dye sensitized solar cells have engendered perovskite solar cells that have recently revolutionized the whole field of photovoltaics reaching over 22% efficiency only a few years after their inception. This exceeds the performance of polycrystalline silicon solar cells. With never stopping improvement professor Grätzel continues to lead the field of the future solar energy.

Grätzel has received numerous awards including the Millennium 2000 European Innovation Prize, Faraday Medal of the British Royal Society, the Dutch Havinga Award, two McKinsey Venture awards, the Harvey Prize of Technion for pioneered research on energy and electron transfer reactions in mesoscopic-materials and their optoelectronic applications. His most recent awards include Marcel Benoist Prize & Albert Einstein World Award of Science.

How you became interested in the sciences?

I was driven by natural curiosity. I got good grades in science, and wanted to learn more about life in general, the laws of nature, the composition of materials and so on. I became infatuated with light, and the interaction between light and matter, and was very motivated to work in that area. I did my PhD in radiation chemistry, a postdoc in laser photolysis and then I worked on energy conversion, focusing on how to mimic natural photosynthesis.

Is there anything you wish to add about the future of nanotechnology?

Nanotechnology will play a pivotal role for energy generation and storage and will thrive in the future as mankind will rely on nanocrystalline systems to cover its needs in these vital fields.

LIGHT-HARVESTING NANOPARTICLES, CANCER THERAPY AND SOLAR STEAM GENERATION

Naomi Halas

Rice University, USA

Naomi J. Halas is a pioneering nanotechnologist at Rice University and a co-founder of Nanospectra Biosciences, a company developing photothermal therapies for cancer and other diseases. She is an author of more than 250 refereed publications, has more than 15 issued patents and has been cited nearly 60,000 times with an h-index of 120.

Her mission is to create a new type of nanoparticles meant to provide specific functions and evolve the field of nanotechnology. She aims to understand the physical properties of nanomaterials, both at the microscopic and macroscopic level, and to incorporate them into unique applications of societal and technological impact.

Halas is best known for her invention of nanoshells – tiny glass particles coated in gold, a new type of nanoparticles with tunable optical properties especially suited for biotechnology applications. Such nanoparticles have a huge potential in cancer treatment as it could work similarly to chemotherapy but without any toxic side-effects. She dreams of a world without cancer and believes that her team holds the key.

As a great example of interdisciplinary research, she is also a member of the National Academy of Sciences, the American Academy of Arts and Sciences and a fellow of the APS, MRS, OSA, IEEE and SPIE. She is a recipient of the R.W. Wood Prize from the Optical Society of America and 2014 Frank Isakson Prize from the American Physical Society for Optical Effects in Solids.

Your own background was very diverse. Has that served you well in your career?

Starting in music and going to chemistry and physics and laser science, was quite a liability. But it has turned out to be a tremendous asset. To have a background that is very broad and diverse has enabled me to be able to talk to people in many different disciplines and have enough expertise within each of those disciplines that we can develop intelligent and focused collaborations.

Do you ever think about your legacy as a scientist?

Well, as a graduate student, the sort of scientists that really stuck out in my mind were not necessarily the ones who had just done great science but who in addition had a wonderful human legacy. I decided that was the kind of faculty member I wanted to be.

This lecture is sponsored by SPIE.

GENE EDITING: NEW BRAVE WORLD

Robin Lovell Badge

Francis Crick Institute, UK

Robin Lovell-Badge is a Head of the Laboratory of Stem Cell Biology and Developmental Genetics at the Francis Crick Institute, United Kingdom. He is an author of almost 200 publications cited more than 20000 times and is one of the key experts who help society navigate the increasingly complex terrain of the new gene editing technologies.

Lovell-Badge was first thrust into the public limelight in the early 1990s when he co-discovered the Y-chromosome gene that orchestrates male development. He then used this gene to make a genetically female mouse develop as a male. As stem-cell sciences took off at the turn of the century, the British Parliament called upon him for advice in revising the Human Fertilisation and Embryonic Act. Since then he has regularly given scientific counsel in areas of public engagement and policy.

New technology, called CRISPR-Cas9, has given scientists the ability to alter a cell by removing genes, adding genes, or swapping one gene for another. When the first attempts to do this in human embryos happened, a once-fantastical piece of science fiction became an inevitable reality. The technique has made gene editing accurate and efficient enough for hundreds of labs around the world to try their luck. It is being used to change our food plants and other crops, but has even further prospects such as preventing diseases – creating genetically modified humans, which would open a new page in the world as we know it.

Robin Lovell-Badge was elected a member of EMBO in 1993, a Fellow of the Academy of Medical Sciences in 1999, and a fellow of the Royal Society in 2001. He has received the Louis Jeantet Prize for Medicine (1995), the Amory Prize (1996), the Feldberg Foundation Prize (2008), and the Waddington Medal of the British Society for Developmental Biology (2010).

What does CRISPR bring to gene editing that we didn't have before?

The CRISPR-Cas9 methods are simple to use, quick, precise and very efficient. They make the change in a gene just where you want it. They are also inexpensive and can be used in seemingly any species.

How long do you think it will be before we actually see people who have had genetic "corrections"?

Well I hope it's not right now, because I think we still need to understand how to use the methods properly. But at the rate things are going in this field, particularly with the CRISPR-Cas9 technology, you can imagine it could start happening within just a few years. I would much rather it happen in a properly regulated way. It certainly should not be just a free-for-all because that would be horrible — that would be crazy.

LIGHT-BASED BIOMATERIALS STRUCTURING FOR TISSUE ENGINEERING

Frederik Claeyssens

University of Sheffield, UK

Frederik Claeyssens is Lecturer in Biomaterials at the Department of Materials Science and Engineering in University of Sheffield, UK. His research expertise mainly focuses on laser processing of biomaterials, and its applications.

Frederik's research portfolio can be divided into three parts: coatings for biology (biocompatible coatings of semiconductors to be integrated into cell-silicon interfaces for biosensors), bioprinting (laser based techniques for printing biomolecules/cells; his developed technique is able to print viscous fluids containing DNA, proteins and even living cell) and biomaterials manufacture via microstereolithography (3D biocompatible/degradable polymer structures with micrometer resolution; hybrid biomaterials as 3D scaffolds for implants, tissue engineering and pharmaceutical testing).

Additionally, Frederik has also a keen research interest in computational solid state and biological chemistry. His previous work in this area includes predicting the stabilisation mechanism for the growth of polar wurtzite surfaces based on the existence of a low energy graphite-like structure (or h-BN) for ultra-thin wurtzite films. This model has recently been confirmed experimentally and forms the basis for understanding growth of polar surfaces in a large number of key technological materials (e.g. ZnO, GaN, CdSe and SiC). Besides that, Frederik has studied enzyme reactions on an unprecedented high level of theory, providing powerful new tools for modelling enzyme reactions, and enabling for the first time the study of enzyme reactions computationally with chemical accuracy.

Frederik Claeyssens does not shy away from the opportunities to highlight his work to a broader audience, including but not limited to publications on multiple media sites and various interviews. He is also a member of scientific editorial board for "The Open Materials Science Journal", member of Royal Society of Chemistry and Materials Research Society.

Thoughts on scaffold technology for nerve repair:

> *The nerve has small regions of 'cable' that go through from one end to the other end, you have a whole bunch of little cables inside a larger cable, that's what we tried to reproduce with this type of scaffold. <...> This technology could make a huge difference to patients suffering severe nerve damage.*

Oral session 1

Astrophysics and Astronomy

EFFECTS OF STOCHASTICITY IN THE EVOLUTION OF ISOLATED DWARF GALAXIES

Eimantas Ledinauskas[1,2], Kastytis Zubovas[1,2]

[1]Faculty of Physics, Vilnius University, Lithuania
[2]Department of Fundamental Research, National Centre for Physical Sciences and Technology, Lithuania
eimantasl@gmail.com

Isolated dwarf galaxies are scientifically interesting because of several reasons: 1) According to the most acknowledged cosmological model, ΛCDM, galaxies form and grow by hierarchical merging of smaller galaxies into bigger ones. If this paradigm is correct, then the presently observed isolated dwarf galaxies represent primordial building blocks out of which massive galaxies formed; 2) Because of shallow gravity potentials of dwarf galaxies their evolution is very sensitive to various baryonic processes (stellar feedback, heating by intergalactic radiation field, etc.). This could be useful in constraining models of these processes; 3) Mass-luminosity ratios of dwarf galaxies are several orders of magnitude larger than in massive galaxies. This means that dwarf galaxies should have relatively a lot more dark matter and could be very important in determining its nature; 4) Isolated dwarf galaxies are simpler systems than massive galaxies (no AGN, no mergers etc.) so their evolution could be modeled more easily and more reliably.

In this work I will present a semi-analytic isolated dwarf galaxy evolution model which tracks the stochastic accretion of baryonic and dark matter, star formation, stochastic stellar feedback and chemical evolution of a galaxy. Its basic structure is similar to other semi-analytic galaxy formation and evolution models (e.g.[1, 2]). Stochastic growth of the dark matter halo is modeled by using merger trees generated by a Monte Carlo algorithm based on the extended Press-Schecter theory [3]. Star formation is modeled by using an analytic model of star formation rate in molecule-poor galaxies [4]. Stochastic stellar feedback and metal enrichment is modeled by generating random stellar masses from an empirical probability density function [5]. This model is used to investigate how stochastic galaxy growth and stellar feedback could affect the evolution of an isolated dwarf galaxy and its observable properties. We find that stochasticity can create significantly different star formation histories in galaxies with the same present dynamical masses and this results in up to 40 % scatter in present-day stellar mass, gas mass and metallicity. Also we find that because of non-linear effects the most probable evolution and observable properties differ from the average model without stochastic effects. This might lead to disagreement between results of a model without stochastic effects and observations even if that model is correct.

[1] D. J. Croton, A. R. H. Stevens, C. Tonini, T. Garel, M. Bernyk, A. Bibiano, L. Hodkinson, S. J. Mutch, G. B. Poole, G. M. Shattow, Semi-Analytic Galaxy Evolution (SAGE): Model Calibration and Basic Results, Astrophysical Journal, Supplement **222**, 22 (2016).
[2] C. G. Lacey, C. M. Baugh, C. S. Frenk, A. J. Benson, R. G. Bower, S. Cole, V. Gonzalez-Perez, J. C. Helly, C. D. P. Lagos, P. D. Mitchell, A unified multiwavelength model of galaxy formation, Monthly Notices of the Royal Astronomical Society **462**, 38543911 (2016).
[3] H. Parkinson, S. Cole, J. Helly, Generating dark matter halo merger trees, Monthly Notices of the Royal Astronomical Society **383**, 557564 (2008).
[4] M. R. Krumholz, The star formation law in molecule-poor galaxies, Monthly Notices of the Royal Astronomical Society **436**, 27472762 (2013).
[5] P. Kroupa, On the variation of the initial mass function, Monthly Notices of the Royal Astronomical Society **322**, 231 (2001).

TIME DELAY OF RADIATION FROM PULSAR IN A BINARY SYSTEM THAT MOVES IN FIELD OF SCHWARZSCHILD BLACK HOLE

Alexander Gorbatsievich, Stanislav Komarov*, Alexander Tarasenko

Department of Theoretical Physics and Astrophysics, Belarusian State University, Nezavisimosti av., 4, 220030 Minsk, Belarus

*staskomarov@tut.by

Observation and analysis of pulsar radiation give us possibilities both to study our Universe and to perform various tests of theories of gravity. The studying of the Galactic Center (Sgr A*) for many years provides information about of the pulsars that are on tight orbits around the supermassive black hole (see, e. g., [1]). This allows us to perform study of gravity in a strong field regime. Some theoretical approaches of reconstruction of a compact object motion that moves in the field of a supermassive black hole are presented in many papers (see, e. g., [2, 3]).

Most of this works, that consider the general case of orientation of the orbit, use the post-Newtonian expansion of the arrival time of the pulse, to perform calculations (see, e. g., [4, 5, 6]). Our approach is based on full general relativistic treatment of the problem of calculating of time dilation. The presented formalism gives us possibilities to obtain the analytical expression for the pulses time of arrival in both cases: for the motion of a single point-like object and for the motion of a binary system in external gravitational field of a supermassive black hole.

Firstly, by using the tetrad formalism we infer the equations of motion of compact binary system in external gravitational field. Secondly, we obtain an general expression for the time dilation of the pulsar pulses under the assumption of the compactness of the system. And finally, we complete the calculation for the model binary system, that moves in external Schwarzschild field.

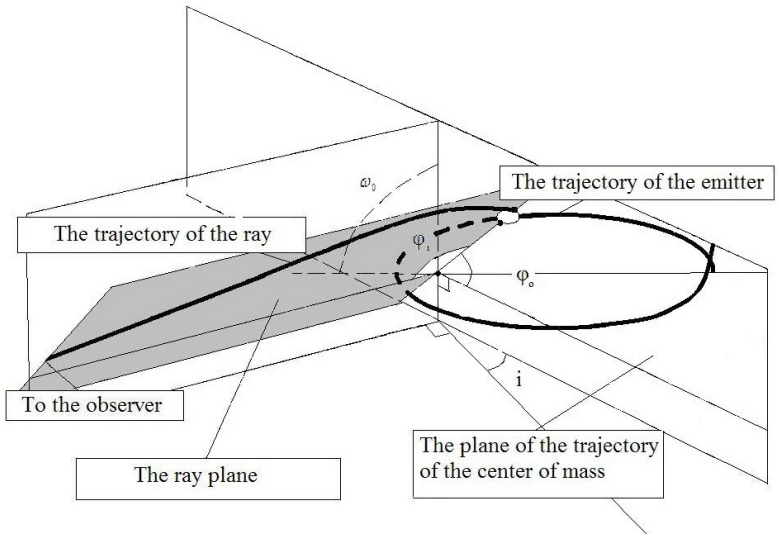

Fig. 1. Orbital parameters of the binary: ϕ_0 — the polar angle in the orbital plane; ϕ_r — the polar angle in the ray plane; i — the orbital inclination; ω_0 — the longitude of periastron (the set of parameters for the relative motion of the stars is not presented).

This approach without difficulties can be generalized on the case of Kerr, or Kerr-Newman supermassive black hole. By using the general expression for the time dilation that is discussed in our work, one can perform fitting of the time dilation data to reconstruct of the parameters of the motion (see Fig. 1) of the binary system near the Galactic Center.

[1] K. Perez, at. all. Extended hard-X-ray emission in the inner few parsecs of the Galaxy, Nature, **520**, P. 14353 (2015).
[2] A. Herrera-Aguilar, U. Nucamendi, Kerr black hole parameters in terms of the redshift/blueshift of the photons emited by geodesic particles, Phys. Rev. D, **92**, P. 045024, (2015).
[3] A. Tarasenko, Reconstruction of a compact object motion in the vicinity of a black hole by its electromagnetic radiation, Phys. Rev. D, **81**, P. 123005 (2010).
[4] Y. Zhang, Y. Lu, Q. Yu, On testing the Kerr metric of the massive black hole in the Galactic Center via stellar orbital motion: full general relativistic treatment, ApJ, **809**, P. 127 (2015).
[5] R. Angelil, P. Saha, D. Merrit, Toward relativistic orbit fitting of Galactic Center stars and pulsars, ApJ, **720**, P. 1303 (2010).
[6] K. Stovall, at. all. Observability of pulsar beam bending by the Sgr A* black hole, ApJ, **744**, P. 143 (2012).

ANALYSIS OF HYDRODYNAMIC MODEL OF ACTIVE GALACTIC NUCLEUS - INDUCED OUTFLOW

Aidas Sadauskas[1], Kastytis Zubovas[1,2]

[1] Faculty of Physics, Vilnius University, Lithuania
[2] Department of Fundamental Research, Centre for Physical Sciences and Technology, Lithuania
a.sadauskass@gmail.com

Active Galactic nuclei (AGN) are arguably one of the most important ingredients in Galaxy formation and evolution theories. Some observational facts indicate that Milky Way's central super massive black hole SgrA* might have been active in the past. Recently discovered giant gamma-ray structures called Fermi bubbles could be one of the SgrA* activity footprints. Therefore understanding the origin and evolution of these structures may help us better understand how AGN feedback influences host galaxies.

In this work we study the results of AGN outflow simulations designed to reproduce the Fermi bubbles. We are trying to determine whether it is possible to reproduce the observable properties of Fermi bubbles – their morphology and kinematics – by using a model of their recent origin 6 Myr ago. We find that for certain sets of AGN episode parameters (luminosity and duration), the outflow bubbles reach a size comparable to the Fermi bubbles, while their gas maintains projected velocities comparable to those observed. This research contributes to the understanding of the history of Galactic evolution.

INVARIANT MANIFOLDS AND SPACE MISSION DESIGN

Azem Hysa, Marsida Klemo

Department of Engineering Sciences, "Aleksandër Moisiu" University, Durrës, Albania
azemhysa@gmail.com

A more profound understanding of the available mission options has also emerged due to the theoretical, analytical, and numerical advances in many aspects of libration point mission design. We first find two periodic orbits around equilibrium points. One condition to be able to find such an orbit is to compute an intersection between two manifolds. To find an intersection, we introduce two dimensional sections $\Sigma_1 = \{(x,y) \in \mathbb{R}^2, x = 1-\mu, y < 0\}$, and $\Sigma_2 = \{(x,y) \in \mathbb{R}^2, x = 1-\mu, y > 0\}$ [1].

The instability of periodic orbits and similar periodic solutions can be exploited to analyze paths to and from every point on a given orbit. This work presents a systematic method for the designin of impulsive low-energy transferes between the Earth and the Moon by the explicit using invariant manifold theory. Invariant manifolds are tube-like structures along which a spacecraft may travel using no energy and this techniques usually only provied trajectories for uncontrolled spacecraft [2].

To generate trajectories that meet a variety of mission constraints, tools that provide insight into the available solution space are essential. The Poincare map is a powerful tool that, in combination with a constraint on the energy level, allows a reduction in dimension such that, for the planar problem, the system is reduced two-dimensions and the phase space is fully represented by the projection onto a plane [3].

We compute the intersection of the unstable manifold M_{L1}^U from L_1 and the stable manifold M_{L2}^S from L_2 with the space Σ_1. Of course, we can do the symmetric counterpart: stable manifold M_{L1}^S from L_1 and unstable manifold M_{L2}^U from L_2 with the space Σ_2 (see Fig. 1).

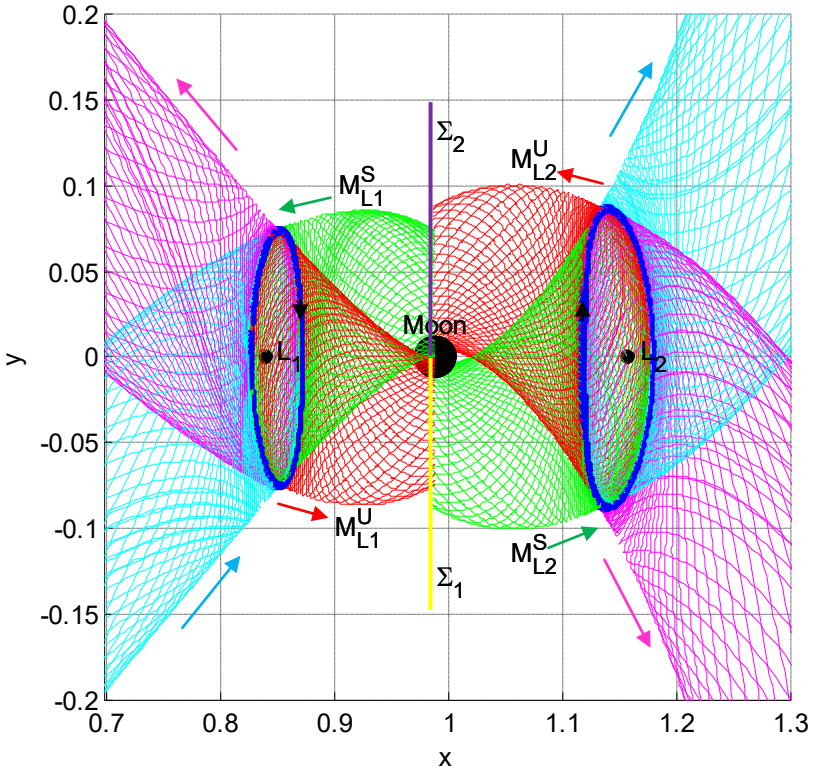

Fig.1. Stable (green) and unstable (red) manifolds associated with L_1 and L_2 periodic orbits (blue), respectively. The location of the Poincare sections Σ_1 (yellow) and Σ_2 (purple) are also shown.

Figure 1 shows 4 manifolds in the "neck" region in the Earth-Moon system, two periodic orbits around fixed points and the location of the Poincare sections. Unstable M_{L1}^U and stable M_{L2}^S manifolds respectively from L_1 and L_2 stopping at the plane Σ_1. Stable M_{L1}^S and unstable M_{L2}^U manifolds stopping at the plane Σ_2. Arrows indicate the direction of the motion of the spacecraft.

[1] M. Chupin, Th. Haberkorn, E. Trelat, Low-thrust lyapunov and halo to halo missions with L^2 minimization, 1511.02089v2 [math.OC] (2016).
[2] N.Truestadle, Using Invariant Manifolds of the Sun-Earth L_2 point for Asteroid Mining Operations, ASEN 5050 Spaceflight Dynamics (2012).
[3] A.F. Haapla, K.C. Howell F. Representations of higher-dimensional Poincaré maps with applications to spacecraft trajectory design, Acta Astronautica 96 23–41 (2014).

Oral session 2

Theoretical Physics

STRONG INTERACTIONS INVESTIGATION METHODS AT NA61/SHINE EXPERIMENT

Maciej Lewicki

Faculty of Physics and Astronomy, University of Wrocaw
malewick@cern.ch

NA61/SHINE [1] is an experiment nested at the CERN's *Super Proton Synchrotron* devoted to an investigation of the strong interactions – one of the four elementary forces present in our Universe. The experiment's programme focuses mainly on the phase transition between hadronic matter – the matter as we know it – and the *quark-gluon plasma* [2] – a new state of matter created at extreme conditions of high energy denisity.

The first part of my presentation will provide a didactic introduction into the World of sub-atomic interactions and the theory of *Quantum Chromo-Dynamics* (QCD). I will briefly invoke the main properties of the *Standard Model*, highlighting the recent development in the area of nucleon structure. The definition of quark-gluon plasma will be introduced.

In the second part of my talk I will explain a role of hadron collisions in the process of the investigation of QCD. I will present a connection between accelerator experiments and sub-atomic physics, with a special focus devoted to the **NA61/SHINE** research programme.

I will conlcude my presentaion with a description of particle identification methods in the **NA61** experiment, showing my own contribution to this large international project.

[1] N. Abgrall *et al.* [NA61 Collaboration], *NA61/SHINE facility at the CERN SPS: beams and detector system* JINST **9** (2014) P06005 doi:10.1088/1748-0221/9/06/P06005 [arXiv:1401.4699 [physics.ins-det]].

[2] E. Shuryak, *Physics of Strongly coupled Quark-Gluon Plasma* Prog. Part. Nucl. Phys. **62**, 48 (2009) doi:10.1016/j.ppnp.2008.09.001 [arXiv:0807.3033 [hep-ph]].

SIGNALS OF THE ONSET OF DECONFINEMENT @ CERN

Michał Naskręt[1,2]

[1]Department of Physics and Astronomy, University of Wroclaw, Poland
[2]CERN, Geneva, Switzerland
michal.naskret@uwr.edu.pl

The quark model of hadron classification proposed by Murray Gell-Mann [1] and George Zweig [2] in 1964 motivated the opinion that a new state of matter, namely strongly interacting matter composed of subhadronic constituents, may exist. Soon thereafter, quantum chromodynamics (QCD) was formulated as the theory of strong interactions, with quarks and gluons as elementary constituents.

At low temperatures and baryonic chemical potentials (e.g. in the nuclei) quarks are always confined in hadrons. Increasing temperature and density of hadrons lets us unleash the elementary constituents of matter. The state that is formed is called the quark-gluon plasma (QGP)[3, 4, 5]. The characteristic of this phenomenon is often presented in form of the phase diagram of strongly interacting matter (Figure 1). It demonstrates the conditions which have to occur for the quark-gluon plasma to be created. Exact position of the critical point and the onset of deconfinement remain the subject of intensive experimental and theoretical studies.

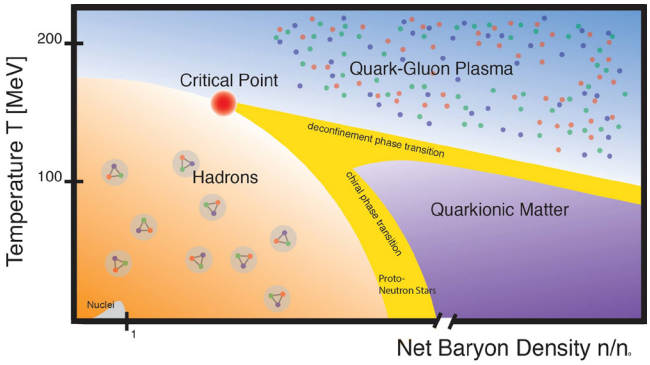

Fig. 1. Phases of strongly interacting matter.
Courtesy: Mark Alexander Randolph Kaltenborn

The quark-gluon plasma is a very mysterious and elusive state of matter. Probing signals of the existence of this deconfined phase is the main goal of the NA61/SHINE experiment at CERN. The task is performed by numerous measurements of particles produced in heavy-ion collisions. Three of the most distinct signals are: the kink, the dale and the step[6]. These mysterious names are related to shapes of different particle properties plotted against the collision energy.

In my talk I will describe one of the signals of deconfinement - the kink. This will be done with a description of the full process of heavy-ion collision data analysis in background. Based on the data obtained recently in the NA61/SHINE experiment I will follow through the whole path - from data acquisition to obtaining the final particle yields. In the end I will relate the results to the kink plot.

[1] M. Gell-Mann,Physics Letters 8, 214-125 (1964),
[2] G. Zweig,CERN Report No.8182/TH.401 (1964),
[3] Collins Perry, Phys. Rev. Lett. 34, 151 (1975),
[4] J.Rafelski, Phys. Rep. 88, 331–347 (1982),
[5] Müller, Rep. Prog. Phys. 58, 611–636 (1995),
[6] M. Gaździcki, M.Gorenstein and P. Seyboth, Acta Phys.Polon. B42, 307-351 (2011),

SUPERSYMMETRY BASED ALGEBRAIC APPROACH TO THE SCHRODINGER EIGENVALUE PROBLEM

Kiryl Piasotski

Research Institute for Nuclear Problems, Belarusian State University, Belarus
kirillpias@gmail.com

The ideas inspired by supersymmetry (SUSY) from quantum field theory provide an elegant basis for solving the Schrodinger equation. Supersymmetry in the context of nonrelativistic quantum mechanics was introduced by E. Witten, it is well understood since mid-eighties and had been extensively applied to solve numerous problems [1]. Various methods have been developed during last decades, for example, supersymmetry is often used to generate new potentials with known spectra [2], to study shape invariant and self-similar potentials [3], to solve bound and continuum states problems, as well as, qualitatively analyzing the scattering setups.

In this report general theory of Witten's $N = 2$, supersymmetric quantum mechanics is revised. Non-relativistic supersymmetry is established as a particular representation of the supercharges through the Schrodinger operators on the Hilbert space being a direct sum of bosonic and fermionic Hilbert spaces $\mathbf{H} = \mathbf{B} \oplus \mathbf{F}$. Theory in then applied to various types of problems mentioned above, including those which are not solvable otherwise. It is shown how SUSY method allows one to very quickly display some important characteristics of a given problem such as the eigenvalues, say avoiding the determination of function spectrum of the given operator. SUSY is then applied to the Flessas' [4], [5] anharmonicity problem in one dimension, the problem of conditional solvability of the anharmonic oscillator. It is shown that the problem of the bound states for the potential of the inharmonicity $n = 2m$ where m is odd admits an exact solution via the supersymmetry technique when the certain conditions on the potential parameters are satisfied.

[1] Fred Cooper, Avinash Khare, Uday Sukhatme 251; Physics Reports (1995)
[2] J. David and C. Fernndez; AIP Conference Proceedings 1287; (2010)
[3] Khare, A., Sukhatme, U. P.; Journal of Physics A: Mathematical and General 26; (1993)
[4] G. P. Flessas; Physics Letters A 72; (1979)
[5] G. P. Flessas; Physics Letters A 81; (1981)

DIFFUSION IN HETEROGENEOUS MEDIA

Rytis Kazakevičius, Julius Ruseckas

Institute of Theoretical Physics and Astronomy, Vilnius University, Lithuania
rytis.kazakevicius@tfai.vu.lt

There are many systems and processes where the time dependence of the central second moment is not linear as in the classical Brownian motion. Such family of processes is called anomalous diffusion [1]. Recently [2] it was suggested that the anomalous diffusion can be a result of heterogeneous diffusion process, where the diffusion coefficient depends on the position. The heterogeneous diffusion processes can yield subdiffusion as well as superdiffusion, depending on the behavior of the diffusion coefficient. Spatially dependent diffusion can occur in heterogeneous systems. For example, heterogeneous medium with steep gradients of the diffusivity can be created in thermophoresis experiments using a local variation of the temperature [3]. Here we consider heterogeneous diffusion processes with the power-law dependence of the diffusion coefficient on the position and investigate the influence of external forces on the resulting anomalous diffusion. We assume that not only the diffusion coefficient but also the external force has a power-law dependence on the position [4].

$$\mathrm{d}x = \sigma^2 \left(\eta - \frac{\nu}{2}\right) x^{2\eta-1}\mathrm{d}t + \sigma x^{\eta}\mathrm{d}W_t\,. \tag{1}$$

Here η is the power-law exponent of multiplicative noise, σ is the amplitude of noise and W_t is a standard Wiener process (Brownian motion). This stochastic differential equation is interpreted in Itô sense. Here ν is a new parameter describing the additional drift term. The meaning of the parameter ν is as follows: when the reflective boundaries at small positive $x = x_{\min}$ and large $x = x_{\max}$ are present, the steady-state PDF is a power-law function of position with the power-law exponent ν, $P_0(x) \sim x^{-\nu}$.

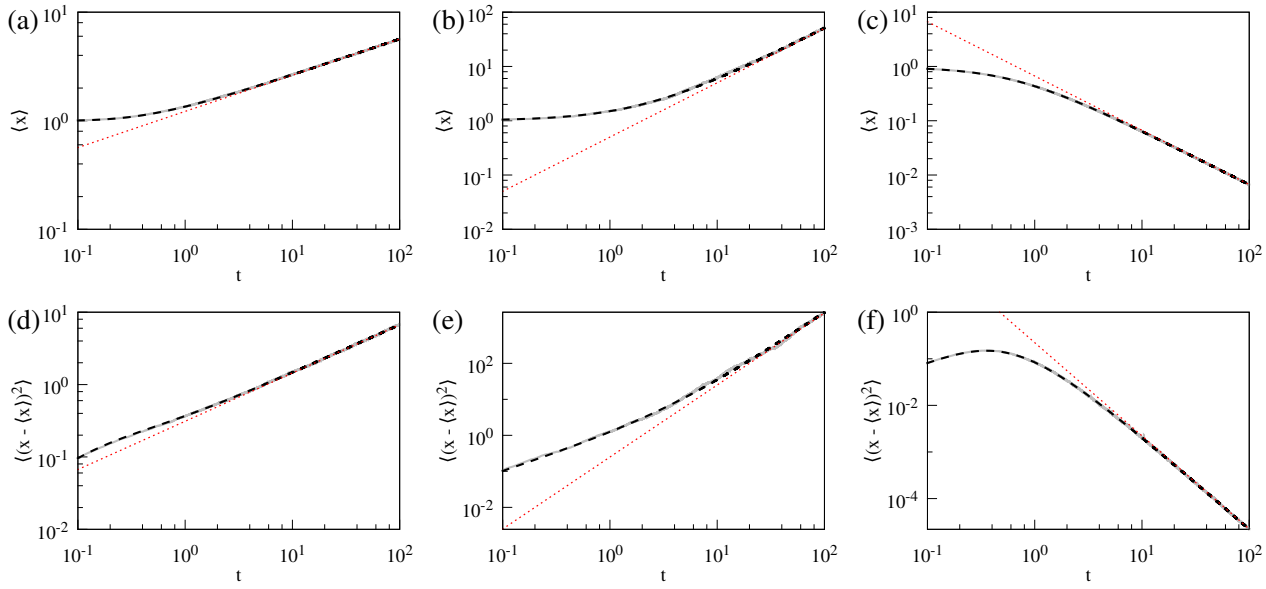

Fig. 1. Dependence of the mean (a,b,c) and variance (d,e,f) on time for various values of the parameters η and ν when the position of the diffusing particle changes according to Eq. (1). Dashed black lines show numerical result, dotted lines show the power-law dependence on time $\sim t^{1/[2(1-\eta)]}$ for (a,b,c) and $\sim t^{1/(1-\eta)}$ for (d,e,f). The parameters are $\sigma = 1$ and $\eta = -\frac{1}{2}$, $\nu = -1$ for (a,d); $\eta = \frac{1}{2}$, $\nu = 0$ for (b,c); $\eta = \frac{3}{2}$, $\nu = 5$ for (c,f). The initial position is $x_0 = 1$.

We found that the power-law exponent in the dependence of the mean square displacement on time does not depend on the external force; this force changes only the anomalous diffusion coefficient (see Fig. 1 (d) and (e)). Anomalous diffusion occur only for specific parameters values if $\nu < 3$ and $\eta < 1$ (or $\nu < 1$ and $\eta < 1$). As we can see in Fig. 1 (c) and (f), in other cases anomalous diffusion do not occur due localization of particles. Also, we obtain analytic expressions for the transition probability in two cases: when the power-law exponent in the external force is equal to $2\eta - 1$, where 2η is the power-law exponent in the dependence of the diffusion coefficient on the position, and when the external force has a linear dependence on the position.

[1] J. P. Bouchaud and A. Georges,Anomalous diffusion in disordered media: Statistical mechanisms, models and physical applications , Phys. Rep. **195**, 127-293 (1990).
[2] A. G. Cherstvy and R. Metzler, Nonergodicity, fluctuations, and criticality in heterogeneous diffusion processes, Phys. Rev. E **90**, 012134 (2014).
[3] C. B. Mast, S. Schink, U. Gerland and D. Braun, Escalation of polymerization in a thermal gradient, Proc. Natl. Acad. Sci. USA **110**, 8030-8035 (2013).
[4] J. Ruseckas and B. Kaulakys, Scaling properties of signals as origin of 1/f noise, J. Stat. Mech. P06005 (2014).

STATIONARY SOLUTIONS OF STOCHASTIC EQUATIONS WITH QUANTUM FLUCTUATIONS FOR ULTRACOLD GASES

Karolina Borek[1], Piotr Deuar[2]

[1]Faculty of Physics, University of Warsaw, Poland
[2]Institute of Physics, Polish Academy of Science, Warsaw, Poland
k.borek@student.uw.edu.pl

Experiments with ultracold quantum gases in recent years have come down to such low temperatures, that the effect of both classical and quantum fluctuations is noticeable. Therefore it became necessary to improve methods for numerical simulations that can let quantum fluctuations survive in the new physical regime. Several methods, which give promising results and represent the two types of fluctuations, have been proposed so far. However, they are unstable (Positive P) or lead to the equilibrium state which is not fully correct (Truncated Wigner). The aim of the study was to determine the physical constraints on the range in which the correct many body quantum state can be obtained by the Truncated Wigner method. To this end we have characterized an equilibrium states of Wigner stochastic equations and their properties.

- Ultracold gases at non-zero temperatures are fairly well described by the Stochastic Gross Pitaevskii Equation (SGPE)[1,2,3]:

$$\hbar\frac{\partial\varphi(x)}{\partial t} = -i(1-i\gamma)\mathscr{L}_{GP}\varphi(x) + \sqrt{2\gamma\hbar k_B T}\,\eta(x,t), \tag{1}$$

$$\langle\eta(x,t)^*\eta(x',t')\rangle = \delta(x-x')\delta(t-t'), \qquad \mathscr{L}_{GP} = -\frac{\hbar^2}{2m}\nabla^2 + V(x) - \mu + g|\varphi(x)|^2.$$

- Equation (1) does not include quantum fluctuations which become important at lower temperatures.
- WSGPE evolution equation (recently developed):

$$\frac{\partial\varphi(x,t)}{\partial t} = -i(1-i\gamma)\left(-\frac{1}{2}\frac{\partial^2}{\partial x^2} + V(x) - \mu + g\left(|\varphi|^2 - \frac{1}{\Delta x}\right)\right)\varphi + \sqrt{\gamma(2T + E - \mu + \frac{g}{\Delta x}\left(|\varphi|^2 - \frac{1}{\Delta x}\right))}\,\eta(t). \tag{2}$$

- Equation (2) includes also quantum fluctuations.

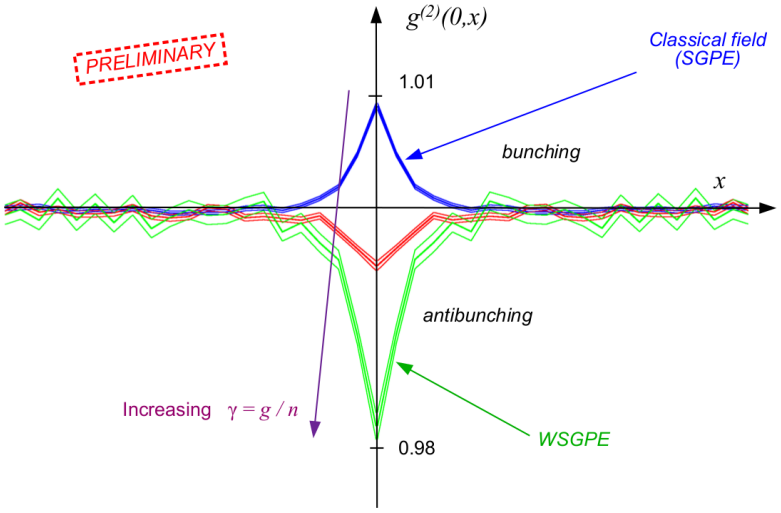

Fig. 1. $g^{(2)}(0,0) < 1 \longrightarrow$ antibunching. Only possible in nonclassical states. Here due to quantum fluctuaions.

- We have studied the local (one-mode) stationary solution in detail and found its asymptotic behaviours when the number of particles is large and when it is small. Importantly, we confimed that the virtual vacuum noise characteristic for quantum fltuations in the Wigner description is present even in the stationary solution. This is something that could not be achieved with previous standard truncated Wigner simulations.

[1] H.Stoof Journal of low temperature physics 114 (1-2), 11-108.
[2] Gardiner+Davis, J. Phys. B 36, 4732 (2003).
[3] A. S. Bradley and P. B. Blakie, Phys. Rev. A 90, 023631 (2014).

OPTICALLY DETECTABLE MAGNETIC RESONANCE SIGNALS IN NITROGEN - VACANCY CENTRES IN DIAMOND NEAR GROUND STATE LEVEL CROSSING

Laima Busaite, Marcis Auzinsh, Andris Berzins, Ruvin Ferber, Florian Gahbauer, Reinis Lazda

Laser Centre, University of Latvia, 19 Rainis Boulevard, Riga, Latvia, LV-1586
laima.busaite@lu.lv

Nitrogen-vacancy (NV) centres are powerful instruments in many areas of research, such as magnetometry, quantum information, nanoscale sensing. They have been used to detect individual electron spins and spin ensembles, measure the magnetic field distributions in biological signals, measure temperature and electric fields [1].

NV centres are defects in diamond crystal consisting of paired nitrogen (N) and vacancy (V) with two electrons in it. The NV centre has a triplet ground state with a zero-field splitting between the $m_s = 0$ and $m_s = \pm 1$ ground state sublevels of 2.87 GHz. The NV centre can be optically polarized due to nonradiative decay path from the excited state via singlet state that preferentially populates the $m_s = 0$ ground-state sublevel. This is the reason why the fluorescence from exciting $m_s = 0$ sublevel is more intense than the fluorescence from exciting the $m_s = \pm 1$ sublevels. In presence of microwave field population of $m_s = 0$ can be transferred to $m = \pm 1$ levels, decreasing the total detected fluorescence. The quanzation axis is defined by the NV centre axis direction. If the magnetic field is applied along this axis, the $m_s = \pm 1$ energies are shifted by $g_e \mu_B B_z$ or 2.8 MHz/G. At around 1025 G a crossing of ground state sublevels $m_s = 0$ and $m_s = -1$ appear and due to nuclear spin interaction of ^{14}N, the hyperfine states of $m_s = 0$ and $m_s = -1$ (states $|0,0\rangle$, $|-1,1\rangle$ and states $|0,-1\rangle$, $|-1,0\rangle$) are mixed and anticrossing is formed, creating complex energy level system (Fig. 1).

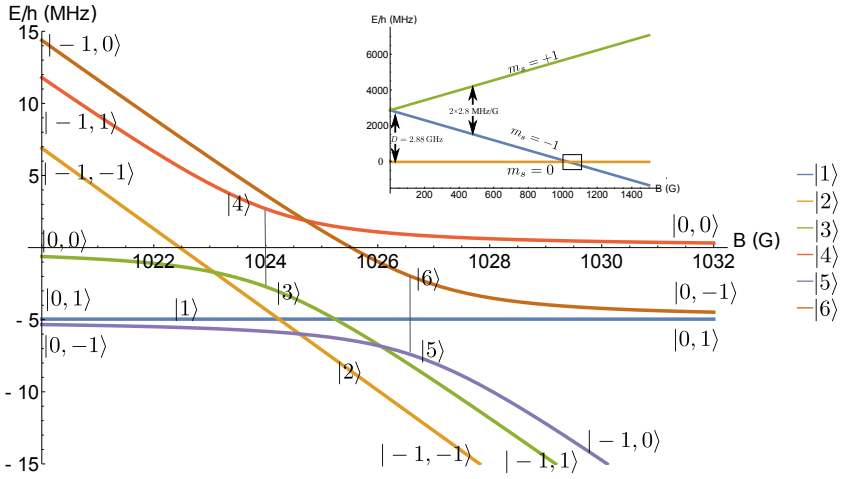

Fig. 1 Anticrossing of ground state hyperfine sublevels of $m_s = 0$ and $m_s = -1$ levels.

At the point of the anticrossing the wave functions of the ground state $m_s = 0$ and $m_s = -1$ hyperfine sublevels are mixed, modifying the probabilities for magnetic-dipole transition of microwave field.

System Hamiltonian of NV centre ground state including interaction of nuclear spin, magnetic field at the range of level crossing, is calculated as [2]

$$\hat{H} = g_e \mu_B \mathbf{B}\hat{\mathbf{S}} + \hat{\mathbf{S}}\hat{D}\hat{\mathbf{S}} + \hat{H}_{HFI}, \tag{1}$$

where $g_e \mu_B \mathbf{B}\hat{\mathbf{S}}$ describes interaction with magnetic field, $\hat{\mathbf{S}}\hat{D}\hat{\mathbf{S}}$ - describes spin - spin interaction of two unpaired electrons of NV centre and $\hat{H}_{HFI}$ - describes the hyperfine interaction of ^{14}N ($I_N = 1$).

To simulate microwave interaction spin step-up and step-down operators for magnetic-dipole transitions are used.

This research was kindly supported by the M-ERA.NET project MyND no. Z/15/1366.

[1] L. Rondin et al., *Magnetometry with nitrogen-vacancy defects in diamond, Reports on Progress in Physics*, **77**, 056503 (2014), arXiv:1311.5214

[2] G. D. Fuchs et al., *A quantum memory intrinsic to single nitrogenvacancy centres in diamond* Nature Physics **7**, 789793 (2011)

Oral session 3

Chemistry and Chemical Physics

CHARGE SEPARATION AND BAND SHIFT PHENOMENA IN REACTION CENTERS OF PURPLE BACTERIA

Eglė Bašinskaitė[1], David Paleček[1], Petra Edlund[2], Emil Gustavsson[2], Sebastian Westenhoff[2], Donatas Zigmantas[1]

[1] Department of Chemical Physics, Lund University, Sweden
[2]Department of Chemistry and Molecular Biology, University of Gothenburg, Sweden
egle.basinskaite@chemphys.lu.se

Reaction centers (RCs) from photosynthetic purple bacteria are pigment-protein complexes responsible for initial charge separation steps of photosynthesis. Following the isolation of RCs from photosynthetic bacteria, done in the late sixties, both arrangement of chromophores and the approximate structure of energy levels were determined. Nevertheless, due to the simple structure as well as high energy and charge transfer efficiency, which are not fully understood, the RCs is still one of the most investigated photosynthetic systems in the world [1].

The structure of quinones-depleted RCs (QDRCs) from purple non-sulfur bacteria *Rhodobacter sphaeroides* has six co-factors: two bacteriochlorophyll *a* molecules forming a strongly excitonically coupled dimer — a special pair (P), two monomeric bacteriochlorophyll *a* molecules (B_A and B_B) on each side of the dimer and two bacteriopheophytin *a* molecules (H_A and H_B). All pigments are arranged into two branches "A" and "B" featuring C_2 symmetry (see Fig. 1, (a)) [2]. Remarkably, although excitations are absorbed and transferred to the special pair through both branches, the electron is transferred just through the active "A" branch [3]. After the charge separation in the special pair and formation of the $P^+H_A^-$ state, the monomeric bacteriochlorophyll molecule B_A undergoes the electrochromic blue shift (indicated by an arrow in Fig. 1, (b)), which results in a well-known derivative shape signal, observed in the pump-probe measurements [4].

In this study, the QDRCs were investigated by the broadband two dimensional electronic spectroscopy at cryogenic temperature (77K). The study revealed dynamics with three characteristic lifetimes, which were observed also in the earlier studies: energy transfer of 100 fs, charge separation and electron transfer during 1.7 ps and a long (> 1 ns) lifetime for charge recombination. We also recorded the signals in the 2D spectra, arising from the band-shift phenomena and characterized them with the help of the double-sided Feynman diagram analysis. In addition, we observed the detailed features of the initial charge separation process, which have not been observed before.

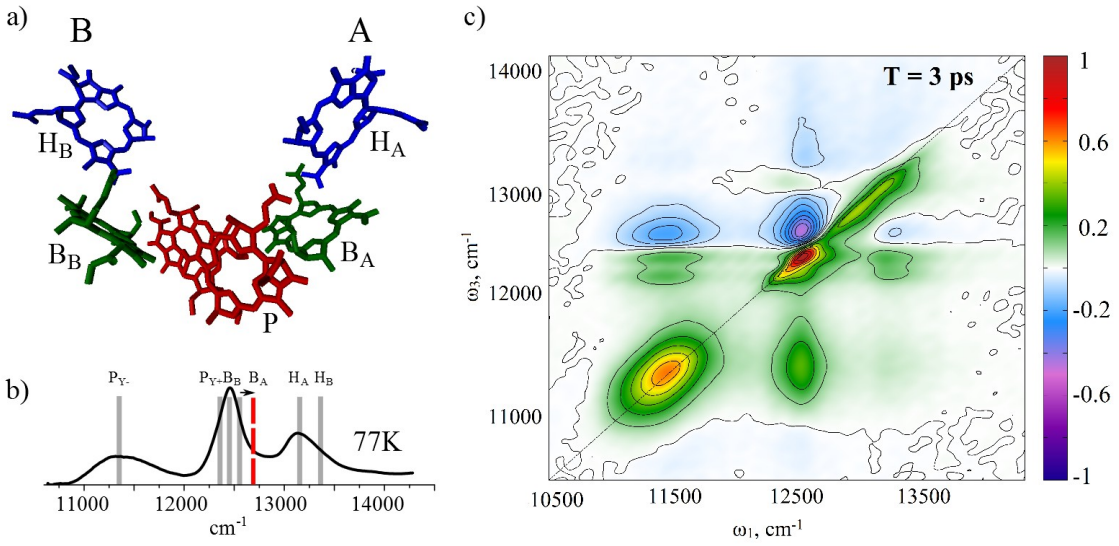

Fig. 1. Structure of quinones-depleted reaction center from *Rhodobacter sphaeroides* (a): special pair (P), two monomeric bacteriochlorophyll *a* molecules (B_A and B_B) and two bacteriopheophytin *a* molecules (H_A and H_B) [2]. Low temperature absorption spectrum (b), dashed line shows electrochromic shift of B_A level, and two-dimensional spectrum at the 3 ps population time (c).

[1] J. Breton, A. Vermeglio, *The photosynthetic Bacterial Reaction Center Structure and Dynamics,* (Plenum Press, New York, 1988).
[2] U. Ermler, G. Fritzsch, S.K. Buchanan, H. Michel, Structure of the photosynthetic reaction centre from Rhodobacter sphaeroides at 2.65 A resolution: cofactors and protein-cofactor interactions, Structure **2**, 925-936 (1994).
[3] C.K. Chan, T.J. DiMagno, et al., Mechanism of the initial charge separation in bacterial photosynthetic reaction centers, Biophysics **88**, 11202-11206 (1991).
[4] D.C. Arnett, C.C. Moser, P.L. Dutton, N.F. Scherer, The first events of photosynthesis: electronic coupling and energy transfer dynamics in the photosynthetic reaction center from Rhodobacter sphaeroides, Journal of Physical Chemistry B **103**, 2014-2032 (1999).

IMPACT OF ARYL-SUBSTITUENTS IN 3*H*-NAPHTHOPYRANS ON THE RATES OF PHOTOCHROMIC REACTION

Sabina Brazevic[1], Michel Sliwa[2], Yoichi Kobayashi[3], Jiro Abe[3], Gotard Burdzinski[1]

[1] Quantum Electronics Laboratory, Faculty of Physics, Adam Mickiewicz University in Poznań, Poland
[2] Laboratoire de Spectrochimie Infrarouge et Raman, LASIR, CNRS, UMR 8516, Université de Lille, France
[3] Department of Chemistry, School of Science and Engineering, Aoyama Gakuin University, Japan
sabina.brazevic@amu.edu.pl

Photochromic compounds, such as 3*H*-naphthopyrans, have been applied in commercially available photochromic lenses, for which one of the serious issue is a residual color. 3*H*-naphthopyrans generate the transoid-*cis* (TC) form and the transoid-*trans* (TT) form by UV light irradiation. Typically thermal back reaction of TC form takes from several seconds to tens of seconds while TT form needs much more time. Recently, the suppression of the generation of the TT form was achieved simply by substituting a bulky substituent to the 2-position of the naphthopyrans [1]. However, there are still open questions whether the bulky substituent may also interfere the ring-opening reaction and, as a result, decrease the photochromic reaction efficiency. On the other hand it is important to answer the question whether the TT form is completely suppressed or the lifetime of the TT form is accelerated faster than microseconds.

Herein, naphthopyrans with various aryl substituents (phenyl, naphthalenyl and pyrenyl, Fig. 1) at the 2-position were studied. Time-resolved UV-vis and mid-IR optical spectroscopies were applied to detect the transient species involved in the photoreaction over time-scale from subpicosecond to hundreds of microseconds. The early steps of the photoreaction through detection of C=O group (absorption band at ≈ 1650 cm^{-1}) as a result of the photoinduced ring-opening reaction were revealed by mid-IR ultrafast spectroscopy. Femtosecond UV-vis transient absorption data show an initial broad spectrum corresponding to the S_1 excited state of the closed-ring. At delays of few nanoseconds absorption band of TC form can be clearly observed (Fig 1).

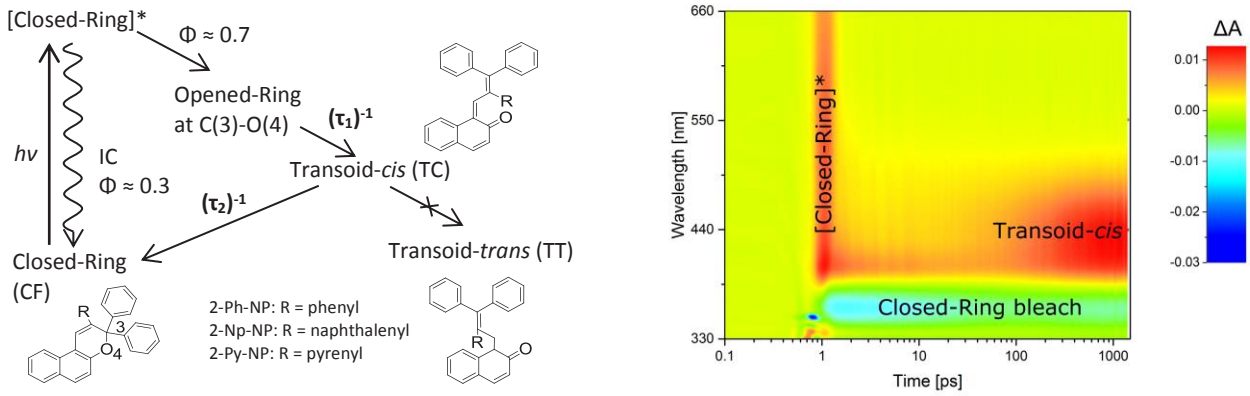

Fig. 1. Photochromic reaction mechanism for derivatives of 3*H*-naphthopyrans and transient UV-vis absorption data obtained in acetonitrile after photoexcitation of 2-Ph-NP at 320 nm (time zero was shifted to 1 ps in order to present the time axis in logarithmic scale)

On the basis of time-resolved data a following reaction mechanism emerges (Figure 1). At the beginning, closed-form (CF) absorbs the UV photon, which brings the molecule to the singlet excited state. The S_1 excited state lifetime τ_{S1} is very short (≈ 0.3 ps). In the next, the $S_1 \rightarrow S_0$ internal conversion repopulates back the initial CF (with yield $\Phi \approx 0.3$) or C(sp^3)-O bond cleavage occurs (with yield ≈ 0.7). The nascent opened-ring form structurally relaxes to the transoid-*cis* (TC) form with a rate of $(260\ ps)^{-1}$, $(400\ ps)^{-1}$ and $(950\ ps)^{-1}$ for phenyl, naphthalenyl and pyrenyl derivative, respectively, in acetonitrile. Over microsecond time-scale TC→TT reaction path is suppressed by the efficient TC→CF ring-closure reaction with color-fading rate equal to $(\text{tens of } \mu s)^{-1}$. The substituent R (Fig. 1) exerts a great impact on the rates of TC formation and the subsequent decay TC→CF. Important role is played by steric and electrostatic repulsions between the aryl substituent group and C=O group. Moreover, solvent viscosity and polarity affect the kinetics: a viscous solvent decelerates TC formation, while the opposite effect is caused by high solvent polarity. A polar solvent stabilizes the polar TC species and decelerates the subsequent TC→CF reaction.

In summary, the photocycle is free from TT isomer and fast TC→CF back-reaction takes place. These findings are not only important for fundamental photochemistry but also demonstrate the potential of these molecular designs for developing optimal photofunctional materials.

[1] K. Arai, Y. Kobayashi, J. Abe, Rational Molecular Designs for Drastic Acceleration of the Color-Fading Speed of Photochromic Naphthopyrans, Chem. Commun. **51**, 3057-3060 (2015)

NOVEL BRANCHED HOLE TRANSPORTING MATERIALS FOR PEROVSKITE SOLAR CELLS: SYNTHESIS AND PERFORMANCE

Artiom Magomedov[1], Paul Gratia[2], Michael Saliba[3], Tadas Malinauskas[1], Maryte Daskeviciene[1], M. Khaja Nazeeruddin[2], Vytautas Getautis

[1] Department of Organic Chemistry, Kaunas University of Technology, Lithuania
[2] Group for Molecular Engineering of Functional Materials, École Polytechnique Fédérale de Lausanne, Switzerland
[3] Laboratory for Photonics and Interfaces, École Polytechnique Fédérale de Lausanne, Switzerland
artiom.magomedov@ktu.edu

In 2009, perovskite (methylammonium lead iodide) absorbing layer was for the first time applied in the dye-sensitized solar cell (DSSC) resulting in a not very exciting 3.81 % efficiency [1]. Just in a few years efficiencies have reached 21.1 % for the small area devices [2] and 20.5 % for the >1 cm^2 area devices [3] making it promising technology for the low-cost modules manufacturing.

Architectures of the most efficient devices were translated and further developed from the field of the solid-state dye-sensitized solar cells (ssDSSC) and, therefore, 2,2',7,7'-tetrakis-(*N,N*-di-*p*-methoxyphenylamine)-9,9'-spirobifluorene (Spiro-OMeTAD) is used as a hole transporting material for the vast majority of the devices. However, price of the Spiro-OMeTAD is very high and hinders progress towards low-cost manufacturing (e.g. 349.5 EUR/g at Sigma-Aldrich). The reason resides in the complicated multi-step synthetic procedure [4], which is affordable in small quantities but is hardly scalable. Therefore, it is important to find alternative synthetic schemes with minimized number of steps and simple workup procedures.

Spiro-OMeTAD structure consists of two MeO-TPD (N^4,N^4,$N^{4'}$,$N^{4'}$-tetrakis(4-methoxyphenyl)[1,1'-biphenyl]-4,4'-diamine) fragments connected by non-conjugated spiro-linkage. The concept was introduced in 1996-1997 by J.Salbeck et al. [5] in order to get molecular glasses with relatively high glass transition temperatures while retaining good electronic properties.

In our work, instead of spiro-carbon, carbazole fragments are interconnected by non-conjugated small fragments. Synthesis scheme consists of only two steps starting from the commertially availible materials. In the first step “click” reaction of brominated carbazole with (bromomethyl)benzene derivatives was used for the core synthesis. This stage is very fast (10 min), does not require high temperature and the product is purified by non-chromatographic methods. On the second step diphenylamine fragment is introduced by palladium-catalysed Buchwald−Hartwig reaction. Even very large molecules (Mw=2613.11 Da) can be synthesised adopting general scheme.

Synthetized compounds are well soluble in common solvents and demonstrated similar performance in comparison to Spiro-OMeTAD.

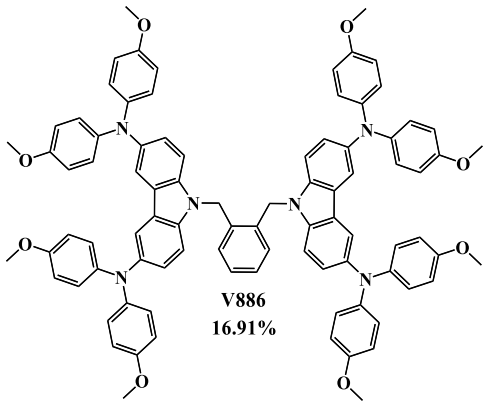

Fig. 1. Best performing material **V886** from the series of branched dimethoxydiphenylamine substituted carbazole derivatives.

[1] A. Kojima, K. Teshima, Y. Shirai, Organometal halide perovskites as visible-light sensitizers for photovoltaic cells**,** J. Am. Chem. Soc. **131**, 6050–6051 (2009).

[2] M. Saliba, T. Matsui et al., Cesium-containing triple cation perovskite solar cells: improved stability, reproducibility and high efficiency, Energy Environ. Sci **9**, 1989–1997 (2016).

[3] X. Li, D. Bi et al., A vacuum flash–assisted solution process for high-efficiency large-area perovskite solar cells, Science **353**, 58–62 (2016).

[4] T. P. I. Saragi, T. Spehr et al., Spiro compounds for organic optoelectronics, Chem. Rev. **107**, 1011–1065 (2007).

[5 J. Salbeck, Electroluminescence with organic compounds, Berichte der Bunsengesellschaft für Phys. Chemie **100**, 1667–1677 (1996).

MODIFIED PEROXIDASE-MIMMICKING DNAZYMES AND THEIR POTENCIAL USE AS BIOSENSORS

Krzysztof Żukowski, Joanna Kosman, Bernard Juskowiak

Laboratory of Bioanalitycal Chemistry, Faculty of Chemistry, Adam Mickiewicz University in Poznan, Poland
krzysztof.zukowski@amu.edu.pl

Four-strand DNA structures are nowadays one of the most interesting objects in research. The most popular of them is G-quadruplex (G4-DNA) formed by oligonucleotides rich in guanines. This structures are stabilized by a Hoogsteen's hydrogen bonds between guanines and also by a cation which is located in the channel between the guanine tetrads. There are exist few type of G-quadruplex topology: parallel, antiparallel and hybrid which formation depends on the direction of the DNA strands. [1,2]

The planar G-quartet is able to interact with other planar structures such as porphyrin molecule of hemin. It is proven that this complex is able to catalyze peroxidation reaction. The guanine's oxygen atoms interact with iron atom, located in a hemin molecule (cofactor of this DNAzyme). The increase of strength of this type of interaction affects also the peroxidase activity of this complex. Enzymes formed by nucleic acids are more stable in high temperature than protein enzymes which results in determination of a broader range of analytes. Other advantage of this system is facilitating the development of a new analytical strategies based on the phenomenon of hybridization between complementary DNA strands.[2,3]

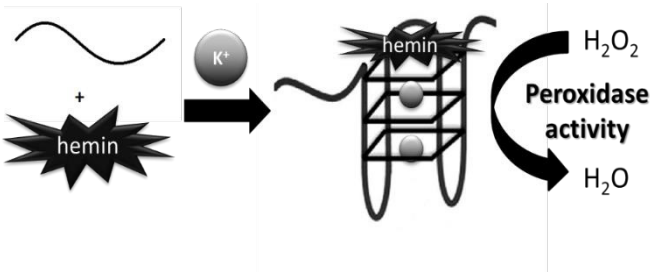

Fig. 1. Scheme of formation peroxidase mimicking DNAzyme.

Appropriate modification of DNAzyme allows on the improvement of the analytical signal produced during peroxidase reaction. This is possible through the covalent attachment of hemin, which allows to reduce the analytical signal from reference probe (hemin activity) and to avoid addition of surfactant. The second approach is the covalent attachment of the functionalized quantum dots to DNAzyme. This approach allows to apply the unique photochemical properties of quantum dots like high fluorescence. This modification enables also the generation of reactive forms of oxygen on the surface on quantum dots and allows to avoid the addition of hydrogen peroxide to the reaction medium. In our research we used amino modified oligonucleotides and NHS-active hemin ester in the reaction of amine coupling to create DNA-hemin covalent conjugate. We also used quantum dots functionalized by 3-mercaptopropionic acid to create a DNA-QD system. [3,4] This compounds were characterized spectroscopically. And in the next step we measured the most important feature of DNAzymes, the peroxidase activity. Our research prove that modified DNAzyme are a better alternative to horseradish peroxidase commonly used in ELISA or Western blot tests.

Acknowledgements:
This project was financed by National Science Center Poland grant no. 2013/10/M/ST4/00490.

[1] D. E. Gomez, R.G. Armando, H.G. Farina, P.L. Menna, C.S. Cerrudo, P.D. Ghiringhelli, D.F. Alonso, Int. J Oncol. **41,** 1561-1569 (2012)
[2] P. Travascio, Y. Liu, D. Sen, Chem. Biol. **5,** 505-517 (1998)
[3] S. Nakayama, J. Wang, H.O. Sintim, Dhem. Eur. J. **17,** 5691-5698 (2011)
[4] A.V. Gribas, S.P. Korolev, T.S. Zatsepin, M.B. Gottikh, I.Y. Sakharov, RSC Adv **5,** 5162-5167 (2015)

SORPTION PERFOMANCES OF $MgFe_2O_4$ SPINEL TOWARDS Mn^{2+}, Cu^{2+}, Co^{2+}, Ni^{2+} IONS

Marina Roshchina[1], Andrei Ivanets[2], Vladimir Prozorovich[2], Elena Petrova[1], Vladimir Pankov[1]

[1] Department of Physical Chemistry, Belarusian State University, Belarus
[2] Laboratory of adsorbents and adsorption processes, Institute of General and Inorganic Chemistry, National Academy of Sciences of Belarus
che.roschina@bsu.by

Due to industrialization the global production of products containing toxic metal ions has increased as well as amount of toxic metal-containing wastewater released by industries [1]. Removal of these metal ions from water has a high priority because even low concentration can cause severe damage to living organisms and the environment [2]. In recent years nanosized spinel ferrites (SFs) with a general formula MFe_2O_4 have been widely used as adsorbent due to their high surface area, simplicity of separation and superparamagnetic properties [3-4]. MFe_2O_4 nanoparticles have stronger magnetic features and higher chemical resistance to oxidation in comparison with iron oxide [5-7]. Also, SFs can be characterized by a high stability in acidic medium (pH 2.0-6.0) which allows to use it within a wide pH range. In addition, SFs are used as heterogeneous Fenton-like catalyst for oxidation destruction of organic materials in the presence of H_2O_2, O_3 and other ·OH precursors [8]. For all these reasons, SFs are attractive materials for the development of effective adsorbents and Fenton-like catalysts.

In this work $MgFe_2O_4$ was used as a non-toxic sorbent of heavy metal ions. Magnetic particles of $MgFe_2O_4$ were prepared by different methods: spray pyrolysis, glycine-nitrate combustion synthesis, co-precipitation, spray-drying synthesis. The phase composition and morphology of the powdered samples were investigated with X-ray diffraction (XRD), scanning (SEM) and transmission electron microscopy (TEM). Analysis of residual concentration of ions in aliquot was carried out using atomic absorption spectrometry (AAS). Percentage removal of metal ions and amount of metal ions adsorbed onto $MgFe_2O_4$ nanoparticles were calculated by the following equations:

$$\text{Removal ions } (\%) = \frac{(C_i - C_e)}{W} \cdot 100 \quad (1)$$

$$q_e = \left(\frac{C_i - C_e}{W}\right) \cdot V \quad (2)$$

Where q_e is the adsorption capacity (mg/g), W is the mass of adsorbent (g), V the volume of the solution (L), C_i and C_e are the initial and the equilibrium concentrations of metal ion (mg/L).

According data of adsorption different metal ions (Mn^{2+}, Cu^{2+}, Co^{2+}, Ni^{2+}) onto SFs, the method of SFs synthesis does not significant effect on the capacity of obtained magnetic adsorbents. It was determined that the highest adsorption affinity SFs demonstrate towards Mn^{2+} (101,8 mg/g) and Cu^{2+} (85,0 mg/g) ions. However, adsorption capacity slowly decreases with increasing of their crystallinity structure and magnetic properties. Therefore, it is necessary to determine the optimal conditions to preserve high sorption and magnetic properties of SFs.

[1] J.O. Nriagu, J.M. Pacyna, Quantitative assessment of worldwide contamination of air, water and soils by trace metals, Nature 333 134-139 (1988).
[2] S.L. Begg, B.A. Eijkelkamp, Z. Luo et al., Dysregulation of transition metal ion homeostasis is the molecular basis for cadmium toxicity in Streptococcus pneumoniae, Nat. Commun. 6 (2015).
[3] V. Srivastava, Y.C. Sharma, M. Sillanpää, Application of nano-magnesso ferrite (n-$MgFe_2O_4$) for the removal of Co^{2+} ions from synthetic wastewater: Kinetic, equilibrium and thermodynamic studies, Applied Surface Science 338 42-54 (2015).
[4] V. Srivastava, T. Kohout, M. Sillanpää, Potential of cobalt ferrite nanoparticles (CoFe2O4) for remediation of hexavalent chromium from synthetic and printing press wastewater, Environmental Chemical Engineering Vol 4 Iss 3 2213-3437 (2016).
[5] J. Liu, Y. Bin, M. Matsuo, Magnetic Behavior of Zn-Doped Fe_3O_4 Nanoparticles Estimated in Terms of Crystal Domain Size, J. Phys. Chem. C 116 134-143 (2012).
[6] Q. Song, Z.J. Zhang, Correlation between Spin−Orbital Coupling and the Superparamagnetic Properties in Magnetite and Cobalt Ferrite Spinel Nanocrystals, J. Phys. Chem. B 110 11205-11209 (2006).
[7] N.M. Jacob, P. Kuruva, G. Madras, T. Thomas, Purifying Water Containing Both Anionic and Cationic Species Using a (Zn, Cu)O, ZnO, and Cobalt Ferrite Based Multiphase Adsorbent System, Ind. Eng. Chem. Res. 52 16384-16395 (2013).
[8] Y. Wang, H. Zhao, M. Li, J. Fan, G. Zhao, Magnetic ordered mesoporous copper ferrite as a heterogeneous Fenton catalyst for the degradation of imidacloprid, Applied Catalysis B: Environmental 147 534-545 (2014).

SPOTTING THE UNUSUAL GEOMETRY IN CRYSTAL STRUCTURES

Andrius Merkys[1], Antanas Vaitkus[1], Saulius Gražulis[1,2]

[1]Vilnius University Institute of Biotechnology, Saulėtekio 7, LT-10257 Vilnius, Lithuania
[2]Vilnius University Faculty of Mathematics and Informatics, Naugarduko 24, LT-03225 Vilnius, Lithuania
andrius.merkys@gmail.com

X-ray crystallography, a method for the determination of 3D atomic structure of the matter, has been used extensively for more than a hundred years. X-ray structure determination, if carried out with adequate attention, has the power to provide incontrovertible evidence, upon which our knowledge is built [1], sometimes presenting scientists with unprecedented features of the matter, for example, the recent characterisation of six-coordinated carbon atom [2]. However, this method is not immune to errors, and the amount of crystal structures, submitted for publication each year, outnumbers experienced referees by orders of magnitude, resulting in incorrect structures being built [1]. Addressing this problem, we have developed an automated tool for the detection of unusual features in crystal structures. The tool is based on the knowledge of molecular geometry parameters – interatomic bond lengths, bond and dihedral angles, and crystal voids – extracted from the Crystallography Open Database (COD, http://www.crystallography.net) [3], the largest open-access resource of experimentally determined small molecule crystal structures. We have devised methods allowing automatic unsupervised extraction of molecular geometry parameters [4] and drawing conclusions about the geometry of crystal structures that are stored in the COD [5]. Our tool could be used to detect geometric outliers in crystal structures both by referees and model builders, having in mind that, obviously, “unusual” does not necessary mean “wrong”.

[1] Spek, A. L. Single-crystal Structure Validation With the Program PLATON. Journal of Applied Crystallography, 2003, 36, 7-13,
[2] Malischewski, M. & Seppelt, K. Crystal Structure Determination of the Pentagonal-Pyramidal Hexamethylbenzene Dication $C_6(CH_3)_6^{2+}$. Angewandte Chemie International Edition, 2016, 1, 368-370, http://dx.doi.org/10.1002/anie.201608795
[3] Gražulis, S.; Daškevič, A.; Merkys, A.; Chateigner, D.; Lutterotti, L.; Quirós, M.; Serebryanaya, N. R.; Moeck, P.; Downs, R. T. & Le Bail, A. Crystallography Open Database (COD): an open-access collection of crystal structures and platform for world-wide collaboration. Nucleic Acids Research, 2012, 40, D420-D427, http://nar.oxfordjournals.org/content/40/D1/D420.abstract
[4] Gražulis, S.; Merkys, A.; Vaitkus, A. & Okulič-Kazarinas, M. Computing stoichiometric molecular composition from crystal structures. Journal of Applied Crystallography, 2015, 48, 85-91, http://dx.doi.org/10.1107/S1600576714025904
[5] Merkys, A.; Long, F.; Murshudov, G. N. & Gražulis, S. Stereochemical statistics in Crystallography Open Database. Acta Crystallographica Section A, 2013, 69, s388-s389, http://scripts.iucr.org/cgi-bin/paper?S0108767313096621

Oral session 4

Spectroscopy, Methods and Devices for Physical Diagnostics

HEAVY METAL IONS SENSING BY SURFACE-ENHANCED RAMAN SCATTERING SPECTROSCOPY USING HYBRID MAGNETIC Fe_3O_4/Ag NANOPARTICLES

Marcin Witkowski[1,2], Agata Królikowska[1], Janusz Cukras[1], Jacek Szczytko[2], Jolanta Bukowska[1]

[1] Laboratory of Molecular Interactions, Faculty of Chemistry, University of Warsaw, Poland
[2] Institute of Experimental Physics, Faculty of Physics, University of Warsaw, Poland
mw358335@okwf.fuw.edu.pl

Innovation in modern spectroscopic methods, including surface-enhanced Raman scattering (SERS) spectroscopy, allows the emergence of new and relatively inexpensive procedures for chemical analysis. In this report we present our results on employing hybrid magnetic Fe_3O_4/Ag nanoparticles (NPs) fuctionalized with 5-(4-dimethylaminobenzylidene)rhodanine (DBRh) for sensing heavy metal ions.

Use of the magnetic NPs in SERS proves to be beneficial over pure noble metal NPs, as they can be easily and evenly distributed on the substrate, using external magnetic field, resulting in greater SERS signal intensity and uniformity across the surface sample. As the effect, we are able to perform more accurate and sensitive analysis using SERS signals. Such magnetic nanostructures are also great candidates for adsorption and place-exchange reactions, designed for selective removal of toxic species.

Hybrid Fe_3O_4/Ag NPs were prepared in a three-step synthesis [1,2]. In the first step, pure Fe_3O_4 NPs were obtained by coprecipitation of iron (II) and (III) salts with ammonia solution under hydrothermal conditions. In the second step, Fe_3O_4 NPs were modified using (3-aminopropyl)trimethoxysilane, serving as a linker. In the third step, Ag NPs were obtained by reduction of silver ions in the colloidal dispersion of modified Fe_3O_4 NPs, resulting in hybrid Fe_3O_4/Ag NPs connected *via* the linker. NPs were thoroughly examined after each step using various methods, including scanning electron microscopy (SEM), transmission electron microscopy (TEM), energy-dispersive X-ray spectroscopy (EDX), superconducting quantum interference device (SQUID) magnetometry and Raman spectroscopy, assessing the size distribution, magnetic properties and possible background signals in further Raman analysis.

DBRh was chosen as a probe molecule for SERS detection of heavy metals, as it is used in a colorimetric analysis of silver [3], mercury [4], gold [5] and palladium [6] ions. SERS response to solutions of heavy metal ions of varying concentrations was analysed in order to verify quantitative abilities of the proposed system.

[1] J. Du and C. Jing, Preparation of Fe_3O_4@Ag SERS substrate and its application in environmental Cr(VI) analysis, J. Colloid Interface Sci. **358**, 54–61 (2011).
[2] W. Yu, Y. Huang, L. Pei et al., Magnetic Fe_3O_4/Ag Hybrid Nanoparticles as Surface-Enhanced Raman Scattering Substrate for Trace Analysis of Furazolidone in Fish Feeds, J. Nanomater. **2014**, 1–8 (2014).
[3] S. Rastegarzadeh and V. Rezaei, A silver optical sensor based on 5(p-dimethylaminobenzylidene)rhodanine immobilized on a triacetylcellulose membrane, J. Anal. Chem. **63**, 897–901 (2008).
[4] G. Jangg, Die Bestimmung geringer Mengen Quecksilber, Z. Anal. Chem. **183**, 255–262 (1961).
[5] I. E. Lichtenstein, Improved rhodanine method for the spectrophotometric determination of gold, Anal. Chem. **47**, 465–468 (1975).
[6] G. H. Ayres and B. D. Narang, Spectrophotometric determination of palladium(II) with 5 (p-dimethylaminobenzylidene)rhodanine, Anal. Chim. Acta **24**, 241–249 (1961).

pH INFLUENCE ON SPECTROSCOPIC PROPERTIES OF GLUCOSE OXIDASE

Raminta Mazėtytė[1,2], Urtė Bubnienė[3], Arūnas Ramanavičius[2,3], Renata Karpič[2]

[1] Faculty of Physics, Vilnius University, Saulėtekio Ave. 9-III, LT-10222 Vilnius, Lithuania
[2] Institute of Physics, Center for Physical Sciences and Technology, Saulėtekio av. 3, LT-10257 Vilnius, Lithuania.
[3] Department of Physical Chemistry, Faculty of Chemistry, Vilnius University, Naugarduko Str. 24, LT-03225 Vilnius, Lithuania
raminta.mazetyte@gmail.com

The usage of biosensing systems is promising - rapid and accurate method for detection and analysis of various compounds. Nowadays one of the best-known and the most common biosensors are the glucose biosensors. They can accurately detect concentration of glucose in blood during a short period of time – it is very important to people with diabetes [1]. The active part of the biosensor is a glucose oxidase (GOx) enzyme immobilized on the surface of the electrode. When constructing an enzymatic biosensor, one of the most important aims is to determine properties of an enzyme under different environmental conditions. Despite the increasing number of studies on GOx, there is little information about the properties of the enzyme at different pH conditions [2].

Spectroscopic properties of glucose oxidase (GOx) and flavin adenine dinucleotide (FAD) were investigated in different acidity environments. The purpose of this research was to evaluate absorption and fluorescence spectra changes. The study of the absorption and fluorescence spectra and the measurements of relaxation times were carried out using a buffer with pH values from 2 to 8.

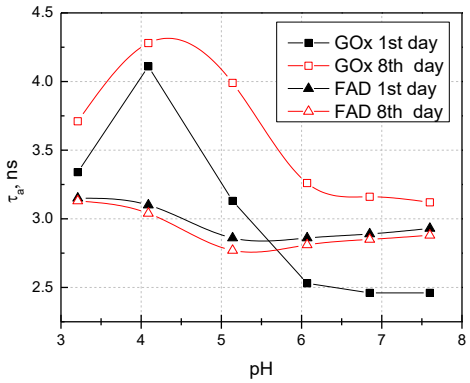

Fig.1. The average fluorescence lifetime dependence of buffer acidity.

GOx is a flavin adenine dinucleotide (FAD) containing glycoprotein. FAD is involved in enzymatic redox reactions and determines the enzyme's activity [3]. Glucose oxidase enzyme can exist in several different spatial conformations, therefore, FAD can also assume “twisted” (stacked) or “planar” (open) structure [4].

Fluorescence lifetimes of GOx and FAD have been measured at fixed 530 nm wavelength. The fluorescence decay kinetics were well approximated by two exponents, those were used to calculate the average relaxation time. Fig.1. shows the changes of average fluorescence lifetimes at different acidity of a buffer in the 1st and 8th days. The short component of fluorescence decay is associated with the "twisted" structure of FAD and the long component is associated with the "planar" spatial configuration of FAD. In a planar configuration, intramolecular electron transfer between the flavin isoalloxazine ring and the adenine moiety takes a longer time.

The data analysis showed that long component of FAD’s and GOx’s fluorescence decay dominated in the acidic environments. In alkaline solutions of FAD, the ratio of a short and long component begins to change from 1:16 to 2:3. The alkylation of GOx solution also starts exchanges of a ratio of short and long component, but it is not as significant as in the FAD’s case.

During this study, it was found that at pH 3 solution acidity, the fluorescence intensities of FAD and GOx at 530 nm were the most intense. At the optimum pH (6) fluorescence intensity of GOx was the lowest. The increased intensity of the fluorescence band of GOx is associated with dissociation of FAD from the enzyme. Also, the increase of GOx fluorescence is due to the substantially increased fluorescence of FAD at the acid buffers (pH 3 - 4).

[1] Eun-Hyung Yoo, Soo-Youn Lee, Glucose Biosensors: An Overview of Use in Clinical Practice, Sensors (2010), 10, 4558-4576.
[2] L. Dumitrascu, N. Stanciuc, G. E. Bahrim, A. Ciumac and I.Aprodu, pH and heat-dependent behaviour of glucose oxidase down to singlemolecule level by combined fluorescence spectroscopy and molecular modelling, J Sci Food Agric 2016; 96: 1906–1914.
[3] V. Leskovac, S. Trivic, G. Wohlfahrt, J. Kandrač, D. Peričin, Glucose oxidase from Aspergillus niger: the mechanism of action with molecular oxygen, quinones, and one-electron acceptors, The International Journal of Biochemistry & Cell Biology 37 (2005) 731–750.
[4] Y. Kao, Ch. Saxena, T. He, L. Guo, L. Wang, A. Sancar, D. ZhongA, Ultrafast Dynamics of Flavins in Five Redox States, J. Am. Chem. Soc., (2008), 130 (39), pp 13132–13139.

SHAPES OF MOLECULAR OPTICAL RESONANCES – TOWARDS A GLOBAL SOLUTION OF THE TRANSPORT-RELAXATION EQUATION

Nikodem Stolarczyk , Piotr Wcisło

Faculty of Physics, Astronomy and Informatics, Nicolaus Copernicus University in Toruń, Poland
280301@stud.umk.pl

One of the most important branch of molecular spectroscopy is modelling of spectral line shapes. Not only it is useful for science itself, like testing if the theoretical descriptions of the way the molecules interact are correct [1] or creating spectroscopic databases [2,3], but also can be applied to analyse human breathing [4], atmospheric measurements of the distant planets or ultra-accurate meteorology, e.g., exact determination of the Boltzmann constant [5].

The more exact results are demanded, the more accurate models need to be implemented. If the molecules do not collide, the shape of the spectral line can be described using a simple Gauss profile, since it is only the Doppler shift which contributes. In general the molecular collisions should be taken into account which makes the model of the line shapes much more complex. To describe the influence of the collisions on the line shapes, the transport-relaxation equation needs to be implemented [6]. It allows calculating the velocity distribution of optical coherence. However, in the general case it is extremely complicated to figure out the exact solution of the equation. Numerical attempts, which are widely used, are either time demanding or not accurate enough.

The main goal of the talk is to demonstrate another way of solving the transport-relaxation equation. In the usual considerations the value of function needs to be numerically found in every point of the parameter space of the model. The new way to tackle this problem is to calculate the value of function and its derivatives for one point only and expand this into a global solution using Taylor series. Since the analytical form of all the derivatives is simply obtainable, it is effortless for the computing engine to calculate the approximated values for the surrounding points. Moreover it would take much less time. Although it still has some drawbacks, the method is very efficient and has a potential for a wide implementation in future research.

[1] P. Wcisło, F. Thibault, H. Cybulski, and R. Ciuryło, Phys. Rev.A 91, 052505 (2015).
[2] P. Wcisło, I. E. Gordon, H. Tran, Y. Tan, S.-M. Hu, A.Campargue, S. Kassi, D. Romanini, C. Hill, R. V. Kochanov,and L. S. Rothman, J. Quant Spectrosc. Radiat. Transfer 177, pages 75-91 (2016).
[3] J. Domysławska, S. Wojtewicz, P. Masłowski, A. Cygan, K. ´Bielska, R. S. Trawinski, R. Ciuryło, and D. Lisak, ´ J. Quant.Spectrosc. Radiat.Transfer 169, 111 (2016).
[4] C. Wang and P. Sahay, Sensors 9, 8230 (2009)
[5] L. Moretti, A. Castrillo, E. Fasci, M. D. De Vizia, G. Casa, G.Galzerano, A. Merlone, P. Laporta, and L. Gianfrani, Phys. Rev. Lett. 111, 060803 (2013)
[6] A. D. May, Phys. Rev.A 59,3495 (1999)

BEAM COMBINATION OF DIODE LASERS FOR OPTO-ACOUSTIC APPLICATIONS

Sandeep Gawali, Luca Leggio, Miguel Sanchez, Sergio Rodriguez,
Daniel Gallego and Horacio Lamela

Department of Electronics technology, Universidad Carlos III de Madrid, Spain
sgawali@ing.uc3m.es

The typical laser sources used for Optoacoustic (OA) imaging are solid state lasers, tunable dye lasers, and optical parametric amplifiers. These sources can provide pulses with energies in the range of mJ, with duration of several ns. However, their use for clinical application is limited by their low repetition rates, high cost and bulky size that is mainly due to the power supply and cooling requirement. On the other hand, the high power diode lasers (HPDLs) could be an alternative to overcome all the limitations of the conventional laser sources [1].

In this works we implement HPDLs system for OA applications. The system consists of 6 diode lasers of stacked layers out of which three are operating at 905 nm and other three operating at 870 nm. The output from these diode lasers coupled into optical fiber bundle with the help of collimating and focusing lens. The fiber bundle consists of 7 input fibers of 200 micron core diameter and output diameter of 675 micron. We characterised the output of fiber bundle by measuring the time synchronization between output pulses and they are perfectly overlapped in time [2].

The measurement setup consists of incoming light from fiber bundle, cuvette holder assembly with 90° provision for ultrasonic transducer, preamplifier, oscilloscope, and PC to record the OA signals. The output of the fiber bundle is collimated by a lens with 12 mm focal length to illuminates the sample uniformly. The beam diameter is 7 mm and the calculated fluence is 37μJ/cm^2 for 905nm and 36 μJ/cm^2. The OA signal was measured in orthogonal direction with respect to the input light using a 1 MHz ultrasonic transducer. In order to test the linear combination of the optical pulses, we characterized the system by measuring the OA signal generated from 1% concentration of ink solution hosted in a 1 cm quartz cuvette.

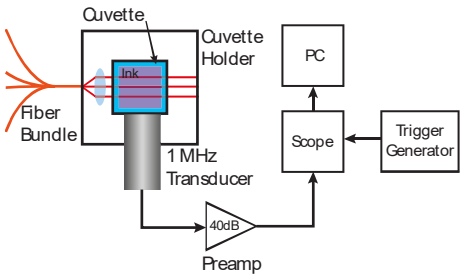

Fig. 1.Block diagram of OA measurement setup

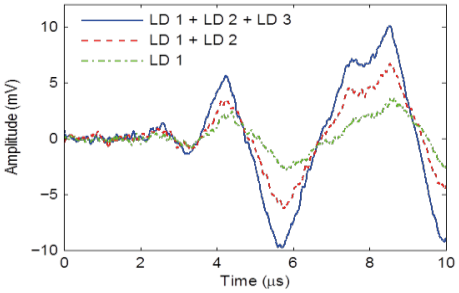

Fig. 2. OA signal generated from 1% ink solution

We have implemented a HPDLs based opto-acoustic system by combining power using optical fiber bundle from several diode lasers. In the OA detection scheme, we used a 90° measurement setup to detect OA signals from 1% ink solution. This 90 degree measurement scheme helps to reduce the signal generating on the surface of the detector in the case of transparent solution. This system can be further be scaled for multiwavelength applications.

[1] T.J. Allan and P.C Beard, Pulsed near-infrared laser diode excitation system for biomedical photoacoustic imaging, Optics letters, Vol. 31, No. 23 (2006).
[2] S. Gawali, L. Leggio, M. Sanchez, S. Rodriguez, E. Dadrasnia, D. Gallego and H. Lamela, Combining high power diode lasers using fiber bundles for beam delivery in optoacoustic endoscopy applications, SPIE Photonics Europe 2016, Proc. SPIE 9892.

Oral session 5

Laser Physics and Optical Technologies

FABRICATION OF PLANAR OPTICAL WAVEGUIDES BY TWO-PHOTON LITHOGRAPHY TO CONTROL BLOCH SURFACE WAVES IN PHOTONIC CRYSTALS

Natalia Kokareva, Kirill Safronov, Dmitrii Gulkin, Ksenia Abrashitova, Vladimir Bessonov, Andrey Fedyanin

Department of Physics, M. V. Lomonosov Moscow State University, Russia
kokareva@nanolab.phys.msu.ru

Bloch surface waves (BSW) are waves propagating along the surface of periodic multilayer structure – one-dimensional photonic crystal (PC). The BSW could be applied in different fields of photonics, for example in photonic integrated circuits. BSW have some advantages over the surface plasmon polaritons (SPP), which had been widely studied in recent years. Firstly, the BSW attenuate slowly than the SPP and have much longer propagation length. The characteristic propagation length of SPP is about 10-100 μm [1], while the propagation length of the BSW in experiments reaches the value of 500 μm [2]. Secondly, the excitation conditions of SPP are determined by the type of metal, while the BSW could be excited in the wide wavelength range. It could be done by selecting materials and thickness of layers of the PC. The possibility of making the dielectric stripe waveguide on the surface of the PC was demonstrated in the paper [3]. However, the photonic circuits such as splitters, interferometers and others haven't been fabricated on the surface of the PC yet. In this paper we would like to present the waveguide structures for the BSW fabricated on the surface of the PC by the method of two-photon lithography (TPL) - the method of direct laser writing based on the phenomenon of two-photon absorption (TPA), which causes the reaction of polymerization of special photosensitive material - photoresist.

By using the TPL scientists can achieve resolution beyond the diffraction limit: the size of voxel (3D pixel) could be less than 100 nm [4]. The TPL is also effective for fabricating planar structures, because this method allows scientists to make many structures in one exposure session. Moreover, if structures are being made in regime of overexposure (when the size of voxel is larger than the thickness of polymer film), it is easy to control shape and thickness of structures. This advantage of the TPL is very important for fabricating waveguide structures for the BSW, because BSW are very sensitive to the thickness of the top layer or the waveguide structure.

In our work we use photoresist SU-8 2015 for fabrication structures by the TPL. The standard procedure allows obtaining films with thickness about 15 mcm. For effective excitation of the BSW in our the PC the films with thickness of 200-400 nm are required. So, we decided to dilute photoresist with developer MR DEV 600. Solutions with different concentrations of SU-8 2015 were made. By using the solution with concentration 14,3% we achieved suitable film thickness and fabricated the waveguide structure, which supports excitation and propagation of the BSW. The Fig.1 and Fig.2 show one of the structures fabricated by our group. It is a waveguide for the BSW (20 mcm long and 2 mcm thick) with diffraction gratings and concentrating triangles. Fig 3. shows propagation of light in the waveguide structure. Furthermore, we have made other types of structures, such as interferometers and splitters and achieved resolution about 200 nm.

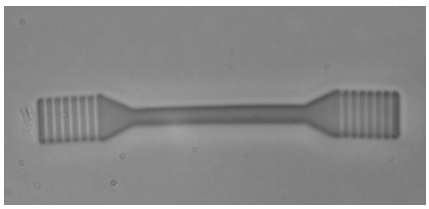

Fig.1 Optical image of the waveguide structure

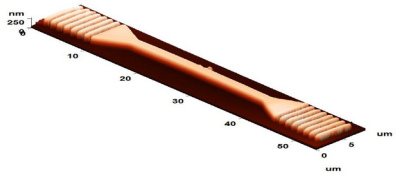

Fig.2 AFM image

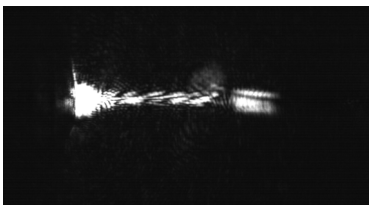

Fig 3. Propagation of light in the waveguide structure

[1] Barnes W. //Nature. – 2003. – Т. 424. – №. 6950. – С. 824-830.
[2]Descrovi E. et al. //Optics express. – 2008. – Т. 16. – №. 8. – С. 5453-5464.
[3]Descrovi E. et al. //Nano letters. – 2010. – Т. 10. – №. 6. – С. 2087-2091.
[4]Malinauskas M. et al. //Physics Reports. – 2013. – Т. 533. – №. 1. – С. 1-31

SUPERHYDROPHILIC PROPERTIES OF SILICON DRIVEN BY FEMTOSECOND PULSES

Iaroslav Gnilitskyi[1*], Alexandr S. Fedotov[2], Alexandr K. Fedotov[2], Leonardo Orazi[1]

[1] DISMI, University of Modena and Reggio Emilia (UNIMORE), Italy
[2] Physics Faculty, Belarusian State University, Belarus
iaroslav.gnilitskyi@unimore.it.com

Material processing by femtosecond lasers has recently drawn a lot of attention due to ablation mechanisms. The possibility of material processing by local heat induced damage has been implemented by using the femtosecond pulses, allowing the ablation of material with excellent precise and flexibility. Femtosecond pulses have also been exploited to generate laser-induced periodic surface structures (LIPSS) in various materials. The LIPSS can be described as a single step, maskless optical patterning techniques. The LIPSS applicability have been demonstrated for solar cells, plasmonics, colorizing metals, wettability and tribology [1]. However, LIPPS technique traditionally have problems with irregularity of structures and irreproducibility over large areas. Highly-regular LIPSS (HR-LIPSS) fabrication is advanced technique to produce LIPSS which can circumvent the periodicity and quality problems of LIPPS by using coherently scanning and laser parameters [2].

The effect of LIPSS on wetting properties has been investigated on metals, whereas the semiconductors had been almost neglected. Here, we present the investigation of effect HR-LIPSS on wetting properties of silicon surface. It also shown possibility to control of drop movement just with pre-drowing any form or shape pattern. Also, the effects of adding additional gases (N_2 and Ar) in laser treated zone and effect on wetting properties of LIPSS patterned Si were investigated.

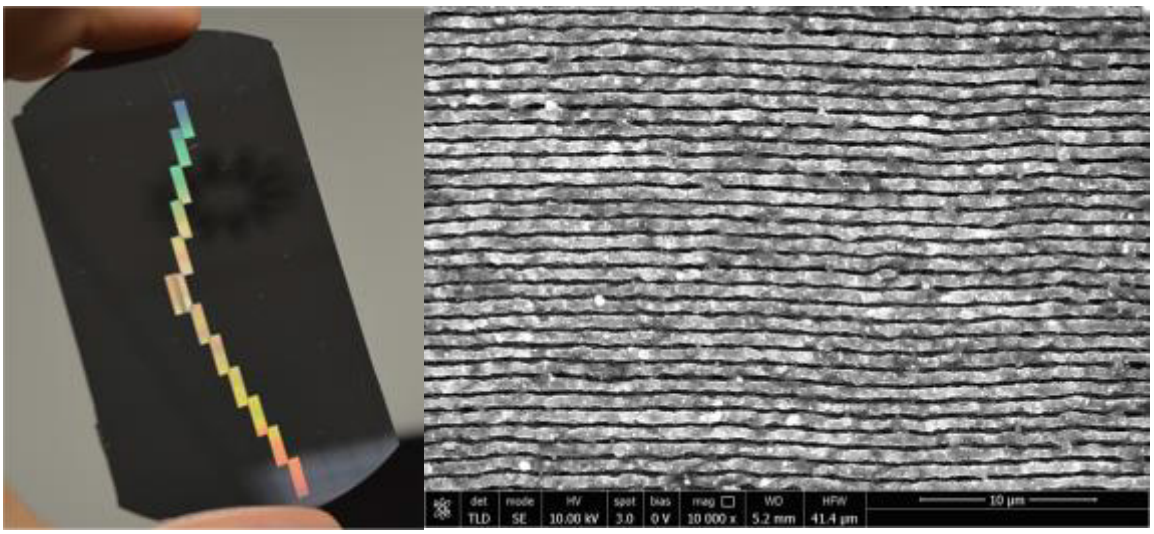

a b

Fig. 1. HR-LIPSS: (a) macroimage of generated path for testing water drops flow control; (b) SEM image with magnification (X 10000).

Fig. 1a reveals macroimage of HR-LIPSS-processed 4-inch silicon waver. Treated path looks with rainbow colours due to light diffraction. The topography of HR-LIPSS (Fig. 1b) present excellent regularity, bifurcation-free periodic structures with the average periodicity ~ 900 nm. The ripples oriented perpendicularly to the laser polarization.

The results demonstrate substantial effect of HR-LIPSS on wetting properties of silicon surface. The hydrophilic surface becomes superhydrophilic after femtosecond nanopatterning. It also shown possibility to control of dropmovement just with pre-drowing any form or shape pattern. The adding of N_2 and Ar in laser treated zone essentially influence on chemistry of the surface. Such advantage allows to control speed of liquid and made HR-LIPSS more flexible, bring up to new level of controlling also chemistry of the surface.

[1] I. Gnilitskyi et al., Nano patterning of AISI 316L stainless steel with nonlinear laser lithography: Sliding under dry and oil-lubricated conditions, Tribology International, **99**: 67-76 (2016)
[2] I. Gnilitskyi et al.,Mechanisms of high-regularity periodic structuring of silicon surface by sub-MHz repetition rate ultrashort laser pulse, Appl. Phys. Lett., **109**, 143101 (2016)

VOLUME HOLOGRAPHIC ELEMENTS ON THE BASIS OF PHENANTHRENEQUINONE – POLYMETHYLMETHACRYLATE COMPOSITE FOR MICROSCOPICAL APPLICATIONS

Sergey Nazarov[1,2*], Alexandra Trofimova[1], Elen Tolstik[2,3], Rainer Heintzmann[2,3], Uladzimir Mahilny[1], Alexei Tolstik[1]

[1] 1Belarusian State University, Nezavisimosti av. 4, 220030 Minsk, Belarus
[2] Leibniz Institute of Photonic Technology, Albert-Einstein-Straße 9, 07745 Jena, Germany
[3] Institute of Physical Chemistry and Abbe Center of Photonics, Friedrich Schiller University of Jena, Lessingstr. 10, 07743 Jena, Germany
sanazarov@tut.by

We present the results of investigation and applications of the volume holographic elements in microscopy. The volume phase holograms are formed in a thin (100-200μm) layers of polymethylmethacrylate containing 2-3 mol. % of phenanthrenequinone (PQ-PMMA) [1]. The idea of the work is to create holographic elements of two types: for the selective excitation and for simultaneously detection of the emission from different depths of the sample [2].

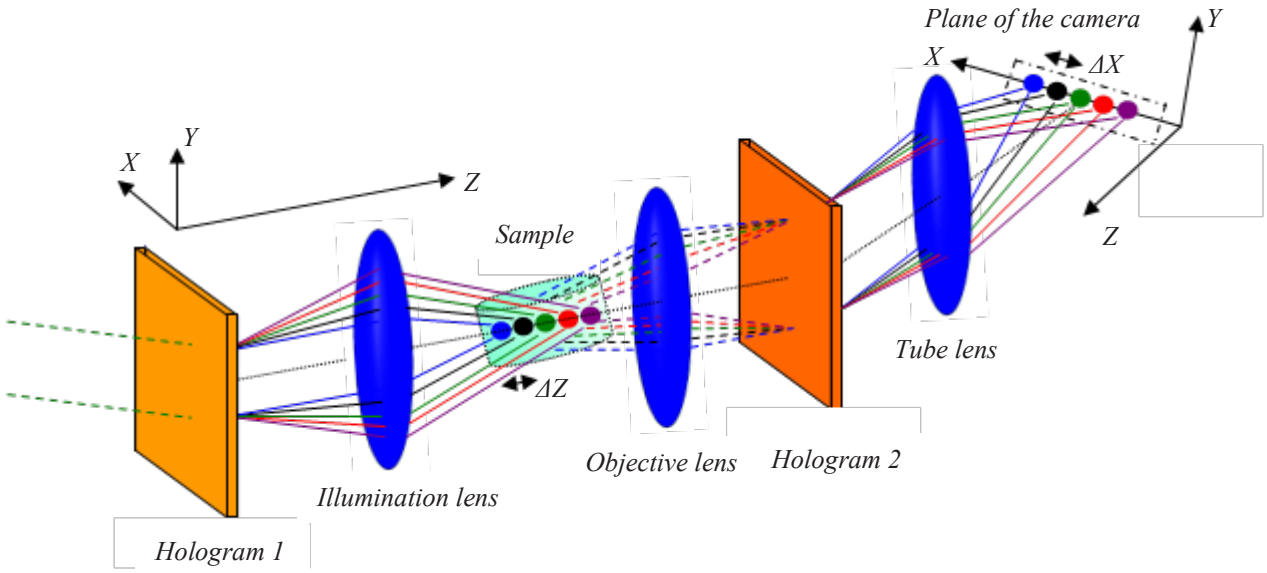

Fig. 1. Scheme of the optical microscope with two holographic elements.

Figure 1 shows the scheme of the realization of the microscope with such holographic elements. Excitation light beam falls on the first holographic element by Bragg angle. *Hologram 1* is the hologram for selective excitation. It forms diffracted beams with different divergence. Then, diffracted light is focused into the different areas within the sample by the *illumination lens*.

Fluorescence light from the sample is captured and transferred to the *Hologram 2* by the *objective lens*. *Hologram 2* is the multiplexed multifocus hologram. Light, illuminated from different *Z* position in the sample, will diffract by different angle in *XZ* plane. *Tube lens* forms images of different depths of the sample along *X* axis on the camera simultaneously.

Characteristics (selectivity, diffraction efficiency) of the holograms are investigated theoretically (by Kogelnik's coupled wave theory [3]) and experimentally. It is also mentioned about the possibility of using of the singular light beams to improve parameters of the volume holographic microscopy.

[1] U. Mahilny, A. Trofimova, S. Nazarov et al., Highly concentrated phenanthrenequinone – polymethylmethacrylate composite for thick reflection holograms recording at 532 nm, Optical Materials Express **6**, №11, 3427-3437 (2016).
[2] Y. Luo, P.J. Gelsinger, J.K. Barton et al., Optimization of multiplexed holographic gratings in PQ-PMMA for spectral-spatial imaging filters, Optics Letters **33,** №6, 566-568 (2008).
[3] H. Kogelnik, Coupled Wave Theory for Thick Hologram Gratings, The Bell System Technical Journal **46**, №9, 2909−2947 (1969).

PROPERTIES OF TERAHERTZ RADIATION GENERATED IN AIR BY TUNABLE FEMTOSECOND LASER PULSES

Karolis Adomavičius, Ernestas Žeimys, Benas Makauskas

Vilnius University Laser Research Center, Saulėtekio Ave. 10, LT-10223 Vilnius, Lithuania
Karolis.Adomavicius@ff.stud.vu.lt

Terahertz (THz) radiation represents the region in the electromagnetic spectrum between far-infrared and microwave radiation and has frequency between 0.1 THz and 10 THz (wavelength varies from 3 mm to 0.03 mm). Terahertz radiation has been investigated by scientists and engineers for over a decade; however compact and efficient THz sources and detectors are still to be developed. Therefore the research efforts in this field are rising, because THz radiation has many interesting and unique properties: for example it is non-ionizing, but safe for the living organisms. Moreover, it can easily pass through wood, paper, clothing, various plastics and ceramics. Furthermore, rotational and vibrational transitions of various molecules have energies in THz frequency range. This leads to a wide range of applications, such as spectroscopy, biological and medical imaging, detection of hazardous materials, security screening, etc.

We have conducted experiments using two different methods. In both of them THz radiation was generated in ambient air. As a pump source the Ti:Sapphire laser system (central wavelength about 790 nm) operating at 1 kHz and delivering 9 mJ pulses of 35 fs (FWHM) duration was used. In the first experiment THz radiation was generated by mixing laser and its second harmonic pulses (bichromatic pump). The second experiment was more complicated, since for the air excitation we have used three laser pulses of different wavelengths: the laser radiation along with the signal (1140-1600 nm) and idler (1600-2600 nm) wavesof the Optical Parametric Amplifier (OPA), pumped by the same Ti:Sapphire laser.

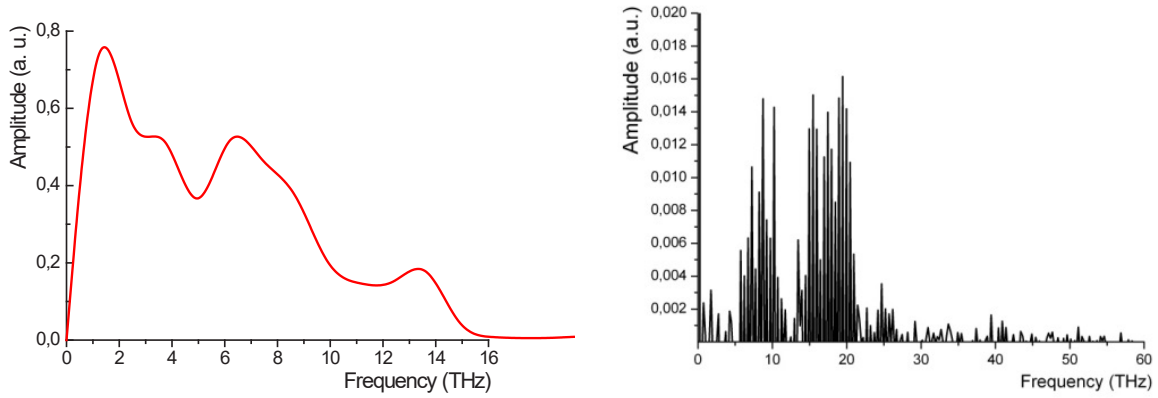

Fig.1. Spectra of THz radiation, obtained using (left) two-colour and (right) three-colour laser pulses.

During the experiments the dependencies of various THz radiation properties (spectral properties, divergence and generation efficiency) on the pump pulse energy and wavelength have been investigated. Though in both cases (two- and three-colour pump) conical THz emission with the apex angle of a few degrees was generated, the three-colour excitation was found to be more efficient than that obtained using the bichromatic pump pulses. In addition, the spectral width of THz emission generated by three-colour pump pulses was considerably larger in comparison with the spectrum of THz radiation, induced by two-colour laser pulses.

In conclusion, spatial and spectral characteristics of THz radiation, generated in air by both the two- and three-colour femtosecond laser pulses have been investigated. The obtained results indicate that both methods are suitable for the broadband (of over 10 THz) THz radiation generation.

FOCAL LINE ENGINEERING OF VECTOR OPTICAL BEAMS WITH PARABOLIC SYMMETRY CROSS-SECTION

Tomas Kontrimas[1,2], Sergejus Orlovas[1]

[1]Center for Physical Sciences and Technology, Sauletekio av. 3, Vilnius, Lithuania
[2]Faculty of Physics, Vilnius University, Sauletekio av. 9, Vilnius, Lithuania
tomas.kontrimas@ff.stud.vu.lt

There is a need in the industry and many applications for beams with long focal lines and small focal spot sizes (so-called "Optical needles" [1]). Nondifracting Bessel beam is a common example of the simplest optical needle and a coherent superposition of Bessel beams can be used to create further optical needles, especially, if the control of the longitudinal distribution of the electric field is desired. However, a controllably asymmetric profile of the beam cross-section is of particular interest for some applications, including laser micromachining of structures with dimensions comparable to the wavelength of incident light.

Using superpositions of nondiffracting parabolic beams we can control their longitudinal profile (Fig. 1a) and parabolically shape transverse distribution profile [2] (Fig. 1b). Because of distinct parabolically shaped cross-section this type of beam profile can be perceived as an "optical shovel".

Classical vectorization method described in [3] ($\mathbf{M}=\nabla\times\mathbf{a}\psi$, $\mathbf{N}=\frac{1}{k}\nabla\times\mathbf{M}$; where $\mathbf{a}$ is Cartesian unit vector, k is wave vector and ψ - scalar parabolic solution) is used to obtain vector solutions, because scalar solutions become not valid when the beam is focused with lens of high numerical aperture and polarization control is needed.

A method of optical engineering of a focal line with controllable longitudinal profile, parabolically shaped cross-section and orientation of electric field will be presented. An optical shovel created by superposition of 101 monochromatic vector parabolic beams is demonstrated - the longitudinal distribution profile on axis and the transverse distribution profile (bending) can be varied independently.

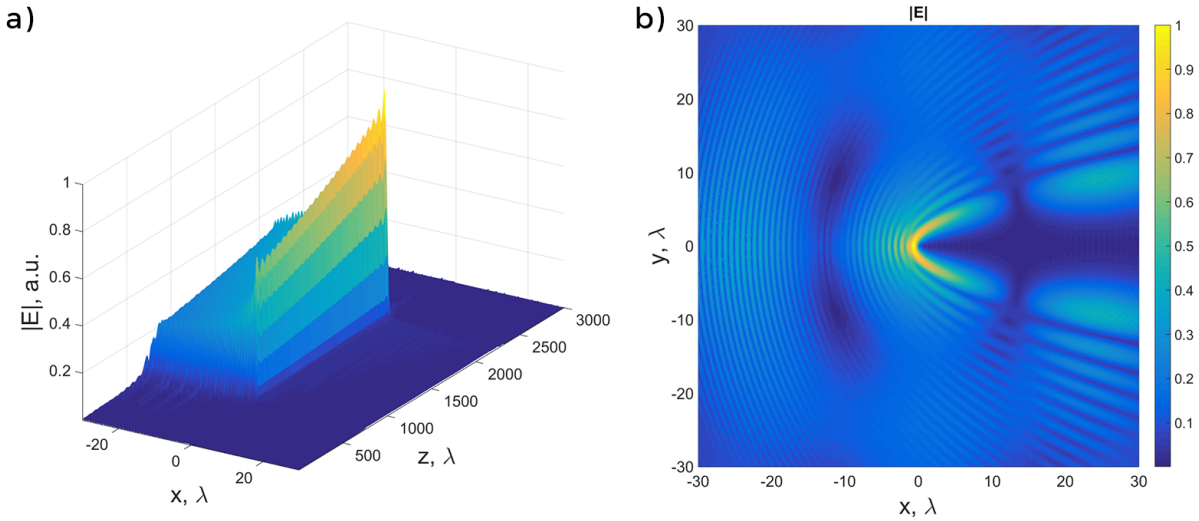

Fig. 1. Longitudinal (a) and transverse (b) distribution of intensity in superposition of monochromatic vector parabolic beams.

[1] M. Zhu, Q. Cao, H. Gao, Creation of a 50,000 long needle-like field with 0.36 width, JOSA A 31, 500504 (2014).
[2] M. A. Bandres, J. C. Gutirrez-Vega, and S. Chvez-Cerda, Parabolic nondiffracting optical wavefields, Opt. Lett. 29 , 44-46, (2004).
[3] J. Stratton, *Electromagnetic Theory*, An IEEE Press classic reissue (Wiley, 2007).

"OPTICAL KNIVES" ENGINEERING USING VECTOR MATHIEU BEAMS

Vitalis Vosylius[1,2], Sergejus Orlovas[1]

[1]Center of Physical Sciences and Technology, Industrial Laboratory for Photonic Technologies, Lithuania
[2]Faculty of Physics, Vilnius University, Lithuania
vitalis.vosylius@ff.stud.vu.lt

Nondiffracting beams define a family of electromagnetic fields that can propagate for certain distances without diffraction. Bessel beams are best known and broadly applied type of nondiffracting beams [1]. Another example of the nondiffrating beams is so-called Mathieu beams that possess elliptical distribution of an electric field in transverse plane [2]. Mathieu beams have some practical applications due to its asymmetrical cross-section [3]. Furthermore, these beams have eccentricity parameter, which provides additional degree of freedom and allows us to perceive them as "optical knives" of controllable width. Also, by controlling the orientation of electric field in "optical knives", long focal lines with small transverse dimensions can be obtained.

In this work we derive vector Mathieu beams from scalar *m*-th order Mathieu beams [2] using classical technique, described in [3]. We analyze the properties of vector Mathieu beams with different *m* values and eccentricity parameters. Also we study the possibility to construct the long focal lines that have elliptical cross sections. As an example, we construct optical knives with desired profiles on axis by superposing monochromatic vector Mathieu beams. The distribution of electric field in transverse plane is presented in Fig 1. (a) and the geometry of defined longitudinal distribution of the beam intensity is depicted in Fig. 1. (b).

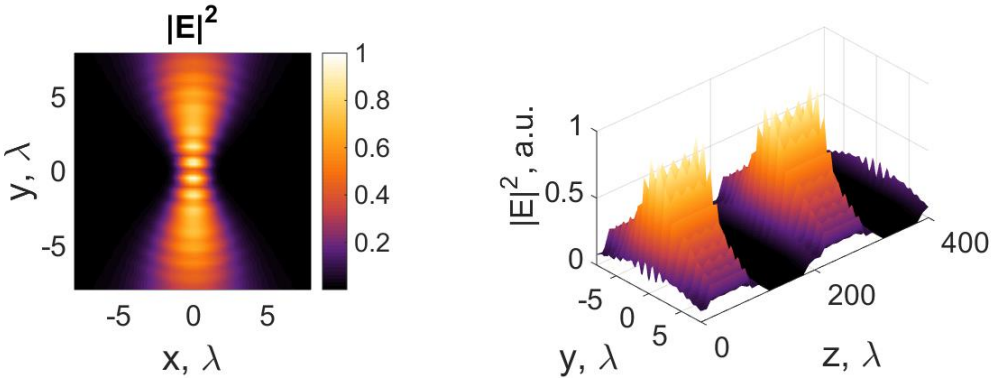

(a) (b)

Fig. 1 Distributions of intensity of superposition of zero order even Mathieu beam in transverse (a) and longitudinal (b) planes.

In conclusion, we have showed that using optical engineering methods, optical knives can be obtained using vector Mathieu beams and width can be controlled by changing the polarization of electric field. Experimental implementation to form Mathieu beams will be discussed as well.

[1] M. Duocastella, C. B. Arnold, "Bessel and annular beams for materials processing, " Laser Photon. Rev. **6**, 607–621 (2012).
[2] A. Chafiq, Z. Hricha, and A. Belafhal. "Propagation properties of vector Mathieu–Gauss beams." Opt. Commun., 275, 165-169 (2007).
[3] C. Alpmann, R. Bowman, M. Woerdemann, M. Padgett, and C. Denz, "Mathieu beams as versatile light moulds for 3D micro particle assemblies," Opt. Express 18, 26084-26091 (2010).
[4] J. Stratton, *Electromagnetic Theory*, An IEEE Press classic reissue (Wiley, 2007).

Oral session 6

Material Science and Modern Technologies

TERAHERTZ EMISSION FROM AlGaN/GaN STRUCTURES WITH GRATING-TYPE ELECTRODE

Vytautas Jakštas, Ignas Grigelionis, Vytautas Janonis, Irmantas Kašalynas

Department of Optoelectronics, Center for Physical Science and Technology, Lithuania
vytautas.jakstas@ftmc.lt

Terahertz (THz) radiation consists of electromagnetic waves occupying an electromagnetic spectrum between microwaves and infrared light (frequencies from 0.3 THz to 3 THz). It denotes a boundary of techniques used for generation of the electromagnetic waves. On the one hand THz frequency is too high for a conventional electronics, but on the other hand it is too low to be effectively covered by photonics. More and more THz applications in medicine, spectroscopy, safety and imaging systems have been reported recently despite the lack of efficient THz sources [1]. Therefore, research on compact and scalable THz sources capable to operate at room temperature are carried out. High-electron-mobility transistor (HEMT) with a plasmonic channel of two-dimensional electron gas (2DEG) is a potential candidate to fulfil these requirements [2].

In this work we report on thermally and electrically excited THz emission from AlGaN/GaN HEMTs grown by metalorganic chemical vapour deposition (MOCVD). Electric contacts were formed using optimized photolithography, thin metal film deposition and rapid thermal annealing in N_2 ambient (in case of ohmic contacts). The gate contact of the HEMT (Fig. 1) consisted of grating with different period (varying from 200 nm to 7 μm) and width of metal fingers (varying from 120 nm to 4 μm). The grating approach was used to couple out THz radiation via the plasma instabilities in the 2DEG channel [2].

At first the samples were heated by an external heater and the THz emission was measured at fixed temperature. The quantitative analysis of the results was done by comparing the spectra of different samples. In general, Planck's law of black-body radiation was used to describe data in a broad spectrum range. An impact of grating electrode to the THz emission was found by normalizing the radiation spectrum of the plasmonic sample by the data of a bare heterostructure. In addition, it was found that THz radiation of the plasmonic sample was strongly polarized.

In order to observe a weak plasmonic emission, the heating of the sample was reduced by cooling the sample to 112 K with a liquid nitrogen and using a voltage pulses with a duty cycle from 0.5% to 2.5%. At the duty cycle values smaller than 2% (pulse duration less than 1.6 ms) and voltage amplitude set in the range of 60-100 V, the shape of the emission spectrum differed from the black-body radiation of the plasmonic sample, i.e. an intense emission was observed in the frequency range of 150-300 cm^{-1}. The observed emission was attributed to the radiation from ungated 2DEG plasmons. At higher voltage values, the THz emission concerning thermal radiation and electroluminescence of impurities were dominant in the spectrum.

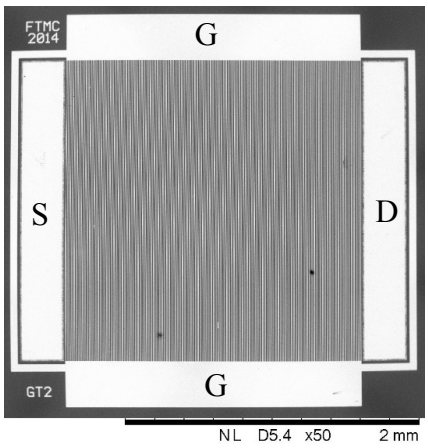

Fig. 1. Scanning electron microscope (SEM) image of a plasmonic THz emitter. Here S, D, and G denotes source, drain, and gate electrodes, respectively.

[1] I. Kašalynas, R. Venckevičius, L. Minkevičius, A. Sešek, F. Wahaia, V. Tamošiūnas, B. Voisiat, D. Seliuta, G. Valušis, A. Švigelj, and J. Trontelj, Spectroscopic Terahertz Imaging at Room Temperature Employing Microbolometer Terahertz Sensors and Its Application to the Study of Carcinoma Tissues, Sensors **16**, 432 (2016);

[2] M. Dyakonov and M. Shur, Shallow Water Analogy for a Ballistic Field Effect Transistor: New Mechanism of Plasma Wave Generation by dc Current, Phys. Rev. Lett. **71** 2465 (1993).

FREE CARRIER ABSORPTION FOR CHARACTERIZATION OF FAST CARRIER DYNAMICS IN SCINTILLATORS

Augustas Vaitkevičius[1], Etiennette Auffray[2], Mikhail Korjik[3], Marco Lucchini[2], Saulius Nargelas[1], Oleg Sidletskiy[4], Yevgeny Tretsiak[5], Gintautas Tamulaitis[1]

[1] Semiconductor Physics Department and Institute of Applied Research, Vilnius University, Vilnius, Lithuania.
[2] CERN, Geneva, Switzerland.
[3] Research Institute for Nuclear Problems, Belarusian State University, Minsk, Belarus
[4] Institute for Scintillation Materials, Lenin av. 60, Kharkov, Ukraine
[5] Research Institute for Chemical Problems, Belarusian State University, Minsk, Belarus
Augustas.Vaitkevicius@ff.vu.lt

The high-energy physics experiments in sight and advanced medical imaging devices based on positron emission tomography (PET), positron annihilation lifetime spectroscopy (PALS) and other techniques require fast scintillation detectors. A 10-ps-resolution is the next target in development of scintillation detectors. The current demand for faster timing of scintillation detectors used both in high luminosity high energy physics experiments and in medical applications inspire deeper studies of the dynamics of nonequilibrium carriers generated in scintillator material. PWO exhibits short emission decay time and has good radiation hardness to γ quanta.

Three scintillation materials have been under study: self-activated led tungstate ($PbWO_4$, PWO) and two cerium-doped garnets, GAGG and $Y_3Al_2Ga_3O_{12}$ (YAGG). The PWO crystal under study was grown by Czochralski technique. The 2x2x0.1 cm3 sample was prepared from the ingot of PWO-II quality [2]. YAGG and GAGG crystals doped with Ce were grown by Czochralski method from the melt containing 1 at.% of Ce in a slightly oxidized neutral atmosphere. The samples under study with dimensions 0.7x0.7x0.5 cm3 were cut from the seed part of the ingots exhibiting higher optical quality. The light yield of YAGG:Ce was found to be by a factor of 7 smaller than that of GAGG:Ce.

The measurements of free carrier absorption have been performed by using a femtosecond Yb:KGW laser PHAROS (Light Conversion Ltd.) emitting at 1030 nm. The laser produced 200 fs pulses at 30 kHz repetition rate. A part of the fundamental laser harmonic was frequency-quadrupled using β-barium borate crystals and the light at 254 nm (4.9 eV) was used as a pump beam for pulsed excitation of free carriers. The excitation beam was focused on the sample surface into a spot of ~350 μm in diameter. The remaining part of laser radiation at 1030 nm was delayed by an opto-mechanical delay line and used as a probe to follow the time evolution of the induced absorption, which is proportional to free carrier density. All measurements were performed at room temperature.

The optical density of the induced absorption in PWO and in other two samples under study was found to be proportional to the energy density in a wide dynamic range, as expected for free carrier absorption. This evidence confirms the assumption that the probe absorption originates exclusively from the carriers created via pumping.

It was determined that the rise time of free carrier absorption in PWO at interband excitation is in the subpicosecond domain. This is a clear indication that the nonequilibrium free electrons appear in the conduction band within subpicosecond time scale.

For YAGG:Ce crystals, pumping at 254 nm coincides pretty good with the upper, third, absorption band due to inerconfiguration electronic transition $4f^15d^0 \rightarrow 4f^05d^1$ of Ce^{3+} ions. The free carrier absorption decay kinetics consists of three components. The fast and intermediate components have characteristic decay times of 2 ps and ~100 ps with no significant dependence on excitation intensity. The decay time of the slow decay component is in nanosecond domain and decreases down to a few nanoseconds as the excitation intensity increases.

The absorption band corresponding to the transition to the third Stark component of $4f^05d^1$ configuration is shifted to short wavelength range in GAGG in comparison with that in YAGG. Therefore, the photons of 254 nm wavelength excite Ce^{3+} ion only into the long-wavelength shoulder of the absorption band due to the third inerconfiguration electronic transition $4f^15d^0 \rightarrow 4f^05d^1$ and Gd^{3+} subsystem directly via $^8S \rightarrow ^6D$ transitions. The FCA decay at low excitation intensities is monoexponential with the characteristic decay time substantially exceeding the time range under study (8 ns). The decay becomes increasingly nonexponential at elevated excitation intensities. The most interesting feature in the free carrier absorption response to a short pulse excitation is the rising part of the response. In contrast to PWO and YAGG:Ce, where the rise time is below the time resolution in our experiments (200 fs), the rise of the free carrier absorption response in GAGG:Ce is considerably slower. The rise time is approximately 10 ps at low excitation of 0.14 mJ/cm2 and decreases to 5 ps as the excitation is increased by an order of magnitude. This is attributed to absorption by free holes.

The time resolved study of free carrier absorption in three scintillation materials, self-activated PWO and cerium-doped GAGG and YAGG showed that the free electrons are instantaneously generated into the conduction band under band-to-band excitation of PWO and at the excitation to the third Stark component of $4f^05d^1$ Ce^{3+} configuration forming a state in the conduction band. Meanwhile in GAGG:Ce, a slow rise of free carrier absorption was observed and attributed to the absorption by free holes. This observation is consistent with the conclusion that the ground state of the $^8S \rightarrow ^6D_{7/2,9/2}$ intracenter transition of Gd^{3+} ions is located within the valence band. The results show that the hole trapping at Gd sublattice is an important factor deteriorating response speed in scintillators based on mixed garnets containing gadolinium.

ROLE OF DOPED AND UNDOPED ELECTRON TRANSPORT LAYER IN VERTICALLY STACKED PHOSPHORESCENT MULTILAYER ORGANIC LIGHT EMITTING TRANSISTOR

Mihirsinh Chauhan[1], Jaishree Vyas[2], Vishwa Bhatt[1], Manoj Kumar[3], Khushdeep Kaur[4], Vaibhav Rao[5], Brijesh Tripathi[3*]

[1]Department of Solar Energy, School of Technology, Pandit Deendayal Petroleum University, Gandhinagar – 382007 (India).
[2]Department of Chemical Engineering, BITS Pilani, Pilani – 333031 (India).
[3]Department of Science, School of Technology, Pandit Deendayal Petroleum University, Gandhinagar – 382007 (India).
[4]Department of Electronic Science, Kurukshetra University, Kurukshetra – 136119 (India).
[5] Ultrasound Research Institute (Electrical and electronic Engineering),Kaunas University of Technology, Kaunas, 44249(Lithuania).
jaishree0491@gmail.com

Many known advantages of organic light-emitting diode (OLED) displays in power consumption, pixel brightness, viewing angle, response time, and contrast ratio over liquid crystal displays (LCDs) have been driving research and development in this area [1]. A major technical challenge, which prevents their commercial utilization remains the drive transistor in the active matrix (AM) backplane. Organic material based channels are useful due to their homogeneity, low cost, and the variety of deposition possibilities, but they have low electron-hole mobility [2]. During operation, the thin-film transistor (TFT) having low-mobility channel layer would need a large source-drain voltage to drive the necessary current. This consumes more power in the transistor as compared to the light production in the OLED, compromising the power savings. This problem cannot be addressed by increasing the channel width of the drive transistor to increase source current, because it would reduce the fraction of pixel area available to the OLED. It needs a higher current density through the electroluminescent emitter to maintain the display brightness which degrades the OLED [3].

Vertical-type organic light-emitting transistors (VOLETs) have advantage of short channel length without the need of high resolution patterning and provide on-current sufficient to drive OLED pixels at low operating voltages [4]. In this article, An organic light emitting transistor (OLET) with tris(8-hydroxyquinoline) aluminium (Alq_3) as an electron transport layer (ETL) and 1% 4-(dicyanomethylene)-2-methyl-6-[p-(dimethylamino)styryl]-4H-pyran (DCM) doped Alq_3 was fabricated for studying the light emission behaviour of small molecules. The doping was done to achieve color tuning of emitted light. In this device electrons at source-dielectric interface and holes at ETL-LiF interface create an electric field which reduces the injection barrier at the ETL-source electrode (Al) interface. This electric field helps in the injection of electrons from the source electrode into the organic layer and these electrons recombine with holes injected from the drain electrode at emissive layer ($Ir(Ppy)_3$:CBP) to produce electroluminescent photons. An increased recombination of electron - hole is observed in undoped Alq_3 OLET with light emission of ~3500 cdm^{-2} (510-520 nm) and comparatively less emission of ~750 cdm^{-2} (600 nm) is observed in DCM doped Alq_3 OLET. The results give an insight for the development of next generation small molecule based OLET display technology.

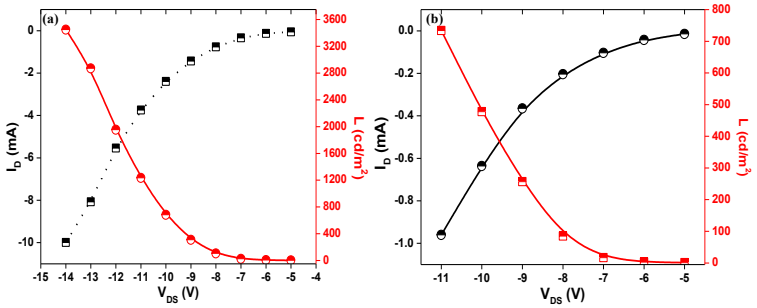

Fig.1: The output characteristics along with the corresponding brightness for: (a) Device A, and (b) Device B (L represents Luminescence).

[1] G. Gu, P.E. Burrows, S.R. Forrest, Design of flat-panel displays based on organic light-emitting devices, IEEE Journal of Selected Topics in Quantum Electronics 4 (1998) 83-99.
[2] M.A. McCarthy, B. Liu, E.P. Donoghue, I. Kravchenko, D.Y. Kim, F. So, A.G. Rinzler, Low voltage, low-power, organic light-emitting transistors for active matrix displays, Science 332 (2011) 570-573.
[3] S. Ohta, T. Chuman, S. Miyaguchi, H. Satoh, T. Tanabe, Y. Okuda, M. Tsuchida, Active matrix driving organic light-emitting diode panel using organic thin-film transistors, Japanese Journal of Applied Physics Part 1 44 (2005) 3678-3681.
[4] M.A. McCarthy, B. Liu, A.G. Rinzler, High current, low voltage carbon nanotube enabled vertical organic field effect transistors, Nano Letters 10 (2010) 3467-3472.

NOVEL DESIGN OF SOLAR SIMULATOR EMPLOYING HIGH POWER LIGHT EMITTING DIODES

Žygimantas Vosylius[1], Algirdas Novičkovas[2], Vincas Tamošiūnas[1]

[1]Faculty of Physics, Vilnius University,Saulėtekio al. 9, bldg. III, LT-10222 Vilnius, Lithuania
[2]Institute of Applied Research, Vilnius University,Saulėtekio al. 9, bldg. III, LT-10222 Vilnius, Lithuania
zygimantas.vosylius@ff.vu.lt

Rapid production growth of solar cell and modules also increases a need of novel device characterization equipment. One of quality control stages in solar cell production is device testing under standardized irradiation conditions, provided by solar simulators. The most commonly used irradiance and spectral distributions aim to match so-called AM1.5G conditions [1]. IEC 60904-9 Ed.2.0[2] standard defines criteria of how A, B or C class can be assigned to solar simulator in three categories: spectral distribution match, temporal stability, irradiance distribution uniformity.Traditionally, Xenon arc lamps were the mostly used light source of solar simulators. However, they suffer from issues related to a relatively short lamp life and stability. Therefore, development of simulators based on light-emitting diodes, such as one reported in [3], are getting more and more attention due stability and long-time performance of light sources.

Results of simulation of solar simulator employing arrays of 5 different types of light emitting diodes and mirrors, as well as properties of the irradiance generated by a produced simulator, are covered in this paper. The influence on irradiance and spectral distributions at the measurement plane made by a system of mirrors was investigated. After that models for solar simulator were created using 19-25 LED's. According to this model, real simulator has been produced and the generated irradiance was compared to simulation results. Moreover, possibility of incorporation of light beam induced current (LBIC) measurement technique and possibility of making simulator for large area modules are investigated.

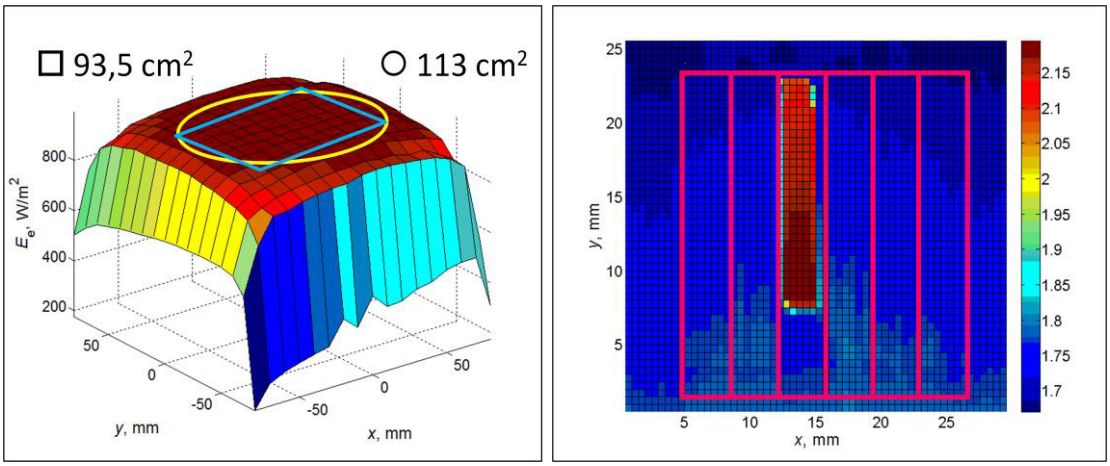

(a) (b)

Fig.1 Irradiance distribution generated by *Simulator No.2*(a) and photocurrent response (mA) of 6-part solar cell irradiated with white LED matrix and scanned with red laser beam, while ~25% of one part is covered (b).

It has been demonstratedtheoretically that there is possible to create AAA-class simulator for (16 × 16) cm2 area while using one *Bridgelux BXRA series,* 4 types of *LedEngin LZ4* LEDs and a square system of mirrors. Real simulator provided A-class irradiance and B-class spectral distributions in (8 × 8) cm2 area. Replacing one big white LED with seven smaller ones lets us achieve AAA-class irradiance in 1,5 times greater area (93,5 cm^2), as shown in Fig.1a. It has also been established that it is possible to incorporate LBIC method in order to reveal the current limiting cells of the solar panel (Fig. 1b). 9 × 9 matrix of imitator modules without mirrors could provide AAA-class irradiance in 1 m^2 area from the height of 270 mm.

[1] *Photovoltaic Devices–Part 3: Measurement Principles for Terrestrial Photovoltaic (PV) Solar Devices With Reference Spectral Irradiance Data*,IEC 60904-3 Ed.2.0, 2006.
[2] *Photovoltaic Devices–Part 9: Solar Simulator Performance Requirements*,IEC 60904-9 Ed.2.0, 2007.
[3] Algirdas Novickovas, Artūras Baguckis, Algirdas Mekys, and Vincas Tamošiūnas, "Compact Light-Emitting Diode-Based AAA ClassSolar Simulator: Design and Application Peculiarities", *IEEE Journal Of Photovoltaics*, VOL. 5, NO. 4, July 2015.

DEVELOPMENT AND CHARACTERIZATION OF PHOSPHOR CONVERTED LED LAMPS FOR NICHE APPLICATIONS

Henrikas Dapkus, Akvilė Zabiliūtė-Karaliūnė, Pranciškus Vitta

Institute of Applied Research, Vilnius University, Lithuania
henrikas.dapkus@ff.stud.vu.lt

Phosphor-converted light-emitting diodes (pcLEDs) are designed for outdoor lighting applications, because a better luminous efficiency of radiation (LER) can be achieved compared to traditional high intensity discharge (HID) lamps. Typically all LED based luminaires are enriched in blue light, which is found to have influence on suppressing sleep hormone - melatonin production. Lack of melatonin in the evening can disrupt human circadian rhythm causing sleeplessness, which can lead to insomnia and other sleeping disorders. The property of the spectral power distribution (SPD) of a light source to suppress the production of melatonin can be characterized by the circadian action factor (CAF). Higher CAF values indicate the increased suppression and vice versa. Luminaires with pcLEDs are an alternative to luminaires of multicolor LEDs, especially in low illuminance lighting applications, where broad orange spectra of phosphors can provide less blue-light pollution and thus achieve lower circadian action, while having better color rendition index (CRI) and the potential to save energy [1,2].

In this work, solid state lamp prototypes for outdoor lighting were designed by using a royal-blue LED (440 nm), a reflector and a remote phosphor converters. The reflector was made of a cone shaped white plastic for even light distribution. The phosphor converters were made from phosphors powders and silicone mixes. Commercial Intematix (O5446 and O6040) and PhosphorTech (BUVOR02) orange phosphors were used. The concentrations of investigated phosphors converters were between 15 wt% and 35 wt% and the thicknesses of the converters varied between 0.5 mm and 1.6 mm. The prototypes SPDs were measured and compared with each other in order to find the optimal concentration and thickness for white light generation. For the best prototypes LER, CAF and CRI were calculated. Optimal phosphors concentrations and thicknesses of the converters for each phosphor were: 35 wt% and 1.2 mm for BUVOR02 (1), 20 wt% and 0.8 mm for O5446 (2) and 20 wt% and 1.2 mm for O6040 (3). The *xy* CIE chromaticity coordinates of the mentioned light sources are presented in Fig. 1.

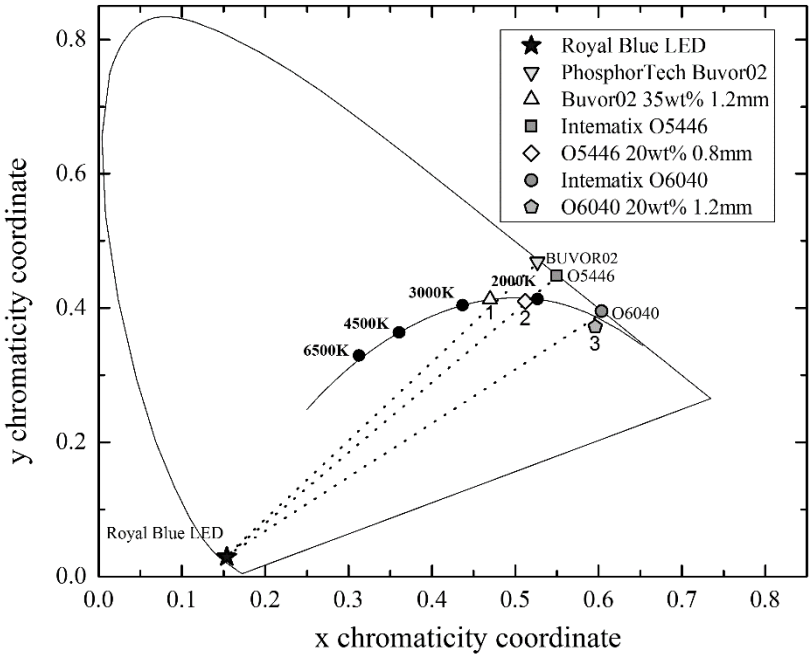

Fig. 1 *xy* chromaticity coordinates of designed pcLEDs in CIE (1931) chromaticity diagram.

Designed prototypes light is perceived as white because of small distances from the Planckian locus ($D_{uv} < 0.02$). Evaluated CRI values are better than typical HID lamp values. Prototype with O5446 and O6040 can be called firelight because of their extra low CCTs and can provide more visual comfort and lower circadian action for low-illuminance night lighting applications.

[1] A. Zabiliūtė, R. Vaicekauskas, P. Vitta, and A. Žukauskas, Phosphor-converted LEDs with low circadian action for outdoor lighting, Optics Letters **39**(3), 563–566 (2014).

[2] A. Žukauskas, R. Vaicekauskas and P. Vitta, Optimization of solid-state lamps for photobiologically friendly mesopic lighting, Applied Optics, **51**(35), 8423–32 (2012).

THREE-DIMENSIONAL STRESS-STRAIN STATE AND VOLUMETRIC DAMAGEABILITY OF TIRE–ASPHALT CONTACT PAIR

Gleb Gribovskii

Mechanics and Mathematics Faculty, Belarusian State University, Belarus
mmf.gribovskiy@gmail.com

Computer models for describing the spatial stress-strain state of a system automobile tire-asphalt are of great practical importance for road transport. Also important challenge for manufacturers of tires and road services is the assessment of volume damageability and wear of the tire tread and the asphalt pavement, which work in conditions of contact, mechanical and sliding fatigue. Today, there are many works dedicated to analytical and computer simulation of stress-strain state of the "rim–tire–asphalt" system components [1,2]. However, the problem of estimating the simultaneous contact interactions of system elements, their 3D stress-strain state and the state of the volumetric damageability is still not fully investigated.

The main goal of this work is to use finite-element modeling for the analysis of simultaneous contact interactions of the multielement system "rim–tire–asphalt", loaded by the inner pressure (850 kPa) and radial load (2500 N) on rim, 3D stress-strain state and the state of volumetric damageability.

Truck tire geometric model of 22.5″ radius with a simplified rim was taken for the calculation in ANSYS [3]. The following components were added to the model of tire (Fig. 1-b): layers of steel belt, radial ply, wire bead, rubber tread.

Calculation of damageability is based on the model of deformable solid mechanics with dangerous volume. According to this model dangerous volume is the volume where acting stresses are greater than limiting stress [4].

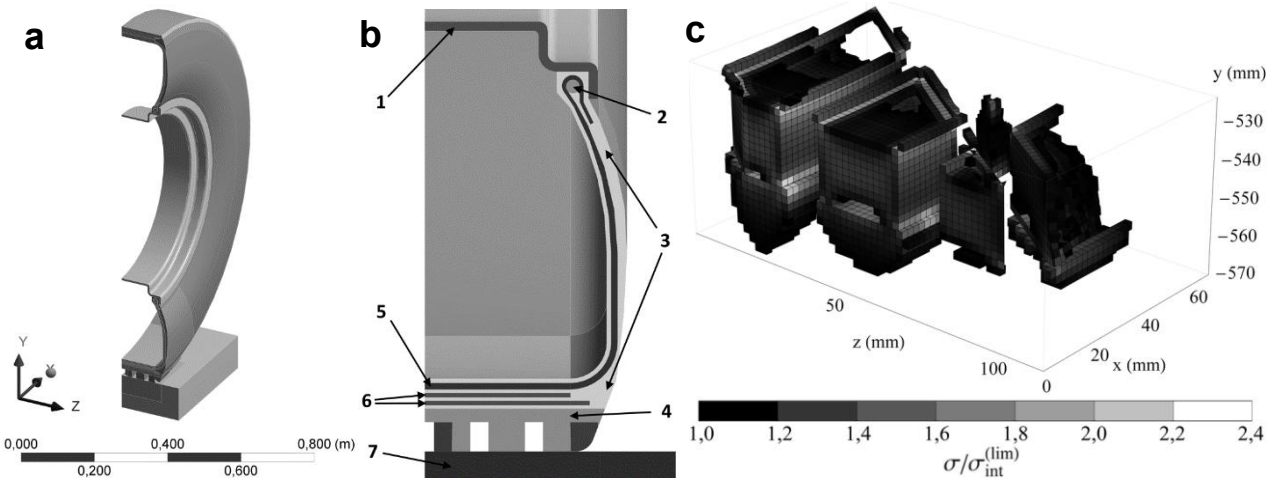

Fig. 1. (a) Geometric model of the system. (b) schematic notation of materials: 1 – steel rim, 2 – wire bead, 3 – rubber, 4 – rubber tread, 5 – radial ply, 6 – steel belt, 7 – asphalt. (c) Dangerous volume by stress intensity V_{int} in contact zone

In this work the computer simulation of stress-strain state of the "rim–tire–asphalt" system for the action of inflation air pressure in the tire and weight on the rim was made.

Distributions of stresses in the system are obtained. In these distributions we considered contact interaction between tire and asphalt-concrete pavement. Maximum of contact pressure is 3.4 MPa. Stresses in rubber are about 1.5 orders less than in other system elements, but strains are higher, because other system elements are harder.

Volume damageability of tire and asphalt in the contact zone were calculated. Obtained dangerous volume (Fig. 1-c) in the tread are 2-2.5 times higher than in the pavement (Table 1), because asphalt is harder. Dangerous volume based on stress intensity in rubber and asphalt is twice greater then dangerous volume based on minimum principal stress.

Table 1. Dangerous volume V and damageability Ψ by stress intensity and minimum principal stress in contact zone

	V_{int}, mm^3	Ψ_{int}, mm^3	V_3, mm^3	Ψ_3, mm^3
Tire	168 238,4	221 018,0	322 635,2	477 016,0
Asphalt	77 540,8	91 878,4	139 151,6	170 961,6

[1] Imad L. Al-Qadi, Hao Wang, Prediction of tire pavement contact stresses and analysis of asphalt pavement responses: a decoupled approach, Journal of the Association of Asphalt Paving Technologists **80**, 289–316 (2011).
[2] S. L. Sokolov, Experimental and computational analysis of stress-strain state of pneumatics in breaker zone under mechanical effects, Journal of Machinery Manufacture and Reliability **40**, 568–572 (2011).
[3] G. V. Gribovskiy, S. S. Sherbakov, Volume damageability of rim–multicomponent tire–asphalt-concrete tribo-fatigue system, International Scientific and Technical Collection Theoretical and Applied Mechanics **32**, 277 – 282 (2017).
[4] L. A. Sosnovskiy, TRIBO-FATIGUE: Wear-Fatigue Damage and its Prediction (Springer-Verlag, Berlin, Heidelberg, 2005)

Oral session 7

Functional Materials and Derivatives

FACE-ON ORIENTED DOPANT-FREE HOLE TRANSPORTING MATERIAL FOR 19% PEROVSKITE SOLAR CELLS

Kasparas Rakstys,[1] Sanghyun Paek,[1] Peng Gao,[1] Tomasz Marszalek,[2] Kristijonas Genevicius,[3] Vygintas Jankauskas,[3] Wojciech Pisula,[2] Mohammad Khaja Nazeeruddin[1]

[1]Group for Molecular Engineering of Functional Materials, Institute of Chemical Sciences and Engineering, École Polytechnique Fédérale de Lausanne, CH-1951 Sion, Switzerland
[2]Organisch-Chemisches Institut, Ruprecht-Karls-Universitt, Im Neuenheimer Feld 270, 69120 Heidelberg, Germany
[3]Department of Solid State Electronics, Vilnius University, Sauletekio 3, Vilnius 10222, Lithuania
kasparas.rakstys@epfl.ch

Hybrid lead halide perovskite-based solar cells (PSCs) have attracted significant attention in the photovoltaics due to inexpensive precursors, simple fabrication methods, and remarkably high power conversion efficiency (PCE), which already exceeds commercialized polycrystalline silicon solar cells.[1] Typical PSC configurations are n-i-p mesoscopic or planar and inverted p-i-n architecture. The n-i-p configuration devices composed of an electron transporting material TiO_2 (ETM), infiltrated with the perovskite absorbing material and coated with a hole transporting material (HTM), which plays an important role facilitating the extraction and transportation of holes from perovskite to the corresponding contact and is essential to reach high light-to-current conversion efficiency. To date, a great number of new promising molecular organic HTMs have been reported, but only very few candidates reached PCE values close to or exceeding 20%.[2] However, although PSCs have achieved high PCE values, the stability remains an issue due to dopant-induced degradation of PSC.[3]

Traditionally, the hole transporting layer (HTL) for PSCs is heavily doped with bis(trifluoromethane)sulfonimide lithium salt (LiTFSI), 4-*tert*-butylpyridine (TBP), and tris(2-(1*H*-pyrazol-1-yl)-4-*tert*-butylpyridine)cobalt(III) tri[hexafluorophosphate] (FK209). TBP is commonly used as HTL morphology controller, while LiTFSI and FK209 provide the necessary electrical conductivity. However, the use of additives is problematic, since hygroscopic nature of lithium salt makes the HTL highly hydrophilic and Co(III) dopant tends to chemical degradation, negatively influencing the stability of the entire device.[4] Therefore, a promising solution for stabilizing PSCs is the appropriate choice of dopant-free HTMs. However, the PCE of pristine HTL based devices are consistently lying around 10%, with only very few examples over 15%. Therefore, development of dopant-free HTMs with both enhanced moisture resistance and charge transporting properties is desired to probe their structure-performance correlations towards the realization of stable and high-efficiency PSCs.

In this work, we have synthesised novel dopant-free star-shaped donor – π-bridge – acceptor (D–π–A) type HTM, featuring a planar triazatruxene central core (D), inducing π-stacking for vertical hole conduction, thiophene-based multiple conjugated arms (π) and malononitrile (A). Due to strong intermolecular interaction, this molecule has a great potential to show high charge carrier mobility, minimizing Ohmic losses of the contact. Moreover, it combines the advantages of both small molecules, i.e. well-defined structures and polymers like good thermal, electrochemical and photochemical stability, together with high solubility, proper wetting on the perovskite. Molecularly engineered HTM has been applied in PSCs and for the first time, we show that a highly ordered characteristic face-on organization could favor vertical charge carrier transport in the perovskite solar cell and a PCE over 19% with improved stability was achieved using **KR321** (Fig. 1). This result is on par with the heavily doped spiro-OMeTAD reference, clearly showing the importance of proper molecular engineering and the great perspective of dopant-free HTMs in perovskite solar cells and outperforms most of the other dopant-free HTMs reported to date.

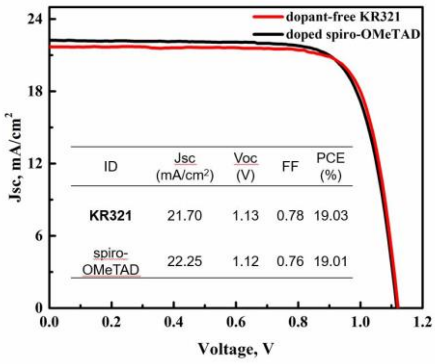

Fig. 1. Current-voltage curves of devices based on novel dopant-free HTM **KR321** and doped spiro-OMeTAD as reference and their photovoltaic performance parameters.

[1] L. Meng, J. You, T.-F. Guo, Y. Yang, *Acc. Chem. Res.* **2016**, *49*, 155–165.
[2] P. Gao, M. Graetzel, M. K. Nazeeruddin, *Energy Environ. Sci.* **2014**, *7*, 2448–2463.
[3] C. Huang, W. Fu, C.-Z. Li, Z. Zhang, W. Qiu, M. Shi, P. Heremans, A. K.-Y. Jen, H. Chen, *J. Am. Chem. Soc.* **2016**, *138*, 2528–2531.
[4] L. Calio, S. Kazim, M. Graetzel, S, Ahmad, *Angew. Chem. Int. Ed.* **2016**, *55*, 14522 –14545.

NANOCRYSTALLIZATION OF $NA_3V_2(PO_4)_2F_3$ GLASS

Paulina E. Kruk, Tomasz K. Pietrzak, Jerzy E. Garbarczyk

Faculty of Physics, Warsaw University of Technology, Poland
paulina.kruk.93@gmail.com

The demand for new power storages for electric cars and electronic devices is increasing each year. However, the need for developing materials useful for such applications, coupled with concerns about the cost and availability of metals used in Li-ion battery cathodes caused invigoration of interest in the study of sodium-ion batteries. One of the most studied material of this type is $Na_3V_2(PO_4)_2F_3$ with capacity up to 128 mAh/g at an average voltage of 3.75 V. Moreover, recently, it was shown that its capacity is not redox-limited, but, with high probability, site-limited [1]. Although mentioned material is considered as prospective, its capacity should be improved to be competitive with existed Li-ion cathodes.

The recent studies performed by J.E. Garbarczyk and co-workers have revealed an alternative method of the conductivity enhancement – thermal nanocrystallization of glassy analogs of the crystalline cathode materials [2, 3]. Glass systems, such as: V_2O_5, $LiFePO_4$ and $Li_3V_2(PO_4)_3$ was obtained to verify this route. Ability of obtaining active cathode materials (without carbon additives) as well as simplicity of the sythesis are considered as main advantages of the performed process. In that case procedure consists of (i) glass preparation by melt-quenching (two-step method was used to obtain glassy samples) and (ii) thermal treatment of the glass to induce its nanocrystallization. Our previous studies have shown that an enormous and irreversible conductivity enhancement could be gained by the appropriate heat-treatment.

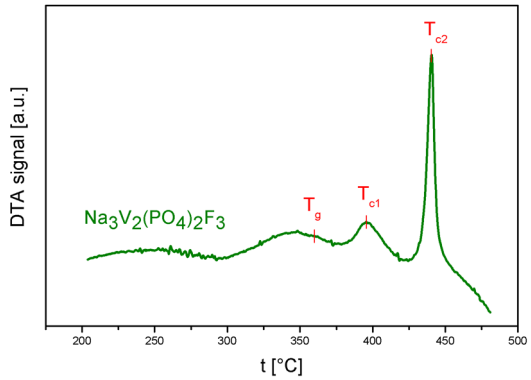

Fig. 1. DTA trace of the sample θ=1°/min.

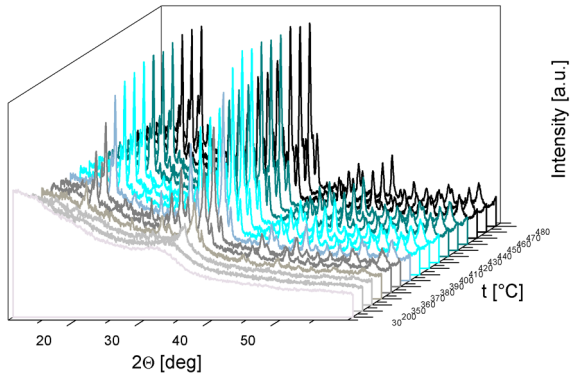

Fig. 2. Temperature XRD patterns of the sample.

In this studies, we aimed to obtain $Na_3V_2(PO_4)_2F_3$ glass from appropriate amounts of precursors (NaF, V_2O_5, $NH_4H_2PO_4$), using two-step method similar to described in [4]. The batch was melted at ca. 1300°C in reducing atmosphere and rapidly cooled between two stainlesssteel plates (melt-quenching technique). X-ray diffractometry (Phillips XPert Pro) was performed to verify amorphousness of the samples, as well as to observe crystallization process upon heating procedure in Anton-Paar HTK 1200 furnace. In order to observe thermal events occurring in obtained samples, additional examination was carried out using TA Q600 apparatus.

DTA trace for the obtained material proved to be typical for amorphous materials. The temperatures of glass transition (T_g) and crystallization (T_c) were 359°C and 465°C, respectively (Fig. 1.). This outcome corresponds to the XRD results, which consisted only in amorphous halo (Fig. 2.). Temperature dependent XRD measurements, conducted in nitrogen atmosphere, showed that heating the glassy material to the temperature higher than T_c resulted in crystallization in NASICON-like phase (ICDD card no. 04-012-2207). The average size of grains was estimated using Sherrer's formula to be within 40–60 nm range. Performing further examinations should reveal the answer, whether the influence of nanocrystallization process results in enhancement of electrical properties of examined material.

[1] I.L. Matts, S. Dacek, T.K. Pietrzak et al., Explaining Performance-Limiting Mechanisms in Fluorophosphate Na-Ion Battery Cathodes through Inactive Transition-Metal Mixing and First-Principles Mobility Calculations. Chemistry of Materials **27** (2015) 6008–6015.

[2] J.E. Garbarczyk, T.K. Pietrzak, M. Wasiucionek et al., High electronic conductivity in nanostructured materials based on lithium-iron-vanadate-phosphate glasses. Solid State Ionics **272** (2015) 53–59.

[3] T.K. Pietrzak, M. Wasiucionek, P.P. Michalski et al., Highly conductive cathode materials for Li-ion batteries prepared by thermal nanocrystallization of selected oxide glasses. Materials Science and Engineering B **213** (2016) 140–147.

[4] T.K. Pietrzak, P.P. Michalski, M. Wasiucionek et al., Synthesis of nanostructured $Li_3Me_2(PO_4)_2F_3$ glass-ceramics (Me = V, Fe, Ti). Solid State Ionics **288** (2016) 193–198.

HIGHLY EFFICIENT RARE-EARTH DOPPED RED-EMITTING PHOSPHORS

Julija Grigorjevaitė, Arturas Katelnikovas

Institute of Chemistry, Faculty of Chemistry and Geosciences, Vilnius University, Naugarduko 24, LT-03225 Vilnius, Lithuania

julija.grigorjevaite@chf.vu.lt arturas.katelnikovas@chf.vu.lt

White light can be generated in different ways. The simplest one is to mix blue and yellow/orange. However, it is also possible to mix blue, green and red. Blending a number of emission bands into a continuous spectrum also yields, of course, white light [1]. The object of this work was to find new and efficient red emitting inorganic phosphors that could be applied in white LEDs.

Powder samples of inorganic phosphors were prepared by conventional high temperature solid-state reaction. The stoichiometric amounts of high purity starting materials (Bi_2O_3, Sm_2O_3, MoO_3, K_2CO_3/ Rb_2CO_3 and $NH_4H_2PO_4$) were blended in the mortar employing acetone as grinding media. The obtained powders were transferred to the porcelain crucibles and annealed at 600 °C for 10 h in air. The calcination procedure was repeated another two times [2].

Three different series were made as follows: $K_2Bi(PO_4)(MoO_4)$ and $Rb_2Bi(PO_4)(MoO_4)$ doped with Eu^{3+} and $K_2Bi(PO_4)(MoO_4)$ doped with Sm^{3+} ions. The structural, morphological and optical characteristics of the compounds were investigated by powder X-ray diffraction (XRD), scanning electron microscopy (SEM) analysis and UV-Visible spectroscopy. The reflection, excitation and emission spectra of the single phase compounds were measured and analyzed. The temperature dependent emission spectra and decay curves in 77 – 500 K temperature interval were also recorded and discussed.

Moreover, colour points, luminous efficacies (LE) and decay times were also calculated. Eu^{3+} doped samples were red emitting and showed quantum efficiencies close to unity, whereas their Sm^{3+} counterparts possessed around 55% efficiency.

Differences between colour points (see Fig. 1), colour purity, luminous efficacy of mentioned series as a function of Eu^{3+} or Sm^{3+} concentration will be presented and discussed.

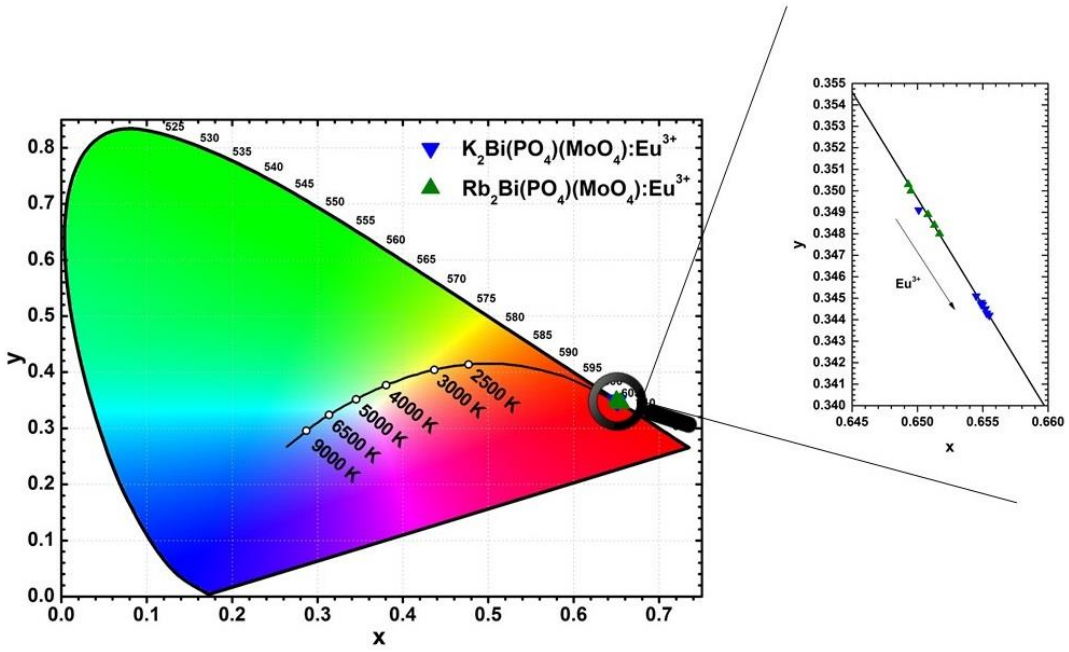

Fig. 1. CIE 1931 colour space diagram with colour points of $K_2Bi(PO_4)(MoO_4)$ and $Rb_2Bi(PO_4)(MoO_4)$ doped with Eu^{3+} excited by 265 nm radiation.

[1] G. Blasse, B.C. Grabmaier, Luminescent materials, Springer-Verlag, Berlin, New York, 1994.
[2] H. Huang, G. Chen, S. Wang, L. Kang, Z. Lin, Y. Zhang. Mater. Res. Bull., **51** (2014) 455-459.

BIFLUORENE SINGLE CRYSTALS FOR ORGANIC LASERS

Paulius Baronas[1], Gediminas Kreiza[1], Patrik Scajev[1], Vladislavas Čerkasovas[1], Edvinas Radiūnas[1], Povilas Adomėnas[1], Ona Adomėnienė[1], Karolis Kazlauskas[1], Jean-Charles Ribierre[2], Chihaya Adachi[2] and Saulius Juršėnas[1]

[1] Institute of Applied Research, Vilnius University, Saulėtekio 3, LT-10222 Vilnius, Lithuania
[2] Center for Organic Photonics and Electronics Research (OPERA), Kyushu University, Kyushu University, 744 Motooka, Nishi, Fukuoka 819-0395, Japan
paulius.baronas@tmi.vu.lt

Organic solid state lasers are often associated with easy and low-cost fabrication, broad tunability of emission wavelength, low temperature-sensitivity of stimulated emission and other features competitive to their inorganic counterparts [1]. One of the key problems associated with electrically driven laser action in organic materials is high amplified spontaneous emission (ASE) threshold, which must be reduced given the poor charge transport properties of the organic materials. Organic single-crystalline materials offering numerous advantages due to their long-range molecular order are considered to be a promising gain medium for realization of electrically pumped organic lasers [2]. Unfortunately, ASE thresholds of the crystals are typically more than one order of magnitude higher (in the range of tens of kW cm^{-2}) as compared to those of amorphous neat or doped films.

Rational design of bifluorene compounds presented in this work lead to extremely low ASE thresholds (down to 700 W cm^{-2}), which were found to be the lowest among sublimation-grown single crystals reported in the literature [3]. Recorded single crystal ASE thresholds were proven to be lower than optimized polymer blend films (see Fig 1.). Such low thresholds were found to originate from high radiative rates (1.5×10^9 s^{-1}) arising from pronounced fluorescence properties of bifluorene molecules and specific orientation of molecular transition dipole moments in the crystals. The efficient lasing was also related to the absence of excited-state absorption in the gain region accompanied by excellent waveguiding properties of the single crystals.

Further studies of exciton diffusion and annihilation dynamics in organic single crystals were performed to evaluate the high excitation density effects, which play a major role in organic solid state laser applications. Results obtained by light induced transient grating experiment revealed highly anisotropic singlet exciton transport with diffusion length reaching 100 nm in bifluorene single crystals.

All above-mentioned findings will contribute to designing and producing our first organic single-crystal light-emitting field-effect transistor in the later stages of the Lithuania-Japan project.

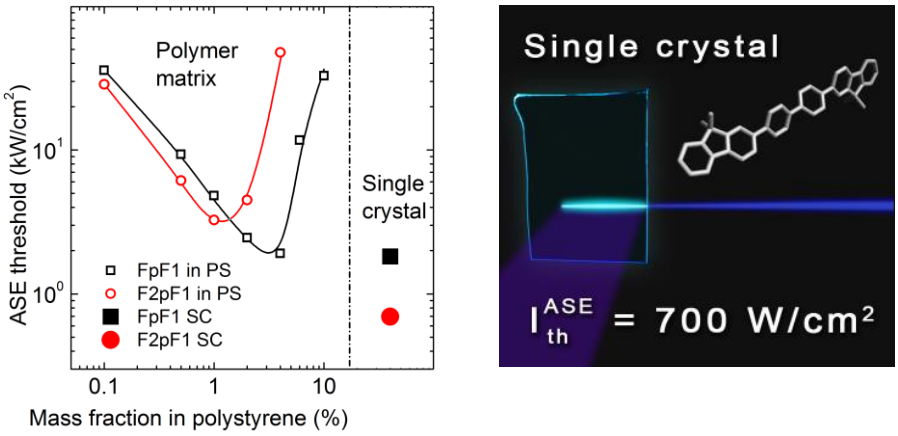

Fig. 1. Optimization of ASE threshold values in polymer films and lowest recorded values for single crystal.

[1] A. J. C. Kuehne, M. C. Gather, "Organic Lasers: Recent Developments on Materials, Device Geometries, and Fabrication Techniques" Chem. Rev. **116**, 13823-12864 (2016).
[2] S. Hotta, T. Yamao, S. Z. Bisri, T. Takenobu, Y. Iwasa, "Organic single-crystal light-emitting field-effect transistors", J. Mater. Chem. C **2**, 965 (2014).
[3] G. Kreiza, P. Baronas, E. Radiunas, P. Adomėnas, O. Adomėnienė, K. Kazlauskas, J. C. Ribierre, C. Adachi, S. Juršėnas, "Bifluorene single crystals with extremely low-threshold amplified spontaneous emission", Adv. Opt. Mater. (2017).

Oral session 8

Semiconductor and Condensed Matter Physics

INFLUENCE OF METALORGANIC PRECURSORS FLOW INTERRUPTION TIMINIG ON GREEN InGaN MULTIPLE QUANTUM WELLS

Mantas Dmukauskas[1], Arūnas Kadys[1], Tadas Malinauskas[1], Tomas Grinys[1], Ignas Reklaitis[1], Kazimieras Badokas[1], Martynas Skapas[1,3], Roland Tomašiūnas[1], Darius Dobrovolskas[2], Sandra Stanionytė[3], Ines Pietzonka[4], Martin Strassburg[4], Hans-Jürgen Lugauer[4]

[1]Institute of Applied Research, Vilnius University, Lithuania
[2]Semiconductor Physics Department, Faculty of Physics, Vilnius University, Lithuania
[3]Department of Characterization of Materials Structure, Institute of Chemistry, Centre for Physical Sciences and Technology, Lithuania
[4]OSRAM Opto Semiconductors GmbH, Germany
mantasdmuk@gmail.com

III-nitrides semiconductor technology has undergone tremendous development and recognition. Numerous GaN-based devices, including light emitting diodes (LEDs), laser diodes, photodetectors and high power electronics, have emerged on the market. InGaN-based quantum well (QW) LEDs became important for solid state lighting [1, 2]. Yet, challenges such as creating green light LEDs still remain a major problem. Compared to the blue LEDs, green or yellow ones have lower efficiency. Attempts to manufacture effective LEDs emitting light at longer wavelengths are problematic due to increased defect density, high influence of carrier localization and the internal electric field. Du et al achieved a remarkable enhancement of emission efficiency for yellow-green LEDs by using multiple interruptions, while maintaining an unchanged ammonia flow. [3].

In this abstract, we present fully strained green light emitting InGaN/GaN multiple quantum wells, grown by metalorganic vapor phase epitaxy, using metalorganic (MO) precursor multiple flow interruptions during InGaN quantum well growth. Optimization of the interruption timing during the growth of QWs lets us reach the integrated photoluminescence (PL) enhancement up to two times for the green light emitting InGaN/GaN MQWs, when MO pulse durations is 20 s and pause durations is 12s (Fig. 1). The enhancement, as a function of pause duration, appeared to be pulse duration dependent: a lower enhancement can be achieved using shorter pulses with optimized relatively shorter pauses. Indium evaporation during the interruption time was interpreted as the main issue to keep the layers intact. Quantum wells revealing the highest PL enhancement were inspected for the interface quality, layer thickness, growth speed, strain, surface morphology and roughness by transmission electron microcopy, X-ray diffraction and atomic force microscopy techniques, and compared with the one grown in the conventional mode.

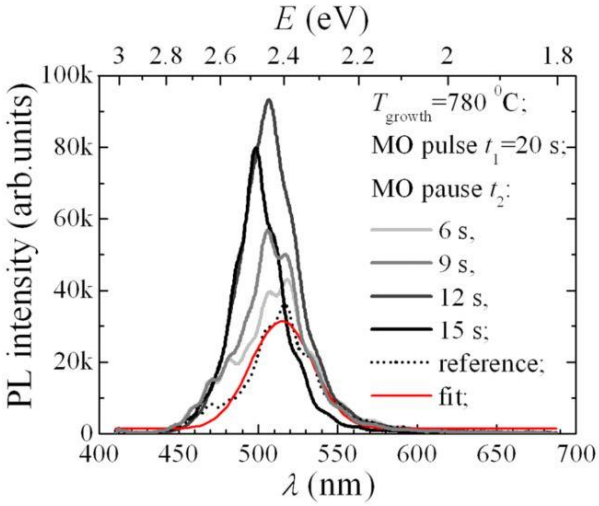

Fig. 1. PL spectra of the reference and the samples grown by the pulse mode.

[1] F. A. Ponce and D. P. Bour, Nitride-based semiconductors for blue and green light-emitting devices, Nature **386**, 351-359 (1997).
[2] A. Žukauskas, M. S. Shur and R. Gaska, *Introduction to Solid-State Lighting* (New York: Wiley, USA, 2002).
[3] C. Du, Z. Ma, J. Zhou, T. Lu, Y. Jiang, P. Zuo, H. Jia, and H. Chen, Enhancing the quantum efficiency of InGaN yellow-green light-emitting diodes by growth interruption, Appl. Phys. Lett. **105,** 071108, (2014).

TEMPERATURE-DEPENDENT PHOTOLUMINESCENCE STUDY OF THERMALLY ANNEALED GaAsBi/AlAs QUANTUM WELLS

Evelina Pozingytė, Renata Butkutė, Bronislovas Čechavičius, Martynas Skapas, Algirdas Selskis, Gediminas Niaura, Arūnas Krotkus

State research institute Center for Physical Sciences and Technology, Lithuania
evelina.pozingyte@ftmc.lt

The ternary GaAsBi compound attracts attention due to its potential application in long wavelength optoelectronic devices [1]. Adding small amount of bismuth to GaAs lattice leads to a large reduction of the bandgap, enabling access to important wavelengths in the infrared region [2]. However, the successful incorporation of Bi within the GaAs lattice requires the use of low-temperatures growth. At low temperatures grown GaAs contains high density of defects, such as As antisites (As_{Ga}) and Ga vacancies (V_{Ga}). These defects act as non-radiative recombination centres and are responsible for reduction of PL intensity. In order, to improve the quality of GaAsBi structures post-growth annealing is usually used. However, thermal annealing of GaAsBi at higher temperatures not only reduces non-radiative recombination rate, but also leads to the appearance of additional peaks in PL spectra at energies well below GaAsBi bandgap, due to formation of nanoclusters, with high Bi content [3]. Several works have been published concerning the effects of GaAsBi thermal annealing to Bi nanocluster formation, but no clear conclusions can be made yet [3, 4].

This work presents an investigation of optical and structural properties of as-grown and annealed GaBiAs/AlAs quantum wells (QWs) by temperature-dependent photoluminescence spectroscopy. Additionally, high-resolution transmission electron microscopy (HRTEM) and Raman spectroscopy results are presented in this work. Investigated samples, containing several GaAsBi/AlAs QWs, were grown by molecular beam (MBE) and migration-enhanced (MEE) epitaxy. Moreover, samples were annealed at $600-750^{o}$C temperature for 180 s in nitrogen atmosphere.

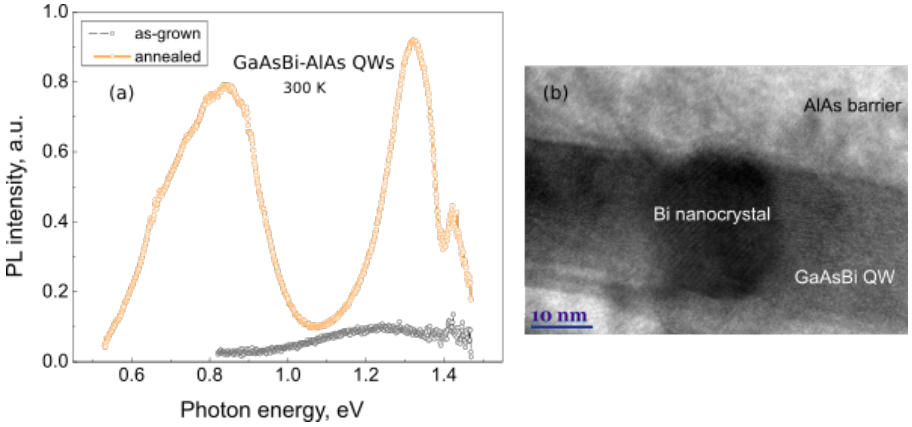

Fig. 1. Room temperature PL spectra of as-grown and annealed at 750^{o}C temperature twenty-GaAsBi/AlAs QWs structure (a) HRTEM image (b).

Firstly, PL spectra of as-grown and annealed at 750^{o}C temperature GaAsBi/AlAs QWs structures were compared (see **Fig. 1(a)**). PL spectra showed that thermal annealing of GaAsBi/AlAs QWs sample induced increase of PL intensity and appearance of additional PL peak at low energies. This peak was attributed to Bi nanoclusters. Furthermore, HRTEM (**Fig. 1(b)**) and Raman scattering measurements evidenced that these nanoclusters are predominantly composed of Bi atoms. Low-temperature PL spectra of GaAsBi/AlAs structure containing 10 nm- and 20 nm-width QWs showed that PL band related to Bi nanocrystals is rather complex; it is composed of several separate peaks with distinguished photon energies at 0.67 eV, 0.88 eV and 0.98 eV (spectrum at 3 K temperature). These peaks were assigned to Bi nanoparticles with various sizes, which formed in 10 nm- and 20 nm-width QWs. That indicates that GaAsBi/AlAs QW width possibly sets size of Bi nanoclusters, which forms after thermal annealing.

This work was supported by the Reseach Council of Lithuania under the grant No. MIP-71/2015 (BiNano).

[1] V. Pačebutas, K. Bertulis, G. Aleksejenko, A. Krotkus. Molecular-beam-epitaxy grown GaBiAs for terahertz optoelectronic applications. Journal of Materials Science: Materials in Electronics, **20**(1), 363-366 (2009).

[2] R. D. Richards, C. J. Hunter, F. Bastiman, A. R. Mohmad, J. P. R. David. Telecommunication wavelength GaAsBi light emitting diodes. IET Optoelectronics, **10**(2), 34-38 (2016).

[3] R. Butkutė, V. Pačebutas, B. Čechavičius, R. Adomavičius, A. Koroliov, A. Krotkus. Thermal annealing effect on the properties of GaBiAs. Physica Status Solidi (c), **9**(7), 1614-1616 (2012).

[4] O. Donmez, K. Kara, A. Erol, E. Akalin, H. Makhloufi, A. Arnoult, C. Fontaine. Thermal annealing effects on optical and structural properties of GaBiAs epilayers: Origin of the thermal annealing-induced redshift in GaBiAs. Journal of Alloys and Compounds, **686**, 976-981 (2016).

DETERMINATION OF TERAHERTZ RADIATING ELECTRIC DIPOLE ORIENTATION BY TERAHERTZ EMISSION MEASUREMENTS

Ieva Beleckaitė, Ramūnas Adomavičius

Center for Physical Sciences and Technology, Saulėtekio av. 3, Vilnius, Lithuania
ieva.beleckaite@ftmc.lt

In recent years terahertz (THz) spectroscopy finds its application in various fields. It could be used in security systems for drugs and explosives detection [1], in medicine as non-invasive way for cancer diagnostic [2], in food industry for quality control [3], in art for heritage restoration [4] and ect. Moreover THz spectroscopy is a good tool to investigate semiconductors and their nanostructures: it could be used for electron mobility and relaxation time measurements [5] as well as for determination of semiconductor band gap and intervalley separation [6]. For all these applications an effective, compact, easy to use and cheap THz emitter is needed. It was shown that THz radiation from surface based THz emitters could be determined by the photo-excited electric dipoles which orientation is essential for an efficiency of THz emission. In this work we present an experimental method which together with theoretic calculations based on W. Lukosz [7] theory could be used to determine the orientation of THz radiating electric dipole.

Experiments have been performed using Ti:sapphire oscillator generating 150 fs, 800 nm pulses at the repetition rate of 76 MHz. THz electric field transients were detected with a GaAs THz detector (Teravil Ltd) which was positioned to detect only p polarized THz radiation. THz emission measurements were carried out in transmission geometry. THz pulse amplitude dependencies on an angle between an incident laser beam and a normal to the sample surface, so called an excitation angle, have been obtained. To change THz radiating electric dipole orientation an external magnetic field ranging from 0.0 T to 0.4 T was applied using an electromagnet. The magnetic field was parallel to the sample surface and perpendicular to the incidence plane. Critical excitation angle $\alpha_{critical}$ (where THz pulse amplitude equals zero) was determined from THz pulse amplitude dependence on an excitation angle measurements. According to obtained results a tilt angle θ of THz radiating electric dipole was calculated. It was shown that our suggested theoretical model is in a good agreement with measurement results (Fig. 1). Described method was adjusted for investigation of non-stoichiometric GaAs layer. It was determined that THz radiating electric dipole in this structure is tilted by an angel $\theta = 8^\circ$ in respect to surface normal which leads to effective THz pulse generation. Investigated structure was used for fabrication of compact, bias-free, polarization rotating THz emitter [8].

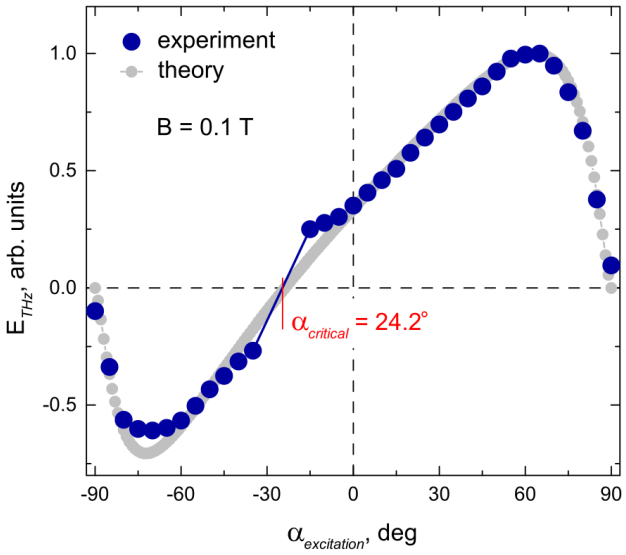

Fig. 1. Measured THz pulse amplitude dependence on an excitation angle (dark blue) compared with theoretical calculations (light grey) based on determined electric dipole orientation.

[1] M. Tonouchi, *Nature Photon*,**1**(2), pp. 97–105, 2007.
[2] Biaobin Jin *el al*, *Terahertz Science and Technology*, **3**(4), pp. 192, 2010.
[3] Hu Tao *el al*, *Advanced Materials*, **24**(8), pp. 1067-1072, 2012.
[4] M. Picollo *el al*, *Journal of Cultural Heritage*, **16**(1), pp. 73–80, 2015.
[5] A Urbanowicz *et al*, *Semicond. Sci. Technol.*, **20**(10), pp. 1010–1015, 2005.
[6] G. Molis *el al*, *Applied Physics Letters*, **94**(9), pp. 91104, 2009.
[7] W. Lukosz, *J. Opt. Soc. Am.*, **69**(11), pp. 1495, 1979.
[8] I. Beleckaitė *el al*, *Electronics Letters*, **54**(23), pp. 1954-1956, 2016.

OPTICAL PROPERTIES OF EPITAXIAL $Sn_{1-x}Mn_xTe$ LAYERS STUDIED BY FOURIER TRANSFORM INFRARED SPECTROSCOPY

Jakub Polaczyński[1, 2], Andrzej Witowski[1], Michał Szot[2], Monika Zięba[2], Tomasz Story[2]

[1] Faculty of Physics, University of Warsaw, Pasteura 5, 02-093 Warsaw, Poland
[2] Institute of Physics, Polish Academy of Sciences, Al. Lotników 32/46, 02-668 Warsaw, Poland
Jakub.Polaczynski@ifpan.edu.pl

SnTe is a well-known, narrow-gap semiconductor which found a broad application e.g. in infra-red optoelectronics due to the tunability of the band-gap and the ease of fabrication. It was also shown recently that SnTe belongs to the new class of materials, known as *topological crystalline insulators*. Moreover, alloying of SnTe with MnTe (which results in $Sn_{1-x}Mn_xTe$ ternary alloys) can improve it's thrmoelectric properties [1]. An importan feature of $Sn_{1-x}Mn_xTe$ material is the high intrinsic concentraion of holes, which strongly affects its optical and magnetic properties. However, very few studies were performed on this material to date, focusing mostly on it's magnetic properties (see e.g. [2]).

Optical spectroscopy, as a non-invasive and relatively easy experimental method, can be used for the characterization of the new materials and to the determination of their parameters. Results thus obtained can be used in turn for the theoretical calculations and modelling of the novel thermoelectric devices of higher performance.

During the presentation, the first results of optical characterization of $Sn_{1-x}Mn_xTe$ crystals will be presented. Six samples were studied, all consisting of app. 1 μm-thick epitaxial layers grown on BaF_2 substrate. Similarily to the SnTe, our samples are intrinsically p-type. The Mn content, x, and hole concentration, p, varie in the range $0.03<x<0.05$ and $2\cdot10^{20}$ cm$^{-3}\leq p\leq 9\cdot10^{20}$ cm^{-3}, respectively. The room temperature reflectivity and transmittance spectra were measured for all samples in the spectral region 100 meV – 1000 meV by Bruker 113v Fourier Transorm Infra Red Spectrometer.

The optical properties of the samples under investigation turned out to be strongly concentration-dependent. The Burstein-Moss shift was observed for all the samples and will be discussed. The analysis of interference fringes allowed the estimation of the refractive index of $Sn_{1-x}Mn_xTe$ in the studied region, as can be seen in the Fig. 1. It will also be shown that the simple model of a free-carrier dielectric function, extended by interband transitions, is sufficient for the explanation of basic optical properties of studied crystals.

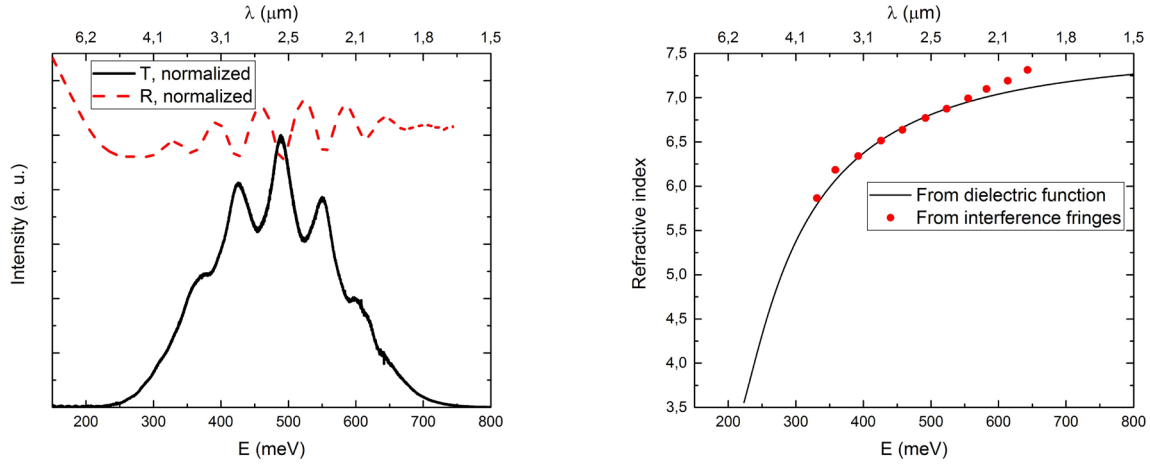

Fig. 1. Normalized room-temperature reflectivity and transmittance spectra obtained on a sample with Mn content of x= 0.045 and holes concentration p= $3.7\cdot10^{20}$ cm^{-3} (left). Refractive index of the same sample as a function of energy, calculated from the free-carrier dielectric function (solid line) and from interference fringes in the reflectivity spectra (points) (right).

[1] G. Tan et al., Valence Band Modification and High Thermoelectric Performance in SnTe Heavily Alloyed with MnTe, J. Am. Chem. Soc. **137**, 11501-11516 (2015).
[2] A. J. Nadolny et al.,Carrier induced ferromagnetism in epitaxial $Sn_{1-x}Mn_xTe$ layers, J. Mag. And Mag. Mat. **248**, 134-141 (2002).

THE EVALUATION OF THE CHARGE CARRIERS PARAMETERS AND FERMI LEVEL IN MULTICARRIER BI-BASED ALLOYS

Alexander Fedotov[1], Sergey Perevoznikov[2], Aliaksei Pashkevich[1]

[1]Physics Faculty of Belarusian State University
[2]Research Institute for Physical Chemical Problems of the Belarusian State University
fedotov.alehandro@gmail.com

The Bi polycrystalline films and coatings found many industrial applications the last years. Bi is being used in medical implants due to its biocompatibility. Bi electrodes promise to replace toxic Hg electrodes for potentiometry analytical chemistry methods. Bismuth coatings serves as protection from electro-magnetic pulses and some types of radiation. The Bi-based alloys can serve as thermoelectric materials in low-medium range of temperatures.

The applications mentioned above make the understanding of Bi-based systems electronic properties crucial for the scientific community. We have focused on polycrystalline Bi-based films. the most cheap and industrially attractive form of samples.

Our study consists of three main stages. First, we estimate the influence of grain boundaries on electric transport properties in pure Bi films. We've calculated mobilities and concentrations of charge carriers from measurements of Hall coefficient, Seebeck coefficient and magnetoresistance in temperatures range 4−300 K in magnetic fields up to 8 T. It was shown that precise control of mobilities is possible by the controlling of the mean crystallites diameter ($10^{-1} - 10^{1}$ μm). It was experimentally proved that character of resistivity temperature dependece may be switched from metallic to semiconductor one using the mentioned mechanism of mobility reduction [1].

Secondly, we've developed the technique to predict Bi film Seebeck coefficient[2]. The model uses the Electron Backscatter Diffraction crystalline texture mapping as input data. Computation is based on differential equations in partial derivatives describing coupled heat and charge transfer (see Fig. 1(a)) with transport coefficients related to single crystal. The technique has succesfully proved itself for the samples with the grain sizes larger than mean free path of charge carriers.

Third, we've characterized the charge carrier parameters for Bi_x-Sn_{1-x} alloys ($x \leq 0.08$ at. %), the promising candidate for the *p*-type thermoelectric material. The standard galvanomagnetic methods of characterization through Hall coefficient and magnetoresistance are not suitable for those materials due to presence of several charge carrier types (up to three in some temperature region). To extract charge carriers mobilities and concentrations the Quantitative Mobility Spectrum Analysis code was developed with advanced error definition and Fourier-space adjustment mechanism (see Figs. 1(b,c)). The Fermi level position was estimated relatively to extrema of electronic bands in T- and L-points. It was shown that the temperature increase from liquid He to room fully compensates the effect of doping Fermi level shift for the T-point ellipsoid in *k*-space. However, the effect of Sn additions does not vanish with temperature for the L-point and becomes determinative for the electronic properties at room tepmerature.

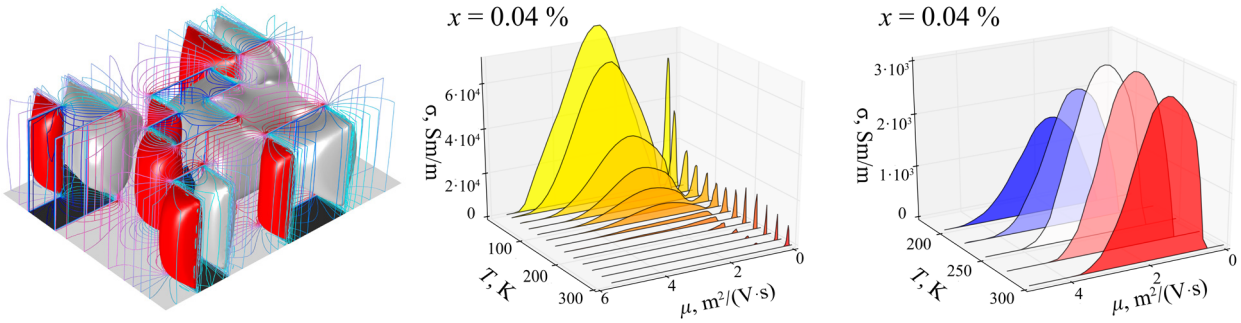

(a) (b) (c)

Fig. 1. (a) - the example of visualization of computed temperature (isothermal surfaces) and current (streamlines) fields. (b), (c) - distribution of partial conductivity vs. charge carriers mobility in $Bi_{0.9996}$-$Sn_{0.0004}$ for holes and electrons, respectively.

We thank the Belarusian Republican Foundation for Fundamental Research for the financial support given to project F16M-067 which made this research possible.

[1] A. Fedotov, S. Poznyak, L. Tsybulskaya et al., Polycrystalline bismuth films: Correlation between grain structure and electron transport, Physica Status Solidi (b) **252** (2015). DOI: 10.1002/pssb.20155205

[2] A. Fedotov, V. Shepelevich, S. Poznyak et al., Simulation of polycrystalline bismuth films Seebeck coefficient based on experimental texture identification, Materials of Chemistry and Physics **177**, 413-416 (2016). DOI: 10.1016/j.matchemphys.2016.04.047

TOWARDS TRANSMISSION STUDIES OF POLARITONS: II-VI SEMICONDUCTOR MICROCAVITIES LIFT-OFF

Bartłomiej Seredyński, Piotr Starzyk, Wojciech Pacuski

Faculty of Physics, University of Warsaw, Poland
b.seredynski@student.uw.edu.pl

Monocrystalline substrate is a key component for grow a thin layers by molecular beam epitaxy (MBE). The choice of the substrate is typically determined by the lattice constant and crystalline structure of designed layer. However physical properties of some substrates may significantly affects measurements of grown epitaxial layers, e.g. opaque substrate limits measurements of light transmission and absorption.

The problem of opaque substrate can be solved by epitaxial layers lift-off. The purpose of this experiment was to develop and verify the method of producing free-standing microcavity containing three (Cd,Zn,Mn)Te quantum wells (QW).

On the black GaAs substrate we have gown the 1 μm thick CdTe buffer and 1 μm hygroscopic MgTe layer. Next we have grown 22 pairs of Bragg mirror based on (Cd,Zn,Mg)Te with 40% and 10% of Mg in low and high refractive index layers respectively. The width of layers was optimized to reach cavity resonance at emission wavelength of (Cd,Zn,Mn)Te quantum wells (about 760 nm). Inside cavity we have grown three of those QWs containing 1% of manganese. Finally we have grown 22 pairs of top Bragg mirror.

Such a structure was stable in atmosphere. Reflectance at both room and helium temperature showed characteristic stopband with sharp cavity mode. The photoluminescence measurements at helium temperature revealed narrow spectral line at 760 nm corresponding to QWs energy.

To separate epitaxial layer with microcavity from the rest of the structure, the sample was glued to a quartz glass and immersed in deionized water for 2 hours. After rinsing, MgTe layers was removed by water and the glass plate with microcavity containing QWs was lifted-off from the substrate. Images of the sample on the glass showed continuous surface of area more than 1 mm^2. At low temperature we observed photoluminescence of QWs and characteristic reflectivity of microcavity what confirms that Mg in Bragg mirror and cavity was not harmed despite long contact with water.

Only after removing the substrate it was possible to measure optical transmission through the microcavity. This measurement gives complementary information to reflectivity spectra, but also it opens possibility of experiments on superfluidity of exciton-polaritons with magnetooptical properties enhanced by presence of Mn in quantum wells.

Oral session 9

Nanomaterials and Nanotechnology

THE RAMAN SCATTERING ENHANCEMENT OF CdS QUANTUM DOTS

Anna Matsukovich[1], Elena Shabunya-Klyachkovskaya[1], Olga Kulakovich[1], Mikhail Smirnov[2], Aleksey Perepelitsa[2], Sergey Gaponenko[1]

[1] B.I. Stepanov Institute of Physics, National Academy of Sciences of Belarus, Belarus
[2] Voronezh State University, Russia
a_matsukovich@tut.by

Quantum dots have attracted considerable interest in the fields of solid state lighting, displays, and medicine. Their tunable optical properties by changing the size and solution processability lead to commercial applications [1]. The small spatial volume of quantum dots and, consequently, the small Raman scattering cross section make it necessary to search for possibility of the Raman scattering enhancement of quantum dots.

Raman scattering enhancement factor depends on nature, form and sizes of metal nanoparticles, configurations of nanoparticles and analyte. It was shown [2] the surface enhancement Raman scattering of the analyte between two layers of gold nanoparticles is up to 5 times higher compared to the "analyte under gold film" arrangement and up to 60 times higher than for the "analyte on gold film" case. In the present work, the enhancement of Raman scattering (RS) by CdS quantum dots in various „analyte-plasmonic silver film" configurations have been studied.

A water solution of CdS quantum dots in thioglycolic acid (TGA) was investigated. The quantum dots size is about 3 nm. Optical density spectrum of QDs solution has absorption in the ultraviolet range 350-450 nm.

The water solution of QDs ($C=3*10^{-7}$ M) has been deposited on the glass, on the silver film substrate and between two layers of silver nanoparticles (so-called „sandwich" configuration) and dried at the room temperature in the horizontal position. Silver sol was prepared by reduction of silver nitrate with sodium citrate as described in [3]. Average silver nanoparticle size is about 50 nm. Optical density spectrum of silver film has the broad peak of plasmon resonance at 485 nm (Fig.1a).

Raman spectra of CdS QDs have an intensive peak at 294 cm^{-1} (LO phonon) [4] on the silver film substrate and in "sandwich" configuration. The double and triple frequency of the LO phonon (593 and 892 cm^{-1}, respectively) are shown overtone bands of the first and second-order (2LO and 3LO) (Fig. 1b).

The intensity of LO phonon at 294 cm^{-1} is about 3000 a.u. in case of CdS deposition on silver film. Raman spectrum of CdS QDs on the glass was not registered. So, it is possible to obtain the RS enhancement of CdS QDs on 3 orders of magnitude. When CdS nanocrystals are located between two layers of silver nanoparticles provides the additional Raman scattering enhancement in 2 times. Theoretical calculations predicted [5] that if the dipole momentum orientation is normal, the density of photonic states in the region between two spherical nanoparticles may be 5 times higher than that near one isolated nanoparticles. Other cases of the dipole momentum orientation can give minimal density of photonic states. In our experiment the forming of "sandwich" configuration based on the principle of self-organization and the dipole momentum orientation could be random. However, the increasing of intensity of the band LO phonons in 2 times for "sandwich" configuration can be seen as an experimental result that is consistent with the theory.

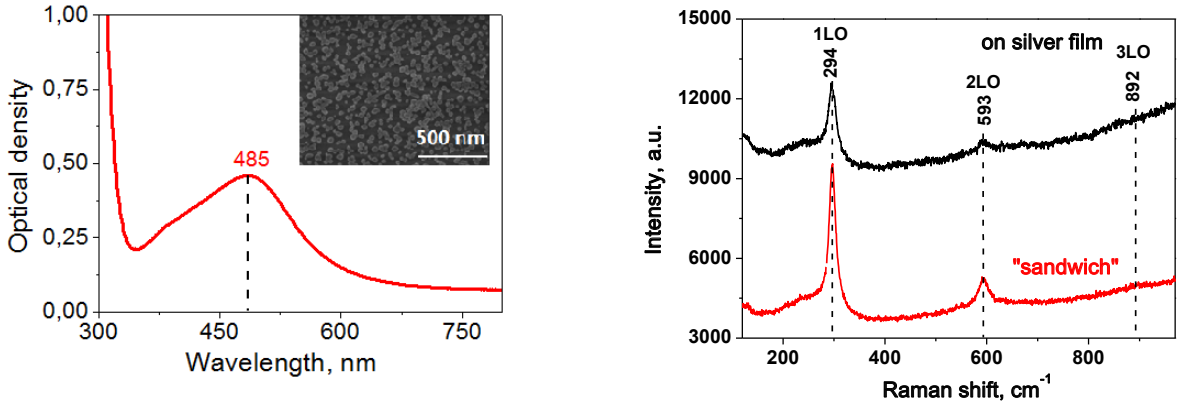

a) b)

Fig. 1. a) Optical density spectrum and SEM imaging of Ag film; b) SERS spectra (λ_{ex}=488 nm) of CdS QDs on silver film and at "sandwich" configuration.

[1] T. Frecker.et al., Review – Quantum dots and their applications in lighting, displays, and biology. ECS J. of Solid St. Sci. and Tech.**5 (1).** R3019-R3031 (2016)
[2] O.S. Kulakovich et al., Plasmonic enhancement of Raman scattering for sandwich metal-analyte configuration. JAS. **83(5).**824–828 (2016).
[3] P. C. Lee, D. Meisel, Adsorption and surface-enhanced Raman of dyes on silver and gold sols. J. Phys. Chem**. 86(17)**. 3391–3395(1982).
[4] A.G.Milechin et al., Surface enhancement Raman scattering of CdS quantum dots. JETPH Letters **88(12)**. 918-921 (2008).
[5] S. Gaponenko. *Introduction to Nanophotonics. (*Cambridge, 2010).

CHARACTERIZATION OF Bi_2Se_3 NANORIBBONS BY *IN-SITU* SCANNING ELECTRON MICROSCOPY

Jelena Kosmaca, Liga Jasulaneca, Raimonds Meija, Jana Andzane, Donats Erts

Institute of Chemical Physics, University of Latvia, Latvia
jelena.kosmaca@lu.lv

Combining a nanomanipulation and electrical measurement set-up together with real-time visualization provides a powerful tool for control and investigation of processes occurring at the nanoscale.

We will present an experimental approach for characterization of nanostructures and their electrical and mechanical properties by *in-situ* scanning electron microscopy (SEM). One-dimensional bismuth selenide (Bi_2Se_3) nanostructures – nanoribbons, have thermoelectric and topological insulator properties, prospective for applications in energy conversion, as well as spintronic and quantum information devices. Besides, due to their size, shape, and elasticity, they can act as active elements in nanoelectromechanical systems and sensors. We investigate nanoelectromechanical switching and electrical breakdown parameters of individual Bi_2Se_3 nanoribbons, analyze their vibrations and finally, determine the Young's modulus.

Experiments are performed *in-situ* SEM Hitachi S-4800. The set-up is configured using a Smaract 13D nanomanipulation system and Au tips, which are used as electrodes for electrical measurements (Fig. 1a) and electrostatic excitation of the nanoribbon resonance (Fig. 1b).

The results are important for interpretation of nanoscale processes, as well as characterization of nanomaterial properties and their application in nanodevices.

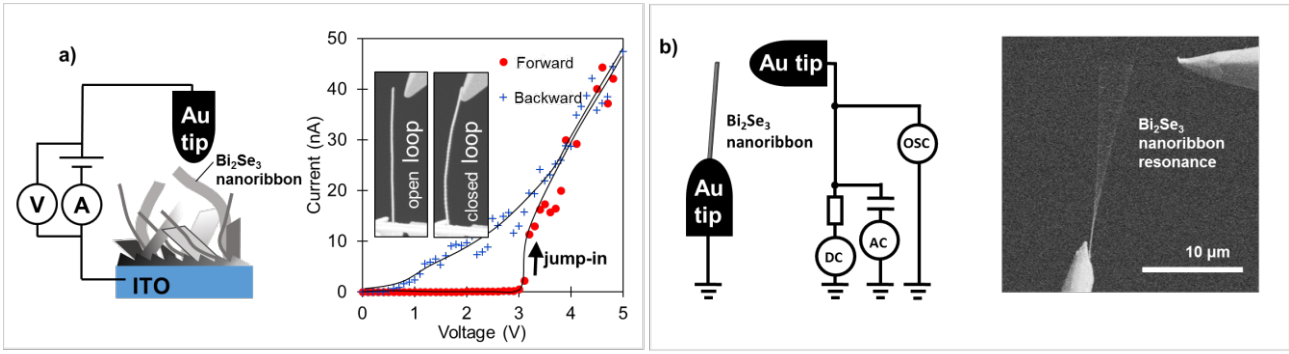

Fig. 1. a) Set-up for electrical measurements and nanoelectromechanical switching of an individual nanoribbon and corresponding voltage-current curve [1]; b) Set-up for the electrostatic excitation for mechanical vibrations and individual nanoribbon resonance [2]

[1] J. Kosmaca, J. Andzane, M. Baitimirova, F. Lombardi, D. Erts, Role of Nanoelectromechanical Switching in the Operation of Nanostructured Bi_2Se_3 Interlayers Between Conductive Electrodes, ACS Applied Materials & Interfaces, **8**, 12257-12262 (2016)

[2] J. Kosmaca, L. Jasulaneca, R. Meija, J. Andzane et al., Cross-sectional analysis and determination of Young's modulus of Bi_2Se_3 nanoribbons by *in-situ* resonance measurements – submitted manuscript (2017)

RANDOM CIRCUIT METHOD FOR MWCNT-NH_2 COMPOSITES MODELING

Gleb Gorokhov[1], Darya Meisak[1], Dzmitry Bychanok[1], Silvia Bistarelli[2], Stefano Bellucci[2]

[1]Research Institute for Nuclear Problems, Belarusian State University, Belarus
[2]INFN-Laboratori Nazionali di Frascati, Italy
glebgorokhov@yandex.ru

Polymer-based composites containing carbon nanostructures are prospective for a wide range of applications such as electromagnetic shielding, next-gen wireless communications, and many others. A few wt% of multi-wall carbon nanotubes (MWCNT) can significantly modify the electromagnetic response of composite increasing its electric conductivity and shielding effectiveness[1, 2, 3]. In the case of epoxy resin there is less than 0,25 % of MWCNT needed to create percolation network, but due to the nanotubes strong agglomeration ability, a significant amount of nanotubes is excluded from percolation network. To reduce the number of agglomerates NH_2–radicalization was used[4]. The dispersion of radicalized MWCNT in the epoxy resin is more homogeneous due to amino radicals taking part in epoxy resin curing.

The permittivity of composite MWCNT-NH_2 composites was measured in the range up to 10 MHz. For modeling such a composite system simple 2D–circuit consists of resistors, capacitors, diodes (constant phase elements), i.e. RCD-model[5] was used. In this case, resistors correspond to metallic nanotubes, capacitors to polymer matrix (epoxy resin) and diodes to contacts between nanotubes.

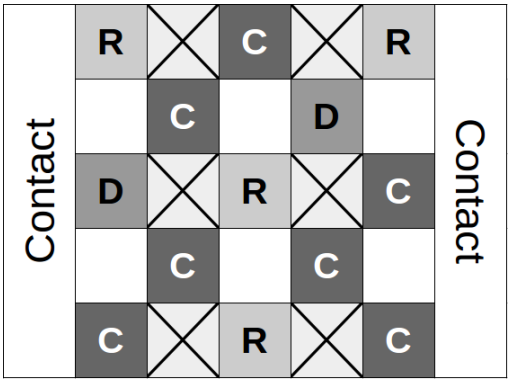

Fig. 1. Typical random circuit used for approximation. R, C and D corresponds to resistor, capacitor and diode, respectively. Crossed cells correspond to connections between elements.

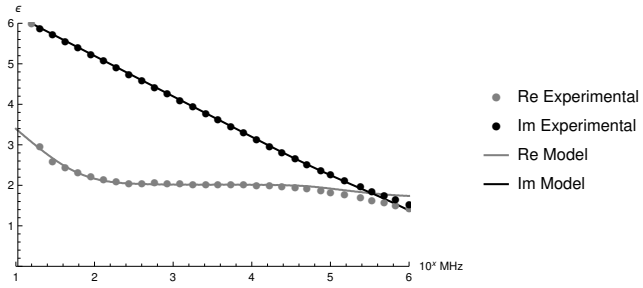

Fig. 2. Complex permittivity for 1 % MWCNT–NH_2 composite. Dots correspond to experimental data, lines for approximation. Grey and black colors corresponds to real and imaginary parts of permittivity, respectively.

The result of modeling with random circuit method strongly depends on network properties. To obtain realistic results the circuit must provide at least one connection between the left and right sides consisting of only resistors and capacitors. It corresponds to percolation network in the real composite. Additionally, there must be an alternative connection containing only capacitors because more than 98 % of the composite is the dielectric matrix.

Results of modeling using equivalent RCD network are shown in Fig. 2. They are in good agreement with experimental data. The model gives better fitting for samples with bigger MWCNT concentrations. The permittivity of samples with MWCNT-NH_2 concentrations larger than 0,5 % can be successfully approximated, but for lower concentrations in the experimental setup, the model does not reproduce experimental data. That means that for low concentrations close to percolation threshold the RCD–model needs to be modified. There exist also other possibilities to fit experimental data, e.g. variation of relative R, C, D concentrations; introducing of any dispersion of diodes by the scale parameter C_1 and exponent k; it is also possible to present statistic data and to model R-C-D network by different morphology (i.e. the network consisting of not square but triangle hexagonal parts). Hereinafter our future efforts will be focused on the experimental verification and improvement of described here methodology using above strategies.

[1] F. Qin and C. Brosseau, A review and analysis of microwave absorption in polymer composites filled with carbonaceous particles, Journal of Applied Physics, **111**, no. 6, p. 061301, (2012).
[2] D. Bychanok, P. Kuzhir, S. Maksimenko, S. Bellucci, and C. Brosseau, Characterizing epoxy composites filled with carbonaceous nanoparticles from dc to microwave, Journal of Applied Physics, **113**, no. 12, p. 124103, (2013).
[3] G. Gorokhov, A. Moiseenko, D. Bychanok, P. Kuzhir, Improved absorption properties of nanocabon/magnetite composites in 2637 GHz, 59th scientific conference for young students of physics and natural sciences Open Readings 2016, ISSN 2029-4425, Vilnius University, 203 (2016).
[4] Chen X, Wang J, Lin M, Zhong W, Feng T, Chen X, Chen J, Xue F., Mechanical and thermal properties of epoxy nanocomposites reinforced with amino-functionalized multi-walled carbon nanotubes. Materials Science and Engineering: A. **492(1)**, 236-242 (2008).
[5] D. S. Bychanok, A. G. Paddubskaya, P. P. Kuzhir, S. A. Maksimenko, C. Brosseau, J. Macutkevic and S. Bellucci, A study of random resistor-capacitor-diode networks to assess the electromagnetic properties of carbon nanotube filled polymers, Appl. Phys. Lett. **103**, 243104 (2013).

TEMPERATURE TUNING OF LOCALISED SURFACE PLASMON RESONANCE IN GOLD NANOPARTICLES BASED ON ANTI-GALVANIC REDUCTION

Grzegorz Kolodziej, Michal M. Wojcik

Laboratory of organic nanomaterials and biomolecules, Department of Chemistry, University of Warsaw, Poland
grzegorz.kolodziej@student.uw.edu.pl

Noble metals nanoparticles with controlled geometrical and optical properties are the subject of intensive studies and materials applications due to thier excelent stability derived from organic monolayer. As a deeply investigated system, they make excellent reference material for studying behavior of larger structures build from nanoparticles. [1][2]

Gold nanoparticles inherit property of LSPR (localized surface plasmon resonance) that makes them interesting subject in field of optical properties of condensed matter materials, particularly metamaterials, SERS (surface enhanced Raman spectroscopy), sensing etc. [3][4] LSPR in nanoparticles can be tuned by a number of features. Starting from nanoparticle shape or size, ending on their spatial arrangement and relative distances between them.

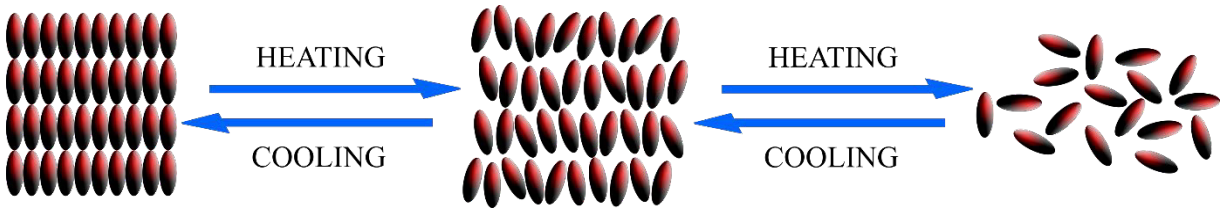

Fig. 1. Phase transitions of thermotropic liquid crystal: from solid to liquid crystal to isotropic liquid.

Thermotropic liquid-crystalline molecules manifest property of changing their spatial arrangement and degree of order in material they make. These behaviour can be seen when material of this type change its phase from solid to liquid-crystalline, liquid-crystalline to isotropic liquid or between diffrent liquid-crystalline phases. These changes are tuned by changes of temperature.

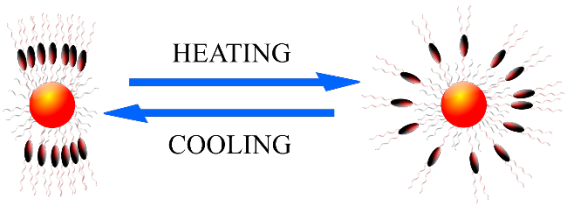

Fig. 2. Phase transition of gold nanoparticle functionalized with thermotropic liquid crystals: from liquid crystalorganisation to isotropic liquid.

Terminating liquid-crystalline molecules by thiol group allow to utilize them as surface-coating agent. This allows self-assembly of gold nanoparticles into ordered structures in liquid-crystalline manner, therefore offering reliable means of changing optical properties of material given by presence of LSPR. [5]

In this research, small gold nanoparticles in size of 2-3 nm were functionalized with liquid crystal molecules. They were also subjected to procedure causing phenomenon called Anti-Galvanic Reduction. [6] That lead to appearance of strong LSPR enhancemen, that can be dynamically controlled.

[1] M. C. Daniel, D. Astruc, Gold Nanoparticles: Assembly, Supramolecular Chemistry, Quantum-Size-Related Properties, and Applications Toward Biology, Catalysis, and Nanotechnology, Chemical Reviews **104**, 293-346 (2004).
[2] Y. Sun, Y. Xia, Shape-Controlled Synthesis of Gold and Silver Nanoparticles, Science **298**, 2176-2179 (2002).
[3] J. N. Anker, W. P. Hall, O. Lyandres, N. C. Shah, J. Zhao, R. P. Van Duyne, Biosensing with plasmonic nanosensors, Nature Materials **7**, 442-453 (2008).
[4] N. Engheta, Circuits with Light at Nanoscales: Optical Nanocircuits Inspired by Metamaterials, Science **317**, 1698-1702 (2007).
[5] M. M. Wojcik, M. Gora, J. Mieczkowski, J. Romiszewski, E. Gorecka, D. Pociecha, Temperature-controlled liquid crystalline polymorphism of gold nanoparticles, Soft Matter **7**, 10561-10564 (2011).
[6] Z. Wu, Anti-Galvanic Reduction of Thiolate-Protected Gold and Silver Nanoparticles, Angewandte Chemie **51**, 2934-2938 (2012).

OPTICAL RESPONCE OF COMPOSITE PLASMONIC STRUCTURES

Nikolai Mitetelo, Sergey Svyakhovskiy, Alexandra Gartman, Anton Maydykovskiy

Department of Physics, M. V. Lomonosov Moscow State University, Russia

nickm@shg.ru

In this paper we would like to present composite structure based on porous quartz with silver nanoparticles [1] prepared by different methods. Such structures could be used for SERS- investigations (Surface enhanced Raman scattering) to define small quantities if substances. In such experiments molecules of investigated substance should be close to metallic nanoparticles which concentrate the incident electromagnetic field in small area near them.

Main application of this structure may be the enhancement of Raman-signal and second harmonic (SH) signal, because the intensity of both signals is proportional to the local field factor which depends on the size, form, origin and arrangement of nanoparticles. For characterization of the enhancement it is better to study second harmonic generation in this structure, because only one of the scattered or incident field is enhanced while both raman frequencies (stokes and anti-stokes) are in the range of enhancement. This range depends on the location of the localized surface plasmon resonance (LSPR).

So we suggest an idea of a 3D-porous quartz plate with metallic nanoparticles on its walls. This object with thickness of ~ is more efficient than 2D-structures due to its larger space of interaction with the incident wave. Here rather crucial is the low linear and nonlinear absorption [2] of the matrix which will also be observed. With the help of electrochemical etching [3] of silicon followed by thermochemical oxidation there is a possibility to make structures with wide range of pore-diameters (electron microscope image of the structure on Fig. 1). Silver nanoparticles were inserted inside the pores by vacuum infusion, supercritical fluid impregnation and by chemical synthesis. Transmission spectra of the structure prepared with the help of the method of using infusion in vacuum box is shown on Fig.2.

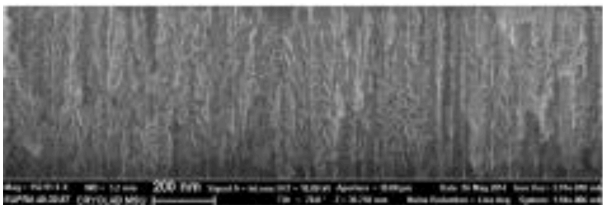

Fig. 1. SEM-image of a porous structure.

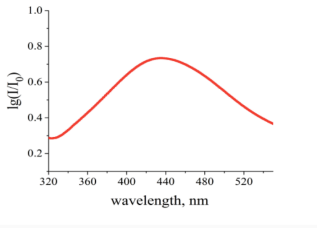

Fig. 2. Transmission of the 3D composite structure

Main prediction of this work is that 3D-composite structure will show bigger enhancement than 2D-plate because of the large space of interaction of the structure surface with the radiation with wavelength placed in the range of localized surface plasmon resonance of the composite structure. Method of producing the matrix for investigated composite structure gives a possibility to make structures with different porosity and pore-diameters which gives a possibility to vary the distance between small metallic “antennas” and to change plasmonic properties in this way. These facts are observed and described in the work.

[1] Chan, S., et al., Adv. Mater. (2003) 15,1595.

[2] M. Sheik-Bahae, A. A. Said, T. H. Wei, D. J. Hagan, and E.W Van Stryland, IEEE J.Quantum Electron. 26, 760 (1990).

[3] Lehmann V. Electrochemistry of Silicon: Instrumentation, Science, Materials and Applications. - Wiley, 2002.

PREPARATION OF MAGNETIC Fe_3O_4 NANOPARTICLES WITH POTENTIAL APPLICATION IN BIOMEDICINE

Paulina Grzączkowska[1,2], Jakub Mikulski[1], Przemysław Kowalik[1], Tomasz Wojciechowski[1], Krzysztof Fronc[1],Rafał Rudniewski[1], Roman Minikayev[1], Mariusz Łapiński[3], Jarosław Rybusiński[2], Anita Gardias[2], Jacek Szczytko[2], Danek Elbaum[1] and Bożena Sikora[1]

[1]Institute of Physics Polish Academy of Sciences, Poland
[2]Institute of Experimental Physics, Faculty of Physics, University of Warsaw, Poland
[3]Institute of Optoelectronics, Military University of Technology, Poland
p.grzaczkowska@hotmail.com

Anti-cancer treatment has become the vital point in medicine. Thus development of nanotechnology is one of the alternative ways of therapy. Iron oxide-based nanoparticles have been widely used for examining and treating cancer cells due to their magnetic properties in hyperthermia therapy.

Fe_3O_4 magnetic nanoparticles were synthesized in two different ways. Morphology and characterization of nanoparticles were measured with X-ray diffraction method, Scanning Electron Microscope and Superconducting Quantum Interference Device. First synthesis of Fe_3O_4 is based on high temperature decomposition of the self-synthesized Fe(III)-oleate. Different concentration of Fe(III)-oleate and time of the reaction resulted in various size of each nanoparticles. In second synthesis the magnetic particles were obtained by chemical precipitation from ferric ($FeCl_3$) and ferrous salts ($FeSO_4$) in alkali medium (ammonia hydroxide). To increase magnetic properties nanoparticles were doped with Yttrium in several concentrations.

X-ray diffraction method confirmed a cubic single phase of Fe_3O_4 in both syntheses. SEM images showed different average size of nanoparticles from 10nm to 25nm. Nanoparticles from Fe(III)-oleate reaction had distribution of size around 2nm and those obtained from precipitation around 6nm. Measurements of relation between applied magnetic field (H) (Oe) and magnetization (M)(emu/g) varied from 9 to 84 (emu/g)(at 2000 Oe), where maximum value is obtained by doped Fe_3O_4. In 200 Oe field precipitated nanoparticles reached higher magnetization values quicker than those from Fe(III)-oleate, which went in favour of these nanoparticles obtained in the second reaction.

Measurements of influence of changing magnetic field on nanoparticles showed their ability to generate heat, which may be used in hyperthermia therapy.

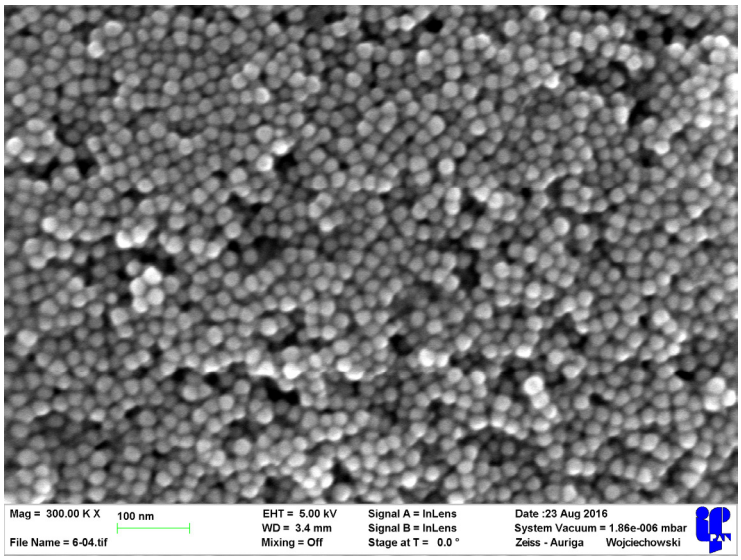

Fig. 1. SEM image of Fe_3O_4 nanoparticles

Acknowledgements: The research was partially supported by the project „Development of the cluster center of biomedical engineering" implemented under Economy Operational Program (project no. UDA-POIG.05.01.00-00) and the grant and DEC-2014/15/D/ST5/02604.

Oral session 10

Biochemistry, Biophysics and Biotechnology

HUMAN AMNIOTIC FLUID-DERIVED MESENCHYMAL STEM CELLS: FEATURES AND DIFFERENTIATION POTENTIAL

Monika Glemžaitė[1], Sandra Baronaitė[1], Aistė Zentelytė[1], Jūratė Savickienė[1], Natalija Krasovskaja[2], Audronė Arlauskienė[2], Rūta Navakauskienė[1]

[1] Department of Molecular Cell Biology, Institute of Biochemistry, Life Sciences Centre, Vilnius University, Lithuania
[2] Clinic of Obstetrics and Gynaecology, Faculty of Medicine, Vilnius University, Lithuania
monika.glemzaite@bchi.vu.lt

Human amniotic fluid-derived mesenchymal stem cells (AF-MSCs) are a new potential stem cell source for regenerative medicine and therapy. These cells are obtained from amniotic fluid by amniocentesis from pregnant women under the necessity of prenatal diagnostics. Amniotic fluid is known to contain multiple cell types derived from the developing foetus and extra-embryonic tissues including foetal skin, placenta membranes, epithelial and mucosa of foetal digestive, respiratory and urinary tract [1]. Among these, there is a fraction of cells exhibiting stem-cell like properties and characteristics of mesenchymal stem cells that were termed amniotic fluid-derived mesenchymal stem cells [2]. AF-MSCs have high proliferation and self-renewal potential and are able to differentiate towards multiple lineages *in vitro*, such as osteogenic, adipogenic, myogenic, neurogenic, etc. They show no evident antigenicity and tumorigenicity and can be obtained securely and avoiding ethical issues related to embryonic stem (ES) cells [3]. Considering these features, AF-MS cells are a promising subject for researches *in vitro* as well as *in vivo*.

The aim of our work was to characterize human AF-MS cells phenotypically, genetically and to assess their differentiation potential.

AF-MSCs were obtained from second trimester amniotic fluid from healthy women who needed prenatal diagnostics but no foetus abnormalities were detected by genetic analysis (protocols approved by the Ethics Committee of Biomedical Research of Vilnius District, No 158200-123-428-122). They were evaluated phenotypically as having typical spindle shape. Flow cytometry analysis revealed that AF-MS cells are strongly positive for mesenchymal cell surface markers CD105, CD90 and CD44 and negative for hematopoietic marker CD34 (Fig. 1). These cells also expressed pluripotency markers of stem cells, such as *Oct4, Nanog, Sox2* and *Rex1* as determined by RT-qPCR. AF-MSCs were also confirmed for their multilineage differentiation potential towards adipogenic, myogenic, neurogenic [4], osteogenic [5] and cardiomyogenic lineages by cell staining and expression of genes-markers.

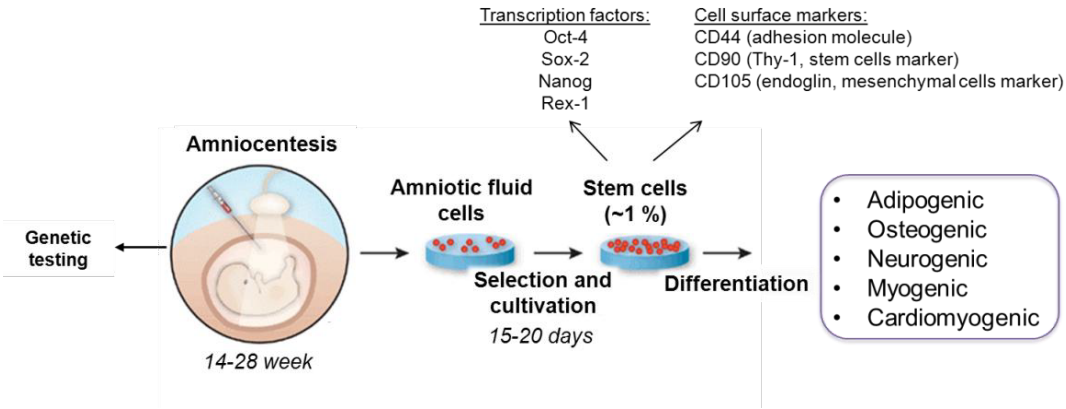

Fig. 1. Characterization of human amniotic fluid-derived stem cells.

In conclusion, our results complement knowledge about mesenchymal stem cells derived from human amniotic fluid confirming that these cells can be considered as multipotent stem cells and used for successful differentiation *in vitro* towards various lineages. This provides new insights for further investigations of human AF-MSCs and their applications in cell therapy and regenerative medicine.

[1] De Coppi P, Bartsch G Jr, Siddiqui MM, Xu T, Santos CC et al. Isolation of amniotic stem cell lines with potential for therapy. Nat Biotechnol. 2007 Jan; 25(1):100-6. Epub 2007 Jan 7.
[2] Prusa AR, Marton E, Rosner M, Bernaschek G, Hengstschlager M. Oct-4-expressing cells in human amniotic fluid: a new source for stemcell research? Hum Reprod. 2003 Jul; 18(7):1489-93.
[3] Roubelakis MG, Pappa KI, Bitsika V, Zagoura D, Vlahou A, Papadaki HA, et al. Molecular and proteomic characterization of human mesenchymal stem cells derived from amniotic fluid: comparison to bone marrow mesenchymal stem cells. Stem Cells Dev. 2007 Dec; 16(6):931-52.
[4] Savickiene J, Treigyte G, Baronaite S, Valiuliene G, Kaupinis A, Valius M, Arlauskiene A, Navakauskiene R. Human Amniotic Fluid Mesenchymal Stem Cells from Second- and Third-Trimester Amniocentesis: Differentiation Potential, Molecular Signature, and Proteome Analysis. Stem Cells Int. 2015; 2015:319238. doi: 10.1155/2015/319238. Epub 2015 Aug 17.
[5] Glemžaitė M, Navakauskienė R. Osteogenic Differentiation of Human Amniotic Fluid Mesenchymal Stem Cells Is Determined by Epigenetic Changes. Stem Cells Int. 2016; 2016:6465307. Epub 2016 Oct 12.

THE EFFECT OF LONG-TERM ELECTRICAL STIMULATION ON MEMBRANE POTENTIAL OF C6 RAT GLIOMA CELLS

Tatiana Kochetkova, Yuliya Kunitskaya, Elizaveta Kavalenka, Elena Golubeva, Pavel Bulai

Department of Biophysics, Belarusian State University
kochetkovatan@gmail.com

Electrical stimulation is a rapidly developing method of cellular and tissue engineering. Recently, both cellular and molecular approaches have demonstrated that electrical stimulation can change cell behavior such as migration, proliferation and differentiation [1]. Nevertheless, the relationship between cell response and electrical stimulation remains to be established. We assume electrical stimulation causes changes in transmembrane potential. The membrane potential plays a central role in many essential biological processes and is actively maintained by ion pumps and transporters [2]. In this study, we exposed C6 rat glioma cells *in vitro* to long-term electrical stimulation with different parameters of electric field and compared resting membrane potentials of cells.

C6 rat glioma cells were cultivated at 37 °C under a humidified atmosphere with 5 % CO_2. Stimulation by the external electric field was applied for 12 hours and was launched 8 hours after cell passaging. Electrical stimulation was provided by application of uniform electric field with biphasic stimuli (0.2 ms pulse duration, 10 Hz) of different strength (6 or 20 V/m) and the number of pulses in train (1, 3, 5 or 7) (Fig. 1 A). The measurements of membrane potentials were performed 2 hours after the exposure and were carried out using patch-clamp technique.

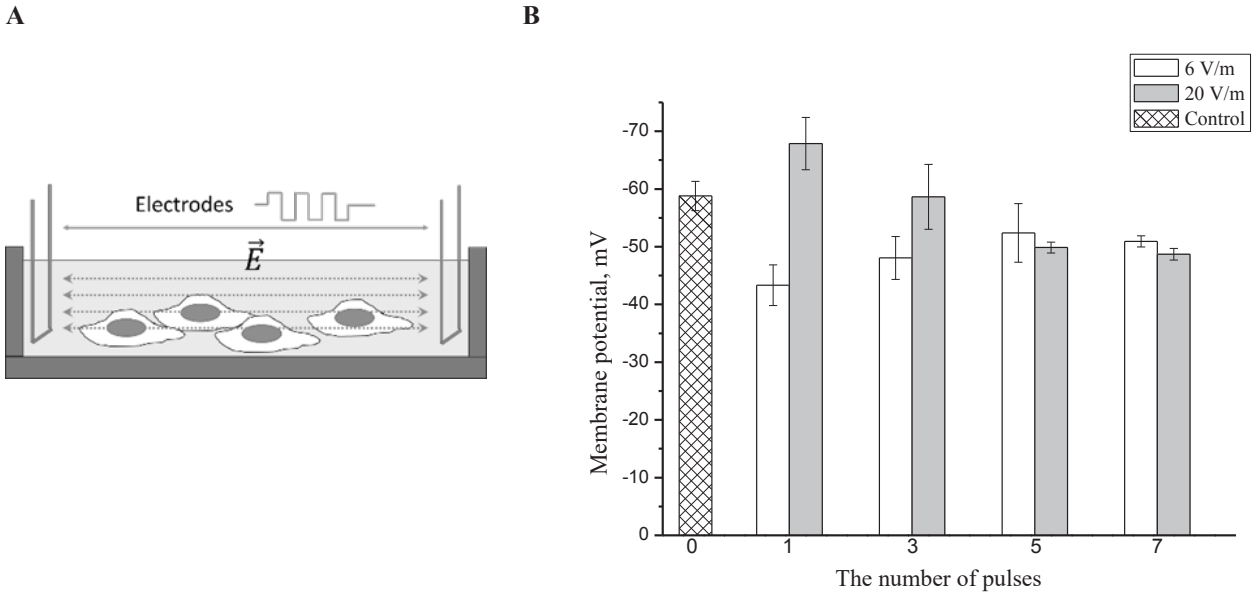

Fig. 1. Experiment design and results. A – Electrical stimulation. B – The resting membrane potential of C6 rat glioma cells after electrical stimulation with different parameters of the stimulatory electric field (Values are shown as mean ± standard deviation).

It was found that electrical stimulation of C6 rat glioma cells causes a change in resting membrane potential. The results obtained depend on the number of pulses and elecrtic field strength (Fig. 1 B). Membrane potential tends to the control value with the increase of pulses quantity both at 6 and 20 V/m. At one-pulse stimulation hyper- and depolarisation of membrane is observed depending on the strength of the electric field. The value of resting membrane potential can affect the cell cycle propagation and, consequently, the cell proliferation [3]. Thus, discovered correlation between electrical stimulation parameters and resting membrane potential can be used to develop cell engineering methods.

[1] R. Balint, N.J. Cassidy, S.H. Cartmell, Electrical stimulation: a novel tool for tissue engineering, Tissue Eng Part B Rev, 19(1):48-57 (2013).
[2] S. Sundelacruz, M. Levin, D.L. Kaplan, Role of Membrane Potential in the Regulation of Cell Proliferation and Differentiation, Stem Cell Rev and Rep, 5:231 (2009).
[3] D. Urrego, A. P. Tomczak, F. Zahed, W. Stühmer and Pardo L. A. Potassium channels in cell cycle and cell proliferation, Philos Trans R Soc Lond B Biol Sci, 369: 20130094 (2014).

ACTIVATION OF MACROPHAGES WITH VARIOUS STRUCTURE OLIGOMERS AND THEIR IMMUNE COMPLEXES

Asta Luciunaite, Indre Dalgediene, Aurelija Zvirbliene

Institute of Biotechnology, Life Sciences Center, University of Vilnius, Vilnius, Lithuania
asta.luciunaite@gmail.com

Macrophages are a part of organism defense system. They remove pathogenic microorganism and other pathogenic compounds, give an activation signal to the immune system cells. They also can detect antigens opsonized with antibodies and internalize them [1]. Therefore, macrophages might have an impact on the efficiency of antigen elimination in certain diseases. However, in many cases it is unknown how macrophages are activated with potentially pathogenic proteins. For example, detailed mechanism of macrophage/microglia activation with β-amyloid (Aβ) during Alzheimer‘s disease is unknown [2]. As well as, the pathway of macrophage activation with immune complexes (IC) is unclear as certain side effects of anti-Aβ therapy have been shown in treatment of AD [3].

The aim of the current research was to investigate the influence of Aβ oligomers and viral oligomers (measles virus, WU polyomavirus and metapneumovirus) and their immune complexes (IC) on macrophage phenotype. The research model was primary spleen cell culture from BALB/c mice. We generated macrophage from splenic monocytes and used this culture in our research. The variations in the levels of cell markers – inflammatory macrophage M1 markers and anti-inflammatory macrophage M2 markers – were investigated by flow cytometry and ELISA.

Our results showed generation of both M1 and M2 phenotype after macrophages treatment with Aβ oligomers and their IC. The IC induced higher expression of M2-related marker IL-10 compared to Aβ oligomers alone. Higher levels of IL-10 may indicate a negative impact of IC on the phagocytic degradation of Aβ oligomers. Macrophage treatment with oligomeric viral antigens and their IC induced the inflammatory phenotype of macrophages. However, the activation signal was lower compared to Aβ oligomers. In conclusion, the activation of macrophages with oligomeric proteins and their IC can induce different signals and lead either to the inflammatory or anti-inflammatory phenotype depending on the origin and structure of the oligomeric proteins.

[1] P. J. Murray, T. A. Wynn, Protective and pathogenic functions of macrophage subsets, Nature reviews Immunology **11**, 723-737 (2011).
[2] D. Tejera, M. T. Heneka, Microglia in Alzheimer's disease: the good, the bad and the ugly, Curr Alzheimer Res. **13(4)**, 370-380 (2016).
[3] D. J. Marciani, Alzheimer's disease vaccine development: A new strategy focusing on immune modulation, J Neuroimmunology **287**, 54-63. (2015).

DELETION ANALYSIS OF MULTISUBUNIT CRISPR-CAS EFFECTOR COMPLEX

Irmantas Mogila, Miglė Kazlauskienė, Gintautas Tamulaitis, Virginijus Šikšnys

Institute of Biotechnology, Life Sciences Center, Vilnius University, Lithuania
mogirmantas@gmail.com

CRISPR-Cas systems provide prokaryotes with adaptive immunity against foreign plasmids and viruses. During the infection short fragments of invading nucleic acids can be integrated into the CRISPR region of host genome. The CRISPR region is transcribed and resulting transcript is processed into separate crRNA (CRISPR RNA) molecules. crRNAs together with Cas proteins assemble into effector complexes which guided by the crRNA seek and destroy foreign nucleic acids during subsequent infections. The best studied effector complexes of Type I and Type II CRISPR-Cas systems target invading DNA [1]. Type II effector complex comprising of a single Cas9 protein is widely established as genome editing tool [2]. In contrast, Type III effector Csm and Cmr complexes function as RNA-guided DNA nucleases: upon recognition of RNA target they start to degrade *in cis* both RNA and the DNA that is being transcribed [3]. It has been shown that Csm3 is the ribonuclease subunit of Csm complex [4] and Cas10 is the deoxyribonuclease which is activated upon the Csm complex binding to an RNA target [5]. However, the roles of remaining Csm complex subunits are not fully understood.

The aim of this study was to determine the functions of *Streptococcus thermophilus* CRISPR-Cas subtype III-A effector Csm complex (StCsm) subunits. For this reason we expressed in *Escherichia coli* and purified StCsm complexes lacking individual subunits. We analyzed i) the composition of StCsm complex in the deletion variants, ii) the RNA target binding affinity and cleavage rate, iii) the RNA-dependent DNA degradation rate. We show that Cas6 protein is responsible for *S. thermophilus* CRISPR transcript processing to individual crRNA molecules. Our data suggest that Csm4, which forms a subcomplex with deoxyribonuclease Cas10, specifically binds and anchors 5'-end of crRNA during the formation of StCsm complex. Next, we conclude that proteins Cas10, Csm4 and Csm5 are important for the maturation of crRNA. We also show how effector complex subunits promote the activity of StCsm. These results may pave the way for development of novel molecular tool for programmable RNA silencing both *in vitro* and *in vivo*.

[1] A. Plagens, H. Richter, E. Charpentier, L. Randau. DNA and RNA interference mechanisms by CRISPR-Cas surveillance complexes. *FEMS Microbiol Rev* **39**(3), 442–63, (2015).
[2] A. V. Wright, J. K. Nuñez, J. A. Doudna. Biology and Applications of CRISPR Systems: Harnessing Nature's Toolbox for Genome Engineering. *Cell* **164**(1-2), 29–44, (2016).
[3] G. Tamulaitis, Č. Venclovas, V. Siksnys. Type III CRISPR-Cas Immunity: Major Differences Brushed Aside. *Trends Microbiol* **25**, 49–61, (2017).
[4] G. Tamulaitis, M. Kazlauskiene, E. Manakova, Č. Venclovas, A. O. Nwokeoji, M. J. Dickman, P. Horvath, V. Siksnys, Programmable RNA shredding by the type III-A CRISPR-Cas system of *Streptococcus thermophilus*. *Mol Cell* **56**, 506-517, (2014).
[5] M. Kazlauskiene, G. Tamulaitis, G. Kostiuk, Č. Venclovas, V. Siksnys. Spatiotemporal Control of Type III-A CRISPR-Cas Immunity: Coupling DNA Degradation with the Target RNA Recognition. *Mol Cell* **62**, 295–306, (2016).

Oral session 11

Biology, Genetics and Biomedical Sciences

MODELLING RESPONSES TO VISUAL STIMULI IN ALZHEIMER'S DISEASE

Eglė Maksimovaitė , Daniel Herring , Dr Marc Goodfellow

Department of Natural Sciences, University of Exeter, United Kingdom
em409@exeter.ac.uk

Approximately 5.2% of the elderly population worldwide suffers from some form of dementia, of which Alzheimer's disease (AD) is the most common cause. Currently there is no definite diagnostic test for AD, other than post-mortem examination. However, one of the early symptoms of AD is the impairment of visual processing. Studies show that the amplitudes of visual evoked potentials (VEPs) are reduced in AD and amnestic mild cognitive impairment (aMCI), an interim stage between healthy aging and dementia. (Fig.1) [1]. VEPs are peaks in electrical potentials within neural populations as a response to a visual stimulus, measured using an Electroencephalogram (EEG). Mathematical modelling can be used to investigate neural mechanisms causing reduced VEPs, and identify biological parameters that could be biomarkers of AD in the brain. In this work, we fitted a neural mass model [2] to clinical VEP data [1] using an evolutionary algorithm. We analysed subject-specific sets of model parameters to understand the effect of AD on the neural architecture and dynamics of the visual pathway.

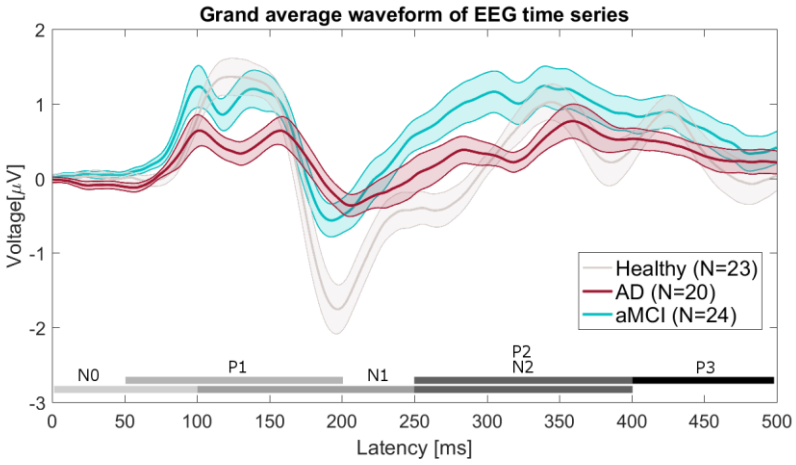

Fig. 1 Grand average waveform of EEG timeseries (shaded regions indicate standard error of the mean).

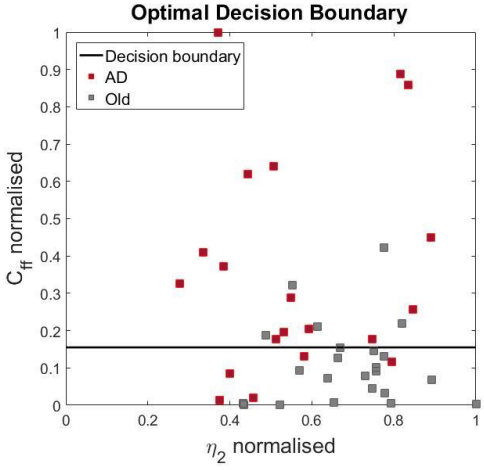

Fig. 2 Clustering of subjects in parameter space (C_{ff} plotted against η_2 for clarity).

We found that self-inhibition of fast-spiking inhibitory interneuron population (FS) is increased in AD and aMCI compared to healthy aging subjects, whereas the inhibition of pyramidal population by FS cells is reduced in aMCI and AD. Based on the self-inhibition parameter (C_{ff}), we classified subjects into healthy and AD on the one hand (Fig.2) and healthy and aMCI conditions on the other with an accuracy of 76.7% and 72.3% respectively. Our results are in line with previous findings, whereby impaired inhibitory function of FS cells has been linked to deficits in information processing, indicating the potential for AD drugs to target inhibitory neuron populations. The success of classification suggests that parameter-based VEP analysis could provide a novel non-invasive tool in the diagnosis of aMCI and AD.

[1] G. Stothart, N. Kazanina, R. Näätänen et al., Early visual evoked potentials and mismatch negativity in Alzheimer's disease and mild cognitive impairment, J Alzheimers Dis **44**, 397-408 (2015).
[2] F. Cona, M. Zavaglia, M. Massimini et al., A neural mass model of interconnected regions simulates rhythm propagation observed via TMS-EEG, Neuroimage **57**, 1045-1058 (2011).

ATHEROSCLEROSIS RISK FACTORS INFLUENCE ENDOTHELIAL MICROVESICLE COUNT IN PERIPHERAL BLOOD

Vytautas Žėkas[1], Reda Matuzevičienė[1], Dovilė Karčiauskaitė[1], Asta Mažeikienė[1], Neringa Burokienė[1], Mantas Radzevičius[1], Aušra Janulionienė[2], prof. Zita Aušrelė Kučinskienė[1].

[1] Departament of Physiology, Biochemistry, Microbiology and Laboratory Medicine, Faculty of Medicine, Vilnius University, M. K. Čiurlionio str. 21/27, LT-03101 Vilnius, Lithuania.

[2] Center for Laboratory Medicine, Vilnius University Hospital Santariškių Clinics, Santariškių str. 2, LT-08661 Vilnius

Vytautas.zekas@mf.vu.lt

High numbers of circulating microvesicles of different cell origin have been associated with subclinical atherosclerosis. Microvesicles shed from endothelial cell may participate in the pathogenesis of oxidative stress, inflammation, coagulation and angiogenesis [1]. The objective of this study was to test the relationship between known atherosclerosis risk factors and counts of two different populations of endothelial microvesicles (EMV)**.** We included 81 male individuals in the study aged between 25 and 55 years who were apparently healthy or without any acute clinical condition. Informed consent was obtained from all the subjects and the study protocol was approved by the local ethics committee of Vilnius University. Laboratory tests including concentration of C-reactive protein, glucose, total cholesterol, triglycerides, HDL- and LDL-cholesterol were performed using routine techniques. Fresh blood samples were collected in Lithium and Sodium Heparin contained tubes after night fasting. Tubes were centrifuged for 10 minutes at 3000g within one hour from collection to obtain platelet free plasma (PPP). Three quarters of said plasma were transferred to sterile tube and centrifuged again at 15000g for 30 minutes in angle head motor to pellet microvesicles. Resulting EMV pellet was reconstituted with 1ml serum free freezing medium containing DMSO (Biological Industries, Israel) and analyzed by flow cytometry. All samples were labeled with anti CD144-FITC, anti CD105-BV421, anti CD42a-PerCP, anti CD62e-PE, anti CD31-APCy7, anti CD61-APC (BD, San Jose) and tested using BD Fortessa cytometer (BD, San Jose). All events were gated by forward and side light scatter parameters. In our research we examined two endothelial microvesicle (EMV) populations: 1) expressing CD144, CD42b-, CD61- and 2) CD105, CD42b-, CD61- markers. Furthermore in each population we determined a percentage of EMVs, expressing CD62e. The men were grouped according to their blood pressure: 1) having blood pressure equal to or more than 140 mm/Hg (n=17); 2) having blood pressure less than 140 mm/Hg (n=64). Percentage of EMVs expressing CD 144 and CD62e was significantly higher in group with higher blood pressure (d=8.24%±4.67 vs d=5.20%±3.36, P=0,03). We also have found significant positive correlation with diastolic blood pressure (d=79.94±8.84, P<0.001), total cholesterol (d=5.84±3.85, P<0.001) and triglycerides concentration (P<0.001), especially with the microvesicles, expressing CD62e. The results of this study suggest a strong direct association between different atherosclerosis risk factors and EMV count in peripheral plasma of apparently healthy individuals.

[1] R. P. Keshav, P. Nisha, K. Dong-Wook. Circulating Endothelial Microparticles: A Key Hallmark of Atherosclerosis Progression. Scientifica **2016:9** (2016)

mTHPC NANODELIVERY SYSTEM BASED ON CYCLODEXTRINS

Yakavets Ilya[1,2,3*], Yankovsky Igor[1,2,3], Lassalle Henri-Pierre.[2,3], Bezdetnaya Lina[2,3], Zorin Vladimir[1,4]

[1] Department of Biophysics, Belarussian State University, Minsk, Belarus
[2] Centre de Recherche en Automatique de Nancy, CNRS, Université de Lorraine, Nancy, France
[3] Institut de Cancérologie de Lorraine, Vandoeuvre-lès-Nancy, France
[4] International Sakharov Environmental Institute, 220070 Minsk, Belarus.
**viprorok@gmail.com*

Application of meta-tetra(hydroxyphenyl)chorin (mTHPC), one of the most effective photosensitizer (PS), in photodynamic therapy of solid tumors encounters several complications resulting from its insolubility in aqueous medium [1]. To improve its solubility and pharmacokinetic properties, two modified β-cyclodextrins (β-CDs): methyl-β-cyclodextrin (Me-β-CD) and 2-hydroxypropyl-β-cyclodextrin (Hp-β-CD) were proposed (Figure 1). The aim of this work was to evaluate the effect of β-CDs on mTHPC behavior at various stages of its distribution in vitro and in vivo.

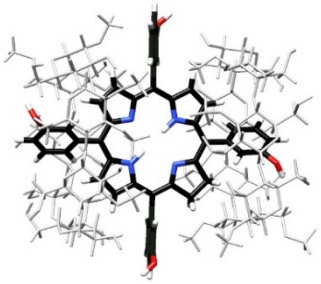

Fig. 1. The structure of mTHPC/β-CDs complex [2].

For this purpose, we have studied the influence of the β-CDs on mTHPC binding to the serum proteins, its accumulation, distribution and photodynamic efficiency in HT29 monolayer and spheroid models. In addition, the processes of mTHPC biodistribution in HT29 tumor bearing mice after intravenous injection of PS alone or with the β-CDs were compared.

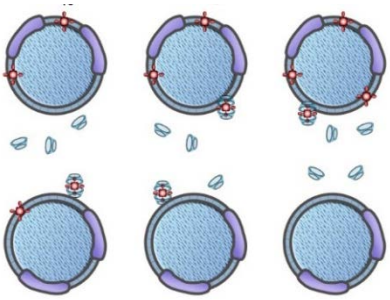

Fig. 2. Representative scheme of nanoshuttle mechanism.

Interaction of mTHPC with studied β-CDs leads to the formation of inclusion complexes that completely abolishes its aggregation after introduction into serum [2]. The β-CDs increase diffusion movement of mTHPC molecules by nanoshuttle mechanism (Figure 1B). The presence of β-CDs significantly improve distribution of mTHPC tumor cell cultures *in vitro* [3]. *In vivo* studies confirm the fact that application of β-CDs allows to modify mTHPC distribution processes in tumor bearing mice.

The data obtained confirm the interest of CDs in mTHPC-PDT.

Acknowledgements. This study was supported by Belarussian Republican Foundation for Fundamental Research, the Ministry of Education of the Republic of Belarus and French "Ligue National contre le Cancer". The authors thank Biolitec Research GmbH (Jena, Germany) for providing mTHPC.

[1] M. Senge, mTHPC – A drug on its way from second to third generation photosensitizer? Photodiagnosis and Photodynamic Therapy **9**, 170-179 (2012).
[2] I. Yakavets, I. Yankovsky, L. Bezdetnaya, and V. Zorin. Soret band shape indicates mTHPC distribution between β-cyclodextrins and serum proteins. Dyes and Pigments **137**, 299–306 (2017).
[3] I. Yankovsky, E. Bastien, I. Yakavets, et al. Inclusion complexation with β-cyclodextrin derivatives alters photodynamic activity and biodistribution of meta-tetra(hydroxyphenyl)chlorin. Eur. J. Pharm. Sci. **91**, 172–182 (2016).

TOXICITY AND ACCUMULATION OF UPCONVERTING NANOPARTICLES IN CANCER CELLS

Evelina Voronovič[1], Greta Jarockytė[1], Artiom Skripka[2], Vitalijus Karabanovas[1,3], Ričardas Rotomskis[1,4]

[1] Biomedical Physics Laboratory of National Cancer Institute, Baublio 3B, LT-08406, Vilnius, Lithuania
[2] National Institute of Scientific Research, University of Quebec, 1650, boulevard Lionel-Boulet, Varennes, Canada
[3] Department of Chemistry and Bioengineering, Vilnius Gediminas Technical University, LT-10223 Vilnius, Lithuania
[4] Biophotonics group of Laser Research Centre, Vilnius University, Saulėtekio 9, c.3, LT-10222, Vilnius, Lithuania
evelina.voronovic@stud.vgtu.lt

Current biomedical imaging methods such as X-ray computed tomography (CT), positron emission tomography (PET) and single photon emission computed tomography (SPECT) imaging are being widely used due to their supremacy of unlimited tissue penetration depth. However, they possess harmful effects for patients and medical personnel on account of radioactive sources usage [1]. The most favorable alternative for these bioimaging methods are new generation contrast agents called upconverting nanoparticles (UCNPs) which acquire optical properties within the „biological transparency window“, are biocompatible and non-toxic for human health. To date, UCNPs show great luminescent properties, biocompatibility, high penetration depth in biological tissues, resistance to photobleaching [2].

The aim of this work was to investigate optical properties of water soluble upconverting nanoparticles in different cell growth media/aqueous solutions and perform *in vitro* studies by testing biocompatibility and uptake dynamics of UCNPs into breast cancer cells with different tumorigenicity.

In this study optical properties of $LiYF_4:Yb^{3+}$, Tm^{3+} UCNPs in different aqueous environments were investigated. Emission spectra of nanoparticles were measured with Edinburgh Instruments spectrometer FLS920. Different concentration of UCNPs were used while evaluating emission spectra. It was observed that colloidal stability of upconverting nanoparticles strongly depends on concentration and presence of fetal bovine serum (FBS). Our results showed that solution was the most stable when concentration of nanoparticles was 10 μg/mL and medium was supplemented with FBS. The highest colloidal stability was found in the solution with the 20 % FBS. Additionally, influence of pH on optical properties of UCNPs was determined. Acidity of aqueous media affects UCNPs properties directly: emission intensity of nanoparticles decreases increasing pH of the solution.

Moreover, the uptake dynamics and cytotoxicity of nanoparticles were evaluated. Human breast adenocarcinoma cell lines with different tumorigenicity (MCF-7 and MDA-MB-231) were used for cell experiments. Cells were treated with different concentrations of UCNPs for 24 h. After incubation with nanoparticles, the viability of cells was evaluated by counting viable and non-viable cells with automatic cell counter ADAM-MC (Digital Bio, Republic of Korea). The uptake dynamics of nanoparticles in cancer cells was observed by measuring emission of $LiYF_4:Yb^{3+}$, Tm^{3+} UCNPs accumulated in cells.

In conclusion, $LiYF_4:Yb^{3+}$, Tm^{3+} UCNPs possess great and stable emission intensity in different cell growth media for several weeks. Our experiments revealed that $LiYF_4:Yb^{3+}$, Tm^{3+} UCNPs accumulate in cells and are non-toxic: after 24 h incubation with UCNPs viability assay was carried and no overt toxicity was found. These results show UCNPs to have great intrinsic properties and suitability for cancer bioimaging.

Acknowledgement: this work was supported by grant „Study of optical properties and biocompatibility of $Na(Gd/Y)F_4$ nanoparticles“ (No.MIP-030/2014) from the Research Council of Lithuania.

[1] V. Ntziachristos et al., Looking and listening to light: the evolution of whole-body photonic imaging, Nature Biotechnology **23**, 313-320 (2005).
[2] M. Wang et al.,Upconversion nanoparticles: synthesis, surface modification and biological applications, Nanomedicine: NBM **7**,710-729 (2011).

ANNIHILATION UPCONVERSION AS AN ALL-OPTICAL TEMPERATURE SENSING TOOL FOR LIFE-SCIENCE

Nadzeya Nazarova[1], Yuri Avlasevich[1], Stanislav Baluschev[1,2], Katharina Landfester[1]

[1] Max Planck Institute for Polymer Research, Mainz, Germany
[2] Optics and Spectroscopy Department, Faculty of Physics, University «St. Kliment Ochridski» of Sofia, Bulgaria
pleshka@mpip-mainz.mpg.de

Optical sensing, based on the process of triplet-triplet annihilation photon energy upconversion[1] (TTA-UC), represents new approach for testing of the material parameters of living objects. The sensing process involves optical excitation of the sensitizer molecule at so-called upconversion regime, followed by ratiometric registration of two optical signals – delayed emitter fluorescence (dEF) and residual sensitizer phosphorescence (rSPh) – as a function of the local temperature in an oxygen-free environment. Excitation at the tissue transparency window combined with extremely low excitation intensity and ratiometric type registration ensures high signal to noise ratio, keeping the sensing procedure minimally invasive.

As stated at the literature, real-time monitoring of the physical parameters in living object could allow creating of a prognostic tool for diagnostics of number of disease, for instance various types of cancer. Deviation of the tissue-temperature from the physiological norm can be used as indicator of physiological changes in the cell[2, 3].

The efficiency of process TTA-UC in organic matrix (paraffin wax) together with the intensity of the residual phosphorescence was investigated at different macroscopic matrix temperatures. As shown in Figure 1a, when the sample-temperature is elevated, the emitter delayed fluorescence is significantly increased, while the residual phosphorescence is strongly decreased. This behavior allows for creating of an unambiguous ratiometric temperature calibration curve demonstrated in Figure 1b.

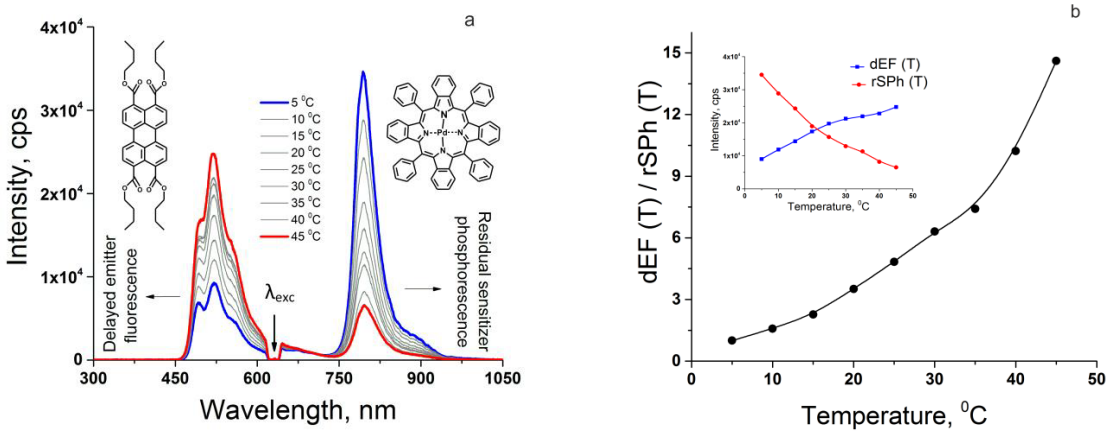

Fig. 1. (**a**) – Temperature dependence of the emission spectra for the sample containing Pd-meso-tetraphenyl-tetrabenzoporphyrin [1×10^{-5} M] as a sensitizer, 3,4,9,10-tetra(butoxycarbonyl)perylene [2×10^{-4}M] as an emitter in the oxygen-free organic matrix, excitation wavelength λ=633 nm with intensity of 50 mWcm^{-2}; The inset of (**a**): Chemical structures of the dyes. (**b**) – Ratiometric temperature calibration curve, derived from the date presented in (**a**). The inset of (b) represents the temperature dependence on the sample temperature for dRF (the blue curve) and for the rSPh (the red curve).

Main advantage of the demonstrated ratiometric-type temperature calibration is the independence of the data obtained on excitation intensity instabilities, local molecular concentration fluctuations and filed-of-view variations. All these advantages reveal the application potential of TTA-UC based temperature sensing tool in field of life-science

[1] M. A. Filatov, S. Baluschev, K. Landfester, Protection of densely populated exited triplet state ensembles against deactivation by molecular oxygen, Chem. Soc. Rev. **45**, 4668-4689 (2016).
[2] D. F. Wilson, Quantifying the role of oxygen pressure in tissue function, Am. J. Physiol.: Heart Circ. Physiol. **294**, H11-H13 (2008).
[3] M. Erecinska, I. A. Silver, Tissue oxygen tension and brain sensitivity to hypoxia, Resper. Physiol. **128**, 263-276 (2001).

HYDRATION OF CYTOCHROME C STUDIED BY VIBRATIONAL SPECTROSCOPY AND CALORIMETRY

Jekaterina Latynis[1*], Vitaly Kocherbitov[2], Justas Barauskas[2], Gediminas Niaura[1]

[1] Vilnius University Life Science Center, Vilnius, Lithuania
[2] Biomedical Science, Faculty of Health and Society, Malmö University, Malmö, Sweden
latynis@gmail.com

Enzyme proteins such as cytochrome c (cyt c) and lysozyme are effective pharmaceuticals and widely used in practices[1]. Biological function of proteins displays in appropriate conformational structure, which occurs in presence of particular water quantity. Most protein folding occurs with water hydrating the peptide backbone and precisely maneuvering the backbone through its secondary and tertiary structural assembly towards its ultimate and unique active structure [2]. Biofilms with immobilized proteins are widely used in biochip science. There is a relationship between the decrease of intermolecular hydrogen bond strength and biofilm mechanical behavior changes, thus film molecular configuration can lead to dissimilarities in its mechanical properties. Thus, to understand a protein function and properties of formed biofilm it is important to know the microscopic dynamics of a protein, i.e., motions of residues and secondary structure, and vision of their bonds' energetics [3, 4]. Recently, we have employed Raman spectroscopy to probe the hydration induced structural changes at various sites of lysozyme under isothermal conditions in the range of water contents from 0 to 44 wt % [5]. This study was aimed to investigate structural and thermodynamic behavior of cyt c during the hydration by means of Fourier Transform Infrared Spectroscopy (FTIR, amide III vibrational bands), Differential Scanning Calorimetry (DSC), Sorption calorimetry studies and compare it to lysozyme hydration studies.

We found a correlation between the spectroscopic and thermodynamic data. There was a reversible structural transition (beta-sheets / unordered structures) in samples containing from 3 to 14 wt % of water with a peak of beta-sheets loss in a sample containing 7 wt %, where an enthalpy of cytochrome c denaturation had a minimum value. We observed an increase of alpha-helix in a sample containing 14 wt % and above content of water, leading a glass transition onset (found using Sorption calorimetry). A loss of beta-sheets and increase in content of unordered structure started from 26 wt % of water content; this point was the end of cytochrome c glass transition. Sample containing 30 wt % showed a peak of the second structural transition which coincided with maximum value of cytochrome c denaturation enthalpy and occurrence of "free water" (a water melting peak appeared in a DSC curve).

Phase transition for both cyt c and lyz c occurred in samples containing relatively close water quantity: the onset of a glass transition was at 13(lyz.)/15(cyt.c) wt % of water in samples; the end of a glass transition and the start of an elastic non-liquid protein phase was in a range of 20 (lyz.)/22 (cyt.c.) wt % of water in samples. Finally, a "free water" in protein molecule occurred in the range of 30 (cyt.c.)/35 (lyz.) wt % of water contents in samples.

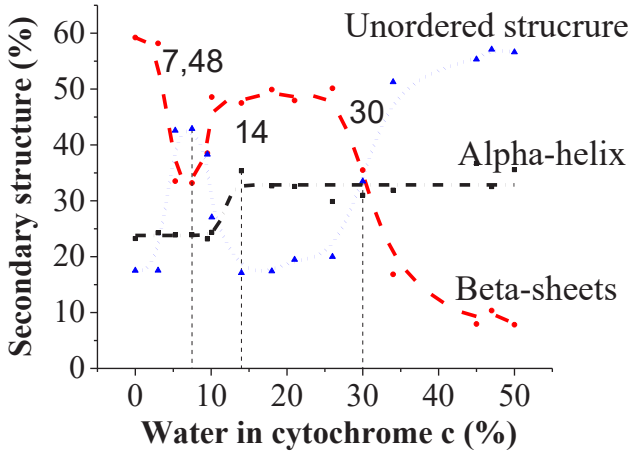

Fig. 1. FTIR studied changes in secondary structure during cytochrome c hydration

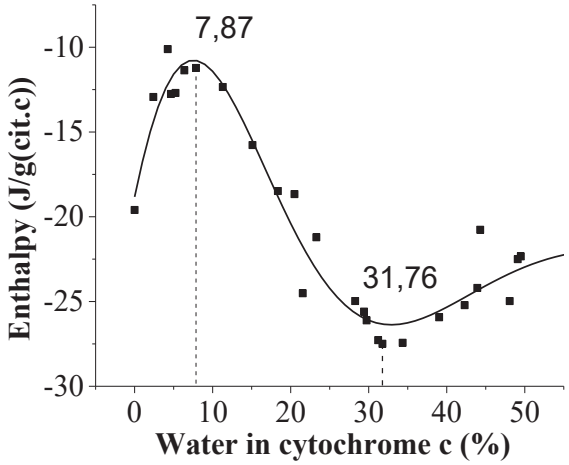

Fig. 2. DSC studied changes of cytochrome c denaturation enthalpy during the hydration of protein.

[1] A. Oleinikova, N. Smolin et al., Influence of water clustering on the dynamics of hydration water at the surface of a lysozyme. Biophysical Journal **93**, 2986-3000 (2007).
[2] M. Chaplin, Do we underestimate the importance of water in cell biology. Nature Reviews Molecular Cell Biology **7** 861-866 (2006).
[3] J.H. Roh et al., Influence of hydration on the dynamics of lysozyme. Biophysical Journal, 2006. **91**(7): p. 2573-2588.
[4] V. Gilbert et al., Characterization and evaluation of whey protein-based biofilms as substrates for in vitro cell cultures. Biomaterials **26**. 7471-7480 (2005)
[5] V. Kocherbitov, J.Latynis et al., Hydration of Lysozyme Studied by Raman Spectroscopy. J. Phys. Chem. B **117**, 4981-4992 (2013).

Poster session 1

PROPER MOTION STUDIES IN G23.657-0.127

Monika Stangret, Anna Bartkiewicz

Centre for Astronomy, Faculty of Physics, Astronomy and Informatics, Nicolaus Copernicus University, Grudziadzka 5, 87-100 Torun, Poland
265911@fizyka.umk.pl

G23.657-0.127 is a high-mass star-forming region. Valuable details about surrounding of the central object is provided by studies of the methanol maser emission at 6.7 GHz [1]. Because of gas and dust extincion, observations of these regions are difficult.

Using the European VLBI Network multi-epoch observations (2004, 2013, 2015) [2] of maser spots in the ring G23.657-0.127, I present a proper motion estimations for individual spots. The ring suggesting expansion because the motions are directed outward. This is probably related to an outflow directed along the line-of-sight. In a relative coordinate system, the shifts depend on the position on the ring, where a reference point is the brightest maser spot. This is consistent with obtained results for individual groups of masers. Calculated velocities of maser spots are: 3.86 km s^{-1} (median) and 4.25 ± 0.4 km s^{-1} (mean value). They are consistent with estimations in other high-mass star-forming regions.

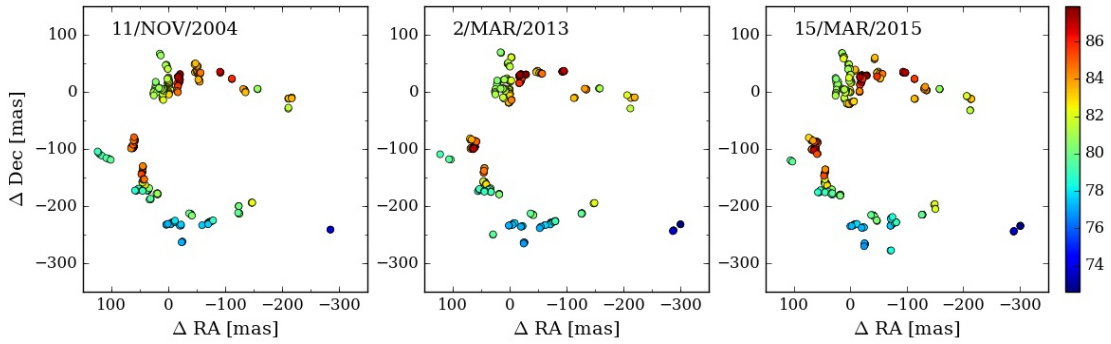

Fig. 1. The distribution of methanol maser spots seen towards G23.657-0.127 in each epoch.

[1] K. M. Menten, The discovery of a new, very strong, and widespread interstellar methanol maser line, The Astrophysical Journal, **380**:L75-L78, 1991.

[2] A. Bartkiewicz, M. Szymczak, and H.J. van Langevelde, Ring shaped 6.7 GHz methanol maser emission around a young high-mass star, Astronomy & Astrophysics, **442**, L64-L64.

THE MODEL OF ORBITAL MOTION AROUND SPHERICAL AND NON-SPHERICAL BODIES

Mateusz Narożnik

Faculty of Physics, Astronomy and Informatics, Nicolaus Copernicus University in Toruń, Poland,
mateusznaroznik1@gmail.com

Motion of the body in central gravitational field is well known and described by three Kepler's law. We know that this is ideal model and is vary rarely encountered. That's why we use several different approaches to this problem (to calculate gravitational potential from non-spherical body) such as: mascons approach, spherical harmonic method and, the most important to me, polyhedral approach. I've chosen the problem of probe's motion in a non-regular gravitational potential because it is a very interesting topic to me and I believe it would have many practical uses in the nearest future [1], [2], [3].

We all remember 2014 and crucial Rosetta mission which opened discussion in the problem, meaning it's not only theoretical divagation but a practical thing. When we launch a probe like Rosetta we want to make such project as efficient as possible. This means, among other things, that the probe should not be heavier than it needs to be. Thanks to newer software, which allows us to make precise calculations of a non-spherical body's potential, we can find a more optimal orbit around an asteroid. Such corrections could save a lot of money, fuel and energy.

In my presentation I will introduce the theme of evaluating gravitational potential in several ways. Firstly, I will describe the motion of an orbiting body, which circles a traditional body like a sphere or a spheroid then I'll move onto more realistic shapes like an asteroid. Thanks to such studies we could learn a lot about morphology of an asteroid and the potential threat it may pose when planet Earth turns out to be standing on its course.

[1] A. Rossi, F. Marzari, P. Farinella*, Orbital evolution around irregular bodies,* Earth Planets Space, **51**, 1173–1180, 1999

[2] Flaviane C.F. Vendetti, Evandro M. Rocco, Antonio F.B.A. Prado*, Orbital Trajectories Control Around Non-spherical Bodies*, AIP Conference Proceedings , Volume 1493, Issue 1, 2012

[3] Robert A. Werner and Daniel J. Scheeres, *Exterior gravitation of polyhedron derived and compared with harmonic and mascon gravitation representations of asteroid 4769 Castalia*, Celestial Mechanics and Dynamical Astronomy 65(3):313-344, September 1996

CROSS-CALIBRATION OF MULTISPECTRAL IMAGES OF BELARUSSIAN SATELLITE AND OTHERS AEROSPACE SYSTEM WITH ATMOSPHERIC CORRECTION

Volha Siliuk[1], Leanid Katkouski[1]

[1] Research Institute of Applied Physical Problems named after A.N.Sevchecnko, Belarusian State University, Belarus
volha.siliuk@gmail.com

For extraction of information about the Earth surface from satellite data, it's necessary to do periodical check of satellite sensors stability. Cross-calibration of two or more sensors is one of the way of such check.

The Belarusian Satellite (BS) was launched in 2012. BS regularly takes pictures of the Earth surface, and this data are used for solving different problems. Cross-calibration of the data from BS and from other known satellites such as Landsat 8, EO-1 (ALI & Hyperion) and AVIRIS (airborne) was done [1,2]. The technique of the cross-calibration is described. The technique is based on calculation of correction factors that take into account the difference in band sensitivities of sensors and the differences in observing conditions (observation time). Cross-calibration techniques for multispectral and hyperspectral (AVIRIS, Hyperion) sensors have some features. These features are described.

Results of cross-calibration show that BS data are reliable enough because derived different sensors ratios of radiances measured quasi-synchronously above the same underlying surface are within the total uncertainties, determined by accuracy of absolute sensors calibrations. Calibration uncertainty of BS, Landsat 8, EO-1 and AVIRIS sensor is no more than 5% [3-6].

The performed technique isn't imply atmospheric correction of satellite data. It is considered that methods of cross-calibration with atmospheric correction are more reliable and accurate. Therefore, as a check on accuracy of the performed technique the cross-calibration of the same satellite data with atmospheric correction was done. For these, method of atmospheric correction is developing. The method are based on calculation of components of the radiative transfer equation by the code LibRadtran. The results of atmospheric correction by this method have a good correlation with results obtained by well-known module FLAASH of program ENVI.

[1] O Siliuk, L. Katkovsky. Inter-calibration of Belarusian Satellite with other imagers, Global Space-based Inter-Calibration System. Quarterly Newsletter: Fall Issue, V. 9, No. 3, 2016, p. 6-8.

[2] O. Siliuk, L.Katkovskii Methods and results of image cross-calibration of the Belarusian satellite and other sensors, V. 13, No. 4, 2016, p. 261-270.

[3] Belyaev, Y., et al., Spectral brightness passing schemes and methods of high-resolution and large aperture equipment calibration. The 10th all-Russia Open Conference "Current Problems in Remote Sensing of the Earth from Space", Book of Abstracts, 2012.

[4] Markham, B., et al., Landsat-8 Operational Land Imager Radiometric Calibration and Stability. Remote Sensing, Vol. 6, Issue 12, 12275-12308, DOI:10.3390/rs61212275, 2014.

[5] Mendenhall, J., Lencioni, D., Evans J., Spectral and Radiometric Calibration of the Advanced Land Imager. Lincoln Laboratory Journal, Vol. 15, No. 2, 2005, p 207-224.

[6]. Chrien, T., et al., Calibration Validation of the AVIRIS Portable Radiance Standard. AVIRIS Workshop Proceeding, 2000,

USING TECHNIQUES OF ALGEBRAIC RENORMALIZATION FOR THE TWO HIGGS DOUBLET MODEL WITH ONE HEAVY NEUTRINO

Vytautas Dūdėnas, Thomas Gajdosik

Department of Theoretical Physics, Faculty of Physics, Vilnius University, Lithuania
vytautasdudenas@inbox.lt

A main ingredient for any model in physics is the collection of its symmetries. In classical physics, Noether's theorem defines the relation between the symmetries and the conserved currents of the model. A classical example of it is that the symmetries of a spacetime lead to the energy-momentum conservation. In field theory, one assigns some intrinsic local symmetries to fields of the theory, which leads to conserved charges. They are called gauge symmetries. An example of such a theory is Quantum electrodynamics(QED), which is a U(1) gauge theory. QED satisfies Noether identities at classical level. However, after the quantization of the theory, the identity is modified to a quantum relation between the correlation functions. These relations in QED are called Ward identites(WI)[1]. The generalization of these identities to non-abelian gauge theories are called Slavnov-Taylor identities(STI)[2]. These identities ensure that the physical amplitudes stay independent of the gauge choice after the quantization and renormalization procedure.

In order to quantize gauge field theories such as the Standard Model one needs to introduce gauge fixing functions into the action, hence explicitly breaking gauge invariance. However it is shown by Becchi, Rouet and Stora[3], that the action stays invariant under the symmetry transformations that include anticommuting fields in place of the commuting gauge parameters. Using this symmetry, one can show that the physical amplitudes are independent of the gauge fixing. In fact, using the STI derived from these symmetries, one can ensure that the renormalization of the SM does not lead to violation of the gauge symmetry. This approach is called algebraic renormalization. The algebraic renormalization is usally employed to formally prove renormalizability of the theory to all orders. However, the practical usage of such an approach is quite uncommon apart from the well known textbook application of WI to QED[4], identifying field and charge renormalization constants. This is due to the fact that STI get increasingly complicated when considering broken non abelian gauge theories such as the SM. However, it is still possible to single out some specific identities of interest for correlation functions at a given order as presented in [5].

We are interested in the neutrinos of the Grimus-Neufeld model[6], which is the SM extended with one heavy neutrino and the second Higgs doublet. We work in Weyl spinor notation, since the chiral structure of the theory is better visible in this formulation [7]. We present and discuss the STI relations at one loop level of this model in Weyl spinor notation that includes the restrictions for the mass and field renormalization of neutrinos.

Acknowledgements: The authors thank the Lithuanian Academy of Sciences for the support (the project DaFi2016).

[1] Y. Takahashi, Nuovo Cim. **6** (1957) 371. doi:10.1007/BF02832514
[2] A. A. Slavnov, Theor. Math. Phys. **10** (1972) 99 [Teor. Mat. Fiz. **10** (1972) 153]. doi:10.1007/BF01090719
[3] C. Becchi, A. Rouet and R. Stora, Annals Phys. **98** (1976) 287. doi:10.1016/0003-4916(76)90156-1
[4] J. C. Ward, Phys. Rev. **78** (1950) 182. doi:10.1103/PhysRev.78.182
[5] P. A. Grassi, T. Hurth and M. Steinhauser, Annals Phys. **288** (2001) 197 doi:10.1006/aphy.2001.6117 [hep-ph/9907426].
[6] W. Grimus and H. Neufeld, Nucl. Phys. B **325** (1989) 18. doi:10.1016/0550-3213(89)90370-2
[7] V. Dūdėnas, T. Gajdosik, Lith. J. Phys. **56** (2016) 148-163. doi:10.3952/physics.v56i3.3364

ANALYSIS OF THE TWO HIGGS DOUBLET MODEL: IN SEARCH OF THE VALID CP-CONSERVING POTENTIAL

Anton Kunčinas, Thomas Gajdosik

Department of Theoretical Physics, Vilnius University, Lithuania
Anton.Kuncinas@protonmail.com

Although the Standard Model (SM) like Higgs boson was discovered in 2012 with the combined measured mass $m_h = 125.09 \pm 0.21(\text{stat.}) \pm 0.11(\text{syst.})$ GeV [1] based on data from the ATLAS and CMS experiments, there is still no experimental verification that it is the only Higgs boson. Therefore there is still place for extending the SM. One of the simplest extensions of the SM Higgs sector is the two Higgs doublet model (2HDM). In the 2HDM a second complex $SU(2)$-doublet is added, which leads to eight scalar fields in total. Out of these fields, five different physical Higgs bosons are generated: two neutral CP-even Higgs bosons h and H, a neutral CP-odd Higgs boson A and a pair of charged Higgs bosons $H^{\pm}$.

During our research we performed both theoretical and numerical analyses of the CP-conserving 2HDM. The generic basis and the physical mass-eigenstates basis were scrutinized. For the numerical analysis the two Higgs doublet model calculator (2HDMC) [2] was used. In order to check how the 2HDMC works a test run of 10^7 points was performed. To achieve that a random number generator (RNG) was implemented along with changing the input format to a convenient form. The theoretical analysis of the model was also performed based on works by Haber [3]. Theoretical and numerical results were compared to get an idea of possible limits of the 2HDM.

The RNG algorithm was constructed to increase efficiency of computing. The algorithm is based on the physical mass-eigenstates basis. The input is the following:

$$\text{4 physical masses} : m_h,\ m_H,\ m_A,\ m_H^{\pm}$$
$$\text{2 mixing angles} : \alpha, \beta$$

First of all, three constraints of the 2HDM potential are checked: stability, S-matrix tree-level unitarity and quartic Higgs boson perturbativity. Based on these calculations and additional limits coming from Higgs bosons masses the range for the value of the coupling coefficient m_{12}^2 is determined. Afterwards it is randomly chosen if parameter point is possible. We call this test the UPS check.

Secondly, if a parameter point passes the UPS check, the oblique parameters [4] S, T and U are estimated. Their values are compared with the ones from the Gfitter group [5]. In our analysis we inspect these values directly without correlation coefficients between the S, T, and U parameters.

Finally, the decay rates are checked. For this check the program Higgs Bounds (HB) [6] is used. Of particular interest is the Type-III 2HDM in which the second 2HDM doublet Yukawa couplings are chosen freely. Such choice allows for flavour changing neutral currents. We check the fermiophobic model where the second 2HDM doublet Yukawa coupling values are zero.

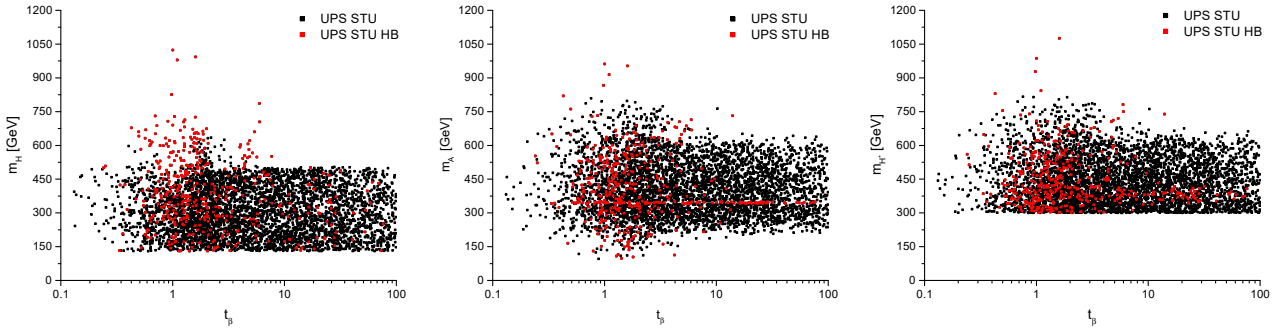

Fig. 1. Different Higgs bosons masses as a function of $\tan\beta$ at various 2HDM potential check steps. Maximum masses are chosen to be 1200 GeV while the minimum are: $m_H^{min} = 130$ GeV, $m_A^{min} = 92$ GeV, $m_{H^{\pm}}^{min} = 300$ GeV.

[1] G. Aad *et al.* [ATLAS and CMS Collaborations], Phys. Rev. Lett. **114** (2015) 191803 doi:10.1103/PhysRevLett.114.191803 [arXiv:1503.07589 [hep-ex]].
[2] D. Eriksson, J. Rathsman and O. Stal, Comput. Phys. Commun. **181** (2010) 189 doi:10.1016/j.cpc.2009.09.011 [arXiv:0902.0851 [hep-ph]].
[3] H. E. Haber and D. O'Neil, Phys. Rev. D **74** (2006) 015018 doi:10.1103/PhysRevD.74.015018 [hep-ph/0602242].
H. E. Haber and D. O'Neil, Phys. Rev. D **83** (2011) 055017 doi:10.1103/PhysRevD.83.055017 [arXiv:1011.6188 [hep-ph]].
[4] M. E. Peskin and T. Takeuchi, Phys. Rev. D **46** (1992) 381. doi:10.1103/PhysRevD.46.381
[5] M. Baak *et al.*, Eur. Phys. J. C **72** (2012) 2205 doi:10.1140/epjc/s10052-012-2205-9 [arXiv:1209.2716 [hep-ph]].
[6] P. Bechtle, O. Brein, S. Heinemeyer, O. Stl, T. Stefaniak, G. Weiglein and K. E. Williams, Eur. Phys. J. C **74** (2014) no.3, 2693 doi:10.1140/epjc/s10052-013-2693-2 [arXiv:1311.0055 [hep-ph]].

CONSTRUCTION OF ANTISYMMETRIC BASIS STATES FOR SIX BODY SYSTEMS IN TRANSLATIONALLY INVARIANT BASIS

Augustinas Stepšys[1], Saulius Mickevičius[2], Darius Germanas[3], Ramutis Kazys Kalinauskas[3]

[1]Department of Theoretical Physics,Faculty of Physics of Vilnius University, Saulėtekio Avenue 9,build. 3, 10222, Vilnius , Lithuania
[2]Vytautas Magnus University, K. Donelaičio str. 58, LT-44248, Kaunas, Lithuania
[3]Center for Physical Sciences and Technology, Savanoriu str. 231, LT-02300 Vilnius, Lithuania
augustinas.stepsys@ff.vu.lt

Ab-initio approach allows solving nuclear physics problems using minimal approximations. Recent developments in ab-initio methods and computing power allows exploration of more complex systems. It also enables us to find out more about the role of nuclear forces[1][2] or structure of exotic nuclei[3][4].

For constructing wavefunction of the nuclear system, we must ensure antisymmetrization of a given system and the center of mass (CM) elimination. CM problem can be solved by direct construction of the CM free wavefunction. For this, the relative (Jakobi) coordinates of an identical fermion system are convenient. If the Jakobi coordinates are used, then the antisymetrization procedure can be done in isospin formalism. Then use of Slater determinants is not necessary and spurious state elimination from antisymmetrized wavefunction sample is avoided. This allows significant reduction of matrix dimensions and certain simplification of whole antisymmetrization procedure.

Construction of antisymmetric wavefunction for a six body system in translationally invariant basis can be based on eigenvalue calculation of two particle transposition operator P of a symmetry group S_6. In this method, six particle system is partitioned into three particle sub-clusters (Fig.1). The separate subcluster nucleon basis states are already antisymmetrized[5]. Then the six body system can be characterized by good quantum numbers: Oscillator quanta E, total angular momentum J, parity π, isospin T and additional integer quantum number Δ for unambiguous enumeration of the basis states.

In presentation, the procedure of antisymmetric basis state construction using symmetry group transposition operators for six particle nuclear system with intrinsic clusterization will be given.

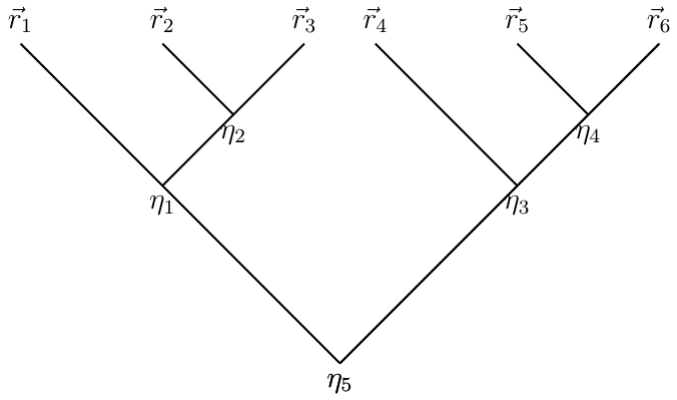

Fig. 1. Six body system in Jacobi coordinates with intrinsic bi-clusterization.

[1] G.Hupin,S.Quaglioni, P. Navratil, Phys. Rev. Lett.**114** 212502 (2015)
[2] S.Binder et al, Phys. Rev. C **93** 044002 (2016)
[3] C. Romero-Redondo et al. Phys. Rev. Lett **117** 222501(2016)
[4] C.Ji et al, Phys Rev. C **90** 044004 (2014)
[5] S. Mickevičius, D. Germanas, R. K. Kalinauskas, Cent. Eur. J. Phys. **11** (2013), 568.

SEMI-SYNTHETIC ZIGZAG OPTICAL LATTICE FOR ULTRACOLD ATOMS

Mantas Račiūnas[1], Egidijus Anisimovas[1], Christoph Sträter[2], André Eckardt[2], Ian B. Spielman[3,4], Gediminas Juzeliūnas[1]

[1]Institute of Theoretical Physics and Astronomy, Vilnius University, Saulėtekio 3, LT-10222 Vilnius, Lithuania
[2]Max-Planck-Institut für Physik komplexer Systeme, Nöthnitzer Straße 38, D-01187 Dresden, Germany
[3] Joint Quantum Institute, University of Maryland, College Park, Maryland 20742-4111, USA
[4]National Institute of Standards and Technology, Gaithersburg, Maryland 20899, USA
mantas.raciunas@tfai.vu.lt

We consider a semi-synthetic "zigzag" lattice, pictured as a two-site wide single strip taken from a triangular lattice, as shown in Fig. 1. The lattice can be created combining a spin-dependent one-dimensional optical lattice with laser-induced transitions between the atomic internal states [1]. It is affected by a tunable homogeneous magnetic flux γ and features nonlocal interactions both in the synthetic and the real dimensions, because atoms in different internal states are trapped in different spatial locations. Nonlocal interactions represent an important goal in recent experiments, and previously such interactions have been engineered via superexchange dipole-dipole coupling or Rydberg dressing.

We numerically investigate the ground-state properties of the proposed system for the case of bosonic atoms with strong interactions using the density-matrix renormalization group calculations. We find that the interplay between the frustration induced by the magnetic field and the interactions gives rise to an exotic gapped phase at fractional per-site filling factors corresponding to one particle per magnetic unit cell [1].

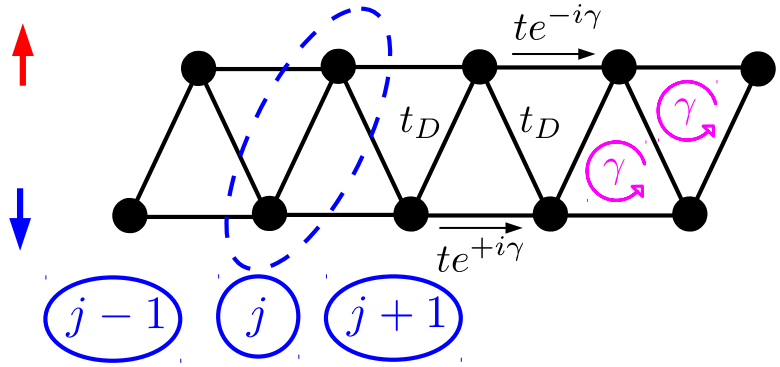

Fig. 1. A semi-synthetic zigzag lattice produced combining an ordinary tunneling along the sites of a one-dimensional spin-dependent lattice (horizontal direction) and laser induced transitions between the two spin states (diagonal direction).

This research was supported by the Lithuanian Research Council (Grant No. MIP-086/2015).

[1] E. Anisimovas, M. Račiūnas, C. Sträter, A. Eckardt, I. B. Spielman, and G. Juzeliūnas, Semisynthetic zigzag optical lattice for ultracold bosons, **Phys. Rev. A 94, 063632 (2016)**.

DIFFUSION OF A BROWNIAN PARTICLE IN A PERIODIC POTENTIAL WITH A FINITE LIFE-TIME

Ulada Vysotskaya, Irina Shapochkina

Department of Physics, Belarusian State University, Belarus
vladavysockaya@mail.ru

Brownian motion appears in a number of physical phenomena and is used for development of artificial nanoscale devices [1-3]. One of the most impressive applications of the theory of Brownian motion is the so-called Brownian motors which model the directional motion of particles in fluctuating periodic potentials [1-3]. In the vast majority of cases, this directional motion takes place in a periodic potential profile with a finite life-time [4]; that makes it important to describe Brownian motion just in such states. The main quantity containing information about the diffusion of a particle is the conditional probability, $P\left(x,t\middle|x_0,0\right)$. Supposing that a state (a certain potential profile) can decay with the rate Γ, i.e, the probability of decay in the time interval $[t,t+dt]$ is $\Gamma\exp(-\Gamma t)dt$ ($t\geq 0$), the probability to find the particle in this state with a finite life-time Γ^{-1} is defined as

$$G\left(x,x_0\right)=\Gamma\int_0^\infty dtP\left(x,t\middle|x_0,0\right)\exp(-\Gamma t). \qquad (1)$$

For the diffusion of a Brownian particle in a periodic potential $V(x)$ (L is the period), the quantity $G\left(x,y\right)$ can be considered as the Laplace representation of the Green's function of the Smoluchowski equation; thus the equation for $G\left(x,y\right)$ appears as

$$\left[1+\Gamma^{-1}\frac{\partial}{\partial x}\hat{J}(x)\right]G\left(x,y\right)=\delta(x-y), \qquad \hat{J}(x)=-De^{-\beta V(x)}\frac{\partial}{\partial x}e^{\beta V(x)}=-D\frac{\partial}{\partial x}-\beta DV'(x) \qquad (2)$$

Here $\beta=(k_BT)^{-1}$ is the inverse thermal energy (k_B is the Boltzmann constant, T is the absolute temperature), D is the diffusion coefficient. Using the conditions of periodicity, of continuity of G-function and the flux discontinuity at point $y=x$, we have got the system of equations for the coefficients of periodic particular solutions of Eq. (2). For piecewise-linear potentials, with two linear links ($[0,l]$ and $[l,L]$) and an energy barrier V, experiencing dichotomous fluctuations with the inverse correlation time Γ, the analytical solution of this system has been found. This result determines the probability density to find the particle, being initially placed at the point y, in the state with a finite life-time Γ^{-1} at the point x. The detailed graphical analysis of this solution has been carried out which gave all the information about the diffusion in the potentials considered; it was shown that the behavior of $G\left(x,y\right)$ strongly depends on the position y relative to the narrow and wide links of the potential profile as well as on the ratio of the potential amplitude to the thermal energy, βV. Thus, the function $G\left(x,y\right)$ is an effective tool to consider the influence of parameters of the model on the average velocity of a Brownian motor. Using the approach suggested, the average velocity of stochastic Brownian motors, of flashing and rocking as well as of combined types, has been calculated and analyzed. Both analytical results and the results of calculation demonstrate good correspondence with the known results [4,5] in limiting cases.

[1] P. Reimann, Brownian motors: noisy transport far from equilibrium, Phys. Rep. **361,** 57 – 265 (1990).
[2] J. Howard, *Mechanics of Motor Proteins and the Cytoskeleton* (Sinauer, Sunderland, MA, 2001).
[3] P. Hänggi and F. Marchesoni, Artificial Brownian motors: Controlling transport on the nanoscale, Rev. Mod. Phys. **81**, 387 - 442 (2009).
[4] R. D. Astumian and M. Bier, Fluctuation Driven Ratchets: Molecular Motors, Phys. Rev. Lett. **72**, 1766 (1994).
[5] V. M. Rozenbaum, I. V. Shapochkina, S. H. Lin et al, High-temperature ratchets with sawtooth potentials, Phys. Rev. E **94**, 052140 (2016).

ADDITIONAL STRANGE RESONANCES FROM LATTICE QCD

Pok Man Lo[1], Michał Marczenko[1], Krzysztof Redlich[1,2,3], Chihiro Sasaki[1,4]

[1]Institute of Theoretical Physics, University of Wrocław, PL-50204 Wrocław, Poland
[2]Extreme Matter Institute EMMI, GSI, Planckstrasse 1, D-64291 Darmstadt, Germany
[3]Department of Physics, Duke University, Durham, North Carolina 27708, USA
[4]Frankfurt Institute for Advanced Studies, D-60438 Frankfurt am Main, Germany
michal.marczenko@ift.uni.wroc.pl

With increasing temperature, the gas of strongly interacting hadronic constituents–baryons and mesons–tends to produce more and more new resonances. At the critical temperature T_c, this picture breaks down and the hadronic matter undergoes a chiral crossover to a new phase with quarks and gluons as the degrees of freedom. The bulk thermodynamic properties of such a gas in the low temperature region are surprisingly well-approximated by a gas of non-interacting hadrons, the so-called hadron resonance gas (HRG). Thanks to the recent progress in the numerical methods of QCD, i.e. lattice QCD, we are now able to look into specific sectors of hadronic matter separately by studying the fluctuations of the net-strangeness and correlations between the net-strangeness and net-baryon number fluctuations. The conventionally used HRG model, despite its success in describing the equation of state below the chiral crossover temperature, fails to reproduce the lattice QCD results for fluctuations. These results suggest that there might be missing resonances in the strange sector of the HRG model [1].

In this talk, we show that the discrepancies between the lattice QCD results and HRG model predictions for the fluctuations and correlators below the chiral crossover can be quantitatively accounted for by inclusion of the Hagedorn mass spectrum in a way consistent with lattice data for both thermodynamics and fluctuations [2].

[1] A. Bazavov, H.-T. Ding, P. Hegde, O. Kaczmarek, F. Karsch, E. Laermann, Y. Maezawa, S. Mukherjee et al., Additional Strange Hadrons from QCD Thermodynamics and Strangeness Freezeout in Heavy Ion Collisions, Phys. Rev. Lett. **113**, 072001 (2014).
[2] P. M. Lo, M. Marczenko, K. Redlich, C. Sasaki, Matching the Hagedorn mass spectrum with lattice QCD, Phys. Rev C **92**, 055206 (2015).

ASYMMETRIC QUANTUM SYSTEMS IN STRONG ELECTROMAGNETIC FIELDS AS TERAHERTZ RADIATION SOURCES

Piotr Gładysz, Dr Karolina Słowik

Institute of Physics, Faculty of Physics, Astronomy and Informatics, Nicolaus Copernicus University, Grudziadzka 5, 87-100 Torun, Poland
pg@atomista.pl

In the last couple of years, technologies based on terahertz radiation have become increasingly interesting due to their numerous applications in fields such as medicine, biotechnology, material engineering and even history of art [1]. For all of these applications, it is essential to use efficient and tunable sources of terahertz frequencies. This presentation is about quantum systems with broken inversion symmetry subject to a strong electric field, which can be used as sources of terahertz radiation.

A two-level quantum system characterized with inversion symmetry and coupled to a classical electromagnetic field undergoes so-called Rabi oscillations where the population flips between the ground and excited levels.

I will discuss how the dynamics is modified if a system of broken inversion symmetry is exploited instead. Then, the eigenstates are characterized with an extra electric dipole moment originating from the polarisation of charges, which plays a significant role. Apart from Rabi oscillations between the energy levels, additional effective oscillations of eigenenergies of these levels can be identified. I will demonstrate how this leads to radiation emission not only at the transition frequency of the system but also with the modified Rabi frequency [2].

The latter could reach the terahertz domain if the quantum system is driven by strong electromagnetic fields, e.g. at close vicinity of plasmonic nanostructures [3]. Final goal is to propose a plasmonic device that could be exploited to implement the above-descibed scenario (Fig. 1).

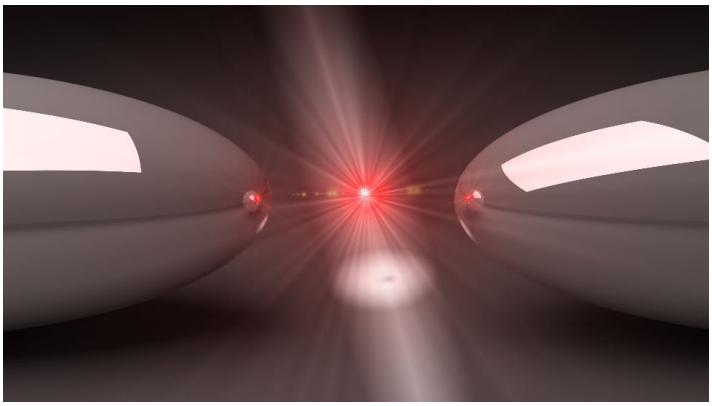

Fig. 1. A visualisation of a quantum system in a spacer gap between plasmonic nanostructures where electromagnetic fields are strongly focused.

[1] A. Y. Pawar, D. D. Sonawane, K. B. Erande, D. V. Derle, Terahertz technology and its applications, Drug Invention Today, 5, 157-163 (2013)
[2] O. V. Kibis, G.Ya. Slepyan, S.A. Maksimienko, A. Hoffman, Matter Coupling to Strong Electromagnetic Fields in Two-Level Quantum Systems with Broken Inversion Symmetry, Physical Review Letters, 2009
[3] L. Novotny, N. van Hulst, Antennas for light, Nature Photonics, 5, 83–90 (2011)

OPTICAL PROPERTIES OF BORON VACANCIES AND BORON VACANCY COMPLEXES IN HEXAGONAL BORON NITRIDE

Mažena Mackoit, Audrius Alkauskas

Center for Physical Sciences and Technology, Vilnius LT-10257, Lithuania
mazena.mackoit@ftmc.lt

Fluorescent defects recently observed under ambient conditions in hexagonal boron nitride (*h*-BN) promise to open novel opportunities for the implementation of on-chip photonic devices that rely on identical photons from single emitters [1], [2], [3]. Despite a flurry of experimental results, the nature of these emitters remain unknown.

In this work we have performed density functional theory calculations of boron vacancies and boron vacancy complexes with oxygen in hexagonal boron nitride. Interaction with oxygen significantly lowers the formation energy of boron vacancies. Therefore, when oxygen is present, complexes are more likely to occur that bare vacancies.

We find that electronic defect states can be of both σ and π type. This suggests that intra-defect luminescence can be polarized both in- and out-of-plane. A multitude of defects levels gives rise to various possible configurations of excited states. This provides a clue to the explanation why polarization of emission and absorption do not necessarily have the same orientation [4]. However, to induce a permanent dipole in bare boron vacancies local strain is needed. More specifically, in negatively charged boron vacancies the dominant transition is of the type $a_1' \rightarrow e'$. In unstrained *h*-BN the emission is unpolarized because transitions to either e'_x or e'_y are equally probable. These states are no longer be degenerate if some strain is present which sets a preferential direction in the *xy* plane. This reasoning is in good agreement with experimental results [4], where observed emitters were oriented in the same direction. We also provide estimates of intra-defect excitation energies and associated Franck Condon shifts, making the connection with recent experimental observations of single photon emitters in this material. These results are a significant step in identifying the structure and electronic states of defect-based single photon sources in *h*-BN.

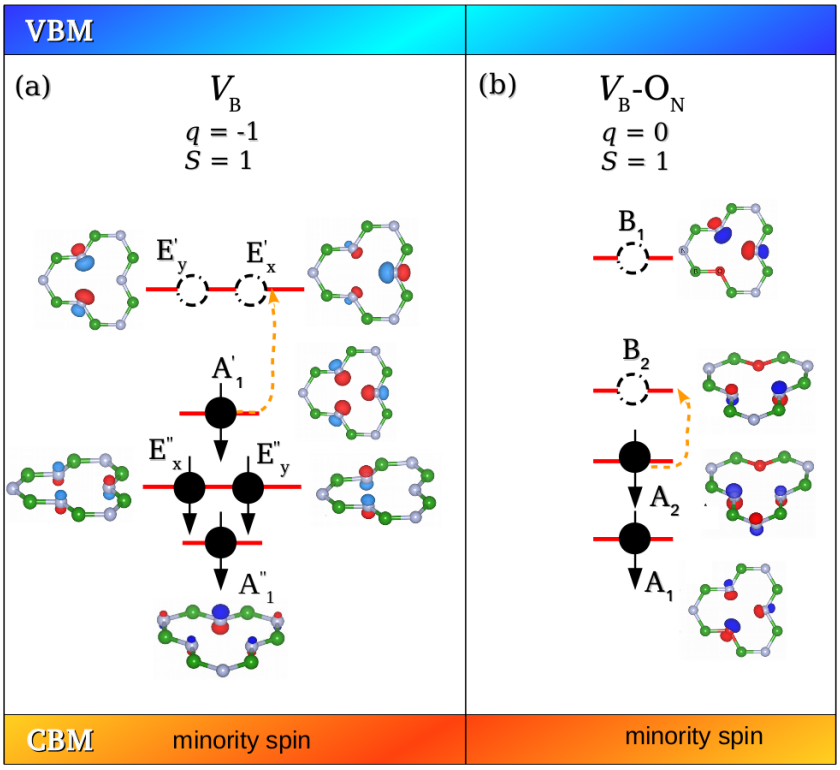

Fig. 1. Single-particle states of the V_B (a) and V_B-O_N (b) defects for charge states q = -1 and q = 0, respectively. In this picture we demonstrate one of possible intra-defect excitations that can occur by promoting an electron from the a_1' state to e' state (a) and from the a_2 state to b_2 state (b).

[1] T. T. Tran, K. Bray, M. J. Ford *et al.*, Nature Nanotechnology **11**, 37-41 (2016).
[2] L. J. Martinez, T. Pelini, V. Waselowski *et al.*, *Phys. Rev. B.* **94**, 121405 (2016).
[3] Z. Shotan, H. Jayakumar, C. R. Considine, M. Mackoit *et al.*, ACS Photonics **3**, 2490 (2016).
[4] N. Chejanovsky, M. Rezal, F. Paolucci *et al.*, Nano Lett. **16**, 7037-7045 (2016).

IDENTIFICATION OF THE ENERGY SPECTRUM OF AUTOIONIZING STATES OF STRONTIUM EXCITED BY ELECTRON IMPACT

Gintaras Kerevičius

Department of the Theory of Atom, Institute of Theoretical Physics and Astronomy, Vilnius University, Saulėtekio Ave. 3, LT-10257, Vilnius, Lithuania

gintaras.kerevicius@tfai.vu.lt

One of the reasons for a complete lack of both experimental and theoretical data [1] on the excitation of $4p^6$ subshell in strontium (Sr) or any core subshell by photon absorption or electron impact is a difficult and sometimes ambiguous assignment of quantum numbers to the states observed. However, sufficiently accurate and unambiguous identification is possible only when relativistic and correlation effects between the electrons are taken thoroughly into account.

Investigation of the energy spectrum of autoionizing (AIS) and Auger (AS) states of Sr is quite a tedious task. Sr I ground state electronic configuration $[Kr]5s^2\ {}^1S_0$ is fully populated, thus spherically symmetric, compared to a previous element in the periodic table – Rb I with the ground state $[Kr]5s\ {}^2S_{1/2}$, so 5.695 eV [1] outer electron binding energy of the former is higher than 4.177 eV [1] of the latter. Sequentially, the binding energies of all electrons in the inner subshells are even higher. Therefore, one could argue that p-core of alkaline earths or any core-excited AIS or AS of an atom become more polarized, and if the initial state was unpolarized – aligned, when the electrons are excited from a fully populated subshell. Sr is a relatively heavy alkaline earth metal atom ($Z = 38$), so relativistic effects play a significant role on the electrons populating different states of the atom. Hence, one can not ignore the fine structure splitting on the energy levels of an atom because of the spin-orbit interaction, which is usually the most dominant relativistic effect. Then, instead of describing the states by an uncoupled total orbital L and spin S angular momenta, one should create a new orthonormal basis by coupling the latter angular momenta to form a total angular momentum J describing each state. One should be aware, that the newly formed $(LS)J$ coupling scheme is just an approximation to real couplings of the angular momenta of electrons present in the atom. This coupling scheme properly describes low to medium energy states of outer and some inner subshells in light to medium and relatively heavy atoms. The scheme is also convenient to experimenters when identifying the states by their properties and excitation dynamics observed in the experiments.

Previously, the works [2, 3] on p-core-excited $mp^5nln'l'\ J$ AS of alkali metal atoms Rb I ($m = 4$) and Cs I ($m = 5$) were relatively simple. These states could autoionize only via one decay channel $mp^6\varepsilon\lambda$, which leaves the resulting ion in the ground state $mp^6\ {}^1S_0$. Other excited states of the ion were energetically forbidden. Consequently, only the width of an Auger line was proportional to the decay probability and not the intensity value. However, after the work [4] on $5p^5n_1l_1n_2l_2n_3l_3\ J$ AIS of Ba I it became apparent that these states can effectively autoionize via more than one decay channel $5p^6n_4l_4\varepsilon'\lambda'$, leaving Ba II in the ground or an excited state. Moreover, it was experimentally observed and theoretically calculated, that given a sufficient amount of energy (more than 21 eV approximately) to Ba I atoms by a photon or electron impact, some high lying AIS could autoionize via $5p^5n_5l_5n_6l_6\ J$ AS of Ba II. This decay path to doubly excited states has proven to be more probable or of the same order as the decay to the ground or singly excited states of Ba II. The same considerations and arguments were applied in this work to study $4p^5n_1l_1n_2l_2n_3l_3\ J$ AIS of Sr I, $4p^5n_5l_5n_6l_6\ J$ AS of Sr II and distributions of intensity from each core-excited to many final states between the two spectra.

Calculations of excitation energies, electron impact excitation cross sections and autoionization probabilities of the $4p^5n_1l_1n_2l_2n_3l_3\ J$ AIS of Sr I and $4p^5n_5l_5n_6l_6\ J$ AS of Sr II were performed by the Flexible atomic code [5]. Relativistic radial orbitals were calculated by solving self-consistent field Dirac-Fock-Slater equations. The potential was optimized on the ground $4p^65s^2\ {}^1S_0$ and singly-excited $4p^65sn_0l_0\ J$, and singly-excited $4p^6n_4l_4\ J$ states for Sr I and Sr II separately, respectively. The exchange part was approximated by the Slater potential. Similarly, the ground, singly-excited and AIS for Sr I, and AS for Sr II were used to take into account the correlation effects between electrons. Cross sections were calculated by using the distorted-wave, autoionization probabilities – distorted-wave and isolated resonance approximations. The angular part of wave functions was transformed from the $(jj)J$ to $(LS)J$ coupling scheme of angular momenta.

Two preliminary papers [6, 7] on identification of the experimental energy spectra of $4p^5n_1l_1n_2l_2n_3l_3\ J$ AIS of Sr I and $4p^5n_5l_5n_6l_6\ J$ AS of Sr II excited by both photon absorption and electron impact will be submitted approximately by the time of this presentation. Theoretical and experimental methods, described in [6, 7], were used for the identification.

[1] A. Kramida, Y. Ralchenko, J. Reader and NIST ASD Team, NIST Atomic Spectra Database (version 5.4), [Online] Available: http://physics.nist.gov/asd [2017 02 02] National Institute of Standards and Technology, Gaithersburg, MD (2016).

[2] A. Kupliauskienė and G. Kerevičius, Theoretical study of the $4p^5nln'l'$ autoionizing states of Rb excited by electron impact, Phys. Scripta **88**, 065305(7) (2013).

[3] G. Kerevičius and A. Kupliauskienė, Classification of the $5p^5nln'l'\ LSJ$ energy levels of Cs excited by 30 eV electrons, Lith. J. Phys. **55**, 84-91 (2015).

[4] V. Hrytsko, G. Kerevičius, A. Kupliauskienė and A. Borovik, The 5p autoionization spectra of Ba atoms excited by electron impact: identification of lines, J. Phys. B: At. Mol. Opt. Phys. **49**, 145201(12) (2016).

[5] M.-F. Gu, The flexible atomic code, Can. J. Phys. **86**, 675-689 (2008).

[6] A. Kupliauskienė, G. Kerevičius, V. Roman and A. Borovik, The energy structure and decay channels of the $4p^6$-shell excited states in Sr, submitted to J. Phys. B: At. Mol. Opt. Phys. (2017).

[7] A. Kupliauskienė and G. Kerevičius, Theoretical study of $4p^5nln'l'\ LSJ$ states of Sr ion excited by electron impact, submitted to J. Phys. B: At. Mol. Opt. Phys. (2017).

WAVE MODELING USING SMOOTHED PARTICLE HYDRODYNAMICS

Gleb Bogomol, Janek Laanearu

Department of Science, University of Technology
gbogomol@gmail.com

The computational fluid dynamics contains two basic approaches to modeling: the Euler's method, based on a mesh grid and the Lagrangian method based on the particles. Today, computing power is large enough to use the mechanics of particles effectively. The main method in this area is smoothed particle hydrodynamics. This approach can effectively simulate various processes not only of liquids and gases, but also solid and elastic materials. Apart from obvious applications in engineering and classical hydrodynamics, the method allows to simulate fluid and tissues in living organisms, including at the cellular level.

The main objective of this research is a computer simulation of conditions for the formation of the waves by the smoothed particle hydrodynamics and study of the processes related to this (changing the dynamic viscosity, the distribution of energy and the appearance of vortices). The secondary objective was to test methods published by Monaghan [1][2].

Matlab was used as a simulation environment. Simulation was two-dimensional. As the kernel function was used a two-dimensional normal distribution function. Fluid density and incompressibility were the water imitation. Several different equations of state were tested; the best results showed the equation of state described by Batchelor [3]. Lennard–Jones equation was taken as the equation of the boundary conditions. The number of particles in the simulation was varied from 1000 to 8000.

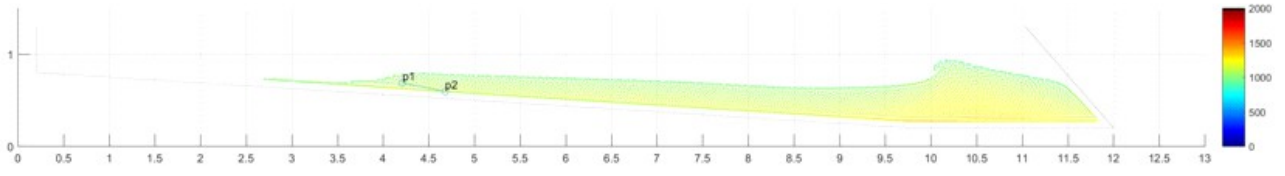

Fig. 1. Density plot .

As a result, the system proved to be very sensitive to initial conditions. Furthermore the high sensitivity also relates to computational aspects as frequency and used number of particles. In eight cases out of ten the energy of particles was dissipated and did not form falling wave crests. Here was discovered and analyzed the conditions of formation of the falling wave crests. The behavior of the fluid in a simulation is similar to the behavior of the fluid in the analogical physical laboratory setup.

These results will help to build more complex models and a deeper understanding of the physical processes under the water surface. The next step may be to move in the third dimension.

[1] J.J.Monaghan “Simulating Free Surface Flows with SPH”, Journal of Computational Physics 110, pp. 399-406, 1994
[2] J.J.Monaghan “SPH without a Tensile Instability”, Journal of Computational Physics 159, pp. 290-311, 2000
[3] G.K.Batchelor, “An Introduction to Fluid Dynamics”, Cambridge Univ. Press, Cambridge, UK, 1973

DICHOTOMOUS MODEL FOR SYSTEM-ENVIRONMENT INTERACTION IN PHOTOSYNTHETIC COMPLEX

Vytautas Bubilaitis, Olga Rancova, Darius Abramavicius

Department of Theoretical Physics, Faculty of Physics, Vilnius University, Lithuania
vytautasbubilaitis@gmail.com

Photosynthesis is an exceptional process with high excitation transfer efficiency. Light harvesting 2 (LH2) complexes are responsible for turning solar energy into excitations in purple bacteria. In LH2 absorption spectrum of purple bacteria's *Rhodoblastus acidophilus* B850 band peak moves to higher frequencies when temperature rises [1]. To describe this unusual behaviour the dichotomous model was developed [2]. In this model it is assumed that proteins have two conformational states and conformation occupancy propability depends on temperature.

In present work dichotomous model is further expanded to include homogeneous spectral line broadening dependency on temperature and to get agreement with two-dimensional electronic spectroscopy (2DES) spectra of LH2 [3].

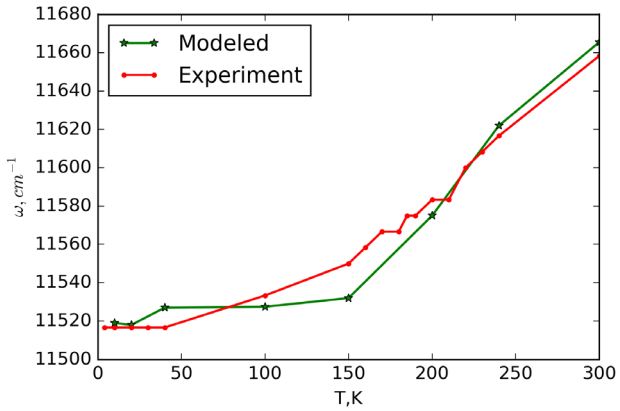

Fig. 1. Modeled LH2 B850 absorption spectrum peak position dependency on temperature.

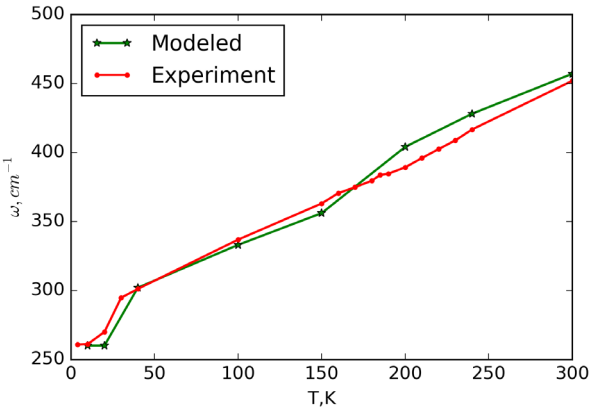

Fig. 2. Modeled LH2 B850 absorption spectrum FWHM dependency on temperature.

Dichotomous model is expanded with an additional third conformation. Each conformation has specific parameters for slow and fast fluctuations. Conformation occupancy propability for expanded dichotomous model:

$$p_i(T) = \frac{n_i \exp(-E_{ai}/kT)}{1 + n_2 \exp(-E_{a2}/kT) + n_3 \exp(-E_{a3}/kT)}. \quad (1)$$

The agreement with experimental data was achieved for simulated LH2 absorption spectra with dominating homogeneous disorder using expanded dichotomous model. Modeled LH2 B850 absorption spectra, with expanded dichomous model, has very good agreement with experimental spectra's FWHM (Fig. 2) and good agreement with band peak position dependency (Fig. 1) on temperature. The analysis of the spectral band shapes and spectral cross-sections showed that in calculated LH2 2DES spectra there is homogeneous broadening dependency on temperature, because of expanded dichotomous model.

[1] O. Zerlauskienė, G. Trinkūnas, A. Gall, B. Robert, V. Urbonienė, L. Valkūnas, Static and dynamic protein impact on electron properties of light-harvesting complex LH2, Phys. Chem. B 112, 15883–15892 (2008).

[2] J. Meldaikis, O. Zerlauskienė, D. Abramavičius, L. Valkūnas, Manifestation of protein conformations in B850 absorption band of light-harvesting complex LH2, Chem. Phys. 423, 9–14 (2013).

[3] A. F. Fidler, V. P. Singh, P. D. Long, P. D. Dahlberg, G. S. Engel, Time scales of coherent dynamics in the light-harvesting complex 2 LH2 of rhodobacter sphaeroides, J. Phys. Chem. Lett. 4, 1404–1409 (2013).

QM/MM PROTOCOL FOR STUDYING INTERACTIONS IN IONIC LIQUIDS: CHARGES OPTIMIZATION

Dovilė Lengvinaite,[1] Sonja Grubisic,[2] Kęstutis Aidas,[1] Ilija Cvijetic,[3] Aatto Laaksonen,[4] Francesca Mocci[5]

[1] Department of General Physics and Spectroscopy, Faculty of Physics, Vilnius University, Lithaunia
[2]Center for Chemistry, IHTM, University of Belgrade, Belgrade, Serbia
[3]Innovation Center of the Faculty of Chemistry, University of Belgrade, Serbia
[4]Division of Physical Chemistry, Arrhenius Laboratory, Stockholm University, Sweden
[5] Departmen t of Chemical and Geological Sciences, University of Cagliari, Italy
dlengvinaite@gmail.com

Ionic liquids (ILs) are organic salts, characterized by a remarkably low melting temperature (<100°), and by many useful properties (e.g. electrical conductivity, high thermal stability, high solvating capability, etc.) which can be tuned by modifying the anion or cation. The need of designing ILs with desired properties had stimulated a large amount of investigations. Among the experimental techniques used to this purpose, we are interested in the nuclear magnetic resonance (NMR) signal of the quadrupolar nuclei, particularly of the halides which are common anions in ILs.

We use classical MD, coupled with QM and QM/MM calculations, to understand how the structure and dynamics of ILs at the atomistic and sub-atomistic level affects the NMR signal of quadrupolar nuclei [1] and what information can be extracted from the experimental signals. The work presented in this symposium concerns stages 1-3 of the scheme in Fig.1, and is focused on the improvement of the currently used force field parameters in order to improve the description of the interactions between anions and cation of 1-decyl-3-methyl-imidazolium chloride (DMimCl). To this aim we improved the partial and total charges by performing QM calculations and varying the van der Waals parameters. The atomic charges were calculated using Gaussian 09 program, with the restrained electrostatic potential (RESP) approach by fitting the electrostatic potential grid computed at the B3LYP DFT level on the optimized geometries. The new set of AMBER parameters has been validated by comparing the structural and dynamical behavior of investigated systems by means of MD simulations with QM data and experimental evidence. A very good agreement with reference data (ab initio [2] and experimental) has been obtained for all of the investigated structural and dynamical properties.

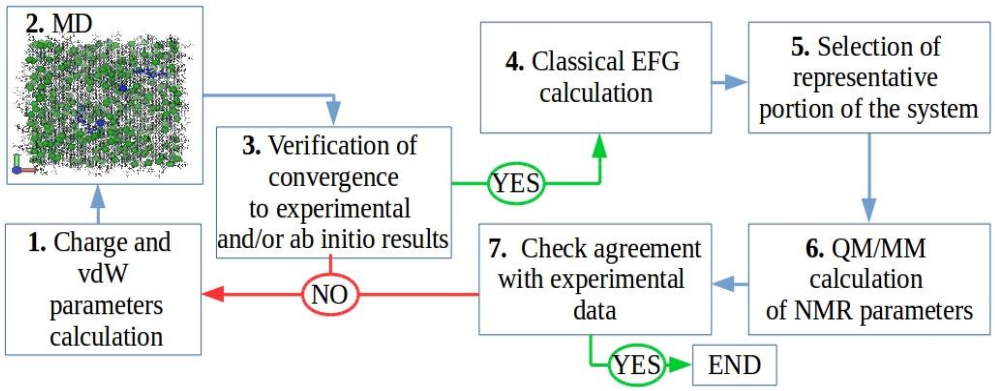

Fig. 1. Proposed scheme for calculation of NMR parameters of ionic liquid

[1] K. Aidas, H. Agren, J. Kongsted, A. Laaksonen, F. Mocci, *PCCP* 2013, **15**, 1621-1631.
[2] A. Bagno, F. D'Amico, G. Saielli, *Chem Phys Chem* 2007 **8**:873-881

NANOANTENNAS FOR INDUCED CIRCULAR DICHROISM

Monika Kubek, Karolina Słowik

Institute of Physics, Faculty of Physics, Astronomy and Informatics, Nicolaus Copernicus University,
Grudziadzka 5, 87-100 Torun, Poland
270018@fizyka.umk.pl

Nanoantennas are nanostructured optical devices, metallic, dielectric, or even made of more exotic materials such as graphene, able to dramatically enhance the light-matter interaction [1]. This is due to their extraordinary ability to concentrate light in subwavelength spatial domains. A molecule placed into such hot spots interacts with a field of extreme strength. However, a nanoantenna can do much more. It allows to overcome paradigms that have been prevalent for long time when considering the light-matter interaction in free-space or in traditional cavities. There, it is assumed that the spatial extent of the molecule is much smaller than the wavelength of light; being a length scale for the spatial variations of the electric field. In consequence, the electric field can be considered as constant across the molecule. This allows to use the dipole-approximation where quantum state transitions are considered as purely electric dipolar. This assumption is

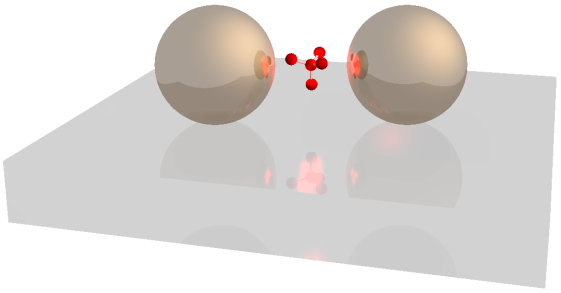

Fig. 1. Artist's view of a dimer nanoantenna coupled to a molecule.

lifted by metallic nanoantennas [2, 3]. They provide not just huge electric fields but also huge electric field modulations, allowing to stimulate quantum state transitions that are usually considered as hardly accessible in free space: in this case magnetic dipolar transitions. We explore the possibility to superimpose them with the usually dominating electric dipolar ones and to coherently control the two pathways of the same transition. This may lead to circular dichroism induced in molecules that normally do not show this property.

For this purpose, we consider specific designs of metallic nanoantennas. Their spectral profiles and characteristics of scattered fields are calculated with a finite element method in the frequency domain. We investigate different multipolar contributions of a quantum transition between the ground and an excited state of specific molecules, using the Fermi golden rule:

$$\Gamma = \frac{2\pi}{\hbar}|\langle f|H|i\rangle|^2 \rho\left(\omega_f = \omega_i \pm \omega\right). \tag{1}$$

Here Γ is the modified transition rate between the initial state $|i\rangle$ and a final state $|f\rangle$, $\rho(\omega)$ is the density of states, and the $\pm$ sign corresponds to an absorption or an emission, respectively. The investigated interaction Hamiltonian H combines the electric and magnetic dipolar contributions:

$$H = -\mathbf{d}\cdot\mathbf{E}(\mathbf{r}_m) - \mathbf{m}\cdot\mathbf{B}(\mathbf{r}_m), \tag{2}$$

where $\mathbf{E}(\mathbf{r}_m)$ and $\mathbf{B}(\mathbf{r}_m)$ are the electric and magnetic fields at the position $\mathbf{r}_m$ of the molecule, while $\mathbf{d}$ and $\mathbf{m}$ are the molecular transition electric and magnetic dipole moments. Our goal is to exploit the nanoantenna to strongly enhance the magnetic field in its vicinity. Therefore, the magnetic transition mechanism of the molecule will be booste: instead of a negligible contribution at the absence of the nanoantenna it might even become comparable to the electric dipolar one. This is especially inetersting if a circularly polarized beam is used for illumination. The 90^o phase shift between the electric and magnetic fields renders a different molecular response to illumination with right- and left-circularly polarized light. This is referred to as circular dichroism.

[1] P. Biagioni, J.-S. Huang, and B. Hecht, Nanoantennas for visible and infrared radiation, Rep. Prog. Phys., **75**, 024402, 2012.
[2] T. Feng, Y. Zhou, D. Liu and J. Li, Controlling magnetic dipole transition with magnetic plasmonic structures. Opt. Lett., **36**, 2369–2371, 2011.
[3] R. Filter, S. Mühlig, T. Eichelkraut, C. Rockstuhl, and F. Lederer, Controlling the dynamics of quantum mechanical systems sustaining dipole-forbidden transitions via optical nanoantennas, Phys. Rev. B, **86**, 035404, 2012.

THEORETICAL STUDY OF THE ROVIBRATIONAL SPECTRUM OF WATER MOLECULE TRAPPED IN ARGON MATRIX IN THE ν_1 AND ν_3 SPECTRAL REGIONS

Yaroslav Zubritsky[1], Alex Malevich[1], Elena Shalamberidze[1], George Pitsevich[1], Valdas Sablinskas[2]

[1] Department of Physical Optics, Belarusian State University, Minsk, Belarus
[2] Vilnius University, Vilnius, Lithuania
yauz_lv@inbox.lv

Matrix isolation methods are very useful for investigating individual molecules and their clusters. It is believed that due to its small size the molecule of water can be in the excited rotational and vibration-rotational states in an isolating matrix in the case of small values J'' and J'. The state of the molecule, which can be considered as an asymmetric top with some effective values of the rotational constants ($A_{v_1v_2v_3}, B_{v_1v_2v_3}, C_{v_1v_2v_3}$), can be described by the following set of quantum numbers ($v_1v_2v_3, J_{k_ak_c}$), where v_1, v_2, v_3 are vibrational quantum numbers characterizing symmetric stretching, bending and asymmetric stretching vibrations of O-H bonds, respectively, and $J_{k_ak_c}$ - standard set of quantum numbers describing the rotational state of an asymmetric top. Recently [1], we analyzed the rovibrational spectrum of the water molecule trapped in Ar matrix in ν_2 region using effective values of the rotational constants from [2,3]. The intensity of a vibration-rotational transition can be calculated using the formula:

$$I_{i\to f} = \frac{(2\pi)^3 N\tilde{\nu}_{if} g_{s(i)} \left[e^{-\frac{E_i}{kT}} - e^{-\frac{E_f}{kT}} \right]}{4\pi\varepsilon_0 3hcQ(T)} \left(3\left\langle \Psi_{vi}\Psi_{ri} \left| \mu_Z \right| \Psi_{vf}\Psi_{rf} \right\rangle \right)^2 \quad (1)$$

Using (1) and effective values of the rotational constants for ν_1 and ν_3 we calculated the rovibrational spectrum of water molecule in Ar matrix at 6 K and 30 K. Calculated spectra are represented in Fig.1

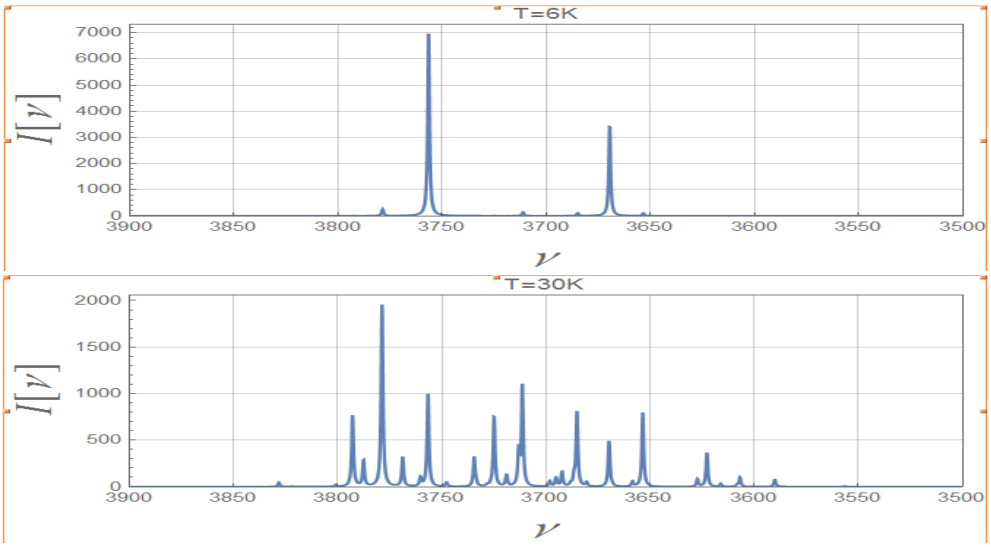

Fig.1 Rovibrational spectrum of water trapped in Ar matrix in ν_1 and ν_3 regions calculated at 6 K (upper spectrum) and 30 K (lower spectrum).

Comparing calculated IR spectra at 6 and 30 K one can see huge changes due to temperature rising. At 6 K trasitions from (000, 0_{00}) level are dominated. At 30 K intensities of these transitions become smaller and intensities of other trasitions become higher. These changes are due to increasing of the population of the exited rotational levels of the ground vibrational state. Calculated and experimental [2,3] intensities of rovibrational bands are compared and some conclusions about lifetime of the exited states and relaxations times of the ortho-para transitions in Ar matrix were made.

[1] G. Pitsevich, I. Doroshenko et al., Temperature dependence of the intensity of the vibration-rotational absorption band ν_2 of H_2O trapped in an argon matrix, Spectrochim.Acta Part A, **172**, 83 (2017).
[2] X. Michaut, A.-M. Vasserot, L. Abouaf-Marguin, Temperature and time effects on the rovibrational structure of fundamentals of H_2O trapped in solid argon: hindered rotation and RTC satellite, Vib.Spectr., **34**, 83 (2004).
[3] J.P. Perchard, Anharmonicity and hydrogen bonding. III. Analysis of the near infrared spectrum of water trapped in argon matrix, Chem.Phys., **273**, 217 (2001).

ANHARMONIC CALCULATIONS OF THE STRUCTURE AND IR SPECTRA OF THE WATER CLUSTERS IN THE VACUUM, ARGON AND WATER MEDIUM

Artem Sosnovsky[1], George Pitsevich[1], Ekaterina Kozlovskaya[1], Valdas Sablinskas[2]

[1] Department of Physical Optics, Belarusian State University, Minsk, Belarus
[2] Vilnius University, Vilnius, Lithuania
leopold7918@gmail.com

Water plays key role in many chemical and biological proccesses, exhibiting unique properties in many aspects and applications. Central role in the ungerstanding of these properties plays ability of the water molecules to form hdrogen bonds and cluster structures. Water molecule is known for its ability to form at least four hydrogen bonds – two as asseptor and two as donor. With this, spectral, structural and energetic perturbations introduced by the formation of hydrogen bonds, are growing non-linearly with the number of hydrogen bonds for single molecule. These cooperative effects are poorly investigated, although they can be responsible for some unque water properties.

Equilibrium configurations of some water molecules clusters, as well as their conforamtional diversity were calculated at B3LYP/cc-pVTZ level of theory. For obtained configurations IR and Raman spectra were calculated at the same level of theory. Both type of calculations were performed for 1) free clusters, 2) clusters in Ar, 3) clusters in water. For the second and third cases, the PCM model of taking into account the solvation effects was used. Besides, based on computational facilities, for some cases IR spectra were calculated both in harmonic and anharmonic approximations. Equilibrium configurations of water dimer and trimer are presented in Fig.1.

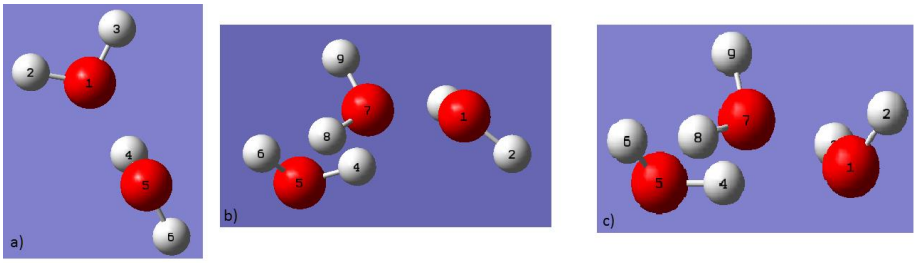

Fig. 1. Equilibrium configurations of water dimer (a) and stable water trimer (b and c) calculated in B3LYP/cc-pVTZ approximation.

Calculated IR spectra of the water trimer presented in Fig. 2.

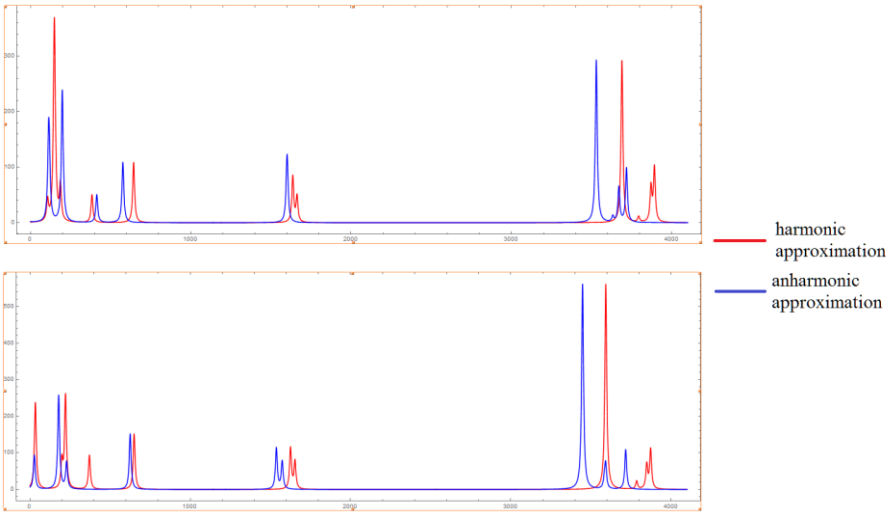

Fig. 2 Calculated in B3LYP/cc-pVTZ approximation IR spectra of free water dimer (top) and in water media (bottom).

As can be seen from Fig.2, accounting of the anharmonicity effects leads to the red-shift of the stretching and bending vibrations of the hydroxyl groups of water monomers, and in case of water dimer value of this shift indicates insignificant increase of anharmonicity of the donor O-H bond comparing to the free one. For water dimer in water, additional red-shift of the stretching vibrations can be noted. In forthcoming presentation investigations of the IR spectra of water clusters with different number of molecules will be introduced. Influence of intrinsic anharmonicity of vibrations and medium polarity on the positions of the absorption bands will be analyzed.

DFT STUDY OF THE IR SPECTRA AND STRUCTURE OF THE $H_5^+O_2$+X COMPLEXIS (X=Ar,Ne,He) IN HARMONIC AND ANHARMONIC APPROXIMATIONS

Anton Paltsev[1], Alex Malevich[1], George Pitsevich[1], Ekaterina Kozlovskaya[1], Vitas Balevicius[2]

[1] Department of Physical Optics, Belarusian State University, Minsk, Belarus
[2] Vilnius University, Vilnius, Lithuania
danny.mad@yandex.com

Measuring the IR absorption spectrum of the protonated water dimer (PWD) in the gas phase has been challenging. Only in the late 80s of the last century the group of Lee has developed two methods of measuring the IR spectra of the PWD in the gas phase. The first method is based on use of a carrier gas such as hydrogen or some other inert gas [1]. The second technique involves infrared multiphoton dissociation (IRMPD) [2]. However, the IR spectral range used in this work was very narrow (3500-3800 cm^{-1}). Later IR absorption spectra of the PWD in the gas phase were obtained in the spectral region of vibrations of the central proton (600-2000 cm^{-1}) [3]. The authors of [4] carried out a number of experiments on measuring IR spectra of the PWD using the "carrier gas" method. This time, in addition to the experiments with Ar gas, similar studies were performed using Ne as carrier gas. The authors convincingly show that, due to the smaller perturbation in case of Ne, the IR spectrum is closer to the C_2 configuration than in case of Ar, where the PWD presumably has the C_S configuration. Recently, new experimental IR spectra investigations of the PWD with helium atom as the carrier [5] are found close enough, in terms of basic characteristics, to the IR spectra of the PWD+Ne. In particular, the doublet of bands around 1000 cm^{-1} is red-shifted by only 7 cm^{-1} (to 921 and 1040 cm^{-1}). Taking into account the decrease of the perturbation effects caused by a helium atom compared to neon, the authors of [5] suggested that the PWD+He IR spectrum is practically equivalent to the free PWD IR spectrum.

Although one can see progress in experimental investigation of the PWD+X (X=Ar,Ne,He) [1,4,5], the only theoretical work [6], where structure and IR spectrum of the PWD+Ar complex were calculated, was published only recently. In order to understand this situation in more detail, harmonic and anharmonic calculations of IR spectra of $H^+{}_5O_2$+Ar and $H^+{}_5O_2$+Ne complexes were carried out in the PBEH1PBE/acc-pVTZ approximation. The optimized structures of these complexes are presented in Fig. 1.

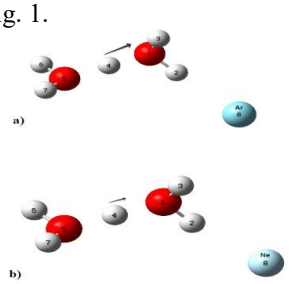

Fig. 1. Optimized geometries of $H_5^+O_2$+Ar (a) and $H_5^+O_2$+Ne (b) complexes calculated at the PBEH1PBE/acc-pVTZ level of theory.

As indicated in Fig.1 and as can be seen from the results of the calculations, the proton tends to move towards the water molecule that is closer to Ar/Ne/He. In case of Ar atom, this shift is more significant. So we can assume that addition of the Ar/Ne/He atom to the PWD molecule stabilizes the H_3O+ fragment of the PWD. Our calculations confirm the deformation of the C_2 configuration, but for both complexes ($H_5^+O_2$+Ar, $H_5^+O_2$+Ne, $H_5^+O_2$+He) the water molecules are still oriented relative to each other similarly as in the case of the C_2 configuration, i.e. only the proton shifts towards one of the monomers without relative rotation of the water molecules; the shift in the case of $H_5^+O_2$+Ar is significantly bigger than in the case of $H_5^+O_2$+Ne and $H_5^+O_2$+He, but the O_1O_5 distance is in neither case hardly affected compared to the case without carrier gas. Harmonic and anharmonic spectra of the complexes will be discussed in details in a forthcoming report.

[1] M. Okumura, L. I. Yeh, J. D. Myers, Y. T. Lee, Infrared spectra of the solvated hydronium ion: vibrational predissociation spectroscopy of mass-selected H_3O^+*($H_2O)_n$ *($H_2)_m$, J. Phys. Chem. **94**, 3416 (1990).
[2] L. I. Yeh, Y. T. Lee, J.T. Hougen, Vibration-rotation spectroscopy of the hydrated hydronium ions $H_5O_2^+$ and $H_9O_4^+$, J. Mol. Spectr. **164**, 473 (1994).
[3] K. R. Asmis, Nicholas L. Pivonka, Gabriele Santambrogio, Mathias Brümmer, Cristina Kaposta, Daniel M. Neumark, Ludger Wöste, Gas-phase infrared spectrum of the protonated water dimer, Science, **299**, 1375 (2003).
[4] N.I. Hammer, E.G. Diken, J.R. Roscioli, M.A. Johnson, E.M. Myshkin, K.D. Jordan, A.B. McCoy, X. Huang, J.M. Bowman, S. Stuart, The vibrational predissociation spectra of the H_5O_2 $^+$RGn(RG = Ar,Ne) clusters: correlation of the solvent perturbations in the free OH and shared proton transitions of the Zundel ion, J. Chem. Phys. **122**, 244301 (2005).
[5] C.J. Johnson, A.B. Wolk, J.A. Fournier, E.N. Sullivan, G.H. Weddle, M.A. Johnson, Communication: He-tagged vibrational spectra of the SarGlyH+ and H+(H_2O)2,3 ions: Quantifying tag effects in cryogenic ion vibrational predissociation (CIVP) spectroscopy, J.Chem.Phys., **140**, 221101 (2014).
[6] M. Kaledin, D.T Adedeji, Driven molecular dynamics studies of the shared proton motion in the $H_5O_2^+$.Ar cluster: The effect of argon tagging and deuteration on vibrational spectra, J. Phys. Chem. A **119**, 1875 (2015).

POTENTIAL ENERGY SURFACE OF THE GROUND TRIPLET STATE OF UO_3 MOLECULE

Darya N. Meniailava, Maksim B. Shundalau

Physics Department, Belarusian State University, Belarus
darhon.yo@gmail.com

Apart from the obvious practical significance of uranium trioxide, for example in the production and reprocessing of nuclear fuel and uranium enrichment, such a molecule is also of great interest from a fundamental point of view due to its complicated electronic structure and geometry features. For most trioxides the D_{3h} point group is typical. Experimental studies of the molecular uranium trioxide were carried out at high temperatures in the gas phase [1-2], as well as at low temperatures in argon matrix [3]. The last indicated C_{2v} point group for the molecule (T–shaped structure with nonequivalent bonds). *Ab initio* calculations [4] verified C_{2v} point group and determined the more symmetrical D_{3h} point group for a saddle point, as an explanation a second-order Jahn–Teller effect was proposed. Computational study [5] showed besides of all mentioned an existence of Y–shaped structure. All the *ab initio* calculations for the UO_3 molecule are performed in single configuration approximation, which is not always reliable. That is why research of the electronic structure using quantum chemical methods of high-level theory is worthwhile.

We carry out calculations of potential energy surfaces (PESs) of low-lying electronic states as functions of internal coordinates at the multiconfiguration CASSCF level of theory. The active space for CASSCF calculations included six electrons on eight orbitals. The SA-procedure was done for two states (triplet and singlet). For uranium atom we used Stuttgart large fully relativistic ECP, replacing eighty inner electrons, and corresponding TZ basis set, for oxygen atom we used cc-pVTZ basis set. We firstly determined triplet to be a ground state of the uranium trioxide molecule. The potential energy contour map of the ground triplet electronic state is presented in Fig. 1. The PES of the first exited singlet state has a similar character. The fixed internal coordinates α and β are the angles between each of the equivalent bond and the one along the symmetry axis. The PES has tree minima, marked in Fig. 1, at (118.14˚,118.14˚), (118.14˚,123.71˚) and (123.71˚,118.14˚) angles with bond length of 1.90, 2.25 and 2.25 Å and two evident valleys. Energy strictly increases, saddle points do not appear. A symmetrical D_{3h} geometry predicted earlier for the UO_3 molecule also absent and a second-order Jahn–Teller effect is not implemented. Thus, for an explanation of geometry of the molecule we provide a lack of electron density to form the equivalent chemical bonds.

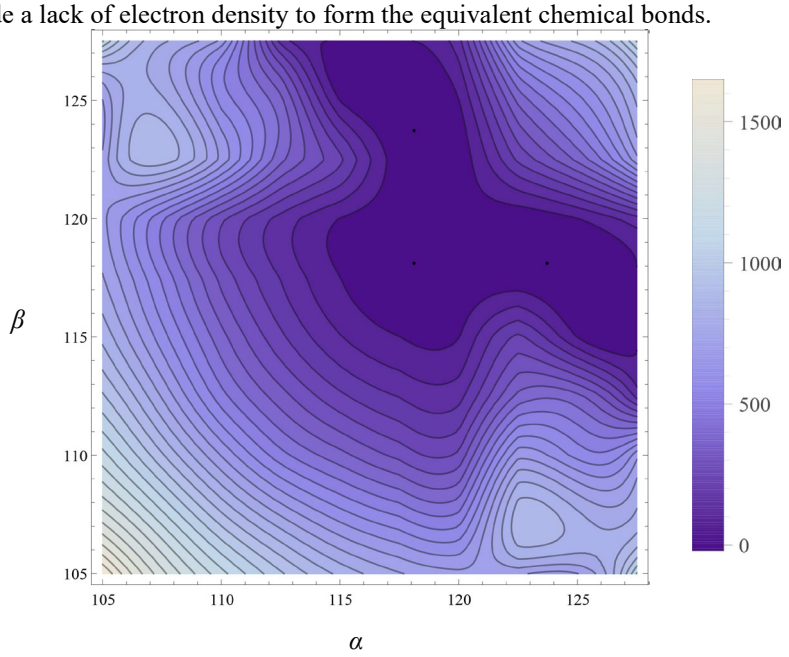

Fig. 1. The PES contour map for the ground triplet state of the UO_3 molecule, obtained at the CASSCF(6,8) level of theory

[1] R. J. Ackermann, P. W. Gilles, R. J. Thorn, High-temperature thermodynamic properties of uranium dioxide, J. Chem. Phys. **25**, 1089-1097 (1956).
[2] C. A. Alexander, Volatilization of urania under strongly oxidizing conditions, J. Nucl. Mater. **346**, 312-318 (2005).
[3] S. D. Gabelnick, G. T. Reedy, M. G. Chasanov, Infrared spectra of matrix-isolated uranium oxide species. II: Spectral interpretation and structure of UO_3, J. Chem. Phys. **59**, 6397-6404 (1973).
[4] P. Pyykkö, J. Li, N. Runeberg, Quasirelativistic pseudopotential study of species isoelectronic to uranyl and the equatorial coordination of uranyl, J. Phys. Chem. **98**, 4809–4813 (1994).
[5] M. B. Shundalau, A. P. Zajogin, A. I. Komiak et al., A DFT modeling of the uranium trioxide vibration spectra characteristics, J. Spectrosc. Dyn. **2**, 1-6 (2012).

QUANTUM CHEMICAL MODELING OF AQUEOUS ACIDITIES FOR 2-, 3- AND 4-PHENACYLPYRIDINES

Sonata Kvedaravičiūtė[1], Andrés Cedillo[1,2], Kęstutis Aidas[1]

[1] Dept. of General Physics and Spectroscopy, Faculty of Physics, Vilnius University, Lithuania
[2] Dept. of Chemistry, Metropolitan Autonomous University, Mexico City, Mexico
sonata.kvedaraviciute@chf.stud.vu.lt

The family of phenacylpyridine compounds (Fig. 1) are substances, which are essential in pharmacy as well as organic synthesis due to their biological activity. These molecules have different protonation states and they in addition exhibit keto-enol tautomerization [1]. Different protonation states and tautomeric forms can differ in their biological activity rather significantly. Because experimental determination of aqueous acidities of different tautomeric species is not a trivial task, it is important to find cheap and fast means to predict these parameters with high certainty, particularly to facilitate drug development. The main purpose of this study is to benchmark quantum chemical methods rooted in density functional theory for the prediction of the aqueous acidity constants, pK_a, as well as tautomeric equilibrium constants, pK_T, of 2-, 3- and 4-phenacylpyridine compounds following the lines as documented in our previous study [2].

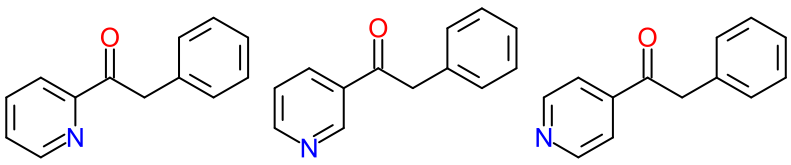

Fig. 1. Neutral keto forms of 2-, 3- and 4-phenacylpyridines

This study consists of two major parts – the conformational analysis of all the compounds in different protonation states and tautomeric forms, and calculation of pK_a and pK_T values using two different thermodynamic cycles. The direct and proton exchange thermodynamic cycles have been considered in this work. Free energy calculations were performed using the B3LYP and M05-2X functionals in combination with the 6-31G* and cc-pVTZ basis sets. The SMD solvent model was used to model solvent effects. All calculations were performed using the Gaussian09 program.

Our careful conformational analysis has allowed us to predict all relevant pK_a and pK_T values for 2-, 3- and 4-phenacylpyridines. The agreement between predicted and experimental acidity constants varies. Generally, better match is seen for the acidity constants of cationic rather than neutral forms. Even though proton exchange cycle was generally found to provide more accurate acidity constants, the accuracy of the results depends on the chosen reference compound prominently. We have also seen that different electronic structure methods can give qualitatively different gas-phase stabilities of different tautomeric forms. The predicted tautomeric equilibrium constants agree with experimental data in qualitative terms.

The authors are grateful to the High Performance Computing Center “HPC Saulėtekis” at Faculty of Physics of Vilnius University for computational resources.

[1] A. R. E. Carey, S. Eustace, R. A. M. O'Ferrall and B. A. Murray, Keto-Enol and Imine-Enamine Tautomerism of 2-, 3- and 4-Phenacylpyridines, J. Chem. Soc. Perkin Trans. **2**, 2285- 2296 (1993).
[2] K. Aidas, K. Lanevskij, R. Kubilius, L. Juška, D. Petkevičius, & P. Japertas, Aqueous acidities of primary benzenesulfonamides: Quantum chemical predictions based on density functional theory and SMD, J. Comp. Chem. **36**, 2158-2167 (2015).

THE ANHARMONIC COUPLINGS OF THE SHARED PROTON STRETCHING VIBRATION IN THE PROTONATED WATER DIMER: MP4 STUDY

Alex Kozhanovsky[1], George Pitsevich[1], Ekaterina Kozlovskaya[1], Vitas Balevicius[2]

[1] Department of Physical Optics, Belarusian State University, Minsk, Belarus
[2] Vilnius University, Vilnius, Lithuania
sanches-cop@mail.ru

Water is the key element for life and, therefore, attracts strong attention by the scientists. Properties of water are investigated and discussed constantly, however we are still far from their full understanding. Studies of the hydrated proton in bulk water or in compounds containing water are important for many areas of chemistry and biology. The protonated water dimer (PWD) $H_5O_2^+$ or Zundel ion takes a special place among these clusters. It is one of the simplest protonated water clusters, and its properties are important for a better understanding of mechanisms of proton transfer as well as of properties of the hydrogen bond. The available literature data indicate extremely strong anharmonic modes coupling of the shared proton vibrations in PWD. However to this day there are no full data on the degree of anharmonicity couplings of this vibration with other vibrational modes.

Equilibrium configurations of the PWD and its IR absorption spectra were calculated in the harmonic approximation for the cases of C_2 and C_S symmetry as well as without symmetry limitation (C_1) using the acc-pVTZ basis set at the MP4 level of theory. The anharmonic calculations of the IR spectrum of the PWD for the configurations with C_2, C_S and C_1 symmetry were carried out using B3LYP/acc-pVQZ, B3LYP/acc-pVTZ and MP2/acc-pVTZ. In the latter case, the standard second-order perturbation theory (PT2) model for inclusion of anharmonicity effects is used. The calculations of 1D - 3D PESs for some vibrational coordinates of the PWD with C_2 and C_S symmetry were carried out at the MP4/acc-pVTZ level. Calculations of the 2D PES were carried out using normal coordinates Q_7 and Q_i; $i \neq 7$; the normal coordinates were varied in the range $-0.6 \le Q_7, Q_i \le 0.6$; with a step 0.1. Since both for the coordinate Q_7 and for the coordinate Q_2 the central proton shifts, there were some points of the 2D grid where the energy could not be calculated because of a too small distance between the proton and one of the oxygen atoms. We, however, did not reduce the range of variation of the coordinates, but instead the energy at these points was set large enough. The vibrational Schrödinger equation in this case can be written as:

$$-\frac{\hbar^2}{2\mu_{Q_7} l_0^2}\frac{\partial^2\Psi}{\partial q_7^2} - \frac{\hbar^2}{2\mu_{Q_i} l_0^2}\frac{\partial^2\Psi}{\partial q_i^2} + U(q_7, q_i)\Psi = E\Psi \qquad (1)$$

The Hamiltonian matrix was constructed and diagonalized using the program Mathematica. In order to obtain the most complete information, besides the 2D vibrational problem, two 1D vibrational problems were solved. Anharmonic interactions of ν_7 with other modes can be divided into three groups: 1) modes, interactions with which lead to a blue-shift of ν_7, 2) modes, interactions with which lead to a red-shift of ν_7, 3) modes, interactions with which insignificantly affect the ν_7 frequency. The first group includes interaction of ν_7 with ν_1 and ν_2. The blue-shift of the ν_7 frequency due to the interaction with the antisymmetric twisting vibration of the water monomers leads to a blue-shift of ν_7 by only 13 cm^{-1}, while a similar shift due to interaction with the second mode was not noted previously although it increases the ν_7 frequency by more than 100 cm^{-1}. It should be remembered that the ν_2 and ν_7 normal modes are mixtures of the shared proton stretching vibration and antisymmetric wagging vibration of the water molecules. With this, the second type of the vibrations is prevailing in the first mode, and the first type – in the second mode. Interaction of ν_7 with stretching O-H vibrations of the water monomers and with the third, fourth and fifth normal modes should be included in the third group of the interactions. Interaction with the remaining five modes $(\nu_6, \nu_8 - \nu_{11})$ decreases the ν_7 frequency. The maximal red-shift (more than 200 cm^{-1}) is due to the intermolecular interaction with water monomers. This fact was previously noted in a series of works, despite the fact that the description was limited to proton movement along the hydrogen bridge. The next, in terms of the value, is a red-shift due to the interaction with the antisymmetric bending vibration of the water monomers (ν_{11}). This fact was previously noted, but in our case, when normal coordinates are used, the value of the red-shift is significantly smaller (less than 35 cm^{-1}) than the results of [1], where the red-shift was found to be more than 120 cm^{-1}. It is interesting to note that anharmonicity constants, calculated at the PBEh1PBE/acc-pVTZ and especially at the MP2/acc-pVTZ levels of theory at least correlate with the values of "effective" anharmonicity constants, but in case of ν_{11} there is a notable contradiction between their values. Such contradiction is probably associated with the intricate topology of the 2D PES, constructed by varying Q_7 and Q_{11}, that leads to an incorrect interaction estimation in the frame of the standard model of accounting for anharmonicity effects. Indeed, the 2D PES for these coordinates is quite flat around the minimum. Accounting of intrinsic anharmonicity and anharmonic double modes coupling ν_7, and using column elements of the "effective" anharmonicity constant matrix, we can evaluate the frequency of the shared proton stretching vibration.

[1] O. Vendrell, F. Gatti, H.-D. Meyer, Full dimensional (15-dimensional) quantum-dynamical simulation of the protonated water dimer. II. Infrared spectrum and vibrational dynamics, J. Chem. Phys. **127**, 184303 (2007).

QUANTUM CHEMICAL PREDICTIONS OF AQUEOUS ACIDITIES FOR SECONDARY BENZENESULFONAMIDES

Milda Koreivaitė[1], Greta Majauskaitė[1], Kęstutis Aidas[2]

[1]Faculty of Chemistry and Geosciences, Vilnius University, Lithuania
[2]Department of General Physics and Spectroscopy, Faculty of Physics, Vilnius University, Lithuania
milda.koreivaite@chf.stud.vu.lt, greta.majauskaite@chf.stud.vu.lt

Benzenesulfonamides are organic compounds based on sulfonamide moiety fused to a benzene ring with different substituents. Due to their antibacterial and antiviral activity, they are widely used as drugs. Their pharmacological activity depends on their protonation state. In the development of the new benzenesulfonamide based drugs, it is thus highly important to have computational tools for reliable prediction of their acidity constants. The main task of this study is to benchmark several quantum chemical schemes for the prediction of aqueous acidities of several prototypical benzenesulfonamides aiming to find the most accurate model.

We have analysed six different secondary benzenesulfonamides including (where S means sulfonamide) 4-S-1,2,4 triazole, 4-S-5-methylfurazan, 4-S-5-methyloxadiazole, 2-S-4-methylthiazole, 2-S-1,3,4-thiadiazole, 2-S-5-methylthiadiazole, see Fig. 1 [2]. Even though these compounds contain structurally similar five membered organic heterocycles, the presence of three different heteroatoms, sulfur, oxygen or nitrogen, poses an additional challenge for the applied theoretical methods. We have performed a careful conformational analysis using the B3LYP exchange-correlation functional along with the modest 6-31G* basis set. The aqueous acidities were predicted using direct and the proton exchange thermodynamic cycles where the free energy changes were evaluated using B3LYP and M05-2X functionals in combination with the 6-31G* and cc-pVTZ basis sets. We have relied on the SMD method for modelling of molecules in the condensed phase.

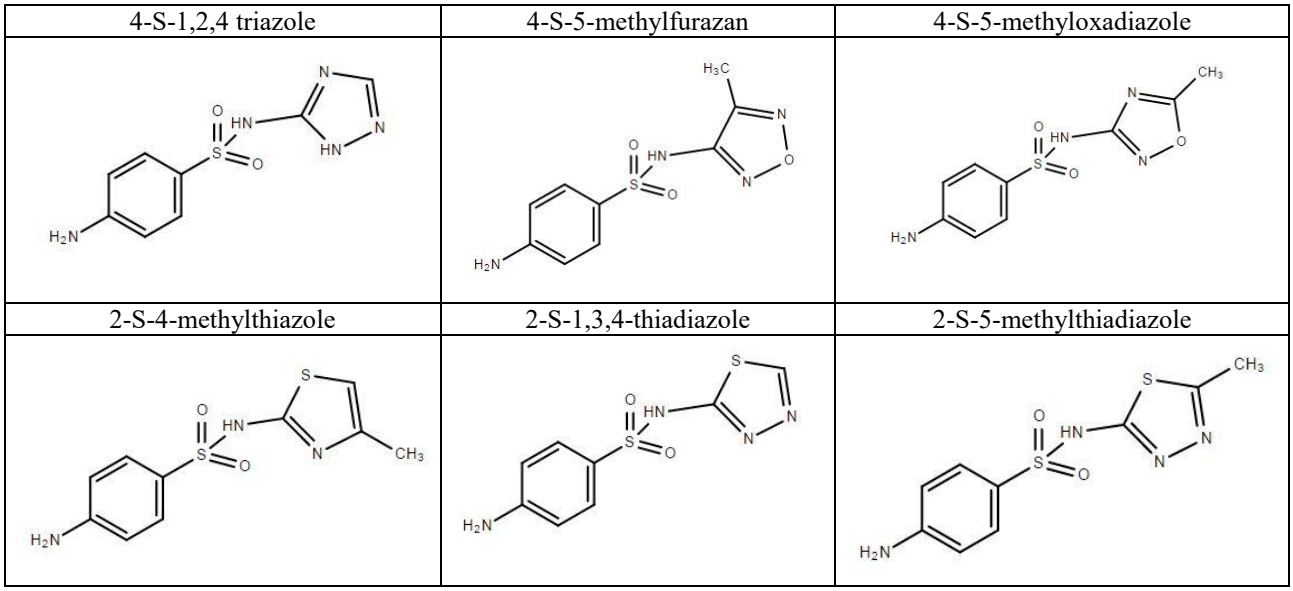

Fig. 1. Secondary benzenesulfonamides

The predicted pKa values using the direct thermodynamic cycle strongly depend on the electronic structure method used for the computation of the free energies. When the direct cycle is employed, the best agreement between computational results and experimental data was obtained using the M05-2X functional and the cc-pVTZ basis set. In this case, the mean absolute deviation (MAD) of computed values with respect to experimental data is as low as 0.51 pKa unit, meaning that in this case the scheme is much more reliable as compared to the case of primary benzenesulfonamides [3]. The MAD was further reduced to 0.36 pKa unit using the proton exchange cycle, yet the results are seen to depend on the choice of the reference compound rather strongly.

Computations were performed on resources at the High Performance Computing Center "HPC Sauletekis" in Vilnius University Faculty of Physics.

[1] C. T. Supuran, A. Innocenti, A. Mastrolorenzo, A. Scozzafava, Mini Rev. Med. Chem. 2004, 4, 189
[2] P. H. Bell, R. O. Robblin, Jr., J. Am. Chem. Soc. 1942, 64, 2905
[3] K. Aidas, K. Lavenskij, R. Kubilius, L. Juška, D. Petkevičius, P. Japertas. J. Comput. Chem. 2015, 36, 2158-2167

THE APPLICATION OF NEURAL NETWORKS FOR ACTIVATED CARBON SYNTHESIS

Ivan Reznikov

Chemistry Department, Belarusian State University, Belarus
ivanreznikov@gmail.com

Activated carbons are effective sorbents, as they can be characterized by their large surface area, high porosity, great adsorption capacity. Other applications include using AC as storages and catalysts.

Nowadays regenerating AC is problematic, so from the commercial point of view synthesizing AC from renewable source seems as a perspective. Different kind of agricultural, industrial and animal wastes, as long as polymers were tried as the source for the production of AC.

The synthesis of AC is a complex procedure with many variables [1]. Most of the synthetic plans consist of two stages: carbonization, at which raw materials are being heated up to 800°C to produce char and activation - to obtain high porosity and surface area. AC can be synthesized by physical or chemical methods. The main difference is upon using activating agent - CO, CO_2 or steam in physical process and chemical where alkalis and salts are used to activate carbon.

Despite the amount of publications, it is hard to say that the process is well studied. Dependent on the carbonization and activation temperatures, temperature rates and procedure time, concentrations and the nature of activators and raw materials, not speaking about the atmosphere and the flow rate — the result may significantly vary. The following parameters are independent and differently affect, dependent on other parameter values, on the final product characteristics.

An interesting decision here might be using artificial neural networks (ANNs), as the problem can be considered not formulated [2]. A great amount of input information from scientific articles allows to train the network for certain popular carbon precursors. The application of ANN allows to model above mentioned procedures, what can result in achieving effective methods for activated carbon synthesis. An example of the ANN for activated carbon synthesis can be shown on Fig. 1.

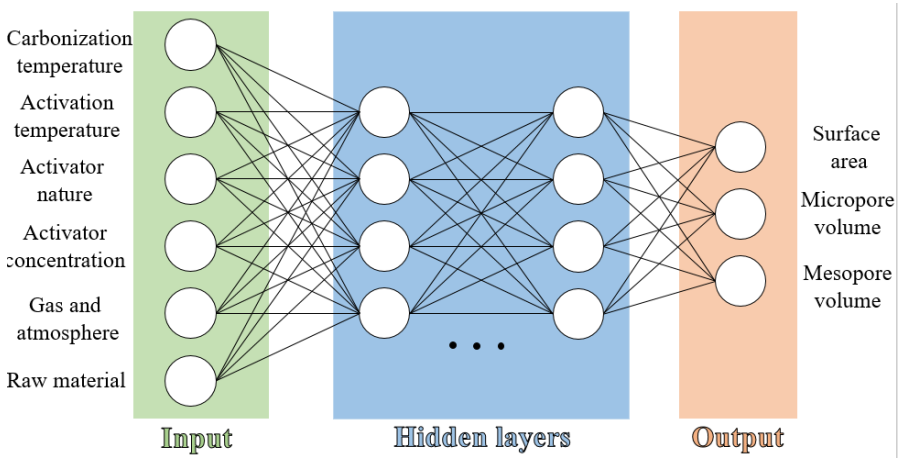

Fig. 1. ANN for activated carbon synthesis.

The number of input factors on Fig. 1 are combined into groups: carbonization temperature (temperature and rate), activation temperature (temperature and rate), activator's nature (cation size, iconicity, hygroscopicity, etc.), activator concentration, gas and atmosphere (nature and flow), raw material (element percentage, structure parameters, etc.). The optimal number of hidden layers and neurons is to be found. Three outputs were chosen, as most describable in literature. For commercial proposes the forth output 'yield' can be described.

The described neural network allows better understanding of the processes of activated carbon production, as the suggested experiment performed, have shown significant growth in surface area and micropore value.

[1] Nor, N. M., Lau, L. C., Lee, K. T., & Mohamed, A. R. (2013). Synthesis of activated carbon from lignocellulosic biomass and its applications in air pollution control—a review. Journal of Environmental Chemical Engineering, 1(4), 658-666.
[2] Yegnanarayana, B. (2009). Artificial neural networks. PHI Learning Pvt. Ltd..

AUTOMATING THE DERIVATION OF CHEMICAL INFORMATION FROM CRYSTALLOGRAPHIC DATA

Antanas Vaitkus[1], Andrius Merkys[1], Saulius Gražulis[1,2]

[1]Vilnius University Institute of Biotechnology, Saulėtekio 7, LT-10257 Vilnius, Lithuania
[2]Vilnius University Faculty of Mathematics and Informatics, Naugarduko 24, LT-03225 Vilnius, Lithuania
antanas.vaitkus90@gmail.com

The emergence of new interdisciplinary fields stipulates the ever growing need of greater connectivity between scientific data from a diverse range of research areas. The process of establishing such relationships differs from field to field with the need of creating an identifier common for both fields remaining a constant. In the case of crystallography, generating a chemical descriptor of a molecule from its crystallographic structure opens up the possibility of identifying chemical compounds and relating the crystal structure to the properties of the compounds it encompasses. Carrying out this task manually for larger datasets might have been viable a century ago, but with the arrival of big data it is no surprise that there have been multiple attempts at automating the process [1, 2, 3]. However, none of the approaches were sufficient enough for the processing of the open-access Crystallography Open Database (COD) [6] due to incompatible licenses or the lack of functionality. As a result, we have developed an automated approach of extracting the chemical data such as atom connectivity, bond orders and atom charges from the crystallographic atom coordinates and thus enabling the generation of chemical descriptors and the cross-linking of the COD with other open resources. Our approach strictly adheres to the principles of open science by making all of the data open-access and all of the developed programs [4, 5] open-source.

[1] Altermatt, D. and Brown, I. D. The automatic searching for chemical bonds in inorganic crystal structures. Acta Crystallographica Section B, 1985, 41, 240-244, doi: 10.1107/S0108768185002051.
[2] Baber, J. C. and Hodgkin, E. E. Automatic assignment of chemical connectivity to organic molecules in the Cambridge structural database. Journal of Chemical Information and Modeling, 1992, 32, 401406, doi: 10.1021/ci00009a001.
[3] Zhang, Q.; Zhang, W.; Li, Y.; Wang, J.; Zhang, L. and Hou, T. A rule-based algorithm for automatic bond type perception. Journal of Cheminformatics, 2012, 4, 26, doi: 10.1186/1758-2946-4-26.
[4] Gražulis, S.; Merkys, A.; Vaitkus, A. & Okulič-Kazarinas, M. Computing stoichiometric molecular composition from crystal structures. Journal of Applied Crystallography, 2015, 48, 85-91, doi: 10.1107/S1600576714025904
[5] Merkys, A.; Vaitkus, A.; Butkus, J.; Okulič-Kazarinas, M.; Kairys, V; and Gražulis, S. COD::CIF::Parser: an error-correcting CIF parser for the Perl language. Journal of Applied Crystallography, 2016, 49, 292-301 doi: 10.1107/s1600576715022396
[6] Gražulis, S.; Daškevič, A.; Merkys, A.; Chateigner, D.; Lutterotti, L.; Quirós, M.; Serebryanaya, N. R.; Moeck, P.; Downs, R. T. & Le Bail, A. Crystallography Open Database (COD): an open-access collection of crystal structures and platform for world-wide collaboration. Nucleic Acids Research, 2012, 40, D420-D427, doi: 10.1093/nar/gkr900

AGGREGATION AND SPECTROSCOPIC PROPERTIES OF GEMINI SURFACTANTS WITH ESTER GROUPS

Marta Pakiet, Iwona Kowalczyk, Bogumił Brycki

Laboratory of Microbiocides Chemistry, Department of Chemistry, Adam Mickiewicz University in Poznań, Poland
mpakiet@amu.edu.pl

Surfactants are one of the most important groups of chemical compounds having a fundamental meaning in household chemicals, mining, petrochemical and pharmaceutical industries. Quaternary alkylammonium are one of surfactant group, which have some special applications due to the ability to create differentiated morphologically systems in aqueous solutions and an excellent antimicrobial and anticorrosion activity. Gemini surfactants, which are double quaternary ammonium salts, possess surface, antimicrobial and anticorrosion activity of two to three orders of magnitude better than the corresponding monomeric cationic surfactants [1]. That is why so many attention is devoted to gemini surfactants.

Activity of gemini surfactants is strongly influenced by alkyl chain length, type of spacer, number of charged nitrogent atoms and the type of functional group present in the molecule [2–4].

One of the most important parameter which characterize properties of surfactants in aqueous solution is the Critical Micelle Concentration (CMC), i.e. the concentration of surfactant at which molecules begin to aggregate. The structure and stability of spherical micelles is due to the mutual compensation of two factors: the attraction between the alkyl chain and repulsion resulting from the electrostatic interactions between polar groups localized on the surface of the micelles formed. There are many ways to determine CMC , however the most favorable and accurate technique is conductometric titration [5] .

This work present results of physicochemical and spectroscopic study of novel gemini surfactants functionalized by ester groups.

[1] F. M. Menger, C. A. Littau, Gemini Surfactants: Synthesis and Properties, Journal of American Chemical Society, **113**, 1451-1452 (1991).
[2] S. M. Tawfik, Synthesis, surface, biological activity and mixed micellar phase properties of some biodegradable gemini cationic surfactants containing oxycarbonyl groups in the lipophilic part, Journal of Industrial and Engineering Chemistry, **28**, 171-183 (2015).
[3] M. T. Garcia, O. Kaczerewska, I. Ribosa, B. Brycki, P. Materna, M. Drgas, Biodegradability and aquatic toxicity of quaternary ammonium-based gemini surfactants: effect of the spacer on their ecological properties, Chemosphere, **154**, 155-160 (2016).
[4] B. Brycki, I. Kowalczyk, A. Kozirog, Synthesis, molecular structure, spectral properties and antifungal activity of polymethylene-α,ω-bis(*N,N*-dimethyl-*N*-dodecyloammonium bromides), Molecules, **16**, 319-335 (2011).
[5] K. Łudzik, K. Kustrzepa, H. Piekarski, Thermodynamics of micelle formation of gemini surfactants hexylene-1,6-bis(dimethyloctylammonium bromide) and dodecylene-1,12-bis(dimethyloctylammonium bromide) by electric conductance measurements, Journal of Chemical and Engineering Data, **59**, 4165-4172 (2014).

LOW-TEMPERATURE SYNTHESIS AND MAGNETIC PROPERTIS OF NANOSIZED Mn-FERRITES

Maksim Kutuzau, Dzmitry Kotsikau, Vladimir Pankov

Department of Physical Chemistry, Belarusian State University, Belarus
che.kutuzov@bsu.by

Ferrites have been widely studied due to their diverse potential applications including telecommunication device, ferro-fluid technology, chemical sensor, electrophotographic developer, hyperthermia treatment, drug delivery, and magnetic resonance imaging [1, 2].

As magnetic nanoclusters, which have a low (even zero) coercivity over a wide range of particle sizes, exhibiting desired magnetization can be useful in a broad range of applications [3].

In this work, we studied Mn-ferrites because of their promising magnetic properties. As seen in Fig. 1, Mn-substituted ferrites are characterized by a high magnetization at room temperature.

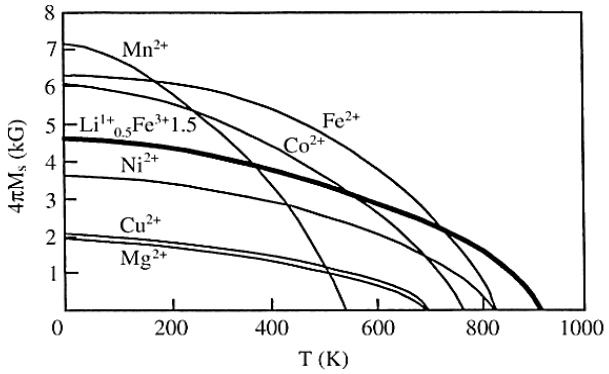

Fig 1. Thermomagnetic properties of spinel ferrites [4].

The magnetic properties of Mn-ferrites are known to depend on their phase composition and other structural features. The studied ferrites are $Mn_xFe_{2-x}O_4$ solid solutions differing in structural and concentration inhomogeneity. To achieve the best magnetic characteristics, the preparation of a product consisting of single spinel-type phase with no traces of individual iron or manganese oxides is required. The oxidation state manganese and iron cations, and manner of their distribution over the spinel crystal lattice also influence the magnetic behavior of the Mn-ferrites. According to the Neel theory, maximum magnetization value is reached when bivalent cations (Fe^{2+}, Mn^{2+}) occupy tetrahedral positions of the spinel lattice, while trivalent cations (Fe^{3+}) – octahedral ones [5].

During the synthesis, it is very important to consider the possibility of $Mn^{2+} \rightarrow Mn^{3+}$ oxidation reaction, which influences the ferrite properties. In the technological cycle of the ferrite fabrication, $Mn^{2+} \rightarrow Mn^{3+}$ oxidation reaction may occur at high temperature, which is likely accompanying by a reduction of Fe^{3+} ions to Fe^{2+} state, and also by a redistribution of the metal cations between the sublattices. Namely, a partial swap of the generated Fe^{2+} and Mn^{3+} ions between tetrahedral and octahedral lattice sites is possible. The described processes have an adverse effect on the magnetic features of the material [5]. In our work, we used low-temperature co-precipitation method of synthesis, which allows avoiding undesired oxidation reactions. A series of $Mn_xFe_{2-x}O_4$ ferrites with $x = 0 \div 1.5$ has been synthesized. The structural features and the magnetic properties of the prepared materials have been studied.

In order to prepare $Mn_xFe_{2-x}O_4$ ferrites, a combined hydrolysis of Fe^{3+}, Fe^{2+} and Mn^{2+} salts with NaOH was used. The metal salts were taken in the corresponding proportions. The suspension was stirred for 1 h followed by magnetic decantation and drying.

Transmission electron microscopy shown that all the samples consist of nearly spherical particles with an average size of about 10 nm and low polydispersity index.

According to X-ray diffraction analysis, the powders of $Mn_xFe_{2-x}O_4$ were single-phased and had a spinel structure up to $x = 1$. Individual MnO_2 phase was distinguished in the diffraction patterns of the powders with $x > 1$.

The magnetic properties of the prepared samples have been estimated. The saturation magnetisation values were measured to be in the range of 50–65 emu/g. All the powders were superparamagnetic at room temperature.

[1] D. Carta, M. F. Casula, P. Floris et al., Synthesis and microstructure of manganese ferrite colloidal nanocrystals, Phys. Chem. Chem. Phys. 12, 5074-5083 (2010).
[2] C. Cheng, Y. Wen, X. Xu, H. Gu, Tunable synthesis of carboxyl-functionalizedmagnetite nanocrystal clusters with uniform size, J. Mater. Chem. 19, 8782-8788 (2009).
[3] W. H. De Jong and P. J. A. Borm, Drug delivery and nanoparticles:applications and hazards., Int. J. Nanomed. 3, 133-149 (2008).
[4] G.F. Dionne, Molecular-field coefficients of $MnFe_2O_4$ and $NiFe_2O_4$ spinel ferrite systems, J. Appl. Phys. 63, 3777-3779 (1988).
[5] D. Kotsikau, M. Ivanovskaya, V. Pankov, Y. Fedotova, Structure and magnetic properties of manganese–zinc-ferrites prepared by spray pyrolysis method, Solid State Sci. 39, 69-73 (2015).

UNEXPECTED COURSE OF REACTIONS OF HETARYL AND FERROCENYL SUBSTITUTED SECONDARY METHANOLS WITH LAWESSON'S REAGENT (L.R.)

Róża Hamera-Fałdyga, Małgorzata Celeda, Grzegorz Mlostoń

Department of Organic & Applied Chemistry, University of Łódź,
Tamka 12, PL-91-403 Łódź, Poland
roza.hamera@gmail.com, *gmloston@uni.lodz.pl*

Thiols constitute a class of organosulfur compounds with great importance for both, laboratory and industrial organic synthesis. For that reason new methods for their preparation have extensively been studied. Recently we described the conversion of (ferrocenyl)(aryl)(trifluoromethyl)methanols to corresponding thiols. Thus, the reaction of tertiary alcohols with L.R. is a straightforward method for preparation of corresponding tertiary thiols [1]. Encouraged by this success, we decided to examine reactivity of thienyl/ferrocenyl secondary alcohols of type **1** towards L.R..

It is known that secondary diphenyl alcohol (benzhydrylalcohol) (**1a**) can be easily converted into the corresponding thiol **2** by treatment with Lawesson's reagent in wet toluene [2]. Unexpectedly, the study showed that in this series, replacement of Ph group by ferrocenyl and/or by thienyl group results in the formation of tetra-substituted ethanes **3** or sulfides **4**, respectively, which were isolated in good to excellent yields [3].

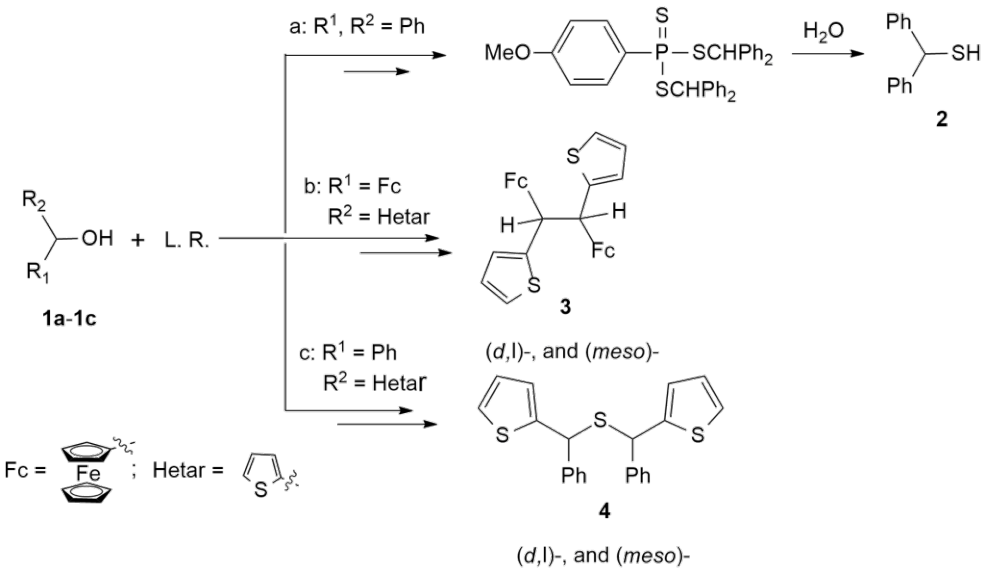

Scheme 1. Different courses of reaction secondary alcohols **1**with L.R..

Unexpectedly, in reactions of aryl/hetaryl and dihetaryl methanols **1** with L.R. the respective sulfides of type **4** were formed exclusively [3]. In the case of chiral alcohols **1**, sulfides **4** were obtained as 1:1-mixtures of *dl*- and *meso*-diastereoisomers. Mechanisms of reactions leading to thiole **2**, ethane **3** or sulfides **4** will be discussed.

Acknowledgement: *Financial support by the National Science Center (PL-Cracow) within the research grant Grant Maestro-3 (Dec-2012/06/A/ST5/00219) is acknowledged.*

[1] G. Mlostoń, R. Hamera-Fałdyga, M. Celeda, K. Gębicki, H. Heimgartner, J Fluorine Chem **188**, 147-152 (2016).
[2] G. Mlostoń, M. Celeda, R. Hamera-Fałdyga, H. Heimgartner, Heteroatom Chem. (2017), submitted.
[3] G. Mlostoń, R. Hamera-Fałdyga, H. Heimgartner, Phosphorus Sulfur Silicon Rel. Elem., (2017),in print DOI:10.1080/10426507.2017.1286491

ENANTIOSELECTIVE SYNTHESIS OF EPOXYKETONES VIA AEROBIC OXIDATION OF CYCLOPROPANOLS

Gábor Zoltán Elek, Victor Borovkov, Margus Lopp, Dzmitry Kananovich*

Department of Chemistry and Biotechnology, School of Science, Tallinn University of Technology, Estonia
gaelek@ttu.ee

Enantiomerically pure epoxyketones are valuable intermediates for production of pharmaceuticals and bioactive compounds [1]. One of the most effective methods to synthesize epoxyketones is based upon the Weitz-Scheffer epoxidation reaction. However, despite of extensive development of its asymmetric versions in recent decades [1], there are still several practical shortcomings, e.g. a limited scope of substrates. For example, vinyl ketones cannot be transformed into the corresponding epoxides [2,3].

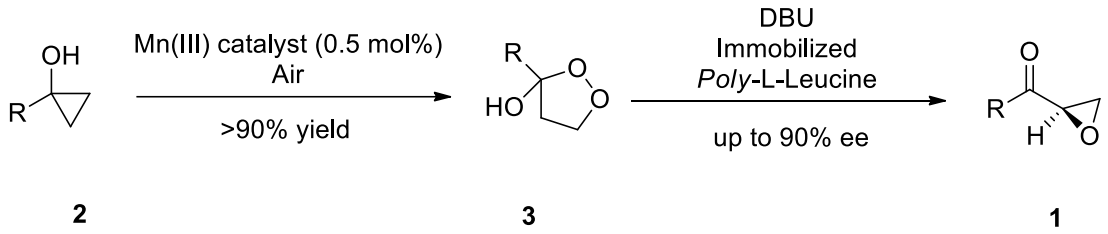

Fig. 1. Synthesis of enantiomerically enriched epoxyketones

To fill this gap, we have developed a facile two-step approach for asymmetric synthesis of epoxyketones **1** from easily available cyclopropanols **2**. Aerobic oxidation of cyclopropanols **2** proceeds readily in the presence of various Mn(III) catalysts to afford 1,2-dioxalan-3-ols **3** in high yields (>90%) [4]. The latter can be further transformed into the corresponding enantiomerically enriched epoxyketones (with up to 90% ee) by treatment with organic base (DBU) in the presence of immobilized *poly*-L-leucine catalyst. Further details and implications of this synthetic strategy will be presented and discussed.

[1] C. Reisinger, *Epoxidations and hydroperoxidations of α,β-unsaturated Ketones* (Springer-Verlag, Germany, 2012).
[2] C. Lauret, S. M. Roberts, Asymmetric epoxidation of α,β-unsaturated ketones catalyzed by Poly(amino acids), Aldrichimica Acta **35**, 47-51 (2002).
[3] O. Lifchits, B. List et al., The cinchona primary amine-catalyzed asymmetric epoxidation and hydroperoxidation of α,β-unsaturated carbonyl compounds with hydrogen peroxide, J. Am. Chem. Soc **135**, 6677-6693 (2013).
[4] O. G. Kulinkovich, D. A. Astashko et al., Synthesis of α,β-epoxy ketones from alkyl- and arylsubstituted cyclopropanols, Synthesis 1453-1455 (2001).

MAGNETIC NANOPARTICLES FOR SHINERS MEASUREMENTS

Robert Ambroziak

Department of Chemistry, University of Warsaw, Poland
rambroziak@chem.uw.edu.pl

Silver and gold nanoparticles can be used for achieving so-called surface enhanced Raman scattering (SERS) effect. The SERS enhancement factor can reach $10^4 – 10^6$. Interesting modification of SERS spectroscopy is SHINERS (shell-isolated nanoparticle-enhanced Raman spectroscopy). In SHINERS spectroscopy the same plasmonic nanoparticles as in standard SERS measurements are used but they are capped by very thin protective layer of SiO_2, AlO_2 or MnO_2, that protects nanoparticles from contact with the sample and agglomeration [1]. If one uses a magnetic core in this type of nanoparticles (Fig. 1), application and removal from sample surface can be easier.

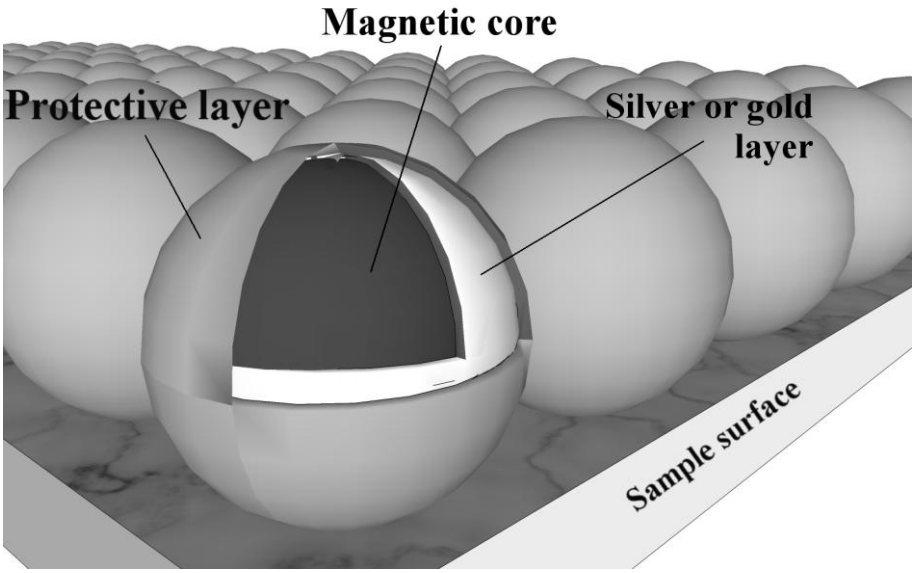

Fig. 1. Magnetic nanoparticles for SHINERS measurements on sample surface

Synthesis of this type of material is not easy. Silver and gold is hard to attach to magnetic core. Strong magnetic effects are observed for ferric and cobalt oxide, which, unfortunately have different crystalline structure than gold and silver. So it can be necessarily to use silica for linking these materials. Next problem is that magnetic nanoparticles used as core can be too small to show a macroscopic magnetic properties for these nanomaterials.

In this approach we used methods from literature [2] for coating Fe_3O_4 by gold layer. In the other approach we are trying to use a silica layer on magnetic core for coating [3]. The silica layer may be relatively easy cover with gold or silver [4]. These silver or gold layers can be covered by next silica layer [5]

These multistage type synthesis is hard to make because problems on one stage can make all synthesis impossible to carry out but these type of material can be used for applications were normal SHINERS can't be used.

[1] J. Li, Y. Huang, Y. Ding et al., Shell-isolated nanoparticle-enhanced Raman spectroscopy, Nature **464**, 392-395 (2010).
[2] Q. Lu, K. Yao, D. Xi et al., Synthesis and characterization of composite nanoparticles comprised of gold shell and magnetic core/cores, J. Magn. Magn. Mater. **301,** 44-49 (2006)
[3] K. Woo, J. Hong, J-P. Ahn, Synthesis and surface modification of hydrophobic magnetite to processible magnetite@silica-propylamine, J. Magn. Magn. Mater. **293,** 177-181 (2005)
[4] B. Jankiewicz et al., Silica-metal core-shell nanostructures, Adv. Colloid Interfac. **170,** 28-47 (2012)
[5] H. Abdulrahman et al., Silica-Protected Hollow Silver and Gold Nanoparticles: New Material for Raman Analysis of Surfaces, J. Phys. Chem. C. **119,** 20030 - 20038 (2015)

FLUORESCENCE QUANTUM YIELD OF PERYLENEDIIMIDE COMPOUNDS

Austėja Bukauskytė[1,2], Alytis Gruodis[1], Renata Karpič[2]

[1] Faculty of Physics, Vilnius University, Saulėtekio Ave. 9-III, LT-10222 Vilnius, Lithuania
[2] Center for Physical Sciences and Technology, Saulėtekio Ave. 3, LT-10257 Vilnius, Lithuania
bukauskyte.austeja@gmail.com

Perylenediimides (PDIs) are organic materials of high photo and thermal stability, high fluorescence quantum yields (QY) and chemical inertness. First PDIs had very low solubility so they were used as high quality industrial pigments, especially for automobiles [1]. New potential applications for PDIs arose when solubility increasing substituents were introduced (Figure 1 positions R, 1-8).

Due to high fluorescence QY, high thermal and photo stability, PDI compounds are used in luminescence solar concentrators. Wide absorption in visible region allows application of these compounds in dye sensitized solar cells. Also, PDI compound possess *n*-type conductivity, so they can be used in organic solar cells, organic field effect transistors and organic light emitting diodes. Broad fluorescence spectrum and high photo stability make PDIs excellent material for developing organic solid-stat lasers [2].

Most of PDIs properties can be modified by introducing different substituents at different positions (Figure 1). Although, while some substituents can alter PDI's properties in desired way (for example, increase solubility, widen absorption or emission spectra), they can also do some negative influence on some properties (for example, substituents at 1-8 positions can decrease fluorescence QY).

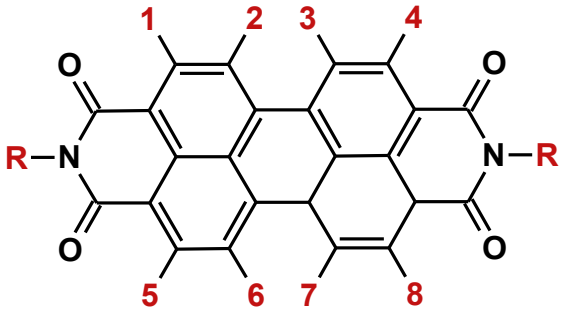

Fig. 1. Molecular structure of PDI molecule with possible substituents positions (R, 1-8)

In this research, properties of newly synthesized PDIs were investigated. These compounds were synthesized by Dr. Linas Labanauskas group from Center for Physical Sciences and Technology. Dependence of absorbance and fluorescence spectra on different substituents was discussed. Furthermore, fluorescence QY of all PDIs were determined employing the comparative method and using two different standards – Fluorescein and Rhodamine 101 [3]. Strong dependence of QY on different substituents was shown. Different substituents have different effects on charge distribution in excited state. This was also confirmed by quantum chemical calculations. Finally, radiative and non-radiative fluorescence lifetimes of all PDIs were determined and presented.

[1] W. Herbst, K. Hunger, Industrial Organic Pigments Production, Properties, Applications, 3rd ed. WILEY-VCH Verlag GmbH & Co. KGaA, Weinheim, (2004).
[2] E. M. Calzado, J. M. Villalvilla, P. G. Boj, J. A. Quintana, R. Go´mez, J. L. Segura, M. A. Dı´az-Garcı´a, Effect of Structural Modifications in the Spectral and Laser Properties of Perylenediimide Derivatives, J. Phys. Chem. C, **111**, 13595-13605 (2007).
[3] H. Langhals, J. Karolin, L. B-A. Johansson, Spectroscopic properties of new and convenient standards for measuring fluorescence quantum yields, J. Chem. Soc., Faraday Trans., **94**, 2919-2922, (1998)

SYNTHESIS AND PROPERTIES OF PHENOTHIAZINE-BASED DERIVATIVES

Tadas Cepulis, Eigirdas Skuodis, Dalius Gudeika

Department of Polymer Chemistry and Technology, Kaunas University of Technology, Radvilenu pl. 19, LT-50254 Kaunas, Lithuania
ktultu@gmail.com

The electroactive low-molecular mass materials known as molecular glasses are using in OLEDs, OFETs, organic electronics and photoreceptors. Organic electron-donating materials were described by lots authors but bipolar materials explored lower and it are really perspective because of well characteristics. Phenothiazine is cheap structural element which is explored low. Cianophenyl substituents are usually using for electron-accepting part [1-3]. Donor – acceptor structure materials are perspective because of small energy gap between singlet and triplet energies and are possibility to observe thermally activated delayed fluorescence (TADF) properties. Compounds were synthesised by Ullman coupling reaction and the thermal, photophysical and electrochemical properties of derivatives were studied.. The route of synthesis is shown at Fig. 1.

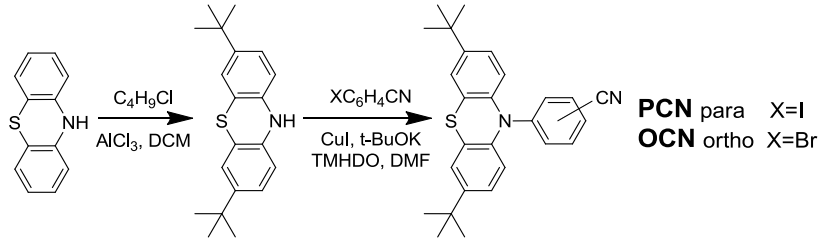

Fig. 1. Structures of phenothiazine-based derivatives.

The derivatives were obtained as crystalline materials but *Ortho*-substituted derivative **OCN** consisted stabile molecular glasses. The compounds exhibit green colour emission. The ortho-substituted derivative **OCN** exhibit lower ionisation potential and higher electron affinity. The electronic spatial distribution of the HOMO is mainly distributed over the phenothiazinyl moieties, while that of the LUMO is completely localized over the 4-cyanophenyl and 2-cyanophenyl moieties, respectively.

---

[1] Walzer, K.; Maennig, B.; Pfeiffer, M.; Leo, K. Highly Efficient Organic Devices Based on Electrically Doped Transport Layers. *Chem. Rev*. **2007**, *107*, 1233–1271.
[2] Chaskar, A.; Chen, H.-F.; Wong, K.-Ts. Bipolar Host Materials: A Chemical Approach for Highly Efficient Electrophosphorescent Devices. *Adv. Mater*. **2011**, *23,* 3876–3895.
[3] Cho, Y.J.; Yook, K.S.; Lee, J.Y. High efficiency in a solution-processed thermally activated delayed fluorescence device using a delayed fluorescence emitting material with improved solubility*Adv Mater.* **2014***, 26*, 6642-6666.

AQUEOUS SOL–GEL SYNTHESIS AND THERMOANALYTICAL STUDY OF $La_{1.9}Ca_{0.1}Mo_2O_{8.95}$

Giedrė Gaidamavičienė[1], Artūras Žalga[1], Edvardas Kazakevičius[2]

[1] Faculty of Chemistry and Geosciences, Vilnius University, Naugarduko Str. 24, LT-03225 Vilnius, Lithuania
[2] Faculty of Physics, Vilnius University, Sauletekio av. 9/3, LT-10222 Vilnius, Lithuania
giedre.prievelyte@chf.stud.vu.lt

Manufacturing of solid oxide fuel cell (SOFC) components nowadays remains a key point for the industrial development of this technology. Especially, the deposition of dense electrolyte layer which is sandwiched between the porous anode and cathode attracts a lot of attention [1]. Nevertheless, the practical application of these devices is hindered by the high operation temperature (up to 800 °C) required to allow the conduction of oxygen ions through conventional electrolytes (i.e., yttria-stabilized zirconia (YSZ)) [2]. Concerning the electrolyte production, a number of many different compositions have been found which present higher ionic conductivity than YSZ. The drawbacks such as lower stability under reducing conditions, undesired phase transformations or interaction with cathode or anode materials should be eliminated in order to replace YSZ by other electrolyte. The reducing of operating temperature also plays important role in the production of SOFC. Solid electrolytes that possess high conduction below 600 °C overcomes the YSZ. One of the most promising electrolyte that operates at low temperature is lanthanum molybdate with general formula $La_2Mo_2O_9$ (LAMOX). This compound is well known for more than a decade because of its high ionic conductivity that increases up to two orders of magnitude during the reversible phase transition from monoclinic α to cubic β structure at about 560 °C and reaching conductivity higher than the one corresponding to YSZ. Despite lower chemical stability of LAMOX at high temperatures, comparing with YSZ, the possibility to increase the resistance to the environment conditions and to stabilize the high temperature cubic phase at room temperature with increased ionic conductivity is really attractive and desirable.

In this respect, the substitution of La by Ca (i.e., $La_{2-x}Ca_xMo_2O_{9-\delta}$) was reported to improve the stability against reduction of this kind of materials with a slight decrease of ionic conductivity and retaining the high temperature β-cubic phase. Moreover, it is well known that the size of the particles for standard practice powder usually reaches 50 μm to 100 μm in diameter. Accordingly to that in this work the aqueous sol-gel synthesis method was successfully used in order to obtain lanthanum molybdate substituted by calcium. In addition, the influence to the possible formation of final material according to the starting compounds by thermal analysis (TG/DSC) was investigated in detail. Besides, the surface morphology of annealed ceramic was analyzed by scanning electron microscopy (SEM) in order to prove the formation of dense structures. Finally, X-Ray diffraction (XRD) was used to assess the composition of the crystalline phases in the sample.

Acknowledgements The research leading to these results has received funding from Lithuanian–French Programme "Gilibert" under project agreement n° S-LZ-17-7.

[1] P. Coddet, H. L Liao, C. Coddet, A review on high power SOFC electrolyte layer manufacturing using thermal spray and physical vapour deposition technologies, Advances in Manufacturing 2 [3], 212–221 (2014).
[2] L. Baqué, J. Vega-Castillo, S. Georges, A. Caneiro, E. Djurado, Microstructural and electrical characterizations of tungsten-doped $La_2Mo_2O_9$ prepared by spray pyrolysis, Ionics **19**, 1761–1774 (2013).

THIA-DIELS-ALDER REACTIONS OF DIHETARYL THIOKETONES WITH 2,4-HEXADIENE; A RARE CASE OF STEPWISE, DIRADICAL [4+2]-CYCLOADDITIONS

Paulina Grzelak, Grzegorz Mlostoń

Department of Organic & Applied Chemistry, University of Łódź,
Tamka 12, PL-91-403 Łódź, Poland
paulinagrzelak88@gmail.com, *gmloston@uni.lodz.pl*

The thia-Diels-Alder reactions constitute an important group of [4+2]-cycloadditions, which offer an attractive access to six-membered sulfur-containing heterocycles [1]. They are of special interest for the preparation of 3,6-dihydro-2*H*-thiopyrans, which are known as relevant components of natural products and biologically active compounds [2].

Dihetaryl thioketones of type **2** substituted with thiophen-2-yl and seleophen-2-yl rings react as 'superdienophilic reagents' with non-activated 1,3-dienes such as 2,3-dimethylbuta-1,3-diene, cyclopentadiene and isomeric hexa-2,4-dienes **1a** to produce the expected 2*H*-thiopyrans **4a**-**4b**in good to excellent yields [3]. In the latter case, starting with a mixture of (*E*,*E*)-, and (*E*,*Z*)-isomers, the corresponding *cis*-3,6-dihydro-3,6-dimethyl-2,2-dihetaryl-2*H*-thiopyrans (*cis*-**4a**-**4b**) are formed as the sole products in a stereoconvergent thia-Diels-Alder reaction. A step-wise mechanism via delocalized intermediate diradicals **3** is postulated to rationalize the observed reaction course [3-5].

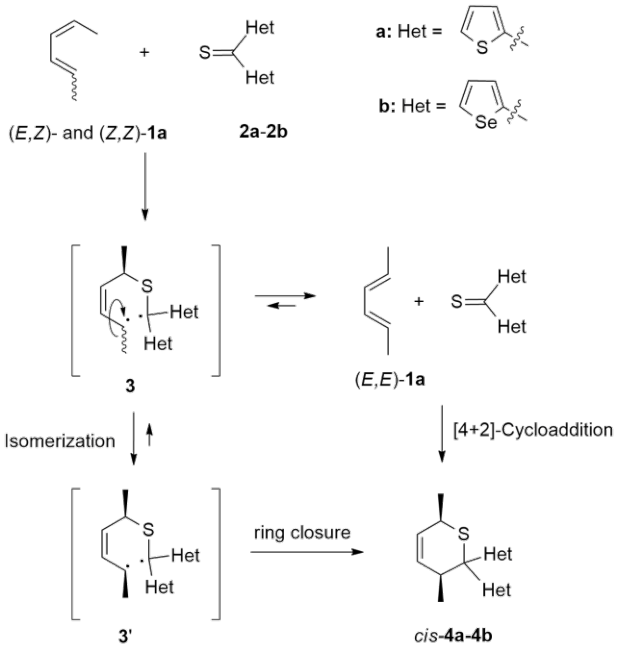

Fig. 1. Mechanistic interpretation of the step-wise reaction course of the thia-Diels-Alder reaction with (*E,Z*)- and (*Z,Z*)-hexa-2,4-diene **1a** and dihetaryl thioketones **2**.

Finally, products obtained in thereaction 2,3-dimethyl buta-1,3-diene with selected thioketones, i.e. corresponding 2*H*-thiopyrans were treatedwith excess *m*-CPBA at room temperature in CH_2Cl_2 solution. In these reactions oxidation of both the C=C bond and the *S*-atom in the six-membered ringwas observed. Remarkably, the *S*-atom of the thiophene ring did not undergo the oxidation reaction under the applied conditions.

Acknowledgement:*Financial support by the National Science Center (PL-Cracow) within the research grant Grant Maestro-3 (Dec-2012/06/A/ST5/00219) is acknowledged.*

[1] G. Blond; M. Gulea, V. Mamane, Curr. Org. Chem. **20**, 2161–2210 (2016).
[2] a) E. Block, in *Science of Synthesis*, Ed. A., G. Molander, Vol. 33, Chapter 33, pp. 235–259, G. Thieme Verlag, Stuttgart (2007).
b.) F. Tavakolinia, T. Baghipour; Z Hossaini; D. Zareyee; A. Mohammad, M. A., Khalilzadeh; M. Rajabi, Nucleic Acid Ther., **22**, 265–270.
[3] G. Mlostoń, P. Grzelak, A. Linden, H. Heimgartner Chem. Heterocycl. Comp. (2017), in press.
[4] S. Wilker, G. Erker, J. Am. Chem. Soc. **117**, 10922–10930 (1995).
[5] R. A. Firestone, Int. J. Chem. Kinet., **45**, 415−428 (20013).

SYNTHESIS AND PROPERTIES OF DONOR-ACCEPTOR CARBAZOLE-BASED DERIVATIVES

Dainora Jankunaite[1], Dalius Gudeika[1]

[1] Department of Polymer Chemistry and Technology, Kaunas University of Technology, Radvilenu pl. 19, LT-50254 Kaunas, Lithuania
taipsakant@gmail.com

The materials are useful for the preparation of optoelectronic devices, such as light-emitting diodes, electrophotographic photoreceptors, solar cells as charge-transporting compounds [1,2].

In this report we are presenting thė synthesis and studies of the series of carbazole derivatives there derivatives of benzene were merged with the 9th atom of carbazole by Ullmann or modified Ullmann coupling reactions (Fig 1).

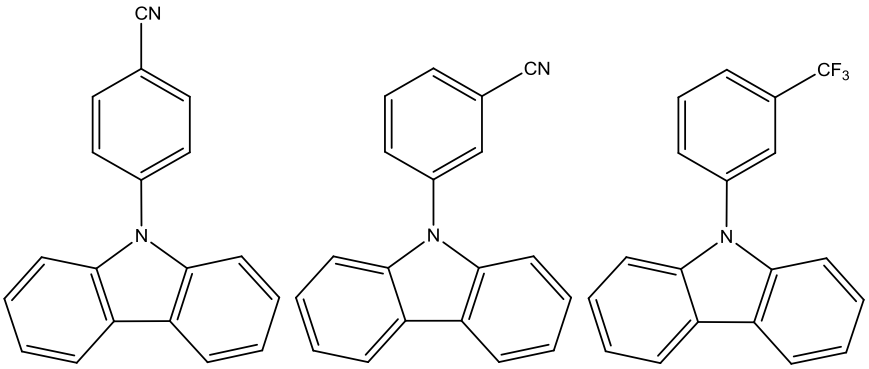

I II III

Fig. 1. Structures of **I-III**.

The structures of the synthesized compounds were proved by ^{1}H and ^{13}C NMR, IR and mass spectrometries. The thermal, optical, electrochemical and photophysical properties of the compounds were investigated.

---

[1] Forrest, S. R.; Thompson, M. E. Eds. Organic Electronics and Optoelectronics. *Chem. Rev.* **2007**, *107*, 923−1386.
[2] Shirota, Y.; Kageyama, H. Charge Carrier Transporting Molecular Materials and Their Applications in Devices. *Chem. Rev.* **2007**, *107*, 953−1010.

RAMAN STUDY OF WATER STRUCTURES IN 1-BUTYL-3-METHYLIMIDAZOLIUM BROMIDE AND NITRATE AND WATER MIXTURES

Vytenis Jočys, Valdemaras Aleksa, Jonas Kausteklis

Department of general physics and spectroscopy, Faculty of Physics, University of Vilnius, Lithuania
vytenis.jocys@ff.stud.vu.lt

Ionic liquids (ILs) has become extremely attractive study material in spectroscopy due to their variable abilities and wide range of applications. Most notably, ionic liquids are great designer solvents, as their abilities can be tuned to match a specific solute and negligible vapor pressure let them serve as "green" solvents by replacing volatile and toxic industrial solvents.

It is crucial to study the effects water on ionic liquids, because water, as a co-solvent or impurity, can drastically change the properties of ionic liquids and even hydrophobic ionic liquids tend to absorb water from atmosphere [1]. The main goal of this work was to investigate the effect of two specific room temperature ionic liquids, namely 1-butyl-3-methylimidazolium bromide and nitrate, on O-H stretch band of water using polarized Raman spectroscopy.

There are three O-H stretch band components, namely: ν_{3270}, ν_{3450} and ν_{3650} corresponding to network forming (strong H-bonds), intermediate (weaker H-bonds) and free (no H-bonds) water O-H stretch bands, accordingly [2].

Three slope change points (at X_{H2O}=0.4±0.02, X_{H2O}=0.68±0.02 and X_{H2O}=0.84±0.02) were determined in the $S_{x/}(S_{3270}+S_{3450}+S_{3650})$ integral intensity ratio for [BMIM]Br/H_2O mixture and two (at X_{H2O}=0.38±0.02 and X_{H2O}=0.6±0.02) for [BMIM]NO_3/H_2O mixture as the free water O-H band component in the latter mixture formed only in very high water concentration.

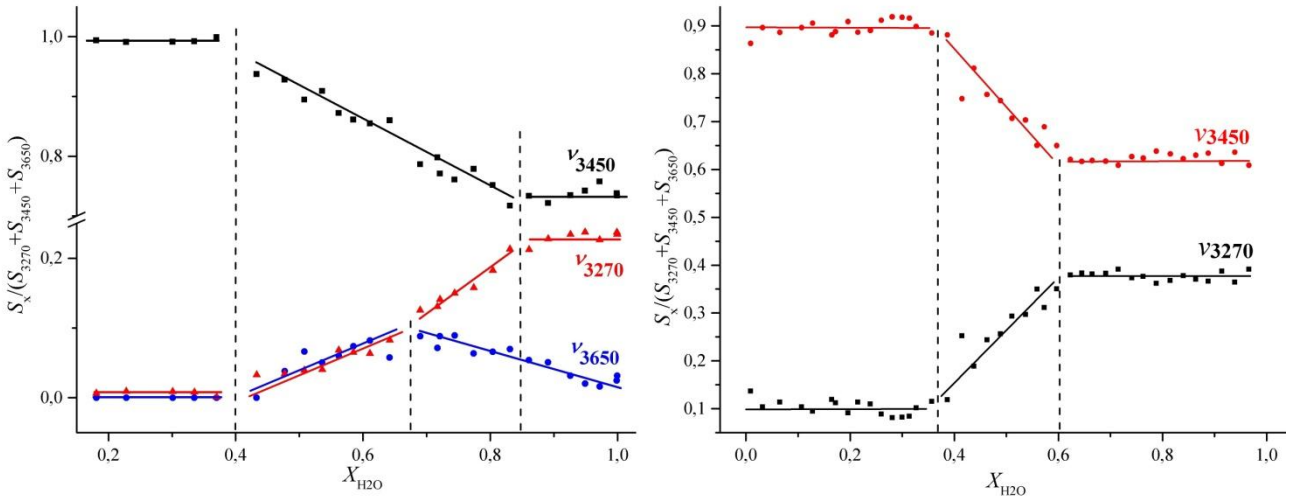

Fig. 1. All three water structure O-H band integral intensities, normalized to the sum of network, intermediate and free water O-H band integral intensities, dependencies on water molar fraction in the mixture of [BMIM]Br/H_2O on the left and [BMIM]NO_3/H_2O on the right

The slope change point at X_{H2O}=0.4±0.02 in the case of both ionic liquids is probably due to the start of forming of network water. The change point at X_{H2O}=0.84±0.02 for [BMIM]Br/H_2O and at X_{H2O}=0.6±0.02 for [BMIM]NO_3/H_2O could be attributed to the weakening of ionic liquid polar network and simultaneous increase in both network and intermediate water.

Moreover, the polarized Raman spectra of the ionic liquid aqueous solution were measured and the depolarization ratios for ν_{3270} and ν_{3450} O-H bands were determined. For the [BMIM]Br/H_2O mixture, the ν_{3270} band's depolarization ratio is 0.2±0.15 and remains nearly constant throughout the whole concentration range, whereas ν_{3450} band's depolarization ratio decreases from 0.3±0.1 to 0.1±0.05 upon water fraction increase. In the case of [BMIM]NO_3/H_2O mixture - the ν_{3450} band the depolarization ratio is 0.05±0.02 and remains constant throughout the whole concentration range, while ν_{3270} band's depolarization ratio has a break point at X_{H2O}=0.5±0.1. The symmetry changes could be due to the growth of symmetric anion-water complexes, but further analysis is required to be certain.

[1] I. Khan, K.A. Kurnia, F. Mutelet, S.P. Pinho, J.A.P. Coutinho, Probing the interactions between ionic liquids and water: Experimental and quantum chemical approach, J. Phys. Chem. B. 118 (2014) 1848–1860. doi:10.1021/jp4113552.

[2] B. Fazio, A. Triolo, G. Di Marco, Local organization of water and its effect on the structural heterogeneities in room-temperature ionic liquid/H2O mixtures, J. Raman Spectrosc. 39 (2008) 233–237. doi:10.1002/jrs.1825.

SYNTHESIS OF 3,5-DIARYL-2-SUBSTITUTED-THIOPHENES

Mantas Jonušis, Indrė Misiūnaitė, Girius Kisielius, Inga Čikotienė

[1] Faculty of Chemistry and Geosciences, Vilnius University
Naugarduko 24, LT-03225, Vilnius, Lithuania
mantas.jonusis@chf.vu.lt

Thiophene based compounds are widely explored and applied in pharmaceutical and physical sciences [1]. Classical routes to thiophene synthesis are Gewald reaction and Paal-Knorr thiophene synthesis. Nowdays many other synthetical methods are developed towards the substituted thiophene synthesis [2].

We have derived series of 3,5-diaryl-2-substituted-thiophenes from 1,3-diarylprop-2-yn-1-ones **1** by treating them with active methylene group containing thiols in methanol solvent and DBU as a base.

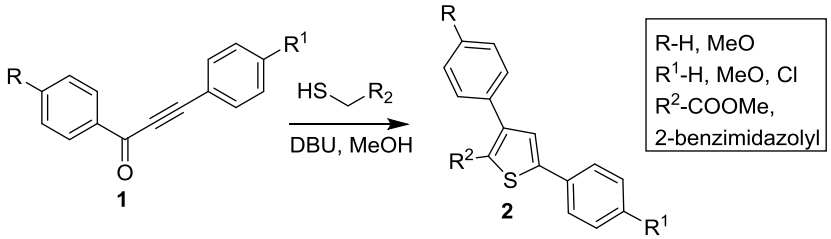

Compounds **1** were synthesized in excellent yields from substituted phenylacetylenes and corresponding commercially available benzoyl chlorides in Et_3N as a base and solvent and CuI catalyst. Compounds **2** with R^2 = COOMe were reduced to alcohols using $LiAlH_4$ and oxidized to aldehydes **3** with PCC in DCM. Series of compounds **4** and **5** were derived from **3**.

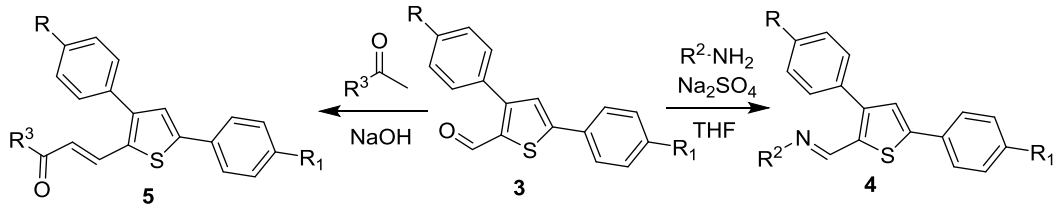

In summary, we have synthesized list of previously unexplored 3,5-diaryl-2-substituted-thiophenes which exhibited fluorescent properties and good solubility in organic solvents and could potentially find their applications in electronics or dye industry.

[1] S. C. Rasmussen, S. J. Evenson, C. B. McCausland, Fluorescent thiophene-based materials and their outlook for emissive applications, Chem. Commun. **51**, 4528-4543 (2015).
[2] R. Mancuso, B. Gabriele, Recent Advances in the Synthesis of Thiophene Derivatives by Cyclization of Functionalized Alkynes, Molecules **19**, 15687-15719 (2014).

SYNTHESIS AND PHOTOPHYSICAL PROPERTIES OF (1,2,3-TRIAZOL-4-YL)-7-DEAZAPURINES AND PURINES

Karolis Karpavičius[1], Jonas Bucevičius[1], Maris Turks[2], Tadas Bucevičius[3], Paulius Baronas[3], Saulius Juršėnas[3], Sigitas Tumkevičius[1]

[1] Department of Organic Chemistry, Faculty of Chemistry and Geosciences, Vilnius University, Naugarduko Str. 24, LT-03225 Vilnius, Lithuania
[2] Faculty of Materials Science and Applied Chemistry, Riga Technical University, P. Valdena Str. 3, LV-1048 Riga, Latvia
[3] Institute of Applied Research, Vilnius University, Saulėtekio Str. 3, LT-10222 Vilnius, Lithuania.
karolis.karpavicius@chf.vu.lt

Purine and 7-deazapurine heterocycles constitute an important class of compounds widely spread in nature and exhibiting diverse biological activities. On the other hand, heterocycles containing embedded 1,2,3-triazole moiety have found application in fields of bioconjugation, material science, chemical sensors, drug discovery and related areas [1,2]. Recently, we have shown that triazole – (deaza)purine conjugates exhibit strong fluorescence and are promising candidates as functional materials [3, 4]. Continuing our work aimed to the search of novel fluorescent materials a series of 2,6-bis(1-aryl-1,2,3-triazol-4-yl)- and 2-aryl-6-(1-phenyl-1,2,3-triazol-4-yl)-7-deazapurines and purines (**I**, **II**) (Fig. 1) were synthesized and their photophysical properties investigated.

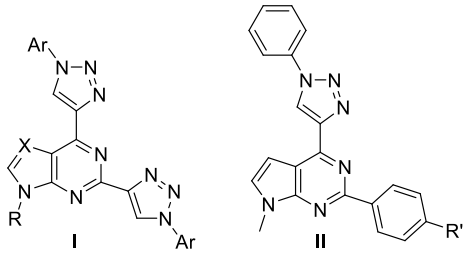

X = CH, N
R = Me, $SO_2C_6H_4Me$-4, CH_2CO_2Et, n-$C_{12}H_{25}$,
R' = H, 4-Me_2N, 4-F, 4-CF_3,
Ar = Ph, 4-$Me_2NC_6H_4$, 4-$MeOC_6H_4$, 4-MeC_6H_4, 4-FC_6H_4, 2-naphthyl, 1-naphthyl,

Fig. 1. Structures of (1,2,3-triazol-4-yl)-7-deazapurines and purines

Construction of 1,2,3-triazole moieties in positions 2 and/or 6 of the heterocycles (**I**, **II**) was accomplished by a synthetic route consisting of the Sonogashira cross-coupling reaction of 2,6-dichloro-(7-deaza)purines with trimethylsilylethyne and following removing of trimethylsilyl group and copper(I)-catalyzed azide-alkyne cycloaddition reactions of the formed ethynyl(deaza)purines with the appropriate arylazides. Introduction of aryl groups into the second position of 7-deazapurines to give compounds **II** was achieved under the microwave irradiation by using cross-coupling reaction of 2-chloro-6-(1-phenyl-1,2,3-triazol-4-yl)-7-deazapurine with the corresponding aryl(tributyl)stannanes in the presence of $Pd(PPh_3)_2Cl_2/AsPh_3$ as a catalyst system.

Optical properties of the synthesized 7-deazapurines **I** (X=CH)**, II** and purines **I** (X=N) were assessed by performing absorption and fluorescence spectroscopy, fluorescence quantum yield (Φ_F) and fluorescence lifetime measurements. Most of the studied compounds exhibited blue fluorescence with emission maxima in the range 353-501 nm. Absorption and fluorescence properties were found to depend on the heterocycle origin and electronic nature of substituents at triazole ring and at position 9 of (deaza)purines. The largest Stokes shift (up to 200 nm) was observed for compounds bearing 4-dimethylaminophenyl group at triazole ring (**I**, X=CH, N, Ar=4-$Me_2NC_6H_4$). 7-Deazapurine derivatives (**I**, X=CH) exhibited stronger absorption and more efficient fluorescence in comparison with corresponding compounds of a purine series (**I**, X=N). In a 7-deazapurine series, molecules with (ethoxycarbonyl)methyl group at N9 (**I**, X=CH, R=CH_2COOEt) were more efficient emitters (Φ_F = 43.4%-63.5%) than *N*-tosyl derivatives (**I**, X=CH, R= $SO_2C_6H_4Me$-4) (Φ_F = 14.5%-34.5%).

Some other peculiarities of photoluminescence properties of the synthesized molecules will be presented in a report.

Acknowledgements
The research was funded by a grant (No. TAP-LLT-01/2015) from the Research Council of Lithuania.

[1] J. E. Moses, A. D. Moorhouse, Chem. Soc. Rev. **36**, 1249-1262 (2007).
[2] Y. H. Lau, P. J. Rutledge, M. Watkinson, M. H. Todd, Chem. Soc. Rev. **40**, 2848-2866 (2011).
[3] J. Bucevicius, J.; Skardziute, L.; Dodonova, J.; Kazlauskas, K.; Bagdziunas, G.; Jursenas, S.; Tumkevicius, RSC Adv. **5**, 38610-38622 (2015).
[4] A. Koval, I. Novosjolova, E. Bizdena, I. Bizane, L.Skardziute, K. Kazlauskas, S. Jursenas, M. Turks, Tetrahedron Lett. **54**, 850-853 (2013).

SYNTHESIS OF NEW STEROIDAL PYRIMIDOBENZIMIDAZOLE DERIVATIVES

Urszula Kiełczewska, Agnieszka Wojtkielewicz, Paulina Uścinowicz, Leszek Siergiejczyk, Artur Radkiewicz, Jacek W. Morzycki

Institute of Chemistry, University of Białystok, K. Ciołkowskiego 1K, 15-245 Białystok, Poland
ulakielczewska@interia.eu

Synthesis of benzimidazo[1,2-a]pyrimidines has gained considerable interest because of the pronounced biological activity of these compounds. They were reported to have antibacterial, anticancer, sedative, and antiarrhythmic. Some of them (fasiplon, taniplon, divaplon) have found application as anxiolytic drugs. However only a few steroid fused pyrimido[1,2-a]benzimidazoles have been described so far. Since nowadays there is a tendency to combine two pharmocophores in one hybrid molecules, which potentially is more effective than its individual components, we attempted to connect steroid skeleton with benzimidazo[1,2-a]pyrimidine.

To synthesize the steroidal pyrimidobenzimidazole derivative we have carried out the condensation of 16-dehydropregnenolone acetate with 2-aminobenzimidazole under various reaction conditions (Fig.1). As 2-aminobenzimidazole possesses two nucleophilic nitrogen atoms (NH2 and N3) the condensation may lead to two isomeric pyrimidines. However, the aromatic product was formed regioselectively, by conjugated addition of N3 of benzimidazole to C16 of steroid, followed by cyclization, autoxidation, and aromatization. Unexpectedly, the major product was accompanied by the D-homo ketone produced by competitive α-ketol type rearrangement of the hydroperoxide intermediate. The tentative mechanism is postulated. The elucidation of the product structures was carried out by NMR, IR, MS and X-ray methods as well as chemical evidences.

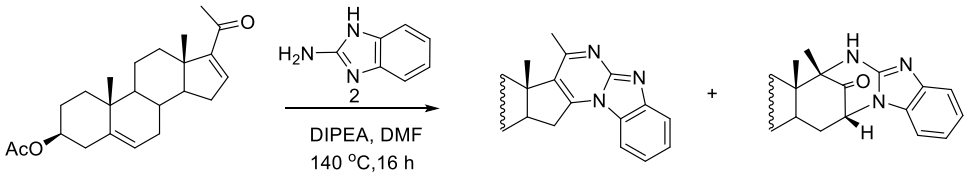

Fig. 1. The reaction between 16-dehydropregnenolone acetate and 2-aminobenzimidazole.

The authors thank the Polish National Science Centre for the grant support (2015/17/B/ST5/02892)

[1] X. He, S.E. Kassab, G. Heinzl, F. Xue, Base-catalyzed one-step synthesis of 5,7-disubstituted-1,2,4-triazolo[1,5-a] pyrimidines Tetrahedron Letters 56, 1034-1037 (2015).
[2] A. Wojtkielewicz, P. Uścinowicz, L. Siergiejczyk, U. Kiełczewska, A. Ratkiewicz, J.W. Morzycki, A study on the reaction of 16-dehydropregnenolone acetate with 2-aminobenz-imidazole , Steroids 117, 71-76 (2017)

COMPARISON OF BIOGENIC AND BY MICROEMULSION POLYMERIZED POLYPYRROLE MICROSPHERES

Monika Kirsnytė[1], Arūnas Stirkė[1], Algimantas Janarauskas[2], Roxana-Mihaela Apetrei[3]

[1] Department of Material Science and Electrical Engineering, Center for Physical Sciences and Technology, Lithuania
[2]Faculty of Chemistry and Geosciences, Vilnius University, Lithuania
[3]"Dunarea de Jos", University of Galati, Romania
monika.kirsnyte@ftmc.lt

Among conjugated polymers polypyrrole (PPy) is well known for its semiconductor properties [1], quick and simple polymerization and wide use in chemical sensors, electrochemical devices and batteries [2]. Due to its ability to convert electrogamnetic energy into thermal energy PPy could be used for engineering electromagnetic wave absorbers [3]. Polypyrrole can be synthesized by electrochemical, chemical and biocatalytic polymerization methods with variety of oxidizing agents. Here we observe two methods for PPy microsphere formation. A "green" method when microspheres are obtained in biocatalytic medium (BPPy) and microemulsion polymerization (MPPy)[4].

Bacteria *Streptomyces spp*. and pure pyrrole were used to carry out "green" biocatalytic microsphere synthesis. Optimal material proportions were assessed varying different pyrrole concentrations in bacteria medium. 30 mM pyrrole concentration was selected because it had no effect on bacteria vitality. After 10 days of inoculation in the bacterial medium with pyrrole monomer, changes in flasks were noticed. Samples were prepared for morphological and structural analysis by centrifugation and drying overnight in air at 25 °C. Optical microscope and FIB-SEM images confirmed oval and hollow BPpy microsphere structure. X-ray photoelectron spectroscopic analysis was measured using " Escalab MK II " with radiation source MgKα, registrating C 1s, N 1s and O 1s compound spectrum areas. XPS spectra analysis processed using the Avantage software [5].

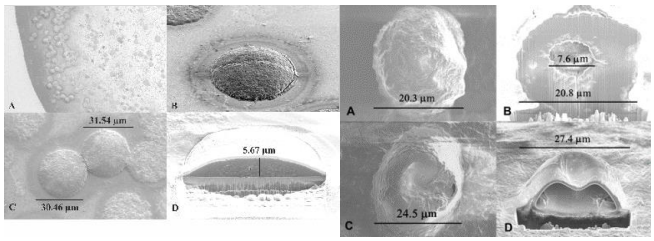

Fig. 1. Polypyrrole microspheres: left MPPy; right BPPy

Microemulsion polymerization was carried out using a special 5 tubular microfluidic system. Microemulsion formation was observed with optical microscope and "Guppy" camera set. As a separating phase for the iron (III) chloride and pyrrole monomer, a solution of propylene carbonate (PC) was used. In this microfluidic system 2 microchanels are for oil, 2 for pyrrole and PC solution and 1 for oxidant iron (III) chloride solution with PC. The medium chosen for experiment is fluorinated oil with surfactant. Experimental inlet velocities: oil and surfactant D2000 240µl/h, iron (III) chloride and PC solution125µl/h, pyrrole and PC solution 75µl/h.

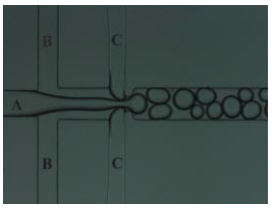

Fig. 2. Microfluidic system used for microemulsion polymerization: A – $FeCl_3$ and PC, B – oil and D2000, C – pyrrole and PC

Results indicate that by selection of a particular polymerization process chemical or biocatalytic, hollow and/or oval shaped BPPy and MPPy microspheres are formed. Polypyrrole microspheres are lighter in weight and have a bigger surface area then PPy layers so they could be used in electomagnetic wave absorber improvement.

[1] Bocchi, V., G. Gardini, and S. Rapi, *Highly electroconductive polypyrrole composites.* Journal of materials science letters, 1987. **6**(11): p. 1283-1284.
[2] Wang, N., et al., *Conductive polypyrrole/viscose fiber composites.* Carbohydrate polymers, 2015. **127**: p. 332-339.
[3] Saville, P., *Polypyrrole, Formation and Use*. 2005, DTIC Document.
[4] Mitchell, M.C., et al., *Microchip-based synthesis and total analysis systems (µSYNTAS): chemical microprocessing for generation and analysis of compound libraries.* Journal of the Chemical Society, Perkin Transactions 1, 2001(5): p. 514-518.
[5] Stirke, A., et al., *Synthesis of polypyrrole microspheres by Streptomyces spp.* Polymer, 2016. **84**: p. 99-106.

ELECTRODEPOSITION AND STUDY OF MOLYBDENUM SULFIDE FILMS

Ramūnas Levinas[1], Natalija Tsyntsaru[2], Henrikas Cesiulis[1]

[1] Vilnius University, Naugarduko 24, Vilnius, Lithuania
[2] Institute of Applied Physics of ASM, 5 Academy str., Chisinau, Moldova
ramunas.levinas@chf.vu.lt

The renewable energy field constantly looks for improved catalysts for hydrogen evolution and solar energy conversion reactions. Various semiconductor materials can be applied, but a common issue is a large band gap energy. This usually limits photocatalytic activity of materials in the visible light range. However, some transition metal sulfides exhibit lower band gaps, and are being explored as potential photocatalysts. One of them is MoS_2 having a band gap of ~1.7eV.

Although other methods exist, this study was aimed at obtaining molybdenum sulfide films by electrodeposition technique. This methodology has been proposed in other studies [1,2] as well, there precursor tetrathiomolybdate / MoS_4^{2-} is used as a source of both sulfide and molybdenum ions in the deposition bath. We chose copper as the substrate and performed cyclic voltammetry in a 40 mM MoS_4^{2-} solution to film deposition. A control test performed in 0.1M Na_2SO_4 solution (see Fig. 1. solid line) showed anodic and cathodic peaks, possibly caused by the formation of copper oxides but the current was otherwise stable. Upon addition of tetrathiomolybdate current densities increase significantly. After 25 cycles a broad peak at -0.3 V became apparent, which indicates the anodic deposition of amorphous MoS_3. When the potential is scanned cathodically film dissolves in part and a reductive deposition of amorphous MoS_2 can occur.

Films obtained by potential cycling are nonstoichiometric MoS_x. Potentiostatic cathodic and anodic depositions are also possible, although the use of anodic potentials on copper is hindered by a sharp increase in current at 0.1 V and films exhibit poor adhesion. The obtained molybdenum sulfide films have also been tested for photocatalytic activity.

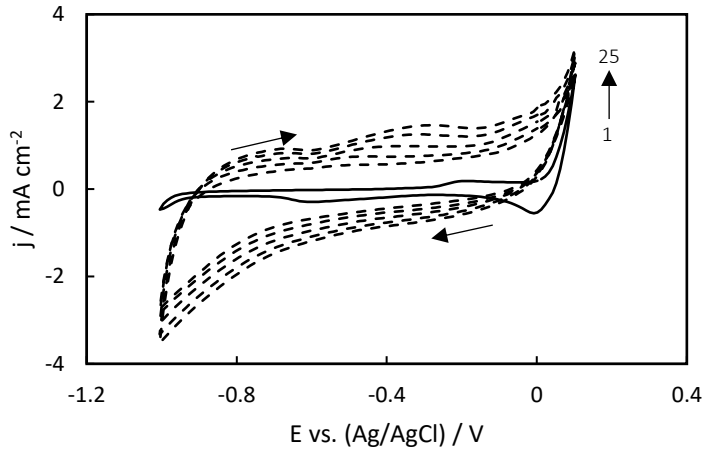

Fig. 1. Cyclic voltammograms of MoS_x deposition on a copper substrate over 25 cycles; c(MoS_4^{2-}) = 40 mM. 0.1M Na_2SO_4 as the supporting electrolyte. Scan rate – 50 mV s^{-1}. Solid line – no MoS_4^{2-}.

[1] H. Vrubel, X. Hu, Growth and Activation of an Amorphous Molybdenum Sulfide Hydrogen Evolving Catalyst, ACS Catal. **3**, 2002-2011, (2013).
[2] S. K. Gosh, C. Srivastva, S. Nath, J. P. Celis, Simple Formation of Nanostructured Molybdenum Disulfide Thin Films by Electrodeposition, Int. J. Electrochem, **2013,**, Article ID 138419.

Ln-CONTAINING HETEROPOLY TUNGSTATES WITH PEACOCK–WEAKLEY ANION: SYNTHESIS AND CRYSTAL STRUCTURE OF ISOSTRUCTURAL SALTS $Na_9[Ln(W_5O_{18})_2]\cdot 35H_2O$ (Ln=Gd, Er)

Oleksandra Yu. Mariichak[1], Vyacheslav N. Baumer[2], Georgii M. Rozantsev[3], Serhii V. Radio[3]

[1] Unit for Research, Research Group in Inorganic Chemistry, Vasyl' Stus Donetsk National University (in exile in Vinnytsia), UKRAINE, Vinnytsia, vul. 600-richchia 21

[2] State Scientific Institution "Institute for Single Crystals" of NAS of Ukraine, Kharkiv, UKRAINE

[3] Faculty of Chemistry, Department of Inorganic Chemistry and Analytical Chemistry, Vasyl' Stus Donetsk National University (in exile in Vinnytsia), UKRAINE, Vinnytsia, vul. 600-richchia 21-215

o.marijchak@donnu.edu.ua

The conditions for the synthesis of a new isostructural heteropoly tungstates $Na_9[Ln(W_5O_{18})_2]\cdot 35H_2O$ (Ln = Gd, Er) from the aqueous solution, acidified to $Z=\nu(H^+)/\nu(WO_4^{2-})=0.80$, were determined. Single Crystal X-ray Diffraction Analysis, and FTIR spectroscopy were used to show that the anion within the synthesized salts has a Peacock-Weakley structure.

Nature of stretch and deformation vibrations in the tungsten-oxygen framework within FTIR spectra of air-dry samples of salts indicates to the presence of Peacock-Weakley heteropoly anion of 10th row in them [1]. In this anion, two lacunar tetradentate pentatungstate-anions $W_5O_{18}^{6-}$ are coordinated to Ln-heteroatom, thus forming a coordination polyhedron in the shape of a square antiprism.

Fig. 1 depicts the atomic numbering scheme and the structure of the main building block in $Na_9[Ln(W_5O_{18})_2]\cdot 35H_2O$ (Ln = Gd, Er). The W—O bond lengths in WO_6 octahedra are in a range of 1.610–2.371Å, bond angles are significantly distorted. The variety of Ln—O bond lengths in LnO_8 square antiprism is much smaller (2.334–2.420 Å). In general, geometry of the anion has close agreement with the literature data [2]. Despite the fact that the structures of $Na_9[Ln(W_5O_{18})_2]\cdot 35H_2O$ (Ln = Gd, Er) are similar to the reported structure of $Na_8H[Gd(W_5O_{18})_2]\cdot 30H_2O$ [2], the structure of the cation sublattice considerably differs from the data in [2].

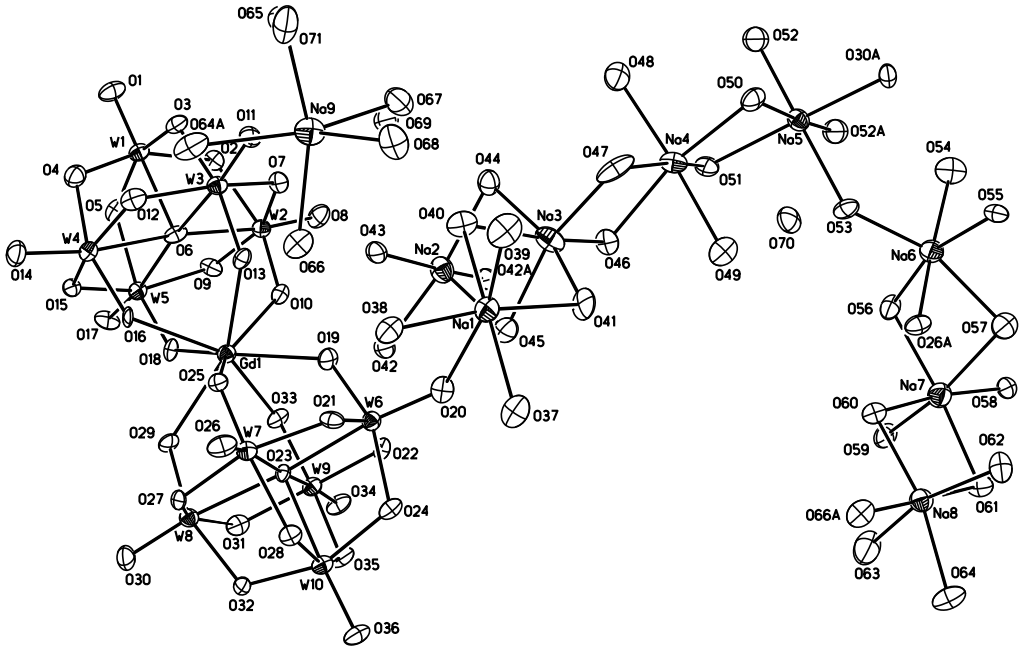

Fig. 1. Structure of the main building block and thermal ellipsoids (50 % probability level) in $Na_9[Ln(W_5O_{18})_2]\cdot 35H_2O$ (Ln = Gd, Er) and the scheme of atomic numbering in the structure. The equivalent atoms used to complete the polyhedra, are denoted by the letters A.

It worth mentioning that this is the second case when the synthesis of isostructural heteropoly compounds with Peacock-Weakley anion is described in the literature.

Acknowledgements. The study was carried out within the Fundamental Research Programme funded by the MES of Ukraine (Project No. 0116U002521).

[1] R. Shiozaki, I. Inagaki, A. Nishino et al., Spectroscopic investigation of a series of sodium lanthanide decatungstates, $Na_7H_2Ln^{(III)}(W_5O_{18})_2\cdot nH_2O$ (Ln: La–Yb): the contribution of $4f^n$ electrons to bonding interaction among $Ln^{(III)}$ and polyoxotungstates, J. Alloys Compounds **234**, 193-198 (1996).

[2] T. Yamase, T. Ozeki, M. Tosaka, Octasodium hydrogen decatungstogadolinate triacontahydrate. Acta Cryst. **C50**, 1849-1852 (1994).

OXIDATIVE DESTRUCTION OF METHYL VIOLET AND METHYLENE BLUE DYES BY FENTON REACTION

Lyubov Makarova[1], Yuliya Sergienko[1], Yuliya Ivanova[1], Svitlana Zhiltsova[1], Iosyp Opeida[1,2]

[1] Department of Biochemistry and Physical Chemistry, Faculty of Chemistry, Vasyl' Stus Donetsk National University, Ukraine

[2] Department of Physical Chemistry of Fossil Fuels, L. M. Litvinenko Institute of Physical Organic and Coal Chemistry, National Academy of Sciences of Ukraine, Ukraine

makarova.l@donnu.edu.ua

Fenton reaction is widely used to generate hydroxyl radicals in water media: $Fe^{2+} + H_2O_2 \rightarrow Fe^{3+} + OH^{\cdot} + OH^{-}$ [1, 2]. One of the ways to use this system is oxidative destruction of different organic compounds, including ecotoxicants and water pollutants. Dyes are common models for the investigation and development of methods for water purification [3, 4]. The goal of the present paper was investigation of oxidative destruction of methyl violet and methylene blue by Fenton reagent under different conditions.

Spectrophotometry was used to investigate the kinetics of dyes decoloration by Fe^{2+}/H_2O_2 system. All the experiments were carried out at ambient temperature. The parameters that have been varied were concentrations of each component – dye, hydrogen peroxide, Fe^{2+}, and pH value.

The kinetic curves demonstrate that the oxidation process includes two main stages – faster (up to 10 min) and 5–12 times slower. The duration of each stage and the reaction rate in it strongly depend on the concentrations of components in the reaction media. It was shown that the rate of degradation is dependent non-linearly on the initial concentration of dye, hydrogen peroxide, and Fe^{2+}, as well as pH value. The optimal conditions were determined to provide conversion of the dye 90 % after 20–30 minutes of reaction at pH 2.2.

The additional experiments also showed that some compounds of natural origin (e.g. amino acids, carbohydrates) could be used to effectively control the reaction rate. The higher the content of the additives the higher the dye conversion. It was shown that the most catalytic effect in Fenton reaction in our case demonstrates fructose.

[1] S. Goldstein, D. Meyerstein, D. Czapski, The Fenton reagents, Free Radical Biol. Med. **15**, 435-445 (1993).

[2] E. Chamarro, A. Marco, S. Esplugas, Use of Fenton reagent to improve organic chemical biodegradability, Water Research, **35**, 1047-1051 (2001).

[3] K. Dutta, S. Mukhopadhyay, S. Bhattacharjee, Chemical oxidation of methylene blue using a Fenton-like reaction, Journal of Hazardous Materials, **84**, 57-71 (2001).

[4] S. Hashemian, M. Tabatabaee, M. Gafari, Fenton Oxidation of Methyl Violet in Aqueous Solution, Journal of Chemistry, **2013**, Article ID 509097, 6 pages, (2013).

Ce-CONTAINING POLYOXOTUNGSTATES: SYNTHESIS, FTIR SPECTROSCOPY, AND SURFACE MICROMORPHOLOGY

Oleksandra Yu. Mariichak[1,2], Tetiana O. Arzamastseva[1], Illia V. Kapitanov[2,3], Yevgen Karpichev[2,3], Georgii M. Rozantsev[1,4], Serhii V. Radio[1,4]

[1] Unit for Research, Research Group in Inorganic Chemistry, Vasyl' Stus Donetsk National University (in exile in Vinnytsia), vul. 600-richchia 21, Vinnytsia, UKRAINE
[2] Department of Chemistry, Chair of Green Chemistry, Tallinn University of Technology, Tallinn, ESTONIA
[3] L.M. Litvinenko Institute of Physical Organic & Coal Chemistry NAS of Ukraine, Kyiv, UKRAINE
[4] Faculty of Chemistry, Department of Inorganic Chemistry and Analytical Chemistry, Vasyl' Stus Donetsk National University (in exile in Vinnytsia), vul. 600-richchia 21-215, Vinnytsia, UKRAINE
o.marijchak@donnu.edu.ua

Polyoxometalates are a class of metal oxide clusters of early transition metals (V, Mo, W, Nb, etc.), and they show strong Brönsted acidity, fast reversible multi-electron redox transformations under mild conditions, and adjustable acid-base and redox properties over a wide range. Therefore, the use of POMs as acidic and redox-bifunctional catalysts in homogeneous and heterogeneous systems is their most popular and important application area. Thus, cerium decatungstate $[Ce^{IV}(W_5O_{18})_2]^{8-}$ modified with cetylpyridinium cations was found to be an active and selective catalyst for the oxidation of secondary alcohols to ketones with hydrogen peroxide [1].

In present work we have studied the interactions of cerium (III) chloride with aqueous solutions of Na_2WO_4 at various acidity $Z = \nu(H^+)/\nu(WO_4^{2-}) = 0 – 1.50$. As known [2], during them isopoly tungstate anions of different composition $[H_{m-2k}W_nO_{4n-k}]^{(2n-m)-}$ are formed.

Presence of Ce(III) ions and other lanthanide ions can lead to the formation of heteropoly anions [3-4]:

$Ce^{3+} + 10\ WO_4^{2-} + 8\ H^+ \leftrightarrows [Ce(W_5O_{18})_2]^{9-} + 4\ H_2O$, (Z = 0.80);

$2\ Ce^{3+} + 22\ WO_4^{2-} + 30\ H^+ \leftrightarrows [Ce_2(H_2O)_{10}W_{22}O_{72}(OH)_2]^{8-} + 4\ H_2O$, (Z = 1.36).

From aqua-acetone media (v/v = 50/50) at Z = 0.80 the sodium heteropoly decatungstocerate (III) $Na_9[Ce(W_5O_{18})_2]\cdot 28H_2O$ with Peacock-Weakley anion structure was synthesized. From acidified up to Z = 0.80 aqueous solution of sodium tungstate without acetone adding the acid sodium heteropoly decatungstocerate (IV) $Na_6H_2[Ce(W_5O_{18})_2]\cdot 30H_2O$ with Peacock-Weakley anion structure was synthesized. Salts of these heteropoly compounds have different micromorphology (Fig. 1) and different positions of vibration maxima in the FTIR spectra (FTIR data for $Na_9[Ce(W_5O_{18})_2]\cdot 28H_2O$, cm^{-1}: 416, 485, 542, 575, 711, 787, 845, 955; FTIR data for $Na_6H_2[Ce^{IV}(W_5O_{18})_2]\cdot 30H_2O$, cm^{-1}: 436, 491, 553, 583, 677, 783, 828, 941).

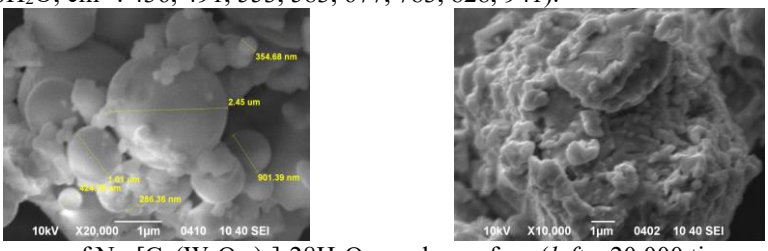

Fig. 1. SEM images of $Na_9[Ce(W_5O_{18})_2]\cdot 28H_2O$ powder surface (*left* – 20,000 times magnification), and $Na_6H_2[Ce(W_5O_{18})_2]\cdot 30H_2O$ (*right* – 10,000 times magnification)

From the solution with Z = 1.00 the cerium heptatungstate $Ce_2W_7O_{24}\cdot 20H_2O$ was synthesized, and by XRD it was shown that it thermal decomposition accompanied with crystallization of $Ce_4W_9O_{33}$ and WO_3 phases.

By the chemical analysis and FTIR spectroscopy it was shown that the $Ce_5[HW_7O_{24}]_3\cdot 56H_2O$ was synthesized from solution with Z = 1.17, and by XRD method it was shown that calcination of $Ce_5[HW_7O_{24}]_3\cdot 56H_2O$ at 500^0C occurs with only WO_3 phase crystallization, and calcination at 700^0C accompanied with crystallization of $Ce_4W_9O_{33}$ phase. By the chemical analysis and FTIR spectroscopy it was shown that the cerium paratungstates B – $Ce_{10}[W_{12}O_{40}(OH)_2]_3\cdot 94H_2O$ and $Na_{10}Ce_{20}[W_{12}O_{40}(OH)_2]_7\cdot 180H_2O$ were synthesized from equilibria solutions with Z = 1.17 and 1.29, respectively, and $Na_2Ce_2[Ce_2(H_2O)_{10}W_{22}O_{72}(OH)_2]\cdot 35H_2O$ with lacunar metatungstate-anions as ligands was synthesized from the solution at Z = 1.364.

Acknowledgements. The study was carried out within the Fundamental Research Programme funded by the MES of Ukraine (Project No. 0116U002521). OM acknowledges funding from Dora Plus Visiting Fellowship and EU 7th Framework Programme for research, technological development and demonstration activities under grant agreement No. 621364 (TUTIC-Green).

[1] R. Shiozaki, H. Kominami, Y. Kera, H_2O_2 Oxidation by Ce(IV) Contained Weakley-Type Heteropolyoxometalate for Various Alcohols. Synth. Commun. **26**, 1663-1668 (1996).
[2] G.M. Rozantsev, S.V. Radio, N.I. Gumerova, Strontium Isopoly Tungstates: Synthesis and Properties. Pol. J. Chem. **82**, 2067-2080 (2008).
[3] R.D. Peacock, T.J.R. Weakley, Heteropolytungstate complexes of the lanthanide elements. Part I. Preparation and reactions. J. Chem. Soc. Sect. A. 1836-1839 (1971).
[4] A.H. Ismail, M.H. Dickman, U. Kortz, 22-Isopolytungstate Fragment $[H_2W_{22}O_{74}]^{14-}$ Coordinated to Lanthanide Ions. Inorg. Chem. **48,** 1559-1565 (2009).

SYNTHESIS AND COMPLEXING ACTIVITY OF NEW POLYMERIZABLE N-HETEROCYCLIC CARBENE PRECURSORS

Iwona Misztalewska-Turkowicz, Agnieszka Z. Wilczewska

Institute of Chemistry, Department of Biology and Chemistry, University of Bialystok, Poland
i.misztalewska@uwb.edu.pl

The N-heterocyclic carbenes (NHCs) are widely used in organocatalysis[1] also as excellent ligands in transition-metal complexes.[2] A large variety of NHC-metal complexes is used in organometallic catalysis for example NHC-Pd complexes in C-C coupling reactions[3] or NHC-Cu complexes in "click" type reactions[4]. NHC ligands successfully replaced phosphines in this area because of their lower toxicity and better electron-donating properties.[5] Some of the NHCs are crystalline species, stable for several weeks at the inert atmosphere.[6] The five-membered NHC are mainly formed by deprotonation of azolium salts, e.g., imidazolium or imidazolinium salts.[7]

RAFT/MADIX (Reversible Addition-Fragmentation Chain Transfer and Macromolecular Design *via* the Interchange of Xanthates) polymerization is the type of a living (controlled) radical polymerization which utilizes dithiocarbonates (xanthates) to mediate the polymerization *via* a reversible chain-transfer process. This polymerization technique allows control of the chain growth and the polydispersity.[8] Also dithiocarbonates show a great tolerance towards most of the functional groups.[9] In our research we used the covalently-bonded, to the surface of magnetic nanoparticles, chain transfer agent for mediate the polymerization.

In this presentation synthesis of two new imidazolium salts - NHC precursors will be presented. These imidazolium salts were prepared in terms of obtaining polymerizable NHC-metal complexes (ruthenium and palladium complexes). Furthermore these salts and also their complexes will be polymerized by RAFT/MADIX polymerization technique on magnetic core to prepare magnetically-separable catalytically-active complexes.

The project was financially supported by National Science Centre, Poland, grant no. 2016/21/N/ST5/01316.
Analyses were performed in Centre of Syntesis and Analisys BioNanoTechno of University of Bialystok.
The equipment in the Centre of Synthesis and Analysis BioNanoTechno of University of Bialystok was funded by EU, as a part of the Operational Program Development of Eastern Poland 2007-2013, project: POPW.01.03.00-20-034/09-00 and POPW.01.03.00-20-004/11.

[1] Bugaut, X. and Glorius, F. Organocatalytic umpolung: N-heterocyclic carbenes and beyond. *Chem. Soc. Rev.* **41,** 3511–3522 (2012).
[2] Díez-González, S., Marion, N., Nolan, S. P. N-Heterocyclic Carbenes in Late Transition Metal Catalysis. *Chem. Rev.* **109,** 3612–3676 (2009).
[3] Wilczewska, A. Z., Misztalewska, I. Direct Synthesis of Imidazolinium Salt on Magnetic Nanoparticles and Its Palladium Complex Application in the Heck Reaction. *Organometallics* **33,** 5203–5208 (2014).
[4] Díez-González, S., Correa, A., Cavallo, L., Nolan, S. P. (NHC)Copper(I)-Catalyzed [3+2] Cycloaddition of Azides and Mono- or Disubstituted Alkynes. *Chem. - Eur. J.* **12,** 7558–7564 (2006).
[5] Crudden, C. M., Allen, D. P. Stability and reactivity of N-heterocyclic carbene complexes. *Coord. Chem. Rev.* **248,** 2247–2273 (2004).
[6] Arduengo III, A. J., Harlow, R. L., Kline, M. A stable crystalline carbene. *J. Am. Chem. Soc.* **113,** 361–363 (1991).
[7] Dröge, T., Glorius, F. The Measure of All Rings-N-Heterocyclic Carbenes. *Angew. Chem. Int. Ed.* **49,** 6940–6952 (2010).
[8] Perrier, S., Takolpuckdee, P. Macromolecular design via reversible addition-fragmentation chain transfer (RAFT)/xanthates (MADIX) polymerization. *J. Polym. Sci. Part Polym. Chem.* **43,** 5347–5393 (2005).
[9] Destarac, M. Controlled Radical Polymerization: Industrial Stakes, Obstacles and Achievements. *Macromol. React. Eng.* **4,** 165–179 (2010).

SYNTHESIS AND INVESTIGATION OF PHENYL CARBAZOLE DERIVATIVES CONTAINING INDOLE UNITS

Karolis Norvaisa, Dalius Gudeika

Department of Polymer Chemistry and Technology, Kaunas University of Technology, Radvilenu pl. 19, LT-50254 Kaunas, Lithuania
mentinas@gmail.com

Compounds with electroactive moieties are widely studied due to their good processability and applications in various optoelectronic devices including organic light emitting diodes [1,2]. Their thin films on the different substrates can be fabricated by using simple techniques, i.e. casting or spin-coating from solutions. Such advantages are important in the fabrication of low cost, large area devices. In this work the synthesis and properties of carbazole and indole derivatives **1-3** will be presented (Fig 1).

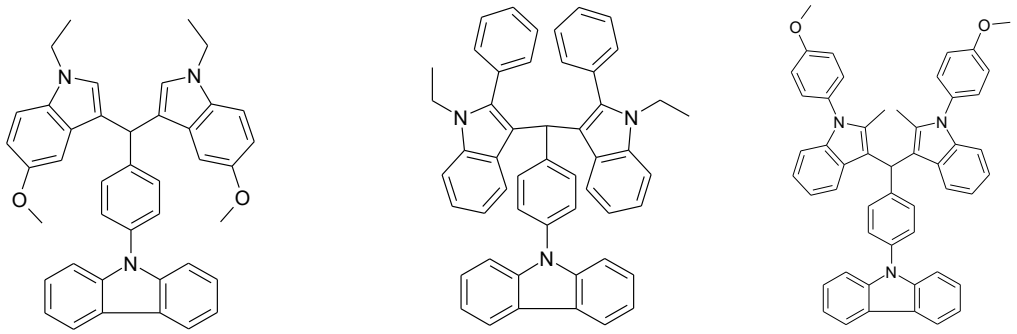

1 **2** **3**

Fig. 1. Structures of **1-3**.

All the compounds demonstrated high thermal stability: their 5% weight loss temperatures were found to be higher than 390 °C. The glass-transitions were observed in the range of 89-130 °C. The ionization potentials of the derivatives were estimated by cyclic voltammetry. They were found to be comparable and ranged from 5.59-5.66 eV. Photophysical properties of the synthesized compounds were studied.

---

[1] Forrest, S. R.; Thompson, M. E. Eds. Organic Electronics and Optoelectronics. *Chem. Rev.* **2007**, *107*, 923−1386.
[2] Shirota, Y.; Kageyama, H. Charge Carrier Transporting Molecular Materials and Their Applications in Devices. *Chem. Rev.* **2007**, *107*, 953−1010.

HYDROGEN-BONDED SUPRAMOLECULAR NANOTUBES FROM SMALL BUILDING BLOCKS

Edvinas Orentas*, Algirdas Neniškis, Dovilė Anderson, Tomas Javorskis

Department of Organic Chemistry, Vilnius University
edvinas.orentas@chf.vu.lt

The tubular nanoscale self-assembled systems represent one of the most versatile constructs in the field of supramolecular chemistry.[1] The wall of the tube separates the bulk environment into two distinct regions- interior and exterior, having different chemical and physical properties. Moreover, the open-ended topology of these aggregates allows the facile entry of different molecular entities and therefore, they are very attractive for the application in transport, flow-through catalysis, separation and detection. The molecular scaffold of the tube may also act as a protective shell to isolate and stabilize otherwise very sensitive or highly aggregative molecules, such as conjugated polymeric nanowires. In another approach, the merging of organic and inorganic chemistries is possible when organic molecular tubes are used as a growth template to construct coaxial, inorganic shell coated tubular architectures. For the successful realization of all the above envisioned applications, a reliable and flexible access to synthetically modifiable tubular structures is necessary.

Herein we present two conceptually new strategies to achieve tubular polymerization using the hydrogen-bonding building blocks, the scaffold of which is composed of only nine carbon atoms. The careful design of hydrogen-bonding units and their spatial arrangement allowed the construction of both, discrete and polymeric tubular assemblies possessing large cavity.[2,3]

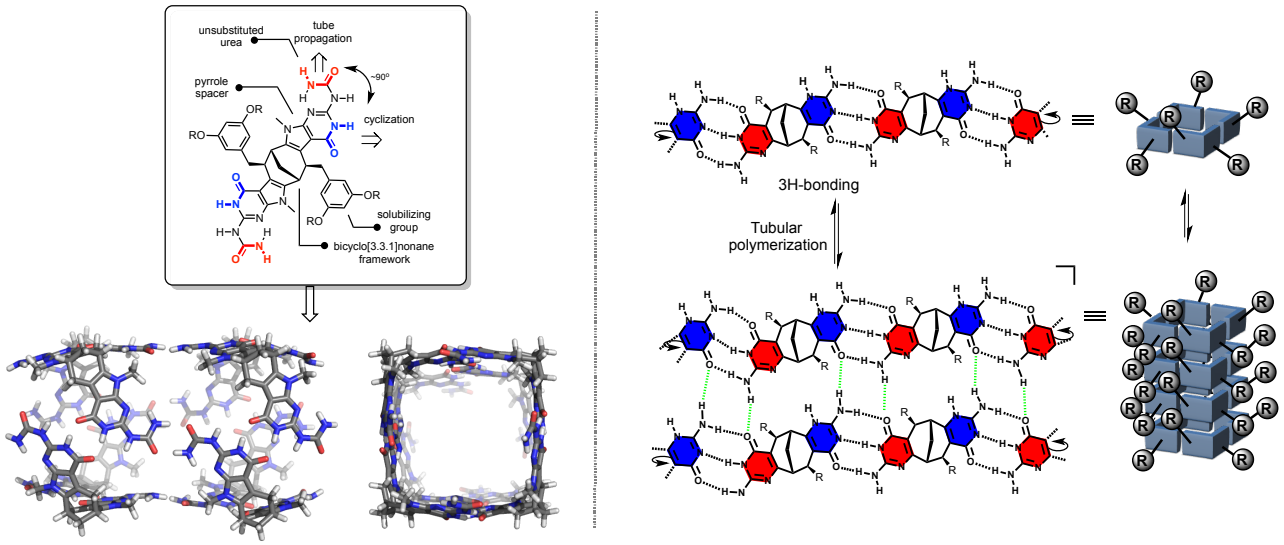

Fig. 1. Supramolecular hydrogen-bonding monomers and their aggregation into tubular polymers.

[1] M. A. B. Block, C. Kaiser, A. Khan, S. Hecht, *Top Curr Chem* **2005**, *245*, 89.
[2] D. Račkauskaitė, R. Gegevičius, Y. Matsuo, K. Wärnmark, E. Orentas, *Angew, Chem. Int. Ed.* **2016**, *55*, 208.
[3] S. Stončius, E. Orentas, E. Butkus, L. Öhrström, O. F. Wendt, K. Wärnmark, *J. Am. Chem. Soc.* **2006**, *128*, 8272.

INVESTIGATION OF STRUCTURAL PROPERTIES OF Eu^{3+}-DOPED $Y_{3-x}Sm_xAl_3O_{12}$ GARNETS

Lina Pavasarytė[1*], Vytautas Klimavičius[2], Vytautas Balevičius[2], Aivaras Kareiva[1]

[1]Faculty of Chemistry and Geosciences, Insitute of Chemistry, Vilnius University, Naugardukas str. 24, LT – 03225, Vilnius, Lithuania

[2]Department of General Physics and Spectroscopy, Vilnius University, Saulėtekio al. 3, LT – 10222 Vilnius, Lithuania

lina.pavasaryte@gmail.com

$Y_3Al_5O_{12}$ is commonly called yttrium aluminium garnet (YAG) and adopts the cubic garnet structure. Rare earth element doped YAG has been thoroughly investigated for application in various fields, such as lasers, scintillators, cathode ray tubes (CRT), field-emission displays (FEDs), plasma display panels (PDPs,) and optical windows, due to its attractive optical properties, outstanding chemical stability, low creep rate and high thermal resistance[1,2,3,4]. Luminescent materials based on YAG are stable under conditions of high irradiation with an electron beam[5,6].

Luminescent materials containing europium (Eu^{3+}) and samarium (Sm^{3+}) ions have attracted a special attention during the past decades for their superior optical properties such as narrow emission bands for high colour purity, high quantum efficiency, large stokes shifts and long life time. These materials have important applications in the display field due to their excellent fluorescence properties in the visible region[7].

In this work YAG samples doped with different amount of Sm^{3+} and Eu^{3+} were prepared by sol-gel method. To our best knowledge, YAG:Sm,Eu garnets with various doping levels of europium have not been synthesized yet. Therefore, the main aim of this study was to fabricate these garnets and investigate their structural properties.

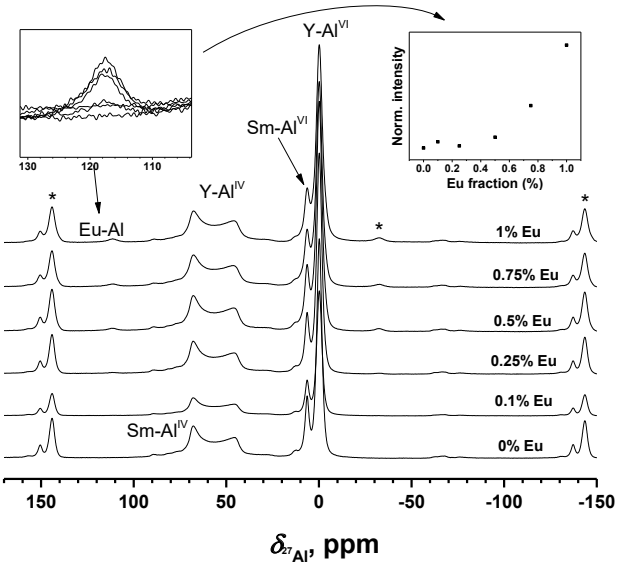

Fig. 1. ^{27}Al MAS NMR spectra of the $Y_{2.9}Sm_{0.1}Al_5O_{12}$:Eu samples.

Photoluminescent properties of YAG:Sm,Eu materials are largely determined by the local environments of Eu^{3+} and Sm^{3+} ions. In non-doped $Y_3Al_5O_{12}$, yttrium cations reside in the dodecahedral interstices formed by the network of corner-sharing AlO_4 and AlO_6 polyhedra[4,8,9]. Since it is expected that the Eu^{3+} and Sm^{3+} ions will occupy the same dodecahedral interstices, the local environment of these cations could be inspected by solid-state NMR spectroscopy, which uses NMR-active ^{27}Al nuclei as local probes. Peaks of Al^{IV} and Al^{VI} with samarium and yttrium in their vicinities increases increasing doping element. A simple calculation of expected aluminium intensities based on probabilities for a normal distribution shows a very nice agreement with the experimentally detected intensities and thus reveals that the Sm^{3+} ions are randomly dispersed throughout the crystal lattice of YAG:Sm,Eu (Figure 1). The linear relation between the Al(1Eu) line intensity and the Eu^{3+} indicates that, as for samarium, the spatial distribution of europium ions in these samples is also homogeneous.

[1] W. Q. Chen, D. S. Jo, Y. H. Song, T. Masaki and D. H. Yoon, *J. Lumin.*, 2014, **147**, 304–309.
[2] Y. Pan, M. Wu and Q. Su, *J. Phys. Chem. Solids*, 2004, **65**, 845–850.
[3] M. S. Kurrey, A. Tiwari, M. S. K. Khokhar, R. S. Kher and S. J. Dhoble, *J. Lumin.*, 2015, **164**, 94–98.
[4] A. Kareiva, *Medziagotyra*, 2011, **17**, 428–437.
[5] H. M. Lee, C. C. Cheng and C. Y. Huang, *Mater. Res. Bull.*, 2009, **44**, 1081–1085.
[6] X. Li, H. Liu, J. Wang, H. Cui, F. Han and R. I. Boughton, *J. Am. Ceram. Soc.*, 2004, **87**, 2288–2290.
[7] K. N. Kumar, L. Vijayalakshmi and Y. C. Ratnakaram, *Opt. Mater. (Amst).*, 2015, **45**, 148–155.
[8] S. Alahrach, J. Lambert, M. R. Suchomel, D. D. S. Meneses, G. Matzen, D. Massiot and V. Emmanuel, 2011, 20499–20506.
[9] R. S. Azis, D. Holland, M. E. Smith, A. Howes, M. Hashim, a Zakaria, N. M. Saiden and M. K. Ikhwan, 2013, **49**, 74–80.

RECYCLING OF RUBBER BY SUPPRESSION OF MOLECULAR SELF-HEALING PROCESS

Karolis Petrauskas, Svajus Asadauskas

Tribology lab., Institute of Chemistry of Center for Physical Sciences and Technology, Vilnius, Lithuania
Karolis.Petrauskas@ftmc.lt

Turning waste rubber into a material, that could be reused has always proved to be a challenge. Reducing the particle size of end-of-life rubber products proved to be a promising path. Rubber that is reduced to crumb could be used as a filler while very fine rubber powder could even be incorporated into new rubber articles to a certain extent [1]. One of the methods of rubber powder production is cryogenic grinding, unfortunately due to the need of liquid nitrogen the process is not very cost efficient. Another way of rubber powder production is mechano-chemical treatment of rubber [2].

In our experiments we subjected truck tire buffings to mechanical shear in a two-roll mill (XSK-360, *Wuxi Double Elephant Rubber and Plastic Machinery Co. Ltd.*, China) at certain processing conditions: without any additives (Sample 1); with the addition of 3% (w/w) of water (Sample 2); 3% (w/w) of water and 0.4 % (w/w) of NaCl (Sample 3); 3% (w/w) of water and 1 % (w/w) of acetamide (Sample 4); 3% (w/w) of water, 1% (w/w) of acetamide and 0.4% (w/w) of NaCl. All tribological conditions were kept constant during the experiments, processing temperature was ambient. After 16 processing cycles rubber samples were visually inspected and, if possible, the granulometric composition of processed rubber was determined (Figure 1A).

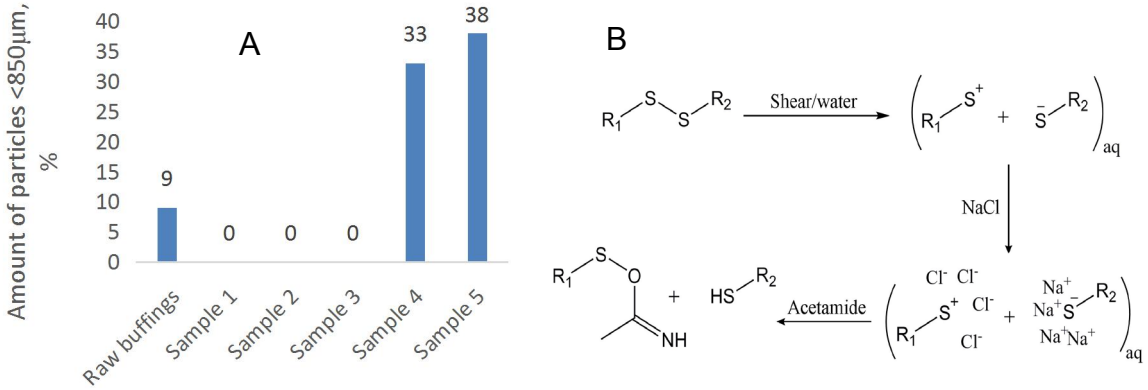

Fig. 1. Granulometric composition of processed rubber (A); proposed mechanism of ionic self-healing suppression of rubber (B)

Rubber, due to it's structure, is a self-healing material at molecular level. When subjected to shear forces, weak cross-link bonds in the rubber matrix break and are able to recombine or react with adjacent polymeric chains, thus reforming a broken network. This could be illustrated by samples 1, 2 and 3 - rubber buffings, after being subjected to mechanical shear, started sticking together and forming a sponge like structure. It proved that neither water, nor NaCl alone could be used in mechano-chemical production of rubber powder. An interesting outcome was reached when acetamide was used as a chemical aid in mechno-chemical processing of rubber (sample 4) - the rubber particles not only did not stick together but were considerably reduced in size. This effect was increased even further when NaCl together with acetamide was added to the processing mixture. The action of acetamide and NaCl could be explained by suppression of rubber's self healing process: when rubber's cross-links break, they can break into charged species, instead of radicals as in thermal reclamation of rubber. These charged species could then react with acetamide, instead of polymeric chains, and thus be deactivated. The addition of NaCl helps in providing a shielding barrier between active charged species. Proposed mechanism is given in figure 1B.

When rubber's self healing process is suppressed by chemical aids, mechanical energy could be efficiently utilized in production of fine rubber powder by breaking down the rubber network. Another important conclusion, that could be drawn from the experiment, is that when rubber is subjected to moderate mechanical stress and polar environment [3], heterolytic, rather than homolytic, cleavage of bonds could be the dominant reaction.

Authors would like to thank Arturas Jukna and Tadas Ikanevicius from JSC "Gumos technologijos" for providing rubber samples and carrying out mechano-chemical experiments.

[1] R. Mujal-Rosas et al., Study on dielectric, thermal and mechanical properties of the ethylene vinyl acetate reinforced with ground tire rubber, Journal of Reinforced Plastics and Composites **30**, 581-592 (2011).
[2] S. Asadauskas, A. Jukna, Devulcanizing agent for production of reclaim rubber powder, patent WO2014062043A1 (2014).
[3] D. Aktah, I. Frank, Breaking Bonds by Mechanical Stress: When do Electrons Decide for the Other Side?, Journal or American Chemical Society **124**, 3402-3406 (2002).

SCANNING ELECTROCHEMICAL MICROSCOPY COMBINED WITH FAST FOURIER TRANSFORM IMPEDANCE SPECTROMETER FOR LOCAL ELECTROCHEMICAL IMPEDANCE MEASUREMENTS

Jurate Jolanta Petroniene[1], Inga Morkvenaite-Vilkonciene[2], Aušra Valiūnienė[1], Almira Ramanaviciene[3], Arunas Ramanavicius[1,4]

[1] Vilnius University, Faculty of Chemistry, Department of Physical Chemistry, Vilnius, Lithuania
[2] Vilnius Gediminas Technical University, Department of Mechatronics and Robotics, Vilnius, Lithuania
[3] Vilnius University, Faculty of Chemistry, Department of Analytical and Environmental Chemistry, Vilnius, Lithuania
[4] State Research Institute Centre for Physical Sciences and Technology, Laboratory of Bio-nanotechnology, Vilnius, Lithuania
arunas.ramanavicius@chf.vu.lt jurate.petroniene@chf.vu.lt

EIS is a powerful, non-destructive and informative technique, which has been successfully applied for the characterization of biosensor surfaces [1]. However, conventional EIS based techniques represent only averaged response of the entire electrochemical system. In order to get more advanced mapping of electrochemical system scanning electrochemical microscopy (SECM) merged with EIS (SEIM) eventually could be applied. In SEIM based technique localized impedance measurements could be performed in the range of frequencies when the surface of interest is scanned by ultramicroelectrode (UME). The result of SEIM could be visualized by mapping one of calculated parameters, e. g. charge transfer resistance or double layer capacitance as a function of 3D coordinates [2,3]. Fundamental aspects of SEIM were investigated comparing UME responses while it was approaching to different surfaces e.g.: (i) insulator surface, (ii) conducting surface not-connected to electric circuit, and (iii) conducting surface, which was connected to electric circuit and was held at constant potential [4]. By this research it has been shown that the admittance of the UME located at relatively small distance from the surface of interest mostly depends on the distance between UME and the surface and on interfacial properties of the surface. Therefore the SEIM based imaging is informative even without any redox mediators. Using SECM, combined with Fast fourier transform (FFT) impedance spectrometer, the impedance spectra could be registered at very high speed. In the frequency range between 1.5 Hz and 25 kHz the measurement time of the electrochemical impedance spectrum continues 1.3 s. This combined technique allows to obtain additional information to common measurements of impedance spectra: system-generated noise, and reliability of spectra. Thus, this technique is very informative, reliable, and suitable for measurements of quickly changed processes in the electrochemical cell. Combined with SECM, this technique could be applied for local characterization of not-stabile surfaces.

[1] I. Morkvenaite-Vilkonciene, P. Genys, A. Ramanaviciene, A. Ramanavicius, Scanning electrochemical impedance microscopy for investigation of glucose oxidase catalyzed reaction, Colloids and Surfaces B: Biointerfaces, 126 (2015) 598-602.
[2] A.S. Bandarenka, K. Eckhard, A. Maljusch, W. Schuhmann, Localized Electrochemical Impedance Spectroscopy: Visualization of Spatial Distributions of the Key Parameters Describing Solid/Liquid Interfaces, Anal. Chem., 85 (2013) 2443-2448.
[3] V. Kuznetsov, A. Maljusch, R.M. Souto, A.S. Bandarenka, W. Schuhmann, Characterisation of localised corrosion processes using scanning electrochemical impedance microscopy, Electrochem. Commun., 44 (2014) 38-41.
[4] A.S. Baranski, P.M. Diakowski, Application of AC impedance techniques to Scanning Electrochemical Microscopy, J. Solid State Electrochem., 8 (2004) 683-692.

DRAG FORCE AND QUARTZ RESONATOR ADMITTANCE STUDY OF AQUEOUS SOLUTION LAYER PROPERTIES AT POLYMER COATED ELECTRODE SURFACE

Arūnas Pulmanas, Filipas Ambrulevičius

Department of Applied Chemistry, Vilnius University, LT-01513 Vilnius, Lithuania
arunas.pulmanas@chf.stud.vu.lt; ambrulevicius.filipas@gmail.com

Reduction of water flow friction by applying electric potential to the pipe wall [1] can contribute to the ability to actively manipulate a wall-bounded liquid flow field to effect a desired change. This effect has been tested in two Norwegian hydroelectric power stations [2]. However, the mechanism of this effect is not entirely clear, but it is hypothesized that this phenomenon is related to structural changes of water due to electric field in a double layer region. Piezoelectric resonator measurements show that there is a minimum of interfacial viscosity of aqueous solutions (approximately 1% of the bulk viscosity) at the potential of zero charge of gold electrode [3], [5]. Drag force measurements confirm interfacial viscosity dependence on the potential obtained from piezoelectric resonator measurements but the minimum is lower (approximately 5% of the bulk viscosity) [5].

Computer controlled fluid circulation system for measuring the drag force of the body, whose electrode potential can be controlled independently, was built. By using this technique the potential dependence of the drag force on a polymer (PV butyral) coated sphere was measured in a stream of 0.1 M sodium fluoride (99%, Roth) solution prepared in distilled water. Then the drag coefficients were calculated for the sphere via Eq. (1) and corrected for the wall effect [4].

$$C_D = 8F_D /(\pi\rho v^2 d^2) \quad (1)$$

The LOESS (local smoothing technique with tri-cube weighting and polynomial regression, (sampling proportion and polynomial degree equal to 0.3 and 1, respectively) procedure was used to smooth the drag force data as a function of the potential. Viscosity values were calculated from drag force values by using empirical relationship, which for the Reynolds number range from 1.5×10^3 to 1.2×10^4 are [4]

$$\lg C_D = 2.4751 + 2.5558w - 0.9295w^2 + 0.1049w^3 \ (w = \lg \mathrm{Re_d}) \quad (2)$$

Quartz resonator admittance is $\vec{Y} = \vec{G} + \mathbf{j}\vec{B}$, where G is conductance and B is sucseptance. In present work for the non-damped resonator (resonator in contact with air) or for the fixed electrode potential, when resonator is in contact with solution, frequency spectra of admittance magnitude $Y = \sqrt{G^2 + B^2}$ and phase angle $\Theta = \arctan B/G$ were measured and recalculated into G and B frequency spectra. From these spectra, a set of elements of the electrical equivalent of quartz resonator (Butterworth-Van-Dyke equivalent circuit) was calculated. Then, the obtained sets of circuit element values were used to calculate the changes of electrode mass and liquid properties (viscosity and density product).

In present work, it was observed that change of interfacial viscosity with potential correlates with the dependence of interfacial viscosity and density product on the potential, which was obtained by using quartz sensor. It should be noted and emphasized that the character of interfacial viscosity change with potential of polyvinyl butyral coated electrode is the same as in case of electrode with clean metallic surface.

The results obtained demonstrate that polymer coated surfaces can be used instead of metallic surfaces. That increases the technological potentiality of the effect observed because the disadvantage of metallic surface is their corrosion when they are positively polarized.

The results obtained increase the ability to actively manipulate a wall-bounded liquid flow field to effect a desired change what is of great technological importance: lower wall viscosity ($\partial\eta/\partial x > 0$) will cause the curvature of the velocity profile at the wall to become more negative what increases the lower critical Reynolds number and reduces amplification rates of unstable waves and, hence, increases the flow stability and its resistance to boundary-layer separation.

[1] M. Waskaas, *US Patent No US 6,334,957* (2002).

[2] M. Waskaas , V. Daujotis , K. E. Wolden , R. Raudonis , D. Plausinaitis, *Russ. J. Electrochem*. **44**, 609 (2008).

[3] V. Daujotis, D. Plausinaitis, M. Waskaas, R. Raudonis, *9th Spring Meeting of the ISE*, May 8 to 11, 2011, Turku, Finland.

[4] R. Clift, J.R. Grace, M. E. Weber, *Bubles, drops and particles*, Academic Press, New York, 1978.

[5] D. Plausinaitis, F. Ambrulevicius, V. Daujotis, *Int. J. Electrochem. Sci.* **10**, 7251 – 7260 (2015).

LIGHT DRIVEN SYNTHESIS OF NANOSTRUCTURES

Eva Raudonyte-Svirbutaviciene[1], Alexandra Neagu[2], Cheuk-Wai Tai[2], Arturas Katelnikovas[1]

[1] Faculty of Chemistry and Geosciences, Vilnius University, Naugarduko 24, LT-03225 Vilnius, Lithuania
[2] Department of Materials and Environmental Chemistry Arrhenius Laboratory, Stockholm University, SE-106 91 Stockholm, Sweden
eva.raudonyte@chf.stud.vu.com

Photochemical water compatible synthesis is a promising route to the formation of nanostructures, especially when it is desired that the products obtained would have catalytic/photocatalytic properties. Light assisted synthesis, if compared to standard chemical approaches, provides advantages of a uniform distribution of the reducing agent in the entire solution and rather mild reaction conditions [1]. Organic compounds, employed in colloidal synthesis, would be able to block a number of active sites of catalytic materials due to the strong interaction with the metal surface and to the sterical hinders, thus leading to the loss of catalytic activity to a great extent [2]. The proposed photochemical approach enables to produce semiconductor-silver system without employing organic stabilizers and additives, thus resulting in formation of nanoparticles with "clean", highly reactive metal surface.

In this research, photochemically synthesized CeO_2 nanoparticles (NPs) were applied as photoactive compounds in order to generate formation of silver nanoparticles. Irradiation was performed using 40 W low pressure mercury discharge lamp NIQ 40/18 – 45000024 (Heraeus – Amersil, Germany), emitting a spectrum with lines at 185, 254, 313, 365, 405, 436, 546, and 579 nm. Irradiation of deaerated CeO_2 suspensions in the presence of $AgNO_3$ resulted in the rise of a strong band with the maximum at 393 – 422 nm in the absorption spectra of the solutions, indicating formation of small metallic silver particles.

Faster formation of Ag NPs with the lower amount of silver being required was observed when ethanol was introduced to the reaction solution before the irradiation. Alcohols with α-hydrogens are known to easily form α-hydroxyalkyl radicals upon α-H atom abstraction. Hence, reductive reactions can be strongly enhanced in deaerated ethanol containing solutions with respect to the pure aqueous media.

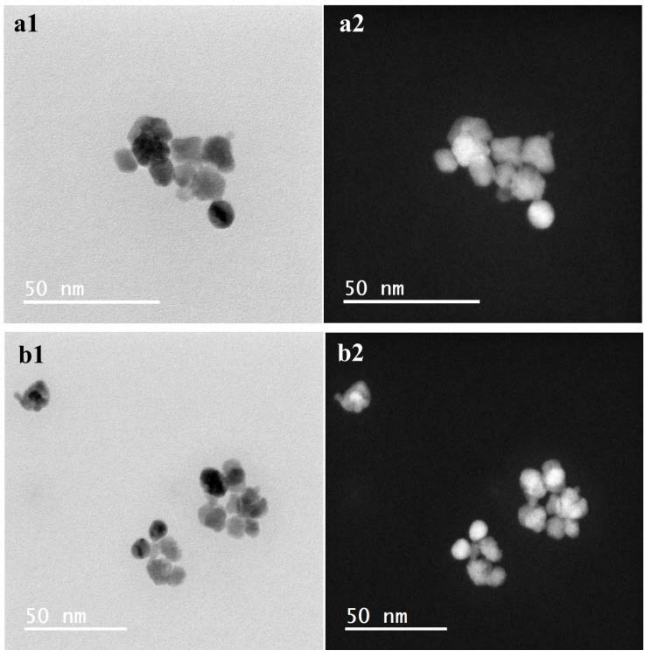

Fig. ~~ure~~ 1. BF- (a1 & b1) and HAADF-STEM (a2 & b2) images of 0.039 mmol/l $AgNO_3$ ethanol containing solution irradiated for 30 min. Bright Z contrast is attributed to silver NPs in HAADF-STEM images

Not only was the overall efficiency of the process remarkably increased by the use of alcohol, but also smaller and more uniform silver nanoparticles with a size comparable to that of ceria nanoparticles (around 15 nm) were formed with regard to those synthesized without radical scavengers as revealed by TEM analysis. Moreover, there were no signs of particularly small Ag NPs, nor were observed large silver nanoparticles, formed separately from ceria, which were present in the samples with higher silver concentration.

[1] M.Grzelczak, L. M. Liz-Marzan, The relevance of light in the formation of colloidal metal nanoparticles, Chemical Society Reviews **43(7)**, 2089-2097 (2014).
[2] Y. Li and M. A. El-Sayed, The Effect of Stabilizers on the Catalytic Activity and Stability of Pd Colloidal Nanoparticles in the Suzuki Reactions in Aqueous Solution, The Journal of Physical Chemistry B **105(37)**, 8938-8943(2001).

SYNTHESIS OF STEROID *VIC*-DIAMINO LIGANDS USING STRECKER REACTION

Barbara Seroka[1], Jacek W. Morzycki[1], Rafał R. Siciński[2], Zenon Łotowski[1]

[1]Institute of Chemistry, University of Białystok, K. Ciołkowskiego 1K, 15-245 Białystok, Poland
[2]Faculty of Chemistry, University of Warsaw, L. Pasteura 1, 02-093 Warsaw, Poland
barabara_17@o2.pl

Cytotoxic complexes of platinum (II) are still the leading group of drugs used in anticancer therapy. One of the most potent anticancer agents widely used against many severe forms of cancers is cisplatin (Fig. 1.).

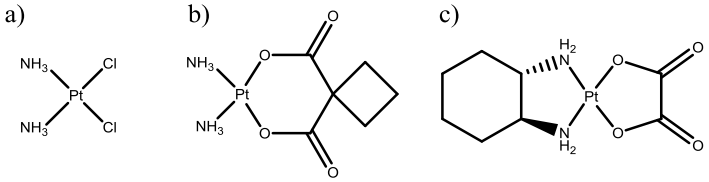

Fig. 1. a) cisplatin, b) carboplatin, c) oxaliplatin

An example of a substrate for the synthesis of bidentate ligands was lithocholic acid and its utility requires indispensable modifications in the structure of side chain in the steroidal backbone. Multistep synthesis has allowed to obtain two amino groups in this part of the molecule, where the key step of the synthesis was Strecker reaction in which *O*-pivaloylated D-galactosylamine has been used as an auxiliary.[1,2] All new compounds will be tested for their ability to form the complexes with platinum and their biological activity.

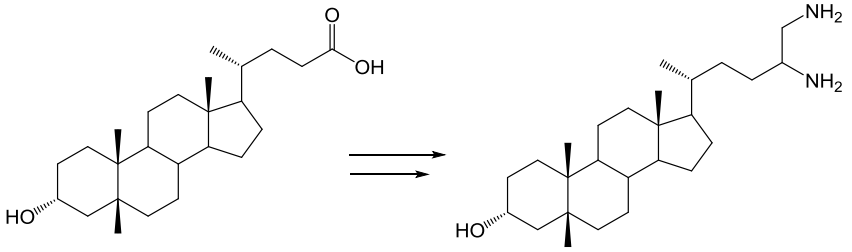

Fig. 2. Synthesis of steroidal *vic*-diamino ligands

The authors thank the Polish National Science Centre for the grant support (2014/15/B/ST5/02129)

[1] H. Kunz, W. Sager, D. Schanzenbach, Carbohydrates as chiral templates: Stereoselective Strecker synthesis of D-α-amino nitriles and acids using *O*-pivaloylated D-galactosylamine as the auxiliary, Liebigs Ann. Chem., 649-654 (1991).
[2] J. Wang, X. Liu, X. Feng, Asymmetric Strecker Reactions, Chem. Rev., 111, 6947-6983 (2011).

SYNTHESIS AND PROPERTIES OF THE $Ca_{1-2x}Ce_{2x}Mo_{1-x}Ge_xO_4$ ($0 \le x \le 0.2$) CRYSTALS

Alina Slepets[1], Tetiana Voitenko[1], Sergiy A. Nedilko[1*], Sergiy G. Nedilko[2*]

[1] Faculty of Chemistry, Taras Shevchenko National University of Kyiv, Ukraine .
[2] Physics Faculty, Taras Shevchenko National University of Kyiv,Ukraine.
giva@online.ua

Materials which based on $CaMoO_4$ are used as luminescence materials for blue– green emission depending on the particle size and crystallinity [1, 2]. The functionality of this materials increases, if molecules are doped in Ca^{2+} sites They can be used in in different areas such as solid state lasers, LED (light emitting diodes), scintillators, microwave dielectrics, cryogenic detectors and fluorescent lamps [3].

The $Ca_{1-2x}Ce_{2x}Mo_{1-x}Ge_xO_4$ ($0 \le x \le 0.2$) samples were made by using high temperature solid state procedure. Cerium nitrates $Ce(NO_3)_3$, calcium carbonate $CaCO_3$, germanium (IV) oxide GeO_2 and molybdenum (VI) acid H_2MoO_4 were used as starting materials. The powders of starting materials were weighted and grinded thoroughly for 30 min in an agate mortar to achieve uniformity. Then, the mixtures were taken into the porcelain crucibles followed by calcinations in a furnace 400 – 950 ºC.

Infrared spectra (IR) of the samples were recorded on PerkinElmer IR spectrometer using the KBr pellet method in the range 1400-400 sm^{-1}.

The phase composition and crystal lattice parameters were determined using x-ray diffractometers DRON-3M ($Cu_{K\alpha}$-radiation with a Ni filter). The diffraction patterns were taken at a step of 2 deg./min.

The microstructure of the compounds were studied by a scanning electron microscope (SEM) Hitachi S – 2400.

Photoluminescence of the $Ca_{1-2x}Ce_{2x}Mo_{1-x}Ge_xO_4$ ($0 \le x \le 0.2$) samples were taken under UV and visible light excitations in 4.2-300 K range of the samples temperature.

The X-ray diffraction rezults are illustrated in Fig. 1. In general, $CaMoO_4$ compound crystallizes in a tetragonal zircon-type structure (space group: *I41/amd*, Z = 4) [2].

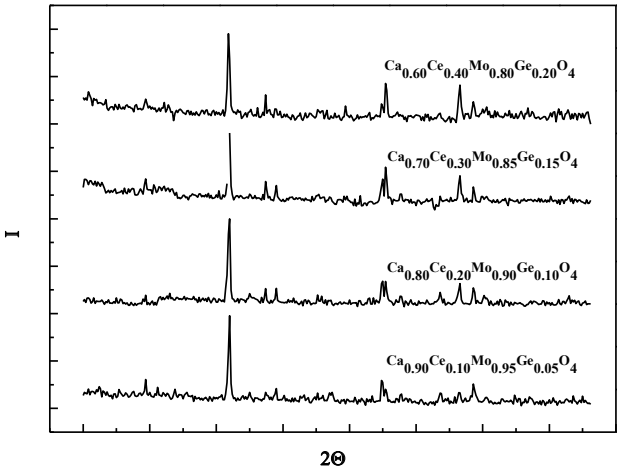

Fig. 1. X-ray diffraction pattern of $Ca_{1-2x}Ce_{2x}Mo_{1-x}Ge_xO_4$ ($0 \le x \le 0.2$) samples.

The crystal lattice parameters of the investigated compounds are shown in Table 1. The calculated unit cells of $CaMoO_4$ are a = 5.2187(3) Å, c = 11.4660(1) Å, V = 311.731(1) $Å^3$.

Table 1.Crystal lattice parameters of the $Ca_{1-2x}Ce_{2x}Mo_{1-x}Ge_xO_4$ ($0 \le x \le 0.2$) samples

Samples	a, Å	c, Å	V, $Å^3$
$Ca_{0.90}Ce_{0.10}Mo_{0.95}Ge_{0.05}O_4$	5.2444(3)	11.4784(1)	315.693(1)
$Ca_{0.80}Ce_{0.20}Mo_{0.90}Ge_{0.10}O_4$	5.2400(3)	11.4804(1)	315.229(1)
$Ca_{0.70}Ce_{0.30}Mo_{0.85}Ge_{0.15}O_4$	5.2387(1)	11.4819(2)	315.109(1)
$Ca_{0.60}Ce_{0.40}Mo_{0.80}Ge_{0.20}O_4$	5.2363(1)	11.4797(3)	315.050(2)

[1] D.K. Avasthi, Y.K. Mishra, F. Singh, J.P. Stoquert, Ion tracks in silica for engineering the embedded nanoparticles, Nucl. Instrum. Methods Phys. Res. Sect. B, 268 (2010), 3027-3034.
[2] S. Park, M. Lang, C.L. Tracy, J. Zhang, F. Zhang, C. Trautmann, M.D. Rodriguez, P. Kluth, R.C. Ewing, Response of $Gd_2Ti_2O_7$ and $La_2Ti_2O_7$ to swift-heavy ion irradiation and annealing, Acta Mater., 93 (2015), 1-11.
[3] S. Dutta, S. Som, S.K. Sharma, Luminescence and photometric characterization of K^+ compensated CaMoO4: Dy^{3+} nanophosphors, Dalton Trans., 42 (2013), 9654-9661.

THE SYNTHESIS CONDITIONS EFFECT ON LUMINESCENT PROPERTIES OF $BaI_2:Eu^{2+,3+}$ FINE POWDERS

Solomakha Tatsiana, Tratsiak Yauhen

Research Institute for Physical Chemical Problems, Belarusian State University, Belarus
tanja_313@mail.ru

Nowadays there is a large variety of scintillation materials which find apply as detectors of photons and high-energy particles in areas such as high energy physics, nuclear physics, medicine, national security, exploration and so on. Despite the sufficient variety of both the scintillation materials and areas of their application there is a list of characteristics that the ideal scintillator should possess. These characteristics include: high density of scintillator and atomic numbers of the elements used, a high light yield and energy resolution, short decay time, no afterglow, low cost, high radiation and mechanical resistance, absence of self-radioactivity [1, 2]. At present time the scintillation material which could simultaneously combine all the above mentioned properties does not exist. Among the scintillation materials halide compounds in comparison with oxide holds the record in energy resolution and light output. Due to the relatively low cost and availability halides of alkaline earth elements are sufficiently attractive for mass use, in particular BaI_2, which has high Z_{ef}, is not radioactive and has the smallest band gap among the alkaline earth metals halides. In accordance with the foregoing, the synthesis methods development and study of the synthesis conditions effect on the properties of the obtained BaI_2 is of practical interest.

$BaI_2:Eu^{2+},Eu^{3+}$ powder has been obtained by heat treatment in iodinating agent atmosphere of precursor $BaCO_3:Eu^{3+}$ obtained by coprecipitation [3]. The use of the two-step approach to the synthesis of $BaI_2:Eu^{2+},Eu^{3+}$ opens up opportunities for the control of its structural, morphological, and as a result, luminescent properties, both due to the modification of the precursor and varying its heat treatment parameters.

Synthesis conditions (inert atmosphere, synthesis temperature 400°C, duration – 30 minutes), allowing to obtain $BaI_2:Eu^{2+},Eu^{3+}$ powders containing no impurity phases have been found. It was discovered that obtained powder is a mixture of crystalline hydrates of different composition with a predominance of $BaI_2 \cdot 2H_2O$. It is shown that in $BaI_2:Eu^{2+},Eu^{3+}$ powders synthesis a transition $Eu^{3+} \rightarrow Eu^{2+}$ occurs, which completeness is defined both by the $BaI_2:Eu^{2+},Eu^{3+}$ synthesis conditions (the reactants ratio, the ion-activator concentration, atmosphere, synthesis temperature and its duration) and morphology characteristics of the precursor particles. The possibility of controlling the Eu^{2+} ions luminescence band displacement in $BaI_2:Eu^{2+},Eu^{3+}$ powders by codoping powders with cations of alkaline-earth elements has been demonstrated.

Thus, in present work the optimal conditions of $BaI_2:Eu^{2+},Eu^{3+}$ powders formation have been determined and the synthesis conditions effect on their morphological, structural and luminescent properties has been studied.

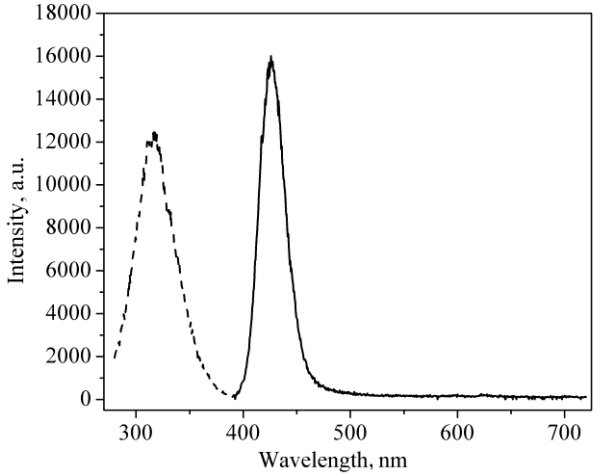

Fig. 1. Luminescence excitation ($\lambda_{reg.}$~425 nm) and luminescence ($\lambda_{ex.}$~315 nm) spectra of $BaI_2:Eu^{2+},Eu^{3+}$.

[1] M.Nikl, A.Yoshikawa, Recent R&D Trends in Inorganic Single-Crystal Scintillator Materials for Radiation Detection, Advanced Optical Materials **3**, 463-481 (2015).

[2] W.W. Moses, Current trends in scintillator detectors and materials, Nuclear Instruments and Methods in Physics Research **487**, 123–128 (2002).

[3] E.V Tret'yak., G.P.Shevchenko, T.A.Solomakha, M.V. Korzhik, Effect of Precursor Morphology on the Structural Properties, Optical Absorption, and Luminescence of $BaI_2:Eu^{2+},Eu^{3+}$, Inorganic Materials **53**, 1–6 (2017).

FTIR MATRIX ISOLATION AND CPMD METHODS IN CONFORMATIONAL ANALYSIS OF THF MOLECULE

Joanna Stocka

Department of General Physics and Spectroscopy, Vilnius University, Lithuania
joana.lach@university.com

Tetrahydrofuran (THF, oxolane), cyclic ether with formula $(CH_2)_4O$, is widely used the industry applications[1] despite its probable toxic effect to the environment. Nowadays THF is used as a precursor of biologically active molecules, as a monomer in polymerisation reactions, what is more THF might be treated as a simple model of deoxyribose in the DNA chain in electron interactions researches[2].

The high-level ab initio calculations show that the global minimum of the THF molecule in a gas phase has an envelope (C_s) structure[3,4,5]. According to the latest benchmark calculations the absolute energy difference between the global minimum (C_s) and the first local minima, the twisted conformation (C_2), is only 0,59 kJ/ mol^{-1}.[6] Such low differences between global and local minima suggest almost barrierless adaptation from one conformer to another at finite temperature.

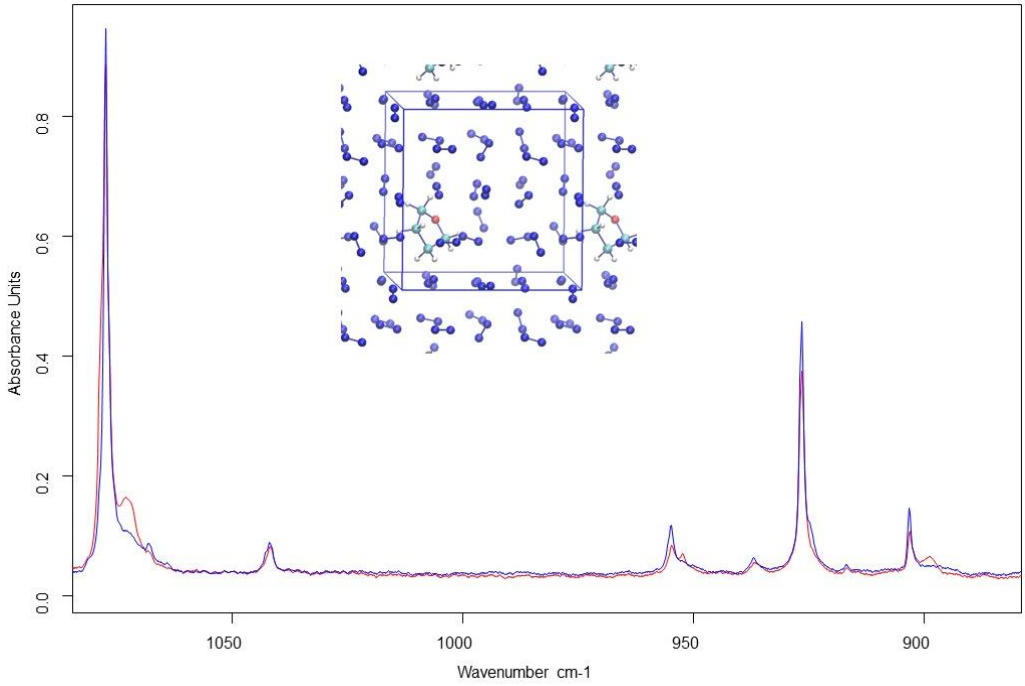

Fig. 1. THF@N_2 FT-IR spectra from matrix isolation experiment for 9K (red), and 9K after annealing (blue).

The spectra were collected after 1 hour deposition of the THF:N_2 mixture (ratio 0.5:500 mba) in 9 K and after annealing (heating up to 25 K and cooling down to 9 K.Matrix isolation infrared absorption experiments reveled that both conformers are observable in the low temperature nitrogen matrices.

The dynamics of the model THF in N_2 system and the structural rearrangements between the local and global minima have been studied at finite temperature by Car-Parrinello molecular dynamics (CP-MD) simulations. CP-MD calculations proves that the global minimum structure is envelope conformer. We can observe transformation of the conformation from envelope to twisted and backward, what suggest that the nitrogen matrix might induce the pseudorotation even in such low temperatures.

[1] B. Thiemer, J. Andreesen, T. Schrder, Arch. Microbiol. (179) (2003) 266–277.
[2] M. Lepage, S. Letarte, M. Michaud, F. Motte-Tollet, M.-J. Hubin-Franskin, D. Roy, L. Sanche, J Chem Phys 109 (14) (1998) 5980.
[3] D. G. Melnik, S. Gopalakrishnan, T. A. Miller, F. C. D. Lucia, J. Chem. Phys. 118 (2003) 3589.
[4] V. M. Rayon, J. A. Sordo, J. Chem. Phys. 122 (2005) 204303.
[5] A. D. Boese, R. Boese Cryst. Growth Des. 15 (2015) 1073.
[4] T. Yang, G. Su, C. Ning, J. Deng, F. Wang, S. Zhang, X. Ren, Y. Huang, J. Phys. Chem. A 111 (2007) 4927.

ELECTROCHEMICAL SERS STUDY OF PHENYL-TERMINATED SELF-ASSEMBLED MONOLAYERS WITH AMIDE GROUP

Marija Špandyreva*, Ieva Matulaitienė, Ilja Ignatjev, Zenonas Kuodis, Gediminas Niaura

Department of Organic chemistry, Center for Physical Sciences and Technology, Lithuania
marija.spandyreva@gmail.com

Self-assembled monolayers (SAMs) on metal surfaces can serve as useful models for analysis of the interaction of functional groups of amino acids with ions, solvent molecules, biomolecules, and other components. In particular, the effect of electric field on the structure and spectral properties of the functional group is important for understanding the function of biomolecules. To probe the structure of phenylalanine ring at different conditions, we have synthesized the thiol molecule with terminal phenyl-ring and intrachain amide group (MOPHE, N-(2-phenylethyl)-8-sulphanyloctanamide). In this work, we studied the effect of electrochemical potential on the structure of monolayer by using the surface enhanced Raman spectroscopy (SERS).

Fig. 1 shows the potential-dependent SERS spectra from MOPHE monolayer self-assembled on gold electrode surface. Defined bands of MOPHE phenyl ring were observed in SERS spectrum at 496 (γ Phe), 620 (F6b), 823 (νC7-C1), 1003 (F12), 1030 (F18a), 1064 ($\nu C\text{-}C)_T$, 1103 ($\nu C\text{-}C)_T$, 1203 (F7a), 1436 (δCH_2), 1583 (F8b), 1603 (F8a), 2849, 2896 $\nu_s(CH_2)$, and 3063 (F2) cm^{-1} [1]. The intense band near 1064 cm^{-1} is due to C-C stretching vibration of alkyl chain in all-*trans* conformation [2]. Thus, monolayer is well-ordered and exhibits alkyl chain in extended *trans* configuration. The low intensity band near 1643 cm^{-1} was assigned to Amide-I (Am-I) vibrational mode. The main contribution for Am-I mode comes from the C=O stretching vibration. Relatively low frequency of this band indicates involvement of intrachain amide group in strong hydrogen bonding interaction. Such interaction might be responsible for the stabilization of the monolayer. The low frequency band near 277 cm^{-1} corresponds to metal-adsorbate stretching vibration ν(Au-S) [2]. Presence of this band provides direct evidence on formation of covalent bond between the thiol and gold substrate. One can see (Fig. 1) that the monolayer is stable in the wide potential region (from -1.1 to 0.4 V vs. Ag/AgCl electrode). Relative intensity of the SERS bands provides information on orientation of functional groups with respect to the electrode surface. Thus, intensity of ν(Au-S) increases at more positive electrode potentials. This might be associated with more vertical alignment of Au-S bonds. Slight increase in relative intensity is also visible for the ring C-H stretching mode near 3063 cm^{-1} indicating more vertical orientation of phenyl-ring at more positive electrode potentials.

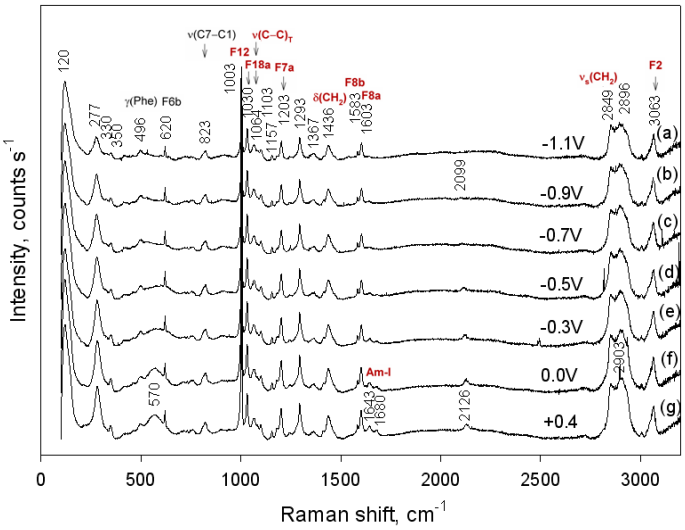

Fig. 1. Surface enhanced Raman spectra of self-assembled monolayers formed from MOPHE (N-(2-phenylethyl)-8-sulphanyloctanamide), obtained on gold electrode at potential range (-1.1V to +0.4 V) by immersion of gold in 10 mM MOPHE methanolic solution for 18h, revealing ordering of the phenyl rings C6H5 in 0.01M $H_2NaPO_4^{3-}$ /0.1M $Na_2SO_4^{3-}\cdot H_2O$ buffer solution. The laser power at λ = 785 nm is 50mW. The arrows indicate the major peaks due to phenyl ring.

[1] E. Proniewicz, D. Skoluba et al., Influence of applied potential on bradykinin adsorption onto Ag, Au, and Cu electrodes, J. Raman Spectrosc. **44**, 655-664 (2013).
[2] I. Matulaitiene, Z. Kuodis et al., SERS of the positive charge bearing pyridinium ring terminated self-assembled monolayers: structure and bonding spectral markers, J. Phys. Chem. C **119**, 26481-26492 (2015).

DIRECTED HIGH-THROUGHPUT SCREENING OF AQUEOUS-PHASE SONOGASHIRA COUPLING REACTION FOR SYNTHESIS OF BIOTIN-11-dNTPs

Justina Šulgaitė[1, 2], Rytis Vincentas Urbonas[1, 2], Inga Čikotienė[1, 2]

[1] Thermo Fisher Scientific Baltics UAB, Lithuania
[2] Institute of Chemistry, Faculty of Chemistry and Geosciences, Vilnius University, Lithuania
justina.sulgaite@thermofisher.com

Manual high-throughput screening was applied in order to discover the best suited conditions for the last step of biotin-11-dNTP synthesis. Our goal for this research was to establish more effective and less time-consuming synthesis pathway which we achieved. We have developed three-step synthesis of biotin-11-dNTP where two steps are in parallel and the last step is aqueous-phase Sonogashira cross-coupling reaction (Fig. 1). Conventional method to obtain such products is a linear five-step synthesis [1], [2], consisting of propargylamine blocking and Sonogashira coupling with iodinated nucleoside, following up with the synthesis of corresponding 5'-triphosphate. Subsequently, deprotection of amino group and biotinylation via 7 atoms linker yielding the desired product. In comparison both conventional and our developed methods have been fulfilled. Moreover, during this research the phosphorylation reaction screening of iodinated nucleosides utilizing different phosphorylation agents and reaction conditions have been carried out.

Liquid chromatography-mass spectrometry was used for product identification and conversion determination.

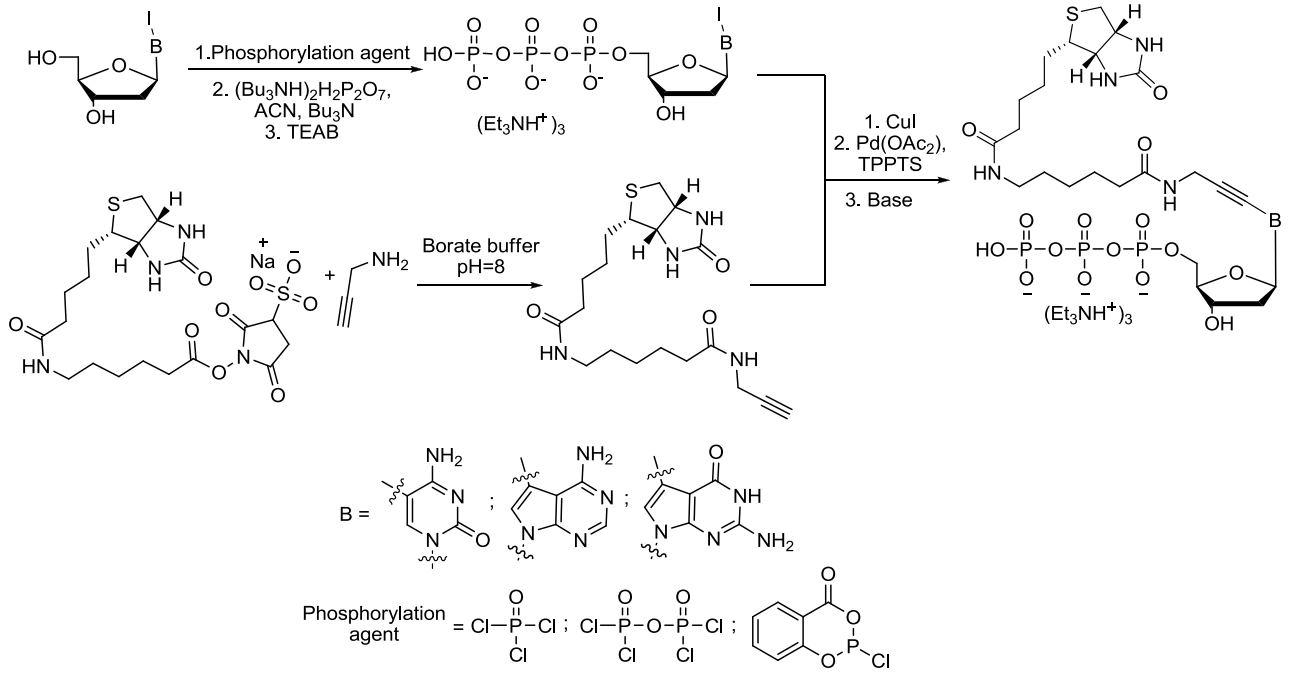

Fig. 1. Parallel three-step synthesis pathway for biotin labeled 2'-deoxynucleoside-5'-triphosphates.

In conclusion, we have developed alternative synthesis route in order to obtain biotin-11-dNTPs. To our knowledge it is a first study for synthesis of biotin labeled 2'-deoxynucleoside-5'-triphosphate by utilizing aqueous-phase Sonogashira coupling.

[1] S. Jager, G. Rasched, H. Kornreich-Leshem, M. Engeser, O Thum, M. Famulok., A Versatile Toolbox for Variable DNA Functionalization at High Density, J. Am. Chem. Soc. **127**, 15071 – 15082 (2005).
[2] M. Hollenstein, Deoxynucleoside triphosphates bearing histamine, carboxylic acid, and hydroxyl residues – synthesis and biochemical characterization, Org. Biomol. Chem. **11**, 5162 – 5172 (2013).
[3] P. Pan, Q. Zhang, J. Hou, Z. Liu, F. Bai, M. Cao, T. Sun, G. Bai., Cell surface glycoprotein profiling of cancer cells based on bioorthogonal chemistry, Anal. Bioanal. Chem. **403**, 1661 -1670 (2012).
[4] S. Ikonen, H. Macickova-Cahova, R. Pohl, M. Sanda, M. Hocek, Synthesis of nucleoside and nucleotide conjugates of bile acids, and polymerase construction of bile acid-functionalized DNA, Org. Biomol. Chem. **8**, 1194 – 1201 (2010).
[5] P. Brazdilova, M. Vrabel, R. Pohl, H. Pivonkova, L. Havran, M. Hocek, M. Fojta, Ferrocenylethynyl Derivatives of Nucleoside Triphosphates: Synthesis, Incorporation, Electrochemistry, and Bioanalytical Applications, Chem. Eur. J. **13**, 9527 – 9533 (2007).
[6] L. H. Thoresen, G. Jiao, W. C. Haaland, M. L. Metzker, K. Burgess, Rigid, Conjugated, Fluoresceinated Thymidine Triphosphates: Syntheses and Polymerase Mediated Incorporation into DNA Analogues, Chem. Eur. J. **9**, 4603 – 4610 (2003).

DETERMINATION OF THE DEGREE OF PES ANHARMONICITY

Nikita Tsimbrovsky[1], George Pitsevich[1], Ekaterina Kozlovskaya[1], Vitas Balevicius[2]

[1]Department of the Physical Optics, Belarusian State University, Minsk, Belarus
[2] Vilnius University, Vilnius, Lithuania
tsin-1995@yandex.by

Knowledge of the full potential energy or at least its part is a key element of different fields – molecular dynamics, vibrational and UV spectroscopy, photoexcitation and etc. It is well known one of the ways to determine the PES is to use ab-initio calculations. If during vibrations atoms dispacements from their equilibrium positions are insignificant, then one can use harmonic approximation for calculations of the potential energy surface. However, vibrations of the small atoms, especially the ones that involve hydrogen atom, are anharmonic vibrations due to large amplitudes of the atoms motions. Analysis of the calculated PESs can provide scientists with valuable data on the properties of the investigated molecules. This data can be especially valuable in case of large amplitude motions.

Here we propose a new way of evaluation of the PES anharmonicity degree. Our method is based on the quantitative expression of the differences between the harmonic and calculated PESs. We detmine the degree of anharmonicity for 1D and 2D PESs as follow:

$$\eta = \frac{1}{N}\sum_{i=1}^{N}\frac{\left|U(x_i)-U^h(x_i)\right|}{U^h(x_i)} \qquad U^h(x)=\frac{f_{xx}x^2}{2} \qquad f_{xx}=\frac{d^2U(x)}{dx^2}\Big|_{x=0};\ldots \tag{1}$$

$$\eta = \frac{1}{N}\sum_{i,j=1}^{N_i,N_j}\frac{\left|U(x_i,y_j)-U^h(x_i,y_j)\right|}{U^h(x_i,y_j)} \qquad U^h(x,y)=\frac{f_{xy}x^2}{2}+\frac{f_{xy}y^2}{2}+f_{xy}xy \qquad f_{xy}=\frac{d^2U(x,y)}{dx\cdot dy}\Big|_{x=0,y=0} \tag{2}$$

where x,y - natural vibrational coordinates, characterizing variations in the length of a hydroxyl group, $U(x_i, y_i)$ – potential energy, calculated at point (x_i, y_i), $U^h(x_i, y_i)$ – potential energy, calculated at point (x_i, y_i) in harmonic approximation.

Values of the parameter η were calculated for O-H group of the number of molecules and complexes with different type of the hydrogen bond: methanol dimer, malonaldehyde, formic acid dimer, pyridine N-oxide and trichloroacetic acid free complex and comples in acetonitrile, protonated water dimer. Calculations were performed using different number of points N and different ranges where x and y coordinates are varying. In case of 2D PESs two methods of the anharmonicity degree calculations were implemented. The first one is similar to the case of 1D potential curves, where η was calculated as difference between harmonic and calculated PESs in a number of points along two axis. The second method was implied in order to perform more uniform investigations of 2D PESs. For this method harmonic and calculated PESs were intersected by a cylinder (see Fig.1) and differences between harmonic and calculated energy values were calculated at points of the cylinder intersections of two surfaces.

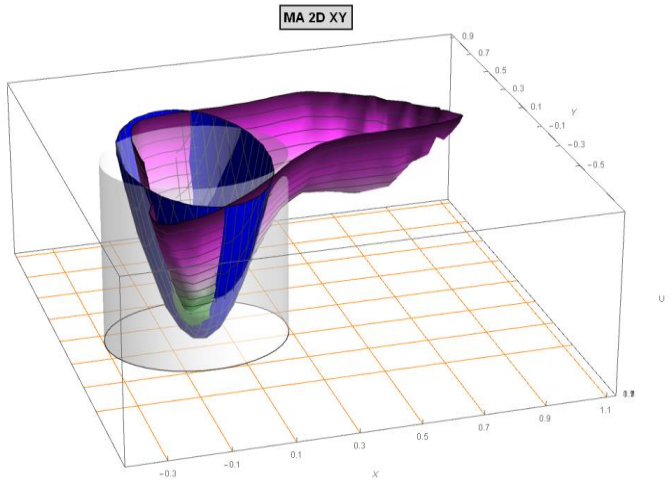

Fig. 1. Harmonic (blue) and calculated (colored) 2D PESs of the malonaldexyde molecule.

While analyzing PES anharmonicity it can be noted that from phsical point of view with the right choise of vibrational coordinates there should be one coordinate, which can be characterized by the maximal deviation of the calculated PES from the harmonic one. We performed calculations that allowed to analyze which linear combination of the vibrational coordinates allows to characterize the PES more percisely in terms of anharmonicity. To permorn such calculations we constructed the section planes for PESs with the step equals to 5° and then analyzed obtained 1D curves to indicate the direcction where calculated and harmonic energy values have the greatest difference.

SYNTHESIS OF POLYSUBSTITUTED PYRROLES *VIA* TANDEM 1,3-ADDITION-5-*ENDO*-DIG CYCLIZATION OF 1-(1-ALKYNYL)CYCLOPROPYL IMINES

Aurelija Urbanaitė, Inga Čikotienė*

Faculty of Chemistry and Geosciences, Vilnius University, Lithuania
aurelija.urbanaite@chf.vu.lt

Polysubstituted pyrroles are important class of organic compounds. This heterocycle is valuable do to its chemical, photophysical and biological properties [1].

Transition metal salts mediated 5-*endo*-dig cyclizations of alkynes, bearing imino groups in close proximity are typicall for the preparation of pyrroles [2]. Whereas there are only few publications about catalyst-free intramolecular cyclizations of these compounds in the literature [3]. Herein we present mild and efficient tandem intramolecular cyclizations – cyclopropane ring opening of *in situ* generated cyclopropyl-tethered 3-alkynyl imines with polarized-covalent-bond-containing compounds. This provides an effective method for the introduction of chalcogen, halogen or hydrogen groups to the 3-position of the pyrrole ring, together with the incorporation of alkoxy/aryloxy, azide or halogen groups into the ethyl side-chain.

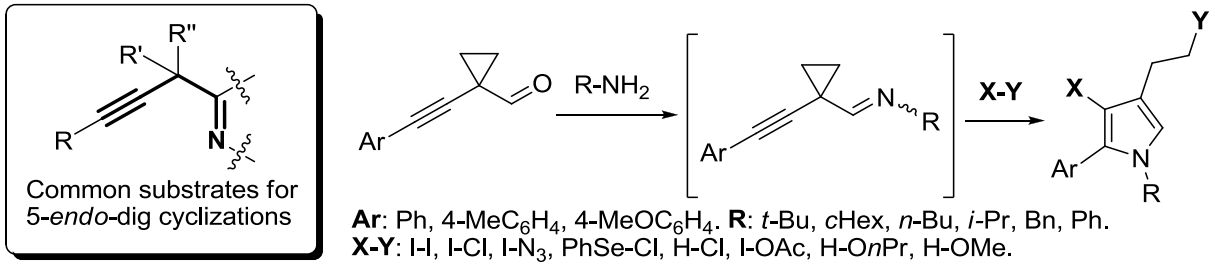

Fig. 1. Reaction between *in situ* generated 1-arylalkynylcyclopropyl imines and polarized covalent bond containing compounds.

The scope and limitations of this catalyst-free addition-cyclization reaction will be discussed.

[1] a) Bhardwaj, V.; Gumber, D.; Abbot, V.; Dhiman, S. *RSC Adv.* **2015**, *5*, 15233. b) Biava, M.; Porretta, G.C.; Poce, G.; Battilocchio, C.; Alfonso, S.; Logu, A.; Manetti, F.; Botta, M. *ChemMedChem* **2011**, *6*, 593. c) Mohamed, M.S.; Fathallah, S.S. *Mini Rev. Org. Chem*., **2014**, *11*, 477. d) Gabriel, S.; Cecius, M.; Fleury-Frenette, K.; Cossement, D.; Hecq, M.; Ruth, N.; Jerome, R.; Jerome, C. *Chem. Mater*., **2007**, *19*, 2364. e) Domingo, V. M.; Aleman, C.; Brillas, E.; Julia, L. *J. Org. Chem*., **2001**, *66*, 4058. f) Novák, P.; Muller, K.; Santhanam K. S. V.; Hass, O. *Chem. Rev*., **1997**, *97*, 207.

[2] a) Chen, G.-Q., Zhang, X.-N., Wei, Y., Tang, X.-Y. Shi, M. *Angew. Chem. Int. Ed.*, **2014**, *53*, 8492. b) Liu, R.-R.; Ye, S.-C.; Lu, C.-J.; Xiang, B.; Gao, J.; Jia, Y.-X. *Org. Biomol. Chem*. **2015**, *13*, 4855. c) Cadierno, V.; Crochet, P. *Curr. Org. Synth*, **2008**, *5*, 343.

[3] Aggarwal, T.; Kumar, S.; Dhaked, D.K.; Tiwari, R.K.; Bharatam, P.V.; Verma, A.K. *J. Org. Chem*., **2012**, *77*, 8562.

ELECTRODEPOSITED COBALT FOAMS AS CATALYSTS FOR WATER ELECTROLYSIS

Modestas Vainoris[1], Henrikas Cesiulis[1], Natalia Tsyntsaru[1,2]

[1]Deptment of Physical Chemistry, Vilnius University, Lithuania
[2]Institute of Applied Physics of ASM, Chisinau, Moldova
modestas.vainoris@chf.stud.vu.lt

Cobalt and its alloys are widely used, e.g. as superalloys, anticorrosion and wear-protecting coatings, magnetic recording devices and medical equipment. However the depletion of fossil fuels and growing rate of global warming are increasing the need for eco-friendly and efficient energy sources, such as O_2 and H_2 fuel cells. Currently obtaining pure H_2 gas is very expensive. Metallic foams, that have high surface area, could be used as efficient and cheap catalyst for oxygen evolution reaction (OER) and hydrogen evolution reaction (HER). The aim of this work was to design a simple and cheap procedure to manufacture Co foams by means of electrodeposition, using hydrogen bubbles as dynamic template.

Co metallic foams were deposited under galvanostatic conditions at high current densities (0.6-2.5 A/cm²) onto copper substrate from acidic solution (pH 2) containing 0.2 M $CoCl_2$ and 2 M NH_4Cl. Obtained Co foams were characterized by Scanning Electron Microscope (SEM) and Energy Dispersive Spectroscopy (EDS) and Electrochemical Impedance spectroscopy (EIS). Cylindrical pores were clearly visible on the coatings, however the density of the pores was rather low and neither pores diameter nor their density was dependent on the current density applied. In order to increase the porosity of Co coatings, solution surface tension was reduced by adding 2 M isopropanol. The increase of diameter of pores, overall porosity as well as surface area was observed, however the addition of 2M isopropanol has significantly reduced the current. Even though obtained Co-foam coatings after synthesis were blown dry with hot air stream, according to EDS data they contain up to 50 at.% of oxygen and 3 at. % of chlorine. The surface area of cobalt foams was estimated from capacitance of double electric layer (C_{DES}) obtained from EIS data.

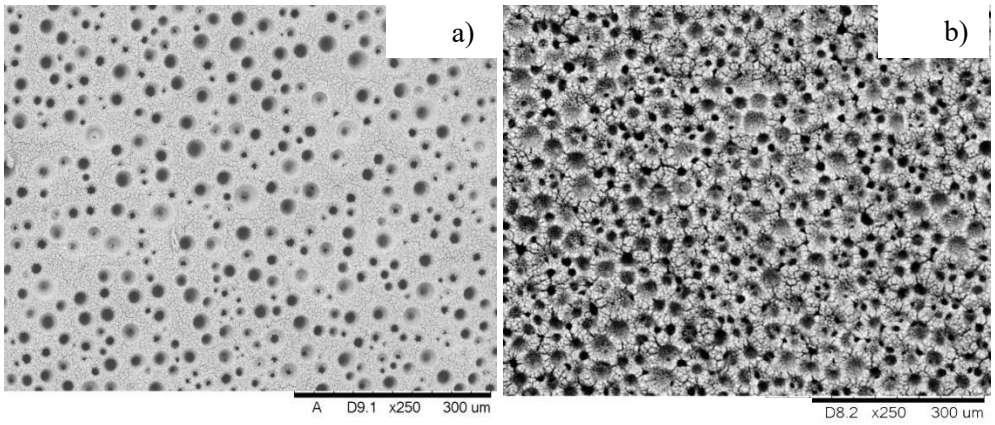

Fig. 1. SEM images of Co foams obtained from a) 0.2 M $CoCl_2$ and 2 M NH_4Cl, j = 2A/cm² t= 100s, b) 0.2 M $CoCl_2$, 2 M NH_4Cl and 2M isopropanol j = 2,2A/cm² t= 100s

In the interest of increasing the surface area of Co-foams, the effect of angle between working electrode and counter electrode during galvanostatic electrodeposition also was investigated. The working electrode was situated in parallel, at 45° and 90° angles in regard to counter electrode. Samples obtained at 45° angle contained more pores on both sides. Porosity of Co-foams obtained at 90° angle has also increased, but only on the side facing the bottom of the electrochemical cell. Catalytic activity of Co foams for hydrogen evolution reaction was tested in 0.1 M KOH solution by voltammetry. HER started at the potential region of -0.75-0.85 V. Some peaks which might be attributed to the partial reduction of cobalt compounds have been observed at -0.3 V (CoO and $Co(OH)_{2)}$ and at -0.7 V (CoOOH and Co_3O_4).

Acknowledgments: Authors acknowledge funding from H2020 (SELECTA 642642) and the Moldavian national project (15.817.02.05A).

THERMAL DESORPTION METHODOLOGY FOR VOLATILE ORGANIC COMPOUNDS (VOC'S) IDENTIFICATION: POSSIBLE APPLICATION IN INVASIVE FUNGAL INFECTIONS

Adrián Vicent Claramunt[1], Algimantas Paškevičius[2], Jurgita Švedienė[2] , Eglė Gudeliūnaitė[2], Silvija Kiverytė[3], Roberta Petrauskaitė[3], Laimonas Griškevičius[3], Audrius Zolumskis[1], Evaldas Naujalis[1]

[1]Center for Physical Sciences and Technology, Savanorių Ave. 231, LT-02300 Vilnius, Lithuania.
[2]Nature Research Center, Akademijos 2, LT-08412 Vilnius, Lithuania.
[3]Vilnius University Hospital Santariškių Klinikos and Vilnius University, Santariškių 2, LT-08661 Vilnius, Lithuania
adrian.vicent@ftmc.lt

There are almost 2000 volatile organic compounds (VOC's) found in healthy humans [1]. The identification of unusual compounds or variations in their levels could be used as biomarkers for several diseases, including invasive fungal infections such as Invasive pulmonary Aspergillosis (IA) [2]. IA is caused by Aspergillus *Fumigatus* fungus (Fig. 1) and is a major contributor to mortality of patients with weak immune system. Diagnosing IA in early stages is still difficult as several tests have to be conducted to confirm the presence of the fungi [3]. Aspergillus *Fumigatus* fungus emits a VOC profile that is distinctive from other pathogenic molds [4]. Human breath analysis could be used as a non-invasive methodology for IA diagnosis. Thermal Desorption is used for VOC analysis among other techniques [5]. A home-made sampling system is being developed for detection of VOC's from *Aspergillus* fungi in-vitro and in-vivo. For in-vitro samples a study of different parameters was performed.

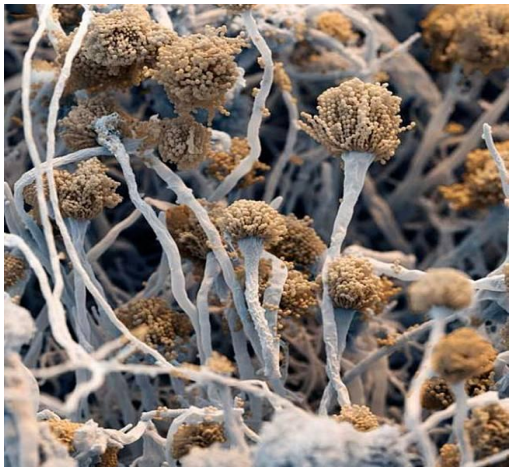

Fig.1: Fungi *Aspergillus fumigatus*. "Microcosmos" by Brandon Broll

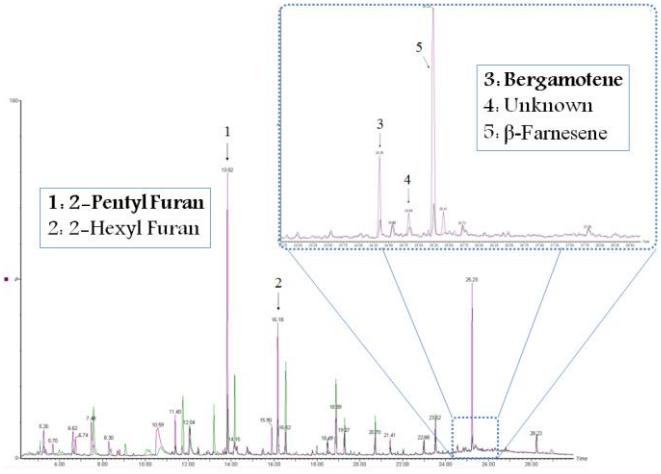

Fig.2: Chromatogram for *Aspergillus* sample overlapped with "Control"

Thermal desorption tubes were run on a GC-HDMS system for prior separation and identification of all compounds emitted by fungi. After we optimized the method, we could find the key components that allowed us to discriminate the fungi presence from natural compounds emitted in the breath of healthy humans.

The chromatogram (Fig. 2) illustrates that we found 2 compounds that are emitted by the fungi that are not found in healthy humans. 2-Pentyl Furan and Bergamotene could be considered as biomarkers for IA.

[1]Chambers et al. "Novel diagnosis: progress toward a breath test for invasive Aspergillus Fumigatus" *Medical Mycology*. April 2011, 49(Suppl. 1), S54-S61.
[2] Sethi et al. "Clinical Application of Volatile Organic Compounds Analysis for Detecting Infectious Diseases. *Clin. Microbiol*. Rev. 2013, 26(3):462
[3]Moularat et al. "Detection of fungal development in a closed environment through the identification of specific VOC: Demonstration of a specific VOC fingerprint for fungal development" *Science of total Environment* 407 (2008) 139-146
[4]Lin et al. " Identification of Unique Volatile compounds of Aspergillus Fumigatus for Potential diagnostic Breath Test by HS-SPME and GC-MS" *J Immunol Tech Infect Dis* 2013, 2:3
[5] Koo et al. "A breath Secondary Metabolite Signature to Diagnose Invasive Aspergillosis" *Clinical Infectious Diseases* October 22, 2014

STAINLESS STEEL CAPILLARY COLUMNS FOR GAS CHROMATOGRAPHY. PREPARTION AND USAGE

Audrius Zolumskis, Audrius Sadaunykas, Audrius Markevičius

Faculty of Chemistry, Vilnius University, Vilnius Lithuania
audrius.zolumskis@gmail.com

This poster will be about stainless steel capillary columns usage in gas chromatography. Recently the most popular capillary columns in gas chromatography are made of fused silica and coated with some stationary phase. But there are few problems with these type of capillary columns they are limited by temperature range and also they aren`t mechanically firm. So as the solution of high temperature gas chromatography analysis the stainless steel capillary columns are used. [1] Furthermore, the stainless steel capillary columns are mechanically firm so they can be used not only for the solution as a high temperature analysis, but also for saving the space and energy crafting new series gas chromatograph.

In our laboratory to reach some of our objects we decide to use stainless steel capillary columns not only as the solution of the high temperature analysis, but mostly as mechanically firm material. [2] To find out what kind of stainless steel capillary columns are best for our research we decide to craft some stainless steel capillary columns by ourselves (the sample of coating is shown in Fig. 1.). So in this conference we will make a poster which will show what achievements we reached and our plans in near future to develop most effective usage of stainless steel capillary columns for gas chromatography analysis.

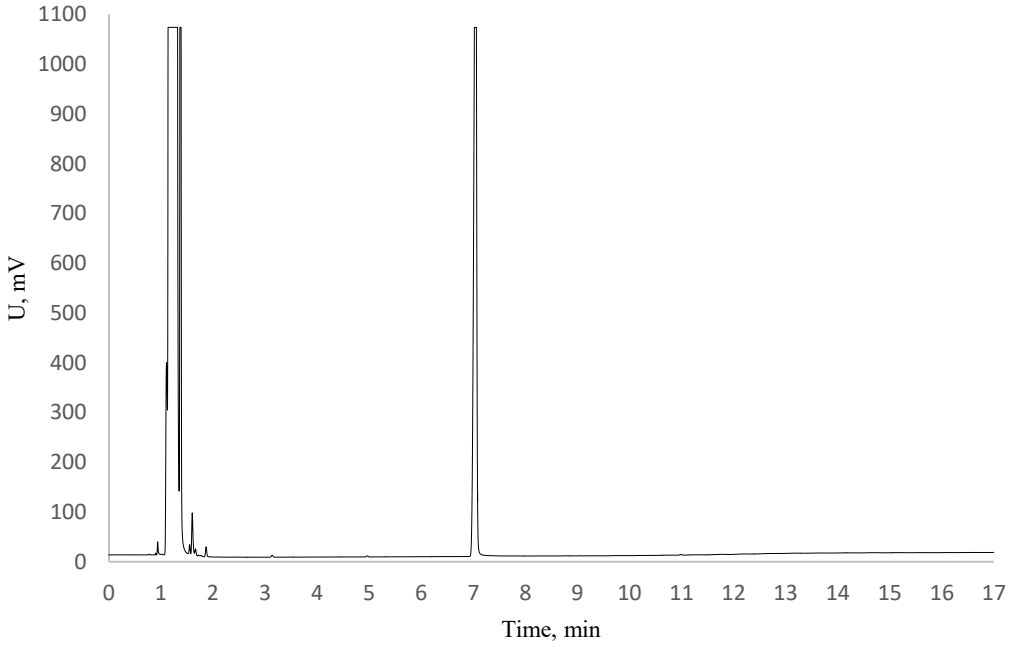

Fig. 1. The example of stainless steel capillary column coating with 100 % dimethylpolysiloxane

[1] CF Poole, Wayne State University, Detroit, MI, USA, GAS CHROMATOGRAPHY, Column Technology, 2013, 3–7.
[2] A. Bemgard and L. Blomberg, Journal of High Resolution Chromatography and Chromatography Communications, Vol 10, May 1987, 302-318.

SOL–GEL SYNTHESIS, CRYSTAL STRUCTURE, SURFACE MORPHOLOGY, AND FT-IR SPECTROSCOPICAL INVESTIGATION OF ALKALINE-EARTH METAL MOLYBDATES

Gediminas Braziulis, Giedrė Gaidamavičienė, Artūras Žalga*

Faculty of Chemistry and Geosciences, Vilnius University, Naugarduko Str. 24, 03225 Vilnius, Lithuania
arturas.zalga@chf.vu.lt

Among various metal oxides, molybdates play a key role in potential and technological applications such as optic fibers, humidity sensors, catalysts, scintillation detectors, solid-state lasers, photoluminescent devices, microwave applications and so on [1, 2].

From the structural point, the differences between alkaline earth metal molybdates ($AMoO_4$, A = Mg, Ca, Sr, and Ba) mainly consist in ionic radius of the A-site. If the ionic radius of the A-site ion is smaller than 1.0 A ° as is the case for $MgMoO_4$ ceramic, the compounds show a wolframite structure with octahedral coordination. Alternatively, if the ionic radius of the A-site is larger than 1.0 Å as is the case for Ca^{2+}, Sr^{2+}, and Ba^{2+} in $AMoO_4$, the compounds show a scheelite structure with tetrahedral coordination [3].

Up to now, various techniques have been developed to synthesize molybdates, such as traditional solid-state reaction, the coprecipitation synthesis, the combustion method, Czochralski method, solvothermal process, reverse micellar reaction, microwave irradiation, spray pyrolysis, the facile microemulsion-mediated hydrothermal process, electrochemical method, sonochemical preparation and sol-gel synthesis. Among these different synthesis routes the solution based synthetic methods play a crucial role in the design and production of fine ceramics and have been successful in overcoming many of the limitation of the traditional solidstate, high-temperature methods [4]. Such kind synthesis techniques can eliminate major problems, such as long diffusion paths, impurities, and agglomeration, and result in products with improved homogeneity. Moreover, the sintering temperature that usually strong affects the properties of final compounds is crucial factor for the preparation of both nano-sized materials and thin films on different substrates [3–5].

In this work, the samples $MMoO_4$ (where M = Mg, Ca, Sr, and Ba) were successfully prepared by an aqueous sol–gel synthesis route taking tartaric acid (TA) as a ligand in order to prevent the crystallization and precipitation of both the initial and final compounds during the sol–gel processing. Afterwards, M–Mo–O tartrate gel precursors were additionally annealed at 500, 600, 700, 800, 900, and 1000 °C temperatures and investigated by X-Ray diffraction (XRD), scanning electron microscopy (SEM), and Furier Transform infrared spectroscopy (FT-IR). According to the XRD results is clear that the crystallization of final compound starts below 500 °C in all cases except for $BaMoO_4$. It is obvious that the formation of barium molybdate really depends on the synthesis conditions (pH, temperature, mixing rate and etc.) during the sol–gel processing. SEM measurements revealed that by increasing annealing temperature the size of the particles also tends to increase. Besides, the results obtained from FT–IR spectra of investigated samples showed that there exist the relation of changes between the surface morphology and appearance of submitted curves.

[1] M. G. Amini, M. Bazarganipour, M. S. Niasari, Calcium molybdate octahedral nanostructures, hierarchical self-assemblies controllable synthesis by coprecipitation method: Characterization and optical properties, Journal of Industrial and Engineering Chemistry **21**, 1089–1097 (2015).

[2] Y. Wang, L. Yang, Y. Wang, X. Wang and G. Han, Controlled synthesis of $CaMoO_4$ and $SrMoO_4$ rods by a simple sonochemical method, Journal of the Ceramic Society of Japan **120**, [9] 378-381 (2012).

[3] G. Braziulis, R. Stankeviciute, A. Zalga, Sol-gel Derived Europium Doped $CaMoO_4:Eu^{3+}$ with Complex Microstructural and Optical Properties, Materials Science-Medziagotyra **20** [1] 90-96 (2014).

[4] G. Braziulis, G. Janulevicius, R. Stankeviciute, A. Zalga, Aqueous sol-gel synthesis and thermoanalytical study of the alkaline earth molybdate precursors, Journal of Thermal Analysis and Calorimetry **118** [2], 613-621 (2014).

[5] A. Zalga, A. Kareiva, A. Zarkov, S. Tautkus, B. Abakeviciene, UV-Vis spectroscopical investigations of the YSZ thin films on corundum, silicon and silica substrates, Chemija **25** [1], 29-33 (2014).

PULSE PROPAGATION FOR CLOSED LOOP QUANTUM SYSTEMS

Hamid Reza Hamedi, Gediminas Juzeliunas

Institute of Theoretical Physics and Astronomy, Vilnius University Saulėtekio 3, LT-10222 Vilnius, Lithuania
Hamid.r.hamedi@gmail.com

The dynamics of pulse propagation [1] is theoretically investigated for a closed- loop five- level atomic configuration, in which a probe laser beam couples a ground level to a four- level closed loop system [2]. By solving the coupled Maxwell-Bloch equations for the field and atomic scheme, the probe pulse dynamics through the atomic medium is studied. It is shown that under the resonance condition, a weak Gaussian- shaped probe pulse can be transmitted through the medium nearly without any significant loss, broadening and distortion, so that it can preserve its shape for quite a long propagating distance.

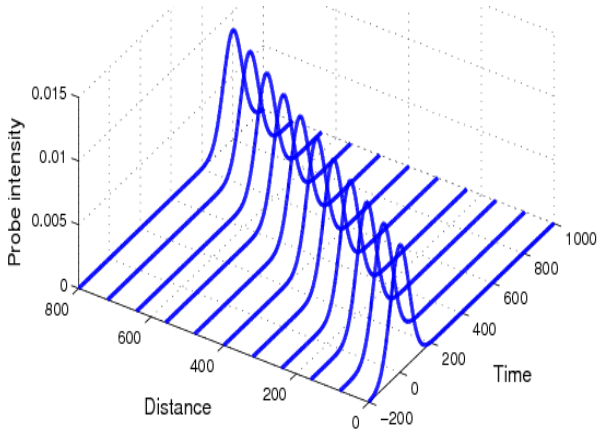

Fig. 1. Pulse propagation against time and distance.

Subsequently the propagation of probe pulses is considered which are not necessarily weak [3]. It is realized that an intense probe pulse experiences a considerable absorption during its propagation. Analytical solutions are obtained to elucidate the behaviour of pulse propagation in our atomic model [4].

[1] R. Fleischhaker and J. Evers, Phys. Rev. A 77, 043805 (2008)
[2] H. R. Hamedi and G. Juzeliūnas, Phys. Rev. A 91, 053823 (2015)
[3] T. N. Dey and G. S. Agarwal, Phys. Rev. A 67, 033813 (2003)
[4] H. R. Hamedi and Gediminas Juzeliūnas, Phys. Rev. A 94, 013842 (2016)

SPONTANEOUS EMISSION FACTOR INFLUENCE ON OUTPUT PARAMETERS OF THE VERTICAL-CAVITY SURFACE-EMITTING LASERS

Labatsevich Pavel

Department of Physics, Belarusian State University, Belarus
pavel.lobatsevich@mail.ru

The magnitude of spontaneous emission factor contribution into the lasing mode (parameter β) is very important characteristic, that determines energetic and dynamic characteristics of semiconductor lasers. For vertical-cavity surface-emitting semiconductor lasers (VCSEL) the experimental values and theoretical estimates give a very wide variation in the range from 10^{-2} to 10^{-6}, and there are no criteria that would significantly clarify the range of the parameter β determination nowadays. This work presents the results of numerical simulation of the intensity and the degree of polarization of the output radiation, in which the β acts as a fitting parameter. The initial model was analyzed on the base of the polarization components method [1,2]. Previously, this method has shown high efficiency for the description the polarized light formation in VCSEL polarization instability area.

It has been shown that increase of the parameter β results in effective reduction of the induced anisotropy that leads to a significant reduction in the degree of the output radiation polarization. As a result, the latter does not reach the limiting values even far from the point of polarization switching, which corresponds to a significant expansion of the polarization switching area, even in the case of stationary excitation, that has not been experimentally observed. This effect may occur already at β values greater or equal to 10^{-4}.

Since β is usually determined as a particular value at the lasing threshold, the possible dependence of β on the injection current density has been investigated. Calculation results have shown that the dependence of the polarization degree on the injection current is weak even for a significant change of β.

Thus, the numerical simulation results showed that the optimal β values belong to the range 10^{-5} -10^{-6}, in which the calculated dependences match well with the experimental data.

According to the classical theory of semiconductor lasers, the spontaneous emission intensity fluctuations determine the statistical characteristics of the output radiation. The analysis of the statistical modeling results for the VCSELs in polarization instability area has shown that the numerical value of the distribution function dispersion is substantially lower than experimentally observed, especially for the intensity providing the distribution function for the intensity and degree of polarization are qualitatively similar to those observed experimental data. Thus, we can assume that the spontaneous emission is an important, but not dominated factor. However, there are other factors (for example, fluctuations in the concentration of nonequilibrium carriers and injection current), which may be more significant in terms of the statistical parameters formation of the output radiation, at least for the VCSEL in polarization instability area. Probably this overestimation of the spontaneous radiation is reflected to the fact that experimentally observed values of β are two or three orders of magnitude higher than the values used in the theoretical calculations.

---

[1] M. Jadan, L.I.Burov, A.S.Gorbatsevich, E.S.Sokolov, Polarization switching in single-mode injection semiconductor laser, Journal of Applied Spectroscopy 76, 717-724 (2009).
[2] M. Jadan, L.I.Burov, A.S.Gorbatsevich, E.S.Sokolov, Dynamics of polarization switching in single-mode injection semiconductor lasers, Journal of Applied Spectroscopy 77, 65-72 (2010).

DENSITY OF QUANTUM STATES IN PERIODICAL STRUCTURES

Vitali Ghoghoberidze[1], David Kakulia[1], Akaki Lomia[1], Avto Tavkhelidze[2]

[1] Faculty OF Exact and Natural Sciences, Ivane Javakhishvili Tbilisi State University, 3 Ilia chavchavadze ave.,Tbilisi, Georgia

[2]Faculty Of Engineering, Ilia State University, Kakutsa Cholokashvili Ave 3/5, Tbilisi 0162, Georgia

Vitali_gogoberidze@hotmail.com

New quantum effects have been studied in thin nanograting layers. Nanograting on the surface imposes additional boundary conditions on the electron wave function and reduces the density of states. When the dimensions of the nanograting are close to the De Broglie wavelength the density of states reduction is considerable and leads to change in the layer properties. Calculations of the density of states are challenging to perform and are related to the quantum billiard problem. Performing such calculations requires to find solutions for the time-independent Schrodinger equation with Dirichlet boundary conditions [1].

It was one of the goals of this work to solve this problem using numerical methods. There is a full mathematical analogy between quantum billiards and electromagnetic resonators. Therefore, it is reasonable to use the Method of Auxiliary Sources (MAS) for quantum billiard calculation, as it is most efficient numerical approach for solving eigen value problems. It was one of the goals of the project to solve this problem using digital methods. MAS has been proposed by Georgian mathematician V. Kupradze [2]. Method was adopted by Georgian scientists for solving eigen value problems related to wave guides with arbitrary cross-section [3, 4]. In the MAS for EM boundary value problems are solved numerically by representing the electromagnetic fields in each domain of the structure by a finite linear combination of fundamental solutions of the relevant field equations, corresponding to sources situated at some distance from the boundaries of each domain. The "auxiliary sources" producing these solutions are chosen to be elementary currents/charges located on fictitious auxiliary surface, usually conforming to the actual surface of the structure. The method only requires points on the auxiliary and actual surfaces, without resorting to the detailed mesh structures as required by other methods. Finally the problem is reduced to linear system of algebraic equations which solutions are coefficients of the decomposition. Coefficients should be obtained by solving of the mentioned linear system where one of the coefficients is fixed. It means that the field inside area of interest becomes non-trivial only when the main parameter of the problem is near to eigenvalues and we can easily observe the forming of eigenfunctions. Intensity of the field reaches maximum on eigenvalues. The calculations are performed in Fortran.

[1] N. Peranio, M. Winkler, D. Bessas, Z. Aabdin, J. König, H. Böttner, R.P. Hermann, O. Eibl, Journal of Alloys and Compounds, 521, pp. 163–173, 25, (2012).

[2] A. Tavkhelidze, V. Svanidze , International Journal of Nanoscience, Vol. 7, No. 6, pp. 333-338, (2008).

[3] A. Tavkhelidze, J. Appl. Phys. 108, 044313 (2010).

[4] V. Kupradze, in Success of Mathematical Sciences, vol. 22, Moscow, 1967, pp. 59-107

ON THE QUESTION OF POISSON'S RATIO IN MULTI-SCALE MODELLING OF BCC-LATTICES

Klaidas Grigaravicius[1], Tomas Vaitkunas[1], Audrius Jutas[1*]

[1] Department of Mechanical Engineering, Kaunas Univerity of Technology, Lithuania
klaidas.grigaravicius@ktu.lt

This study describes an atomic system dynamics from the bifurcation view point [1]. Also, there is modeling of BBC-lattice deformation presented in the theory of computation of elastic constant like Poisson's ratio from the atomic perspective in close connection with experiment data obtained at macro-scale [2]. This study is made in so named "analytical atom lab". Parallel to development in statistical mechanics, atomistic modeling is shown as a maturing and perspective tool in materials science and for the fine investigations of physical properties of crystalline materials. In order to render the present study more comprehensive, there basic principles and equations of infinitesimal strain field were applied [3]. To stimulate further interests in this area of research, it is firstly presented procedure of model creation, evaluation techniques and related analysis on atomistic modeling of elastic characteristic. The research presents explanation of elastic behavior starting with the atomistic level within the interacting atomic clusters and finishing with modeling results (Figure 1).

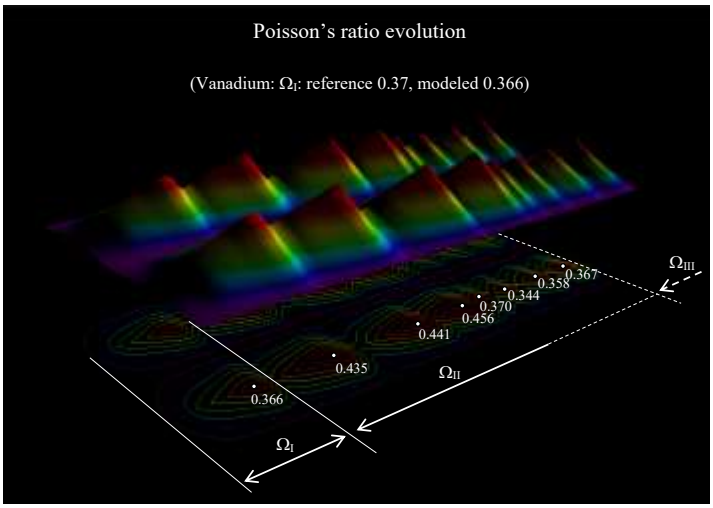

Figure 1: Bifurcations are presented as the picks in Poisson's ratio evolution for excited states Ω_i

Also, as the procedure for verification and calibration of modeled quantity, the prior and posterior probabilities were used. The averaged value of Poisson's ratio related directly to number of resonances (or superposed quantum jumps) was used as the controlled physical characteristic influenced by geometrical heterogeneity of bcc-lattices.

It was assumed that full event set Ω consists of events $H_1, H_2, ..., H_n$ that satisfy number of transformations of differently oriented microstructures. Then Bayesian equation looks like

$$P(H_i|w_i) = \frac{P(H_i)P(w_i|H_i)}{P(H_1)P(w_1|H_1) + P(H_2)P(w_2|H_2) + ...}; \quad (1)$$

here $i = \overline{1, N}$, $P(H_i) = \frac{N_{wi}}{N}$, $N_{wi} \in Q$, $Q = \{N_{wi}, ...N_{wn}\}$, $P(w_i|H_i)$ is prior probability influenced by modeled number of transformations of event w_i according to the chosen objective function $f_N(Q)$ and one asseses relative accuracy of simulated Poisson's ratio $P(w_i|H_i) = \frac{\nu(w_i)}{\nu}$, if $\nu(w_i) < \nu$ and $P(w_i|H_i) = \frac{\nu}{\nu(w_i)}$, if $\nu(w_i) > \nu$. Simulated results demonstrate some disagreement between prior and posterior probabilities. It means that chosen number of features with various lattice directions is not enough because of other physical character inside the atomic structure.

[1] I. Prigogine, I. Stengers, *The end of certainty: time, chaos and the new laws of nature*, Simon & Shuster Inc., New York, p. 228 (1997)
[2] D. Raabe, M. Sachtleber, Z. Zhao, F. Roters, S. Zaefferer, Micromechanical and macromechanical effects in grain scale polycrystal plasticity experimentation and simulation Acta Materialia 17, pp. 3433-3441 (2001)
[3] L. Kubin, J. P. Hirth, Dislocations in solids, Volume 15, Elsevier, UK, p.310 (2009)

MODELLING MICRO-REACTOR WITH AN NERNST LAYER

Linas Petkevičius, Romas Baronas

Faculty of Mathematics and Informatics, Vilnius University, Naugarduko g. 24, LT-03225 Vilnius, Lithuania
linas.petkevicius@mif.vu.lt

Various acids transformation from fluids and water to clean water and harmless product is challenging task. It takes into consideration not only chemical reaction, but technological process [1], designed [3] and various dependencies from system parameters to be useful and adaptable in practice.

We consider the following chemical reactions taking place in the micro-reactor visualized at Figure 1a:

$$\mathrm{L} + \mathrm{E_{1ox}} \xrightarrow{k_1} \mathrm{P} + \mathrm{E_{1red}}, \quad \mathrm{E_{1red}} \xrightarrow{k_2} \mathrm{E_{1ox}} + 2\mathrm{e}^-, \tag{1}$$

$$\mathrm{E_{2ox}} + 4\mathrm{e}^- \xrightarrow{k_3} \mathrm{E_{2red}}, \quad \mathrm{E_{2red}} + \mathrm{O_2} \xrightarrow{k_4} \mathrm{E_{2ox}} + \mathrm{H_2O}. \tag{2}$$

where L is laccase, O_2 - oxygen, H_2O - water, $E_{i(ox)}$ and $E_{i(red)}$ are the oxidized and reduced forms of the enzyme E_i, $i = 1, 2$, P - reaction product, k_1 and k_4 are the rate constants of the enzyme reactions, and k_2, k_3 are the rate constants of the electron transfer (ET) reactions.

It is assumed that both enzyme catalyzed processes (1)-(2) obey the Michaelis-Menten kinetics.

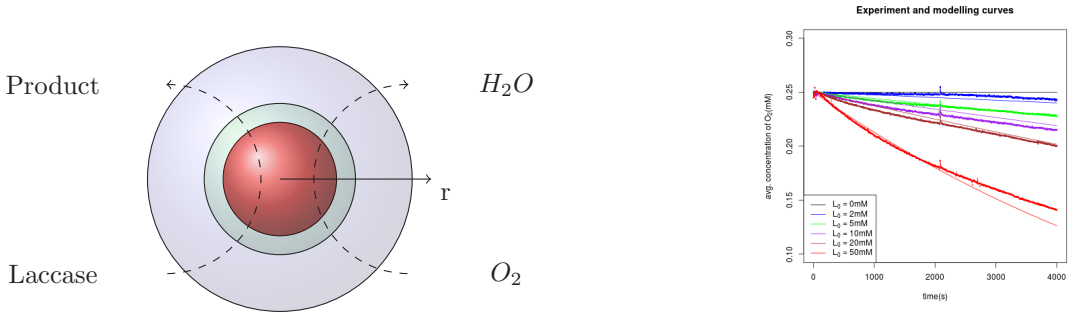

(a) Model in polar coordinates. Micro-reactor with radius R_0, Nernst size $R_1 - R_0$ and convection layer $R - R_1$.

(b) Modelling curves(right) and physical experiment(left) curves comparison.

Fig 1. Micro-reactor structure and comparison with physical experiments.

Due to non-linearity of the governing equations of the problem, no exact analytical solutions are possible. Because of this, the initial boundary value problem was solved numerically by applying the finite difference technique [4]. The numerical simulator has been implemented in C++ programming language.

In physical experiments oxygen parameters were measured since system does not have electrode layer [2]. Initial concentration of laccase varied between 2 and 50 mM. Experiments data was compared with simulations see Figure 1b.

A mathematical model of micro-reactor was created and implemented. Results showed that the relative difference between the numerical solution and the experiment data, averaged over time from 0 up 4000(s), was less than 10% for all experimental concentrations of laccase. Since such modelling errors including the measurement errors can be considered as admissible, the model can be used for investigating the kinetic peculiarities bioreactive system.

[1] Kulys, J. J. *The development of new analytical systems based on biocatalysts.* Analytical Letters 14.6, 377-397 (1981).
[2] Velkovsky, Momchil, et al. *Modeling the measurements of cellular fluxes in microbioreactor devices using thin enzyme electrodes.* Journal of mathematical chemistry 49.1, 251-275 (2011).
[3] Harriott, P. *Chemical reactor design.* CRC Press (2002).
[4] Britz, D., Baronas, R., Gaidamauskaite, E., Ivanauskas, F. *Further comparisons of finite difference schemes for computational modelling of biosensors.* Nonlinear Anal. Model. Control, 14, 419-433 (2009).

FEATURES OF XS GENERATION FOR RADIAL REFLECTOR OF THE VVER REACTOR IN SERPENT MONTE CARLO CODE

Krystsina Usheva[1], Semen Kuten[2], Arkadiy Khruschinsky[2], Leonid Babichev[2]

[1]Belarusian State University, Belarus
[2]Institute for Nuclear Problems, Belarusian State University, Belarus
[3]Joint Institute for Power and Nuclear Research - Sosny, National Academy of Sciences of Belarus, Belarus
k.usheva93@mail.ru

The DYN3D is three-dimensional dynamic code used to calculate the dynamics processes in the nuclear core with quadratic or hexagonal fuel assembly geometry [1]. It is successfully applied to conservative estimations and best estimate calculations in safety analyses. The computer code DYN3D can be coupled with the thermohydraulic code (eg ATHLET [2]) to apply to the whole spectrum of operational and transient accidents, small and intermediate leaks, up to large breaks of coolant loops at PWRs/VVERs and BWRs.

The neutron kinetic model is based on the solution of the three-dimensional two-group neutron diffusion equation by nodal expansion methods. To use the DYN3D for NPP safety analysis it is necessary to generate the constants library for each fuel loading of the NPP reactor.

Serpent Monte Carlo reactor physics code [3] can be used as tools for generation of two-group constants library for DYN3D code. For generation of constants library using Serpent code it is necessary to carry out a very large number of simulations. To obtain reliable results in a reasonable time, it can use a supercomputer and parallel computing.

Detailed model of the radial reflector for the VVER reactor core is developed for calculations in Serpent (version 2.1.26) Monte Carlo code. Five types of the radial reflector cells can be considered taking into account design features of the baffle of VVER reactor. Two-group cross sections have been calculated for the two-layer reflector of DYN3D full core model.

The XS library of the reflector in the full core model contains values of the following characteristics, which are calculated in the two-group approximation: transport cross section ($\Sigma_{tr1,2}$), absorption cross section ($\Sigma_{abs1,2}$), group-transfer cross section (Σ_{S12}), reflector discontinuity factor (RDF).

For correct work of the DYN3D two-group version the fast-to-thermal transfer cross-sections (Σ_{s12}) were adjusted taking into account thermal-to-fast transfer (the heating of the thermal neutrons) (Σ_{s21}):

$$\Sigma'_{s12} = \Sigma_{s12} - \Sigma_{s21}\frac{\Phi_2}{\Phi_1} \quad (1)$$

Reflector discontinuity factors were calculated using additional correction which taking to account for the influence of nearby FAs (Kord S. Smith, PHYSOR 2016) [4] :

$$RDF = \frac{DF_{ref}}{Df_{fuel}}ADF \quad (2)$$

Testing of the reflector XS library has been performed using typical first loading of VVER core based on four different FA types [5]. The library has been prepared for radial reflector as well as for each of individual FAs using Serpent. The two-group cross sections were calculated taking into account discontinuity factors at the "FA-FA", "FA-reflector" boundaries (so-called ADF and RDF factors, respectively).

Verification of the two-group XS's for reflector was been carried out by comparing the results of the full core calculations in DYN3D and Serpent codes. The results obtained by using the last code were considered as reference. The resulting XS libraries have been used in DYN3D for calculating the criticality and normalized power distribution in the reactor core during operation at zero power.

The results of the DYN3D calculations with the Serpent cross section sets agree very well with those of the Serpent full core MC calculations. The difference in k_{eff} is 10,7 pcm for detailed models of the reflector, respectively. Maximum difference in the calculation of normalized power distribution does not exceed 5% in the peripheral layer of FAs, its average value is less than 2%.

Detailed model gives good agreements between reference full core calculation in Serpent and DYN3D using two-group XS's. The XS library generation method presented above can be used for developing the model of the radial reflector for Belarusian NPP with VVER-1200 reactor core.

[1] Rohde U., Kliem S., Grundmann U., Baier S., Bilodid Y., Duerigen S., Fridman E., Gommlich A., Grahn A., Holt L., Kozmenkov Y., Mittag S. The reactor dynamics code DYN3D – models, validation and applications / Progress in Nuclear Energy, 2016. №89. P. 170-190
[2] G.Lerchl, H.Austregesilo: The ATHLET Code Documentation Package, GRS-P-1 / Vol.1.: User's Manual, October, 1995;http://www.grs.de/en/computer-code-athlet
[3] Leppänen J. Serpent – a Continuous-energy Monte Carlo Reactor Physics Burnup Calculation Code. User's Manual / VTT Technical Research Centre of Finland, 2015. 164 p.
[4] Smith K.S. Nodal diffusion methods: understanding numerous unpublished details / PHYSOR 2016, Sun Valley, ID, USA, May 1-5, 2016. P. 1227-1241
[5] In-Core fuel Management Code Package Validation for WWERs. IAEA-TECDOC-847, 1995. 156 p.

EFFECT OF CONTROLLING GATE GEOMETRY ON DONOR QUBITS FUNCTIONALITY

Elena Levchuk, Yury Shkliaryk, Olga Lavrova

Department of Applied Mathematics and Computer Science, Belarusian State University,
Independence Ave. 4, 220030 Minsk, Belarus
shkliaryk.yu.n@gmail.com

Size reduction of semiconductor devices has led to increasing role of dopants position in a working area of a device. The abiliby to control accurately the location of dopant atoms allows to create devices with one or several donor atoms, which functionality is based on electron wave function relocation [1]. An example of such devices is a spin-based quantum computer proposal [2]. The effect of external electric field on donor electron has been studied earlier in cases of a thin disc-shaped gate [3] and uniform electric field [4]. However, these cases do not represent real device geometries.

In this work, we consider the following system: the area $z > 0$ is filled with a semiconductor, a donor is positioned at a distance z_0 from a semiconductor surface. External electric field is applied by the gate, situated on the plane $z = 0$. The donor is centered with respect to the gate. Within the effective mass approach, donor electron energy E and wave function Ψ in semiconductor are described by the stationary Schrödinger equation

$$\left(-\nabla^2 + \hat{V}_G^{(i)} - \frac{2}{\sqrt{x^2 + y^2 + (z - z_0)^2}}\right)\Psi = E\Psi, \quad z > 0, \quad i = \{A_1, A_2, B, C\}, \tag{1}$$

$$\Psi\big|_{z=0} = 0; \quad \Psi \to 0 \quad \text{as} \quad |\vec{r}| \to \infty. \tag{2}$$

where $\hat{V}_G^{(i)}$ is external electric field potential induced by the gate. Several types of the controlling gates have been considered:

1) A_1 – the electric field is applied by a thin disc of diameter d, situated at a semiconductor-insulator interface;
2) A_2 – the electric field is applied by a disc of diameter d, surrounded by a grounded shield;
3) B – the gate has a form of unbounded thin strip of width d;
4) C – the external electric field is uniform.

Expressions for $\hat{V}_G^{(i)}$ in cases A_1 and A_2 are given in [4], in case B – in [5].

The problem (1) – (2) has been studied numerically using the finite element method (FEM) and the variational method. Two main characteristics of the system functionality have been studied:a critical potential difference between the gate and the donor position ($\Delta\Phi_C$) and an exchange interaction between electrons bounded to neighbouring donors or quantum dots.

The value of $\Delta\Phi_C$ has been calculated as the minimum point of the difference between first excited and ground state energies. The dependence of $\Delta\Phi_C$ on d is shown in Fig. 1. It has been found that the value of z_0 practically does not affect $\Delta\Phi_C$ in cases A_1 and A_2 ($\Delta\Phi_C$ varies by no more than 2% when z_0 changes from $8a^*$ to $16a^*$) and has more influence in cases B and C (for the uniform electric field the change of $\Delta\Phi_C$ reaches 20%).

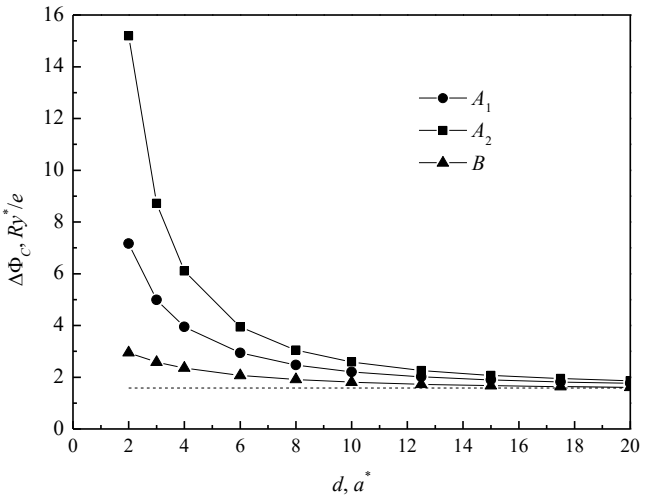

Fig. 1. The dependence of the critical potential difference $\Delta\Phi_C$ on d (diameter or width of the gate). For the uniform electric field (dashed line) and the charged strip (B) $z_0 = 8a^*$; A_1 – thin disc-shaped gate at semiconductor-insulator interface, A_2 – disc-shaped gate surrounded by a grounded shield.

As the exchange coupling between two electrons is essential for qubit entanglement, we have also investigated the effect of geometrical parameters on the overlap integral and the exchange energy, which has been calculated using Heitler-London method.

The results of this work allow to select the most efficient form of the controlling gate used in few-electron nanoelectronic devices.

[1] P.M. Koenraad, M.E. Flatte, Single dopants in semiconductors, Nature materials **10**, 91 (2011).
[2] B.E. Kane, A silicon-based nuclear spin quantum computer, Nature **393**, 133-137 (1998).
[3] M.J. Calderon et al., External field control of donor electron exchange at the Si/SiO_2 interface, Phys. Rev. B **75**, 125311 (2007).
[4] E.A. Levchuk, L.F. Makarenko, On controlling the electronic states of shallow donors using a finite-size metal gate, Semiconductors **50**(1), 89-96 (2016).
[5] N.M. Mirolyubov et al., Solving methods for electrostatic fields, Vischaya Shkola, Moscow (1963).

Poster session 2

HIGH-ENERGY CONTINUUM GENERATION IN AN ARRAY OF THIN PLATES PUMPED BY TUNABLE FEMTOSECOND IR PULSES

Dainius Kučinskas, Rimantas Budriūnas, Arūnas Varanavičius

Vilnius University Laser Research Center, 10 Saulėtekio av., LT-10223, Vilnius, Lithuania
dainius.kucinskas@ff.stud.vu.lt

Supercontinuum generation in bulk solids gathers a lot of interest from both research and practical applicability standpoints. The resulting spatio-temporally coherent radiation has multi-octave spanning spectra and high shot-to-shot stability when pumped by CEP-stabilized pulses. In the anomalous dispersion case the pulses may self-compress to few-optical cycles and have soliton-like spatial structures.

For femtosecond pulses pump energies above a few µJ cause the continuum to lose its spatio-temporal coherence due to multiple pulse splitting and modulational instability. Combined with the low efficiency of the process, the new spectral components account for energies on the order of nJ. A recently demonstrated novel method of continuum generation proposes using multiple thin plates instead of one continuous piece of material [1]. This means that the spectrum is broadened in each successive plate, but because the nonlinear foci are outside the material, the pulse energies can be of several orders higher (hundreds of µJ).

We performed characterization of multi-plate continua pumped by a previously-unexplored wavelength range of 1.1-1.75 µm. We used a mix of 0.1-0.2 mm thick sapphire and fused silica plates. The distances between the plates were chosen as to facilitate the maximum spectral broadening without destroying the spatio-temporal coherence of the pulses or causing optical damage to the plates. The shape of continuum spectra using different pump wavelengths was quite consistent and reminiscent of continua generated in bulk solids. The measured frequency-resolved angular spectra show that for all pump wavelengths almost all the energy and bandwidth is concentrated in the near-axial angular components, which allows for efficient spatial filtering in the Fourier plane. The spectral energy density of the visible part of the spectrum is typically above 10 nJ/nm, 2-3 orders of magnitude higher than in bulk media. Using the SFG-XFROG method, we observed smooth spectral phases except for modulations in spectral phase and intensity around the pump wavelength, which is also the case for continua generated in bulk solids. The temporal structure of the pulses shows several subpulses: the leading sub-pulse contains frequencies lower than the pump and has the larger part of the energy, while the trailing sub-pulse has the higher frequencies and the larger part of the bandwidth (therefore can reach few-cycle durations).

The range of pump energies that can be used is constrained on the low end by the decreasingly small plate spacing, which is required to achieve sufficient intensities in the plates for spectral broadening. On the high end, femtosecond pulses exceed the critical self-focusing power in air, which causes filamentation and the interplay between air and plate nonlinearities to degrade the stability of the continuum. We observed a difference of 30% in pump energies between the onset of normal continuum generation and optical damage. The shot-to-shot energy stability was below 1% for most wavelengths, with exceptions around 1 and 1.5 µm, which can be explained by the narrow bandwidth of interference filters (10nm) and spectral peaks near those wavelengths. The measured CEP noise level in the multi-plate case was very similar to continuum generation in bulk solids.

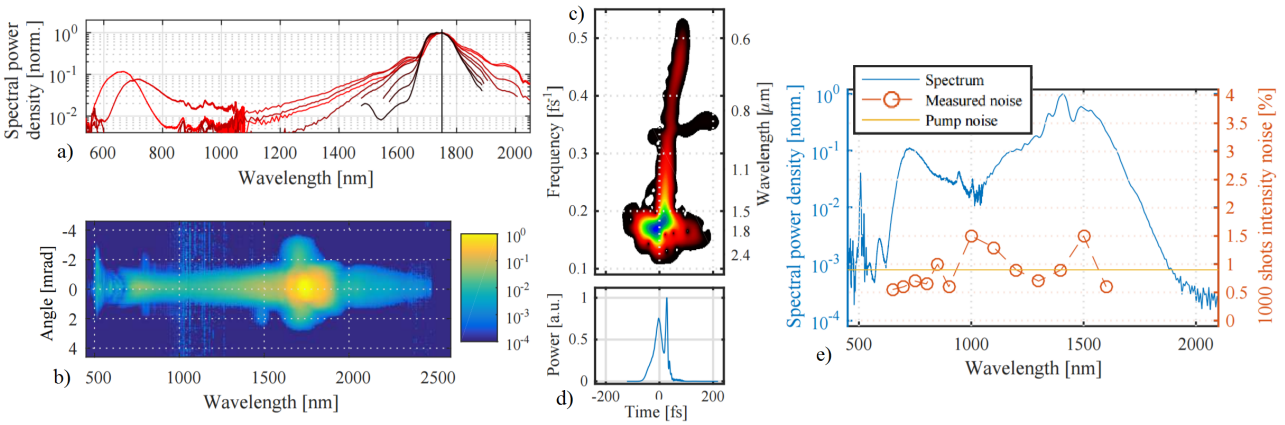

Fig. 1. a) spectra using different numbers of plates b) frequency-resolved angular spectrum c) spectrogram d) pulse temporal profile (all with 1750nm pump) and e) energy noise for different wavelengths (1500nm pump)

[1] C. H. Lu, Y. J. Tsou, H. Y. Chen, B. H. Chen, Y. C. Cheng, S. D. Yang, M. C. Chen, C. C. Hsu, and A. H. Kung. Generation of intense supercontinuum in condensed media. Optica, **1**(6), (Dec 2014).

INVESTIGATION OF SUPERCONTINUUM GENERATION IN PHOTONIC CRYSTAL FIBER USING CHIRPED FEMTOSECOND PULSES

Miglė Kuliešaitė, Julius Vengelis

Laser Research Center, Faculty of Physics, Vilnius University, Lithuania
migle.kuliesaite@ff.stud.vu.lt

Supercontinuum generation is a widely studied topic in nonlinear optics as broadband, high brightness and spatially coherent supercontinuum sources found applications in various fields such as spectroscopy, optical coherence tomography, biomedical optics, etc. [1-2] Photonic crystal fibers (PCF) are an attractive nonlinear medium for supercontinuum generation due to ability to engineer the photonic crystal fiber's dispersion, high nonlinearity and unique waveguide properties [3]. The physics of supercontinuum generation has been investigated and discussed in many research papers, however, there are certain experimental parameters whose influence to supercontinuum generation has not been investigated experimentally. One of such parameters is chirp of pump pulses.

In this study we present experimental results of our investigation of supercontinuum generation in photonic crystal fiber using chirped femtosecond pulses. The pump source was Yb:KGW laser oscillator generating 52 nJ energy 110 fs duration bandwidth limited pulses at 1030 nm with 76 MHz repetition rate. The nonlinear medium was a 32 cm long polarization maintaining photonic crystal fiber with zero dispersion wavelength at 800 nm manufactured by *NKT Photonics A/S*. Pump pulses were chirped by allowing them to propagate back and forth through a pair of SF11 dispersive prisms. The amount of chirp was changed by changing the distance between dispersive prisms and the optical path length of the beam in the prisms.

Supercontinuum generation is a result of many interacting nonlinear phenomena. To investigate the complex nature of supercontinuum formation process, we firstly measured supercontinuum spectrum dependence on pump pulse energy. In case of bandwidth limited pulses at maximum pulse energy supercontinuum spectrum extended from roughly 420 nm to 1500 nm. Further on, we compared supercontinuum spectra generated using bandwidth limited pump pulses (generated by our laser) and supercontinuum spectra generated using chirped pulses. The comparison must be done at the same peak power level as in our case it means the same peak intensity which is the key parameter determining the strength of nonlinear phenomena and their interactions. The results show that at the same peak power supercontinuum spectra obtained using chirped femtosecond pump pulses are broader than the ones obtained using bandwidth limited femtosecond pump pulses (Fig. 1). Left picture in Fig. 1 depicts spectra measured using spectrometer with VIS and part NIR range sensitivity, right picture – spectra measured using spectrometer with NIR range sensitivity. The additional broadening (compared to supercontinuum spectra in case of bandwidth limited pump pulses at the same peak power) depends on the amount of chirp. Under our experimental conditions it varied from several tens of nanometers at chirp values close to zero to more than 100 nm at highest chirp values we could achieve under our experimental conditions (+10600 fs^2). Moreover, the difference between supercontinuum spectrum short-wavelength limits is greater than difference between long-wavelength limits. We believe that chirping pump pulses changes the strength of certain nonlinear phenomena which participate in supercontinuum formation process causing additional spectrum broadening.

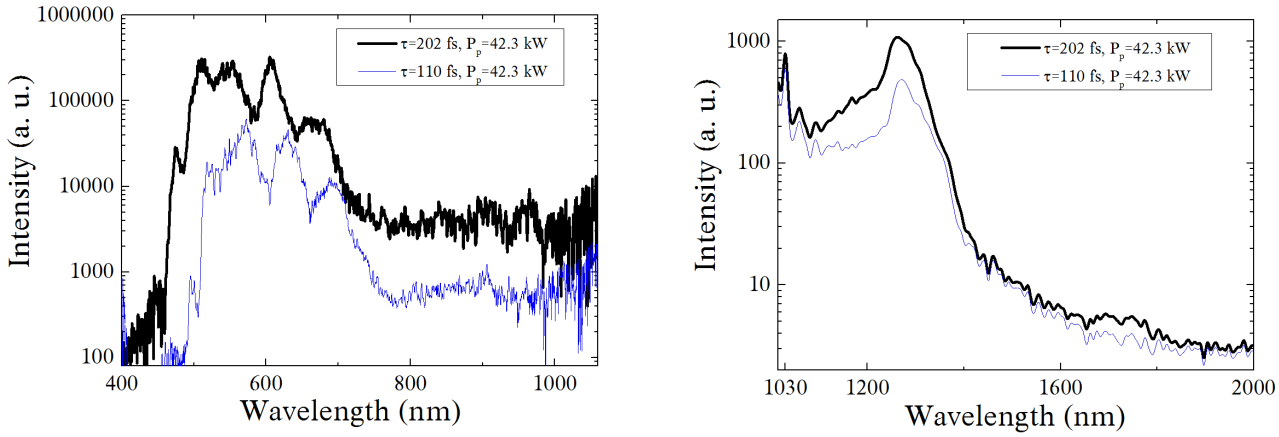

Fig. 1. Comparison of supercontinuum spectra generated using bandwidth limited (thin blue line) and chirped pulses (thick black line). The amount of chirp in this case was +6715 fs^2.

[1] J. M. Dudley, G. Genty, S. Coen, Supercontinuum generation in photonic crystal fiber, Reviews of modern physics **78**, 1135–1183 (2006).
[2] G. Gentry, S. Coen and J. Dudley, Fiber supercontinuum sources, J. Opt. Soc. Am. B **24** (8), 1771-1785 (2007).
[3] P. Russell, Photonic crystal fibers, Science **299**, 358–362 (2003).

MULTI-OCTAVE SPANNING NONLINEAR INTERACTIONS INDUCED BY FEMTOSECOND FILAMENTATION IN POLYCRYSTALLINE ZNSE

Julius Lukošiūnas, Rosvaldas Šuminas, Nail Garejev, Gintaras Tamošauskas, Audrius Dubietis

Vilnius University, Faculty of Physics, Saulėtekio al. 10, LT-10223 Vilnius, Lithuania
julius.lukosiunas@ff.stud.vu.lt

Nonlinear photonic crystals are structures with spatially modulated quadratic nonlinearity [1] offering new possibilities to manipulate the nonlinear three wave interactions in a desired way. Naturally grown disordered polycrystalline materials consisting of a large number of single crystal domains with random orientations, random shapes and random sizes, represent a peculiar class of nonlinear photonic crystals, often termed as random or short-range order nonlinear photonic crystals. The so called "random quasi phase matching", which stems from the disorder of the nonlinear domains [2], greatly extends the fundamental limits of frequency conversion that are imposed by the phase mismatch between the interacting waves, without any additional adjustments. Due to greatly relaxed phase matching conditions, random quasi phase matching allows to phase match any second-order process, therefore enabling a broadband frequency conversion within a wide spectral range, with the limitations of the bandwidth being imposed just by the transparency window of the material.

In this contribution, we investigate self-focusing and filamentation of intense wavelength tunable (in the 1.6 – 2.4 μm range) femtosecond pulses in polycrystalline ZnSe. We observe ultrabroadband supercontinuum (SC) generation in the 650 – 4200 nm range, which is accompanied by efficient simultaneous broadband generation of the second, third and fourth harmonics via randomly quasi-phase matched three wave mixing (Fig. 1).

As confirmed by the near-field intensity measurements, we have accessed both, single and multiple filamentation regimes with the latter possessing exceptionally stable and reproducible patterns, which emerge regardless of the chaotic nature of the process. Moreover, we uncover a number of interesting features regarding the efficiency and polarization of the second and third harmonic generation. First of all, the measured second and third harmonic conversion efficiencies reach up to 20% and 1% respectively, which are the highest values ever achieved in randomly quasi phase matched interactions. Secondly, we show that in the single filament regime the measured second and third harmonic conversion efficiencies follow the expected linear dependence on the sample length [3]. Finally, we demonstrate that as a result, of random orientation of the individual crystallites, the second and third harmonic radiation possess a random polarization, whereas the SC retains the linear polarization of the incident pulse, We believe our findings open fascinating prospects for randomly quasi phase matched interactions in the rapidly developing field of ultrafast mid-infrared nonlinear optics.

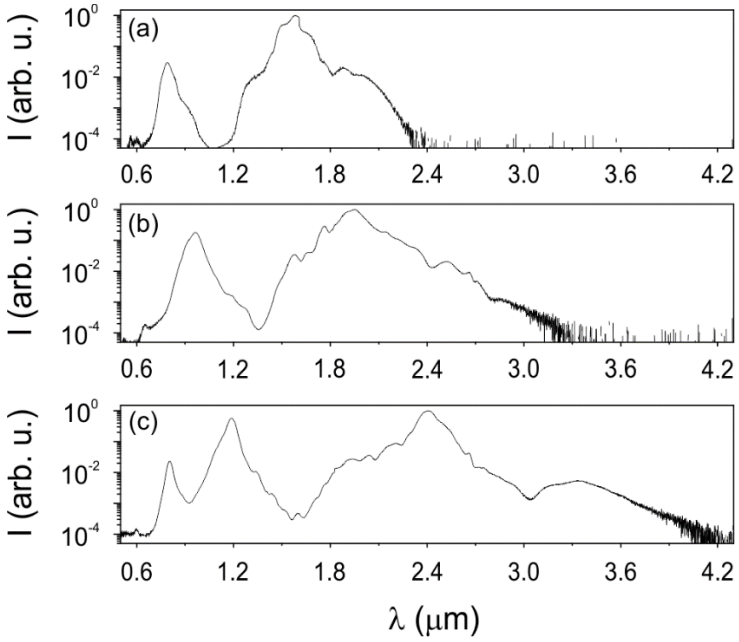

Fig. 1. Supercontinuum spectral dependence as a function of pump wavelength: (a) $\lambda_p = 1.55$ μm, (b) $\lambda_p = 1.9$ μm, (c) $\lambda_p = 2.4$ μm as measured with a constant ratio of $P/P_{kr} \approx 50$.

[1] V. Berger, Nonlinear photonic crystals, Phys. Rev. Lett. 81 , 4136–4139 (1998).
[2] M. Baudrier-Raybaut, R. Haïdar, Ph. Kupecek, Ph. Lemasson, and E. Rosencher, Random quasi-phase-matching in bulk polycrystalline isotropic nonlinear materials, Nature 432, 374–376 (2004).
[3] X. Vidal and J. Martorell, Generation of light in media with a random distribution of nonlinear domains, Phys. Rev. Lett. 97, 013902 (2006).

SIXTH HARMONIC GENERATION IN BBO CRYSTAL AT 224 NM WITH HIGH REPETITION RATE PICOSECOND LASER

Augustinas Petrulenas, Nortautas Ulevicius, Aleksej M. Rodin

Solid State Laser Laboratory,
Department of Laser Technologies, Center for Physical Sciences and Technology, Lithuania
augustinas.petrulenas@gmail.com

Laser emission near 1342 nm has applications in micromachining, deep-UV laser source development for lithography at 224 nm and 192 nm, manufacturing of fiber Bragg gratings and surgical treatment [1,2]. Efficient wavelength conversion into the red 671 nm by second harmonic generation (SHG) or into the blue 447 nm by the sum frequency mixing (THG) is attractive for laser TV, laser printing, medical diagnostics and treatment, underwater communication. Sixth harmonics wavelength at 224 nm is promising for micromachining of polytetrafluoro-ethylene (PTFE), well known commercially as Teflon™. We describe the development of high repetition rate multiply wavelength: NIR-Visible-UV mode-locked laser covering a wide range of these applications with a focus towards the efficient generation of the 6th harmonic at 224 nm.

Picked from the oscillator train, picosecond seed pulses were injected into the cavity of the regenerative amplifier based on pumped at 880 nm wavelength composite Nd:YVO_4 crystal with diffusion-bonded segments of multiple Nd doping concentration [2]. We used 4×4×15 mm^3 type-I LBO ($\theta = 85.2°$, $\varphi = 0°$) nonlinear conversion crystal for SHG and 4×4×10 mm^3 type-I LBO ($\theta = 90°$, $\varphi = 19.6°$) crystal for THG. Two different length of type-I BBO ($\theta = 64°$, $\varphi = 90°$) crystal were used for sixth harmonic generation: 6×5×3 mm^3 and 6×5×6 mm^3.

Developed laser emits 13 ps output pulses of 10 W average power at 1342 nm wavelength and ensures the energy stability of StDev ± 1 % at 300 kHz repetition rate with output beam quality of $M^2 < 1.1$. Conversion to 671, 447 and 224 nm with efficiency of up to 80 %, 50 % and ~ 8 % was achieved. The average power reaches 6 W in red with pulse energy stability of StDev ± 1.5 % featuring beam quality of $M^2 \sim 1.09$ with 0.9 output beam ellipticity, amounts over 4 W in blue with pulse energy stability of StDev ± 1.5 % featuring beam quality of $M^2 \sim 1.12$ with 0.83 beam ellipticity and is limited by ~ 0.7 W in UV featuring beam propagation factor of $M^2 \sim 1.4$ with 0.87 output beam ellipticity.

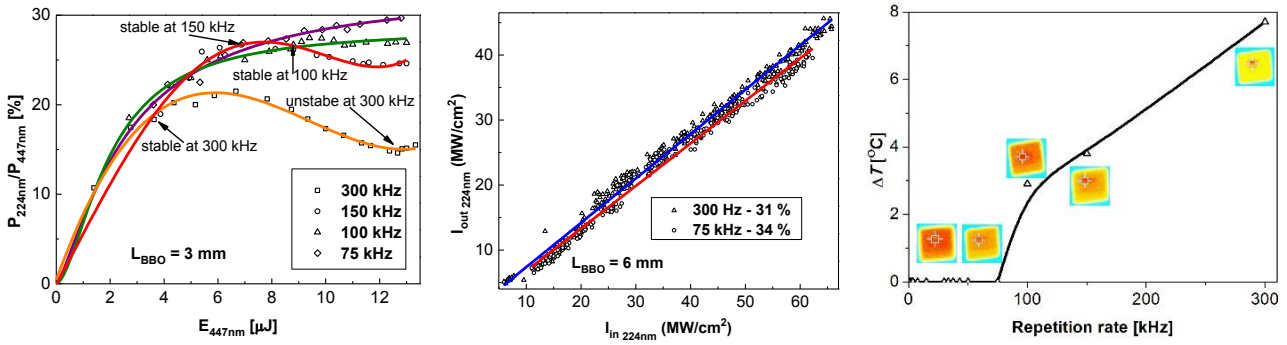

Fig. 1. Conversion efficiency to 224 nm versus pulse energy at 447 nm (left), transmitted versus incident power density in BBO crystal at 224 nm (center) and temperature difference at the output face of BBO versus repetition rate (right).

Conversion efficiency to the sixth harmonic displays a rollover at the repetition rates exceeding 75 kHz (Fig. 1, left) with increasingly unstable behaviour beyond the rollover until the collapse. To identify possible causes for limited conversion we measured transmission in BBO at 224 nm wavelength using another crystal of 6 mm length (Fig. 1, center). It is easily seen that despite considerable scatter of the experimental points caused by the shot-to-shot energy instability of probe pulses, the transmitted versus incident power density is approximated well by a straight line corresponding to linear absorption of ~ 31 ÷ 34 %. Accordingly, we didn't observe an impact of two-photon absorption in the range of incident power densities from 7 to 70 MW/cm^2. Further measurements of temperature gradient induced at the exit face of BBO crystal by linear absorption of UV radiation at 224 nm (Fig. 1, right) demonstrate a threshold at 75 kHz followed by substantial growth of temperature difference up to to 8°C at 300 kHz. Insets (Fig.1, right) show the temperature distribution maps recorded with thermal imaging camera "Fluke Ti10". We enhanced the contrast here to reveal the hot caustic that is clearly seen at 150 ÷ 300 kHz repetition rates.

Designed ultrafast Nd:YVO_4 laser demonstrates the highest average output power achieved at 1342 nm wavelength. Fundamental radiation at 1342 nm from this laser was further converted to the 2nd, 3rd and 6th harmonics at 671, 447 and 224 nm wavelength. To improve the conversion efficiency to 224 nm wavelength at repetition rates exceeding 50 kHz we designed and manufactured special crystal oven providing the longitudinal temperature gradient.

[1] P. Koch, J. Bartschke, and A. L'huillier, All solid-state 191.7 nm deep-UV light source by seventh harmonic generation of an 888 nm pumped, Q-switched 1342 nm Nd:YVO_4 laser with excellent beam quality, Optics Express **22**, 13648 – 13658 (2014) http://dx.doi.org/10.1364/OE.22.013648

[2] A.M. Rodin, M. Grishin, and A. Michailovas, Picosecond laser with 11 W output power at 1342 nm based on composite multiple doping level Nd:YVO_4 crystal, Optics and Laser Technology, **76**, 46 – 52 (2016) http://dx.doi:10.1016/j.optlastec.2015.07.022

COMPACT YB:YAG CPA SYSTEM WITH ALL-IN-FIBER SEED SOURCE

Laurynas Veselis[1,2], Tadas Bartulevičius[1,2], Aleksej Rodin[1,2] and Nerijus Rusteika[1,2]

[1] Solid State Laser Laboratory, department of Laser Technologies, Center for Physical Sciences and Technology, Savanoriu 231, LT-02300 Vilnius, Lithuania
[2] UAB Ekspla, Savanoriu 237, LT-02300 Vilnius, Lithuania
l.veselis@ekspla.com

All-in-fiber seed sources are irreplaceable in laser systems where beam quality, compactness and ease of integration is necessary. However, all-in-fiber laser systems face a challenge handling nonlinearity accumulated in fibers and fiber amplifiers, limiting output energy in 100's μJ level and average power in 100 W level, with pulse durations <1 ps at central wavelength of 1030 nm [1-2]. Although there are demonstrations of energy scaling using all-in-fiber systems to >1 mJ and average power of 1 kW at 100 kHz repetition rate and pulse duration <1 ps, but an Yb-doped, ultra large-core, single-mode photonic crystal fiber (PCF) rod was used for last amplification stage [3]. In this case the term "all-in-fiber" is debatable, as rod itself is large and rigid. Also the compactness of the system suffers.

In this work a hybrid approach of chirped pulse amplification (CPA) system was studied using all-in-fiber seed source and Yb:YAG crystal as a last amplification stage [4-5]. Setup was seeded with ~200 ps pulse duration, 500mW average power pulses at 11 MHz repetition rate. Single end-pumped configuration with 70W high-brightness laser diode at 940 nm coupled into a 105 μm fiber core (NA = 0.15) was used (Fig. 1.). Both seed and pump beams were focused to ~0.4 mm beam width at $1/e^2$ level. 2x2x20 mm Yb:YAG crystal doped 2 at. % Yb was used for experiments. Both crystal and pump diode were water chilled (seperately). Single and double pass setup was studied.

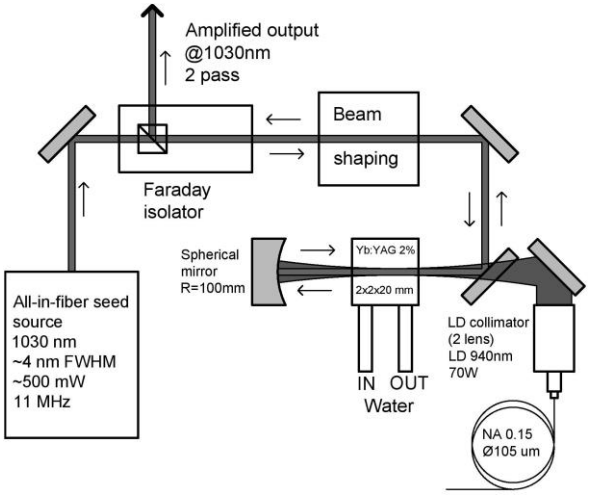

Fig. 1. Experimental setup of single-end pumped double pass Yb:YAG CPA system with all-in-fiber seed source.

Amplified output of 5 W in a single pass and 12 W in double-pass CPA has been achieved at 11 MHz repetition rate, with M^2<1.1 after double-pass. Simulation of amplification was also demonstrated and showed a good agreement with experimental results. More experimental and simulation results will be presented at the conference.

[1] Z. Liu, L. Shah, I. Hartl, G. C. Cho, and M. E. Fermann, High-energy fiber chirped-pulse amplification system based on cubicons, Proceedings of the Conference on Lasers and Electro-Optics (Baltimore, 2005).
[2] A. Galvanauskas, Mode-scalable, fiber-based, chirped-pulse amplification systems, IEEE J. Sel. Top. Quantum Electron. **7** (4), 504–517 (2001).
[3] P. Wan, L. M. Yang, J. Liu, All fiber-based Yb-doped high energy, high power femtosecond fiber lasers, Opt. Express, **21** (24), 29854-9 (2013).
[4] A. M. Rodin, A. Aleknavicius, A. Michailovas, and A. S. Dementjev, Beam quality investigation in Nd:YAG crystal fiber amplifier pumped at > 110 W, Proc. SPIE, **9342**, 934207-16 (2015).
[5] X. Délen, Y. Zaouter, I. Martial, N. Aubry, J. Didierjean, C. Hönninger, E. Mottay, F. Balembois, and P. Georges, Yb:YAG single crystal fiber power amplifier for femtosecond sources, Optics Letters, **38** (2), 109 – 111 (2013).

HIGH GAIN Yb:YAG CHIRPED PULSE AMPLIFIER PUMPED WITH HIGH BRIGHTNESS LASER DIODES

Eimantas Zopelis and Aleksej M. Rodin

Solid State Laser Laboratory, Department of Laser Technologies,
Center for Physical Sciences and Technology, Lithuania
eimantaszopelis@gmail.com

Passively mode-locked fiber lasers are unsurpassed in terms of the beam quality, operation stability, compactness and simplicity of integration. Further power and energy scaling in Nd:YAG [1] and Yb:YAG [2] single crystal fiber (SCF) chirped pulse amplifier (CPA) benefit from the pump guiding and improved heat removal. Compared with Nd:YAG, ytterbium-doped yttrium aluminium garnet (Yb:YAG) has significantly lower fractional heating [3].

We investigated Yb:YAG SCF seeded with 210 ps, 3.8 nm FWHM pulses of over 300 mW average power at 10 – 500 kHz repetition rates in a single and dual-end-pumped configuration. High brightness laser diodes of 50 W and 70 W power at 940 nm wavelength fiber-coupled into a 105 µm core provided the overall pump power of up to 120 W. We studied also a larger aperture Yb:YAG rods with unguided pump propagation of up to 140 W at 940 nm and 100 W at 969 nm wavelength. The main goal of our investigation was to optimize the first cascade of pumping source for 1 TW class optical parametric chirped pulse amplification (OPCPA).

The seed source was based on all-in-fiber passively mode-locked oscillator generating spectrally broadened to 3.8 nm and temporally stretched to ~ 0.2 ns pulses at 1030 nm wavelength. An acousto-optic modulator was used as a pulse picker to control pulse repetition rate in the range of 10 – 500 kHz. These pulses were further amplified up to ~ 500 mW of average power in Yb-doped fiber. Maximum pulse energy was limited to 14 uJ at 21 kHz repetition rate by nonlinear phase distortion in the amplifier.

Collimated seed beam of ~ 0.4 mm diameter was directed to SCF: Ø 1 × 40 mm, 1 % at. or larger aperture Yb:YAG rods: 5 × 5 × 5 mm^3 5 % at., 5 × 5 × 20 mm^3 and 2 × 2 × 20 mm^3 2 % at. bonded to the water-cooled copper heat sink set at 15°C. Single or two fiber coupled laser diodes formed the waist of ~ 0.42 mm diameter at ~ 4 ÷ 5 mm depth inside the crystal. Faraday isolators were used for seed source protection and for decoupling the 2nd pass of amplified output. Induced thermal lens was compensated by tuning the distance between the spherical mirror and laser rod.

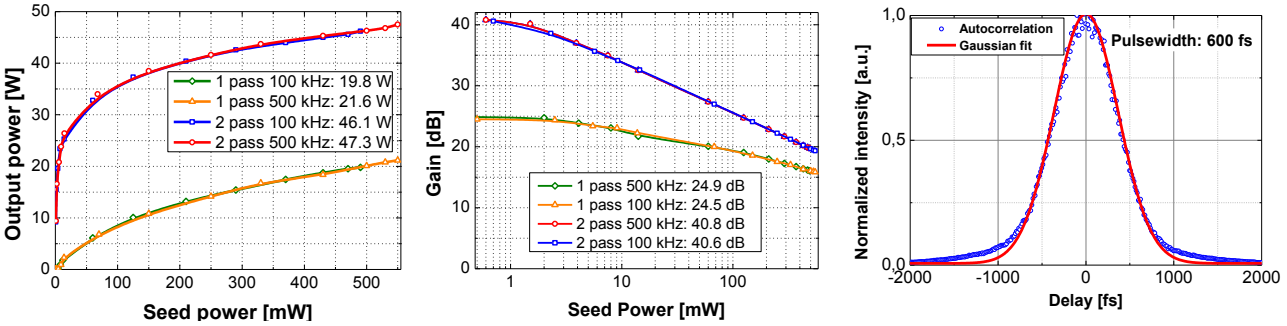

Fig. 1 Output power (left) and gain (centre) versus seed power and autocorrelation trace of compressed pulse (right).

Yb:YAG CPA based on 2 × 2 × 20 mm^3 rod doped 2 % at. surpass the commercially available Yb:YAG SCF in terms of gain and optical-to-optical conversion efficiency while ensures nearly the same output beam quality with low spherical aberration. We achieved the amplified output of up to ~ 30 W in SCF with optical-to-optical efficiency of ~ 27 % and up to ~ 50 W (Fig.1 – left) in the larger aperture rod with ~ 38 % efficiency both featuring a beam quality of M^2 ~ 1.1. The output pulses of ~ 3.5 mJ energy were attained from Yb:YAG rod at 10 kHz repetition rate. The same CPA pumped with ~ 87 W at 969 nm wavelength ensures ~ 19 W output with ~ 21 % optical-to-optical efficiency and M^2 ~ 1.06.

Despite the gain narrowing to ~ 1.8 nm, we obtained ~ 600 fs pulses (Fig.1 – right) with power conversion efficiency of 80 % using compressor based on diffraction grating with 1700 grooves/mm.

Unsurpassed double-pass gain of up to ~ 42 dB, amplified beam quality M^2 ~ 1.1, low cost and alignment simplicity makes the 2 × 2 × 20 mm^3 2% at. Yb:YAG rod the excellent choice for high average output power and energy CPA under pump levels below 140 W.

This work has been funded by Research Council of Lithuania under contract LAT-10/2016.

[1] A.M. Rodin, A. Aleknavicius, A. Michailovas and A.S. Dementjev, Beam quality investigation in Nd:YAG crystal fiber amplifier pumped at > 110 W, Proc. SPIE, vol. 9342, High-Power, High-Energy, and High-Intensity Laser Technology (2015), http://dx.doi.org/10.1117/12.2079294
[2] A.M. Rodin, N. Rusteika et al., 30W thin Yb:YAG rod chirped pulse amplifier with high output beam quality, Conference on Advanced Solid State Lasers, OSA Technical Digest, Paper JTu2A.11, Boston, USA (2016), https://doi.org/10.1364/ASSL.2016.JTu2A.11
[3] W. Koechner and M. Bass, Solid-state lasers: a graduate text, Springer-Verlag, New York (2003).

RESEARCH OF CERAMIC Yb:YAG LASER GENERATION AND SPECIFICATIONS

Justas Girskis, Valerijus Smilgevičius

Department of Physics, Vilnius University, Lithuania
Justas.Girskis@ff.stud.vu.lt

Transparent laser ceramics are acknowledged as the potential replacements for single-crystals counterparts with several remarkable advantages such as easy fabrication, high concentration [1]. Therefore, the ceramics have a higher resistance to thermal shock than single crystal, making them more suitable for high intensity laser pumping [2].

The goal of this work were to approach the difference between Yb:YAG monocrystalline and ceramic CW lasers, to conduct a literature review on the basics of laser technologies. This experiment was conduct using a 10% monocrystalline Yb:YAG with 100,4mm optical resonator (fig 1).

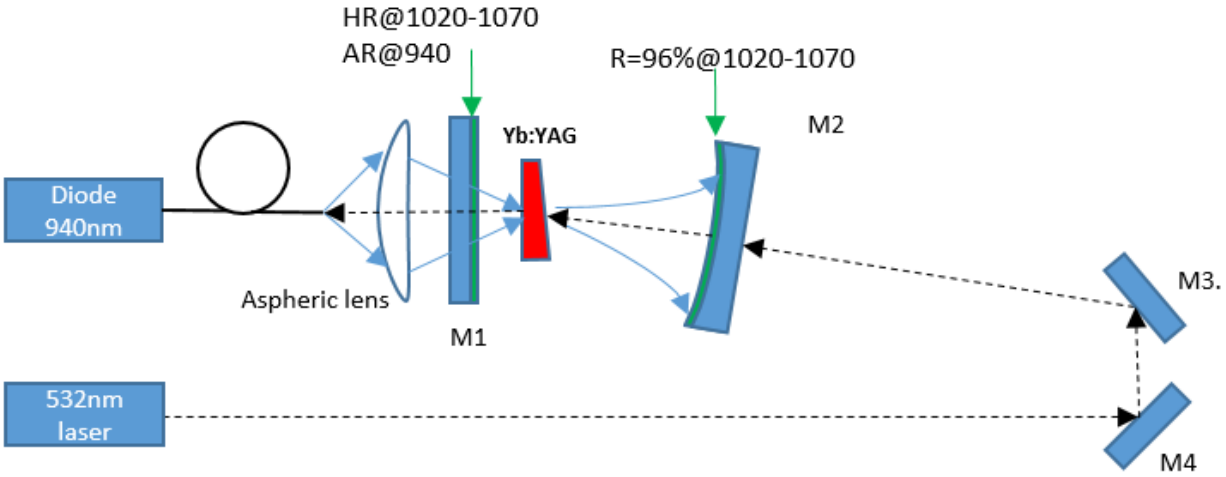

Fig 1. Experimental setup of diode pumped Yb:YAG ceramic lasers: M1, Plano mirror, R = ∞; M2, output coupler, R = -202mm, M3, M4, Yb:YAG ceramic, 10 at %, Ø8 × 2,5 mm.

During this attempt a 1,61W generation threshold and a 1W output power were reached with laser efficiency of 22,5%. In order to compare a monocrystalline with polycrystalline, a 10% Yb:YAG ceramic was used. During this attempt a 2,36W generation threshold and 130mW output power were achieved with laser efficiency of 2,3%. Furthermore, output beam were linear polarized and 15 fold difference between polarization waves was got.

[1] Qiang Hao, Wenxue Li, Haifeng Pan, Xiaoyi Zhang, Benxue Jiang, Yubai Pan, Heping Zeng, Laser-diode pumped 40-W Yb:YAG ceramic laser, Optics Express, Vol. 17, No. 20, (2009).
[2] X. J. Cheng, B. X. Jiang, L. Li, J. L. Wang, Zh. G. Yang, W. B. Cheng, X. Ch. Shi, Y. B. Pan, Diode Pumped Active-Mirror Yb:YAG Ceramic Laser, Laser Physics, 2012, Vol. 22, No. 4, pp. 652–655, (2012)

RADIATION DYNAMICS OF SPACE-DISTRIBUTED MODEL SOLID-STATE LASER WITH HIGH DEFINITION

Sergey Grigoryev

Department of Physics, Belarusian State University, Belarus
sergey.grigoryev.16@gmail.com

One of the most important problems in modern laser physics is the optimization of laser structure and operational regimes relative to concrete range of applications. For a comprehensive solution of such problems it is necessary to utilize rather detailed theoretical models [1].

There are two types of approaches that usually are exploited in practice. The first one, which is usually named as a point (or averaged) model, uses variables averaged over a resonator volume to consider laser dynamics problems. This kind of model is evidently acceptable in the case when variables distributions over the resonator volume are near to a uniform one. The second type of models (the so-called travelling wave approach) can be appropriate for strong inhomogeneous distributions of laser variables, but the known models consider only steady-state regimes [1, 2].Today, space-distributed (the second type) model is the most detailed that we could handle.

But at the same time when using this model there is another problem - the complexity of the calculations.

Using parallel evaluations is one of the ways to solve this. This way could be reached great increasing of calculation powers. Results of implementation parallel evaluation in research of radiation dynamics of space-distributed model solid-state laser with high definition presented in Fig. 1.The same system were solved with different number of kernels that took part in evaluation.

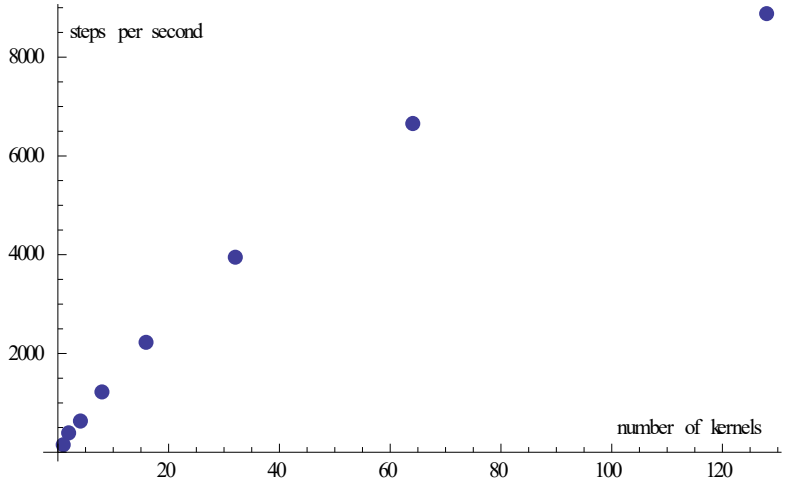

Fig. 1. Number of evaluated numerical grid steps per second with different number of active kernels.

[1] M. Belov, L. Burov, L. Krylova, Influence of the Cr4+:YAG saturable absorber parameters on output characteristics of the Nd3+:LSB laser in Q-switched regime,Nonlinear phenomena in complex systems, vol. 18, no. 2, 2015, pp. 140 - 148.

[2] P. Peterson, Dynamics of passively Q-swiched microchip lasers, IEEE journal of quantum electronics, vol. 35, no. 8, 1999.

OPTICAL PARAMETRIC AMPLIFICATION EXITED BY SPATIALLY INCOHERENT CONICAL RADIATION

Domas Kudarauskas

Department of Quantum Electronics, Vilnius University, Saulėtekio Avenue 10, LT-10223 Vilnius, Lithuania
domas.kudarauskas@ff.stud.vu.lt

The generation and amplification of spatially coherent light waves using spatially incoherent pump is a tempting solution for simplifying and lowering cost of optical parametric systems. The generation and amplification of spatially coherent waves by parametric frequency down- and up- conversions were achieved [1,2]. When conical, also known as Bessel, beam is used as a pump source, in degenerate case, signal and idler waves separates in space. The geometry of separation is determined by noncolinear phase matching. If coherent seed is injected into the axis of a pump cone, it is coherently amplified and spatially incoherent idler cone is generated. This geometry of waves allows one to filter out idler with a simple aperture.

In this thesis it is shown that spatially coherent seed injected in optical parametric amplifier (OPA), exited by spatially incoherent conical radiation, is coherently amplified and all of the pumps incoherency is transferred to idler wave.

Experimental setup was based on diode-pumped Nd:YAG laser emitting 1064 nm 50 ps pulses at 1 kHz repetition rate. Second harmonic of mentioned pulses was used for OPA excitation and fundamental harmonic for the injected seed. Bessel beam was formed using glass axicone with the cone angle equal to 0,067 rad. The beam radius before axicone was 800 μm and the parameter defining quality of Bessel beam (ratio of ring radius to ring width) was ~170. Optical parametric amplification was achieved in 10 mm long nonlinear KTP ($KTiOPO_4$) crystal with 220 μJ pump and 40 nJ seed pulses. When coherent conical pump radiation was used and seed with spatial spectral width of 7,3 mrad was injected, parametrically amplified signal and idler cone were obtained having spatial spectral widths of 4,8 mrad and 3 mrad respectively. When incoherent conical pump radiation was used, amplified signal with spatial spectral width of $2{,}5\ mrad$ and idler cone with spatial spectral width of $6\ mrad$ were obtained. Amplified signals spatial spectrum was with no significant distortions (see Fig. 1).

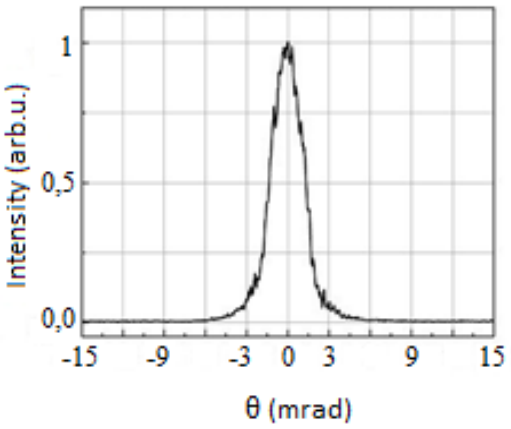

Fig. 1. Normalized spatial spectrum of the amplified signal in OPA exited with spatially incoherent conical radiation.

[1] A. Piskarskas, V. Pyragaite and A. Stabinis, Generation of coherent waves by frequency up-conversion and down-conversion of incoherent light, Phys. Rev. A 82(5), 053817 (2010).
[2] V. Pyragaite, A. Stabinis, A. Piskarskas and V. Smilgevi£ius, Parametric amplication in the eld of incoherent light, Phys. Rev. A, 87(6), 063809 (2013).

INVESTIGATION OF PASSIVELY MODE-LOCKED FIBER YB DOPED FEMTOSECOND OSCILLATOR FOR GENERATION OF PARABOLIC PULSES IN FIBER AMPLIFIER

Saulius Frankinas[1,2], Tadas Bartulevičius[1,2], Andrejus Michailovas[1,2] and Nerijus Rusteika[1,2]

[1] Ekspla Ltd., Savanoriu ave. 237, LT-02300 Vilnius, Lithuania
[2] Center for Physical Sciences and Technology, Savanoriu ave. 231 LT-02300, Vilnius, Lithuania
s.frankinas@ekspla.com

For conventional fiber chirped pulse amplification (FCPA) systems a mode-locked femtosecond laser oscillator is required [1]. Strong normal dispersion of silica glass at wavelength around 1μm limits pulse duration Yb doped fiber oscillators. Passively mode-locked fiber oscillators may be operated in the anomalous dispersion regime if dispersion compensators are introduced in the cavity [2]. The implementation of a chirped fiber Bragg grating (CFBG) as anomalous dispersion source in the cavity was demonstrated [3]. The main advantage of CFBG dispersion control in comparison with bulk optical components such as prisms or diffraction gratings is that it is realized all-in-fiber principle. Moreover chirp and reflection profile of CFBG can be specially selected to achieve solitary pulse formation.

Another important characteristics for seed pulses for FCPA are chirp profile, spectrum smoothness and temporal shape. Seed pulses must be either transform limited or have a linear chirp, which allows compression without pulse distortions. Also, spectrum of the seed pulses must be smooth, as any ripples in the spectrum will be transformed in the ripples of the temporal envelope when pulses are stretched [4]. These temporal ripples will be enhanced in nonlinear fiber amplifier [4]. Finally, temporal shape of the seed pulses also plays a role in FCPA systems. Due to accumulated nonlinear phase, conventionally defined as B integral, recompressed pulses possess side-pulse structure, due to which decreases peak power and reduces pulse contrast. This effect can be minimized by use of parabolically shaped pulses [5].

In this work we present experimental implementation of femtosecond fiber oscillator which utilizes an anomalous dispersion CFBG for dispersion control and spectral filtering. Also we demonstrate generation of parabolically shaped pulses in normal dispersion by doped fiber amplifier using this femtosecond oscillator.

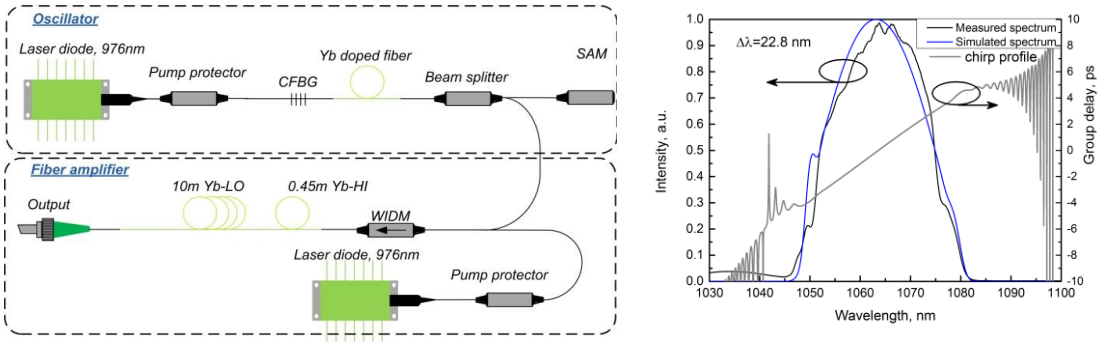

Fig. 1. The layout of experimental setup consisting of femtosecond passive mode-locked fiber oscillator and parabolic fiber amplifier (left), measured and simulated pulse spectrum at the output of system (right).

Linear cavity geometry consisting of CFBG, polarization maintaining single mode Yb doped fiber, beam splitter and saturable absorber mirror (SESAM) was used to generate ultra-short pulses. In stable self-starting single pulse mode-locking regime oscillator emits nearly bandwidth-limited pulses with duration of 380 fs and 15 pJ energy at a repetition rate of 32 MHz at 1064 nm central wavelength. Pulses from the oscillator were amplified in polarization maintaining fiber amplifier that consisted of two gain fibers with different Yb concentration (Yb-LO, Yb-HI). Oscillator pulses due to cumulative action of amplification, nonlinearity and dispersion when propagating in Yb-LO fiber were parabolic shaped. After fiber amplifier, the output pulses had energy of 1.4 nJ, duration of 6.5 ps and the spectral bandwidth of 22.8 nm. The shape of the spectrum (Fig. 1, right) was close to parabolic with typical steep edges. More detailed experimental and simulation results will be presented on a conference.

[1] K. Sumimura, H. Yoshida, et al., "Femtosecond Mode-Locked Yb Fiber Laser for Single-Mode Fiber Chirped Pulse Amplification System," Laser Physics **17**, 339-344 (2007).
[2] M. Baumgartl · B. Ortaç · et al.,"Impact of dispersion on pulse dynamics in chirped-pulse fiber lasers," Applied Physics B **107**, 263-274 (2012).
[3] Ori Katz, Yoav Sintov, "Strictly all-fiber picosecond ytterbium fiber laser utilizing chirped-fiber-Bragg-gratings for dispersion control," Opt. Comm. **281**, 2874-2878 (2008).
[4] D.N. Schimpf, E. Seise, J. Limpert, et al., The impact of spectral modulations on the contrast of pulses of nonlinear chirped-pulse amplification systems, Opt. Express. **16** 10664-10674 (2008).
[5] D. N. Schimpf, J. Limpert, A. Tünnermann, Controlling the influence of SPM in fiber-based chirped-pulse amplification systems by using an actively shaped parabolic spectrum, Opt. Express. **15** 16945-16953 (2007).

PULSE SHAPING IN YB DOPED FIBER CHIRPED PULSE AMPLIFICATION SYSTEM USING FIBER BRAGG GRATING FILTER

Tadas Bartulevičius[1,2], Andrejus Michailovas[1,2] and Nerijus Rusteika[1,2]

[1] Ekspla Ltd, Vilnius, Lithuania
[2] Department of Laser Technology, Center for Physical Sciences & Technology, Vilnius, Lithuania
tadas.bartulevicius@gmail.com

High peak power ultrashort pulse fiber lasers are usually realized using fiber chirped pulse amplification (FCPA) technique [1]. The pulses are temporally stretched to a much longer duration before passing through the amplifier medium by means of a strongly dispersive element. This reduces the peak power to a level where nonlinear pulse distortion effects in the gain medium are suppressed. After amplification laser pulses are compressed using a pair of diffraction gratings. An amplified and compressed femtosecond pulses have an enormous peak power. Due to large level of pulse amplification in fiber amplifiers a phenomenon called gain narrowing takes place. Gain narrowing is an effect caused by the peak of the pulse being amplified more than its wings, reducing the spectral width and therefore increasing the pulse duration. This effect in fiber amplifiers can be minimized with some shaping of the initial pulse [2,3]. Frequency selective optical transmitters such as fiber Bragg gratings can be designed to obtain the desired pulse shape. We investigate both numerically and experimentally the minimization of gain narrowing in Yb doped all-in-fiber FCPA system using fiber Bragg grating filter with desired transmission spectrum.

Our experimental setup consisted of passively mode-locked all-in-fiber picosecond oscillator (1030.4 nm center wavelength, 25 pJ pulse energy). Spectrum of the laser pulses from the oscillator was broadened to 12 nm bandwidth by self-phase modulation in passive fiber and the pulse duration was stretched to about 430 ps by using chirped fiber Bragg grating. Broad spectrum enables to achieve laser pulses of hundreds of femtoseconds in duration in the output of the system. A spectral hole was made in the central part of pulse spectrum using fiber Bragg grating filter with desired transmission spectrum. In our work we investigated separate cases using two different kind of Yb-doped fibers for power amplifier: 10 µm core diameter polarization maintaining large mode area (LMA) fiber and 40 µm core diameter single mode photonic crystal fiber (PCF). Spectrally filtered pulses were amplified up to 1 µJ and 22 µJ pulse energy in these power amplifiers respectively. The minimization of gain narrowing effect was estimated. Pulse spectrum narrowed up to 8 nm and 7.8 nm at energies 1 µJ and 22 µJ respectively due to gain narrowing when no pulse shaping took place. Pulse spectrum was broadened to 12.7 nm (1 µJ) and 11 nm (22 µJ) minimizing gain narrowing effect using fiber Bragg grating filter. The pulse spectrum of shaped and not shaped pulses can be seen in figure 1. Transform limited pulse duration of 196 fs at 22 µJ energy was achieved. Accordingly shorter pulses (approximately 10%) can be obtained at the output of the laser. Detailed information of the experiment and numerical calculations will be presented at the conference.

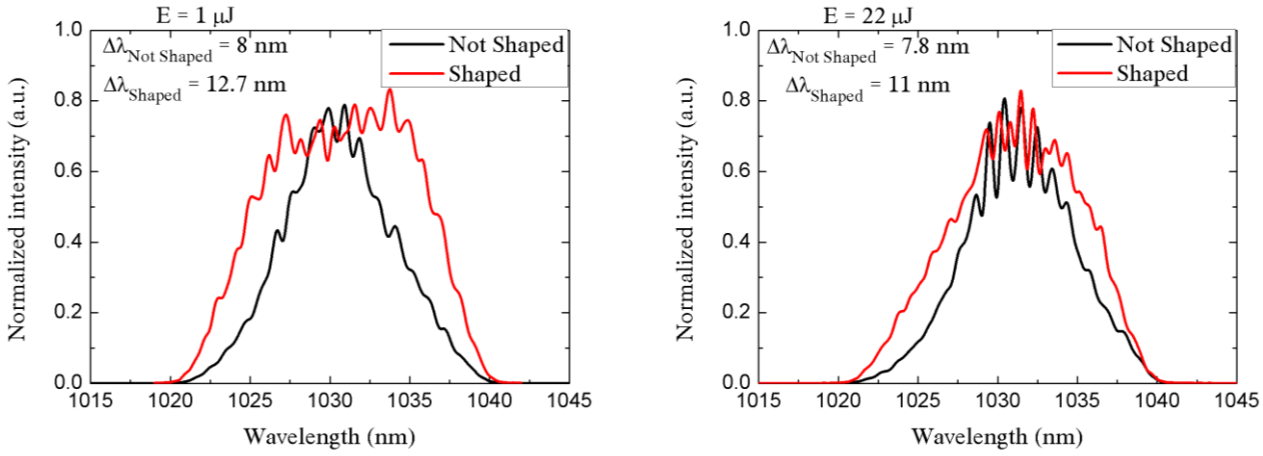

Fig. 1. The comparison of shaped and not shaped pulse spectra at 1 µJ (left) and 22 µJ (right) pulse energy in fiber chirped pulse amplification system using fiber Bragg grating filter.

[1] J. Želudevičius, R. Danilevičius, K. Viskontas, N. Rusteika, and K. Regelskis, Femtosecond fiber CPA system based on picosecond master oscillator and power amplifier with CCC fiber, Opt. Express **21**, 5338–45 (2013).
[2] D.N. Papadopoulos, M. Hanna, F. Druon, P. Georges, Compensation of gain narrowing by self phase modulation in high-energy ultrafast fiber chirped-pulse amplifiers, IEEE J. Sel. Top. Quant. **15**(1), 182-186 (2009).
[3] Y. Chiba, H. Takada, K. Torizuka, K. Misawa, 65-fs Yb-doped fiber laser system with gain-narrowing compensation, Opt. Express **23**(5), 6809-6814 (2015).

PLANE-WAVE EXPANSION MODELLING OF LASER BEAM PROPAGATION IN GYROTROPIC MEDIUM

Yuriy Pilgun

Faculty of Radio Physics, Electronics and Computer Systems, Taras Shevchenko National University of Kyiv, Ukraine
ply@univ.kiev.ua

Growing interest in vortex optics and nanoscopy stimulates development of new methods for modelling laser beam propagation though various media. Scalar theory of light propagation, while being mature and well-tested method, is badly suited for vortex beam simulations, because it doesn't take into account polarization effects. Commonly used paraxial approximation also can't be applied if there is a need to model high-aperture optics. These requirements urge us to develop a method for modelling of light propagation in full vectorial form without approximations. Here we present such a method, which is suitable to model light propagation in gyrothropic media. It is based on plane-wave expansion, where polarization direction and propagation constants of eigenmodes propagating in medium is obtained from matrix formulation of Maxwell equations [1]. We expanded the method presented in [1] to include gyrotropy, making it possible to simulate optical rotation during propagation in optically active media.

Set of Maxwell equations describing electromagnetic wave in gyrotropic media in source-free region are as follows

$$\nabla\times\mathbf{E}=-\frac{\partial\mathbf{B}}{\partial t},\quad \nabla\times\mathbf{H}=\frac{\partial\mathbf{D}}{\partial t},\quad \nabla\cdot\mathbf{D}=0,\quad \nabla\cdot\mathbf{B}=0. \tag{1}$$

$$\mathbf{D}=\varepsilon\mathbf{E}+\mathrm{i}\gamma\mathbf{H},\qquad \mathbf{B}=\mu\mathbf{H}-\mathrm{i}\gamma^{\mathrm{T}}\mathbf{E}. \tag{2}$$

According to [2], constitutive relations stated in form (2) describe both natural and induced optical activity. Natural optical activity is introduced into equations by real-valued chirality tensor γ, while induced optical activity characterized by off-diagonal imaginary components of permittivity tensor ε (or permeability tensor μ). We will consider only monochromatic field in linear, homogeneous, source-free and lossless media, but field distribution at initial plane may be arbitrary. Single plane wave is described by equation

$$\mathbf{E}(x,y,z)=E\exp[\mathrm{i}(k_x x+k_y y)]\exp(\mathrm{i}\,k_z z)\exp(-\mathrm{i}\,\omega t) \tag{3}$$

Dropping dependence on time for stationary field and focusing attention on dependence of the field on z, system of equations (1)-(2) can be restated as matrix equation

$$\frac{\partial}{\partial z}\begin{bmatrix}E_x\\E_y\\-H_y\\H_x\end{bmatrix}=\mathbf{\Delta}\begin{bmatrix}E_x\\E_y\\-H_y\\H_x\end{bmatrix}, \tag{4}$$

where matrix $\mathbf{\Delta}$ depends on media properties and projections of wavevector k_x, k_y. Equation (4) express partial derivatives of field components along z as simple matrix operator $\mathbf{\Delta}$. Advantage of such an approach is that eigenproblem associated with matix $\mathbf{\Delta}$ reveals eigenmodes of plane waves, which may propagate in medium. Solving eigenproblem

$$-\mathrm{i}\mathbf{\Delta}\psi=k_z\psi, \tag{5}$$

we obtain polarizations as eigenvectors $\psi=[E_x\quad E_y\quad -H_y\quad H_x]^{\mathrm{T}}$ and propagation constants k_z as eigenvalues of all possible modes for selected projection of wavevector (k_x; k_y). These can be readily used to decompose arbitrary field $\mathbf{E}(x, y, 0)$ into plane wave spectrum [3]

$$\mathbf{E}(x,y,z)=\int_{-\infty}^{\infty}\int_{-\infty}^{\infty}\sum_{\alpha=1}^{2}a_\alpha\mathbf{A}_\alpha(k_x,k_y)e^{i[k_x x+k_y y+k_z^\alpha z]}dk_x dk_y\,. \tag{6}$$

Amplitude of each mode a_α should be determined from Fourier transform of initial field distribution

$$\widetilde{\mathbf{E}}(k_x,k_y;0)=\frac{1}{4\pi^2}\int_{-\infty}^{\infty}\int_{-\infty}^{\infty}\mathbf{E}(x,y,0)e^{-i[k_x x'+k_y y']}dx'dy'\,. \tag{7}$$

To do full mode decomposition, linear system of equations should be solved for each combination of k_x and k_y

$$\widetilde{\mathbf{E}}(k_x,k_y;0)=\sum_{\alpha=1}^{2}a_\alpha(k_x,k_y)\mathbf{A}_\alpha(k_x,k_y)\,. \tag{8}$$

By taking full range of k_x and k_y we make sure that field is fully described and both evanescent and propagating modes included for every polarization. Presented approach combine well-known plane-wave expansion method with matrix formalism, which simplifies finding of eigenmode parameters, thus allowing to implement computationally effective algorithm for modelling laser beam propagation in gyrotropic media. The method include all polarizations and the resulting field is obtained without approximations.

[1] D. W. Berreman, Optics in Stratified and Anisotropic Media: 4×4-Matrix Formulation, J. Opt. Soc. Am. **62** (4), 502-510 (1972).
[2] F. I. Fedorov, *Theory of Gyrotropy* (Nauka i Tekhnika, Minsk, 1976) [in Russian].
[3] Yu. Pilgun, E. Smirov, Plane-wave expansion based modelling of laser beam propagation in anisotropic medium, Proceedings of IEEE 7th International Conference on Advanced Optoelectronics and Lasers (CAOL 2016), Odessa, Ukraine (12-15 September 2016) [in Press].

OPTICAL FOCAL LINE ENGINEERING METHODS USING VECTOR BESSEL BEAMS

Alfonsas Juršėnas, Sergejus Orlovas

Center for Physical Sciences and Technology, Industrial laboratory for photonic technologies,
Sauletekio av. 3, Vilnius, Lithuania
alfonsas.jursenas@ff.stud.vu.lt

Three dimensional shaping of focused laser beam is of great importance in many modern laser fields. Long focal lines with transverse spot sizes as small as a few wavelengths are called optical needles [1]. Polarization control of the electric field in the optical needle is the next step towards engineering of focal lines suitable for applications, where the orientation of electromagnetic field is important. Optical needles with almost pure longitudinal polarization have a potential application in direct acceleration of charged particles [2].

In this work we consider the formation of optical needle by superposition of monochromatic vector Bessel beams. The longitudinal profile of intensity is fully controlled, while transverse – partly. Vector beams were obtained from scalar Bessel beams using method described in [3]. Firstly, we analyse how combination of topological number *m* and polarization of Bessel beams controls an on-axis orientation and localization of electric field. We demonstrate a successfully achieved control of intensity pattern for three different polarizations: two transverse and one longitudinal. Focal lines, created by superposition of linearly, radially or circularly polarized vector Bessel beams with m=0, have central spots (full width at half maximum) smaller than a wavelength of the beam at certain Bessel cone angles. Furthermore, we get that linear superposition of circularly and radially polarized vector Bessel beams with different topological numbers form focus with almost pure transverse polarization. An example of superposition of twenty radially polarized Bessel beams with m=0, having predefined longitudinal profile of intensity, is shown in Fig. 1.

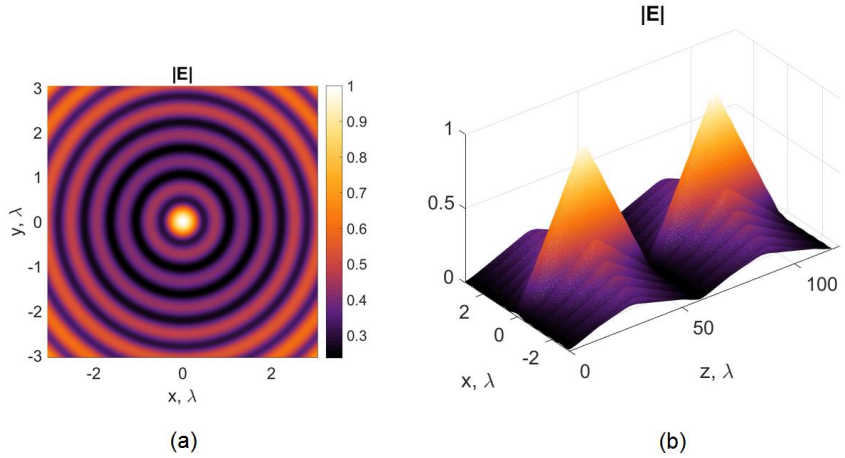

Fig. 1 Transverse (a) and longitudinal (b) distribution of electric field of the superposition result of vector Bessel beams. Axes are normed to the wavelength of the beam.

In conclusion, a method of optical engineering of focal lines will be presented. Examples of calculated intensity profiles with linear focus will be demonstrated. Experimental implementation using spatial light modulators or alternative techniques will be also discussed.

[1] M. Zhu, Q. Cao, H. Gao, " Creation of a 50,000 λ long needle-like field with 0.36 λ width, " JOSA A 31(3), 500–504 (2014).
[2] P. Fortin, M. Piche, C. Varin, " Direct-field electron acceleration with ultrafast radially polarized laser beams: scaling laws and optimization, " J. Phys. B **43** (2009).
[3] J. Stratton, *Electromagnetic Theory*, An IEEE Press classic reissue (Wiley, 2007).

CONVERSION OF ORBITAL-TO-SPIN ANGULAR MOMENTUM OF LIGHT UNDER FOCUSING: THEORETICAL ANALYSIS AND EXPERIMENTAL VERIFICATION

Sergej Orlov[1], Paulius Slevas[2], Valerijus Smilgevicius[2]

[1.] Center for Physical Sciences and Technology, Industrial Laboratory for Photonic Technologies, Saulėtekio 3, LT-10257, Vilnius, Lithuania
[2.] Vilnius University, Department of Quantum Electronics, Sauletekio 10, LT-10223, Vilnius, Lithuania
paulius.slevas@ff.stud.vu.lt

Light can carry linear momentum and together with Angular momentum they are the most important characteristics of light. Photons may possess two distinguishably different types of angular momentum: spin angular momentum (SAM) and orbital angular momentum (OAM). SAM depends on polarization helicity, whereas OAM depends on the vortex charge [1].

It can be expected that some kind of spin-orbit interaction may occur under certain circumstances. For instance, focusing of circularly polarized light by a high-numerical-aperture lens, scattering by a small particle, or in some cases under paraxial propagation in optical fibers and anisotropic crystals a spin-dependent optical vortex (that is, a helical phase) can be generated [2].

Here we present an opposite conversion mechanism, where OAM is converted into SAM under focusing conditions. Our experimental results are based on interferential method and they are in a good agreement with theoretical complex source beam model of optical vortices which also predicts that type of conversion [3].

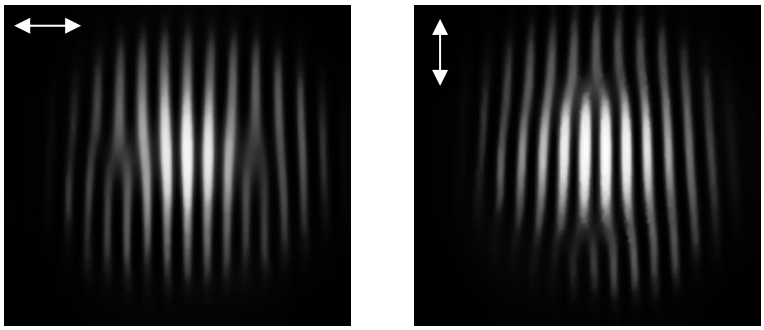

Fig. 1. Interference patterns of a focused radially polarized vortex beam arrows indicates polarization of a reference Gaussian beam. This shows that a radially polarized LG10 mode transforms to LG01 mode

[1] Bliokh K Y, Ostrovskaya E a, Alonso M a, Rodríguez-Herrera O G, Lara D and Dainty C 2011 Spin-to-orbital angular momentum conversion in focusing, scattering, and imaging systems. *Opt. Express* **19** 26132–49
[2] Bliokh K Y, Rodríguez-Fortuño F J, Nori F and Zayats a. V 2015 Spin-orbit interactions of light *ArXiv* **9**1505.02864
[3] Orlov S and Banzer P 2014 Vectorial complex-source vortex beams *Phys. Rev. A* **90** 23832

ANALYSIS OF PULSED VECTOR BESSEL BEAMS

Ada Gajauskaite[1,2], Sergejus Orlovas[1]

[1] Center for Physical Sciences and Technology, Sauletekio av. 3, Vilnius, Lithuania
[2] Department of Quantum Electronics, Faculty of Physics, Vilnius University
ada.gajauskaite@ff.stud.vu.lt

Nondiffracting Bessel beams are known to maintain transverse shape during propagation in large distances compared to Gaussian beams [1]. Superposition of Bessel beams with different frequencies and amplitudes results in nondiffracting pulses, which can propagate without dispersive spreading in linear dispersive medium and exhibit interesting properties such as superluminal velocity [2]. Vector nature of nondiffracting pulses becomes important when angles of plane waves in angular spectrum become large. Linearly polarized vector Bessel X pulses was introduced in [3] and an appearance of longitudinal and cross-components was observed.

In this work we analyse azimuthally and radially polarized nondiffracting vector Bessel X pulses. Analytical solution of scalar Bessel X pulses with near Gaussian frequency spectrum was used [4]. We obtain vector solutions from the scalar ones using method described in [5]. Electric field in transverse electric mode is always orthogonal to propagation direction of the pulse and represents azimuthal state of polarization. Electric field in transverse magnetic mode points along radial vector and thus in this mode pulses are radially polarized. Properties of obtained pulses with different Bessel cone angles and widths of frequency spectrum were analysed. Vector Bessel X pulses with nonzero topological charge (m) are also studied in detail. In case m=0, the distribution of electric field of the azimuthally polarized Bessel X pulse is shown in Fig. 1.

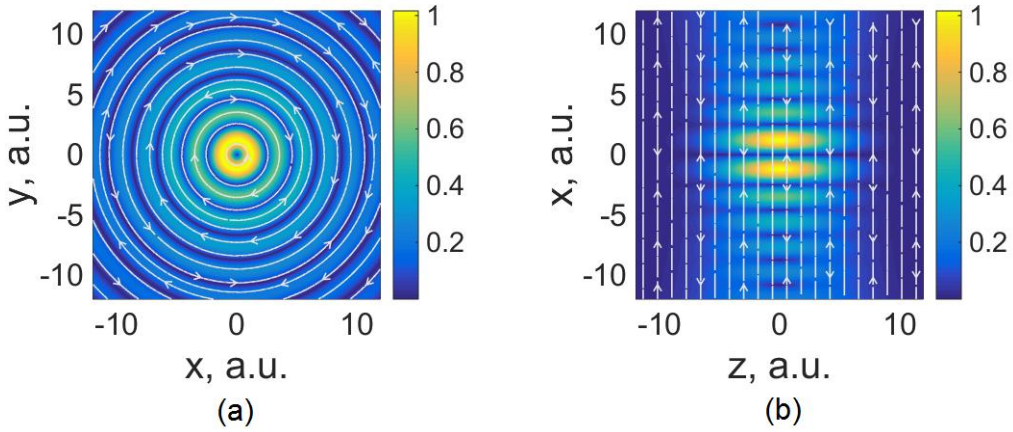

Fig. 1 Distribution of electric field of azimuthally polarized pulsed vector Bessel beam in (a) transverse and (b) longitudinal planes. Arrows show the direction of electric field.

Furthermore, radially polarized nondiffracting Bessel pulses have nonvanishing longitudinal component of electric field, which is concentrated at the center of the beam. Relative magnitude of longitudinal component compared to transverse components can be increased by changing the angle of Bessel cone.

[1] J. Durnin, "Exact solutions for nondiffracting beams, I. The scalar theory," J. Opt. Soc. Am. A **4**, 651 (1987).
[2] P. Saari, and K. Reivelt, "Evidence of X-shaped propagation-invariant localized light waves," Phys. Rev. Lett. **79**, 4135 (1997).
[3] M. Ornigotti, C. Conti and A. Szameit, "Universal form of the carrier frequency of scalar and vector paraxial X waves with orbital angular momentum and arbitrary frequency spectrum," Phys Rev. A **92**, 043801 (2015).
[4] P. Saari, and H. Sonajalg, "Pulsed Bessel beams," Laser Phys. **7**, 32-39 (1997).
[5] P. M. Morse and H. Feshbach, *Methods of theoretical physics*, (McGraw-Hill, New York, 1953).

BESSEL BEAMS AND FOCAL LINE ENGINEERING FOR LARGE SCALE PHOTONIC THRUSTERS

Pavel Gotovski, Sergejus Orlovas

Center of Physical Sciences and Technology, Industrial Laboratory for Photonic Technologies, Lithuania
pavel.gotovski@ff.stud.vu.lt

Laser propulsion became recently a hot topic due to the so-called "Breakthrough Initiative" led by a group of prominent scientists. Photonic thrusters for a long time have been recognized as very efficient for a propulsion of objects with speeds near to the speed of light c. However, they were also considered as quite inefficient due to their low specific thrust at low speeds [1]. Recently, this was addressed with introduction of a so-called "photon recycling" – situation, when a photon bounces many times inside a resonator, where one (moving) mirror is placed on a spacecraft and the second one remains static (see Fig 1(a)) [2]. Thus, a photonic thruster became a viable candidate for the "Breakthrough Initiative".

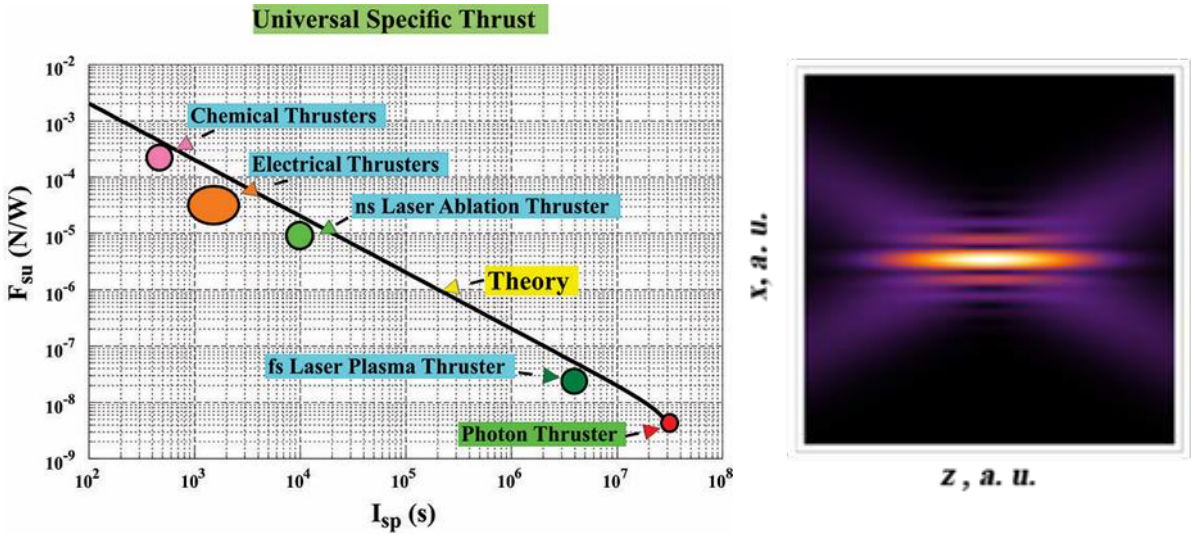

(a) (b)

Fig. 1. (a) The overall specific thrust (thrust to power ratio) of representative propulsion systems, (b) Bessel-Gauss longitudinal intensity distribution.

A combination of beams exhibiting long focal lines are called optical needles [3, 4]. Nondiffracting Bessel beam is a common example of the optical field, which can be perceived as an optical needle, (see Fig 1(b)). Here, we investigate a photonic thruster, enabled by a large scale Bessel-Gaussian beam. Such Bessel based photonic thruster can provide either constant or controllable thrust over large distances. In contrary, the thrust provided by a Gaussian impulse beam is decreasing as the spaceship moves away.

Further we analyze, how the combination of monochromatic superpositions of Bessel-Gaussian beams can be utilized to construct a desired on-axis distribution of the photonic thrust. We demonstrate our achievements in the control of photonic thrust and compare obtained efficiencies with that of a fundamental Gaussian mode.

Moreover, we discuss a practical implementation technique, which enables us not only to estimate sizes and shapes of photonic structures, but we discuss how to further optimize both the photonic thrust and its efficiency.

[1] Young K. Bae, "Prospective of Photon Propulsion for Interstellar Flight", Physics Procedia **38**, 253–279 (2012).

[2] Bae, YK. Photonic Laser Thruster (PLT): Experimental Prototype Development and Demonstration, AIAA 2007-6156-318, Space 2007 Conference Proceedings, (2007).

[3] H. Wang, L. Shi, B. Lukyanchuk, C. Sheppard, C. T. Chong, „Creation of a needle of longitudinally polarized light in vacuum using binary optics", Nature Photonics 2(8), 501–505 (2008).

[4] M. Zhu, Q. Cao, H. Gao, "Creation of a 50,000 λ long needle-like field with 0.36 λ width", JOSA A 31(3), 500–504 (2014).

PROPERTIES AND APPLICATION OF SPIRAL STRUCTURE IN THZ RANGE

Karolina Liebert, Martyna Rachon, Jaroslaw Suszek, Artur Sobczyk, Jaroslaw Bomba, Maciej Sypek.

Faculty of Physics, Warsaw University of Technology, 75 Koszykowa Str. 00-662 Warsaw, POLAND
Karolina.liebert@gmail.com

THz radiation, have many positive aspects such as non-ionizing radiation characteristics which means it is no harm to people, moreover it has the ability to pass through non-metallic minerals and dry substances. Therefore, there are many potential applications for this range of frequencies . However, existing sources of THz radiation have low power. Therefore, there is room for improvement in signal detection to obtain the best signal-to noise ratio possible.

It is not determined which part of the detector collect most of the incident light. The aim of this study is to test whether the pyroelectric antenna detects better illuminated by radiation in shape of the ring. To focus light into ring spiral lenses was modeled and 3D-printed.

The modeling of the optical element was carried out on arrays 4096 x 4096 pixels with the sampling 117 µm x 117 µm. It was designed for the frequency of 300 GHz (DWL 1 mm). Optical element was a spiral structure of dimeter 50 mm and focal length 50 mm.

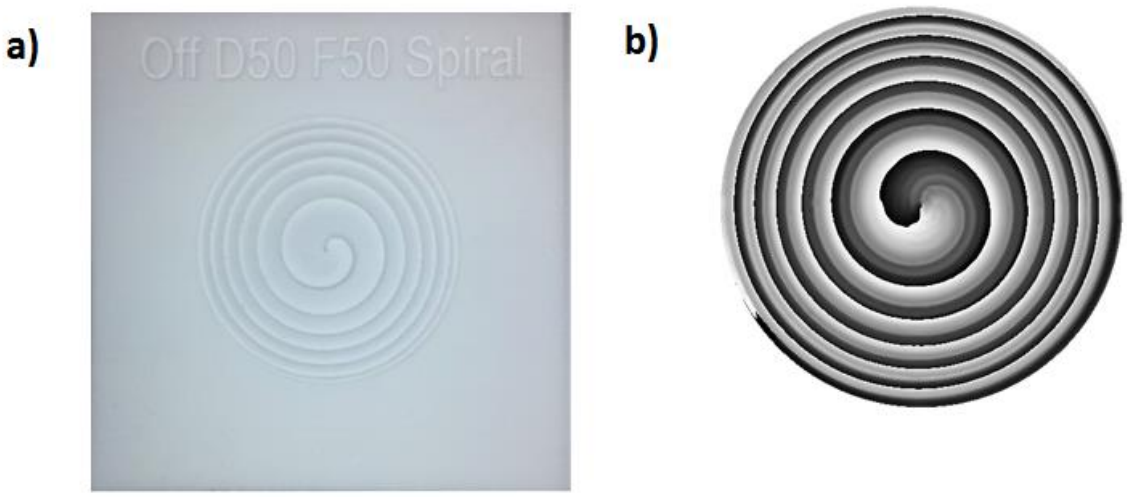

Fig. 1 a) Phase of designed structure. b) Phase of real structure.

SUB-WAVELENGTH CODING TECHNIQUE FOR THZ DIFFRACTIVE LENS

Martyna Rachon, Karolina Liebert, Jaroslaw Suszek and Maciej Sypek

Faculty of Physics, Warsaw University of Technology, 75 Koszykowa Str. 00-662 Warsaw, POLAND
rachon@if.pw.edu.pl

Terahertz frequencies are one of the most promising ranges of electromagnetic waves in these days. There are many applications in which these specific wavelengths are used because of the unique spectrum of multiple chemicals in that range. Through telecommunications, observations of space and widely understood security devices such as THz postal scanner or airports security gates. The development of these technologies is slowed due to poor performance and information-to-noise ratio of THz sources available on the market. Hence it is very important to collect as much incident light as possible and focus it onto a detector. To efficiently collect the incident light large aperture of the diffractive structure is needed. For lens to be compact and useful, it should be located as close to the detector as possible. Hence, it is necessary to create lenses with a diameter greater than the focal length. With this type of parameters lenses modulated with paraxial approach has low efficiency. It can however be increased by the use of the non paraxial approximation, and application fill-factor type of phase structure on the edge of the lens. This poster will present modeling and optimization of the structure and it performance results.

INVESTIGATION OF FEMTOSECOND LASER INDUCED CHEMICAL ETCHING OF FUSED SILICA

Mindaugas Juodėnas[1], Tomas Tamulevičius[1, 2], Linas Šimatonis[1], Sigitas Tamulevičius[1, 2]

[1] Institute of Materials Science, Kaunas University of Technology, Lithuania
[2] Department of Physics, Kaunas University of Technology, Lithuania
mindaugas.juodenas@ktu.lt

Ultra-short laser pulse interaction with matter is a fascinating field that has attracted a lot of attention over the recent years [1]. High peak power, ultra-short electromagnetic pulses interact with matter in a non-linear way, thus creating potential for advanced micro-machining technologies to emerge. A lot of effort has recently been given for investigation of femtosecond laser induced modifications in transparent materials [2, 3]. It relies on non-equilibrium process with photon beams and this provides new access to create materials and micro-devices that cannot be obtained by other means [4]. One of the approaches for such fabrication is femtosecond laser induced chemical etching (FLICE).

Using this technique, a tightly focused femtosecond laser beam is scanned inside a transparent material, drawing an arbitrary shape. Due to non-linear interaction, part of the light is absorbed. This alteration of the material changes its etching selectivity – laser illuminated silicon rich areas become soluble in KOH or HF. By providing proper windows for the etchant to reach laser-exposed parts within the bulk of the material, any arbitrary 3D shape can be fabricated inside a transparent material. However, there are plenty of laser writing parameters to consider when searching for optimal fabrication speed, as both laser writing and subsequent etching are rather time consuming processes. This research is dedicated to figure out the dependencies of pulse density, scanning speed and pulse energy on the etching rate in KOH.

As described in literature [4], three types of transparent material alterations are possible – a slight refractive index change when the pulse energy is below the necessary threshold, formation of nanostructures when it is above the threshold and finally void formation when the pulse energy is exceedingly large. The second type modifications demonstrate reasonable etch selectivity. Fig. 1 and 2 depict channels in fused silica etched by KOH after a single-pass scan of individual lines using a second harmonic of Yb:KGW femtosecond laser PHAROS (Light Conversion) and XYZ sample translation performed with laser microfabrication setup FemtoLAB (Altechna R&D). Thus achieved validation of FLICE technique will enable to further investigate non-linear processes of light-matter interaction and develop an advanced technology for realization of novel 3D microfluidic channels towards lab-on-a-chip devices.

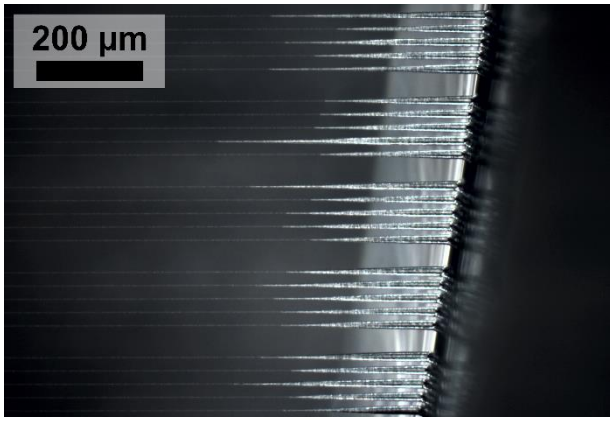

Fig. 1. Optical microscope dark field micrograph of etched channels in fused silica

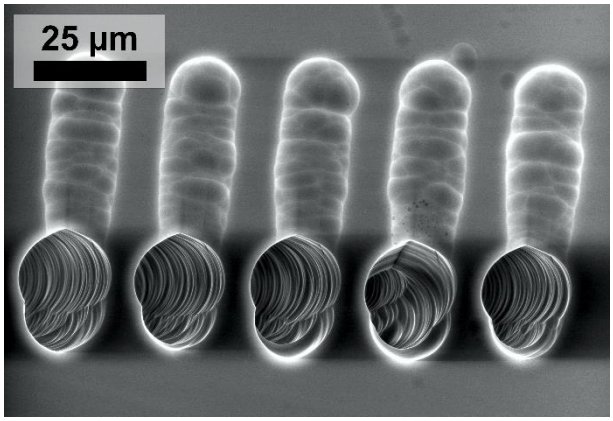

Fig. 2. Scanning electron microscope micrograph of side view of etched channels in fused silica

This research was partly supported by Kaunas University of Technology Interdisciplinary Project No. PP35/161.

[1] K. Sugioka, J. Xu, D. Wu, et al., Femtosecond laser 3D micromachining: a powerful tool for the fabrication of microfluidic, optofluidic, and electrofluidic devices based on glass, Lab on a Chip, **14**, 3447-3458 (2014)
[2] M. Beresna, M. Gecevičius, P. G. Kazansky, Ultrafast laser direct writing and nanostructuring in transparent materials, Advances in Optics and Photonics, **6,** 293-339 (2014)
[3] R. R. Gattass, E. Mazur, Femtosecond laser micromachining in transparent materials, Nature Photonics, **2**, 219–225 (2008)
[4] D. Tan, K. N. Sharafudeen, Y. Yue, et al., Femtosecond laser induced phenomena in transparent solid materials: Fundamentals and applications, Progress in Materials Science, **76**, 154–228 (2016)

FORMATION OF PERIODIC GRATINGS IN STAINLESS STEEL USING FEMTOSECOND LASER INTERFERENCE ABLATION

Linas Šimatonis[1], Artūras Grabusovas[1], Tomas Tamulevičius[1,2]

[1] Institute of Materials Science, Kaunas University of Technology, Lithuania
[2]Department of Physics, Kaunas University of Technology
simatonislinas@gmail.com

Laser ablation is a micro-structuring method where sample is irradiated with high energy fluence ultra-short pulses. High amount of energy is then transferred to the atoms in the material allowing the direct transition from solid state to plasma. By using pulses that have durations of hundreds of femtoseconds the temperature diffusion cannot occur. This way the material is ablated only in the region of irradiation enabling one to create fine structures [1, 2]. Resolution of patterns is diffraction limited and can be overcome only by using interference.

Optical security tags with holographic effects, i.e. arrays of diffraction gratings are used for anti-counterfeiting applications. They are commonly created in light sensitive materials (e.g. photoresists). After many technological steps the final shim is obtained and is used for high throughput replication process in reflective films via mechanical embossing. However, this method can be applied only in relatively soft materials like polymer films.

During current research, Yb:KGW femtosecond laser Pharos (Light Conversion) and micromachining workstation FemtoLAB (Altechna R&D) were employed to create arrays of 60x60 µm squares that contained micrometer pitch interference pattern in stainless steel. Square shape was formed by using square aperture on the expanded beam. Second harmonic (515 nm) laser beam was split into two employing diffractive optical element and then re-focused on the surface of stainless steel sample to create interference field. Circular polarization was chosen to avoid formation of self-reorganized ripple structures [3]. Each square contains a grating of 1.3 µm pitch.

2D array of squares ablated using different parameters was fabricated. In one direction of the array laser fluence was changed. In the other – number of pulses was varied. Different laser ablation effect dependence on combination of these two parameters was observed.

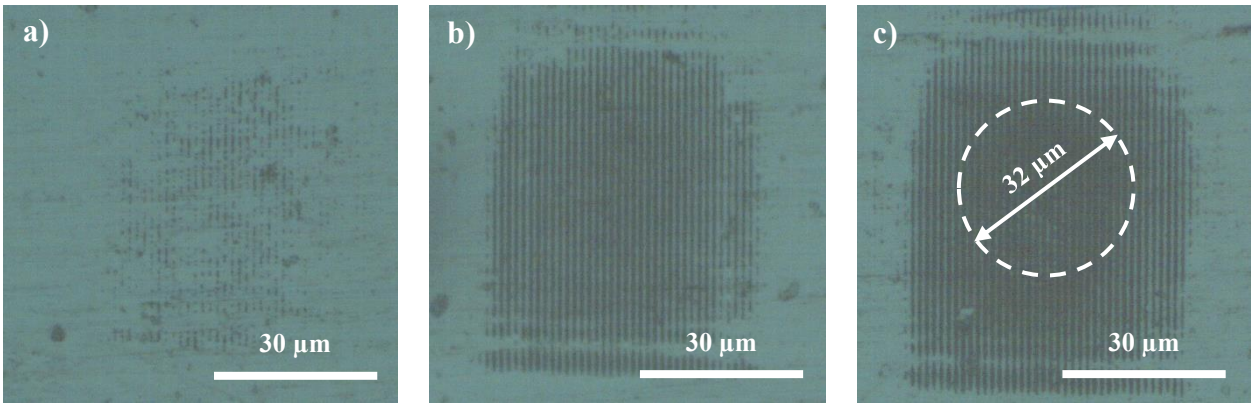

Fig. 1. Squares ablated in stainless steel with 4900 pulses at 40 kHz pulse repetition rate with laser fluence: a) 3.3 J/cm^2 b) 5.1 J/cm^2 c) 6.6 J/cm^2

Two different modes of laser ablation were observed. Using laser fluence higher than 1.1 J/cm^2 the first ablated randomly dispersed lines starts to occur (Fig. 1 a). By increasing the laser fluence the pattern becomes homogenous over all surface (Fig. 1 b). Such patterns provide highest diffraction efficiency of reflected non-zero diffraction maxima. When the fluence reaches 5.1 J/cm^2 strongly ablated pattern occurs at the center of the area (Fig. 1 c). This could be explained as non-uniform Gaussian beam intensity distribution over the aperture. The ablation threshold of the interference was determined at this fluence. The squared diameter of strongly ablated area has logarithmic dependence on pulse fluence. [4-6]. The ablation threshold dependence on the number of pulses was also observed. However, even with a few pulses the undesirable strong ablation area in the middle of the sample occurred while desirable pattern is still weak. The most promising pattern was fabricated with 5 J/cm^2 using from 1000 to 5000 pulses.

[1] D. Bauerle, *Laser Processing and Chemistry* (Springer, Berlin, 2000)
[2] W. M. Steen, *Laser Material Processing, 3rd ed*. (Springer, London, 2003)
[3] G. D. Tsibidis, E. Skoulas, E. Stratakis, Ripple formation on Nickel irradiated with radially polarized femtosecond beams, Opt Lett. **40**, 5172-5175 (2015)
[4] D. Ashkenasi at al., Surface damage threshold and structuring of dielectrics using femtosecond laser pulses: the role of incubation, Applied Surface Science **150**, 101-105, Elsevier, (1999)
[5] A. Ben-Yakar, R. L. Byer., Femtosecond laser ablation properties of borosilicate glass, Journal of Applied Physics **96**, 5316-5323, (2004)
[6] J. Byskov-Nielsen, et al. Ultra-short pulse laser ablation of metals: threshold fluence, incubation coefficient and ablation rates, Applied Physics A **101**, 97-101, (2010)

SUB-WAVELENGHT PERIODIC STRUCTURES AND THEIR FORMATION BY DIRECT LASER INTERFERENCE PATTERNING

Jonas Berzinš

Center for Physical Sciences and Technology, Lithuania
TNO Delft, the Netherlands and Friedrich-Schiller-Universität Jena, Germany
jonasberzins@gmail.com

Sub-wavelength periodic structures, also known as metamaterials, are uniquely designed structures that allow us to manipulate the electromagnetic waves and their properties. This brings us the capabilities of engineering specific devices including but not limited to sensors, filters and others for many promising applications [1].

The very first demonstration of the possibilities emerged in 1998, while using sub-wavelength apertures in a metal previously unpredicted spectral lines were observed [2]. Following experiments proved that such spectra can be adjusted by exploring different parameters of material, but more importantly the distribution and the geometrical size of the structures, making the structures not just wavelength but polarization dependent as well. Main explanation of the phenomena comes from the surface working as a grating and the resonances due to the coupling of electromagnetic wave to the oscillations of the free electrons at the surface of metal, so called plasmons. It should be noted that in the recent year it was proved that dielectric materials might also be used for the above mentioned manipulation of light.

Apart from the work done towards understanding of light propagation, the fabrication by using Direct Laser Interference Patterning (DLIP) was carried out. Even-though there has been some work done with DLIP before, the period of formed structures were in the range of micrometres [3], thus, for the first time to our knowledge, we suggest such method for structuring of plasmonic materials. DLIP was used to pattern thin-films of different types of metal: chromium (Cr), gold (Au) and niobium (Nb). Samples of different thickness (5-100 nm) were analysed and the ablation compared to theoretical predictions. The experiments proved that DLIP method is capable of structuring 600 nm period apertures in Cr and Nb while the method is limited in Au due to thermal processes and this should be further investigated. The study of topology (Fig. 1) as well as the structural dependence on laser parameters: pulse energy and number of pulses, were carried out in order to optimise the effectiveness of laser processing.

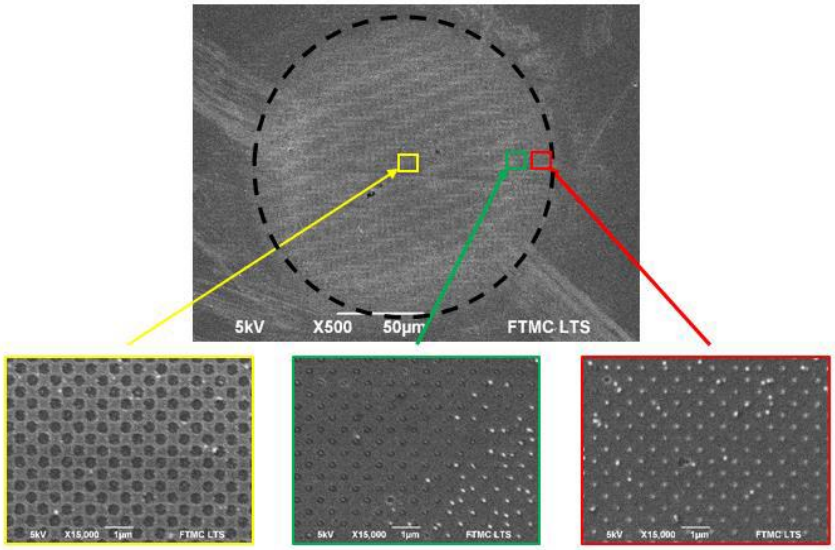

Fig. 1. Example of pattern induced in thin film of metal by a single laser pulse using DLIP.

Light propagation through the structures can be determined by various computational techniques, including the Finite Element Method (FEM) in COMSOL Multiphysics program package, solving partial differential equations. Modelling is critically connected to a proper setting of boundary conditions, properties of materials and description of propagating electromagnetic wave. Results comparable to experimental data can be successfully obtained while changing wide range of parameters: chosen material, periodic arrangement, size and form, as well as the angle of incidence and surrounding environment.

In the scope of this work, dielectric sub-wavelength structures will also be discussed. Appearance of such loss-less structures provides a lot of benefits compared to the metallic ones while sustaining the abilities of manipulation of light, though the usage of DLIP is not a solution for the fabrication of such structures. The metasurfaces based on silicon (Si) nanostructures are extremely promising in the field of multi-dimensional imaging.

[1] S. A. Maier et al., Plasmonics - a Route to Nanoscale Optical Devices, Adv. Mater. **15**(7-8), 2003.
[3] T. Ebbesen et al, Extraordinary Optical Transmission Through Sub-Wavelength hole arrays, Nature **139**, 1998.
[2] B. Voisiat, *Formation of Frequency Selective Surfaces Using Laser Ablation Methods and Characterisation of Their Properties* (PhD thesis in Vilnius University, 2015).

BIOMEDICAL APPLICATION THE PHENOMENON OF LASER-INDUCED OXYHEMOGLOBIN PHOTODISSOCIATION

Anastasia Tabolich[1,2*], Mustafo Asimov[2]

[1] Department of laser physics and spectroscopy, Belarus State University, Minsk, Belarus
[2] Institute of physics named after B. I. Stepanov of NAN Belarus, Minsk
nastya.tabolich@mail.ru

Biophotonics of laser-tissue interaction of low intensity laser radiation with blood oxyhemoglobin is the interesting field of modern photomedicine and photobiology. In the present study we used the combined technology of tissue oxygenation to investigate the elimination of local hypoxia and the modification of the intratumoral oxygen transport *via* oxyhemoglobin complex photodissociation (HbO_2).

The transport of oxygen is carried by hemoglobin through blood circulation through the blood vessels and capillaries. The oxygen deficiency in tissues affects the efficiency of cell metabolism and makes difficult drug treatment of ulcers, wounds and burns. Recovery of oxygen concentration to adequate level for normal cell metabolism becomes critical and is usually can be achieved by additional oxygenation of biotissues. In clinical practice, different methods are used to recovery the shortage of oxygen in tissues, in particular, the method of forced ventilation pure O_2 at atmospheric pressure [1]. Combined effects of laser radiation and acoustic waves allow to increase the local concentration of oxygen in the biotissues. The mechanism of action of this effect can be divided into several stages: a) laser radiation occurs photodissociation of oxyhemoglobin (HbO_2) in the skin with blood-vessels, accompanied by an additional release of molecular oxygen (O_2). The released oxygen penetrates the tissues as a result of the diffusion process and restores the normal glue-accurate metabolism in areas of hypoxia; b) the impact on the fabric of ultra-sound vibrations can significantly increase the diffusivity and enhance the efficiency of oxygenation [2].

The results *in vivo* investigations of laser-induced photodissociation of oxyhemoglobin in cutaneous blood vessels and its role in biomedical processes were presented. Novel optical method of local tissue oxygenation was proposed and developed**.** Different biomedical applications of the effect of laser radiation on gas exchange in biological tissue were discussed.

[1] P.S.Grim, Hyperbaric Oxygen Terapy, JAMA **263**, 2216-2220 (1990).
[2] P.Vaupel, Oxygenation of Human Tumors, Strahlenther, Onkol. **166,** 377-386 (1990).

FABRICATION OF FLEXIBLE MICROPOROUS 3D SCAFFOLDS VIA STEREOLITHOGRAPHY

Giedrė Grigalevičiūtė[1], Evaldas Balčiūnas[2], Linas Jonušauskas[1], Sima Rekštytė[1], Daiva Baltriukienė[2], Virginija Bukelskienė[2], Mangirdas Malinauskas[1]

[1]Department of Quantum Electronics and Laser Research Center, Vilnius University, Saulėtekio ave. 10
[2]Institute of Biochemistry, Life Sciences Center, Vilnius University, Saulėtekio ave. 7
giedre.grigaleviciute@gmail.com

In vivo, cells are embedded in a 3D microenvironment which influences their behaviour and signalling. To mimic that environment, cells can be cultured on 3D scaffolds *in vitro*. There are currently over 40 different 3D printing technologies that can be used for this purpose. Stereolithography is one of them and it may be appealing for the fabrication of customised scaffolds with controlled pore size. Such scaffolds can be applied for tissue engineering purposes or used to study cell-matrix interactions as well as intracellular signalling [1, 2].

The main goal in this research was to test the capabilities of 3D printer *Formlabs Form1+* and the appropriateness of *Formlabs Flexible* and *Formlabs Clear* materials for elastic scaffolds and tissue engineering.

First, the optimal printing parameters were determined by fabricating objects under varying conditions and scaffold porosities (Fig. 1). Then, primary rabbit muscle cells were seeded on the scaffolds and their proliferative activity was measured using a colorimetric assay based on the reduction of a tetrazolium salt. The experimental scheme is depicted in Fig. 2.

We found that scaffold layers tend to overlap in structures that are less than 3 mm tall, resulting in 2D structures. Biocompatibility tests showed that both the materials reduced cellular viability. We hypothesised that the source of such toxicity were uncrosslinked monomers within the material, so additional UV treatment was investigated as a possible solution to the problem. However, our results did not reveal cell viability correlation with UV curing time.

A 3D printer with better control over polymerisation conditions might help improve the biocompatibility of printed scaffolds, so we are currently testing *Autodesk Ember* 3D printer, which has a higher resolution and provides more tuneable printing parameters.

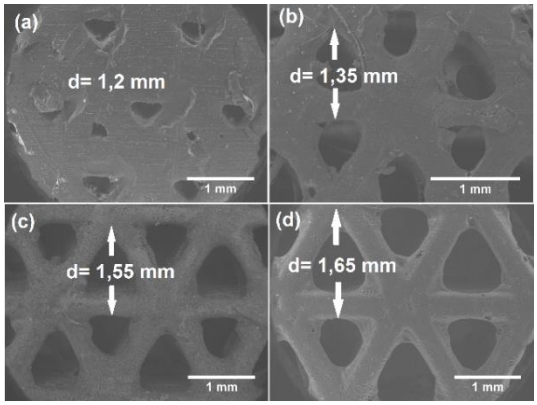

Fig. 1. SEM pictures of the printed structures with different periods – "d".

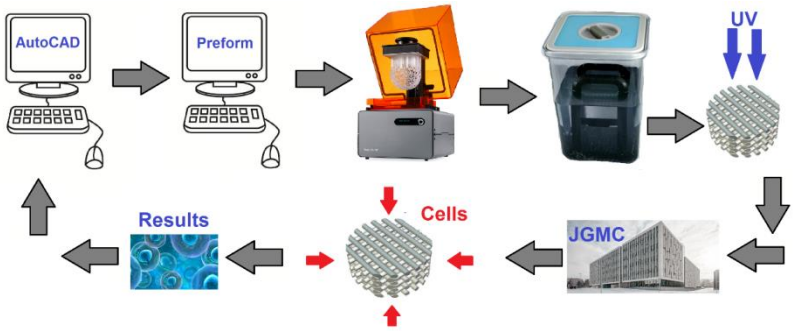

Fig. 2. Experimental scheme. First, a scaffold was designed using CAD software and imported into proprietary Formlabs software. After 3D printing, the scaffolds were developed in isopropanol and UV-cured. Finally, the scaffolds were seeded with cells and their proliferative activity was measured, giving feedback on scaffold design and fabrication conditions.

Acknowledgement. This work is supported by the Research Council of Lithuania, grant No. SEN-13/2015.

[1] J. W. Lee, 3D nanoprinting technologies for tissue engineering applications, J Nanomater. **2015**, 2015:1–14.

[2] J. An, J. E. M. Teoh, R. Suntornnond, Ch. K. Chua, Design and 3D Printing of Scaffolds and Tissues, Engineering 2015, 1(2):261-268.

FUNCTIONALIZATION OF POLY(ETHYLENE GLYCOL) DIACRYLATE FOR PLASMONICALLY ENHANCED 3D LASER LITHOGRAPHY AND TEMPERATURE SENSING APPLICATIONS

Simonas Varapnickas, Linas Jonušauskas, Mangirdas Malinauskas

Laser Research Center, Department of Quantum Electronics, Physics Faculty, Vilnius University, Vilnius, Lithuania
s.varapnickas@gmail.com

In recent years, three-dimensional direct laser writing (DLW) technique has made impressive progress regarding both resolution and feature size of the written structures. However cytotoxicity of virtually all commercially available photoinitiators [1] prevents DLW formed 3D microstructures from wide application in such emerging bio-medical applications as manufacturing of drug delivery agents or bio-compatible, bio-degradable implants. Also, there are only few experimental attempts to evaluate local temperature changes when polymerization reaction takes place during direct laser writing (DLW) process. Furthermore, those few experimental works concludes to completely contrary results even when employing similar experimental set-ups and materials [2, 3].

In this work we investigate the influence of gold nanoparticles (Au NP) (as potentially bio-compatible photoinitiator) to photosensitivity of PEG-DA-700 photopolymer and test bovine serum albumin stabilized Au (BSA-Au) nanoclusters as thermosensitive agent for in-situ temperature change detection during the polymerization reaction in DLW process. Our research shows that doping PEG-DA-700 monomer with Au NP (doping concentrations varying between $3 \cdot 10^3$ and $4.8 \cdot 10^3$ wt%), plasmonically enhances photopolymer sensitivity as measured polymerization threshold values was 25 - 35% lower compared to pure PEG-DA monomers mixture (Fig. 1). We also showed that detection of fluorescent response from PEG-DA photopolymer, doped with BSA-Au nanoclusters, enables to indicate relative temperature gradients during DLW process (Fig. 2) and to prove the thermo-accumulation phenomena when employing $\tau < 300$ fs pulses for polymerization reaction initiation.

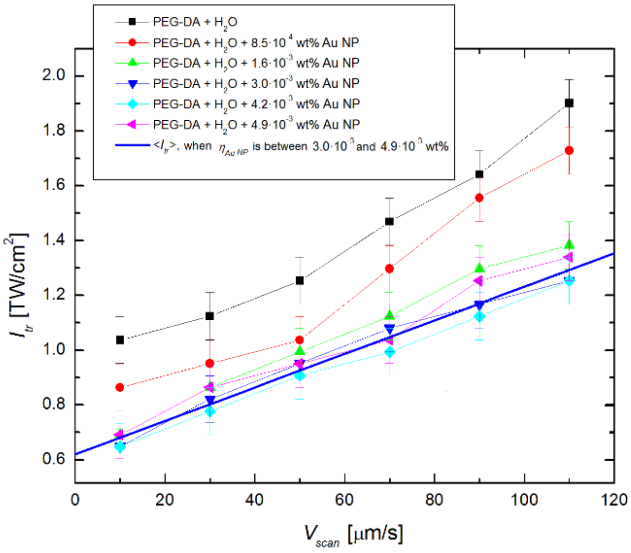

Fig. 1. The change of polymerization threshold when concentration of Au NP in PEG-DA is varied from $8.5 \cdot 10^4$ wt % to $4.9 \cdot 10^3$ wt % and writing speed is changed from 10 μm/s to 110 μm/s.

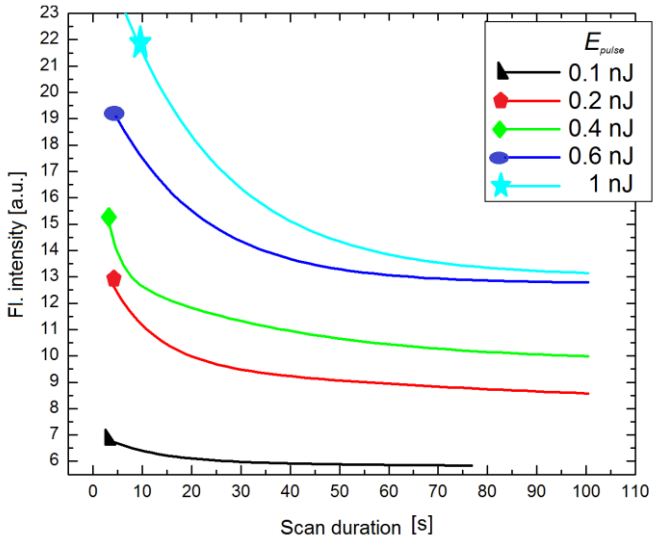

Fig. 2. Fluorescence responses of BSA-Au NC, while structuring periodical gratings in PEG-DA photopolymer, employing different pulse energy beams in DLW setup.

[1] Fairbanks et al., Photoinitiated polymerization of PEG-diacrylate with lithium phenyl-2,4,6- trimethylbenzoylphosphinate: polymerization rate and cytocompatibility, Biomaterials, 2009, 30(35), 6702.
[2] Mueller et al., In-situ local temperature measurement during three-dimensional direct laser writing, Appl. Phys. Lett., 2013, 103, 123107.
[3] Baldacchini et al., Two-photon polymerization with variable repetition rate bursts of femtosecond laser pulses, Opt. Express, 2012, 20, 2989.

A NEW METHOD FOR THE FORMATION OF NORMAL INCIDENCE POLARIZERS

Laurynas Petronis, Tomas Tolenis, Lina Grinevičiūtė

State research institute Center for Physical Sciences and Technology, Savanorių Ave. 231, Vilnius LT-02300, Lithuania
laurynas.petronis@gmail.com

Series of optical systems scientific and technological issues can be solved with interference coatings. Researches include modeling and optimising processes of variuos optical coatings and their manufacturing methods. In these days polarizers have few problems: light beam displacment in Brewster-type polarizers and lower laser-induced damage treshold (LIDT) in absorbing normal incidence polarizers. Unfortunately, dielectric polarizers for normal incidence angle and high LIDT value can not be design using isotropic thin films. Anisotropic layers, namely sculptured thin films, have to be used.

The main aim of this work is to design multilayer coating from anisotropic single-layers and to characterize measuring reflection for different polarization, when illuminating the sample at normal angle. First of all, we explored extinction coefficient and refractive index dispersions of thin films, deposited at diffirent evaporation angles using Al_2O_3 and SiO_2 materials. Secondly, we designed multilayer coatings, which transmission spectra features two mirror relfection areas, which occurs in different spectral region for different incident light polarizations. This transmission distinction perfectly describes polarizer properties.

In present work we use sculptured thin films, which was formed by electron beam evaporation. During the evaporation process columnar structures are formed on substrate due to the self-shadowing effect. This phenomenon causes porosity of thin films, which depends on evaporation angle. Multilayer coatings were formed using a serial bi-deposition (SBD) technique in which a tilted substrate is rotated stepwise by half turn about a normal axis during the evaporation of a material from a single source that causes a columnar structure to grow perpendicular to the substrate [1].

All processes were evaporated in high vacuum of $p_0 = 1.7 \cdot 10^{-5}$ mbar. The evaporation rate was 3 Å/s for both materials and controlled by crystal quartz monitoring. Substrates were rotated in half turns about a normal axis every 5 seconds. The refractive indexes of Al_2O_3 and SiO_2 thin films were determined by modeling transmission spectra using "OptiLayer" program.

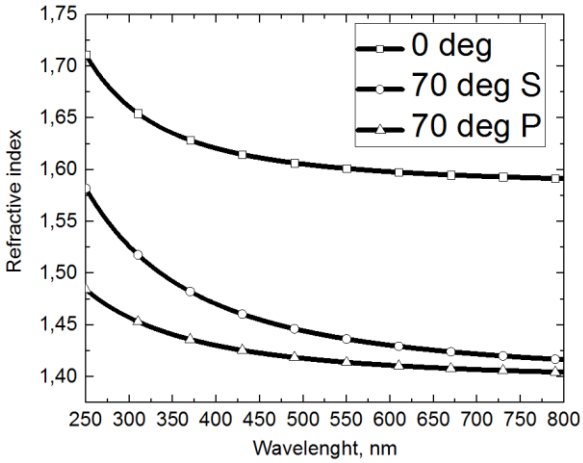

Fig. 1 Refractive index dispersions of Al_2O_3 evaporated at different angle for different polarization

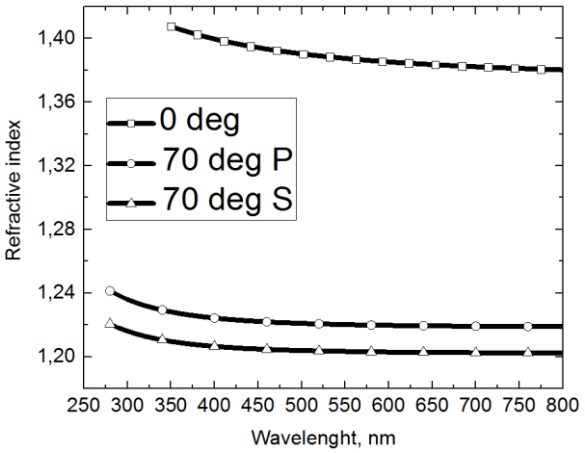

Fig. 2 Refractive index dispersions of SiO_2 evaporated at different angle for different polarization

The dispersions of characterized refractive indexes of materials are represented in Fig. 1 Al_2O_3 and Fig. 2 SiO_2. Anisotropic single-layers Al_2O_3 and SiO_2 refractive indexes decrease due to porosity in thin films, formed by electron beam evaporation technique.

Thin-film polarizers for normal incidence angle is demonstrated. An advantage of the polarizers is compactibility with existing planar technologies. As an example, the thin film polarizers may be combined with spectral filters and diode detectors for simultaneous detection of color and polarization state. As well, variants of the coating may find many uses in laser optics, for example as polarization selective laser cavity mirrors.

[1] I. Hodgkinson and Q. H. Wu, "Birefringent thin-film polarizers for use at normal incidence and with planar technologies," *Applied Physics Letters*, vol. 74, no. 13, pp. 1794–1796, Mar. 1999.

MEASUREMENTS OF PHASE CHARACTERISTICS IN OPTICAL COATINGS BY RESONANCE SCANNING INTERFEROMETER

Laura Šerkšnytė, Mikas Vengris

Department of Quantum Electronics, Vilnius University, Sauletekio Ave. 9, Vilnius LT-10222, Lithuania
lauraserksnyte@gmail.com

In ultrafast lasers it is a hard to maintain extremely short pulse durations, because of the dispersion which the pulse obtains by travelling through space and optical components. Chirped mirrors can be used to compensate this positive dispersion. It is important to know the exact group delay dispersion (GDD) that is created by a chirped mirror. GDD can be measured by white light interferometer (WLI), based on Michelson interferometer, or resonance scanning interferometer (RSI), based on Fabry-Perot interferometer. WLI is the classical choice, but with the RSI it is possible to reach better resolution.

In this work the principles of RSI are examined by creating a theoretical model of RSI and calculating the GD and GDD. The RSI transmittance spectrum consists of spikes at resonant wavelengths. The distance between the resonant frequencies can be related to the average GD within that frequency interval. The GDD is obtained by differentiating GD. This method is limited by the transmittance of the second mirror, the distance between the mirrors and the spectrometer resolution.

The results show, that with a spectrometer resolution of 0.05 nm, signal-to-noise ratio is high enough to distinguish the resonance peaks from noise. It is the optimal resolution because such spectrometer can be easily found in laboratories. The best results can be obtained if the transmittance of the mirror is equal to 0.506%. Then the optimal distance between the mirrors is 10µm. It can be reached experimentally as well. If the distance increases, the intensity of the signal decreases. If the distance between the mirrors is larger (for example, 30µm), a noise occurs in the estimated group delay dispersion.

Theoretical results of a GD and GDD calculated for RSI with such parameters can be seen in Fig. 1.

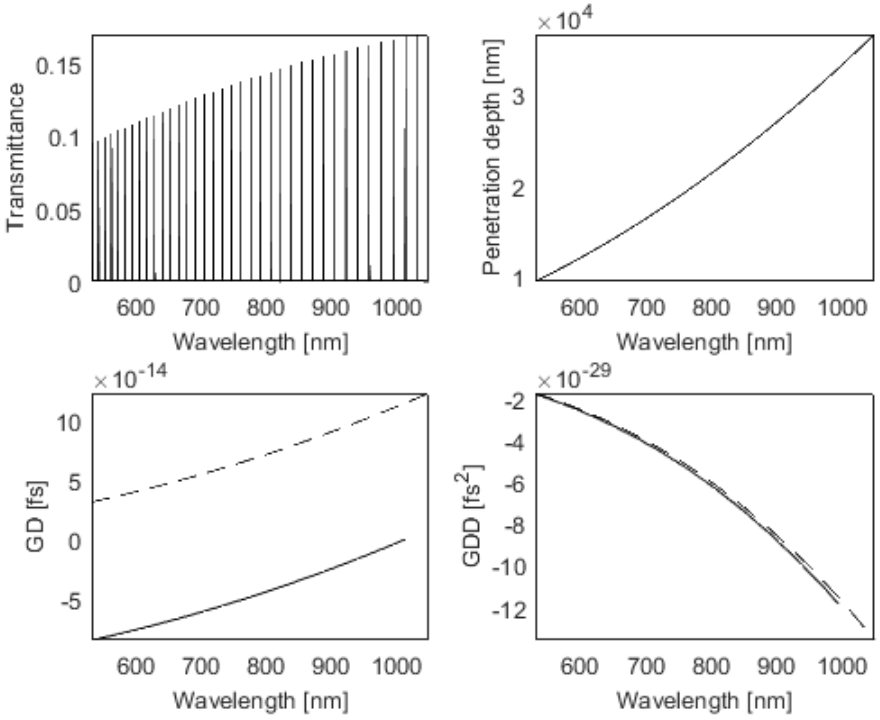

1 Fig. The upper left graph shows the transmittance spectre of the interferometer that is registered by a spectrometer. The penetration depht of the wave is in the upper right graph. In the graphs below the GD (left) and GDD (right) are shown. Dash line represents the function described in the RSI model. The solid line represents the function, calculated from the modeled spectrum. GD is shifted because it is calculated by recurrence relation with a first member equal to 0.

[1] M. K. Trubetskov, M. von Pechmann, I. B. Angelov, K. L. Vodopyanov, F. Krausz, V. Per-vak, Measurements of the group delay and the group delay dispersion with resonance scanning interferometer., Optics express **21**(6), 6658–69 (2013).

OPTICAL AND MECHANICAL PROPERTIES OF AL_2O_3 THIN FILMS PREPARED BY ION BEAM SPUTTERING

Giedrius Abromavičius, Tomas Juodagalvis, Ramutis Drazdys

State research institute Center for Physical Sciences and Technology, Lithuania
giedrius.abromavicius@ftmc.lt

Optical components coated with interference optical coatings play a crucial role in contemporary laser systems. Their optical and other properties often determine the achievable important parameters of lasers, like beam energy, beam quality and others. One of the main tasks for optical coaters is seeking the possible minimal light extinction within the deposited layers. However, other thin film properties like surface roughness, stresses also are the targets of optimization.

Al_2O_3 has the highest bandgap among medium-high refractive index metal oxides which are used for multilayer coating deposition, Therefore it is successfully used for producing multilayer stacks for high power laser systems [1]. Ion beam sputtering technology is well known and widely used as a highly reliable tool capable to achieve superb optical properties as well as very complex spectral and phase properties. For successful production of high quality multilayer coatings it is necessary to know how the process parameters affect the optical and mechanical properties of Al_2O_3 layers, which are the weakest part of multilayer system.

In the present work influence of ion source voltage and background oxygen flow on Al_2O_3 optical constants, surface roughness and stresses is presented. The effect of post deposition annealing is also analyzed. High reflectance coatings for 266 nm wavelength using Al_2O_3 and SiO_2 are prepared and their optical and mechanical properties are characterized.

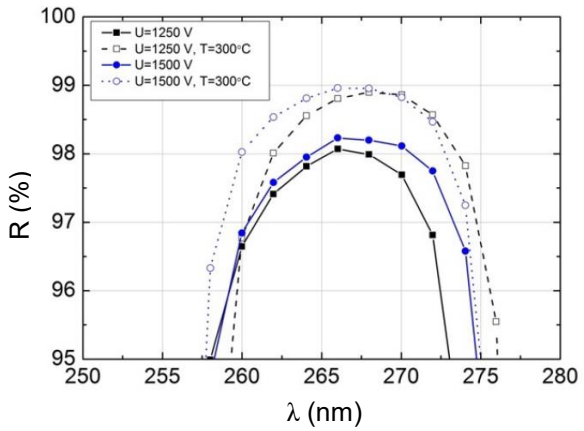

Fig. 1. Reflectance spectra of high reflectance coatings for 266 nm wavelength, prepared using different ion source voltages and additional thermal annealing procedure

[1] N. Kaiser, H. Uhlig, U. Schallenberg, B. Anton, U. Kaiser, K. Mann, E. Eva, High damage threshold Al2O3=SiO2 dielectric coatings for excimer lasers, Thin Solid Films 260, 86–92 (1995).

PHOTOELECTRIC RESPONSE IN NONCENTROSYMMETRIC PHOTOREFRACTIVE CRYSTALS UNDER PULSE EXCITATION

Tatiana Kornienko, Alexei Tolstik

Department of Physics, Belarusian State University, Belarus
tatianakornienko3@gmail.com

Sillenite crystals (bismuth silicon $Bi_{12}SiO_{20}$ (BSO) and bismuth titanium $Bi_{12}TiO_{20}$ (BTO) oxides) are quite complex materials exhibiting piezoelectricity, optical activity, photochromism, photoconductive and electro-optic properties. One more property of electric current generation has already been explored under continuous and pulse illumination and it has been connected with the non-uniformity of radiation beams[1,2]. The aim of the paper is experimental description of the photoelectric-emf with changing the polarity under transverse-moving nanosecond pulse illumination with 532 nm wavelength and 10 Hz repletion rate.

Electrical scheme of experiment include load-circuited sillenites using digital oscilloscope to record photoelectric signals under pulse illumination. Amplitude of such signal signal achieves tens of millivolts on the 550 Om load resistance (fig. 1) and increase with laser intensity increasing. It should be mentioned that in semiconductor crystals photovoltage signal can't exceed the width of the bandgap. The width of bandgap in sillenite crystals is about 3,5 eV. Because of the sillenite crystals haven't the center of symmetry the polarity of observable photovoltage signal varies with the direction of motion. So on figure 1 the first and the third curves correspond to the shift of pulse illuminating stripe in one direction; the second and the fourth curves correspond to the same shift in opposite direction.

Intensity of laser radiation is not only one parameter which influence on the amplitude of signal. As amplitude of recording signal decreases as duration of laser exposure increases. There are black curves (1 and 4) and gray curves (2 and 3) on figure 1 to compare peak value of photoelectric signal immediately when the laser is just switched on, and a few minute later.

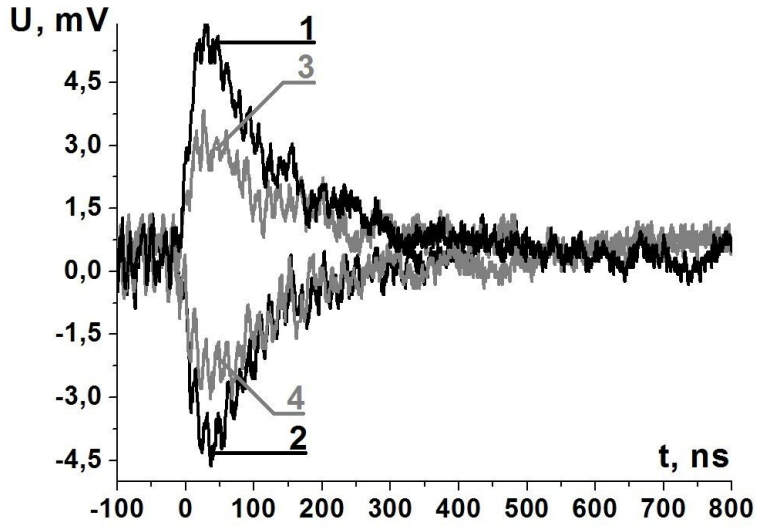

Fig. 1. Amplitude of photoelectric signal *U* during the time at the first second of laser switching-on (black lines 1 and 2) and after laser exposure during a few minute (gray lines 3 and 4)

Obtained results demonstrate that sillenite crystals are very prospective for development on their base different devices of optoelectronics.

[1] M.P. Petrov, A.I. Grachev, Photogalvanic effects in bismuth silicate ($Bi_{12}SiO_{20}$), Pis'ma Zh. Eksp. Teor. Fiz. **30**, no. 1, 15-18 (1979).
[2] R.V. Romashko, A.I. Grachev, Yu.N. Kulchin, A.A. Kamshilin, Fast photogalvanic response of a $Bi_{12}SiO_{20}$ crystal, Optics Express 18, no. 26, 27142 (2010).

TOWARDS WGM RESONATOR STABILISED ON RB 5S-5P TRANSITION LINES

Inga Brice, Antons Pribitoks, Janis Alnis

Institute of Atomic Physics and Spectroscopy, University of Latvia, Riga, Latvia
inga02@inbox.lv

Frequency stability is regarded as absence of frequency drift or maintaining a single fixed frequency as long as possible. Precision play an important role in high speed communications, navigation, frequency standards, spectroscopy and in numerous other important applications [1].

Using femtosecond optical combs the absolute frequency of light can be determined. We use Erbium fiber based optical frequency comb synthesizer that covers a broad optical spectrum 530...1000 nm emitting 150 fs pulses with 250 MHz repetition frequency.

Together with a 780 nm ECFL diode laser and a Rb vapor saturation set-up we are attempting to measure precisely the hyperfine splitting of Rb atoms. The laser is slowly scanned across all the Rubidium saturation peaks to calculate the optical frequency. During different measurements inconsistencies and slight shifting of absolute frequencies of the rubidium lines were observed due to variations of power of the diode laser. This happens as a result of AC Stark shift. This leads to further investigations to observe the frequency depending on the laser power (see Fig. 1).

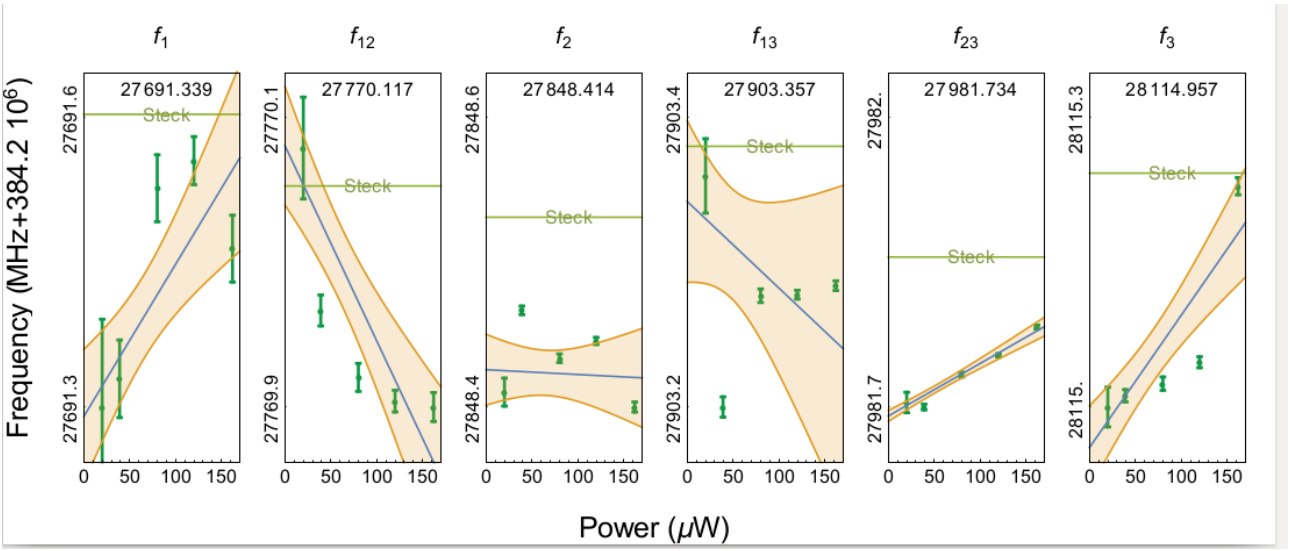

Fig. 1. Absolute optical frequency drift of the Rb^{87} D_2 saturation lines and crossover peaks due to laser power.

Hereafter we want to combine the frequency comb and Rb saturation spectroscopy with the Whispering Gallery Mode (WGM) resonator to compensate for thermal drift and improve the long-term stability. WGM resonators have a high Q factor and resonant frequencies are far apart from each other which provides resonant optical feedback to the laser. As a result the frequency noise and laser line width decreases and stability improves [2, 3]. Also the WGM resonators shaped like micro-spheres, a few hundred micrometers in diameter, can be easily made by melting the tip of an optical fiber.

Acknowledgements:
We thank for support ERAF project Nr.1.1.1.1/16/A/259: “Development of novel WGM microresonators for optical frequency standards and biosensors, and their characterization with a femtosecond optical frequency comb”

[1] K. Predehl, G. Grosche, S.M.F. Raupach et al., A 920-Kilometer Optical Fiber Link for Frequency Metrology at the 19th Decimal Place, *Science* Vol **336**, pp. 441-444 (2012).
[2] W. Liang, V. S. Ilchenko, A. A. Savchenkov et al., Whispering-gallery-mode-resonator-based ultranarrow linewidth external-cavity semiconductor laser, *Optics Letters* Vol. **35**, Issue 16, pp. 2822-2824 (2010)
[3] W. Liang, V.S. Ilchenko, D. Eliyahu et al, Compact stabilized semiconductor laser for frequency metrology, *Applied Optics* Vol. **54**, Issue 11, pp. 3353-3359 (2015)

MULTIPLE PULSE FEMTOSECOND LASER-INDUCED BREAKDOWN SPECTROSCOPY IN MONITORING OF MICROMACHINING PROCESS OF MATERIALS IMMERSED IN WATER

Alok Anand Yadav[1,2], Aurimas Baškevičius[1], Simas Butkus[1], Ona Balachninaitė[1], Valdas Sirutkaitis[1]

[1] Laser Research Center, Department of Physics,Vilnius University, Lithuania
[2] Department of Physics, National Institute of Technology Warangal, India
alkand007@gmail.com

Femtosecond laser micromachining is a quick, precise and flexible procedure. Over the past decade, this technique has been used in a broad range of applications and has been progressed considerably. Laser micromachining related with ablation can benefit from laser-induced breakdown spectroscopy (LIBS) and lead to an insight of the instant characteristics or quality of the micromachining [1]. Double or multiple pulses are used to improve the analytical performance of LIBS and to increase the ablation rate in laser material processing [2].

In this report we present results on the application of the multiple pulse LIBS in monitoring of the micromachining process. The soda-lime glass sample was processed with femtosecond high repetition rate (60 kHz – 1 MHz) pulses. A thin (<1 mm) water layer was applied on the surface of the glass sample. By focusing powerful (energy >30 uJ) femtosecond pulses through a low NA objective, self-focusing and nonlinear absorption phenomena transform the beam to a filament which enables more efficient ablation compared to the conventional focusing in air. It results in high micromachining quality due to additional spatial shaping of femtosecond pulses, cooling and cleaning features of the covering water [3]. This method was successfully applied for fabrication of complex objects from transparent, semiconductor and metallic samples. The experiments were carried out using the Yb:KGW laser system with pulse duration 300 fs and power up to 5 W at 1026 nm wavelength, galvanometric scanner and f- theta lens (f = 100 mm). The interferometric system combined with F-theta lens was used for the formation of multiple femtosecond pulses with decreasing energy. The emission from ablated materials was collected through f- theta lens, scanner and taken away at dielectric mirror used for direction of the laser radiation. The strongest emission line in the spectrum of analyzed soda-lime glass was monitored by single pulse and multiple pulse LIBS.

Figure 1 shows the comparison between single pulse LIBS and multiple pulse LIBS signals from processed soda lime glass in dependence on the number of scans. LIBS signal was estimated during the laser processing using various scanning algorithms, processing speed, focus positions, pulse energies and delay time between the pulses. The correlation between the processed groove volume and LIBS signal was evaluated. In conclusion, by using multiple pulses the improvements in the ablation efficiency and in corresponding LIBS signal were observed and some correlations in the multiple pulses LIBS signal can be used for the implementation of laser processing monitoring.

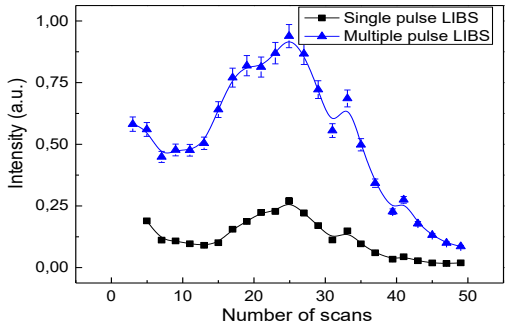

Figure 1 : Na I(at 589 nm) emission line Intensity in relation to the number of scans

[1] A.Baskevicius, O. Balachninaite, S. Butkus, D. Paipulas, R. Sirutkaitis, JLMN -Journal of Laser Micro/Nanoengineering Vol. 11, 381-387 (2016).
[2] V.I. Babushok, F.C. DeLucia Jr., J.L. Gottfried, C.A. Munson, A.W. Miziolek, Spectrochimica Acta B, Vol. 61, 999–1014(2006).
[3] S. Butkus, D. Paipulas, R. Sirutkaitis, E. Gaižauskas, V. Sirutkaitis, JLMN -Journal of Laser Micro/Nanoengineering Vol. 9, 213-220 (2014).

SERS IDENTIFICATION OF ICON PAINTS USING Au NANOPARTICLES IN CHLOROFORM

Yauheniya Korza, Liudmila Trotsiuk, Anna Matsukovich, Olga Kulakovich, Elena Shabunya-Klyachkovskaya

B.I.Stepanov Institute of Physics, National Academy of Science of Belarus, Belarus
korza_ev@list.ru

Today, surface enhanced Raman scattering (SERS) is widely used for various applications. One of them is the identification of art materials in objects of cultural heritage. Since huge enhancement of Raman scattering occur in the close vicinity of metal nanoparticle the extraction of the pigment from the paint layer is commonly used treatment technique for SERS applications in Cultural heritage study [1, 2].

Last year gold nanoparticles in toluene were synthesized and approved as SERS-active substrates for art pigments detection [3]. The toluene dissolving organic binders creates the pores in the paint layer. Gold nanoparticles penetrate thought the pores in the paint layer and have a close interaction with art pigments. However, toluene is more suitable to dissolve varnishes and resins. To dissolve oils and fats it is more preferably to use chloroform.

In present work, gold nanoparticles have been synthesized in chloroform. Moreover, the comparing the efficiency of gold nanoparticles prepared via standard Turkevich technique and proposed gold nanoparticles in chloroform have been carried out.

SERS applications have been performed on the microfragments of paint layers from two Belarusian icons. Both of them are from Brest region and correspond to the depiction "Madonna Hodegetria". The icons have similar stylistic features. The cross-section structures are characterized by two layers of ground and one paint layer. Bottom ground layer is red while upper one is white. The pigments in the paint layers are used as mixture.

Gold nanoparticles in chloroform have been prepared by the modified technique after Brust-Schiffrin [4]. Gold nanoparticles were deposited on the top of paints' microfragments without any pretreatments and dried in the horizontal position at the room temperature.

The obtained spectra are characterized with a high signal-to-noise ratio and low luminescence background. The Chrome yellow, Ultramarine blue, Red ochre and Lead oxides were identified in the paints (Fig. 1). It should be noted, in the case of using Au hydrosol the chromophores peaks appear on the huge luminescence background while the using of organic Au sol provides the efficient enhancement of Raman lines along with luminescence quenching.

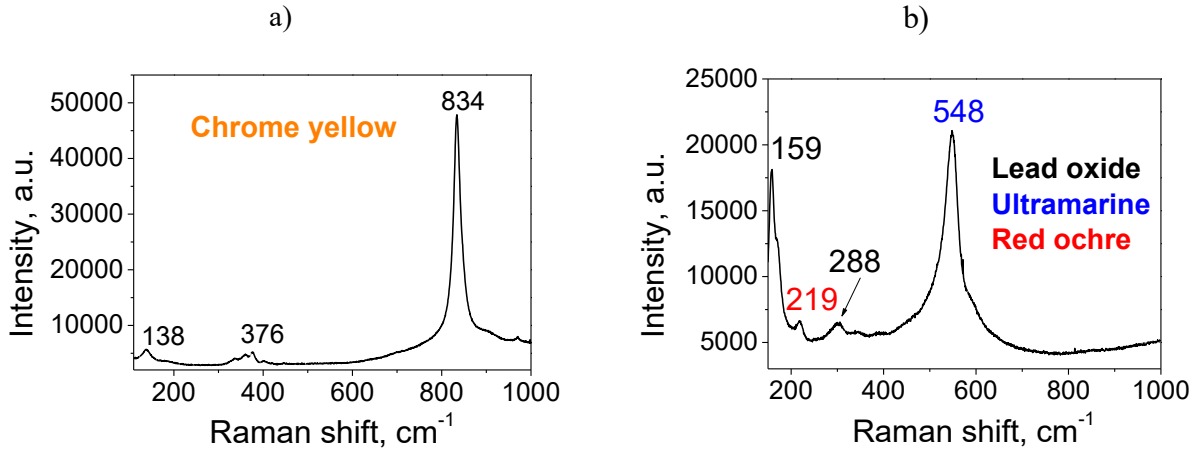

Fig. 1. SERS spectra of paints from icon No.1 (a) and No.2 (b). Excitation wavelength is 488 nm.

So, the using of gold nanoparticles synthesized in chloroform allow to essentially increase the quality of SERS spectra of art pigments from easel paintings avoiding insistent and time-consuming procedure of sample preparation and could be successfully applied for Cultural heritage study and conservation.

[1] E. Shabunya-Klyachkovskaya, O. Kulakovich, S. Vaschenko et al, Surface enhanced Raman spectroscopy application for art materials identification, European Journal of Science and Theology. 12(3) 211-220 (2016).
[2] S. Bruni, V. Guglielmi, F. Pozzi et al, Surface-enhanced Raman spectroscopy (SERS) on silver colloids for the identification of ancient textile dyes. Part II: pomegranate and sumac, J. Raman Spectros. 42, 465–473 (2011).
[3] L. Trotsiuk, Y. Korza, A. Matsukovich, SERS technique optimization for cultural heritage research, 59th scientific conference for young students of physics and natural sciences Open Readings 2016, Vilnius University, 162 (2016).
[4] M. Brust, D. Bethell, C.J. Kiely et al, Self-Assembled Gold Nanoparticle Thin Films with Nonmetallic Optical and Electronic Properties, Langmuir. 14(19), 5425–5429 (1998).

VISIBLE RANGE SPECTROMETER FOR BIOLOGICAL APPLICATION IN SITU

Sopfy Kavalenka, Maryia Bobkova

Department of laser physics and spectroscopy, Belarusian State University, Belarus
sopfykavalenka@gmail

Spectrometric parameters and dimensions of device was developed allows its application in non-laboratory conditions. Device has sizes 160 x 80 x 55 mm. Spectrometer is battery powered, so external electrical socket it not required. Work time of spectrometer using battery is more than 4 hours. Spectral range of this device is 400-720 nm. The range covers most requests of biological issues [1, 2]. Main objects for application of this spectrometer are plants. Most chromophores of plants luminesce in visible range and there are no significant narrow spectral peaks, so spectral resolution of device was developed (2 nm) is enough for accurate experiments [3].

The most distinguishing feature of the spectrometer is way of data transmitting from spectrometer to system of spectra visualization. Bluetooth module HC-05 sends spectral data to some computer data system (CDS). Using wireless way of data transfer makes spectrometer completely portable. Baud rate of transmitting is 921600, it means obtaining of 2 spectra per second at CDS.

There was written app for Android and program for personal computer to visualize, save in dat file and work with spectral data. Also, the app allows choosing of exposure time and snap-shot/active mode regimes. Examples of obtained spectra on smartphone screen shows on Fig. 1.

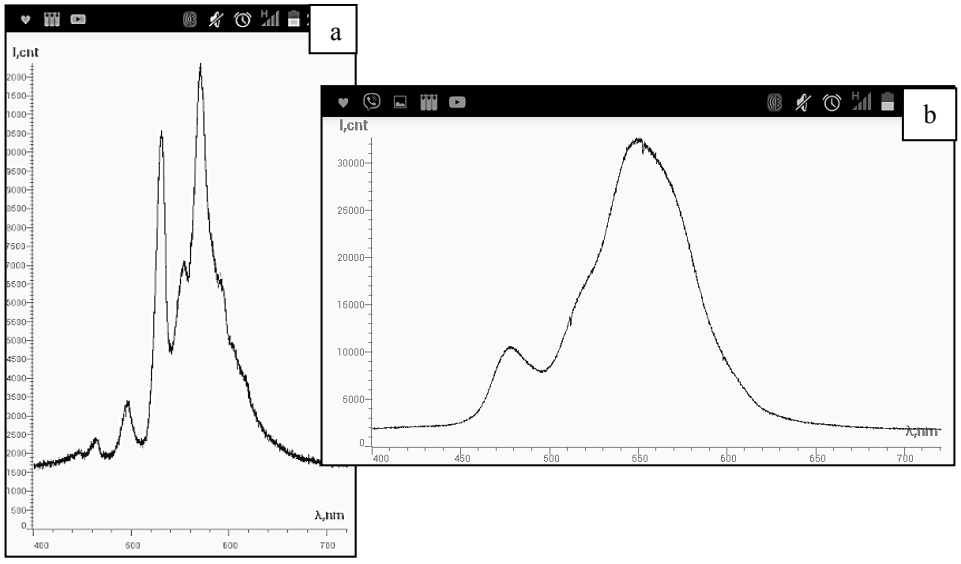

Fig. 1. Spectra of fluorescent (mercury) bulb lamp (a) and led lamp (b) spectra on smartphone screen

During experiment we can obtain reflection spectrum or transmission spectrum. Providing experiments *in situ* (field, forest, any non-laboratory conditions) means, that excitation source is Sun or some portable source. That is why two type of excitation led-source was made. Each led-source made in ring-geometry with hole in the center for simple connection between spectrometer and led-source ring. Wavelength of these modules is 470 nm and 655nm.

Spectral characteristics of plans and tooth enamel was analyzed based on spectral data obtained using the device. Cost of the device extremely small but it‘s characteristics can compete with global peers.

[1] J. Belasque, M. C. G. Gasparoto, and L. G. Marcassa, Detection of mechanical and disease stresses in citrus plants by fluorescence spectroscopy, Applied Optics Vol. 47, Issue 11, pp. 1922-1926 (2008).

[2] Joelson Fernandes, William Ferreira Falco, Samuel Leite Oliveira, and Anderson Rodrigues Lima Caires, Changes in chlorophyll a fluorescence of glyphosate-tolerant soybean plants induced by glyphosate: in vivo analysis by laser-induced fluorescence spectroscopy, Applied Optics Vol. 52, Issue 13, pp. 3004-3011 (2013).

[3] C. T. Phan, E. L. Branch and J. J. Jasmin, Studies on the detection of lettuce maturity: anatomical observation and reflectance measurements in the visible range (350-650 nm). Can. J. Plant Sci. 1067-1075.

CORRECT EVALUATION OF FLUORESCENCE QUANTUM YIELD IN ORGANIC FILMS

Edvinas Radiunas, Karolis Kazlauskas, Saulius Juršėnas

Institute of Applied research, Vilnius University, Lithuania
eradiunas@gmail.com

Lately development of novel organic optoelectronic devices has been at the forefront of scientific interest due to promising convenient and easy solution based device fabrication [1]. Chemically engineered state-of-the-art organic molecules can produce desired optical and physical properties for suitable applications. Electronics based on organic semiconductors can be flexible, wearable, environmentally friendly and in some cases even outperform modern inorganic counterparts. Constantly developing major branches of organic electronics, such as organic light emitting diodes (OLED), organic thin film transistors (OTFT) and others, heavily rely on advanced semiconductor materials and their characterization. Perhaps one of the most essential parameters of fluorescent semiconductor materials used in optoelectronics is fluorescence quantum yield (QY), which determines materials scope to produce photons from energy absorbed.

The current work focused on correct evaluation of QY in the films of organic compounds exhibiting different optical properties. The compounds were selected to have different Stokes shift (from 0.19 *eV* to 1.13 *eV*) and QY (from 43% to 79%). The series of films featuring identical compound concentration in polystyrene matrix (6 *wt*%) and continuously increasing thickness were prepared to deduce the influence of reabsorption on QY estimate. The QY measurements were carried out by using integrating sphere [2] where reabsorption is known to significantly alter QY data thereby preventing its correct evaluation. Our proposed QY evaluation method relies on the reconstruction of reabsorbed, i.e. spectrally distorted, fluorescence spectra (measured inside the sphere) by using the unperturbed spectra obtained outside the sphere. The results of the corrected QY along with the uncorrected data as a function of film thickness (optical density) are displayed in Fig. 1. Clearly, the effect of reabsorption drastically lowers QY of the films (see uncorrected data) as compared to those obtained by employing spectral reconstruction procedure. The reabsorption, obviously, makes QY of the film thickness-dependent. Conversely, spectral reconstruction implies correct QY estimates of the films independently on their thickness, and thus allows determining intrinsic material QY in the solid film.

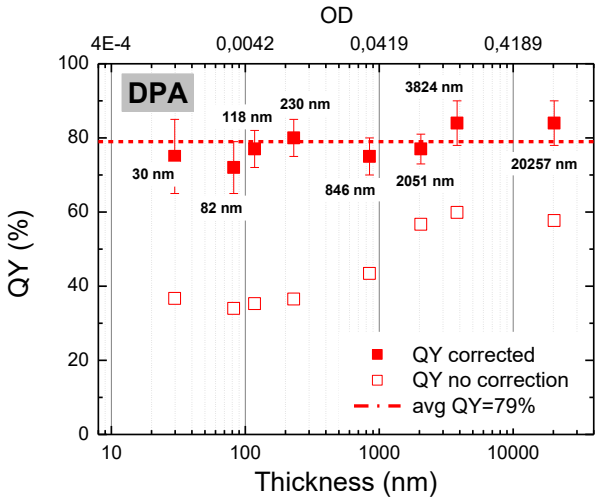

Fig. 1. Fluorescence quantum yield as a function of optical density (thickness) of the DPA/PS film.

[1] R. Søndergaard, M. Hösel and F. Krebs, Roll-to-Roll fabrication of large area functional organic materials, J. Polym. Sci. B Polym. Phys., **51**, 16–34 (2013).

[2] J. C. de Mello, H. F. Wittmann and R. H. Friend, Absolute photoluminescence quantum efficiency measurement of light-emitting thin films, Adv. Mater., **9**, 230–232 (1997).

LOW TEMPERATURE STUDY OF EXTRACELLULAR FLUID OF KIDNEY TISSUE BY MEANS OF SURFACE-ENHANCED RAMAN SCATTERING SPECTROSCOPY

Miglė Radžvilaitė, Martynas Velička, Valdas Šablinskas

Department of General Physics and Spectroscopy, Vilnius University, Lithuania
migle.radzvilaite@ff.vu.lt

The rapid technological development in the medical field has led to implementation of new vibrational spectroscopy methods for research on molecular biology. It was shown that these methods can be used to identify the cells of kidney, breast, and prostate cancer [1].

An overall success of removal of cancerous kidney tissue during the surgery is highly dependent on fast and accurate scoping of kidney tissue. Unfortunately, clinical methods used nowadays cannot ensure this due to time consuming preparation of the samples. Thus a demand for new procedures is growing.

It is known that cancerous and healthy kidney cells differ in metabolism and molecular structure [2]. For this reason, the extracellular fluid of cancerous and healthy kidney tissues also differ since the extracellular fluid composition is closely related to the metabolism of the cells. Thus, due to a simple preparation of the extracellular fluid samples, a faster identification of cancerous cells can be achieved by analyzing the collected vibrational spectra of extracellular fluid. However, conventional Raman scattering cannot be effectively used for thin film analysis and unconventional methods like surface enhanced Raman scattering spectroscopy must be used.

Since biological fluids are composed of different molecules, their experimental spectrum is a combination of many different overlapping vibrational spectral bands. Thus, precise assignment of these bands to the corresponding molecular vibrations is a difficult task. The intensity of SERS spectral bands depends on the distance between the molecule and a metal surface, which is used for the SERS effect. When the samples are cooled, the distance between molecules and the nanoparticles should decrease and the enhancement factor of the SERS signal of the adsorbed molecules should increase. When the sample is composed of different molecules, the adsorption also depends on the functional groups of the molecules in the composition of the sample.

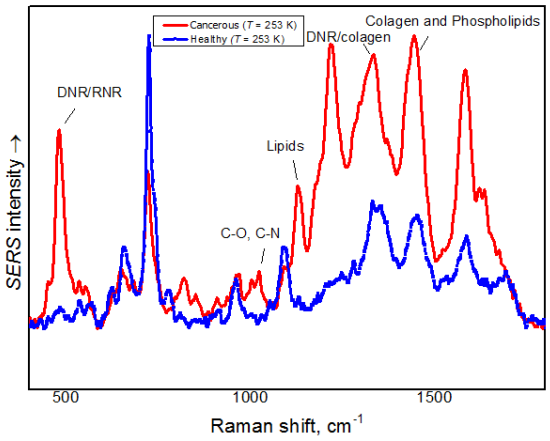

Fig. 1. S*ERS* spectrum of extracellular fluid of healthy and cancerous kidney tissues.

In this study, low temperature SERS measurements of extracellular fluid of cancerous and healthy kidney tissue samples were carried out in order to get a deeper understanding of the nature of vibrational spectral bands present in the experimental spectrum.

[1] Sevda Mert, Mustafa Culha, Surface-Enhanced Raman Scattering-Based Detection of Cancerous Renal Cells, Applied Spectroscopy, 68(6), 617-624, 2014.

[2] Marija Barisienė, Arnas Bakavičius, Henrikas Ramonas, Feliksas Jankevičius, The Treatment Results of Renal Cancer with Invasion in Veins, 21(2), 225- 227, 2015.

SPECTROSCOPIC (FTIR, RAMAN, UV/VIS) AND THEORETICAL (DFT, MRPT, BIOLOGICAL ACTIVITY) STUDIES OF ADAMANTANE-CONTAINING COMPOUNDS, PROMISING FOR THE DEVELOPMENT OF ANTIBACTERIAL DRUGS

Yuliya Mindarava[1], Anna Matsukovich[2], Maksim Shundalau[1]

[1] Department of Physics, Belarusian State University, Minsk, Belarus
[2] B.I. Stepanov Institute of Physics, National Academy of Science of Belarus, Minsk, Belarus
uidja7@mail.ru

The adamantine ($C_{10}H_{16}$) containing compounds have a number of useful properties: a high degree of lipophilicity, highly reactive, etc. In this regard, the adamantane derivatives represent a class of organic compounds finding extensive medical applications owing to their ability to therapeutic activity. It is found that the presence in the structure of compound adamantyl group almost always increases the degree of its biological activity. Thus, the high lipophilicity of an adamantyl fragment provides a slight penetration of the drug through the blood-brain barrier. Adamantane derivatives may act as potential agents for the treatment of neurological diseases, malaria, inflammatory diseases, tuberculosis, and cancer. Currently, at least seven drugs on the basis of adamantane-containing compounds have clinical use and several dozen clinical trials.In this work the structural and spectral characteristics of adamantane derivatives (3-(adamantan-1-yl)-1-[(4-benzylpiperazin-1-yl)methyl]-4-phenyl-1*H*-1,2,4-triazole-5(4*H*)-thione, $C_{30}H_{37}N_5S$, or compound I, and 3-(adamantan-1-yl)-4-ethyl-1-[(4-phenylpiperazin-1-yl)methyl]-1*H*-1,2,4-triazole-5(4*H*)-thione, $C_{25}H_{35}N_5S$, or compound II) (see Fig. 1) were studied. In continuation to our interest in the pharmacological and structural properties of the adamantane derivatives, the results of the present study will help to achieve a better understanding of the properties of such derivatives.

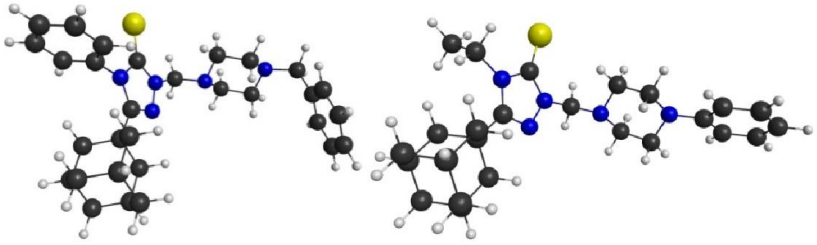

Fig. 1.Equilibrium structures of the compound I (*a*) and II (*b*)

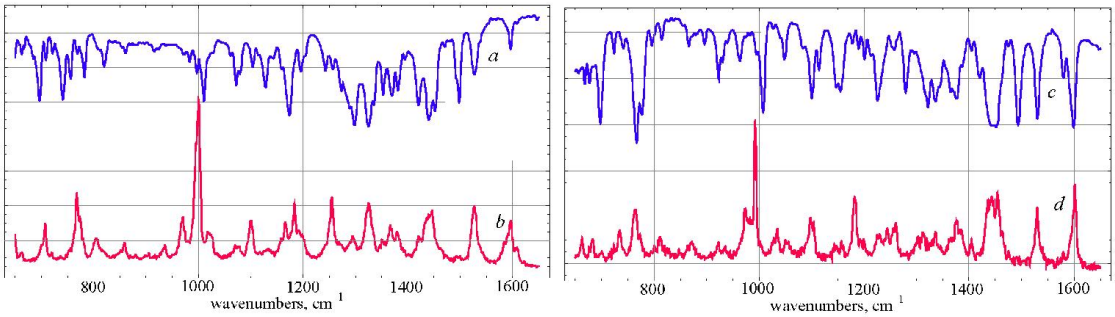

Fig. 2. The fragments of the FTIR (*a*, *c*) and Raman (*b*, *d*) spectra of the compounds I (*a*, *b*) and II (*c*, *d*).

The FTIR spectra (Fig. 2, *a*, *c*) have been measured in reflection mode in the range of 3200–650 cm^{-1}. Raman scattering spectra in the range of 3200–150 cm^{-1} (Fig. 2, *b*, *d*) have been measured using a second harmonic (532 nm) of the Nd:YAG laser. The electronic absorption (UV/Vis) spectra of the solutions of the compounds in ethanol have been measured in the range of 450–200 nm. Calculations of the structural and spectral vibrational characteristics of the molecules were performed using the standard cc-pVDZ basis by DFT methods with the help of the hybrid B3LYP functional. Calculations of the UV/Vis spectra were performed in the TDDFT and MRPT (Multi Reference Perturbation Theory) approximations. On the basis of the calculations the complete interpretation of the spectra was obtained. The biological activity indices Pa (probability to be active) have been predicted. The predicted Pa indices have high values. For example, the Pa value for analgesic activity for the compound I is 0.816.

The comprehensive experimental and theoretical studies of the optical properties of some adamantane-containing compounds carried out, and it may be useful in medicinal chemistry and for the drugs design.

EFFECT OF THE METAL-ANALYTE ARRANGEMENT ON THE EFFICIENCY OF SURFACE ENHANCED RAMAN SCATTERING

Liudmila Trotsiuk, Anna Matsukovich, O. Kulakovich, E. Shabunya-Klyachkovskaya

B.I.Stepanov Institute of Physics, National Academy of Science of Belarus, Belarus
l.trotsiuk@ifanbel.bas-net.by

Surface enhanced Raman spectroscopy (SERS) is an ultrasensitive analytical tool which finds numerous applications [1]. Therefore, an important and urgent task is to search for parameters that affect SERS enhancement factor as well as to develop of effective nanostructured SERS-active metal substrates [2-4].

In this work the effect of the mutual configuration of the analyte with different photostability and the gold nanoparticle films on the intensity of the SERS signal was investigated. The excitation wavelengths was λ = 531 and 632.8 nm. A monodisperse sol of gold was obtained by Turkevich's method [5]. The SERS-active films were formed on glass substrates by layer-by-layer electrostatic deposition of gold nanoparticles. The Raman spectra of malachite green and mitoxantrone on the gold nanoparticles were investigated in three configurations: above the gold film, under the gold film, and between the gold films (so called "sandwich" configuration). The 3 μL of each analyte ($0.8 \cdot 10^{-5}$ M aqueous solutions of malachite green (tetramethyl-4,4-diaminotriphenylmethane chloride) and $1.3 \cdot 10^{-5}$ M mitoxanthrone (1,4-dihydroxy-5,8-bis[[2-[(2-hydroxyethyl)amino]ethyl]amino]-9,10-anthracenedione dihydrochloride) was dropped atop gold plasmonic film or pure glass. In the cases of "analyte under gold film" and "sandwich" configuration the gold sol was dropped atop analyte layer and dried.

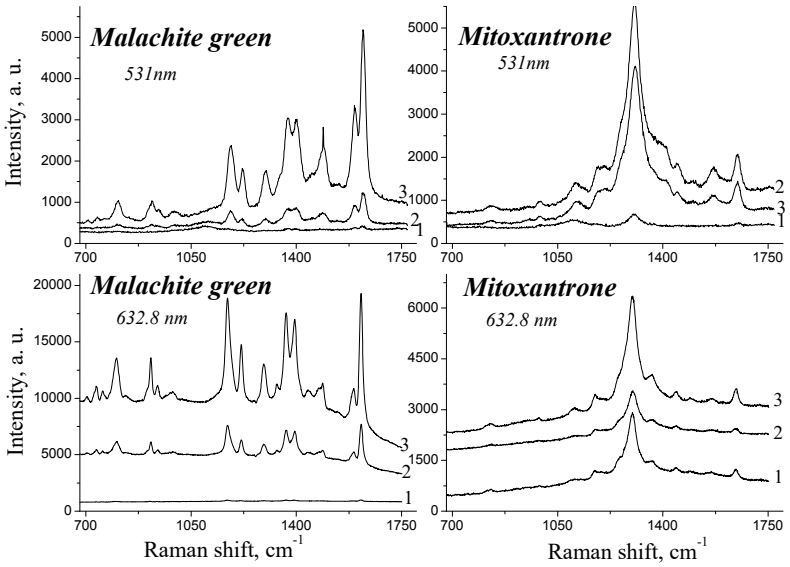

Fig. 1. The SERS spectra of malachite green and mitoxantrone: 1 - analyte above Au film; 2 - analyte under Au film; 3 - analyte between Au films, «sandwich» configuration.

Thus, it was shown that the SERS intensity of the analyte in a sandwich configuration is up to 5 times higher compared to the "analyte under gold film" arrangement and up to 60 times higher than for the "analyte on gold film" case with the using of excitation emission in the plasmon resonance region (531 nm and 632.8 nm). Moreover, the effect is greater, the less photostability of analyte and the higher the power of the exciting radiation. The reason is that the layer of metal nanoparticles above reduces the access of oxygen to the analyte, preventing photodegradation of the molecules.

[1] K. Kneipp et al., Surface-enhanced Raman scattering and biophysics, *J. Phys. Condens. Matter* **14,** R597 (2002).
[2] J. Zheng, et al., Surface-enhanced Raman scattering of 4-aminothiophenol in assemblies of nanosized particles and the macroscopic surface of silver, Langmuir **19**, 632–636 (2003).
[3] 4. T. Abdallah et al., Effect of shape and interstice on surface enhanced Raman scattering (SERS) of molecules adsorbed on gold nanoparticles in the near-dipole and quadrupole regions, J. Raman Spectrosc. **43**, 1924–1930 (2012).
[4] L. Rodríguez-Lorenzo et al., Surface enhanced Raman scattering using star-shaped gold colloidal nanoparticles, J. Phys. Chem. **114**, 7336–7340 (2010).
[5] J. Turkevich et al., A study of the nucleation and growth processes in the synthesis of colloidal gold, Discuss. Faraday Soc. **11**, 55–57 (1951).

CHARACTERISATION OF NON-IRRADIATED AND NEUTRON IRRADIATED GALLIUM NITRIDE BY ESR SPECTROSCOPY

Laimonas Deveikis, Tomas Ceponis, Eugenijus Gaubas

Institute of Applied Research, Vilnius University, Sauletekio av. 3, LT-10257, Vilnius, Lithuania
laimonas.deveikis@ff.stud.vu.lt

GaN is a promising wide band-gap material for fabrication of the solar-blind photo-sensors and radiation tolerant particle detectors applied in high energy physics, radiation monitoring and other fields [1]. Wide band-gap determines low leakage current and proper radiation hardness of devices made of these materials. High luminescence efficiency is an attractive characteristic of GaN. Crystals of large thickness (300-600 μm) and high resistivity ($\geq 10^6$ Ωcm) can also be used for manufacturing of the capacitor type particle sensors with high sensitivity. GaN crystals of such thickness can be synthesised by hydride vapour phase epitaxy (HVPE) and ammono-thermal (AT) techniques. Additionally, acceptor type impurities are often introduced during growth of GaN to reach high resistivity of the material. However, technological defects and impurities introduced during crystal growth affect functional characteristics of devices made of GaN materials. Radiation can also produce damage which determines a degradation of functional parameters of devices. Therefore, it is important to characterise the initial and irradiated material by identifying the existing defects and by evaluating their concentrations in order to produce devices of high quality and to predict their operational characteristics. The spectroscopic methods are highly effective tools for the investigation of technological and radiation defects.

In this work the pristine and reactor neutron irradiated, with different fluences (10^{12} - 5×10^{16} cm^{-2}), GaN samples, grown by HVPE and AT techniques have been investigated by electron spin resonance (ESR) spectroscopy technique. The AT GaN samples were initially doped with manganese and magnesium. ESR spectroscopy has been applied for characterisation of defects and impurities introduced during crystal growth and irradiation. Measurements were performed in the temperature range of 100-300 K using Bruker Elexsys E580 spectrometer.

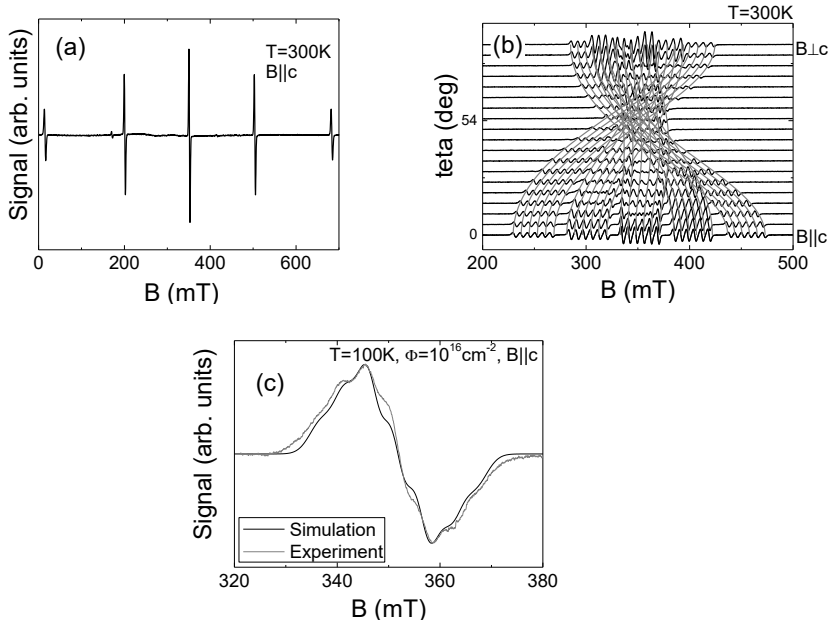

Fig. 1. (a)-ESR spectrum measured in HVPE GaN at magnetic field orientation B||c. (b)-Angular variations of ESR spectra in AT-GaN. Gray lines illustrate the simulated variations of resonance positions. (c)-Experimental (measured at T = 100 K) and simulated ESR spectra in neutron irradiated AT-GaN. Resonance lines are associated with $V_{Ga}O_N$ defect.

Analysis of ESR spectra measured at different temperatures and microwave power levels, as well as using different magnetic field orientations relative to crystal axis (Fig. 1) allowed us to determine the spin-Hamiltonian parameters of spin system and to identify the dominant spin-active defects and impurities in materials under investigation. The density of defects has been evaluated using Bruker software. In the HVPE grown semi-insulating GaN sample the intentionally introduced Fe^{3+} impurities of concentration of 2×10^{17} cm^{-3} have been detected. The concentration of Mn^{2+} impurities has been evaluated to be of 1.3×10^{18} cm^{-3} in AT GaN sample. After irradiation of AT GaN samples the gallium vacancy and oxygen interstitial atom ($V_{Ga}O_N$) defect complexes were identified in both the Mn and Mg doped samples. The analysis of the ESR spectra and procedures for identification of spin-active defects and impurities will be discussed.

[1] S. J. Pearton, *GaN and related materials II*, (Gordon and Breach Science Publishers, Amsterdam, 2000).
[2] E. Gaubas, T. Ceponis, V. Kalesinskas, J. Pavlov, and J. Vysniauskas, Simulations of operation dynamics of different type GaN particle sensors, Sensors **15**, 5429-5473 (2015).

HIGH RESOLUTION SOLAR SPECTROPOLARIMETER SSP-600 FOR DETERMINATION OF RADIATION PARAMETERS

Anton Martenov, Leanid Katkouski, Valeriy Stanchick

A. N. Sevchenko Institute of Applied Physical Problems of Belarusian State University, Belarus
antonmartenov@gmail.com

SSP-600 (Fig.1) is designed to measure the direct sun radiation and radiation scattered by the atmosphere at different angles in the range of 350-950 nm. SSP-600 includes a polychromator with a photo detector based on CCD line with 3648 elements. The lens hood is placed before the projection lens, which leads to 1000-fold reduction in the level of the parasitic illumination. The spectropolarimeter is equipped with a visor for the aiming of the field of view to the relevant portions of the sky with the help of the tripod swivel arm [1]. SSP-600 also includes removable polarizer that lets light rays of a specific polarization pass and blocks light waves of other polarizations. The device is controlled via a smartphone by developed software.

Fig. 1. SSP-600

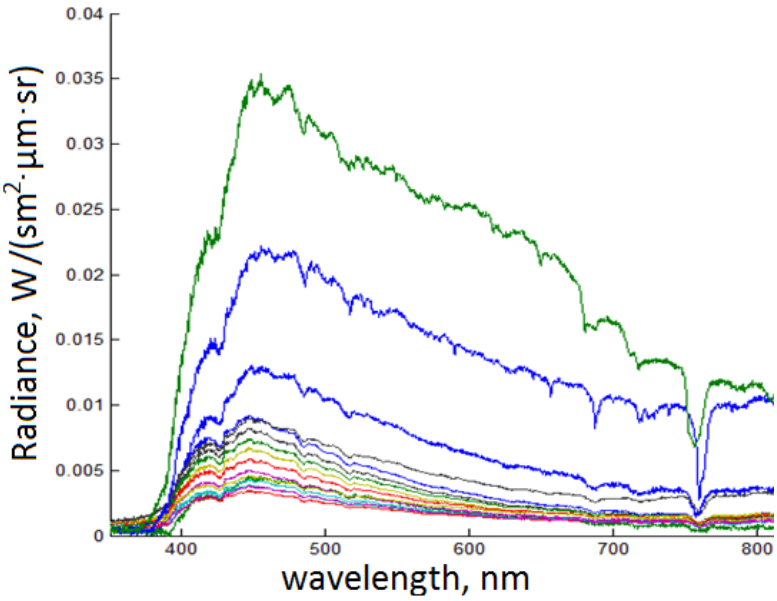

Fig. 2. Spectral profiles of blue sky

Technical characteristics of the SSP-600:

- Working spectral range, nm	350– 950
- Spectral resolution, nm	1.2 - 2.0
- The number of photo detector elements	3648
- The dispersing element	concave holographic diffraction grating
- The number of strokes, lines / mm	315
- Projection lens	"MC Helios 44-3M"
- Focal length, mm	58.0
- Field of view, °	4
- Line CCD photodetector	Toshiba TCD 1304DG

Comparison of measured spectra and spectra obtained by Aeronet station has been carried out. The measured spectra (Fig. 2) can be used to solve the inverse problem of determining the parameters of aerosol atmosphere over Minsk. Such radiation parameters like intensity, degree of linear of the polarization and polarization azimuth were obtained for set of points in the almucantar plane.

A further step in the development of the SSP is its integrating with automatically rotating platform. This platform can position the spectrometer in any direction by sending messages via COM-port. The only thing an operator has to do is press start button and wait for the completion of the measurement process.

[1] Martenov, A., Solar spectropolarimeter SSP-600 / Priborostroenie-2016, 9th International Scientific and Technical Conference, Belarusian National Technical University, 182-183 (2016)

14C MEASUREMENT IN THE TREE RING OF PINUS SILVESTRIS BY SINGLE STAGE ACCELERATOR MASS SPECTROMETER

Algirdas Pabedinskas, Žilvinas Ežerinskis, Justina Šapolaitė, Matas Pocevičius, Laurynas Butkus, Laurynas Bučinskas, Rūta Druteikienė, Andrius Garbaras, Vidmantas Remeikis

Center for Physical Sciences and Technology, Vilnius, Lithuania
algirdas.pabedinskas@ftmc.lt

In January 2016, a single stage accelerator mass spectrometer (SSAMS) from National Electrostatic Corporation (NEC) [1] was installed at the Center for Physical Sciences and Technology. It is the first AMS instrument in Lithuania able to determine the ratio of $^{14}C/^{12}C$. Fig. 1 shows the principal scheme of the machine, which is equipped with one ion source, 240 kV accelerator stage, a gas stripper, two high energy magnets and a detector built on a high voltage deck inside the Faradays cage. The detection limit of the equipped instrument is 53000 years. After a successful start the accelerator mass spectrometer opens many opportunities in the environmental research, elaborates Lithuania's history facts, and serves in the medicine research.

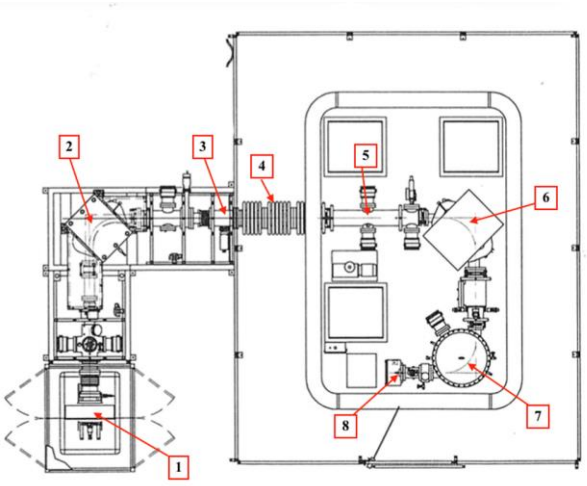

Fig. 1. A SSAMS system: 1. Ion source with the sample wheel of 39 positions. 2. Dipole magnet. 3. Einzel lens. 4. 240 kV accelerator. 5. Molecular dissociator. 6. Dipole magnet. 7. ESA. 8. Solid state detector.

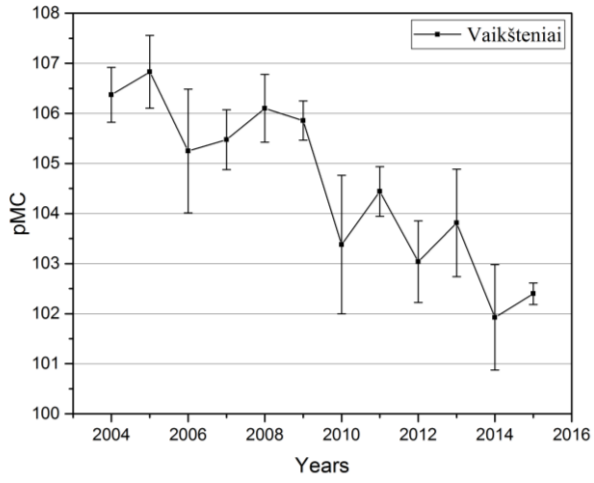

Fig. 2. ^{14}C distribution in the tree rings of Pinus Silvestris.

First results measuring ^{14}C activity in the tree rings of Pinus Silvestris are presented in the Fig. 2. Wood cellulose was extracted prior to ^{14}C analysis [2]. From these results we can observe that ^{14}C activity is decreasing over the investigated period. Further analysis will be performed to evaluate ^{14}C activity in the tree rings of XX century.

[1] J.B. Schroeder, T.M. Hauser, G.A. Norton, G.M. Klody, Initial results with low energy single stage AMS., Radiocarbon 46, 1–4 (2007).
[2] M. Nemec, L. Wacker, I. Hajdas, H. Gaggeler, Alternative Methods for Cellulose Preparation for AMS Measurement, Radiocarbon 52, 1358-1370 (2010).

PECULIARITIES OF BURNING THE GRAPHITE SAMPLES

Vladimir Abdulajev[1], Andrius Garbaras[1,2] , Elena Lagzdina[1], Danielius Lingis[1,2], Jevgenij Garankin[1], Artūras Plukis[1], Rita Plukienė[1], Vidmantas Remeikis[1], Arūnas Gudelis[1]

[1] Institute of Physics, Center for Physical Sciences and Technology, Lithuania
[2] Faculty of Physics, Vilnius University, Lithuania
vladimir.abdulajev@ftmc.lt

Nuclear reactor graphite is a source of dangerous radioactive waste, it is particularly important to determine radiological characteristics of graphite as it is a part of nuclear power plant decommission process. Decommissioning of old reactors and planned use of graphite in the new ones force to look for solutions of irradiated graphite management and disposal [1]. There are several principal solutions possible: disposal of graphite in appropriate repositories, incineration of graphite as a combustible radioactive waste, or recycling and reuse [2]. In order to evaluate radioactive impurities in the graphite is need to burn the graphite. In this work the peculiarities for the burning of graphite were investigated.

Graphite was burned in the oven at 1000 °C in the He flow adding oxygen as oxidiser. It was determined that graphite didn't burn completely during one burning cycle. Burning bigger samples of graphite proved to a challenge for this method as it didn't completely burn down, even after running the cycle for few times. However smaller samples burned down completely. The burning results are presented in the Table 1.

Table 1. The mass of the burned graphite.

Sample nr 1.	Cycle Nr.	Mass of the released carbon, µg
	1	29.85
	2	34.38
	3	38.16
	4	30.77
	5	17.3
Total mass of carbon in the burned sample 150.46		

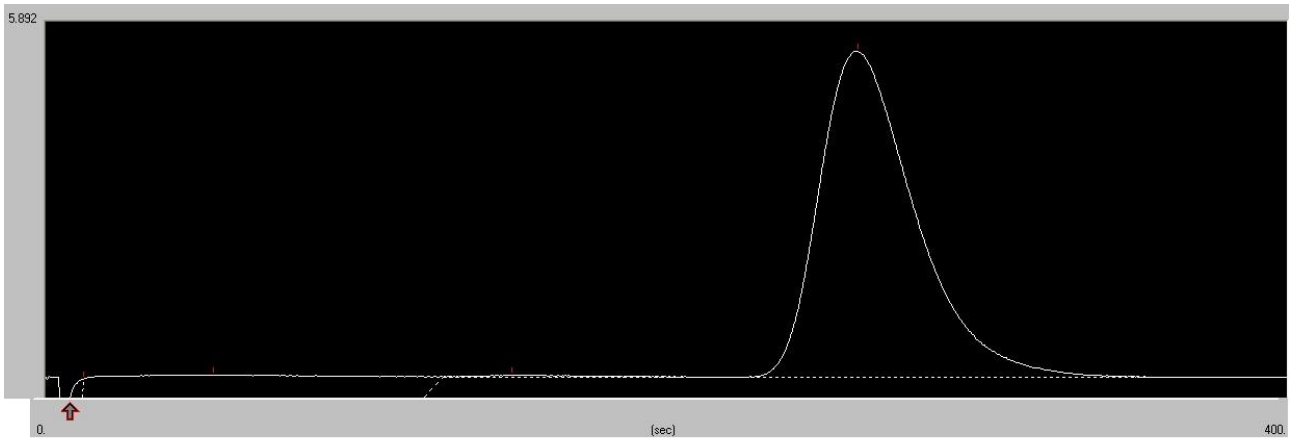

Figure 1. The chromatogram of the burned graphite sample.

The amount of released carbon in the CO_2 form was detected using thermal conductivity detector. The chromatogram of the burned graphite sample is presented in the Figure 1. Further investigations are needed to optimize the instant burning of the graphite sample.

[1] V. Remeikis, A. Plukis, R. Plukiene, A. Garbaras, R. Bariseviciute, A. Gudelis, R. Gvozdaite, G. Duskesas, L. Juodis, Method based on isotope ratio mass spectrometry for evaluation of carbon activation in the reactor graphite, Nuclear Engineering and Design, **240** 2697–2703, (2010).
[2] A. Garbaras, E. Bruzas, V. Remeikis, Stable Carbon Isotope Ratio (δ13C) Measurement of Graphite Using EA-IRMS System, Material Science **21** (2), (2015)

INVESTIGATION OF GRAPHENE LASER ABLATION PARAMETERS EMPLOYING RAMAN SPECTROSCOPY

Aušrinė Jurkevičiūtė[1], Linas Šimatonis[1], Serghej L. Prischepa[2], Tomas Tamulevičius[1]

[1]Institute of Materials Science of Kaunas University of Technology, Baršausko Str. 59, LT-51423 Kaunas, Lithuania
[2]Belarusian State University of Informatics and Radioelectronics, P. Brovka Str. 6, 220013 Minsk, Belarus
ausrine.jurkeviciute@ktu.lt

Graphene has attracted a lot of attention as a novel material, which could replace silicon in semiconductor applications [1]. It is expected to demonstrate exceptional electrical conductivity, absorption, luminescence, etc. [2]. Practical applications of graphene are still limited mainly because of the lithography processes. Femtosecond laser ablation is a non-thermal process in its nature, thus this technique is capable to fabricate high quality structures and has a potential in graphene patterning applications [3]. In this work, we present graphene ablation using various femtosecond laser parameters to find the optimal ablation conditions. Graphene was prepared by atmospheric pressure chemical vapour deposition on copper foil from decane precursor and transferred on Si/SiO_2 substrates.

Graphene was processed employing Pharos femtosecond laser (Light Conversion) and micromachining work station FemtoLAB (Altechna R&D). Laser affected squares of 70 × 70 μm were used for micro Raman spectroscopy (inVia, Renishaw). The 1030 nm wavelength beam was scanned using galvo-scanner system (ScanLab). The 200 kHz repetition rate was selected for this task. The mean power was changed from 3.2 mW to 35.3 mW while the gaps between fabricated lines were varied from 1 μm to 3.8 μm using constant frequency mode with 100 mm/s fabrication speed.

Raman measurements were performed with laser wavelength of 532 nm and 45 mW power employing x50 objective. Spectrum range from 600 cm^{-1} to 3200 cm^{-1} was used for analysis in order to avoid saturation of spectra by silicon peak at 520 cm^{-1}. Measurements were repeated three times. Raman spectra acquired from pristine and under two different conditions laser processed graphene are depicted in Fig. 1.

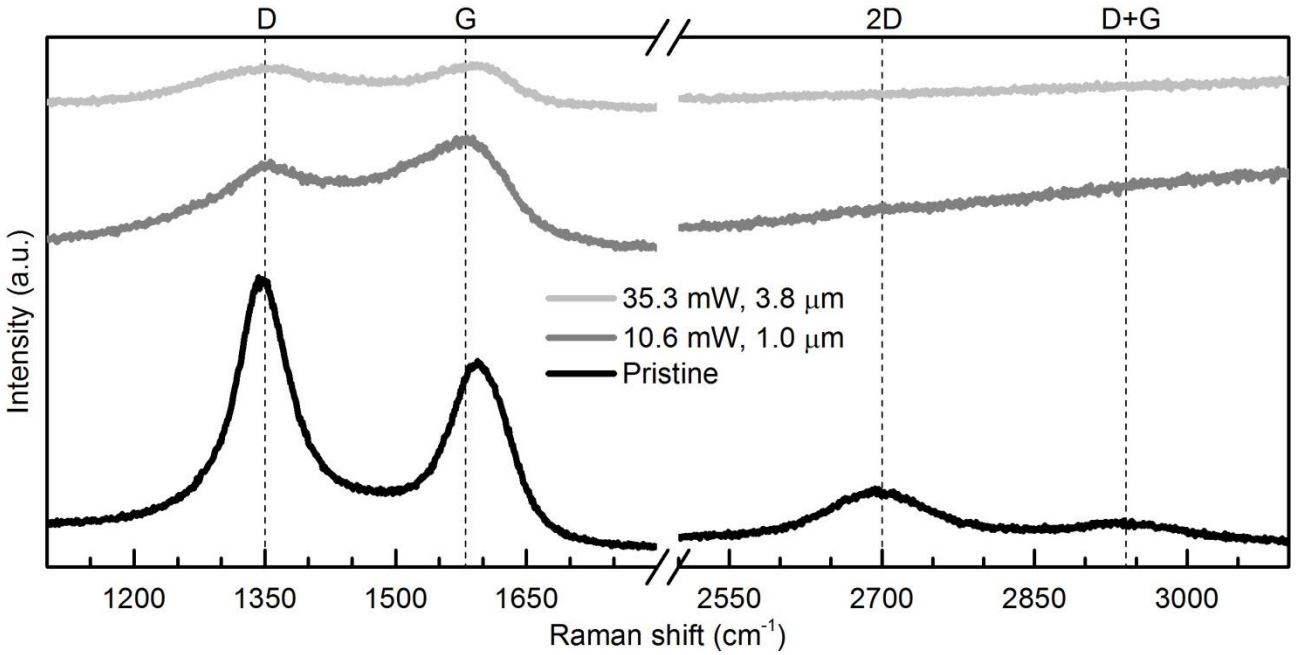

Fig. 1. Raman spectra of three different sample spots: pristine graphene (black); ablated using 10.6 mW power with 1.0 μm hatch gap (dark grey); ablated using 35.3 mW power with 3.8 μm hatch gap. The characteristic Raman peaks of carbon allotropes (D, G, 2D, D+G) are indicated by dashed lines and named above the graph.

It was demonstrated that femtosecond laser ablation can be used as a single step lithography tool for processing of graphene. Raman spectroscopy was used to define the ablation threshold and determine the composition changes on the laser processed graphene. The intensities of D and G peaks change depending on laser ablation parameters. However, it is not totally clear, if 2D and D+G peaks disappear or they are overrun by background signal. They are no longer visible after ablation with 10.6 mW laser power and 1.0 μm hatch gap.

[1] A. Boosalis, T. Hofmann, V. Darakchieva et al., Visible to vacuum ultraviolet dielectric functions of epitaxial graphene on 3C and 4H SiC polytypes determined by spectroscopic ellipsometry, Applied Physics Letters **101**, 011912 (2012).
[2] V. Kiisk, T. Kahro, J. Kozlova et al., Nanosecond laser treatment of graphene, Applied Surface Science **276**, 133-137 (2013).
[3] R. Sahin, E. Simsek, S. Akturk, Nanoscale patterning of graphene through femtosecond laser ablation, Applied Physics Letters **104**, 053117 (2014).

FABRICATION OF PERIODIC MICRO-STRUCTURES USING MULTIPLE BEAM HOLOGRAPHIC LITHOGRAPHY AND MODELLING OF 3D BEAM INTERFERENCE

Artūras Grabusovas[1], Tomas Klinavičius[1], Linas Šimatonis[1], Tomas Tamulevičius[1, 2]
Sigitas Tamulevičius[1, 2]

[1] Institute of Materials Science, Kaunas University of Technology, K. Baršausko St. 59, LT-51923, Kaunas, Lithuania,
[2] Department of Physics, Kaunas University of Technology, Studentų St. 50, LT-51368, Kaunas, Lithuania,
arturas.grabusovas@ktu.edu

Holographic lithography (HL) is a tool offering capabilities to pattern periodic structures with feature sizes from a few micron down to few nanometers and does not require a photomask [1]. Among its advantages are simplicity of the setup and high possible throughput. These features make this technique appealing for certain applications. The patterns may vary only within the limitation of the interference result obtained with certain laser beam arrangement. More complex patterns can be achieved only by using multiple exposures combined with sample rotations. In this work we attempt to experimentally and theoretically demonstrate the polarization influence on the 2D periodic structures patterned employing a multiple beam HL setup.

Proposed multiple beam interference field intensity calculation algorithm enables estimation of the interference patterns in 3D space where all interfering beams overlap. Moreover, it enables calculations with any kind of linear polarization vector angle of each beam, also takes into account the intensity distribution of the individual beams (e.g. Gaussian), evaluates that interference might take place in the corresponding refractive index material (e.g. photoresist) and even addresses the Fresnel reflections from the substrate or antireflective coating underneath. The minimal energy density, necessary to write in the photoresist can be selected based on the intensity threshold that is imposed on the simulation results.

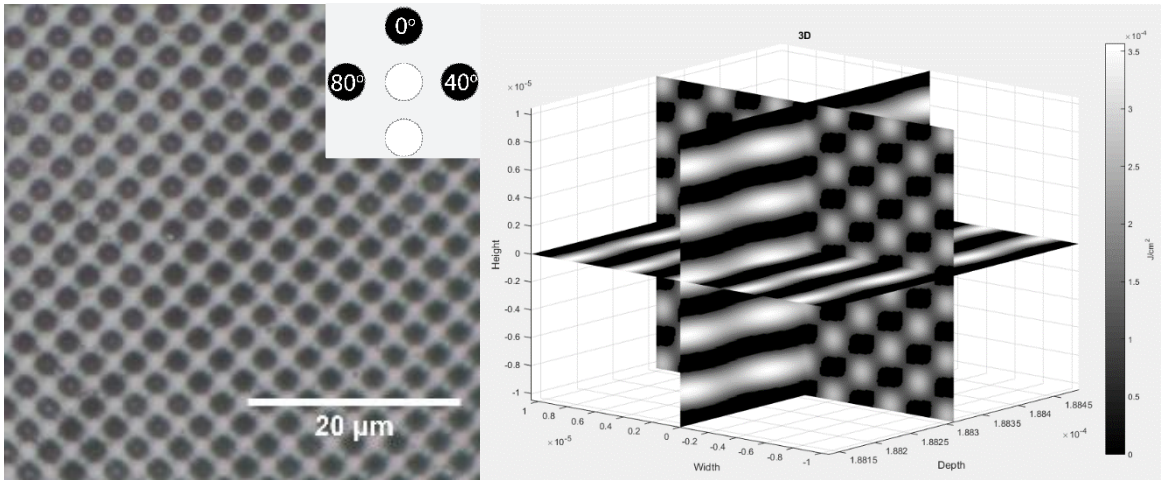

(a) (b)

Fig. 1. (a) Micrograph of the structure patterned in SU-8 photoresist using three interfering beams. The inset depicts the arrangement of the individual beams and orientation of their polarization vectors. (b) Calculated 3D intensity distribution for the same beam arrangement.

Using the HL setup and selecting different arrangements of the interfering beams together with their polarizations we were able to define periodic 2D structures in SU-8 negative tone photoresist (Fig. 1 a). The laser beam is split into multiple beams using a diffractive optical element (DOE). 4f optical system is then used to focus the beams on the sample. Within the 4f system there are two half-wave retarder plates that allow us to rotate the linear polarizations of the individual beams. Finally, slightly in front of the sample there is a metal plate mask which allows to select the beam arrangement from 2-5 beams by blocking the apertures with magnetic strips.

With the aid of computer simulation we can predict the intensity distribution outcomes of many different beam arrangements and expand the range of structures we are able to pattern (Fig. 1 b).

[1] BALACHNINAITĖ Ona, BARGELIS Algirdas, DEMENTJEV Aleksandr, et al. Lazerinė technologija – Vilnius, 2008. P.199-204. ISBN 978-9955-33-456-9

EXAMINATION OF PHOTOPOLYMERIZATION PROCESS IN CASE OF NANOSECOND AND PICOSECOND LASER PULSES

Elena Daugnoraitė, Evaldas Stankevičius, Gediminas Račiukaitis

Department of Laser Technologies, Center for Physical Sciences and Technology, Lithuania
elena.daugnoraite@ff.stud.vu.lt

Interference lithography is a technique for patterning regular arrays of fine features, without the use of complex optical systems or photomasks. It is a very efficient method to make array of periodic microstructures used in tissue engineering, microoptics, microfluidics and photonics. An interference pattern between two or more coherent light waves is set up and recorded in a photosenstive polymer. Light induced photopolymerization reaction starts when photoinitiator molecule absorbs photon and splits into active radicals [1]. There was examined that density of active radicals using different laser pulse durations and pulse repetition rates define geometrical properties of microstrutures. In order to compare microstructures formed by using different laser pulse durations and repetition rates pulse peak intensities were kept comparable for both nano and picosecond pulses.

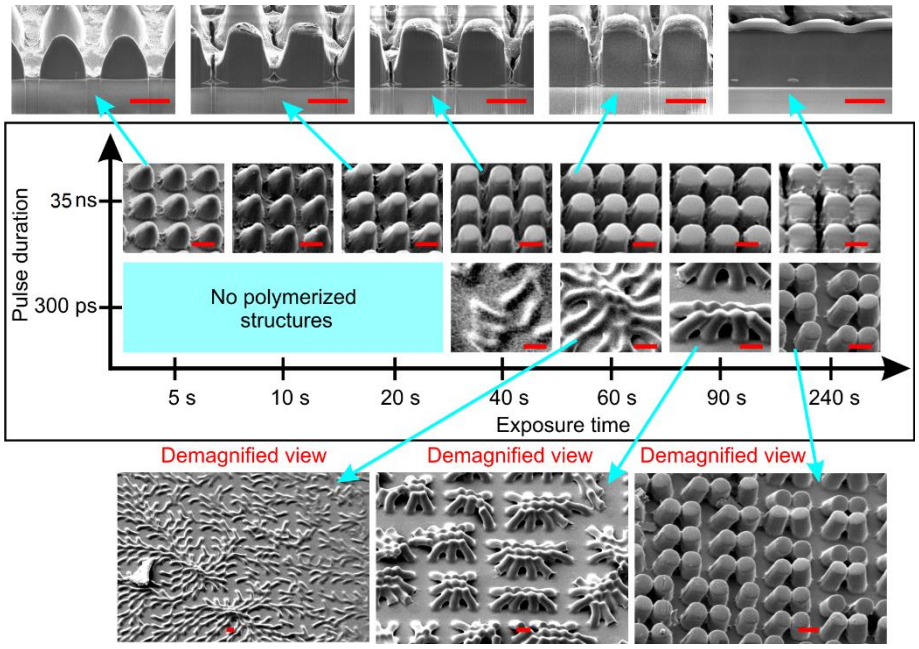

Fig. 1. Micropillar arrays formed using ns and ps pulses with comparable pulse peak intensity. Red scale marks 5 µm.

Radical density generated during laser irradiation (35 ns and 300 ps) is one of the main reasons that leads to geometric differences of the pillars formed in the photopolymer. Also it was demonstrated that using different repetition rates of the same laser pulse different polymerization reaction kinetics and different size microstructures can be achieved [2].

[1] Evaldas Stankevičius "Periodinių mikrodarinių formavimas polimeruose ir jų savybių modifikavimas interferencinės litografijos ir fotojskiepijimo metodais" daktaro disertacija, Fizika (02 P), Vilnius, 2014.
[2] N. Uppal, P. S. Shiakolas "Modeling of temperature-dependent diffusion and polymerization kinetics and their effects on two-photon polymerization dynamics" MEMS MOEMS 7(4), 043002-1, 2008.

GENERATION OF GOLD NANOPARTICLES BY NANOSECOND LASER PULSE IRRADIATION OF THIN GOLD FILMS

Mantas Garliauskas, Evaldas Stankevičius

Department of Laser Technologies, Center for Physical Sciences and Technology, Lithuania
mantas.garliauskas@ftmc.lt

Recently, it has been found that electrochemical biosensors, containing gold nanoparticle (Au NP) coated ITO (indium tin oxide) electrode, exhibit high sensitivity and selectivity to detectable molecules [1,2]. That was attributed to the unique properties of Au NPs, such as large surface-to-volume ratio, high conductivity, excellent biocompatibility and low toxicity [1,3,4]. Commonly and relatively cheaply, deposition of metal nanoparticles on the glass surface is done by immersing the silanized substrate into the colloidal solution of nanoparticles [5]. However, we found that it is difficult to deposit sufficient concentration of Au NPs on the silanized ITO surface. Therefore, the approach of direct Au NP generation by nanosecond laser pulse irradiation of thin Au films [6], coated on the ITO layer, was employed. In this work, we investigated the influence of Au film thickness and laser irradiation parameters on the size distribution and area density of generated Au NPs on the ITO surface.

Firstly, seven different thicknesses of Au films were deposited on the 120 nm-thick ITO layer. Secondly, the samples were irradiated by the second harmonics (532 nm wavelength) radiation of Q-switched Nd:YVO_4 laser *NL220* (*Ekspla*), which has a pulse duration of 30 ns. When the laser radiation was absorbed in the Au film, its temperature was increased above the melting point, causing the film to rupture into nanodroplets due to the dewetting process. After the laser exposure, formed nanodroplets cooled down and solidified into Au NPs. Generated Au NPs were characterized by processing the scanning electron microscope images using the computer software *ImageJ*.

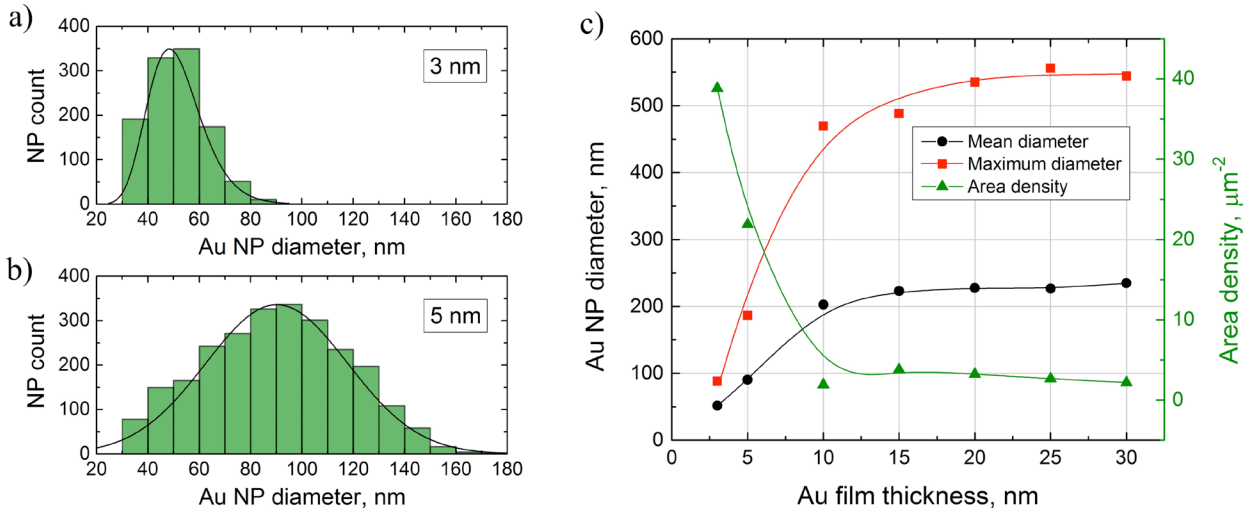

Fig. 1. Size distributions of Au NPs generated using 3 nm-thick and 5 nm-thick Au films (a, b), and Au NP diameter and area density dependence on the Au film thickness (c).

Size distribution histograms of Au NPs generated using 3 nm-thick and 5 nm-thick Au films are depicted in Figures 1a and 1b, respectively. Laser irradiation of 3 nm-thick Au film generated ~50 nm mean diameter Au NPs, whereas irradiation of 5 nm-thick Au film resulted in significantly larger size dispersion of Au NPs with a mean diameter of ~90 nm. Summarized Au NP size and area density dependence on the thickness of Au layer is shown in Figure 1c. The mean diameter reaches the value of ~220 nm and does not depend on the Au film thickness in the range of 15-30 nm. The maximum area density of generated Au NPs was ~40 μm^{-2} for 3 nm-thick Au film and decreased to ~3 μm^{-2} when generating Au NPs in 10 nm and thicker Au films.

In conclusion, it was determined how Au layer thickness and laser irradiation parameters affect the size distribution and area density of generated Au NPs. The results of this work are important for the further research to develop a highly sensitive electrochemical biosensor based on the Au NP textured ITO electrode.

[1] X. C. Song, X. Wang, Y. F. Zheng et al., A hydrogen peroxide electrochemical sensor based on Ag nanoparticles grown on ITO substrate, J. Nanoparticle Res. **13**, 5449-5455 (2011).
[2] J.-H. Lee, B.-K. Oh, and J.-W. Choi, Electrochemical sensor to detect neurotransmitter using gold nano-island coated ITO electrode, J. Nanosci. Nanotechnol. **11**, 6539-6543 (2011).
[3] Y. C. Yeh, B. Creran, and V. M. Rotello, Gold nanoparticles: preparation, properties, and applications in bionanotechnology, Nanoscale **4,** 1871-1880 (2012).
[4] A. Tomar and G. Garg, Short review on application of gold nanoparticles, Glob. J. Pharmacol. **7,** 34-38 (2013).
[5] A. F. Scarpettini and A. V Bragas, Coverage and aggregation of gold nanoparticles on silanized glasses, Langmuir **26**, 15948-15953 (2010).
[6] K. Ratautas, M. Gedvilas, G. Račiukaitis, and A. Grigonis, Nanoparticle formation after nanosecond-laser irradiation of thin gold films, J. Appl. Phys. **112**, 013108 (2012).

BIORESISTS FROM RENEWABLE RESOURCES AS SUSTAINABLE PHOTORESINS FOR 3D LASER MICROLITHOGRAPHY: MATERIAL SYNTHESIS, CROSS-LINKING RATE AND CHARACTERIZATION OF THE STRUCTURES

Edvinas Skliutas[1], Sigita Kašėtaitė[2], Linas Jonušauskas[1], Sima Rekštytė[1], Jolita Ostrauskaitė[2], Mangirdas Malinauskas[1]

[1]Department of Quantum Electronics, Vilnius University, Saulėtekis Ave 10, Vilnius LT-10223, Lithuania
[2]Department of Polymer Chemistry and Technology, Kaunas University of Technology, Radvilėnai Rd. 19, Kaunas LT-50254, Lithuania
edvinas.skliutas@ff.stud.vu.lt

Stereolithography (SLA) allows rapid and accurate materialization of computer aided design (CAD) models into real objects out of photoreactive resin. Nowadays this technology has evolved to a widespread simple and flexible personal tabletop devices 3D optical printers. However, 3D SLA printers use commercially available resins which are not cheap and of limited applicability, often of unknown chemical ingredients and fixed to certain mechanical properties [1]. In our researche, it is important to have bioresin appropriate to 3D print micro-scaffolds for cell proliferation and tissue engineering. This has encouraged us to study synthesis and photostructuring of organic biomaterials applicable for 3DP technology. The primary chosen substances for photosensitive material synthesis were glycerol diglycidyl ether and epoxidized linseed oil which can be obtained from renewable resources. Both materials polymers can be applied as sustainable photoresins [2]. They are some of the cheapest and most abundant, non-toxic, annually renewable natural resources available in large quantities, with a high content of double bonds making them an ideal component for the preparation of bio-based resins.

Chosen composition was the following: glycerol diglycidyl ether or epoxidized linseed oil, 3,4-epoxycyclohexylmethyl-3,4-epoxycyclohexane carboxylate (30 mol%), photoinitiator (mixture of triarylsulfonium hexafluoroantimonate salts, 50 % in propylene carbonate, 3 mol%). UV lithography was employed to determine its photocross-linking rate and describe processed material properties. Small droplets of the composition were casted on the glass. To ensure that the formed structures after UV (λ=365 nm) exposure will adhere to the surface, the droplets were facing downwards. The hydrophilic interaction between glass surface and droplets was strong enough to keep the samples at the substrate. After exposing material to UV radiation through a micro-patterned amplitude mask selective photopolymerization was observed. Acetone was used as a solvent to dissolve UV unaffected area and leaving only formed microstructures on the substrate. The materials were classified according to their: photoreactivity and photomodification selectivity. The resins were compared to FormLabs Form 1+ standard materials, namely Form Clear and AutoDesk Ember PR48.

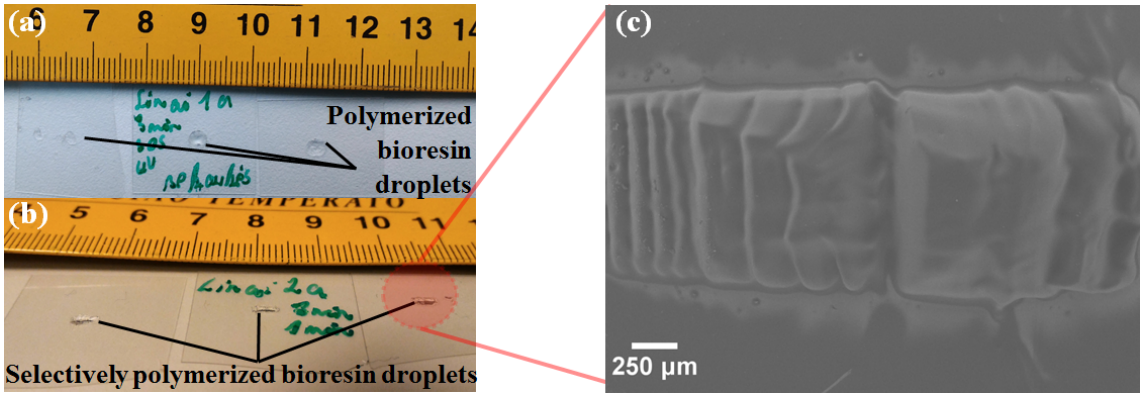

Fig. 1. (a) – polymerized linseed oil-based resin droplets (after 260 s exposure to UV radiation); (b) – selectively polymerized droplets (after 220 s exposure to UV radiation); (c) – enlarged view of the droplet (image obtained with SEM) [3].

The results show that it is possible to induce photopolymerization reaction in linseed oil-based compositions and to control photomodification selectivity using 365 nm wavelength and 270 mW power light source. However, the composition is less photosensitive than commercial resins, thus it requires prolonged exposure, more powerful light source or additional photoinitiator. It motivates to continue studying photoresins from renewable resources towards 3D laser microlithography applications.

[1] M. Malinauskas, et al., Light: Sci. Appl. **5**, e16133 (2016).
[2] S. Kasetaite, et al., Polym. Bull. **72**, 31913208 (2015)
[3] E. Skliutas, et al., Proc. SPIE to be published (2017)

INVESTIGATION OF REFLECTIVITY OF PLASMON–PHONON MODES IN GRATING-COUPLED AlGaN/GaN HETEROSTRUCTURES GROWN ON SiC AND GaN SUBSTRATES

Vytautas Janonis[1], Vytautas Jakštas[1], Irmantas Kašalynas[1], Pawel Prystawko[2]

[1] Center for Physical Sciences and Technology, Saulėtekio al. 3, LT-10222 Vilnius, Lithuania
[2]Institute of High Pressure Physics, Polish Academy of Sciences, Sokołowska 29/37, 01-142 Warsaw, Poland
Vytautas.janonis@ftmc.lt

During last decade, the properties of electron plasma and lattice oscillations have been widely investigated in polar semiconductors GaAs and AlGaAs [1] and heterostructures such as GaAs and InGaAs [2], GaN and AlGaN alloys [3-4]. Gallium nitride (GaN) is one of the most promising materials encouraging rapid development of THz devices. Plasmonic oscillations emerging in the 2D electron gas channel (2DEG) of AlGaN/GaN heterostructure, have been shown as a possible electronic, room environment THz source, yet for technological applications 2DEG THz emission must be further enhanced. This may be done by designing in an optimal way the grating coupler on the surface.

In this research, the reflection spectra of the grating-coupled AlGaN/GaN heterostructures grown on SiC or GaN substrates were investigated with the aim to describe the interaction between grating and phonon modes for efficient electromagnetic radiation coupling with the semiconductor structure.

Two samples were fabricated for the experiment. The first sample consisted of 26/1000 nm thick $Al_{0.19}Ga_{0.81}/GaN$ (with 19% of Al) heterojunction which was grown on the bulk GaN n-type Ammono substrate. Grating with the period of 16 um was fabricated on the surface of heterojunction depositing Ti/Au metals by using standard UV photolithography procedures. For the second sample, a 28/1000 nm thick $Al_{0.25}Ga_{0.75}/GaN$ heterojunction was grown on 500um thick 6H-SiC substrate. In this a case, the period of the grating-coupler was of 7 um.

The reflection spectra were measured using Far Infrared Fourier Transform (FTIR) spectrometer over the frequency range of 400-1500 cm^{-1}. IR reflectance measurements were conducted at room temperature using polarized spectrometer beam. The reflectivity was calibrated using the reflectance spectrum of a gold film on a sapphire plate. Experimentally measured spectra were modeled using classic electrodynamic approach of the dielectric function.

The first grating-coupled sample demonstrated two plasmon modes in the reflection spectrum indicating interaction between plasmon and phonon modes. GaN has only one branch for each vibration direction of transverse optical (TO) and longitudinal optical (LO) phonon modes. Therefore, the first sample was considered as the reference for further investigation of plasmon–phonon modes in AlGaN/GaN heterostructures grown on foreign substrates. The reflection of the second grating-coupled sample demonstrated a more complex reflectivity with up to five peaks of plasmon–phonon modes in the spectrum (Fig. 1). In the case of the second sample, it was observed, that plasmons interact with phonon modes of AlGaN/GaN heterojunction as well as SiC substrate.

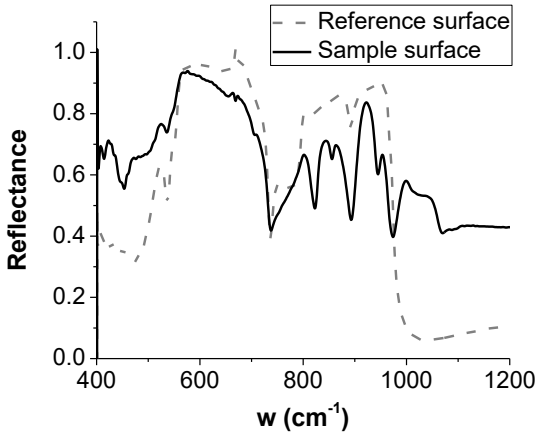

Fig. 1. The reflectivity spectrum of grating-coupled AlGaN/GaN structures grown on SiC substrate. Multiple phonon-plasmon modes were observable as strong peaks.

[1] Požela K, Širmulis E, Kašalynas I, Šilėnas A, Požela J, and Jucienė V, 2014 Selective thermal terahertz emission from GaAs and AlGaAs Appl. Phys. Lett. **105**, 091601.
[2] Ibáñez J, Tarhan E, Ramdas A, Hernández S, Cuscó R, Artús L, Melloch M, and Hopkinson M 2004 Direct observation of LO phonon-plasmon coupled modes in the infrared transmission spectra of n-GaAs and n-InxGa1-xAs epilayers Phys. Rev. B **69**, 075314.
[3] Talwar D.N 2010 Direct evidence of LO phonon-plasmon coupled modes in n-GaN Appl. Phys. Lett. **97**, 051902
[4] Rahbany N, Kazan M, Tabbal M, Tauk R, Jabbour J, Brault J, Damilano B, and Massies J 2013 Measurement of the effect of plasmon gas oscillation on the dielectric properties of p- and n-doped AlxGa1−xN films using infrared spectroscopy J. Appl. Phys. **114**, 053505.

DETECTION OF LOW DENSITY HIDDEN OBJECTS USING TERAHERTZ RADIATION

Domas Jokubauskis, Linas Minkevičius, Rimvydas Venckevičius, Dalius Seliuta, Gintaras Valušis

Center for Physical Sciences and Technology, Saulėtekio al.3, LT-10257 Vilnius, Lithuania
domas.jokubauskis@ftmc.lt

Terahertz (THz) frequency range spanning the range of 100 GHz to 10 THz is being actively exploited for imaging applications in security [1], medical [2] and quality control [3]. As a rule, for screening purposes X-ray radiation is mainly used, however, due to ionizing nature, it is harmful. For more challenging applications such as detection of low density materials (like clothing, plastics, carton etc.) novel solutions are required. Reasonable way to proceed would be employment of THz radiation, which can penetrate through non-conducting materials.

In this work, we demonstrate application of THz radiation for imaging the objects – made of low and high density material, – hidden in cotton fabric.

Experimental setup for THz imaging consists of frequency multiplier chain THz source, high density polyethylene (HDPE) lenses, multiple off-axis parabolic mirrors, electronically controlled X-Y stage and titanium based micro-bolometric THz detectors [4]. Test samples were placed in a focal spot of focusing mirror for transmission and reflection measurements. Transmitted and reflected radiation was detected employing titanium-based micro-bolometer detectors; the output signals were amplified and registered using lock-in amplifiers. Raster scanning technique via custom made computer software was implemented for THz imaging process.

Steel blade, hypodermic needle and a piece of nitrile glove served as samples placed between up to six layers of cotton fabric. Terahertz images were recorded at 100 GHz, 300 GHz, 600 GHz frequencies in transmission as well as reflection geometries.

Distinguishable features of the hidden objects including 0.6 mm diameter needle and separate layers of the nitrile glove were observed indicating that THz imaging can be used to detect low density objects hidden in cotton fabric.

---

[1] M. Kowalski, N. Palka, M. Piszczek, and M. Szustakowski, Hidden object detection system based on fusion of THz and VIS images, Acta Phys. Pol. A, **124**, 490–493, (2013).

[2] F. Wahaia, I. Kasalynas, D. Seliuta et al., Study of paraffin-embedded colon cancer tissue using terahertz spectroscopy, J. Mol. Struct., **1079**, 448-453, (2015).

[3] M. Dohi et al., Application of terahertz pulse imaging as PAT tool for non-destructive evaluation of film-coated tablets under different manufacturing conditions, J. Pharm. Biomed. Anal., **119**, 104–113, (2016).

[4] J. Trontelj and A. Sešek, Micro-machined millimeter wave sensor array for FM radar application, Proc. SPIE 8544, Millimetre Wave and Terahertz Sensors and Technology V, **8544**, 85440G (2012).

TRANSMISSION OF ELECTROMAGNETIC RADIATION THROUGH MODERN WINDOW PANES IN WIFI FREQUENCY RANGE

Evaldas Bilotas, Paulius Ragulis, Žilvinas Kancleris

Center for Physical Sciences and Technology, Saulėtekio Ave. 3, LT-10257 Vilnius, Lithuania
evaldas.bilotas@ftmc.lt

In the past ten years, high energy class buildings became very popular. Various methods were introduced in order to increase thermal isolation. Main approach was to implement low emission (Low-E) coating in window panes, which consists of several layers metal and metal oxide, those form tens of nanometers thick conductive layer. This layer reflects most of the infrared radiation. It was investigated that metal coating also attenuates microwaves up to ten thousand times [1], which means that mobile communication frequencies, GPS and WiFi are reflected and can't reach the user [2]. Frequency selective surfaces (FSS) were introduced as a possible solution for the reduction of metal coating microwave shielding [3]. To realize FSS, conductive layer is removed at specific places forming particular geometrical pattern which acts as a band pass filter for desirable frequency band. In the present paper we propose, in our opinion, the simpler way to reduce the shielding at WiFi frequency band by changing the thickness of glasses and the distance between them in a window pane.

Shielding effectiveness (SE) is a parameter, which shows objects ability to decrease electromagnetic wave amplitude at different frequencies. The decrease can be caused either by reflection or by absorption. SE is defined as ratio between power of incident signal and power of signal passed through the object. SE is measured in dB and is expressed in the following way:

$$SE(f) = 10 * \log\left(\frac{P_{\text{inc}}(f)}{P_{\text{glass}}(f)}\right) \quad (1)$$

In our research, we used theoretical model, in order to find out how shielding effectiveness depends on longitudinal parameters. Calculations were made by using well known matching and propagation matrices theory [4]. The matching matrix was changed accordingly when the boundary conditions of the conductive surface were accounted [5]. All experiments were made by constructing double pane windows with two glasses and by varying the distance between them. Both glasses were obtained from the company Saint Gobain, they are 4 mm thick and one of them has surface conductivity of $\sigma = 0.094$ S. Experiments demonstrate that window panes with 16 mm gap between glasses has the largest SE of 28.5 dB at 5 GHz frequency. It is worthwhile mentioning that such a gap is mostly used in commercially available window panes. By reducing the gap to 2.5 mm, we get the minimum SE of 15.5 dB. At 2.4 GHz frequency, space between glasses has very little influence on shielding effectiveness. Standard window pane with 16 mm gap, shields by 23 dB at 2.4 GHz, while the minimum value of 20.5 dB can be reached with 9 mm gap. Good coincidence was achieved between experimental results and calculated data which proves the viability of the model used. Therefore, we used this model further for the calculation of the dependence of SE on the thickness of metalized and non-metalized glasses and gap between them, searching for the lowest possible SE at the chosen frequencies.

By using accumulated knowledge of the dependence of shielding effectiveness on the thickness of glasses, the optimal window panes were determined demonstrating the lowest SE at WiFi frequencies. The results showed that SE can be lowered by 13.5 dB at 5 GHz and 7 dB at 2.4 GHz only by changing geometry of the window panes. These results might be used in the commercial production of the Low-E window panes.

[1] P. Angskog, M. Backstrom, and B. Vallhagen, "Measurement of radio signal propagation through window panes and energy saving windows," in *Electromagnetic Compatibility (EMC), 2015 IEEE International Symposium on*, pp. 74-79, 2015.

[2] A. Asp, Y. Sydorov, M. Valkama, and J. Niemela, "Radio signal propagation and attenuation measurements for modern residential buildings," *2012 IEEE Globecom Workshops, GC Wkshps 2012,* pp. 580-584, 2012.

[3] M. Gustafsson, A. Karlsson, A. P. P. Rebelo, and B. Widenberg, "Design of frequency selective windows for improved indoor outdoor communication," *IEEE Transactions on Antennas and Propagation,* vol. 54, pp. 1897-1900, 2006.

[4] S. J. Orfanidis, "Electromagnetic Waves and Antennas," ed, p. 2008.

[5] P. Ragulis, R. Simniškis, and Ž. Kancleris, "Shift and elimination of microwave Fabry-Perot resonances in a dielectric covered with a thin metal layer," *Journal of Applied Physics,* vol. 117, p. 165302, 2015.

INVESTIGATION AND OPTIMIZATION OF THE SOLID-STATE LUMINAIRES FOR STREET LIGHTING

Vladislovas Čižas, Pranciškus Vitta

Institute of Applied Research, Vilnius University, Lithuania
vladislovas.cizas@gmail.com

Nowadays, people are getting more and more concerned about saving planet by reducing energy consumption and it was found that a huge amount of energy is being wasted due to inefficient street lighting installations. Therefore, the street lighting market is experiencing the technology changeover when old discharge lamps are replaced by modern LED based luminaires. In parallel to technology change, the expectations of customers and quality requirements evolve significantly requiring much more precise and profound design and development of lighting systems. Keeping in mind the vast need of street lighting renovation the main goal of the work was to develop the method of digital computing to identify the optimal parameters and theoretical limits of the lighting system designed for particular street and particular street lighting class.

Therefore, here we report the analysis of the street lighting standard EN 13201:2016 and methods for assessment of the optimal street lighting parameters under consideration. Several theoretical light spatial distributions were investigated and the "whale-tale" distribution selected for the modelling as the most versatile one. An automated routine generating a set of light spatial distributions (IES files), calculating all standardised lighting parameters and comparing them with EN 13201:2016 standard requirements was developed. The accuracy of the routine was tested in comparison with commercial software Dialux EVO and the errors did not exceed 1%. It is worth to be noticed that commercial lighting design software like Dialux EVO are perfect tools for design and visualization of the installations, but not suitable for optimization and automated modelling exercises performed in this work. Therefore development of the own digital computing application was a necessary part of this work.

In conclusion, the most recent design street examples were modelled, lighting parameters optimized and limiting conditions for pole height and distance revealed.

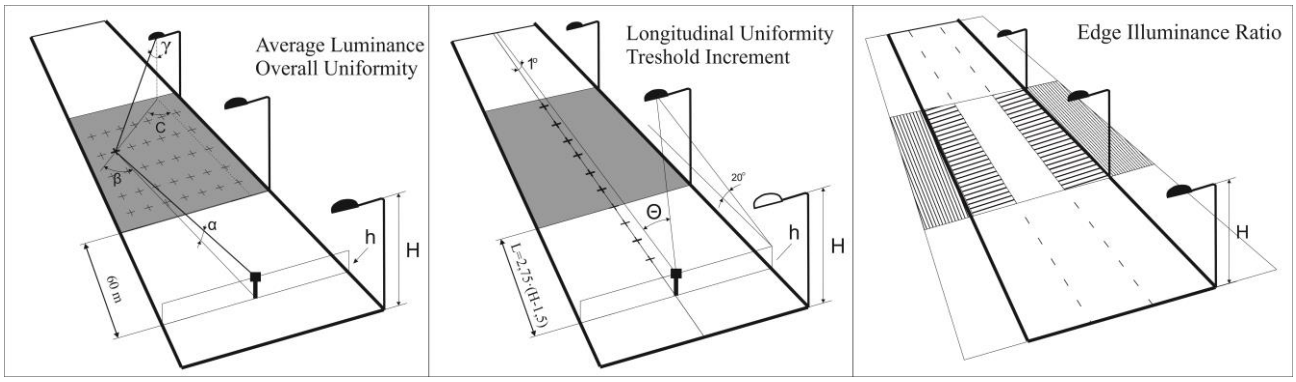

Fig. 1. Calculating methods of standardized parameters.

[1] EN 13201-1:2015 (E), *Road lighting – Part 1-5*, European Committee for Standardisation / Technical Committee 169.
[2] MORENO, I. et al., "Modelling LED Street Lighting", *Applied Optics*, **53** 4420-4430 (2014)

DEVELOPMENT OF THE ZIGBEE RF4CE BASED SMART LIGHTING CONTROL SYSTEM PROTOTYPE

Miglius Budriūnas, Pranciškus Vitta

Institute of Applied Research, Vilnius University, Lithuania
miglius.budriunas@ff.stud.vu.lt

With the growth of lighting market there is an increasing interest in the smart-lighting control systems. Modern illumination systems based on light-emitting diodes (LEDs) together with modern ICT technologies overcome light control standards and even expectations of the customers. Therefore, simple and intuitive way to control sophisticated lighting systems is of high demand and no optimal solutions found yet.

The main goal of this work was to prepare and begin developing the autonomous stand-alone wireless smart luminaire control prototype, which could be operated without any expensive smart devices such as computers, smartphones or tablets. The following tasks were identified in order to achieve the goal:

1. Analyse the most popular wireless communication protocols and standards and choose the most suitable for the particular smart lighting application.
2. Develop the prototype of at least controller end unit and smart-lighting principal control algorithm.
3. Investigate and characterize the wireless communication signal distribution map and suitability for particular application.

The control system of smart luminaire capable to change light intensity, correlated colour temperature and saturation/dulling ratio was set for development and investigation. Commercial wall dimmers were chosen as human interface devices for the simplest and most intuitive way of lighting control. The ZigBee RF4CE wireless communication protocol was chosen as the most suitable for smart lighting controls due to the promising efficiency, signal stability and ability to be powered from battery. Such system setup allows minimizing installation costs in renovated objects, where additional control wires are difficult to install.

The prototype controller endpoint of ZigBee communication was developed basing on ATSAMR21G18A microcontroller. The measurement of ZigBee RF4CE signal distribution map showed that reliable communication could be obtained within a single room if only integrated antennas used. Furthermore, it was noticed that ZigBee RF4CE signal do not penetrate through monolithic walls and reinforced concrete.

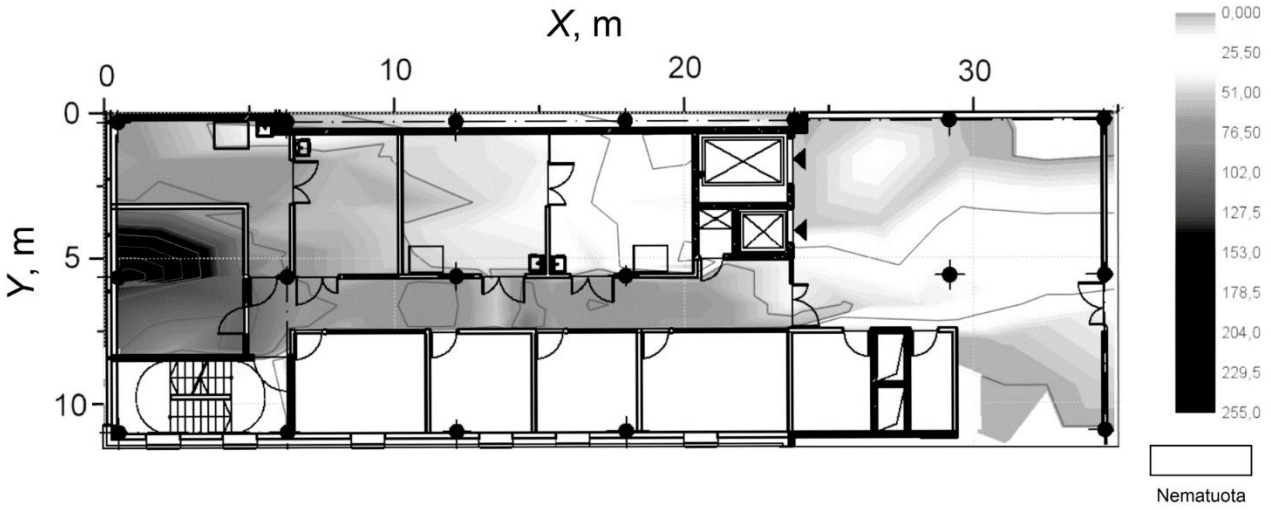

Fig. 1. ZigBee RF4CE signal distribution map.

INVESTIGATION OF RECOMBINATION MECHANISM IN GREEN OLET INCORPORATING TPBI AS ELECTRON TRANSPORT LAYER

Vishwa Bhatt[1], Mihirsinh Chauhan[1], Khushdeep Kaur[4], Vaibhav Rao[2], Pankaj Yadav[3], Brijesh Tripathi[3], U. K. Dwivedi[5], Manoj Kumar[3]*

[1]Department of Solar Energy, School of Technology, Pandit Deendayal Petroleum University, Gandhinagar – 382007 (India).
[2]Ultrasound Research Institute (Electrical and electronic Engineering),Kaunas University of Technology, Kaunas, 44249(Lithuania).
[3]Department of Science, School of Technology, Pandit Deendayal Petroleum University, Gandhinagar – 382007 (India).
[4]Department of Electronic Science, Kurukshetra University, Kurukshetra – 136119 (India).
[5]Amity School of Engineering and Technology, Amity University, Jaipur – 302006 (India).
thevaibhavrao@yahoo.com

OLETs are relatively new opto-electronic devices showing good light emitting proprieties with switching action like a transistor [1-3]. These kind of multifunctionality of the device is very useful in the applications such as cell phones, PDA (Personal Digital Assistance), digital cameras etc. [4,15]. Despite of these developments, many issues such as low device efficiency, poor long term efficiency, low external quantum efficiency etc need to be explored further. In an OLET, electroluminescent emission layer (EL) is sandwiched between electron and hole transport layers and the performance is mainly dependent on the charge-transport properties of the EL emission layer.

In this article, the electric charge transport properties of 1,3,5-tris(N-phenyl benzimidazole-2-yl)benzene (TPBI) as an electron transport layer and its effect on the light emission pattern of the OLETs has been investigated. The mobility, maximum I_{PH}, maximum brightness, ON/OFF ratio, efficiency, and external quantum efficiency (EQE) of the device are explored using the current-voltage characteristics of the device and the light emission properties have been explored using electroluminescence measurements. The maximum current and luminance obtained for TPBI based device is 1.3 mA and 325 cd m^{-2} .The max obtained EQE is 1.271% with the maximum current efficiency of 1.05 cd A^{-1}.

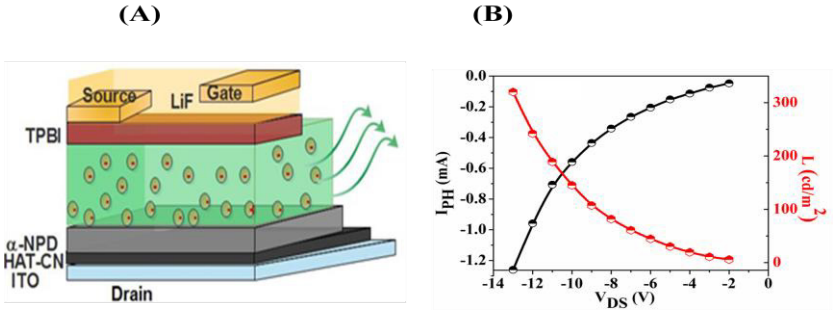

Fig.1. (A) Schematic diagram and (B) Current-Voltage luminance characteristics of OLET

[1] C. Zhang, P. Chen, W. Hu, Organic Light-Emitting Transistors: Materials, Device Configurations, and Operations, Small, 12 (2016) 1252-1294.
[2] S.Z. Bisri, T. Takenobu, Y. Yomogida, H. Shimotani, T. Yamao, S. Hotta, Y. Iwasa, High Mobility and Luminescent Efficiency in Organic Single-Crystal Light-Emitting Transistors, Advanced Functional Materials, 19 (2009) 1728-1735.
[3] M. Kitamura, T. Imada, Y. Arakawa, Organic light-emitting diodes driven by pentacene-based thin-film transistors, Applied Physics Letters, 83 (2003) 3410-3412.
[4] S. Verlaak, D. Cheyns, M. Debucquoy, V. Arkhipov, P. Heremans, Numerical simulation of tetracene light-emitting transistors: A detailed balance of exciton processes, Applied Physics Letters, 85 (2004) 2405-2407.
[5] C. Rost, S. Karg, W. Riess, M.A. Loi, M. Murgia, M. Muccini, Ambipolar light-emitting organic field-effect transistor, Applied Physics Letters, 85 (2004) 1613-1615.

ADDITIVE-FREE POLYMERIC TRIARYLAMINE DERIVATIVES AS HOLE TRANSPORTING MATERIALS FOR STABLE PEROVSKITE SOLAR CELLS

Taisuke Matsui,[1] Ieva Petrikyte,[2] Tadas Malinauskas,[2] Konrad Domanski,[3] Maryte Daskeviciene,[2] Matas Steponaitis,[2] Paul Gratia,[4] Wolfgang Tress,[3] Juan-Pablo Correa-Baena,[5] Antonio Abate,[3] Anders Hagfeldt,[5] Michael Graetzel,[3] Mohammad Khaja Nazeeruddin,[5] Vytautas Getautis,[2] Michael Saliba[3,4]

[1]Advanced Research Division, Materials Research Laboratory, Panasonic Corporation, 1006 Kadoma, Kadoma City, Osaka 571-8501, Japan
[2]Department of Organic Chemistry, Kaunas University of Technology, Radvilenu pl. 19, Kaunas, 50254, Lithuania
[3]Laboratory of Photonics and Interfaces, Institute of Chemical Sciences and Engineering, École Polytechnique Fédérale de Lausanne, Lausanne CH-1015, Switzerland
[4]Group for Molecular Engineering of Functional Materials, Institute of Chemical Sciences and Engineering, École Polytechnique Fédérale de Lausanne, Lausanne CH-1015, Switzerland
[5]Laboratory of Photomolecular Science, Station 6, CH-1015 Lausanne, Switzerland
matas.steponaitis@ktu.lt

Today organic optoelectronics require ability to create devices by solution deposition methods, preferably using simple, inexpensive and easily purified materials. Organic photovoltaic devices are made of multiple layers and high performance is only possible using materials which have good compatibility with each other. Some of those requirements include the stability issue, which derives from additives that are used in the process of increasing the conductivity of hole transporting materials.

Having that in mind triarylamine derivative polymers with different functional groups were synthetized as hole transport materials (HTMs) for perovskite solar cells (PSCs). The novel materials enabled efficient PSCs without the use of chemical doping to enhance the charge transport. Devices employing poly(triarylamine) with methylphenylethenyl functional groups showed better power conversion efficiency then widely used additive-free compound - poly[bis(4-phenyl)(2,4,6-trimethylphenyl)amine] (PTAA). Notably, devices with the foremost polymer enabled stable PSCs under 1 sun at maximum power point tracking for ~40 hours and under elevated temperature (85 °C) for more than 140 hours. The results present remarkable progress towards stable PSC under real working conditions, which is crucial for industrial application.

ELECTROCHEMICAL BARRIER LAYER THINNING OF ANODIC ALUMINUM OXIDE

Edita Vernickaitė[1*], Pavel Globa[2], Henrikas Cesiulis[1], Natalia Tsyntsaru[1,2*]

[1] Department of Physical Chemistry, Vilnius University, Lithuania
[2] Institute of Applied Physics of ASM, Academiei str. 5, Chisinau, Moldova
edita.vernickaite@chf.stud.vu.lt

Anodic aluminum oxide (AAO) template has gained increasing importance in recent years due to its potential industrial and technological applications for nanometric device fabrication. Highly ordered nanopores offer the possibility to use AAO as a template for the formation of nanostructured materials, including nanotubes and nanowires [1]. AAO is usually formed as a result of an inexpensive self-organized two-step anodization of aluminum in various acidic solutions [2]. Reduction of expenses associated with using pure aluminum in anodization process can be achieved by AAO formation on cheaper low-purity aluminum alloy. Still in both cases the non-conductive barrier layer after anodization hinders the electrochemical growth of nanostructures and should be thinned. In this present work the thinning of the barrier layer of AAO membrane produced on AA1050 alloy in 2 M sulfuric acid solution have been performed. It was observed that the treatment of barrier layer is highly correlated with the temperature and time. The treatment of AAO template in this media under potentiostatic mode (E = -0.85 V) permits control of thickness of the barrier layer by changing temperature from 20 to 60 °C. It was found that higher temperature promotes the reaction of dissolution and barrier layer can be reduced from approximately 26 nm (before treatment) to 12 nm at 30 °C. At higher temperature the destruction of nanopores has been noticed. Additional treatment time research has need performed in order to establish a good reproducible control over the dissolution rate of the non-conductive barrier oxide layer of AAO nanotemplate. The results indicated that with increasing the treatment time from 0 to 30 min the barrier layer can be thinned up to 10 nm. With further increase of treatment time the thickness of barrier layer does not change significantly and after the exposure for 60 min in 2 M sulfuric acid solution at 30 °C the structure of nanopores was destroyed.

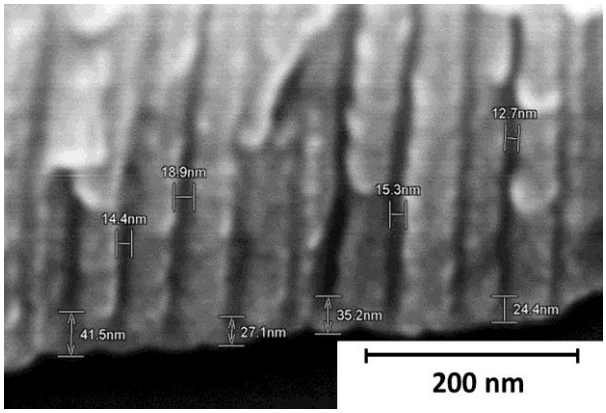

Fig. 1. SEM image of AAO membrane after anodization before chemical etching in 2 M H_2SO_4 solution.

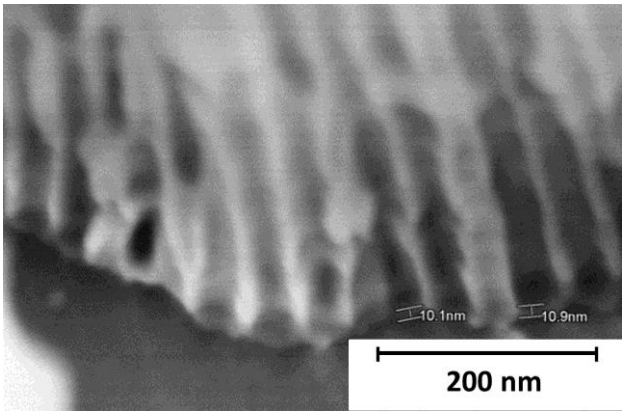

Fig 2. SEM image of AAO membrane after chemical etching under potentiostatic mode in 2 M H_2SO_4 solution at 30 °C for 30 min.

Acknowledgments: The authors acknowledge funding from the Research Council of Lithuania (MIP-031/2014) and Moldavian National Project 15.817.02.05A.

[1] N. Tsyntsaru, S. Silkin, H. Cesiulis, M. Guerrero, E. Pellicer, J. Sort, Toward uniform electrodeposition of magnetic Co-W mesowiresarrays: direct versus pulse current deposition, *Electrochimica Acta* 188 (2016) 589–601.
[2] H. Masuda, F. Hasegwa, S. Ono el al., *Journal of The Electrochemical Society* 144 (5) (1997) L127-L130.

INFLUENCE OF HIGH VOLTAGE STRESS ON THE EFFICIENCY OF C-Si SOLAR CELLS

Zeel Purohit, Manoj Kumar, Brijesh Tripathi*

Department of Science, Pandit Deendayal Petroleum University, Raisan, Gandhinagar-382007, Gujarat, India
zeel.pphd15@sot.pdpu.ac.in

Potential-induced degradation (PID) is the most rapid degradation phenomena that leads to enormous declined of power output over the time in solar PV power plants. Most of the solar PV power plants installed worldwide consisting crystalline silicon (c-Si) PV panels in a string of an array. The potential difference between PV cell matrix and grounded aluminum frame leads to the movement of charge species through the available leakage path, majorly influences the occurrence of PID phenomena [1-5]. The c-Si solar cell has been performed under high voltage stress condition (-800 V) for 24 hours to understand the PID behavior at the cell level. The electrical performance parameters of c-Si solar cell such as short-circuit current density (J_{SC}), open-circuit voltage (V_{OC}), fill factor (FF) and the efficiency (η) drastically decrease under PID effect. The values of FF and η have been reduced from 0.74 to 0.24 and 16.5% to 0.83%, respectively. The decrease in the shunt resistance value R_{SH} is mainly affected due to the diffusion of Na^+ in the P-N junction. The two-diode model has been proposed to further investigate the recombination effect under PID mechanism at cell level. The leakage current increases drastically as the voltage stress increases from 0 to 800 V. The results thus gives an indication that the P-N junction diode and the recombination within the space-charge region are mainly affected under high voltage stress condition.

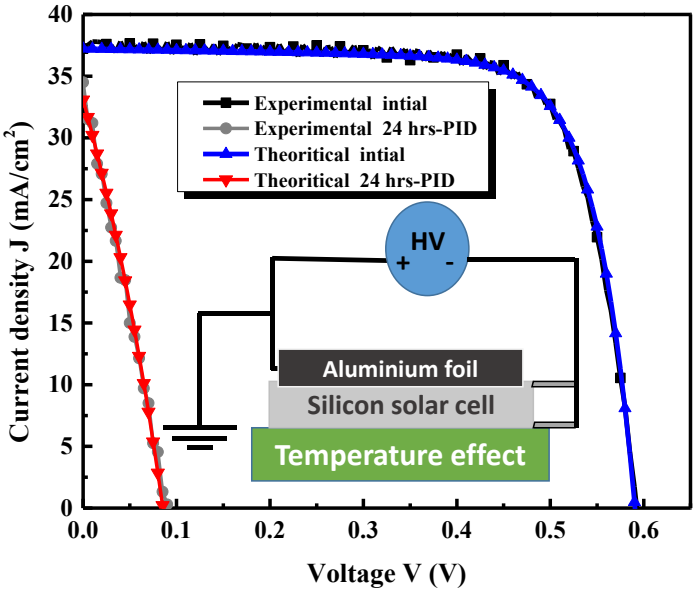

Fig 1: The theoretical and experimental J-V characteristic under high voltage stress (PID) effect. Inset shows the schematic representation of the degradation system for c-Si solar cell.

[1] D. C. Jordan, S. R. Kurtz, Photovoltaic Degradation Rates—an Analytical Review, Progress in photovoltaics: Research and Applications, **21**, 12-29 (2013).
[2] V. Sharma, S. Chandel, Performance and degradation analysis for long term reliability of solar photovoltaic systems: A review, Renewable and Sustainable Energy Reviews, **27**, 753-767 (2013).
[3] J. Bauer, V. Naumann, S. Grober, C. Hagendorf, M. Schutze , On the mechanism of potential-induced degradation in crystalline silicon solar cells O. Breitenstein, physica status solidi (RRL)-Rapid Research Letters, **6**, 331-333 (2012).
[4] V. Naumann, D. Lausch, A. Hähnel, J. Bauer, O. Breitenstein, A. Graff, M. Werner, S. Swatek, S. Grober, J. Bagdahn, Explanation of potential-induced degradation of the shunting type by Na decoration of stacking faults in Si solar cells, Solar Energy Materials and Solar Cells, **120**, 383-389 (2014).

EXCITON AND CHARGE CARRIER DYNAMICS IN ALL-POLYMER TQ1:N2200 SOLAR CELL

Rokas Jasiūnas, Vidmantas Gulbinas

State research institute Center for Physical Sciences and Technology, Saulėtekio Ave. 3, LT - 10222 Vilnius, Lithuania
rokas.jasiunas@ftmc.lt

In most organic solar cell fullerene is used as electron accepting material, but due to it's high production cost much cheaper all-polymer solar cells has gained interest in academic and industrial environments. We investigated exciton and charge carrier dynamics in active layers of all-polymers solar cells.

Exciton stabilization and relaxation dynamics has been investigated in all-polymer blends and their single components prepared from different solvent at various temperatures. Evaluated donor polymer exciton quenching kinetics in blend showed that exciton localize before they are quenched, which is limiting factor for charge carrier generation efficiency.

The extraction and recombination dynamics of photogenerated charge carrier was investigated using transient photocurrent and time-delayed collection field techniques. Charge carrier generation efficiency was found being independent of electric field. Bimolecular charge carrier recombination rate was evaluated and it was shown that recombination process strongly influences efficiency of the investigated solar cells.

ELECTRODEPOSITION OF MANGANESE LAYERS FROM AQUEOUS ELECTROLYTES

Mónica Fernández-Barcia, Volker Hoffmann, Steffen Oswald, Ulrike Wolff, Margitta Uhlemann, Annett Gebert

Institute for Complex Materials, IFW Dresden, P.O. Box 270116, 01171 Dresden, Germany
m.fernandez.barcia@ifw-dresden.de

The research interest in electrodeposition of manganese (Mn) has recently greatly increased due to the wide range of applications as pure metal or alloy constituent. In the alloyed state it can combine high corrosion protection performance with suitable mechanical properties [1]. The present work shows that Mn coatings of good quality can be electrodeposited on polycrystalline Au substrates sputtered on glass from a sulfate electrolyte containing $MnSO_4$, $(NH_4)_2SO_4$ and H_3BO_3 with a constant pH value of 3. Cyclic Voltammetry (CV) curves were recorded in a wide potential range and Electrochemical Quartz Crystal Microbalance (EQMC) measurements were applied to investigate the behavior of the electrochemical system. Scanning Electron Microscopy (SEM) coupled with Energy Dispersive X-ray spectroscopy (EDX), Glow Discharge Optical Emission Spectrometry (GD-OES) and X-ray Photoelectron Spectroscopy (XPS) were applied to investigate the effect of the applied potential and the concentration of ammonium sulfate on the structural and chemical properties of the manganese deposits. Previous studies have reported that $(NH_4)_2SO_4$ is essential to grow Mn coatings with good coverage, to decrease the precipitation of manganese hydroxides and to improve the conductivity of the electrolyte [2]. The morphology of the Mn deposits was found to change with different concentrations of $(NH_4)_2SO_4$ (Fig. 1), but no effect of the applied potential was detected.

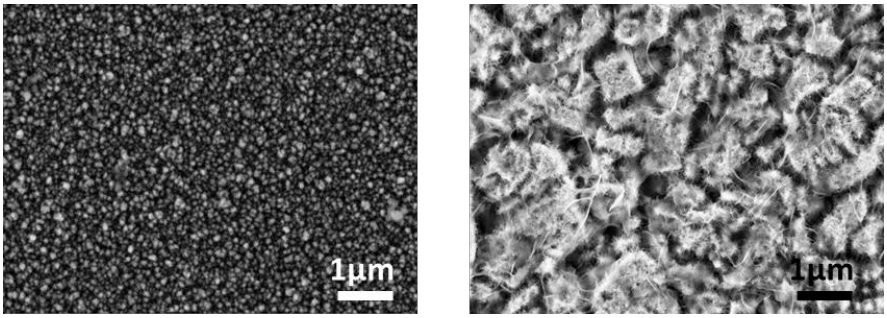

Fig. 1. SEM surface of the Mn deposits at -2.6V_{MSE} in 0.5M (left) and 1M (right) $(NH_4)_2SO_4$ solution.

However, GD-OES measurements revealed an impact of the value of the applied potential on the chemical composition and thickness of the coatings. Electrodeposition of Mn is only possible at very negative potentials in the range of -2.4 V_{MSE} (MSE, Mercury Sulfate Electrode) and long deposition times up to 60 min are necessary. This causes water decomposition as side reaction, resulting in a high hydrogen evolution rate which leads to a significant increase of the pH value in the electrolyte. This is the reason why manganese hydroxides are formed [3]. Therefore, control of the pH value of the bulk electrolyte during the deposition is essential to avoid the precipitation of manganese hydroxides, as confirmed by XPS analysis.

Funding of this work by the European Commission within the H2020-MSCA-ITN-2014 SELECTA, grant agreement no. 642642 is gratefully acknowledged.

[1] J. Gong & G. Zangari, Electrodeposition and Characterization of Sacrificial Copper-Manganese Alloy Coatings, Journal of Electrochemical Society **151** (5), C297-C306 (2004).
[2] J. Gong & G. Zangari, Electrodeposition and Characterization of Manganese Coatings, Journal of Electrochemical Society **149** (4), C209-C217 (2002).
[3] P. Diaz-Arista, et al. EQCM study of the electrodeposition of manganese in the presence of ammonium thiocyanate in chloride-based acidic solutions, Electrochimica Acta **51**, 4393-44040 (2006).

FABRICATION OF STRUCTURES IN Er_2O_3 FILMS USING PHOTOLITOGRAPHY AND WET ETCHING

Tomas Drunga, Tomas Grinys

Institute of Applied Research, Vilnius University, Lithuania
drungatomas@ff.stud.vu.lt

In recent years more and more attention is attributed towards new semiconductors, which would improve the efficiency and clock frequency of devices, compared to silicon. One of those promising materials – gallium nitride (GaN) – is already being used in manufacturing of transistors [1], LEDs [2], lasers and detectors [3].

However, many technical difficulties should be solved in order to grow low cost and high quality GaN. Ideally, GaN thin films could be grown on native - bulk GaN substrates, but this technology is still too expensive for practical applications. Thus, foreign substrates, like sapphire or silicon are usually used. Due to lattice mismatch between GaN and foreign substrates the quality of GaN drops [3].

In the case of heteroepitaxy on silicon, a buffer layer is needed to grow GaN. A promising material for this layer could be erbium oxide. It is distinguished for its high dielectric permittivity, wide band-gap, and high thermal and chemical stability. Also it reduces the lattice mismatch and thermal expansion coefficients between GaN and Si leading to improved efficiency of GaN devices [4],[5]. Furthermore, surface profiling of Er_2O_3 could be employed, which should lead to less-strained and less-defective GaN films grown on such substrate [2].

In this work the fabrication of structures in Er_2O_3 films using photolitography and wet etching was investigated. Etching rates in HCl and activation energies were calculated. Also, the influence of photolitography parameters was shown. Finally, the structures in crystalline Er_2O_3 were formed and the size of etched structures was evaluated as well as the possible etching mechanism was discussed.

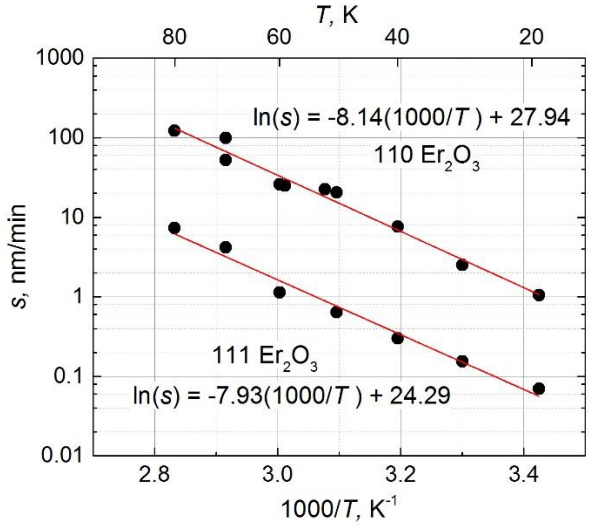

Fig. 1. Etching activation energies of Er_2O_3 in HCl

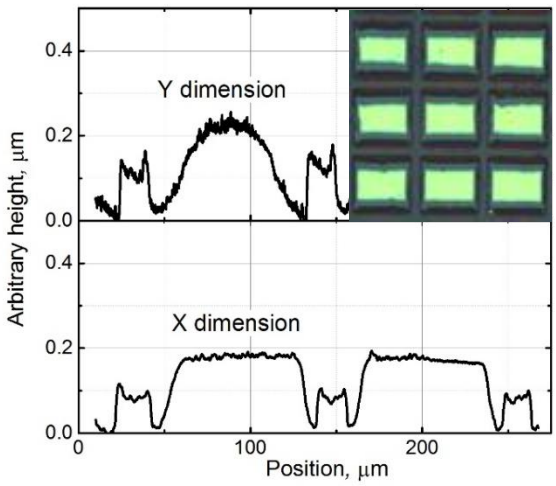

Fig. 2. Surface profile of fabricated structures, graph inset shows optical image of structures

[1] Stephen L. Colino and Robert A. Beach, Ph.D., "Fundamentals of Gallium Nitride Power Transistors", 2009.
[2] Zhu D, Wallis DJ, Humphreys CJ, "Prospects of III-nitride optoelectronics grown on Si", Reg Prog Phys, 2013.
[3] Tanya Paskova, Drew A. Hanser, Keith R. Evans, "GaN Substrates for III-Nitride Devices", Proceedings of the IEEE, Volume: 98, Issue: 7, July 2010.
[4] Chyuan-Haur Kaoa, Hsiang Chenb, Yu Tsung Pana, Jing Sing Chiua, Tien-Chang Luc, "The characteristics of the high-K Er2O3 (erbium oxide) dielectrics deposited on polycrystalline silicon", 504–508, Solid State Communications, Volume 152, Issue 6, 2012.
[5] F. Erdem Arkun, Rytis Dargis, Andrew Clark, Robin S. Smith, Michael Lebby, "Growth of GaN by MOCVD on Rare Earth Oxide on Si(111)", Abstract #1953, 224th ECS Meeting, The Electrochemical Society, 2013.

SELECTIVE PHOTOELECTROCHEMICAL DEPOSITION OF PPy ONTO HYDROGENATED a-Si FOR OPTOELECTRONIC APPLICATIONS.

Denisa Dosenovicova[*1], Jelena Maricheva[1], Alex Neumüller[2], Oleg Sergeev[2], Olga Volobujeva[1], Albert Nasibulin[3], Julia Kois[1], Andres Öpik[1] and Sergei Bereznev[1]

[1] Tallinn University of Technology, Department of Materials and Environmental Technologies, Ehitajate tee 5, 19086 Tallinn, Estonia

[2] NEXT ENERGY - EWE Research Centre for Energy Technology at the University of Oldenburg, Carl-von-Ossietzky-Straβe 15, 26129 Oldenburg, Germany

[3] Laboratory of NanoMaterials, Skolkovo Institute of Science and Technology, Skolkovo Innovation Center, Nobel str., Building 3, 143026, Moscow, Russia

dedose@ttu.ee

In this study, a number of hybrid solar cells (polypyrrole (PPy)/i-a-Si:H/n-a-Si:H/AZO/glass) with an n-i-p structure has been prepared and characterized electrochemically. Hydrogenated amorphous silicon (a-Si:H) was used as a substrate with n-doped (n-a-Si:H) and intrinsic (i-a-Si:H) layers, which acted as a charge separation and photo-absorber layer, respectively. Doped PPy was deposited onto the i-a-Si:H layer using selective photo-assisted electrodeposition (ED) technique under either a red laser illumination or Xe lamp illumination in a standard three-electrode cell. ED was held at room temperature in an aqueous solution containing 1-naphtalene sulfonate or polystyrene sulfonate doping agents for PPy at low potential values ranging from 300 mV to 500 mV vs. SCE. At these potential values, PPy covers selectively only photo-activated area of i-a-Si:H photoabsorber layer. For the first time, photo-assisted ED of PPy onto a-Si:H surface was applied in order to create a working hybrid solar cell with such n-i-p structure. The efficiency of the photo-assisted ED technique for producing of conductive uniform PPy layers onto the i-a-Si:H photoabsorber is confirmed. The overall photoconversion efficiency of the best prepared hybrid solar cells was about 2.9% and comparable for different doping agents for PPy and illumination conditions for ED process.

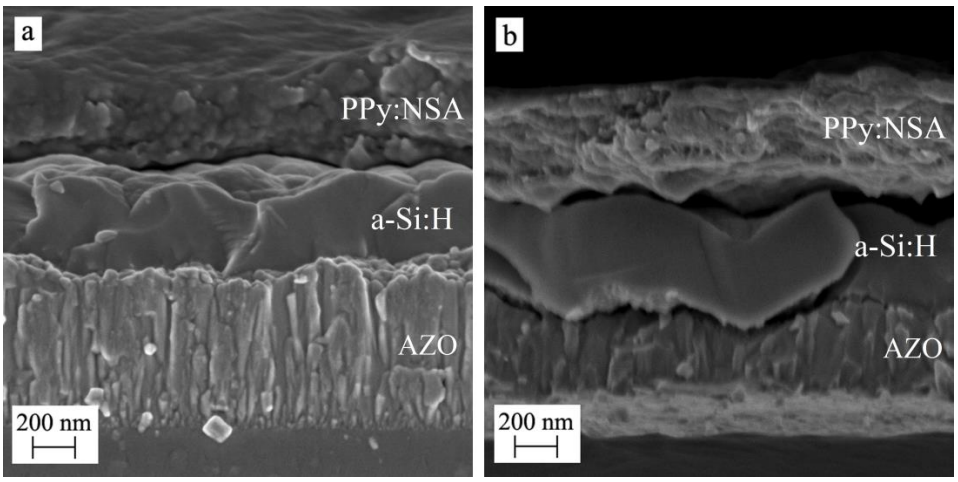

Fig. 1. Cross-sectional HR-SEM micrographs of PPy:NSA/i-Si/n-Si/AZO/glass structures deposited under red (a) laser and (b) Xe lamp irradiation.

STRUCTURE AND PHASE COMPOSITION OF POWDERED QUASICRYSTALLINE Al-Fe-Cr ALLOY AFTER CONSOLIDATION BY QUASI-HYDROSTATIC COMPRESSION

Kravchenko Aleksandra, Guschik Dmitriy, Yurkova Aleksandra.

National Technical University of Ukraine "Igor Sikorsky Kiev Polytechnic Institute",
Kravchenko.kpi@yandex.ru

Nano-size quasicrystalline structures have been a subject of interest over recent years due to their potential use as reinforcement in advanced engineering alloys. The icosahedral phases are hard and brittle due to the difficulty of dislocation movement in the quasiperiodic lattice without long range periodicity [1]. Al-based alloys and, particularly, those containing quasicrystals and related compounds, are of growing attention for researches employed in scientific and engineering applications. Quasicrystalline Al-Fe-Cr–based alloys comprise a number of nano-sized quasicrystalline particles of icosahedral phase (i-phase) dispersed over α-Al matrix. That is why excellent balance between a high strength and sufficient ductility is indicative of quasicrystalline Al–Fe–Cr-based alloys compared to commercial Al-based alloys recommended for service under elevated temperature.

Thus, nanoquasicrystalline Al-based alloys are generally performed as semi-products in form of either melt-spun ribbons/flakes or gas/water atomised powders. Because of this the development of processing routes available in view of semi-product consolidation is of great importance for manufacturing the bulk-shaped material and, as a consequence, further improvement of structural stability is desirable to maximize elevated temperature.

This study devoted to investigation of structure and phase composition of the composite quasicrystalline powder $Al_{94}Fe_3Cr_3$ alloy consolidated under quasi-hydrostatic compression at different pressures of consolidation.

Consolidation of the powder with particle size of 40 μm was performed by quas-hydrostatic compression. Compacting produced in high pressure cells at room temperature (no heating) under pressure of 2.5; 4 and 6 GPa. Structural characterisation of alloy consolidated under quasi-hydrostatic compression was performed by X-ray diffraction (XRD) analysis using Cu K_α radiation and scanning electron microscopy (SEM).

Fig.1 shows the XRD patterns recorded for the feedstock powder, and alloy after consolidation. The presence of diffraction peaks (111) and (200) of α-Al solid solution and i-phase, indexed using Cahn's indexation scheme (6.9) (18, 29) [2], is clearly seen for all of the samples. The presence in the alloy quasicrystalline phase (i-phase), embedded in α-Al matrix of $Al_{94}Fe_3Cr_3$ alloy is confirmed by SEM (Fig. 2).

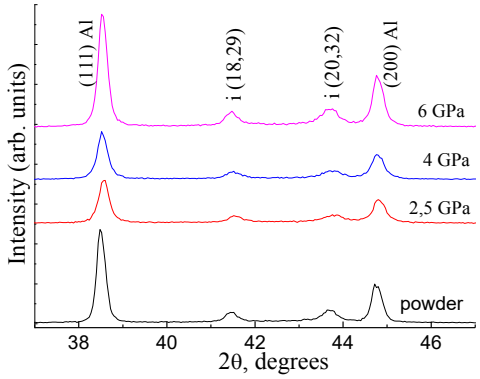

Fig. 1. XRD patterns of quasicrystalline $Al_{94}Fe_3Cr_3$ alloy

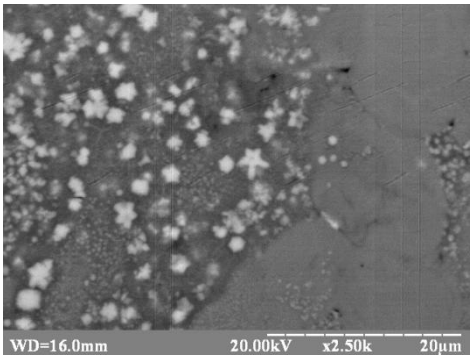

Fig. 2. SEM image of structure quasicrystalline Al94Fe3Cr3 alloy after consolidation

It is important that the integrated intensity of the diffraction peaks of metastable quasicrystalline i-phase in the $Al_{94}Fe_3Cr_3$ alloy consolidated under pressure (2.5, 4, 6 GPa) at room temperature is identical to that in the initial phase powder, indicating complete retaining the unchanged fraction volume of QC i-phase safety of its contents in the structure of the material after consolidation in extrusion at 623 K when quasicrystalline phase loss reach the 23% [3].

Superior advantages of the quasi-hydrostatic compression as alternative solid-state consolidation process for structural performance of quasicrystalline alloys by plastic deformation is discussed by comparison with that resulted from currently employed hot extrusion put into practice at the 623 K. As opposed to extrusion process assisted by unidirectional deformation, comprehensive quasi-hydrostatic compression is primary responsible for creating the mostly effective intimate metallic bonding between the adjacent Al-based powder particles under quasi-hydrostatic compression when the temperature was 293 K.

[1] A. García-Escoriala,, E. Nataleb, V. J. Cremaschib, I. Toddc, M. Lieblicha., Quasicrystalline $Al_{93}Fe_3Cr_2Ti_2$alloys, Metal. **51(4)**,1-6 (2015).
[2] J.W. Cahn, D. Shechtman, D. Gratias. Indexing of icosaedral quasiperiodic crystals, Materials Research Society. **1,** 13-26 (1986).
[3] A.I. Yurkova, A.V. Byakova, A.A. Vlasov. Termostabil'nost' struktury i mehanicheskih svojstv nanokvazikristallicheskogo $Al_{94}Fe_3Cr_3$ splava, konsolidirovannogo jekstruziej, Metallofizika i novejshie tehnologii. (Effect of temperature on structure and mechanical properties of nanoquasicrystalline $Al_{96}Fe_3Cr_3$ alloy consolidated by hot extrusion) **37 № 7**, 1001-1018 (2015).

POLYDIMETHYLSILOXANE - CELLULOSE AND PLANT MATERIAL COMPOSITES THEIR PROPERTY AND ANTIMICROBIAL ACTIVITY

Aistė Lisauskaitė[1], Virginija Jankauskaitė[1], Mindaugas Liaudanskas[2], Akvilė Andziukevičiūtė-Jankūnienė[1]

[1] Faculty of Mechanical Engineering and Design, Kaunas University of Technology
[2] Faculty of Pharmacy, Lithuanian University of Health Science
lisauskait@yahoo.com

Silicone rubber or poly(dimethyl siloxane) (PDMS) is a member of siloxane family. Silicone rubber has many applications owing to its excellent properties, i.e. its thermal and chemical resistivity has led to its usage as an insulator in electrical field. Another major application of the silicones is in the medical field where their excellent biocompatibility, hydrophobicity and elasticity makes them ideal for use in numerous personal care products and medical devices [1]. However, unfilled PDMS usually have low mechanical properties. The reinforcement of rubber is expressed by the enhancement of tensile strength. Beside this, the wider use PDMS in the medical industry, material must be mechanical strong and exhibit antimicrobial activity also. For this reasons PDMS must be combined with fillers [2]. Cellulose microcrystals (CMC) is a linear – chain natural carbohydrate polymer. CMC are being used as potential reinforcing material for many advantages such as abundantly available, biodegradable, nontoxic, cheaper, renewable and have relatively high strength [3]. Also some plants are a very valuable raw material for them biological activity that is way they are used in medicine, pharmacy and other areas. Eucalyptus and sage leaves are known for possesses antibacterial activity. It has been indicated in scientific literature that extracts of sage have particularly strong antioxidant activity compared to other herbal plants [4].

This study focuses to improve polydimethylsiloxane mechanical properties using cellulose microcrystals and to create the antimicrobial activity to use eucalyptus and sage leaves lyophilized extractions.

In this work, polydimethylsiloxane/cellulose microcrystals/eucalyptus and polydimethylsiloxane/cellulose microcrystals/sage composites were characterized for their structure, mechanical properties, morphology and antibacterial effect. The Kirby-Bauer disk diffusion method was used to study the antibacterial activity of composites. Staphylococcus aureus was used as model test strain for Gram-positive bacteria.

SEM imagines reveal the microstructure of particles and polydimethylsiloxane/cellulose/eucalyptus, polydimethylsiloxane/cellulose/sage composites. Eucalyptus and sage particles have irregular shape and agglomerations detected also. Furthermore, the composites surface showed rough surface. Antibacterial activity of polydimethylsiloxane/cellulose/eucalyptus and polydimethylsiloxane/cellulose/sage composites are inhibits S.aureus bacteria growth.

[1] R. D. Paul, J.E Mark. Fillers for polysiloxane ("silicone") elastomers. Progress in Polymer Science **35**, 893-901 (2010).
[2] M.W. Simon, K.Stafford, D.Li Ou. Nanoclay reinforcement of liquid silicone rubber. Journal Inorganic Organoment **18**, 364-373 (2008).
[3] S. Istva, D. Plackett. Microfibrillated cellulose and new nanocomposite materials: a review. Cellulose **17**, 459–494 (2010).
[4] L.S. Nerio, J. Olivero-Verbel, E. Stashenko. Repellent activity of essential oils: a review. Bioresource technology **101 1**, 372-378 (2010).

STRUCTURE AND PHASE COMPOSITION CHANGES IN CARBON STEEL (U9) AFTER COMPRESSION PLASMA FLOW TREATMENT

Alexander Malashevich[1], Nikolai Cherenda[1], Valentin Astashinski[2], Anton Kuzmitski[2]

[1] Physics Faculty, Belarusian State University, Nezavisimosti ave., 4, Minsk 220030, Belarus
[2] A.V Luikov Heat and Mass Transfer Institute, National Academy of Science of Belarus, P. Brovki Str., 15, Minsk 220072, Belarus
alexandermalashevich@gmail.com

Nowadays, the surface modification of solids by means of plasma flows has been intensively investigated. A pulsed plasma sources generating plasma flows with high energy density are also suitable for material processing [1].

A magneto-plasma compressor (MPC) is a quasistationary plasma accelerator capable of producing supersonic compression plasma flows (CPFs)[2]. The weakly diverging and possessing high energy density CPF have been used to modify a surface layer (up to tens of micrometers) in an extremely short time (~100 μs). The surface treatment of ferrous materials and various type of steels by CPFs was found to result in a significant improvement of their mechanical properties. In this connection, the modification of alloyed steels with different elements is of special interest[2].

In the present work, microstructure, phase composition, and mechanical properties of a plasma-mixed „Cromium-U9carbon steel" system have been investigated. In this technique, the action of relatively short (~100 μs) and high-energy (up to 19 J/cm^2) plasma pulses lead to the melting of the near-surface layer of the steel substrate together with the pre-deposited Cr film (~2 μm thick), liquid phase mixing and subsequent high speed cooling resulting in the formation of steel surface layer alloyed with chromium atoms. Such teratment lead to surface layer structure and phase composition changes.

The results of the XRD (X-ray diffraction) analysis of the samples before and after CPF treatment at different energy densities absorbed by the target are presented in figure 1.

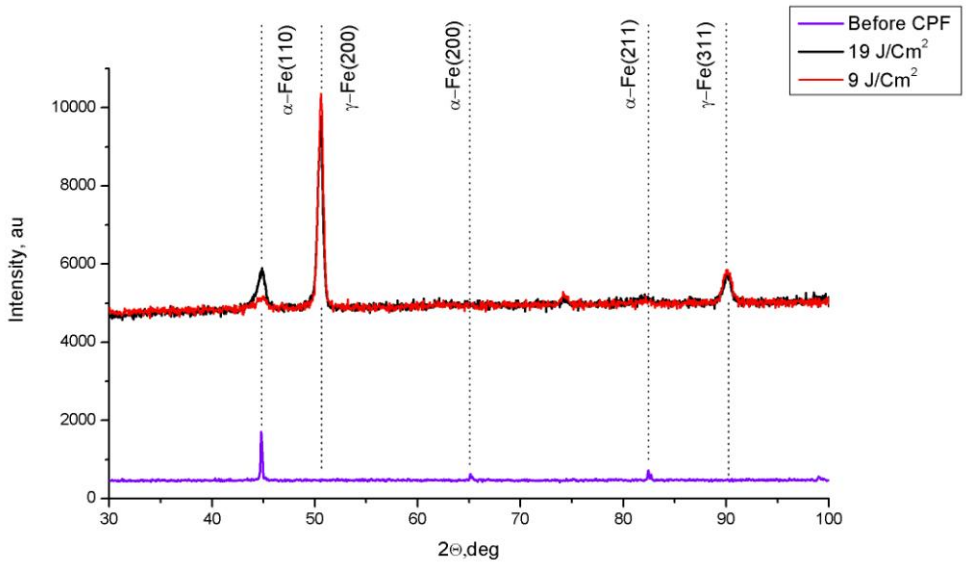

Fig. 1. The XRD patterns of samples before and after CPF treatment at different energy densities absorbed by target and n=3 pulse

The findings showed that the CPF action results in to the formation of metastable austenite phases (γ-Fe) formed as a result of non-equilibrium crystallization. γ-Fe crystallites had preferred orientation (100) according to the XRD pattern. This orientation is typical for phases growing in conditions of high-speed cooling e.g. in case of laser treatment.

Surface morphology analysis showed formation of dendrites at the surface formed during high-speed-cooling from the melt. Their size was about 0,1-1 μm. The increase of the energy absorbed by the surface layer led to the decrease of the alloying element concentration at the surface of the alloyed layer. Cr concentration was changed in the range of 7,5-1,5 wt. % depending on the energy absorbed by the surface.

Compression plasma flows treatment influenced the mechanical properties of steel. CPFs treatment leads to an increase of Vickers microhardness up to 6,1 GPa. Steel microhardness before treatment was 2,3 GPa. Microhardness increase was connected with grain-boundary and solid-solution strengthening.

[1]RotshteinV.P., Ivanov Yu.F., Markov A.B., et.al. Surf. Coat. Technol., 200 (2006) 6378–6383.
[2]Pogrebnjak A.D, Bratushka S., Boyko V.I. et.al. Nucl. Instrum. Methods Phys. Res., B145 (1998) 373-390.

INVESTIGATION OF THE TEXTILE BONDS STRENGTH UNDER SPECIFIED AGEING CONDITIONS

Gerda Mikalauskaitė, Virginija Daukantienė

Department of Materials Engineering, Kaunas University of Technology, Lithuania
gerda.mikalauskaite@ktu.edu

Textile bonding is an alternative for clothing sewing [1]. It is applied for joining two layers of textile material together by using thermoplastic polyurethane adhesive films with the application of high temperature and pressure for certain time duration [2, 3]. The properties of the bonded seams depend on textile properties, bonding conditions, seam construction, and etc. Textile bonds should be resistant to chemical cleaning and laundering during their exploitation process as well as of sufficient strength being worn at different climate temperatures. Thus, the aim of this research was to determine the influence of ageing on textile bonds strength.

One knitted fabric K1 (thickness – 0.56 mm; surface density – 113 g/m^2; warp yarn count – 16 cm^{-1}; weft yarn count – 18 cm^{-1};) and two polyurethane thermoplastic films of different thickness: UAF-472 (1.27 mm) and ET-301 (0.175 mm) suitable for sportswear or leisure clothing manufacture were selected for this study. Textile bonds were pressed at 5.6 kPa at 150 °C bonding temperature for 10 s, 20 s, 30 s and 40 s. Later, bonds were aged at 45 ± 5 °C temperature in an oven chamber with digital temperature controller E5CN for 2 h 30 min; for 5 h and for 7 h 30 min. Bond strength testing was carried out at ambient temperature using computerized CRE type tension machine H10 KT (Tinius Olsen, UK) under 50 mm/min delamination speed. Structure of textile bonds was investigated using SEM method. The summary of the bond strength results is presented in Table 1.

Table 1. Adhesion strength of textile bonded seams

Film code	Bond strength F, N/mm			
	Control specimens (ageing duration t_h = 0 min)			
	t_B* = 10s	t_B* = 20s	t_B* = 30s	t_B* = 40s
ET301	1.919 ± 0.190	4.428 ± 0.480	3.445 ± 0.355	2.601 ± 0.109
UAF472	5.027 ± 0.468	4.578 ± 0.171	3.553 ± 0.388	3.290 ± 0.302
	Ageing duration t_h = 2 h 30 min			
ET301	1.902 ± 0.187	5.430 ± 0.365	3.382 ± 0.247	2.953 ± 0.327
UAF472	5.618 ± 0.379	4.349 ± 0.236	3.561 ± 0.279	3.351 ± 0.486
	Ageing duration t_h =5 h			
ET301	2.539 ± 0.294	4.026 ± 0.397	2.944 ± 0.242	2.877 ± 0.187
UAF472	5.654 ± 0.479	4.418 ± 0.275	3.526 ± 0.432	3.469 ± 0.383
	Ageing duration t_h = 7 h 30 min			
ET301	2.641 ± 0.288	3.760 ± 0.337	3.054 ± 0.280	2.899 ± 0.235
UAF472	5.484 ± 0.360	4.302 ± 0.272	3.686 ± 0.327	3.395 ± 0.115

Note: *t_B – bonding duration.

The higher values of bond strength were determined for the bonds which were laminated using the thicker film (UAF472) compared to the ones of the thinner film (ET301) case. The highest strength is also seen for the bonds which were laminated with thicker film for 10 s duration. The lowest value of bond strength was determined when the bonding duration also was 10 s, but the thinner thermoplastic film (ET301) was used.

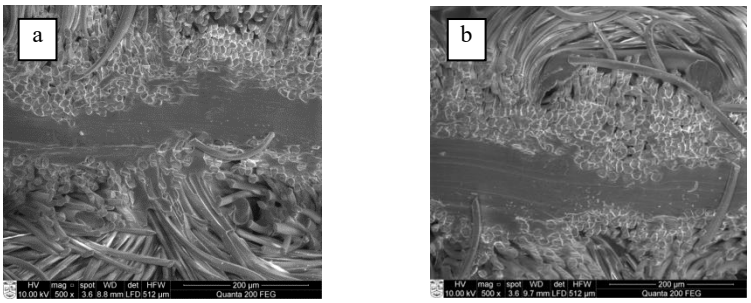

Fig. 1. SEM images of the tested bonds: control (a) and aged for 7 h 30 min duration (b)

The investigation of the influence of the ageing at 45 ± 5 °C temperature on the bonds strength has shown that the bond strength remains almost unchanged compared to the one of control specimen bond. Based on this, it could be concluded that the clothing which are manufactured applying the investigated technological parameters could be worn under the exposure of the high environmental temperatures (Table 1, Fig. 1).

[1] Seram, N; Nandasiri, T 2015, A Comparison between Bonding and Sewing: Application in Sports Performance Wear, Journal of Academia and Industrial Research (JAIR), vol. 3, no. 8, pp. 343-381.
[2] Jakubčionienė, Ž; Masteikaitė, V 2010, Investigation of Textile Bonded Seams, Materials Science (Medžiagotyra), vol. 16, no. 1, pp. 76-79.
[3] JAKUBČIONIENĖ, Ž., et al. Investigation of the Strength of Textile Bonded Seams. Materials Science (Medžiagotyra), 2012, vol. 18, no. 2. pp. 172-176

STRUCTURE AND THERMAL RESISTANCE ANALYSIS OF Fe-W COATINGS ELECTRODEPOSITED FROM GLYCOLATE-CITRATE PLATING BATH

Antonio Mulone[1], Uta Klement[1], Aliona Nicoleno[2]

[1] Materials and Manufacturing Technology, Chalmers University of Technology, Sweden
[2] Department of Physical Chemistry, Vilnius University, Lithuania
mulone@chalmers.se

One of the most important factors determining the structure of electrodeposited Fe-W alloys is the composition of the deposited alloy. Increasing the W content, the structure of Fe-W electrodeposits changes from nanocrystalline to amorphous [1]. The interest in Fe-W coatings has grown in the recent years thanks to Fe-W properties such as hardness, corrosion resistance and thermal stability which makes Fe-W a potential substitute for hard chromium coatings [2]. The thermal stability of amorphous coatings is an important factor which can determine if the material is suited for high-temperature applications. In this perspective this work aims at studying the thermal stability of Fe-W coatings with various W content as well as the change in crystallographic structure, morphology and composition upon annealing.

Fe-W coatings were electrodeposited under galvanostatic conditions from Fe(III)-based glycolate-citrate bath with three different W content: 4at.%, 15at.%, and 25at.% of W. The coating deposited with 4at.% of W has a nanocrystalline structure in the as-plated condition, while the coatings with higher W content are fully amorphous as determined by X-ray diffraction analysis. Cross section imaging by scanning electron microscopy revealed the presence of cracks and oxygen rich areas inside the coating with low W content. The coating with high W content shows also cracks in cross section, but no oxygen was detected.

Annealing of the two amorphous coatings confirms that electrodeposited amorphous Fe-W alloys undergo phase transformation at elevated temperature. As shown in Fig. 1a, the Fe-W coating with 15at.% of W retains the amorphous structure up to 200°C and upon crystallization, a Fe-W solid solution is formed at 400°C. The coating with high W content instead retains the amorphous structure up to 400°C while a partially crystalized α-iron structure is observed at 600°C (Fig. 1b). Hence, Fe-W coatings with higher W content (>25at.%) can be considered as suitable material for application at elevated temperatures.

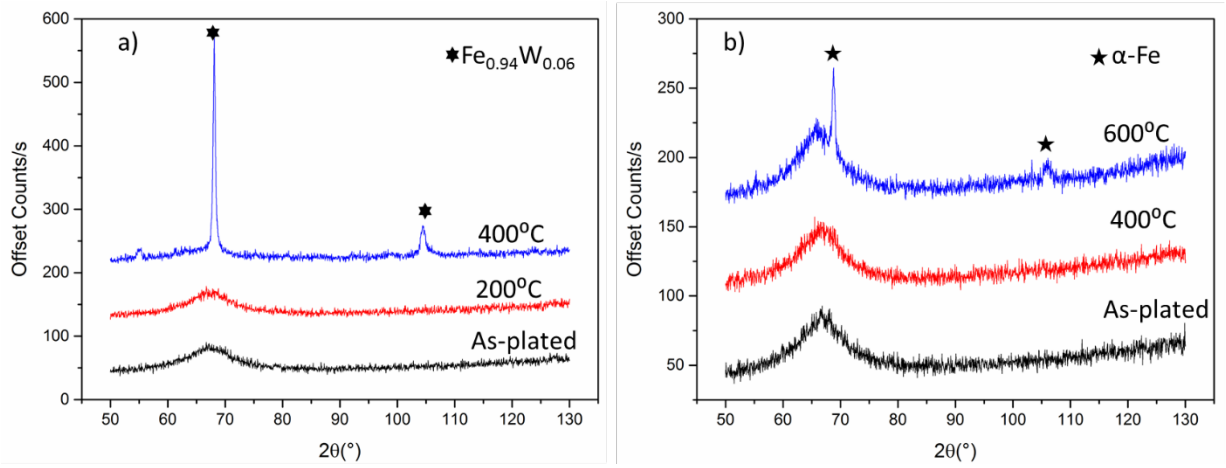

Fig. 1. (a) X-ray spectra for the Fe-W coating with 15at.% of W in the as-plated condition and after annealing for 1 hour in vacuum at the temperature indicated next to the spectra; and (b) X-ray spectra for the Fe-W coating with 25at.% of W in the as-plated condition and after annealing for 1 hour in vacuum at the temperature indicated next to the spectra.

[1] N. Tsyntsaru, H. Cesiulis, M. Donten, J. Sort, E. Pellicer, E.J. Podlaha-Murphy, Modern trends in tungsten alloys electrodeposition with iron group metals, Surf. Eng. Appl. Electrochem. 48 (2013) 491–520.

[2] S. Wang, C. Zeng, Y. Ling, J. Wang, G. Xu, Phase transformations and electrochemical characterizations of electrodeposited amorphous Fe–W coatings, Surf. Coatings Technol. 286 (2016) 36–41.

PHOTOELECTRIC PROPERTIES OF a-SI:H WITH V_2O_{5-X} WINDOW LAYER

Augustas Nekrošius

Semiconductor Physics Department and Institute of Applied Research, Vilnius University, Saulėtekio al. 3, Vilnius LT-10257, Lithuania

nekrosius.augustas@gmail.com

Thin-film solar cells (SC) are attractive due to their low fabrication costs, which mostly depend on the costs of the raw materials of the compounds. We have investigated thin film FTO/V_2O_{5-x}/i-a-Si:H/LiF/Al samples. The deposition technology was based on RF magnetron sputtering, PECVD and thermal evaporation [1] which are optimal for the cheap, fast and relatively low temperature production. Moreover, there are no toxic elements involved in the manufacture process; this makes these SC even more advantageous. However, hydrogenation is associated with light-induced degradation of the material, called the Staebler–Wronski effect.[2] Though the efficiency of a-Si:H solar cells is still relatively low as compared to poly-Si cells, but their energy payback time is much shorter.[3]

The aim of this research was to evaluate photoelectric properties of the thin-film solar cell samples with different intrinsic layer i-a-Si:H thicknesses at 300, 340 and 460 nm. Their thermal activation energies E_A, short-circuit currents I_{SC}, open-circuit voltages U_{OC}, fill factors FF and characteristic resistances R_{CH} were evaluated by measuring current-voltage (IV) dependencies at different temperatures ranging from 80 to 320 K upon 455 nm light illumination.

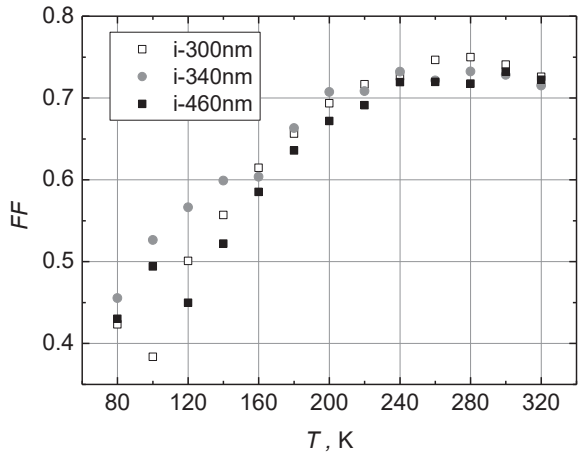

Fig.1. Fill factors FF of the samples with different intrinsic layer thickness depending on the temperature.

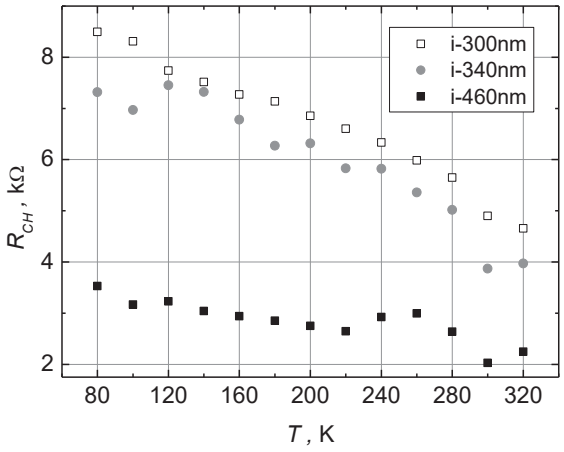

Fig.2. Characteristic resistances R_{CH} of samples with different intrinsic layer thickness depending on the temperature.

Short-circuit currents I_{SC} used to decrease slightly at lower temperatures, while the best results of I_{SC} were observed in the samples with the widest intrinsic region i-a-Si:H=460 nm. Open-circuit voltages U_{OC} did not vary as much, indicating that the characteristic resistance R_{CH} was much lower in these samples. U_{OC} used to increase at lower temperatures, while FF were noticeably reduced below 200 K. Steady growth of R_{CH} was observed while lowering the temperatures.

[1] H. H. Jung, et al., „Doping-free silicon thin film solar cells using a vanadium pentoxide window layer and a LiF/Al back electrode“, *Applied Physics Letters*, **103** (7), 2013.

[2] C. R. Wronski, et al., "Intrinsic and Light Induced Gap States in a-Si:H Materials and Solar Cells - Effects of Microstructure", *Thin Solid Films*, **451**, 470-475, 2004.

[3] K. P. Bhandari, et al., „Energy payback time (EPBT) and energy return on energy invested (EROI) of solar photovoltaic systems: A systematic review and meta-analysis“, *Renewable and Sustainable Energy Reviews*, **47**, 133-141, 2015.

MAGNETIC AND MECHANICAL PROPERTIES OF ELECTRODEPOSITED Fe-W ALLOYS

Aliona Nicolenco[1], Volker Hoffmann[2], NataliaTsyntsaru[1,3], Eva Pellicer[4], Jordina Fornell[4], Jordi Sort[4,5], Henrikas Cesiulis[1]

[1]Department of Physical Chemistry, Vilnius University, Vilnius, Lithuania
[2]Leibniz Institute for Solid State and Materials Research Dresden, Dresden, Germany
[3]Institute of Applied Physics of ASM, Chisinau, Moldova
[4]Departament de Física, Facultat de Ciències, Universitat Autònoma de Barcelona, Bellaterra, Spain
[5]Institució Catalana de Recerca i Estudis Avançats (ICREA), Barcelona, Spain.
aliona.nicolenco@chf.stud.vu.lt

Recently, tungsten alloys with iron group metals have emerged interest as an alternative to replace electrolytic chromium, which involves environmentally hazardous synthetic procedures. Research on Fe-W alloys is very appealing, since such coatings have a unique combination of mechanical, corrosion and magnetic properties, even at elevated temperatures [1]. From this point of view, Fe-W alloys could be considered as suitable materials for certain micro-/nano-electromechanical systems (MEMS/NEMS).

A series of Fe-W coatings have been electrodeposited from ammonia free glycolate-citrate bath. By changing the electrodeposition condition (i.e., pH, temperature and current density) the W content can be varied from 6 to 25 at.% in a controlled way. Taking into account that the functional properties of material are dependent on its composition the quantitative determination of full composition of electrodeposits (including light elements C, O, H, S, etc.) were performed by means of Glow Discharge Optical Emission Spectrometry (GD-OES). Mechanical properties of Fe-W alloys have been determined using nanoindentation techniques on the cross-section of the specimens, and the magnetic properties alloys have been studied using Vibrating Sample Magnetometer (VSM).

Compositional profiles of 10 μm thick coatings obtained by GD-OES show that the distribution of metals is uniform along the entire film thickness (Fig. 1). Oxygen was found in the coatings up to a depth of 1-2 μm, which indicates the presence of "surface-layer" linked with water/air oxidation of top layer after electrodeposition. XRD analysis showed that the grain size of Fe-W alloys decreases with the increase in W content in the alloys. Thus, the structure of the films transforms from nanocrystalline to amorphous-like. This leads to an increase of hardness, which is as high as ~10 GPa for the alloy with the highest W content. Remarkably, the measured hardness of Fe-25 at.%W is comparable to that of electrolytic chromium [2]. The saturation magnetization Ms, coercivity Hc, and squareness ratio (i.e., Mr/Ms, where Mr is the remanent magnetization) also vary with the W content. As expected, increasing of W content leads to the reduction in saturation magnetization and the coatings become magnetically softer. The mapping of mechanical and magnetic properties of Fe-W alloys is summarized in Fig. 2.

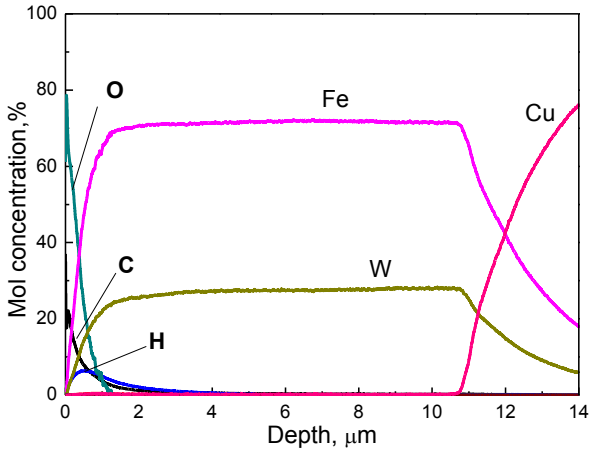

Fig. 1. GD-OES quantitative depth profile for electrodeposited Fe-25 at.% W coating.

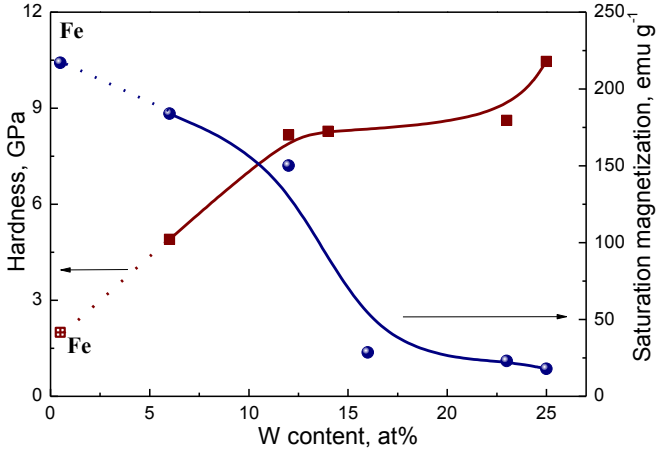

Fig. 2. Mapping of mechanical and magnetic properties of Fe-W alloys depending on tungsten content.

Acknowledgments: Authors acknowledge funding from H2020 (project SELECTA 642642), the Generalitat de Catalunya (2014-SGR-1015), the Spanish Ministry of Science and Competitiveness (MAT2014-57960-C3-1-R, co-financed by the Fondo Europeo de Desarrollo Regional), and the Moldavian national project (15.817.02.05A). We are also grateful for the cooperation with Spectruma Analytical GmbH.

[1] N.V. Myung, D.Y. Park, B.Y. Yoo, P.T.A. Sumodjo, Development of electroplated magnetic materials for MEMS. Journal of Magnetism and Magnetic Materials **265**, 189 (2003).

[2] N. Tsyntsaru, H. Cesiulis, E. Pellicer, J.-P. Celis, J. Sort, Structural, magnetic, and mechanical properties of electrodeposited cobalt–tungsten alloys: Intrinsic and extrinsic interdependencies. Electrochimica Acta **104**, 94-103 (2013)

CRYSTALLINE MATERIALS FOR HADRONIC CALORIMETRY DETECTING MODULES AT HIGH LUMINOSITY COLLIDER EXPERIMENTS

Pavel Orsich[1], Vitaly Mechinski[1], Mikhail Korjik[1], Valera Dormenev[2], Hans-Georg Zaunick[2]

[1] Research Institute for Nuclear Problems, Minsk, Belarus
[2] Justus Liebig University,2nd Physics Institute, Giessen, Germany
lovetreygolnik@gmail.com

The vitality of hadronic calorimeters will be very important for the next generation of collider experiments with high luminosity such as future upgrade of the Compact Muon Solenoid (CMS, CERN) for Large Hadron Collider (LHC, CERN) and Future Circular Collider (FCC) experiment. The FCC would enable proton-proton collisions of 50 TeV center of mass with the present 8.3-T LHC magnets, of 100 TeV with 16-T magnets [1]. The FCC-hh design baseline aims at a peak luminosity $5 \cdot 10^{34}$ $s^{-1}cm^{-2}$ of i.e., the same value as for the LHC luminosity upgrade (HL-LHC) [2].

Radiation damage in experiments at high-luminosity accelerators will play a significant role as limiting factor of the long term stability when operating an experimental setup. In this work we estimated fluence of the high energy protons in the high pseudorapidity region which will reach hadronic detecting blocks depending on the construction of the detector. Following configuration were considered: electromagnetic + hadronic calorimeters (ECAL + HCAL) of the CMS at LHC, spaghetti-type calorimeter (SPACAL) and "shaslyk" sampling-calorimeter + HCAL. We considered three geometry configurations using GEANT4-based simulation toolkit [3], where modules were bombarded by 10, 25, 50, 100 GeV protons.

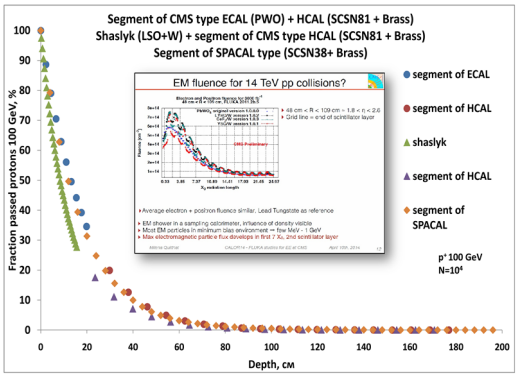

Fig. 1. Residual fluence of 100 GeV protons for different calorimeter geometries.

Our investigations have a good agreements with data, obtained in [4] – the residual proton fractions after ECAL is ~10-20% in comparison with initial flux. As in a case of $PbWO_4$ there are not any addition damage mechanisms under hadron irradiation in the wide energy range 200 MeV – 1 TeV [5] for plastic scintillators.

The obtained data show that in case of high luminosity LHC and FCC experimental facilities the organic plastic material of hadron calorimeter will be vastly damaged by residual hadrons after ECAL-regions, especially in the near beam area of calorimeter (pseudorapidity η=1.6-3) during the first year of operation if the parent hadron flux will be higher than ~10^{13}-10^{14} $s^{-1}cm^{-2}$ [6].

A possibility to apply inorganic scintillation materials in hadron calorimetry is discussed.

[1] F. Zimmermann M. Benedikt, D. Schulte et. Al., Challenges for highest energy circular colliders CERN, Geneva, Switzerland Proceedings of IPAC2014, Dresden, Germany.
[2] G. Apollinari, O. Brüning, L. Rossi, High Luminosity LHC Project Description // CERN ACC-2014-0321, Geneva, Switzerland, December, 2014.
[3] S. Agostinelli et al., Geant4: a simulation toolkit // Nucl. Instr. Meth. A 506 (2003) 250.
[4] Milena Quittnat, FLUKA studies of hadron-irradiated scintillating crystals for calorimetry at the High-Luminosity LHC // CMS Conf. Rep. CMS CR -2014/067, CERN, Switzerland, 2014.
[5] Comparison of Radiation Damage Effects in PWO Crystals Under 150 MeV and 24 GeV High Fluence Proton Irradiation / V. Dormenev, M. Korjik, T. Kuske, V. Mechinski, R.W. Novotny // IEEE Transactions on Nuclear Science. – 2014. – Vol. 61. – P. 501–506.
[6] Borisevitch A.E., Dormenev V.I., Fedorov A.A., Korjik M.V., Kuske T., Mechinsky V. A., Missevitch O.V., Novotny R.W., Rusack R., Singovski A.V., Stimulation of Radiation Damage Recovery of Lead Tungstate Scintillation Crystals Operating in a High Dose-Rate Radiation Environment // Nuclear Science, IEEE Transactions, Vol. 60 (2013), PP.1368-1372.

CALCIUM HYDROXYAPATITE THIN FILMS ON NOVEL SILICON NITRIDE SUBSTRATE

Pranas Usinskas*, Zivile Stankeviciute, Aivaras Kareiva

Faculty of Chemistry, Vilnius University, Lithuania
pranas_usinskas@yahoo.com

As the demand for implants keeps increasing [1], research has focused on the improvement of implant design features and biomaterials in an attempt to accelerate bone healing at early implantation times [2, 3].

Usually metals and metal alloys are used to replace load - bearing bones. Because of their chemical properties, the range of metals is narrow. Due to mechanical differences between bone and metal, after a while implant loses stability [3-5].

Silicon nitride (Si_3N_4) is a non-oxide ceramic that was primary used for industrial applications like internal combustion and high-temperature gas turbines. After improvements were made in its synthesis, processing and properties, Si_3N_4 is now one of the most extensively studied ceramics in history. It is used were extreme toughness, strength, low coefficient of friction and low wear is required and these properties are ideal for medical applications like bearing components of prosthetic hip and knee joints as it is biocompatible and have the ability to propagate human osteoblast cells in vitro [6-8]. The fact, that silicon nitride dissolves in aqueous fluids propose, means that wear particles can dissolve *in vivo*, which may reduce possibility of infection and increase the serving time of the implant [8].

There are many techniques used for implant coating [3]. Amongst all the techniques, plasma spraying is the most used practice, as it was approved by the Food and Drug Administration (FDA), USA for biomedical coatings. However, despite of the advantages this technique provides, it had drawbacks, like poor mechanical properties of coated hydroxyapatite [9]. Although, most of these drawbacks were addressed, other coating techniques are also utilized.

One coating technique is sol-gel dip – coating. It is inexpensive and fast technique that uses simple equipment. What is more, it allows to mass produce coating on big substrates of irregular shapes. The parameters of coating can be controlled through the sol concentration, withdrawal speed and annealing temperature [5]. Sol–gel dip-coating provides other potential advantages: high purity and homogeinity of coating, reduced thickness. On the other hand, it has it's own limitations: brittleness of the coating and high annealing temperatures [5].

In this research, we combine dip-coating of HAp, prepared by sol-gel method, with a novel substrate - silicon nitride. According to our knowledge, this combination of techniques has never been used before. All things considered: substrate properties - high strength and fracture toughness, inherent phase stability, scratch resistance, low wear, biocompatibility, hydrophilic behavior, easier radiographic imaging and resistance to bacterial biofilm formation - and the properties of coating - like excellent biocompatibility and osseointegration - should be interesting for orthopaedic applications . Coatings were prepared with or without calcium titanate sublayer. Samples were investigated using XRD, SEM, AFM and CAM methods.

[1] S. Wu, X. Liu, K.W.K. Yeung, C. Liu, X. Yang, Biomimetic porous scaffolds for bone tissue engineering, Materials Science and Engineering: R: Reports, 80 (2014) 1-36.
[2] R.A. Surmenev, M.A. Surmeneva, A.A. Ivanova, Significance of calcium phosphate coatings for the enhancement of new bone osteogenesis – A review, Acta Biomaterialia, 10 (2014) 557-579.
[3] R.I.M. Asri, W.S.W. Harun, M.A. Hassan, S.A.C. Ghani, Z. Buyong, A review of hydroxyapatite-based coating techniques: Sol–gel and electrochemical depositions on biocompatible metals, Journal of the Mechanical Behavior of Biomedical Materials, 57 (2016) 95-108.
[4] S.V. Dorozhkin, Calcium orthophosphate coatings on magnesium and its biodegradable alloys, Acta Biomaterialia, 10 (2014) 2919-2934.
[5] M. Catauro, F. Bollino, F. Papale, C. Ferrara, P. Mustarelli, Silica–polyethylene glycol hybrids synthesized by sol–gel: Biocompatibility improvement of titanium implants by coating, Materials Science and Engineering: C, 55 (2015) 118-125.
[6] B.S. Bal, M.N. Rahaman, Orthopedic applications of silicon nitride ceramics, Acta Biomaterialia, 8 (2012) 2889-2898.
[7] M. Mazzocchi, A. Bellosi, On the possibility of silicon nitride as a ceramic for structural orthopaedic implants. Part I: processing, microstructure, mechanical properties, cytotoxicity, Journal of Materials Science: Materials in Medicine, 19 (2008) 2881-2887.
[8] M. Pettersson, S. Tkachenko, S. Schmidt, T. Berlind, S. Jacobson, L. Hultman, H. Engqvist, C. Persson, Mechanical and tribological behavior of silicon nitride and silicon carbon nitride coatings for total joint replacements, Journal of the Mechanical Behavior of Biomedical Materials, 25 (2013) 41-47.
[9] K. Thongsuriwong, P. Amornpitoksuk, S. Suwanboon, Structure, morphology, photocatalytic and antibacterial activities of ZnO thin films prepared by sol–gel dip-coating method, Advanced Powder Technology, 24 (2013) 275-280.

INVESTIGATION ON PH GRADIENT FORMATION AT MICROSTRUCTURED ELECTRODES USING SICM

Michele Zanatta[1], Naida El Habra[2], Francesca Visentin[2], Gianluca Pozza[3], Alessandro Zambon[1,4], Nicola Elvassore[1,4], Monica Giomo[1], Giovanna Brusatin[1,4]

[1]Industrial Engineering Department, University of Padova, Via Marzolo 9, 35131 Padova, Italy
[2]Institute of Condensed Matter Chemistry and Technologies for Energy, National Research Council of Italy, Corso Stati Uniti 4, 35127 Padova, Italy
[3]Physics and Astronomy Department, University of Padova, Via Marzolo 8, 35131 Padova, Italy
[4]Venetian Institute of Molecular Medicine (VIMM), Via Orus 2, 35129 Padova, Italy
michele.zanatta.1@phd.unipd.it

In fuel cells, formation of pH gradients at electrodes is a major issue since it may lead to ohmic losses, but it was never measured locally. The availability of data on pH changes in the surroundings of the electrodical surface could create a deeper understanding of the catalytic processes that occur in fuel cells and in other applications where pH plays an important role in determining process performance, such as CO_2 reduction, for example.

In this work we present local pH measurement via open circuit potential (OCP) measurements on a microstructured Pt/Au electrode: this substrate is used to generate H_2 or O_2 via electrolysis and the local consumption of H+ or OH- ions is detected by the device described below as a difference in OCP. The results shown are currently setting the foundations for further studies on photocatalysts' activity towards watersplitting reactions.

Scanning ion conductance microscopy (SICM) is an imaging technique useful for pH mapping (thus revealing the preferential sites of the watersplitting reactions): the integration of this technique with a three-electrode electrochemical system provides simultaneous information on the topographical imaging of a nanostructured sample and on the electrochemical and catalytic activity of the sample itself. This integration is provided by coating the borosilicate micropipette with a 150 nm-thick Pt layer (deposited via MOCVD) that acts as a WE.

In order to achieve maximum resolution for the simultaneous topography and electrochemical measurements just a small area of the coated surface is in contact with the electrolyte: a fully insulating coating was studied, created and tested via cyclic voltammetry (CV), using an industrial spray paint. The thickness of the coating is estimated to be 500 µm. The tip was opened putting it in contact with a small quantity of xylene and the pipettes were then characterized with CVs in $Ru(NH_3)_6Cl_3$.

Before use, each pipette is calibrated performing OCP measurements in solutions with different pH, ranging from 1 to 12. Finally, a microstructured Pt/Au electrodes array was prepared via lithographic technique and the electrochemical process was studied, with the integrated device described above, at a fixed distance of 100 µm from the electrodical surface: resulting curves OCP vs time show clearly the different trend of OCP before, during and after gas generation, due to a different pH of the surrounding environment (Fig. 1). Several experiments were carried with H_2 and O_2 evolution, in various aqueous media and at different buffered pH.

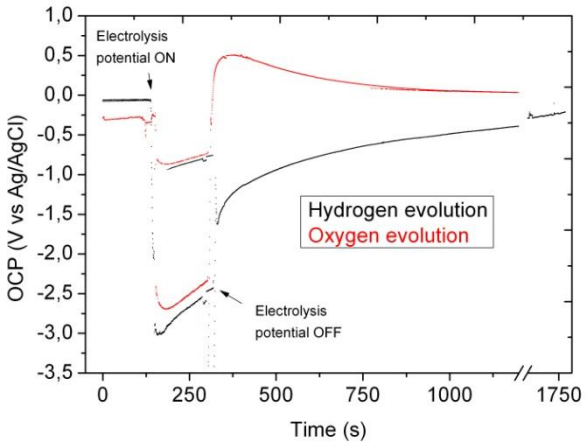

Fig. 1. Different OCP trends, with electrodes performing H_2 and O_2 evolution in KOH 1 M.

THE SIMULATION OF CRACK-LIKE DAMAGE

Liudmila Shemet, Sergei Sherbakov, Aleh Nasan

Department of Theoretical and Applied Mechanics, Belarusian State University, Belarus
shemetla@yandex.ru

Generally the process of fatigue has two stages: the stage before a crack initiation and the stage of development of the crack. The ratio between the lengths of these stages varies widely depending on the level of stresses, loading scheme, size and shape of the object, material properties, etc. In some cases, the stage of development of the main crack can be 60 ... 90% of the overall durability.

Results of two-dimensional computer simulation of crack-like damage propagation in time for different equivalent stresses is considered in the paper. The simulation was made basing on the model of deformable solid with a dangerous volume by deleting the dangerous surfaces at each step of loading [1].

The dangerous volume is the volume which consists of the elements, in which the values of the stress exceeds the limiting stress. While considering a two-dimensional problem dangerous volume becomes dangerous area.

For our work we considered this standard sample used in fracture toughness research. The following dimensions of the sample shown in Fig. 1 were considered for calculations: $L1$=0.0625 m, $H1$=0.06 m, $L2$=0.04 m, $R1$=0.00625 m, Q=15000 N – 20000 N.

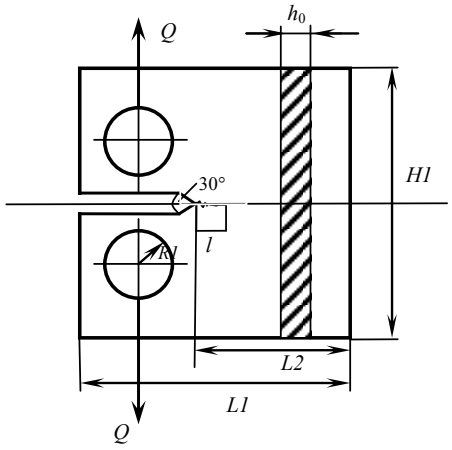

Fig. 1. Diagram of a sample with a crack.

Figures 2 and 3 show the illustration of deformed flat sample at different steps of loading for Q equals 15 000 N. It`s seen from the figures that the crack propagates in the longitudinal direction and the maximum values of the stress intensity are at the crack-like damage tip.

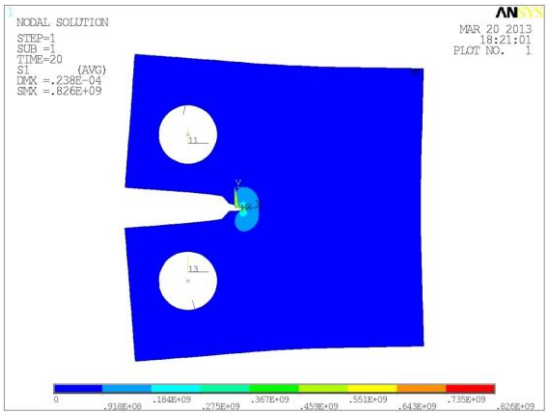

Fig. 2. Development of the crack on the 20th step of loading crack

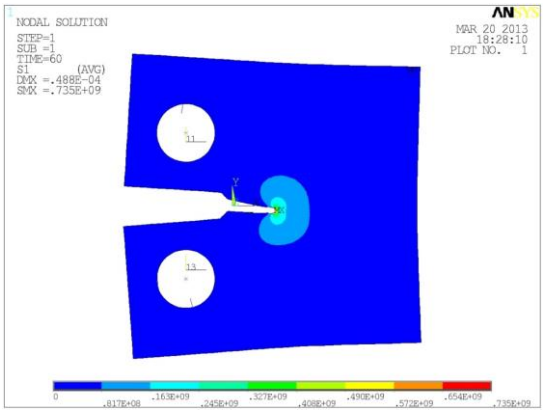

Fig. 3. Development of the crack on the 60th step of loading crack

[1] S. S. Sherbakov, Spatial Stress-Strain State of Tribofatigue System in Roll–Shaft Contact Zone, Strength of Materials 45, 35-43 (2013).

CALCULATION OF WHEEL-RAIL SYSTEM IN TRIBO-FATIGUE STATEMENT

Sergei Sherbakov, Aleh Nasan, Liudmila Shemet

Department of Theoretical and Applied Mechanics, Belarusian State University, Belarus
oleg.nasan@gmail.com

Wheel-rail problem is studied in this work. Two formulations of the problem are considered: classical "tribological", in which wheel interacts with the short segment of the rigidly fixed rail and new "tribo-fatigue", which studies multibody system, containing of some wheels and long rail. Tribo-fatigue approach takes into account both contact interaction of system elements and bending of the rail lying on an elastic Winkler's foundation by a train [1]. Both methods are verified with the help of the analytical solutions, based on the well-known strength of materials and Hertz's contact theories. Another very important purpose of this work was to show that new material Monica (VCHTG high strength cast iron) [2] is more preferred material for rails, than steel.

Mechanical and mathematical models are constructed (see Fig. 1a, 1b) for elastic static statement. Computer finite element modeling is carried out for determination of wheel/rail system spatial stress-strain state and dangerous volumes [3] (see Fig. 1c) as an integral indicators of damageability taking into account contact interaction between the wheel and the rail, bending of the rail on elastic foundation by the adjacent wheels (whole train). Significant increase of volumetric damageability of about 1.5 times is shown for tribo-fatigue formulation of problem in comparison with tribological.

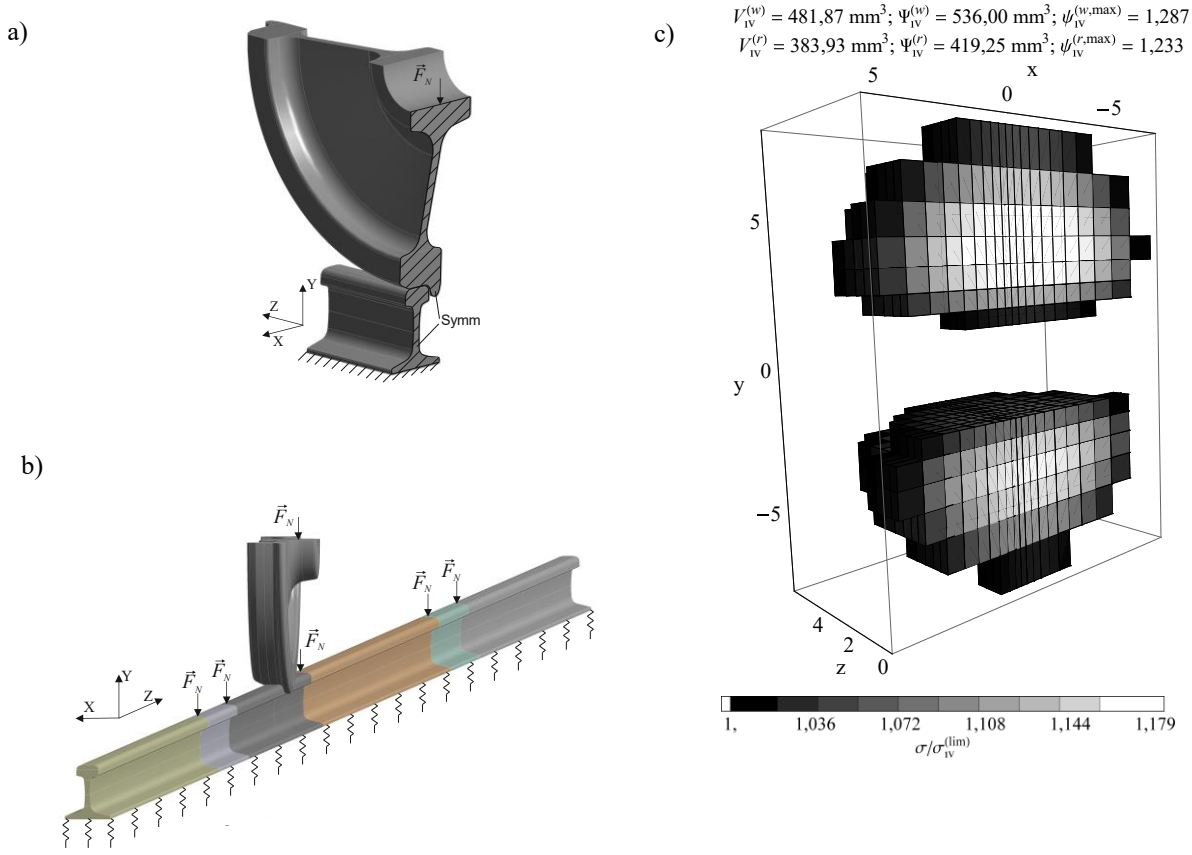

Fig. 1. a) tribological loading scheme; b) tribo-fatigue loading scheme; c) distribution of dangerous volumes in tribo-fatigue system

Using new structural material Monica which has high strength, rolling fatigue limits and ductility decreases volumetric damageability of the system elements by about 47%. It determines the feasibility of railway rails production of Monica.

[1] S.S. Sherbakov, A. A. Nasan Stress-strain state and volume damageability in the vicinity of contact interaction in wheel/rail tribo-fatigue system with the account of non-contact deformation of rail, BelSUT Herald: Science and Transport. – 2016. – № 1 (32). – pp. 234–247.
[2] L.A. Sosnovskiy, Mechanics of wear-fatigue damage, Gomel: BelSUT, 2007. – 434 p.
[3] S.S. Sherbakov, L.A. Sosnovskiy Mechanics of tribo-fatigue systems, Minsk: BSU, 2011. – 407 p.

Poster session 3

THE INVESTIGATION OF TRIPLET STATES IN 1,8-NAPHTHALIMIDE DERIVATIVES

Danielė Anilionytė[1], Dalius Gudeika[2], Juozas V. Gražulevičius[2], Arūnas Miasojedovas[1]

[1]Institute of Applied Research, Vilnius University, Sauletekio ave 3, LT-10257 Vilnius, Lithuania
[2]Department of Organic Technology, Kaunas University of Technology, Radvilenu pl. 19, LT- 50254, Kaunas, Lithuania
daniele.anilionyte@gmail.com

1,8-naphthalimide derivatives destinguish effective fluorescence and they are used in a wide range of applications such as organic light-emitting diodes (OLED) [1], fluorescent markers in biology and medicine [2], pH sensors [3], fluorescent dyes [4], etc. 1,8-naphthalimides contain a nitrogen heteroatom in their structure, which leads to a phosphorescence emission even at room temperature. The aim of this reasearch was to investigate triplet states and their infuence to photophysical properties of the derivatives with 1,8-naphthalimide backbone and different polarity moiety.

Spectral analysis revealed that increasing polarity of moiety determines a shift to longer wavelengths in absorption and fluorescence spectra. Adding a robust donor as a substituent leads to an increase of Stokes shift. These alterations are affected by the increase of dipole moment and intramolecular charge transfer (ICT) through donor-acceptor interaction.

Spectra of luminescence (Fig.1) were investigated at different delay times after optical excitation. After 2 ns signal of fluorescence and after 9 ms signal of phosohorescence were observed. Further spectral analysis revealed that triplet state energy however does not depend on the polarity of substituent and allocates at 570 nm. Phosphorescence of the derivatives is determined by the stucture of 1,8-naphthalimide. Since triplet state energy is equable and energy of singlet state is influenced by the polarity of moiety, the energy gap between singlet and triplet states (ΔE_{ST}) can be modified. Substituents with electron donating properties allow to achieve a small singlet-triplet energy gap. Diminished energy gap increases a chance of reverse intersystem crossing (RISC) and processes of thermally activated delayed fluorescence (TADF).

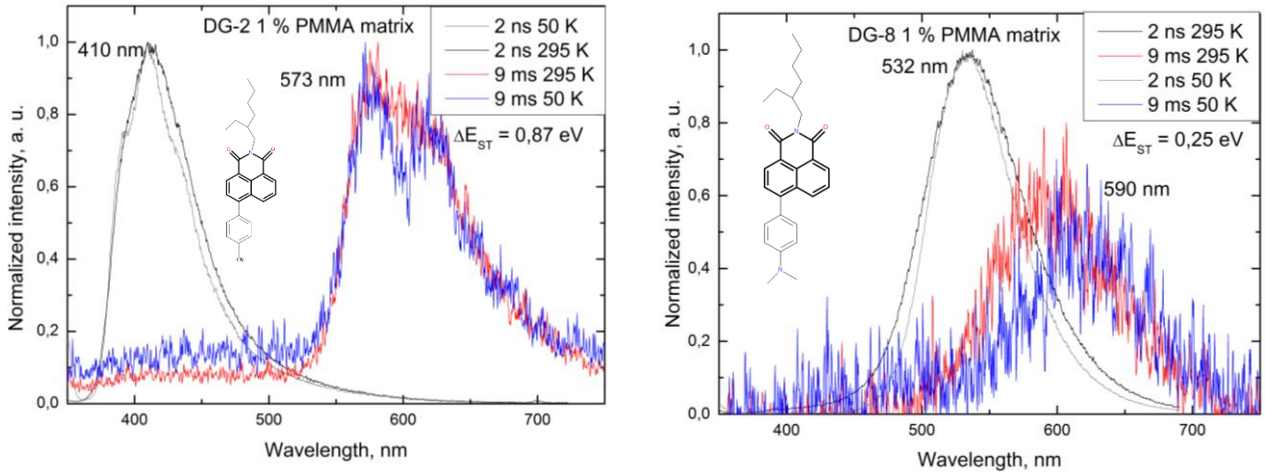

Fig.1 Luminescence spectra of the 1,8-naphthalimide derivatives

[1] H. Ulla, B. Garudachari, M. N. Satyanaryan, G. Umesh and A. M. Isloor, *Blue Light Emitting Materials for Organic Light Emitting Diodes: Experimental and Simulation Study*, International Conference on Optical Engineering (ICOE), (2012).

[2] H. Yin, Y. Zhu, Y. Xu, M. Dai, X. Qian, Y. Li and J. Liu, *Novel aliphatic N-oxide of naphthalimides as fluorescent markers for hypoxic cells in solid tumor* (European Journal of Medicinal Chemistry, 2011).

[3] J. Xie, Y. Chen, W. Yang, D. Xu and K. Zhang, *Water soluble 1,8-naphthalimide fluorescent pH probes and their application to bioimagings* (Journal of Photochemistry and Photobiology, 2011).

[4] L. Zhang, F. Su, X. Kong, F. Lee, S. Sher, K. Day, Y. Tian and D. R. Meldrum, *1,8-Naphthalimide Derivative Dyes with Large Stokes Shifts for Targeting Live-Cell Mitochondria* (ChemBioChem, 2016).

DIELECTRIC PROPERTIES OF $BaTiO_3$-$KNbO_3$ COMPOSITES

Sergejus Balčiūnas[1], Maksim Ivanov[1], Jūras Banys[1], Satoshi Wada[2]

[1] Faculty of Physics, Vilnius University, Sauletekio 9/3 817k., LT10222 Vilnius, Lithuania.
[2] Interdisciplinary Graduate School of Medical and Engineering, University of Yamanashi, Kofu,Yamanashi 400-8510, Japan.
sergejus.balciunas@ff.vu.lt

For the past 40-50 years, lead based perovskite $Pb(Zr_xTi_{1-x})O_3$ (PZT) piezoelectric ceramics have dominated the commercial market of piezoelectric devices due to their remarkable dielectric and piezoelectric properties and ability to operate in wide temperature range.

$BaTiO_3$ (BT) is perhaps the most widely researched perovskite in the last decades. Inserting potassium niobate (KN) into BT structure creates stresses that increase domain wall count and in result piezoelectric coefficient [1]. KNBT has comparable piezoelectric coefficient with PZT, thus making it a great substitute. The fact that KNBT is lead free ceramic makes it of high interest for both researchers and engineers due to environmental concerns.

KNBT composites were prepared in two steps: compact BT particles were heated up to 1000 ℃ and heat-treated at that temperature for 2h to create low-density ceramics, then KN were epitaxially deposited into BT structure. [2].

In this presentation dielectric properties of KNBT with different KN/BT molar ratios will be presented. From Figure 1 we can observe that the bigger the KN/BT ratio is, the more obscured phase transitions of $BaTiO_3$ become. Low dielectric permittivities in KN/BT with molar ratios of 0.22 and 0.5 can be explained by its low relative density.

Furthermore, experimental data of the frequency dependences were approximated by superposition of 3 Cole-Cole equations (Fig 2). Three relaxation processes were distinguished: Maxwell – Wagner relaxation (1), domain wall motion (2) and electro – mechanical resonance (3). Additionally we can see that relaxation times of the third relaxation process has no temperature dependence and it contributes to dielectric permittivity the most.

Lastly, the model proposed by Arlt [3] was used to calculate spontaneous polarization from electro – mechanical resonance contribution to dielectric permittivity and showed promising results. Also, theoretical models of electro – mechanical resonance will be presented.

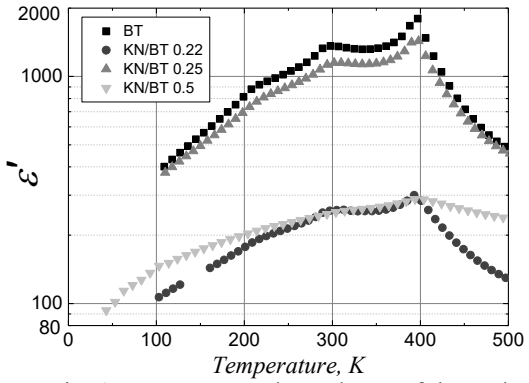

Fig. 1: Temperature dependence of the real part of dielectric permittivity at 1MHz, for: BT, KN/BT 0.22, KN/BT 0.25, KN/BT 0.5 respectively with 60%, 53% 79%, 60% relative

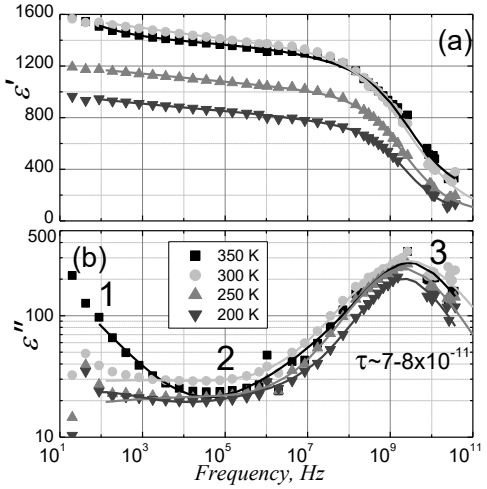

Fig. 2: Frequency dependence of real (a) and imaginary (b) part of dielectric permittivity for BT with 60% relative density.

[1] T. Higuchi, *Journal of mechanical science and technology,* vol. 24, pp. 13-18, 2010
[2] I. Fujii, S. Shimizu, K. Yamashita, K. Nakashima, N. Kumada, C. Moriyoshi*, et al.*, *Applied Physics Letters,* vol. 99, p. 202902, 2011
[3] G. Arlt, U. Böttger, S. Witte, *Annalen der Physik,* vol. 506, pp. 578-588, 1994.

OPTIMIZATION OF NANOCRYSTALLIZATION OF $Li_{3x}Na_{3(1-x)}V_2(PO_4)_3$ GLASSES

Piotr Baranowski, Tomasz K. Pietrzak, Jerzy E. Garbarczyk

Faculty of Physics, Warsaw University of Technology, Koszykowa 75, 00-662 Warsaw, Poland
baranowski_piotr@onet.pl

Low electrical conductivity of many materials proposed for cathodes in lithium and sodium batteries is the main reason for the modest performance of electrochemical cells. There are many propositions to address this issue. In recent years, J.E. Garbarczyk and co-workers have proposed and investigated an alternative route to the conductivity enhancement, namely a thermal nanocrystallization of glassy analogs of the important crystalline cathode materials [1, 2], such as: V_2O_5, $LiFePO_4$ and $Na_3V_2(PO_4)_2F_3$. The advantages of our approach to produce active cathode materials include the absence of carbon additives and simplicity and straightforwardness of synthesis, which consists of two stages only: glass preparation by melt-quenching and thermal treatment of the glass to induce its nanocrystallization. Our experience with that method has shown that one can, by the appropriately chosen heat-treatment conditions, achieve a huge (even by a factor 10^9) and irreversible conductivity enhancement.

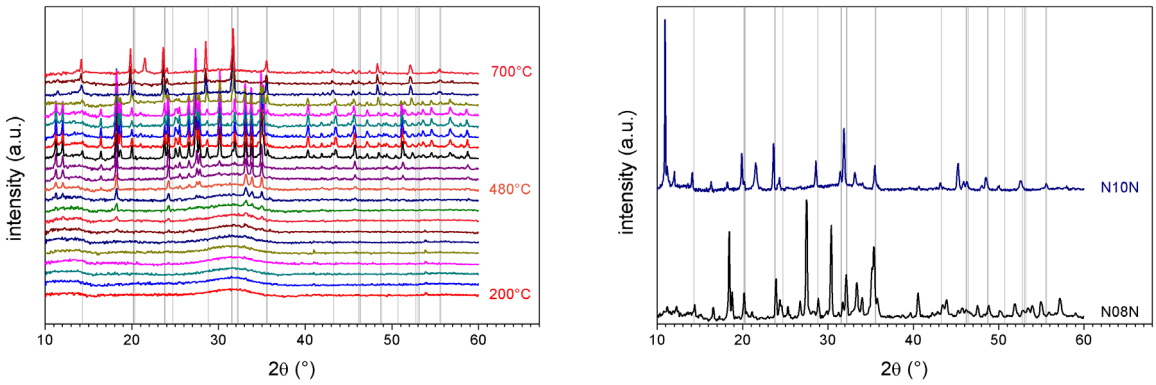

(a) XRD measurements at temperatures in the range of 200–700°C for N10N sample.

(b) XRD measurements for N08N and N10N samples at 30°C after cooling down from 600°C and 700°C, respectively.

Fig. 1. XRD measurements for sodium samples. Gray vertical lines indicate the position of $Na_3V_2(PO_4)_3$ phase

In this work, thermal and structural analysis on $Li_{3x}Na_{3(1-x)}V_2(PO_4)_3$ ($0 \leqslant x \leqslant 1$) materials were carried out. These are promising compounds that can be used as cathode materials in batteries. They have a high specific capacity, but also low electronic conductivity. Samples labeled as N08N and N10N were synthesized with 30% and 50% excess of sodium, respectively. Differential thermal analysis (DTA) study determined the characteristic temperatures of glass transition and crystallization. This temperatures ranged from 401°C to 479°C for glass transition and from 461°C do 615°C for crystallization. This knowledge allows for thermal nanocrystallization of investigated materials. X–ray diffraction (XRD) for samples at room temperature confirmed amorphousness of almost all obtained sodium materials. Samples with lithium had enough time for crystallization. Temperature dependent XRD studies for lithium samples determined presence of two phases: $Li_3V_2(PO_4)_3$ and $LiVOPO_4$, which occured at 440°C.
For sodium samples, XRD study determined $Na_3V_2(PO_4)_3$ and $NaVOPO_4$ phases (Fig. 1a). However, the latter (unwanted) phase disappeared at higher temperatures (Fig. 1b). Sizes of crystallites, calculated with Scherrer's formula are within range 26–150 nm.

[1] J.E. Garbarczyk, T.K. Pietrzak, M. Wasiucionek, A. Kaleta, A. Dorau, J.L. Nowinski: High electronic conductivity in nanostructured materials based on lithium-iron-vanadate-phosphate glasses. Solid State Ionics **272** (2015) 53–59.

[2] T.K. Pietrzak, M. Wasiucionek, P.P. Michalski, A. Kaleta, J.E. Garbarczyk: Highly conductive cathode materials for Li-ion batteries prepared by thermal nanocrystallization of selected oxide glasses. Materials Science and Engineering B **213** (2016) 140–147.

OPTIMIZATION OF MODIFIED ANTHRACENE COMPOUNDS FOR LIGHT UPCONVERSION

Greta Bučytė, Steponas Raišys, Povilas Adomėnas, Karolis Kazlauskas, Saulius Juršėnas

Institute of Applied Research, Vilnius University, Lithuania
greta@fidi.lt

Light upconversion via sensitized triplet-triplet annihilation allows to upconvert polychromatic light even at relatively low excitation power densities [1]. This feature is very attractive for solar energy harvesting, as the radiation power is sufficient for the process to take place. However, for the practical applications the efficiency of upconverting polymer films is still too low due to several factors. One of the main factors is aggregation of the emitter in polymer matrix and aggregation-induced emission quenching [2]. To this end, chemical modification of anthracene compounds to reduce emitter self-quenching and achieve high upconversion efficiency was attempted.

For this study, upconverting films based on sensitized platinum-octaethylporphyrin (PtOEP) and modified anthracene compounds in poly(vinyl butyral-co-vinyl alcohol-co-vinyl acetate) (PVBVAVAc) polymer were fabricated by melt processing technique. The concentration of anthracene compounds in the polymer matrix was chosen to vary from 15 wt% to 50 wt%. The PtOEP/anthracene compound/PVBVAVAc films were evaluated by measuring fluorescence, phosphorescence and upconversion spectra as well as estimating their emission quantum yields.

The obtained data showed that complementary alkyl groups in anthracene compounds (jng2 and jng3) significantly reduce self-quenching effects and enable fabrication of upconverting films with high emitter concentrations, up to 50 wt%. High emitter concentration facilitates triplet exciton migration essential for achieving high upconversion quantum yield in polymer films (Fig. 1). The maximal upconversion quantum yield of 2.1 % was attained in PtOEP/jng2/PVBVAVAc film at 40 wt% of jng2. Upconversion quantum yield of PtOEP/jng3/PVBVAVAc film was found to persistently increase with jng3 concentration reaching its highest value (1.9 %) at 50 wt%.

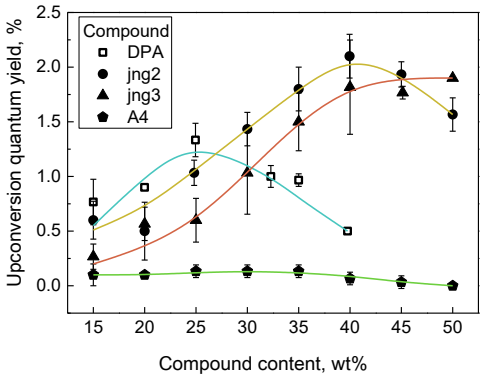

Fig. 1. Upconversion quantum yield of PVBVAVAc/anthracene compound/PtOEP (C_{PtOEP} = 0.01 wt%) films as a function of anthracene compound concentration. Lines are guides to the eye.

[1] S. Baluschev, T. Miteva, V. Yakutkin, et al., Up-conversion fluorescence: noncoherent excitation by sunlight, Physical Review Letters **97**, 7–9 (2006).

[2] S. Raišys, K. Kazlauskas, S. Juršėnas, et al., The role of triplet exciton diffusion in light-upconverting polymer glasses, ACS Applied Materials and Interfaces **8**, 15732–15740 (2016).

HIGHLY EFFICIENT THERMALLY ACTIVATED DELAYED FLUORESCENCE IN TRIAZINE-CARBAZOLE DERIVATIVES

Tadas Buciunas[1], Paulius Baronas[1], Tomas Matulaitis[2], Juozas Vidas Grazulevicius[2] and Saulius Antanas Jursenas[1]

[1] Institute of Applied Research, Vilnius University, Vilnius, Lithuania
[2] Department of Polymer Chemistry and Technology, Kaunas University of Technology, Kaunas, Lithuania
tadas.buciunas@gmail.com

Development of the organic light emitting diodes, OLEDs, experiences a breakthrough due to recent discovery of novel emission mechanism employing delayed florescence generated by thermal activation (TADF) [1]. The delayed emission is established by virtue of the adjacent triplet energy states, corresponding to a mechanism termed as reverse intersystem crossing (RISC). The TADF process enables to reach 100 % internal quantum efficiency of the singlet luminescence recycling the triplet excitations [2]. In the present study, the ability to control the photoluminescence properties of donor-acceptor triazine-triphenyl-carbazole derivatives as a function of varying para (**TTC-p**) or meta (**TTC-m**) position of carbazole substituents was investigated in search of TADF mechanism.

The density functional theory (DFT) calculations revealed twisted molecular conformations (Fig. 1a) for both compounds resulting in a substantial charge transfer (CT) character, and thus a small singlet-triplet energy gap ΔE_{ST} – a fundamental requirement for the efficient TADF process. Investigation of singlet and triplet spectral distributions in 12 K temperature indicated ΔE_{ST} of 0.21 eV and 0.13 eV for **TTC-p** and **TTC-m**, respectively. Gated intensified charge-coupled camera (iCCD) allowed in depth study of the delayed fluorescence. The emission kinetics displayed in Figure 1b demonstrate normalized intensity kinetics of both **TTC** derivatives. Although, **TTC-p** shows higher fluorescence efficiency (φ_{FL} = 63%), the contribution of delayed fluorescence to the total photoluminescence is minute, whereas almost two thirds of **TTC-m** emission (φ_{FL} = 37%) originates from TADF. Furthermore, the measurements of temperature dependency allowed to estimate activation energies E_A for the TADF process, which were found to be 0.2 eV and 0.07 eV for **TTC-p** and **TTC-m**, respectively. The noticeable difference between energies E_A and ΔE_{ST} for **TTC-m** suggests that intermediate band states play an important role in promoting triplet excitations to singlet state manifold.

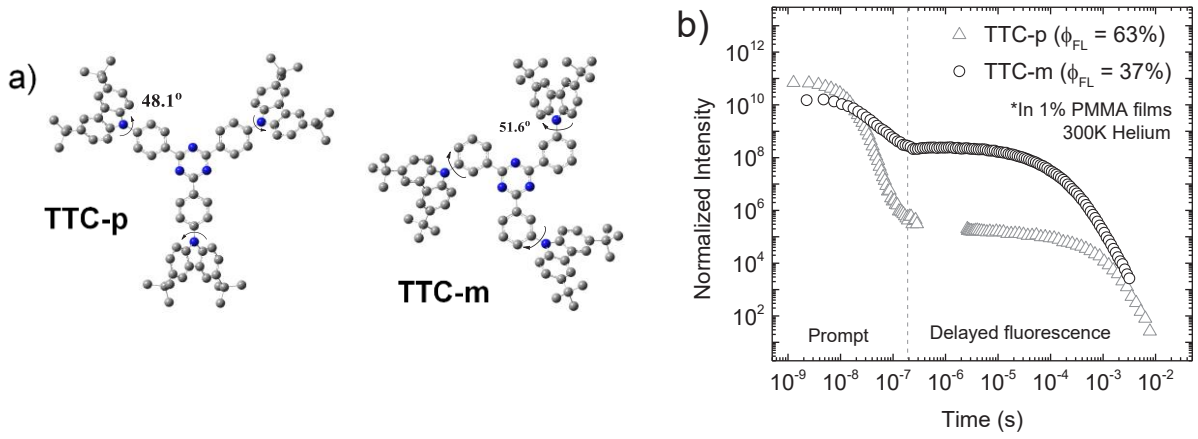

Fig. 1. DFT geometry optimizations of the ground state (a). Prompt and delayed fluorescence kinetics, internal quantum efficiencies φ_{FL} are indicated (b).

This work revealed the ability to manipulate the photoluminescence characteristics by varying para (**TTC-p**) or meta (**TTC-m**) position of carbazole substituents. Meta conformation of donor and acceptor in **TTC-m** derivative resulted in decrease in the energy gap between singlet and triplet energy states and, therefore, highly increased TADF character in comparison to para conformation (**TTC-p**). This knowledge is essential in constructing novel chemical derivatives implemented in highly efficient TADF emitters.

[1] H. Uoyama, K. Goushi, K. Shizu, H. Nomura and C. Adachi, Highly efficient organic light-emitting diodes from delayed fluorescence, Nature, **492**, 234-240, (2012).
[2] F. B. Dias, K. N. Bourdakos, V. Jankus, K. C. Moss, K. T. Kamtekar, V. Bhalla, J. Santos, M. R. Bryce, A. P. Monkman, Triplet harvesting with 100% efficiency by way of thermally activated delayed fluorescence in charge transfer OLED emitters, Adv. Mater., 25, 3707, (2013).

THE EFFECT OF THERMOMAGNETIC TREATMENT ON STRUCTURE AND PROPERTIES OF Cu-Al-Mn SHAPE MEMORY ALLOYS

Lesya Demchenko[1], Anatoliy Titenko[2], Yaroslav Titenko[1], Eduard Udovenko[1]

[1] Department of Physics of Metals, National Technical University of Ukraine "Igor Sikorsky Kyiv Polytechnic Institute", Ukraine
[2] Department of Physics of Magnetic Materials and Nanocrystalline Structures, Institute of Magnetism, Institute of Magnetism, Ukraine
lesyademch@gmail.com

In the market of new materials, the functional materials having unusual properties are in great demand, among which the ferromagnetic shape memory alloys are predominant. The control over such properties is exercised using force, thermal and magnetic fields. An important aspect of improvement in the material properties is to create a nanostructured state, which has significant advantages in magnetic and mechanical characteristics in contrast to the bulk materials in crystalline or amorphous state.

Cu-Al-Mn alloys are ones of the most interesting alloys with shape memory effect. To get their optimal properties. these alloys usually undergo an additional thermal, mechanical or magnetic treatment. Thus, aging of Cu-Al-Mn alloys leads to the formation of a system of nanoscale particles of ferromagnetic Cu_2MnAl phase in a paramagnetic Cu_3Al matrix, and annealing in a magnetic field increases the Tc of Cu-Al-Mn alloys. At the same time, the heat treatment allows to control a number and a size of particles in the alloy, and also the martensitic transformation temperature and hysteresis, which depend on characteristics of precipitated particles [1].

The work is devoted to the influence of a magnetic field on magnetic and mechanical properties of a Cu–Mn–Al alloy under annealing. The comparative analysis of the magnetic-field orientational impact on solid-solution decomposition processes in a fixed annealing procedure is held using the methods of low-field magnetic susceptibility (fig. 1), specific magnetization, and microhardness test. The work highlights changes in the magnetic and mechanical properties of a Cu–Al–Mn alloy associated with the change in a critical size of forming precipitated ferromagnetic phase, and determines correlation in the behaviour of magnetic and mechanical properties of the alloy, depending on a critical nucleus size of forming precipitated ferromagnetic phase.

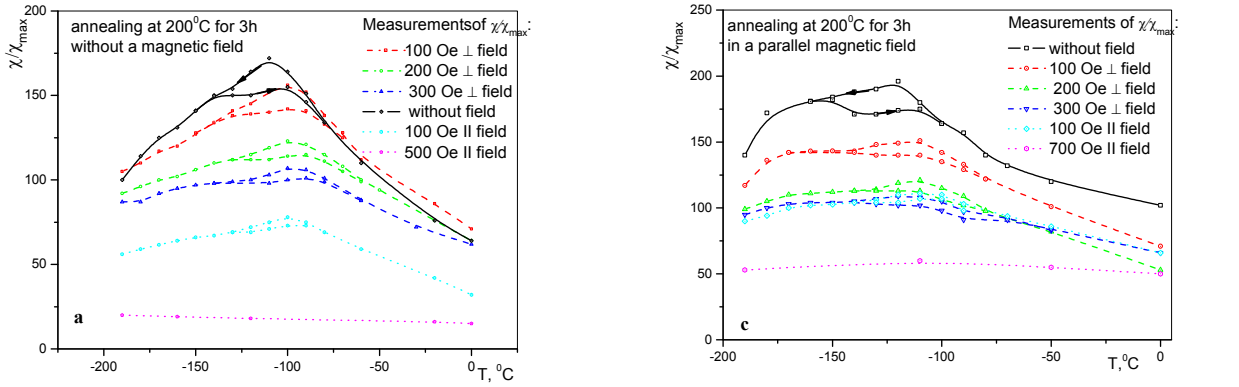

a) b)

Fig 1. Temperature dependence of the low-field magnetic susceptibility of Cu-Al-Mn alloy at different regimes of aging: a) without magnetic field; b) in a parallel magnetic field.

The work was attempted to process control of phase formation at aging of high temperature phase using the constant magnetic field in order to optimize the parameters of martensite transformation behavior in Cu-Al-Mn alloy. With the help of the phenomenological theory of diffusion decay and obtained experimental results, the character and causes of the induced MT behavior in the alloy were determined. One can assume that applying a magnetic field stimulates the formation of ferromagnetic nanoparticles during the decay of solid solution. In addition, thermomagnetic treatment helps to create effective nucleation centers of nanoparticles in Cu-Al-Mn alloy during the aging of high temperature phase. The treatment in the magnetic field causes the reduction in a particle size that appears in the decrease of magnetic characteristics of the alloy, however, increases the alloy microhardness.

[1] A. Titenko, L. Demchenko Effect of Annealing in Magnetic Field on Ferromagnetic Nanoparticle Formation in Cu-Al-Mn Alloy with Induced Martensite TransformationNanoscale Research Letters (2016) 11:237 DOI 10.1186/s11671-016-1453-2

THERMAL AND ELECTRICAL CHARACTERIZATION OF $LiVBO_3F$ GLASSES AND NANOMATERIALS

Jędrzej Doliński, Przemysław Piotr Michalski, Tomasz Karol Pietrzak, Jerzy Edward Garbarczyk

Faculty of Physics, Warsaw University of Technology, Poland
jj.dolinski@gmail.com

Nowadays, take-up in lithium ion (Li-ion) batteries is quickly rising. Thereupon, we are interested in investigation of potential cathode materials for those. The advantages of Li-ion batteries are high energy and power density. One of perspective cathode materials is $LiVPO_4F$ with tavorite crystal structure [1]. This material exhibits good gravimetric capacity (up to 155 $mAhg^{-1}$) and high potential vs metallic lithium (4.2 V) [2]. In this work, we proposed an exchange of phosphate group (PO_4) to borate group (BO_3). Molar mass of borate group is lower than the phosphate one, so theoretical gravimetric capacity of borate-exchanged tavorite is higher, reaching 200 $mAhg^{-1}$.

Materials in this work are obtained in a glassy state and then thermally crystallized to obtain glass-ceramics consisting of nanometric-sized grains. Glasses and glass-nanoceramics seem to be an alternative and interesting way to produce nanometer-sized cathode materials with good electrochemical properties [3].

The investigated material was synthesized using melt-quenching method. Dried chemicals: LiF (Aldrich, 99.995%), H_3BO_3 (Polish Chemicals, 99.5%) and V_2O_5 (Aldrich, 99.5%) were homogenized and put in alumina crucible, which was placed in another crucible filled with carbon to obtain non-oxidizing atmosphere. The batch was melted at 1200 °C for 20 minutes and poured on the metal plate and pressed with another metal plate to obtain the glass by the means of fast cooling. The obtained amorphous material was then heated to elevated temperatures (250–400 °C) to get nanostructured samples.

Obtained $LiVBO_3F$ was investigated using thermal and electrical methods: differential scanning calorimetry (DSC) and impedance spectroscopy (IS). For the first one, TA Q200 DSC apparatus was used. Measurements were performed in 25–450 °C range with different heating rates (1–40 °Cmin^{-1}) in nitrogen flow. For the second one, Solartron 1260 impedance analyzer equipped with tubular furnace was used. Amplitude of voltage was equal to 0.1 V and the measurements were performed in 10^{-2}–10^{7} frequency range and 25–400 °C temperature range.

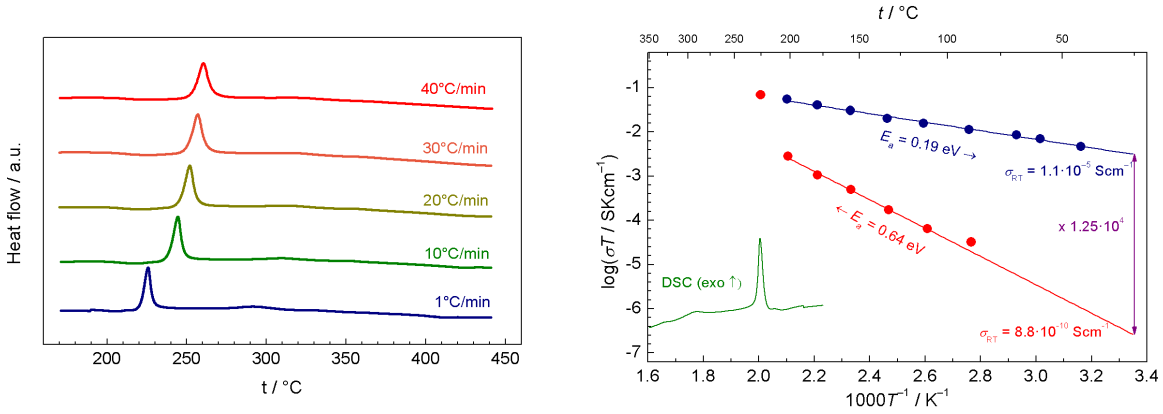

(a) DSC curves for $LiVBO_3F$ sample for diferent heating rates

(b) Arrhenius plot for $LiVBO_3F$ sample heated to 250 °C.

Fig. 1. Exemplary result of thermal (a) and electrical (b) research for $LiVBO_3F$ sample.

[1] B.L. Ellis, T.N. Ramesh, L.J.M. Davis et al., Structure and Electrochemistry of Two-Electron Redox Couples in Lithium Metal Fluorophosphates Based on the Tavorite Structure. Chemistry of Materials, **23**, 5138-5148 (2011)

[2] J.Barker, R.K.B. Gover, P. Burns et al., A Lithium-Ion Cell Based on $Li_{4/3}Ti_{5/3}O_4$ and $LiVPO_4F$, Electrochemical and Solid-State Letters, **10**, A130–133 (2007).

[3] S. Afyon, F. Krumeich, C. Mensing et al., New High Capacity Cathode Materials for Rechargeable Li-ion Batteries: Vanadate-Borate Glasses, Nature Scientific Reports **4**, 7113–7119 (2014)

SYNTHESIS AND CHARACTERIZATION OF $LiFe_{0.44}Mn_{0.44}V_{0.08}PO_4$ GLASS AND NANOMATERIALS

Justyna E. Frąckiewicz, Tomasz K. Pietrzak, Jerzy E. Garbarczyk

Faculty of Physics, Warsaw University of Technology, Poland
frackiewicz.justyna95@gmail.com

Since the pioneering publication by J.B. Goodenough et al. [1], phospho-olivines $LiMPO_4$ (M = Fe, Mn, Co, Ni) had been studied for their application as cathodes for Li-ion cells. From the whole family of isostructural compounds, only cathodes prepared from $LiFePO_4$ had been introduced into mass production. $LiMnPO_4$ cathode has higher potential versus metallic lithium compared to $LiFePO_4$, but synthesis of $LiMnPO_4$ compounds which can work in cathodes with high loads is more difficult [2]. One of the applied ways is to prepare nanomaterials with non-stoichiometry [3]. Other possible way is to synthesize $LiMn_{1-x}Fe_xPO_4$ phospho-olivines [4]. In recent years, J.E. Garbarczyk and co-workers have proposed and investigated an alternative route to the conductivity enhancement, namely a thermal nanocrystallization of glassy analogs of the important crystalline cathode materials [5, 6], such as: V_2O_5, $LiFePO_4$ and $Li_3V_2(PO_4)_3$. The advantages of our approach to produce active cathode materials include the absence of carbon additives and simplicity and straightforwardness of synthesis, which consists of two stages only: (i) glass preparation by melt-quenching and (ii) thermal treatment of the glass to induce its nanocrystallization. Our experience with that method has shown that one can, by the appropriate heat-treatment, achieve a huge (even by a factor 10^9) and irreversible conductivity enhancement.

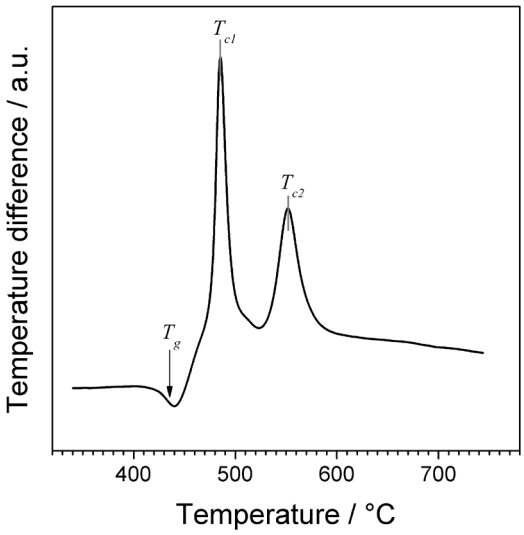

Fig. 1. DTA curve of glassy sample under study (heating rate 10 °C / min).

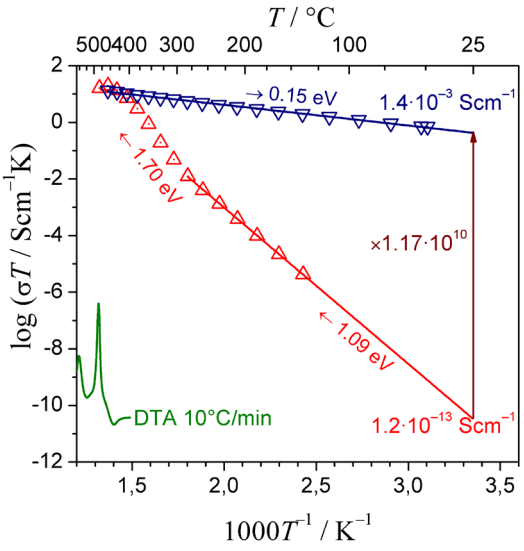

Fig. 2. Electrical conductivity upon heating to 480°C (△) and cooling down to 25°C (▽).

In this research, we aimed to replace some of iron ions in $LiFe_{0.80}V_{0.08}PO_4$ with manganese in order to obtain highly conductive nanomaterial. Appropriate amounts of precursors: Li_2CO_3, $FeC_2O_4{\cdot}2H_2O$, $Mn(CH_3COO)_2{\cdot}4H_2O$, $(NH_4)H_2PO_4$ and V_2O_5 were mixed in a mortar, melted at 1300 °C and rapidly quenched. Their amorphousness was confirmed with X-ray diffractometry (XRD) and thermal events occurring in the sample were observed with differential thermal analysis (DTA). Electrical conductivity was measured upon heating and subsequent cooling with impedance spectroscopy within wide frequency range 10 mHz – 10 MHz.

DTA curve of as-received sample was typical for glassy material (Fig. 1). A glass transition at T_g = 433 °C and two crystallization peaks (T_{c1} = 485 °C and T_{c2} = 552 °C) were observed. Preliminary electrical results (Fig. 2) showed that initial conductivity ($1.2{\cdot}10^{-13}$ Scm^{-1}) can be increased of at least 10 orders of magnitude to $1.4{\cdot}10^{-3}$ Scm^{-1}.

[1] A.K. Padhi, K.S. Nanjundaswamy, J.B. Goodenough: Phospho-olivines as positive electrode materials for rechargeable lithium batteries. Journal of the Electrochemical Society **144** (1997) 1188–1194.
[2] J.O. Herrera, H. Camacho-Montes, L.E. Fuentes, L. lvarez-Contreras: $LiMnPO_4$: Review on Synthesis and Electrochemical Properties. Journal of Materials Science and Chemical Engineering **3** (2015) 54-64.
[3] B. Kang, G. Ceder: Electrochemical Performance of $LiMnPO_4$ Synthesized with Off-Stoichiometry. Journal of The Electrochemical Society **157** (2010) A808–A811.
[4] L. Damen, F. De Giorgio, S. Monaco, F. Veronesi, M. Mastragostino: Synthesis and characterization of carbon-coated $LiMnPO_4$ and $LiMn_{1-x}Fe_xPO_4$ (x = 0.2, 0.3) materials for lithium-ion batteries. Journal of Power Sources **218** (2012) 250–253.
[5] J.E. Garbarczyk, T.K. Pietrzak, M. Wasiucionek, A. Kaleta, A. Dorau, J.L. Nowinski: High electronic conductivity in nanostructured materials based on lithium-iron-vanadate-phosphate glasses. Solid State Ionics **272** (2015) 53–59.
[6] T.K. Pietrzak, M. Wasiucionek, P.P. Michalski, A. Kaleta, J.E. Garbarczyk: Highly conductive cathode materials for Li-ion batteries prepared by thermal nanocrystallization of selected oxide glasses. Materials Science and Engineering B **213** (2016) 140–147.

INVESTIGATION OF STRUCTURAL PROPERTIES OF LITHIUM MANGANESE BORATE

Agata Gołębiewska, Przemysław Piotr Michalski, Tomasz Karol Pietrzak, Jerzy Edward Garbarczyk

Faculty of Physicss, Warsaw University of Technology, Poland
agata.golebie@gmail.com

In this work, synthesis, nanocrystallization and characterization of glassy lithium manganese borate with nominal formula $LiMnBO_3$ were described. The reason for interest in this compound and taking it into account as a potential cathode material for Li-ion batteries is its high theoretical gravimetric capacity reaching 222 $mAhg^{-1}$ [1].

$LiMnBO_3$ was synthesized using melt-quenching method from substrates: Li_2CO_3, $Mn(CH_3COO)_2 \cdot 4H_2O$ and H_3BO_3. This way, three samples with different parameters (maximum melting temperature and time) were obtained. Parameters of the batches and their naming are as follows: 20 min, 1015 ˚C – G02a; 25 min, 1035 ˚C – G02b; 30 min, 1070 ˚C – G02c.

Material was investigated with differential thermal analysis (DTA) and X-ray diffractometry (XRD) methods. Results obtained with differential thermal analysis, carried out within 25–650 ˚C range, proved that typical processes for glassy materials (glass transition and crystallization) appeared in all three samples. In Fig. 1, one can see that increase of temperature leads to increase of peaks intensity meaning that crystallization process in the sample occurs. Cooling down to the room temperature caused only minor changes. X-ray diffractometry measurement confirmed lack of crystalline phases at room temperature, which is typical for amorphous materials. Samples were amorphous till 400 ˚C, and above that temperature, first visible peaks characteristic for different compounds appeared. For all of the diffractograms for a given sample, the background was substracted and the data was normalized to the highest intensity in each graph, respectively. It was due to observe the relative changes between diffractograms in different temperatures. Diffractograms for different parameters of synthesis of the samples vary – different phases are observed after nanocrystallization. The most preferable phases (orthorhombic $MnBO_3$ marked as o-$MnBO_3$, and monoclinic $LiMnBO_3$ marked as m-$LiMnBO_3$) were indicated with dashed and dotted lines; other, less significant phases were marked with various symbols. Grain sizes were estimated in the range from 30 nm to 150 nm, changing for different synthesis parameters and phases.

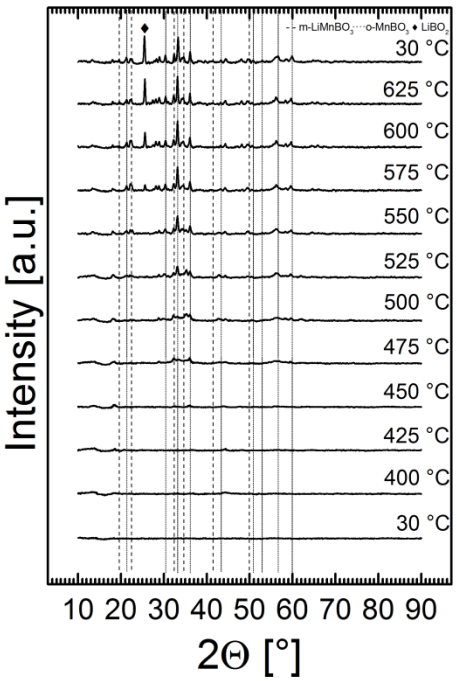

Fig. 1. Diffractograms for G02a sample measured in the temperature range from 30 ˚C to 625 ˚C. m-$LiMnBO_3$ phase is marked with dashed line and o-$MnBO_3$ – with dotted line. Other phases are marked with different symbols on this figure.

[1] J.C. Kim, X. Lin, C.J. Moore, S. Bo, P.G. Khalifah, C.P. Grey, G. Ceder, *Analysis of Charged State Stability for Monoclinic $LiMnBO_3$ Cathode,* Chemistry of Materials **26** (2014) 4200–4206.

OLEDs BASED ON TRIAZINE DERIVATIVES FEATURING THERMALLY ACTIVATED DELAYED FLUORESCENCE

Paulius Imbrasas[1], Karolis Kazlauskas[1], Tomas Matulaitis[2], Juozas V. Gražulevičius[2], Saulius Juršėnas[1]

[1]Institute of Applied Research, Vilnius University, Saulėtekio 9, LT-10222 Vilnius, Lithuania
[2]Department of Polymer Chemistry and Technology, Kaunas University of Technology, Radvilėnų pl. 19, LT-50254 Kaunas, Lithuania
paulius.imbrasas@ff.stud.vu.lt

State-of-the-art OLED devices are fabricated using phosphorescent or triplet-emitting materials. OLEDs based on singlet emitters utilizing thermally activated delayed fluorescence (TADF) phenomena offer an alternative technology, which can also deliver internal quantum efficiency of unity. This allows to reduce the cost and increase operation lifetime of an OLED. TADF is a thermally-assisted process, which enables triplet state harvesting with an efficiency of 100% via reverse intersystem crossing (RISC) to singlet manifold. [1] For the RISC process to be efficient, the energy gap ΔE_{ST} between S_1 and T_1 excited states must be small, i.e., $< k_BT$. This can be achieved by designing emitter molecules with spatially separated donor and acceptor moieties resulting in small overlap of HOMO and LUMO. However, since the separation weakens oscillator strength, and so the quantum efficiency of the optical transitions, a balance must be found. Thus, optimization of new TADF compounds and OLED structures taking into account this balance is a primary task in OLED research.

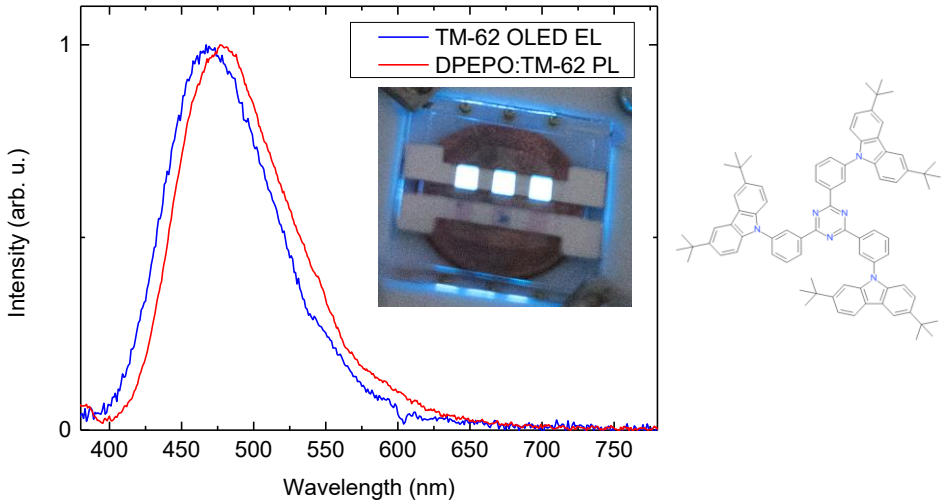

Fig. **1**. Emission spectra of compound **TM-62** dispersed in DPEPO host and of the OLED based on **TM-62.** Inset shows picture of OLED device. Chemical structure of TADF compound **TM-62** (right).

In this work, properties of OLEDs based on triazine TADF compounds are investigated. Spatial separation of donor and acceptor moieties in the compound ensures small HOMO-LUMO overlap, resulting in a small ΔE_{ST}. For triazine compound **TM-62** ΔE_{ST} was found to be as small as 0.12 eV. Luminescence lifetime measurements revealed delayed fluorescence component with a lifetime of 80 μs. The PL quantum efficiency of the DPEPO:**TM-62** emission layer was found to be 9% in oxygen-free atmosphere. This should result in a maximal external quantum efficiency (EQE) of 2% in the OLED based on this emitter (Fig. **1**). However, a somewhat lower EQE was obtained. Additionally, the fabricated OLED showed an irregular I-V curve most likely due to the poor charge injection from the electrodes and non-optimal layer thicknesses. The current results prompt for further device optimization.

[1] Ch. Adachi, *Third-generation organic electroluminescence materials*, Japanese Journal of Applied Physics **53**, 060101 (2014)

CONTROL OF OPTICAL PROPERTIES AND SENSING APPLICATION OF PURINE DERIVATIVE

Justina Jovaišaitė[1], Erika Bizdena[2], Maris Turks[2], Saulius Juršėnas[1]

[1] Institute of Applied Research, Vilnius University, Lithuania
2 Institute of Technology of Organic Chemistry, Riga Technical University, Latvia
jovaisaite.justina@gmail.com

Purine materials, being the core of adenine and guanine, have always generated a wide interest among scientists [1]. It is well known and studied that DNA and RNA nucleobases have very low quantum yields [2], thus there are constant attempts to create fluorescent purine and pyrimidine compounds, making them an excellent tool for bio-system research [3]. Besides, due to the possibility to modulate optical properties [4], there has been an increased focus on sensing applications of nucleobase derivatives [5].

In this work we present the photophysical properties of novel 9-(β-D-ribofuranosyl)-2-(4-phenyl-1H-1,2,3-triazol-1-yl)-N,N-bis(pyridin-2-ylmethyl)-9H-purine-6-amine material (Fig. 1) studied in different polarity, proticity and pH solutions together with complexation analysis upon the addition of various metal ions.

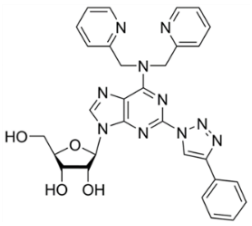

Fig. 1. The molecular structure of 9-(β-D-ribofuranosyl)-2-(4-phenyl-1H-1,2,3-triazol-1-yl)-N,N-bis(pyridin-2-ylmethyl)-9H-purine-6-amine derivative

The initial results have shown that the absorption spectra of purine derivative in dimethylformamide (DMF), dimethyl sulfoxide (DMSO) solutions and DMSO/H_2O mixtures are changing negligible. However, the fluorescence quantum yield increases from 24.5% in DMF to 32.6% in DMSO with fluorescence spectra position (the intensity maximum at 390 nm) and form persistent the same. More surprisingly, the addition of half water to DMSO solution, leads to the red-shift of fluorescence spectrum by 20 nm along with high intensity increase so that the quantum yield reaches 45.5% (Fig. 2 a).

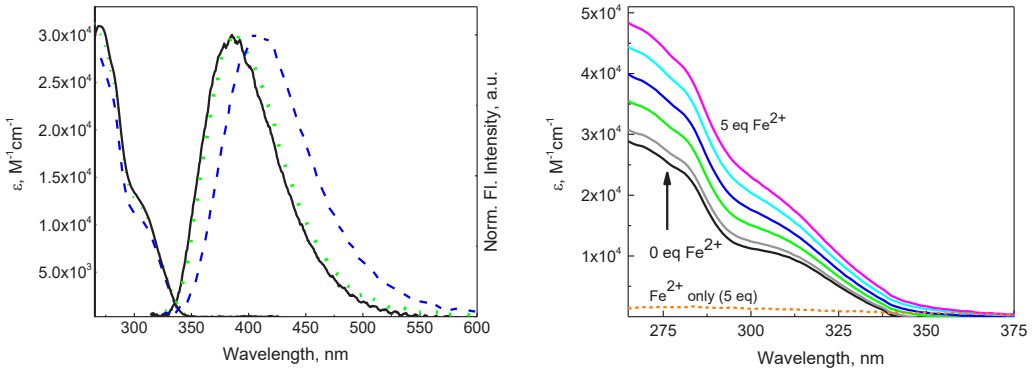

Fig. 2 (a) Absorption and normalized fluorescence spectra of purine derivative (5μM) in different solutions (solid black line – DMF, dotted green line – DMSO and dashed blue line 0.5DMSO/0.5H_2O mixture). (b) Absorption spectra of purine derivative (5μM) in 0.5DMSO/0.5H_2O under the titration of iron ions from 0 to 5 equivalents.

The titration experiments with various metal ions revealed that the absorption spectrum intensity of purine compound is increasing upon the addition of iron (II) ions in DMSO or DMSO/H_2O solutions (Fig. 2 b), allowing further investigation of the compound as a selective sensor.

[1]J. D. WATSON and F. H. C. CRICK, "Molecular Structure of Nucleic Acids," Nature, no. 171, pp. 737–738, 1953.
[2]D. Onidas, D. Markovitsi, S. Marguet, A. Sharonov, and T. Gustavsson, "Fluorescence Properties of DNA Nucleosides and Nucleotides: A Refined Steady-State and Femtosecond Investigation," J. Phys. Chem. B, vol. 106, no. 43, pp. 11367–11374, Oct. 2002.
[3]A. Dierckx et al., "Characterization of photophysical and base-mimicking properties of a novel fluorescent adenine analogue in DNA," Nucleic Acids Res., vol. 39, no. 10, pp. 4513–4524, May 2011.
[4]K. Ozols et al., "Development of N6-methyl-2-(1,2,3-triazol-1-yl)-2′-deoxyadenosine as a novel fluorophore and its application in nucleotide synthesis," 2016.
[5] S. Sahana, S. Bose, S. K. Mukhopadhyay, and P. K. Bharadwaj, "A highly selective and sensitive turn-on fluorescence chemosensor based on a rhodamine–adenine conjugate for Al3+ in aqueous medium: Bioimaging and DFT studies," J. Lumin., vol. 169, pp. 334–341, 2016.

DERIVATIVES OF INDOLE AND BENZO[b]CARBAZOLE AS ELECTROACTIVE MATERIALS

Rasa Keruckiene, Viktorija Mimaite,
Jonas Keruckas, Dmytro Volyniuk, Juozas Vidas Grazulevicius

Department of Polymer Chemistry and Technology, Kaunas University of Technology, Lithuania
rasa.laurinaviciute@ktu.edu

Low-molar-mass and polymer organic light emitting diodes have attracted considerable attention due to their great application potential in large area flat panel displays and solid state lighting [1]. Such devices tend to have multilayer device configuration with a hole transport layer, an electron transport layer and an emissive layer, and some of them also have a hole injection and an electron injection layer [2].

The selection of appropriate materials for each layer is of great importance. Generally, the molecular structures of hole transport materials usually contain electron-donating moieties, such as carbazole, triarylamine, diphenylamine, N-phenyl-1-naphthylamine etc. [3]. However, most of the methods used for the synthesis of electroactive materials suffer from one or several drawbacks such as low yields, prolonged reaction times, use of hazardous, expensive, moisture-sensitive, and large quantity of reagents, involving harsh reaction conditions, tedious workup procedure, and difficulty in recovery, and reusability of the catalysts. Therefore, there is a need to develop efficient and versatile methods for the synthesis of electroactive compounds.

In this work we employed efficient regioselective acid-catalysed reactions of 1*H*, 1-methyl- and 1-naphthylindole with o-phthalbenzaldehyde [4]. New indole and benzo[b]carbazole derivatives (Scheme 1) were synthesized and investigated in order to identify correlations between the molecular structures of the compounds and their optical, electrochemical and photophysical properties. DFT calculations employing the B3LYP functional were performed in vacuum with the Spartan'14 program [5]. Neutral cationic and triplet state geometries of molecules were optimized from conformational analysis data as starting point using 6-31G (d,p) basis set. The newly synthesized derivatives were find to be suitable for the active layers of organic light-emitting layers.

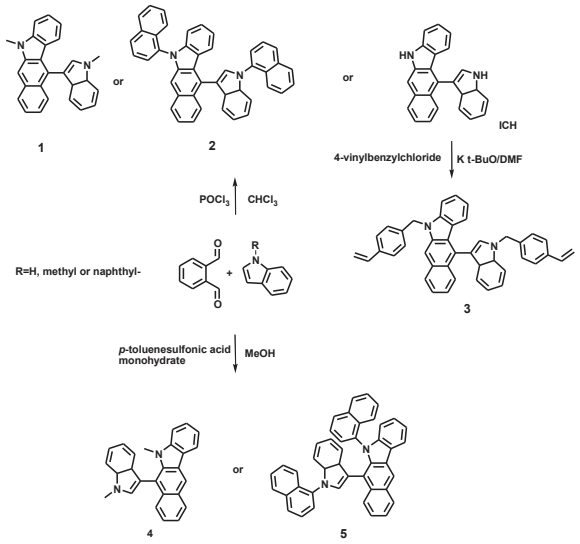

Fig 1. Synthesis of indole and benzo[b]carbazole derivatives **1**–**5**. The reactions were caried out at room temperature for 30 min.

The thermal, optical, photophysical, electrochemical and photoelectrical properties of the materials, as well as photo- and thermally activated polymerization of the monomer containing vinyl group monitored by FTIR will be reported.

Acknowledgment. This work was supported by the research programme of Latvia, Lithuania and Taiwan (project No. TAPLU-2-2016).

[1] A., Holmes, Electronics: Polymers light the way, Nature **421,** 800 –801, 2003.
[2] P., Strohriegl, J.V., Grazulevicius, Charge-Transporting Molecular Glasses, Advanced Materials **14**, 1439–1452, 2002.
[3] Y., Shirota, H., Kageyama, Charge carrier transporting molecular materials and their applications in devices, Chemistry Reviews **107**, 953–1010, 2007.
[4] D. St., Black, D. C., Craig, M., Santoso, Mechanism- controlled Regioselective Synthesis of Indolyl Benzo[b]carbazoles, Tetrahedron Letters **40**, 6653 –6656, 1999.
[5] SPARTAN'14 for Windows Version 1.1.2. 1840 Von Karman Avenue, Suite 370, Irvine, CA 92612: Wavefunction, Inc.; 2013.

STARCH-BASED BIODEGRADABLE FILMS BEHAVIOUR AFFECTED BY COLLAGEN DERIVATIVES INCORPORATION

Olena Ishchenko,Maksym Koliada,Viktoriia Plavan

Department of Applied Ecology, Technology of Polymers and Chemical Fibers,
Kyiv National University of Technologies & Design, Ukraine
maksym.koliada@gmail.com

Recently, environmentally friendly materials from natural and renewable resources have received much attention. Collagen hydrolysates, which can be obtained from tannery waste, has excellent biodegradability and can be used for biodegradable film formation. While performing composites, except collagen, contain hydrophilic polymers, structural reagents (formaldehyde, glyoxal, glutaraldehyde, tanning agents or minerals), organic fillers (starch, cellulose and chitosan) and plasticizers, such as glycerin. As hydrophilic polymers polyvinyl alcohol, polyethylene glycol/polyethylene oxide, polyvinylpyrrolidone, propylene glycol alginate or a combination thereof can be used. Such combination allows adjusting the properties of the composite materials, including moisture content, viscosity, strength, organoleptic properties and biodegradation ability.

Starch, as an abundant raw material with low cost, has been applied in the field of degradable plastics, and blend films containing starch are potential materials in the agriculture, medicine, and packaging industries [1]. To improve the mechanical properties of materials, blending starch with other polymers such as polymethylcellulose and low-density polyethylene is regarded as the simplest way.

Starch blended with synthetic polymer polyvinyl alcohol (PVA) has been studied as a potential biodegradable polymer [2]. The mechanical properties and biodegradability of starch/PVA blended films have been reported by several researchers. However, their wide applicationsare limited by the lack of water resistance and the poor mechanical property of starch/PVA blended films.

Films were obtained by means of the solvent casting procedure after the preparation of film forming dispersions. Starch (10% w/w) was dispersed in an aqueous solution at 95 °C for 30 min to induce starch gelatinization. PVA 10% solution was prepared by stirring for 40 minutes on a water bath. Afterwards, PVA was incorporated into the starch dispersion, the dispersion was maintained at 90 °C for 30 min under stirring until complete dissolution. Finally, glycerol was added as a plasticising agent. We prepared following ratios 3:1, 1:1 and 1:3 of each of the compositions - PVA/starch; starch/gelatine and dialdehyde starch/gelatine.

The film forming dispersions were poured into glass casting plates (15x10 cm) in the right amount to provide stable surface solid density. The films were dried at 50°C and for 1 h and afterwards, peeled off the casting surface.

In order to find the optimal composition of film-forming dispersion we conducted rheological study of the solutions, water absorption, aqueous solubility and release of starch component as well as physical mechanical properties.

Common corn starch is characterized by a high content of hydroxyl groups, which leads to premature decomposition of the polymer composites. Therefore, modification of starch is required to create a water-insoluble film. Therefore we used starch modified by oxidation, using sodium periodate - dialdehyde starch (DS). This modification allows getting a transparent film, which greatly expands its applications. Depending on the expiration period and operational requirements the optimum ratios are 25:75 and 50:50 dialdehyde starch/gelatin/glycerol for the film formation. Films were resistance to water dissolving.

[1] Xiong, H., Tang, S., Tang, H., & Zou, P. (2008). The structure and properties of a starch-based biodegradable film. *Carbohydrate Polymers*, *71*(2), 263-268.
[2] Xiao, C. M., & Yang, M. L. (2006). Controlled preparation of physical cross-linked starch-g-PVA hydrogel. *Carbohydrate Polymers*, 64, 37–40.

SYNTHESIS AND INVESTIGATION OF V-SHAPED HOLE-TRANSPORTING MATERIALS CONTAINING TRÖGER`S BASE CORE AND TPD-TYPE BRANCHES

Regimantas Komskis[1], Titas Braukyla[2], Nobuya Sakai[3], Maryte Daskeviciene[2], Vygintas Jankauskas[4], Egidijus Kamarauskas[4], Tadas Malinauskas[2], Henry J. Snaith[3], Saulius Jursenas[1], Vytautas Getautis[2]

[1] Institute of Applied Research, Vilnius University, Saulėtekio 3, 10257, Vilnius, Lithuania
[2] Department of Organic Chemistry, Kaunas University of Technology, Radvilenu pl. 19, Kaunas, 50254, Lithuania
[3] Department of Physics Clarendon Laboratory, University of Oxford Parks Road, Oxford, OX1 3PU, UK
[4] Department of Solid State Electronics, Vilnius University, Sauletekio 9, Vilnius, 10222, Lithuania
regimantas.komskis@gmail.com

Even though solar cell technology and production from inorganic materials, mainly crystalline silica which currently occupies about 90% of photovoltaic market, is already well developed it also faces problems deriving from their compositional materials themselves – alternatively, organic and hybrid solar cells overcome those drawbacks as these cells are inexpensive, light, flexible, requires less energy to produce and consists of abundant chemical elements. Among these solar cells perovskite layer containing ones seem certainly promising as their relatively new yet constantly evolving technology already allowed to reach power conversion efficiency (PCE) of 22.1% in single-junction perovskite solar cell (PSC).

Efficiency of perovskite solar cell (PSC) highly depends on HTM which is expected to have good hole-drift mobility and high morphological stability as well as to meet certain HOMO and LUMO energy requirements. 2,2′,7,7′-tetrakis(4,4′-dimethoxydiphenylamino)-9,9′-spirobifluorene (spiro-OMeTAD) is the most widely used small-molecule class HTM in both solid-state dye-sensitized solar cells (ssDSSCs) and PSCs. Even though Spiro-MeOTAD is unrivaled efficiency wise by its counterparts in PSC the compound itself also have its flaws. Spiro-OMeTAD is found to exist in semicrystalline state and has a tendency to crystallize in the device, thus impairing cell's performance. Crystallization of the hole conductor layer is undesirable for it would impair the formation of a good contact among the active layer and back contact electrodes. Such findings encourage a search for novel HTM alternatives.

In this paper, we report synthesis and properties of novel V-shaped charge transporting molecules HTM1-HTM3 (Fig. 1) consisting of TPD-type moieties conjoined by Tröger's base core. TB core provides orientation to TPD fragments angle-wise towards each and hampers the crystallization processes making the compound amorphous. Investigated hole transporting materials are promising candidates for application in organic and hybrid optoelectronic devices as they can be handled in air, are amorphous and require no high temperature annealing steps, have high glass transition temperatures, can be solution deposited, and possess comparatively high mobility (up to 0.036 $cm^2 V^{-1} s^{-1}$).

As the most promising property-wise among the synthesized TB derivatives HTM3 have been preliminary tested as hole transporting semiconductor for the perovskite solar cells. The experiments were carried out using perovskite precursor containing a cation and anion mixture in a device stack of fluorine doped tin oxide(FTO)/compact TiO2/ perovskite/HTM/Ag. Respectable maximum power conversion efficiency of 11.27% under AM 1.5 G illumination was recorded in the perovskite device containing HTM3 as hole transporting material. The measured fill factor was 0.61, the current density (Jsc) 20.6 mA cm^{-2}, and the open-circuit voltage (Voc) 983 mV.

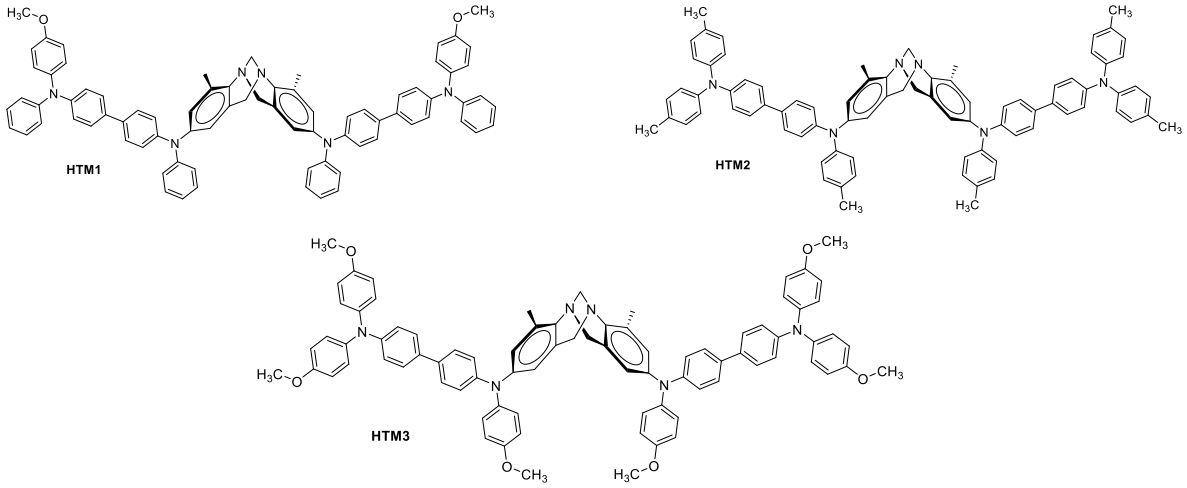

Fig. 1. V-shaped charge transporting molecules HTM1-HTM3 consisting of TPD-type moieties conjoined by Tröger's base core.

DEVELOPMENT OF THE EFFICIENT HOST/GUEST SYSTEMS FOR DEEP-BLUE ORGANIC LIGHT-EMITTING DIODES

Nadzeya A. Kukhta[1*], Dmytro Volyniuk[1], Khrystyna Ivaniuk[2], Juozas Vidas Grazulevicius[1]

[1] Department of Polymer Chemistry and Technology, Kaunas University of Technology, Lithuania
[2] Department of Physics, Lviv Polytechnic National University, Ukraine
*nadzeya.kukhta@gmail.com

Since the discovery of the first organic semiconducting compound, polyaniline, enormous research has been conducted in the field of materials science, resulting in the development of organic electronics and in the industrial production of the first organic diode device several decades ago. Being on par and even outperforming their inorganic analogues, organic semiconductors found wide application in the preparation of such devices as organic field effect transistors (OFETs), organic light-emitting diodes (OLEDs), and organic photovoltaic devices (OPVs) [1]. During the last decades, continuous efforts have been contributed to evolve deep-blue phosphorescent materials with good colour purity [2,3]. Noteworthy, deep-blue emitters can not only be a major constituent in full-colour displays, but also be used as the key element for generating white light in combination with its complementary colour [4]. A suitable blue emitter should comprise such features, as pure colour, high photoluminescence quantum efficiency, long lifetime, remarkable thermal and electrochemical stability, as well as high triplet energy and ambipolar charge transport behaviour, which can make a promising candidate not only for blue OLEDs, but also serve as a desirable host for phosphorescent OLEDs (PhOLEDs). For the achievements of these goals a combination of donating and accepting building blocks can be used.

In current work the design and synthesis of new bipolar derivatives with 1,3,5-triphenylbenzene backbone will be presented. The orientation of the substituents was found to affect greatly the properties of the compounds. Intense deep blue emission with high photoluminescence quantum yields (97% in solution and 30% in solid state) and efficient up-conversion of triplet excitons, on the one hand, and high triplet energy (2.82 eV) and ambipolar charge transport, on the other hand, suggest the application of the new materials as emitters and hosts for OLEDs and PhOLEDs, respectively. By utilization of the derivatives with different substitution pattern as host and guest in the emissive layer, the deep-blue OLED with the external quantum efficiency of 14.1% was fabricated. Theoretical approach (DFT) was employed for the clarification of the characteristics of the bipolar derivatives.

[1] K. Takimiya, K., I. Osaka, Nakano, M.., π-Building Blocks for Organic Electronics: Revaluation of "Inductive" and "Resonance" Effects of π-Electron Deficient Units, Chem. Mater. **26**, 587-593 (2014).
[2] S. H. Kim, I. Cho, M. K. Sim et al., Highly Efficient Deep-Blue Emitting Organic Light Emitting Diode Based on the Multifunctional Fluorescent Molecule Comprising Covalently Bonded Carbazole and Anthracene Moieties, J. Mater. Chem. **21**, 9139 (2011).
[3] R. J. Holmes, S. R. Forrest, Y.-J. Tung et al., Blue Organic Electrophosphorescence Using Exothermic Host–guest Energy Transfer, Appl. Phys. Lett. **82**, 2422 (2003).
[4] W.-Y. Hung, L.-C. Chi, W.-J. Chen et al., A New Benzimidazole/carbazole Hybrid Bipolar Material for Highly Efficient Deep-Blue Electrofluorescence, Yellow–green Electrophosphorescence, and Two-Color-Based White OLEDs, J. Mater. Chem. **20**, 10113 (2010).

LUMINESCENCE AND STRUCTURE OF EUROPIUM(III) *TETRAKIS*-COMPLEXES WITH SULFONYLAMIDOPHOSPHATE (SAPh) LIGANDS

Iryna Olyshevets[1], Sergii Smola[2], Nataliia Kariaka[1], Olena Litsis[1], Vladimir M. Amirkhanov[1]

[1] Taras Shevchenko National University of Kyiv, 12, LvaTolstogo Str., Kyiv, 01033, Ukraine
[2] A.V. Bogatsky Physicochemical Institute, National Academy of Sciences of Ukraine, 65080 Odesa, 86 Lustdorfskaya doroga, Ukraine
olish_i@ukr.net

During last decades the luminescence of lanthanide complexes has attracted increasing interest due to its sharp line and long living emission. The Eu(III) coordination compounds are one of the best luminescent materials, that are widely used in different branches of the science and technology.

Sulfonylamidophosphates(SAPh) are structural analogues of β-diketone ligands, which can serve as an antenna providing efficient energy absorption and its transfer to the lanthanide ion followed by Ln(III) luminescence. In the case of *tetrakis* $[Ln(SAPh)_4]^-$ complexes, additional tuning of the luminescence properties is possible by changing the cation, which can change the structure of the complex and the local coordination geometry of the metal ion. Lanthanide anionic complexes can be used as starting materials for heterometalic compounds and, depending on the nature of the cation, to create conductive solutions or ionic liquids containing luminescent centers.

Europium(III) complexeswithgeneralformula $Kat[Eu(SAPh)_4]$, (where $SAPh^- = (SAPh^1)^-$, $(SAPh^2)^-$ (Fig. 1); $Kat^+ = Li^+$, Na^+, Cs^+, $[N(Et)_4]^+$), were synthesized and characterized by means of elemental, X-ray diffraction, TG analysis, IR, ^1H NMR and UV-Vis spectroscopy.

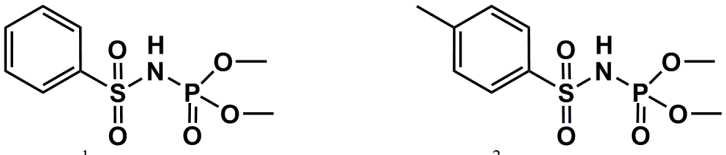

$HSAPh^1$ $HSAPh^2$

Fig. 1.Structural formulas of synthesized ligands

By means of X-ray diffraction method it was found, that each Europium(III) ion of the $[Eu(SAPh)_4]^-$ complex anion is chelated by= oxygen atoms belonging to the phosphoryl and sulphonyl groups of four bidentate chelate ligands, completing coordination number of lanthanide ion to eight (Fig.2). It was also found, that $Na[Eu(SAPh)_4]$ and $Cs[Eu(SAPh)_4]$ has polymeric structures, while $[N(Et)_4][Eu(SAPh)_4]$ has an ionic one.

The emission spectra and emission decay times (τ_{obs}) of the $^5D_0$ state of the both types of europium complexes were measured using excitation into the SAPh ligand singlet state at 298 and 77 K (λ_{exc} = 267 nm). It was found, that in comparison with the earlier known europium *tetrakis*-sulphonylamidophosphates the τ_{obs} for $[N(Et)_4][Eu(SAPh^2)_4]$ is notably higher (3,5 ms), that can be explained by the higher symmetry of europium environment polyhedron in $[N(Et)_4][Eu(SAPh^2)_4]$. For $Cs[Eu(SAPh^2)_4]$ τ_{obs} is equal to 2,28 ms that is in agreement with relatively lower Eu(III) polyhedron symmetry and is comparable with other known SAPhs based Eu(III) *tetrakis*-complexes.

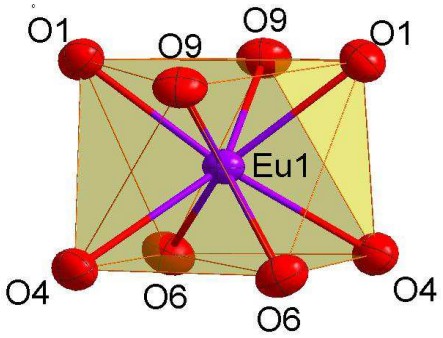

Fig. 2. The structure of coordination polyhedra of Eu^{3+} in $[N(Et)_4][Eu(SAPh^2)_4]$

EUROPIUM COORDINATION COMPOUNDS BASED NANODIMENSION THIN FILMS FOR LIGHT-EMITTING DEVICES

Olena Litsis[1], Tatiana Yu. Sliva[1], Yu.V. Kolomzarov[2], I.E. Minakova[2], Vladimir M. Amirkhanov[1]

[1] Taras Shevchenko National University of Kyiv, 12, Lva Tolstogo Str., Kyiv, 01033, Ukraine
[2] V.E. Lashkaryov Institute of Semiconductor Physics, National Academy of Sciences of Ukraine, Kyiv, Ukraine
olitsis@ukr.net

Light emitting diodes employing heavy-metal complexes are very attractive since the electroluminescence (EL) efficiency, which is limited by the radiative recombination of singlet excitons and can be increased by the addition of the phosphorescent emission from the triplet excitons of the complexes. In order to obtain efficient emission from the complexes, they are usually dispersed in a suitable host displaying the two main properties of: 1) providing efficient energy/charge transfer to the phosphorescent dopants and 2) avoiding concentration quenching effects of the complexes. The use of an electroluminescent polymer as host for the phosphorescent complexes has the further advantage that its own fluorescent component can be exploited for multicolor emission, provided that the energy transfer (ET) from polymer to phosphorescent guest is incomplete and that no direct charge trapping at the dopant site occurs. Thanks to their narrow red emission, Eu^{3+}-complexes have attracted considerable interest in designing organic light emitting diodes (OLEDs) for full color displays. In the last few years, many reports appeared where blends of Eu^{3+}-diketonates in fluorescent π-conjugated polymers polyfluorenes type have been used. Förster resonant energy transfer (FRET) takes place in such blends because of overlap between the polymer emission and complex absorption.

In this paper, we report on a simple and promising approach to realize EL heterostructures using a blend film of blue and red-orange Eu^{3+} complex. Bright blue emission in the 410-450 nm range is characteristic of the **PFD** (poly(9,9-di-*n*-dodecylfluorenyl-2,7-diyl). The overlapping absorption was shown for $EuWi_3 \cdot 2KM$ complex (where Wi^- – carbacylamidophosphate ligand $PhC(O)N^-P(O)(OCH_3)_2$; KM - Michler's ketone $[(CH_3)_2NC_6H_4]_2CO$) in the range 390-440 nm. Also $EuWi_3Phen$ (Phen = 1,10 – phenantroline) complex with absorption in the range 275-350 nm was used. Both complexes under investigation, being excited by UV light, show intensive photoluminescence with maxima at 612.5 nm, observed for $^5D_0 - {}^7F_2$ transition.

The strong correlation between frequency of the spin coating process and film thickness is confirmed by AFM images of $EuWi_3Phen$ films deposited at different resolutions (frequencies of rotation) and concentrations, as shown in Fig. 1. Absolute measurement of the film thickness was made. It can be easily observed that the homogeneity of the film is enhanced when the frequency of the spin coating process rises (Table 1).

Table 1. Thickness of $EuWi_3Phen$ thin films, deposited on the glass substrate (volume of solution 250 µl, time of rotation 15 min)

Deposition parameters		**Thickness, nm**
C, mol/l	*Freqquency of rotation, rpm*	
0,01	500	47
0,001	1000	10
0,01	500	4,5
0,001	1000	10

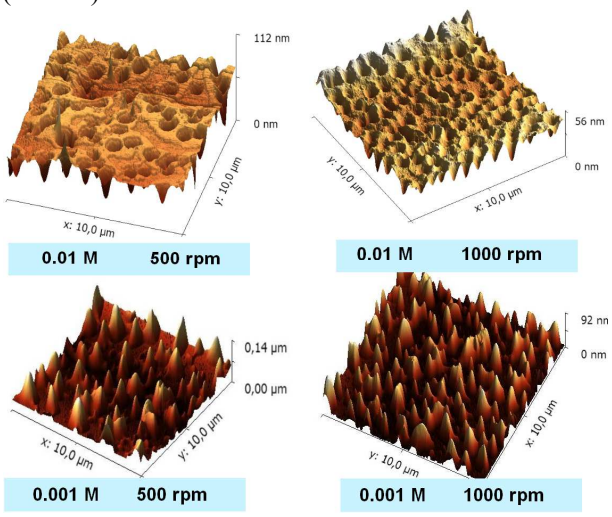

Fig.1. AFM images of $EuWi_3Phen$ thin films deposited at several frequencies of rotation by spin coating of toluene solutions

The polymer-based planar light-emitting heterostructures fabricated in this work have the ITO/PEDOT:PSS/**PFD**/Ca+Al (**1**) structure. Samples of different solution concentration have been created by spin coating and their current-voltage (A-V) characteristics have been investigated. The best A-V values of EL starting and puncture voltage were demonstrated for 5 mg/ml PFD solution. Wherefore this concentration was used for fabrication of polymer-blend-based EL devices. They have the structures ITO/PEDOT:PSS/PFD+$EuWi_3 \cdot 2KM$/Al+Ca (**2**) and ITO/PEDOT:PSS/PFD+$EuWi_3Phen$/Al+Ca (**3**). Diodes prepared with thinner organic films allow higher currents at lower voltages; this can be achieved either by increasing the frequency of the spin coater rotation or by using concentrations of Complex:Toluene lower than 10% weight (the best values was demonstrated for 5%). Fig. 2 shows the I-V characteristics of **1**-**3** heterostructures. The PFD and PFD-Complex layers were deposited at the same spin coater frequencies of rotation (2500 rpm). Bright electroluminescence in all heterostructures was observed. In general, the best performance of the devices made with europium complexes was observed.

CHARACTERIZATION AND OPTIMIZATION OF FUNCTIONAL ORGANIC FILMS PREPARED BY BLADE-COATING

Justina Malakauskaitė, Gediminas Kreiza, Karolis Kazlauskas, Saulius Juršėnas

Institute of Applied research, Vilnius University, Lithuania
Justina@fidi.lt

Organic optoelectronics is one of the most rapidly growing fields of research due to its potential applications in organic light emitting diodes (OLED), organic solar cells, sensors etc. Majority of OLED devices are based on thin organic films fabricated by thermal evaporation in high vacuum. Thermal evaporation enables formation of multi-layered structures composed of charge transport or carrier blocking films and generally ensures high performance of the devices. However, this technology is only suitable for mass production of small- and middle-sized OLED displays. In this case solution processing of multi-layered organic films could benefit in low-cost and large-area devices.

The main goal of the present work was to get acquainted with blade-coating technique used for solution processing of organic films. The technique is advantageous since it can be employed for fabrication of OLEDs on an industrial scale [1]. During this research, functional organic films were processed from two organic polymers: poly(3,4-ethylenedioxythiophene)-poly(styrenesulfonate) (PEDOT:PSS) and poly(9-vinylcarbazole) (PVK), which are typically used for hole injection and transport, respectively. Blade–coating parameters such as the coating speed, the concentration of solution, the space between blade and substrate as well as other external factors (e.g. hot air flow) have been varied to investigate their influence on layer thickness (h) and surface roughness (Rq). Atomic force microscopy (AFM) was employed to estimate these films properties.

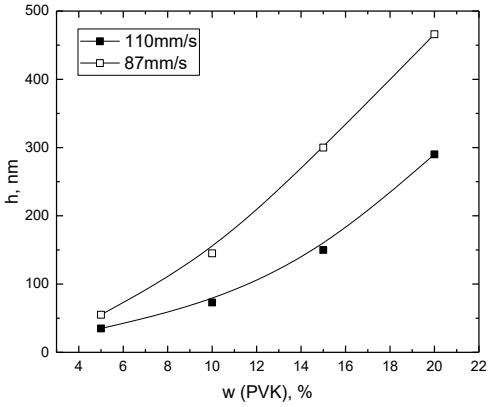

Fig. 1. Film thickness as a function of blade-coating speed and concentration of PVK.

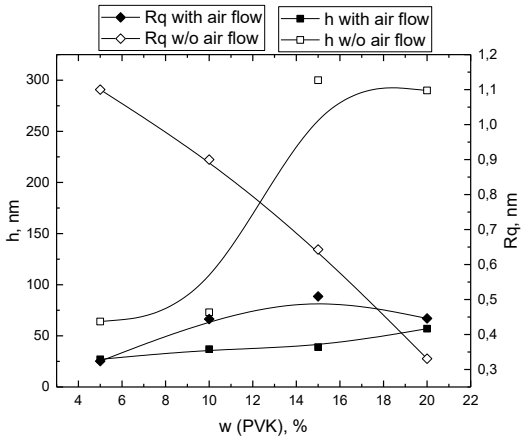

Fig. 2. Film thickness and roughness as a function of concentration of PVK with and without hot air flow.

The preliminary results indicated that the quality (smoothness) of blade-coated films can be improved by utilizing faster coating speeds and by applying hot air flow.

[1] Chen C Y, Chang H W, Chang Y F, Chang B J, Lin Y S, Jian P S, Yeh H C, Chien H T, Chen E C, Chao Y C, Meng H F, Zan H W, Lin H W, Horng S F, Cheng Y J, Yen F W, Lin I F, Yang H Y, Huang K J and Tseng M R 2011 Continuous blade coating for multi-layer large-area organic light-emitting diode and solar cell *J. Appl. Phys.* **110** 1–18

THE INVESTIGATION OF PHOTOPHYSICAL PROPERTIES OF NEW NAPHTALIMIDE CORE DERIVATIVES

Karolina Maleckaitė[1], Dalius Gudeika[2], Juozas V. Gražulevičius[2], Arūnas Miasojedovas[1]

[1]Institute of Applied Research, Vilnius University, Sauletekio ave 3, LT-10257 Vilnius, Lithuania
[2]Department of Organic Technology, Kaunas University of Technology, Radvilenu pl. 19, LT- 50254, Kaunas, Lithuania
karolina.maleckaite@ff.stud.vu.lt

Organic semiconductors let us build high-tech gadgets, which would be impossible with the ordinary, inorganic materials. The new era of the flexible, transparent, and even more biological environment friendly devices has arrived. The hardest task for the physicists and chemists is to make organic semiconductors reach the characteristics of the inorganic ones. Scientists are not giving up not only because organic materials let us have the amazing gadgets in our everyday life, but they also are seeking for a simpler and cheaper production. [1]

One of the conjugated derivatives - 1,8-naphthalimide - is a widely used molecule, which emission colour can be changed by adding different moieties at C-4 position. 1,8-naphthalimide compounds generally have high electron affinity and are very sensitive to the medium polarity. These molecules with the good electron-transporting moieties can be used in fields such as medicine, biology, dyes, organic optoelectronics, sensors, etc. [2]

In this work we investigate photophysical properties of donor-acceptor systems composed of 1,8-naphthalimide with six different moieties linked through acetylene bond at the 4th position. This study includes analyzing of the absorption and photoluminescence (PL) spectra, PL quantum yield and PL decay. The absorption and fluorescence spectra of studied compounds in the different polarity (0 – 3.96 D) solvents revealed intramolecular charge transfer states [3]. The results showed a wide range of Stokes shift (16 – 203 nm), which confirms a strong solvation of the derivatives. Moreover, the PL quantum yields seem to be independent of medium's polarity for molecules with biphenyl [DG-3] and naphthalene [DG-4] moieties (Fig. 1.). The highest PL quantum yields were estimated for the derivatives with electron donating methoxy group [DG-5, DG-6] in the tetrahydrofuran solvent.

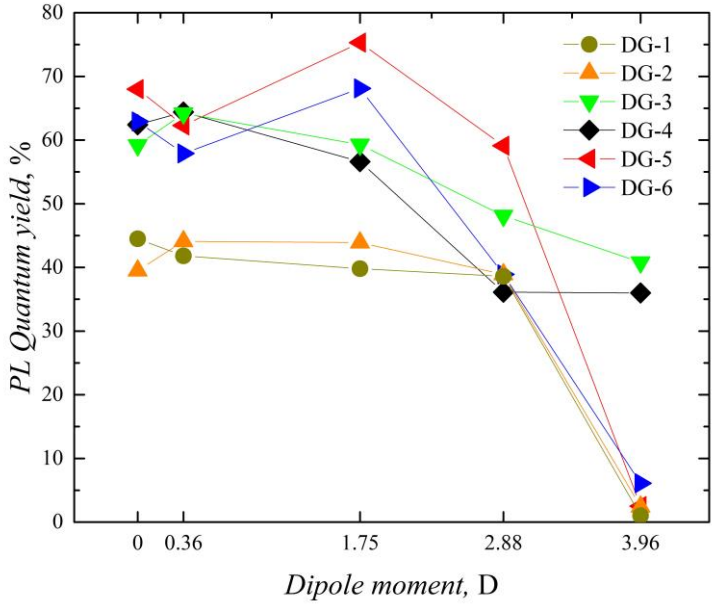

Fig. 1. Evolution of the fluorescence quantum yield of 1,8-naphthalimide compounds in different polarity solvents.

[1] I. Grabchev, I. Moneva, V. Bojinovb, S. Guittonneauc, *Synthesis and properties of fluorescent 1,8-naphthalimide dyes for application in liquid crystal displays*, J. Mater. Chem., 10, 1291-1296 (2000).
[2] D. Gudeika, J. V. Grazulevicius, D. Volyniuk, R. Butkute, G. Juska, A. Miasojedovas, A. Gruodis, S. Jursenas, *Structure-properties relationship of the derivatives of carbazole and 1,8-naphthalimide: Effects of the substitution and the linking topology*, Dyes and Pigments 114, 239-252 (2015).
[3] Z. Tian, Y. Liu, B. Tian, J. Zhang, *The synthesis and fluorescence properties of novel 1,8-naphthalimide derivatives*, Research on Chemical Intermediates (2013)

STRUCTURE-PROPERTY RELATIONSHIP OF BIPOLAR ORGANIC SEMICONDUCTORS

Tomas Matulaitis*, Juozas Vidas Gražulevičius, Dmytro Volyniuk

Department of Polymer Chemistry and Technology, Kaunas University of Technology, Lithuania
*tomas.matulaitis@ktu.lt

In recent years technologies have advanced enormously. This has enabled chemists to perform various types of chemical reactions that were not possible before. The remaining challenge for the material scientists is not only the synthesis and investigation of new compounds, but also a comparison of different molecular systems and establishment of the general trends, relation of the structural modifications of chemical compounds to the different properties. For example, connecting electron donor (D) with acceptor (A) via *para* linkage leads to direct conjugation, the highest oscillator strength, delocalization of frontier orbitals through the molecule, etc. While it is known that *meta*- linkage is responsible for the decreased conjugation strength, as well as reduced photoluminescence quantum yield (PL QY), it localizes the frontier orbitals more on donor and acceptor. Moreover, usage of *meta* linking can lead to more rigid structure. Other important structural modification is the introduction of π-spacer within the D-A system. By physically prolonging the distance between D and A it is possible to achieve higher localization of frontier orbitals on D and A and still to maintain high oscillator strength. Thus, by varying the linkage between the donor, spacer and acceptor it is possible to tune the most of desired properties in the resulting compound.

In our work we mainly focus on the organic semiconductors, dedicated to the field of organic light emitting diodes (OLEDs). More precisely, bipolar donor-acceptor type compounds meant to be used in the emissive layers (EML) in OLEDs. Usage of bipolar molecular architecture is one of the leading approaches to design multifunctional compounds with large variety of desired properties: appropriate singlet and triplet energy levels, high PL QY in solid state, appropriate ionization potential and electron affinity energy levels (depending whether we design emitter/host or exciplex-forming compound), thermal, electrochemical stability, etc.

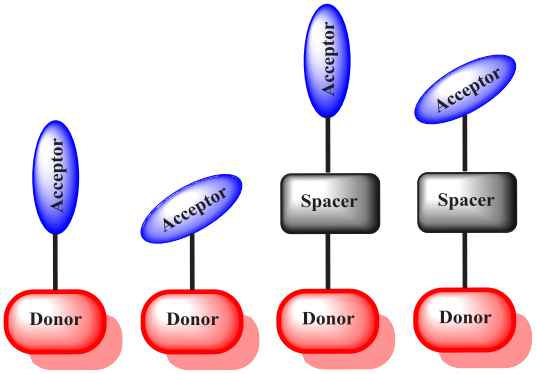

Fig. 1. Schematic representation of design strategy used in the work.

Our aim of this work was to design, synthesize and characterize new bipolar organic semiconductors, based on carbazole (D) and benzonitrile (A). In this presentation we will show how the introduction of spacer, change of linkage between D and A moieties (Fig. 1.) influence the thermal, electrochemical, optical and photophysical properties of these bipolar compounds. In addition, the results of quantum chemistry calculations will be discussed for the better insight on the structure-property relationship.

$LiFeBO_3$ PREPARED VIA THERMAL NANOCRYSTALLIZATION OF AMORPHOUS PRECURSOR

Przemysław Piotr Michalski, Tomasz Karol Pietrzak, Jerzy Edward Garbarczyk

Faculty of Physics, Warsaw University of Technology, Poland
michalski@if.pw.edu.pl

In the previous decade, interesting compound of composition $LiFeBO_3$ emerged as potential cathode material for lithium ion (Li-ion) batteries [1]. Its advantages are: low cost of raw materials and high (220 mAh/g) gravimetric capacity. Unfortunately, the materials in polycrystalline form, prepared by solid state reaction, exhibited low electric conductivity and insufficient gravimetric capacity. The capacity improved, when the material was obtained in nanocrystalline form. Other problems concerned high susceptibility of iron ions to oxidation, when material was kept in air atmosphere [2].

Here, we would like to present an alternative approach to synthesis of $LiFeBO_3$, which allow to preserve its advantages while improving the disadvantages – a thermal nanocrystallization of amorphous precursors. We have successfully applied this method in case of Li_2O–FeO–V_2O_5–P_2O_5 system – the heat-treated materials exhibited structure consisting of nanometer grains, presenting enhanced conductivity by a factor even of 10^8 [3]. This work presents the results of recent studies on $LiFeBO_3$ glass and nanomaterial.

Pre-dried chemicals: Li_2CO_3, H_3BO_3 and $FeC_2O_4{\cdot}2H_2O$ were homogenized and melted in alumina crucibles at 1200 °C for 25 minutes. Glass of nominal composition $LiFeBO_3$ ($25Li_2O{\cdot}50FeO{\cdot}25B_2O_3$) was obtained using melt-quenching method – the molten batch was poured onto metal plate and quickly pressed with another metal plate to guarantee fast cooling of the sample.

Thermal events were investigated using DTA Q600 calorimeter in 30–700 °C range in the argon flow. X-ray diffractometry (Phillips X'Pert Pro) was used to verify the amorphousness of as-received glasses and to examine crystal phases grown after thermal treatment. Temperature XRD measurements were performed in 30–650 °C range in nitrogen flow. Impedance spectroscopy measurements were performed using Solartron 1260 analyser in 10^{-2}–10^7 Hz frequency range and 25–550 °C temperature range. The amplitude of voltage was equal to 0.1 V.

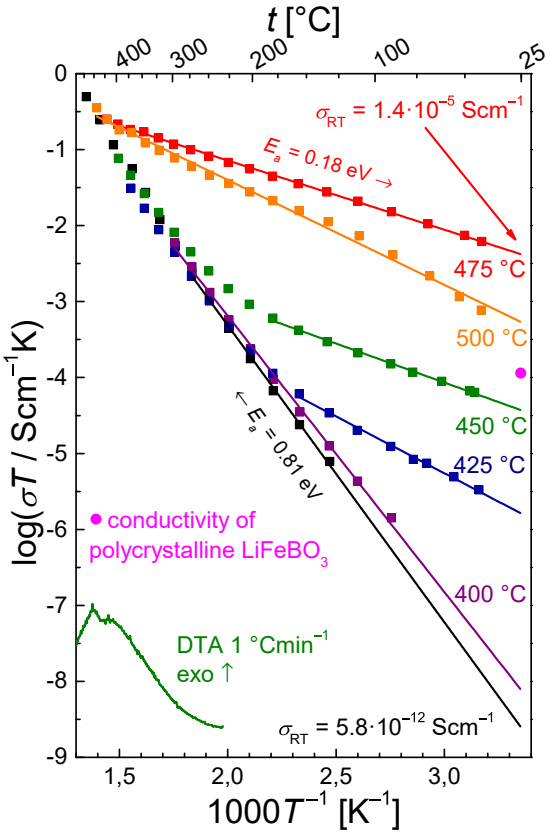

Fig. 1. Temperature dependence of conductivity of $LiFeBO_3$ glass-ceramics.

[1] V. Legagneur, Y. An, A. Mosbah et al., $LiMBO_3$ (M = Mn, Fe, Co): synthesis, crystal structure and lithium deinsertion/insertion properties, Solid State Ionics **139**, 37–46 (2001).
[2] A. Yamada, N. Iwane, Y. Harada et al., Lithium Iron Borates as High-Capacity Battery Electrodes, Advanced Materials **22**, 3583–3587 (2010).
[3] T.K. Pietrzak, M. Wasiucionek, I. Gorzkowska, et al., Novel vanadium-doped olivine-like nanomaterials with high electronic conductivity, Solid State Ionics **251**, 40–46 (2013)

REGULATING THE OPTICAL, ELECTROCHEMICAL AND MORPHOLOGICAL PARAMETERS OF FLUORANTHENE AND P3HT BLEND BY N,N-DIMETHYLACETAMIDE

Jessica Patel[1], Mihirsinh Chauhan[2], Chandrakanth P[1], Maitrayee Trivedi[1], Vaibhav Rao[3], Brijesh Tripathi[1], Manoj Kumar[1], Manoj Kumar Pandey[1*]

[1] Department of Science, School of Technology, Pandit Deendayal Petroleum University, Gandhinagar, Gujarat, India
[2] School of Solar energy, School of Technology, Pandit Deendayal Petroleum University, Gandhinagar, Gujarat, India
[3]Ultrasound Research Institute (Electrical and electronic Engineering),Kaunas University of Technology, Kaunas, Lithuania
pateljessica92@gmail.com

In the present article, the optical, electrochemical and morphological characteristics of the P3HT: Fluoranthene (F5) blend have been studied by using N,N-dimethylacetamide (DMA) as additive. The fluoranthene derivatives are reported as acceptors in organic solar cell (OSC) [1].The focus of this article is to optimize the blend morphology by different parameters such as optical, electrochemical and morphology for the better performance of OSC. 1,6,7,10-tetramethyl fluoranthene (F5) has been synthesized as per the reported procedure [2]. The UV-Visible spectrum of the solution with the addition of solvent additives reveals red shifts in the wavelength which shows a better absorption in the blend and improved local structural order of P3HT [3]. In comparison to pristine solution, the addition of additives causes shift of redox peaks in more positive or negative positions. The curves shows similar redox behavior that indicates additive did not affect the redox reactions and the pairs of redox peaks are consistent. With addition of additive, the cycling performance is significantly improved [4]. The TEM images shows the change in the morphology of the blend with the additive. In the TEM image the brighter phase represents P3HT and darker phase represents F5 moiety. The additive has promoted formation of fibrillar structure in the blend and better phase separation and interpenetrating network. The pristine blend shows large domains, whereas the additive has promoted decrease in the domain size of F5 and forms an interpenetrated network in the P3HT matrix. There is more uniformity and aggregation of F5 which leads to better charge separation and efficient transport of electrons and holes [5].

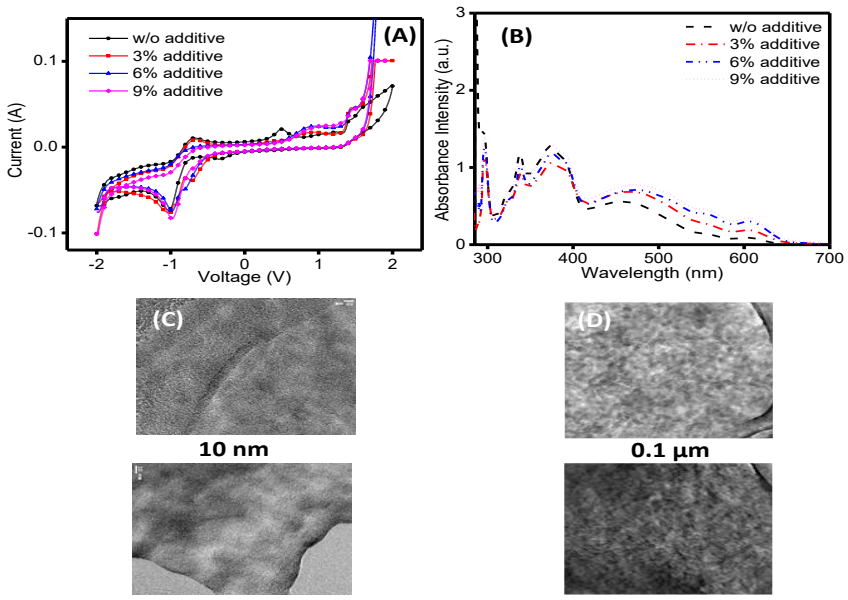

Fig. 1. (A) CV of pristine with different concentration of additive, (B) UV-Visible spectra of pristine with different concentration of additive, (C) TEM images of blend without additive and with additive at 10nm scale, (D) TEM images of blend without additive and with additive 0.1µm scale

[1]Zhou Y, Ding L, Shi K, Dai YZ, Ai N, Wang J, et al. A Non-Fullerene Small Molecule as Efficient Electron Acceptor in Organic Bulk Heterojunction Solar Cells. Advanced Materials. 2012;24(7):957-61.
[2]Butterfield AM, Gilomen B, Siegel JS. Kilogram-scale production of corannulene. Organic Process Research & Development. 2012;16(4):664-76.
[3]P. J. Brown, D. S. Thomas, A. Köhler, J. S. Wilson, J.-S. Kim, C. M. Ramsdale, H. Sirringhaus, R. H. Friend, *Phys. Rev. B: Condens. Matter Mater. Phys.* **2003**, *67*, 642 031.
[4]Bagheri O, Dehghani H, Afrooz M. Pyridine derivatives; new efficient additives in bromide/tribromide electrolyte for dye sensitized solar cells. RSC Adv. 2015;5(105):86191-86198.
[5]Lee J, Jung J, Emrick T, Russell T, Jo W. Synthesis of C60-end capped P3HT and its application for high performance of P3HT/PCBM bulk heterojunction solar cells. Journal of Materials Chemistry. 2010;20(16):3287.

THE EFFECT OF THERMOMECHANICAL TREATMENT ON STRUCTURE AND MECHANICAL PROPERTIES OF FERROMAGNETIC Fe-Ni-Co-Ti ALLOYS

Yaroslav Titenko[1], Andriy Olefir[1], Anatoliy Titenko[2], Lesya Demchenko[1]

[1] Department of Physics of Metals, National Technical University of Ukraine "Kyiv Polytechnic Institute", Ukraine
[2] Department of Physics of Magnetic Materials and Nanocrystalline Structures, Institute of Magnetism, Institute of Magnetism, Ukraine
titenko@imag.kiev.ua

The functional ferromagnetic shape memory materials attract an increasing attention of researchers due to their unusual deformation behavior resulting in a reversible size change under the influence of temperature, applied external stresses, magnetic fields, and their combination, demonstrating the shape memory effect (SME), pseudoelasticity or superelasticity (SE), plasticity of transformation, magnetoelastic deformation, etc. The above mentioned properties have found various practical applications as actuators in robotics, automotive, aerospace and biomedical industries.

The phenomenon of pseudoelasticity consists in an ability of the material to restore its original shape after a plastic deformation that significantly exceeds elastic one. Mainly, copper (Cu-Al-Ni, Cu-Zn-Al, etc.) and nickel based (NiTi) pseudoelastic functional materials were studied and found practical applications. The investigation of deformations induced by external stresses was also carried out for ferromagnetic iron-based alloys, among which Fe-Pd, Fe-Pt and Fe-Ni-Co-Ti are of the greatest interest.

This research is devoted to the study of mechanical behavior of ferromagnetic Fe-Ni-Co-Ti alloy, previously subjected to different regimes of thermomechanical treatment consisting of: quenching in water followed by multiple rolling with different compression degrees and aging. The search for optimal regimes of cold deformation and subsequent aging to obtain a maximum level of pseudoelasticity in polycrystalline ferromagnetic Fe-Ni-Co-Ti alloy was carried out in this work. The measurement of microhardness, low-field magnetic susceptibility, resistivity, mechanical characteristics of alloy in austenitic and martensitic phases was carried out in the work.

The conditions which change the kinetics of martensitic transformation (MT) from nonthermoelastic to thermoelastic and lead to a significant strengthening of austenite at aging when nanoparticles of γ'-phase $(CoNi)_3Ti$ precipitate arise. It was established experimentally that introduction of a new operation, namely, the cold deformation before the aging of quenched austenite, substantially affects the mechanical properties of Fe-Ni-Co-Ti alloy austenite and martensite, as well as characteristics of the magnetic and martensite transformations. With increase of plastic deformation degree, all of the mentioned parameters vary nonmonotonically.

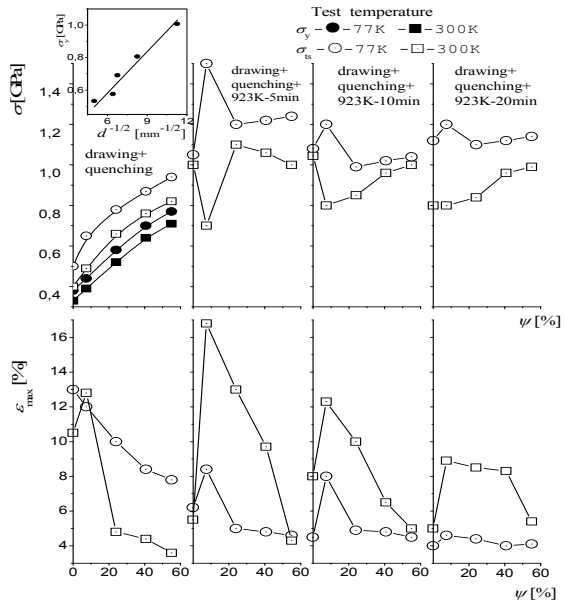

Fig. 1. The dependences of σ_y, σ_{ts} (a) and ε_{max} (b) on preliminary plastic deformation degree (ψ) at different aging time of quenched austenite.

The experimentally determined dependences (fig. 1) of ultimate tensile strength $\sigma_{ts}(\psi)$ show that with the increase of ψ, the strong strain hardening of austenite occurs while the strain before break (ε_{ts}) decreases in 1.5÷2 times. At the same time for the martensite phase, the decrease of strain hardening is observed while ε_{ts} decreases in 2÷4 times. It is found that preliminary plastic deformation of quenched austenite of the ferromagnetic Fe-Ni-Co-Ti shape memory alloy and subsequent aging favours the increase of reversible pseudoelastic deformation.

METAL-TO-INSULATOR TRANSITION IN NANOCRYSTALLIZED $90MgV_2O_5 \cdot 10P_2O_5$ GLASS

Wiktoria K. Zajkowska, Tomasz K. Pietrzak, Jerzy E. Garbarczyk

Faculty of Physics, Warsaw University of Technology, Poland
wiktorex.amorex@gmail.com

Crystalline vanadium oxide (V) has layered structure, so it has the ability of reversible intercalation and deintercalation of many cations, such as e.g. lithium, sodium, magnesium. Its been examined long time ago, that it has features/capability to be used as material for cathodes in lithium batteries. Recently, interest in V_2O_5 increased again, because of possible applications in magnesium [1] and sodium batteries.

Vitreous magnesium-vanadate-phosphate ($90MgV_2O_5 \cdot 10P_2O_5$) samples prepared by melt quenching technique. Weighted chemicals ($NH_4H_2PO_4$ (POCh – Polish Chemicals, 99.5%) and V_2O_5 (Aldrich, 99.6%)), MgO (Aldrich, 99.5%)) were mixed in a mortar and as powder, put into alumina crucibles. The compound was heated to 1300°C in air, and held at this temperature for 15 minutes. The molten batch was rapidly poured onto a stainless-steel plate and pressed with another plate. XRD (X-ray diffractometry) measurements were carried out to check amorphousness of the as-received sample. This research was carried out using Philips XPert aparatus. Glass transition and crystallization temperatures were determined from DSC measurements using a SDT Q200 setup (TA Instruments). Electrical conductivity was meausred with DC method as a function of temperature. The sample was kept in a tube furnace (Czylok) and its temperature was stabilized with Eurotherm 2404 temperature controller. The temperature of the sample was measured with a separate termocouple and Adam 4011.

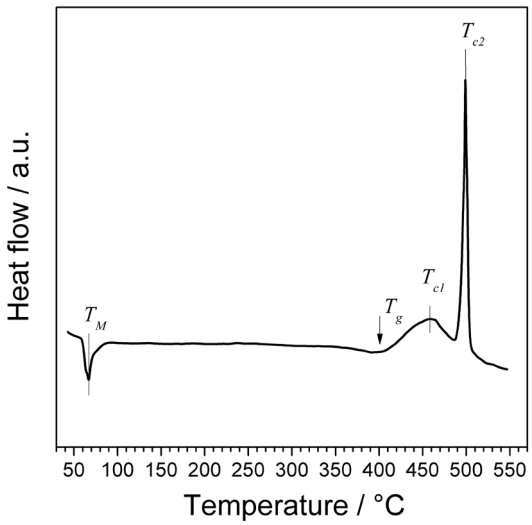

Fig. 1. DSC curve measured at heating rate 10°C/min.

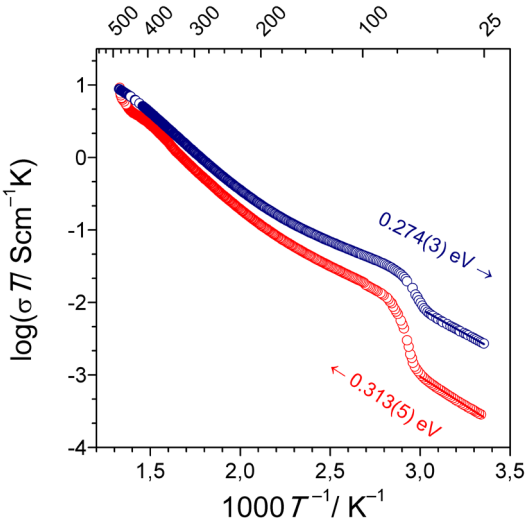

Fig. 2. Electrical conductivity upon heating to 480°*C* and cooling down to room temperature.

DSC trace of as-received sample was typical for glassy material. In Fig. 1 one can see a glass transition followed by two crystallization peaks: a broad one and a narrow one. The characteristic temperatures are as follow: $T_g = 396$°C, $T_{c1} = 455$°C and $T_{c2} = 499$°C. In addition to this, an endotermic peak is observed at low temperatures. The onset is at 60°C and the minimum of the peak at $T_m = 67$°C.

An example of electrical conductivity heated up to 480°C and cooled down to room temperature is presented in the Arrhenius plot (Fig. 2). As expected, graph is typical for vanadate glasses that undergo nanocrystallization. The activation energy of sample was 0.313 eV. The conductivity of glass was equal to $8 \cdot 10^{-7}$ S/cm. Furthermore, one can see a conductivity drop at 60°C. Such transition, which is observable also in DSC trace of the sample, can be ascribed to metal-to-insulator transition in VO_2 [4].

[1] G.S. Gautam, P. Canepa, A. Abdellahi, A. Urban, R. Malik, G. Ceder, The Intercalation Phase Diagram of Mg in V_2O_5 from First-Principles, Chemistry of Materials **27** (2015) 3733–3742.

[2] T.K. Pietrzak, M. Wasiucionek, P.P. Michalski, A. Kaleta, J.E. Garbarczyk, Highly conductive cathode materials for Li-ion batteries prepared by thermal nanocrystallization of selected oxide glasses. Materials Science and Engineering B **213** (2016) 140–147.

[3] T.K. Pietrzak, J.E. Garbarczyk, I. Gorzkowska, M. Wasiucionek, J.L. Nowiski, S. Gierlotka, P. Jowiak, Electrical properties vs. microstructure of nanocrystallized V_2O_5-P_2O_5 glasses, Journal of Power Sources **194** (2009) 73–80.

[4] M.M. Qazilbash A.A. Schafgans, K.S. Burch, S.J. Yun, B.G. Chae, B.J. Kim, H.T. Kim, D.N. Basov, Electrodynamics of the vanadium oxides VO_2 and V_2O_3, Physical Review B **77** (2008) 115121.

PREPARATION OF CUO NANOWIRES BY THERMAL OXIDATION

Naoual Al armouzi, Mustapha Mabrouki, Nourreeddine Kouider

Laboratory of Industrial Engineering, Department of Physics, FST, University Sultan Moulay Slimane, Beni Mellal, Morocco

nalarmouzi@gmail.com

Copper oxide nanowires (CuO) have been synthesized by direct thermal oxidation of copper foils (Cu) in oxygen atmosphere. In comparison with chemical elaboration, the produced CuO nanowires by direct thermal oxidation have excellent crystallinity, and in addition than that, this method is simple, convenient and quick. The textural and structural properties of the films were characterized by atomic force microscopy (AFM) and X-ray diffraction (XRD). The effect of annealing temperature on the morphology of the nanowires is studied; it is found that the annealing temperature plays an important role in the morphology of CuO nanowires and the crystallite size of CuO. Synthesis conditions, such as, temperature and the nature of substrate which is of importance for practical applications.

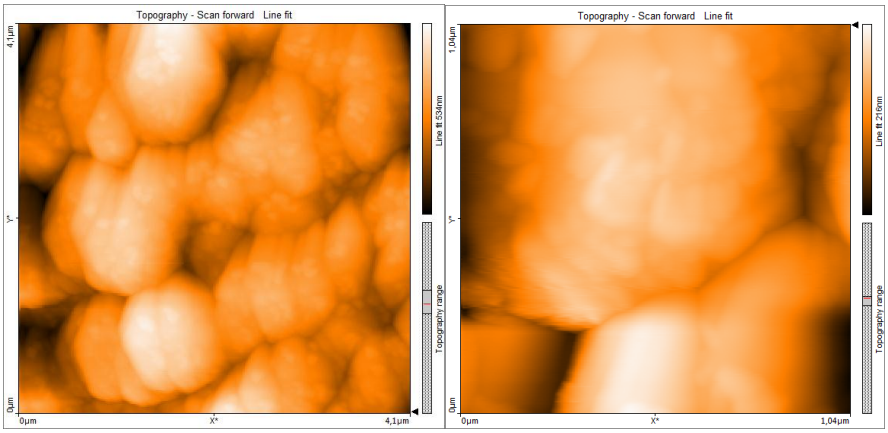

Fig. 1. AFM images for Cu annealing in 300°C and 600°C

[1] Farbod, M., et al. (2012). "Effect of growth parameters on photocatalytic properties of CuO nanowires fabricated by direct oxidation." Materials Letters 81: 258-260.

[2] Dhanasekaran, V. and T. Mahalingam (2013). "Surface modifications and optical variations of (− 111) lattice oriented CuO nanofilms for solar energy applications." Materials Research Bulletin 48(9): 3585-3593.

[3] Anandan, S., et al. (2005). "Room temperature growth of CuO nanorods arrays on copper and their application as a cathode in dye-sensitized solar cells." Materials Chemistry and Physics 93(1): 35-40.

[4] Chandrasekaran, S. (2013). "A novel single step synthesis, high efficiency and cost effective photovoltaic applications of oxidized copper nano particles." Solar Energy Materials and Solar Cells 109: 220-226.

[5] Wang, G., et al. (2012). "A review of electrode materials for electrochemical supercapacitors." Chemical Society Reviews 41(2): 797-828.

SYNTHESIS AND OPTICAL PROPERTIES OF SEMICONDUCTOR COLLOIDAL QUANTUM WELLS

Artsiom Antanovich*, Anatol Prudnikau, Mikhail Artemyev

Institute for Physico-Chemical Problems, Belarusian State University, Minsk, Belarus
artsiom.antanovich@gmail.com

Colloidal semiconductor nanoparticles (NPs) introduced more than 30 years ago became subjects of thorough research and are considered to be highly promising materials for a variety of different applications ranging from light-emitting devices and photovoltaics to medical diagnostics and bioimaging. Such interest resulted in numerous synthetic protocols for the preparation of 2D- and 3D-confined NPs. On the contrary, 1D-confined platelet-shaped atomically flat $A^{II}B^{VI}$ nanoparticles or nanoplatelets (NPls) were discovered only recently. Their shape and strong one-dimensional confinement makes them close analogues of widely used quantum wells (QWs) produced by various methods such as molecular-beam epitaxy or chemical vapor deposition. Unlike QWs, NPls are manufactured by colloidal synthesis that is more versatile, allows preparation of free-standing QWs that are easier to modify and process. NPls were shown to exhibit novel properties that are superior to properties of their counterparts of other dimensionalities such as zero size distribution in confinement direction and narrow absorption and photoluminescence (PL) bands, giant oscillator strength, low lasing thresholds, high intrinsic and two-photon absorption coefficients and electrooptical response.

In this presentation we outline main results of our work on the synthesis and investigation of properties of quantum NPls. We have demonstrated that they possess various unique optoelectronic properties that are superior to other semiconductor nanoparticles. In addition to that we developed a series of protocols for the manufacturing of 2D $A^{II}B^{VI}$ semiconductor nanoheterostructures and a method for controlled organization of NPls into stacks with controlled size. This type of NPs and composite structures on their basis are expected to be highly desirable materials for the fabrication of LEDs and displays with increased brightness and high color resolution, low-threshold lasers, photovoltaic light absorbers and converters and highly sensitive electrooptical switches.

In order to employ semiconductor NPs for practical applications it is often required to overcoat bare NPs with insulating shell consisting of wide-gap semiconductor. It results in the passivation of surface dangling bonds and simultaneous confinement of both charge carriers in the core, thus increasing the probability of radiative recombination what in turn leads to considerably increased luminescence quantum yield. We developed a new approach to overcoating CdSe NPls with ZnS, ZnCdS and CdS shells at mild temperatures using single-source molecular precursor – zinc dithiocarbamate. In comparison with previously reported methods for shell deposition, our approach is less time-consuming, allows continuous tuning of the emission and absorption bands position and opens up a possibility for large scale manufacturing of core-shell NPls. Shell growth on CdSe core NPls is accompanied by the red shift and broadening of absorption and PL bands. However, even these broadened bands are still narrower than bands of core-shell 0D and 1D NPs and allow achieving high emission color purity which is crucial for LEDs and display manufacturing.

Deposition of CdS on CdSe NPls employing different precursors in the presence of acetate-ions results in the formation of novel CdSe-CdS nanoheterostructure with so-called “core-wings” architecture. “Wings” growth is accompanied by the appearance of the absorption band in the blue region attributed to CdS flat wings. At the same time spectral features of the core such as absorption and PL band position and width remain unaffected, while their PL emission increases. In such heterostructures CdS “wings” act as a photonic antenna that concentrates photogenerated charge carriers in the central CdSe-core region what makes such hetero-NPls highly efficient light absorbers and luminescent down-converters.[1] Similar approach can be utilized for the preparation of CdSe-CdTe “core-wings” having a staggered band offset with the lowest energy levels for electrons and holes residing in different parts of nanostructure. Band alignment of this type results in the spatial separation of charge carriers and reduced overlap of carriers’ wavefunctions. Similarly to CdSe-CdS “core-wings” NPls, CdTe overgrowth occurs on the lateral edges of CdSe core and is accompanied by the appearance of new absorption bands. However, in the case of CdSe-CdTe NPls PL bands become considerably red-shifted and broadened and, at the same time, their PL radiative lifetime increases. Unlike other 0D and 1D core-shell heterostructures CdSe-CdTe NPls allow direct contact with both core and wings region and, in turn, simultaneous and selective extraction of both charge carriers. Combined with the large contact area, it makes such NPls of high interest for the preparation of novel photovoltaic and photocatalytic devices and optical sensors.[2]

Recently we also discovered that addition of various organic molecules to the solution of free-standing NPls induces their assembly into elongated stacks with controlled length, interparticle distance and surface composition of these stacks. In such stacks energy transfer process occurs faster than Auger recombination and hence such particles are useful for applications with high pumping intensity and carrier density as optical sensors, light harvesters and LEDs. [3]

A. A. acknowledges financial support from BRFFI grant № X16M-020, A. P. and M. A. acknowledge financial support from the “Chemreagents” program.

[1] A. Prudnikau, A. Chuvilin, M. V. Artemyev, CdSe-CdS nanoheteroplatelets with efficient photoexcitation of central CdSe region through epitaxially grown CdS wings. J. Am. Chem. Soc. **135**, 14476–14479 (2013).

[2] A. V. Antanovich, A. V. Prudnikau, D. Melnikau et al., Colloidal synthesis and optical properties of type-II CdSe–CdTe and inverted CdTe–CdSe core–wing heteronanoplatelets, Nanoscale **7**, 8084–8092 (2015).

[3] A. Antanovich, A. Prudnikau, A. Matsukovich et al., Self-assembly of CdSe nanoplatelets into stacks of controlled size induced by ligand exchange, J. Phys. Chem. C **120**, 5764–5775 (2016).

NANOSECOND RESOLUTION CALORIMETRY USING DAYEM NANOBRIDGES

Marcin Bartmanski[1,2], Marek Foltyn[2], Konrad Norowski[1,2], Maciej Zgirski[2]

[1]Faculty of Physics, University of Warsaw, Poland
[2]Institute of Physic Polish Academy of Sciences, Poland
m.bartmanski@student.uw.edu.pl

The presentation will cover calorimetry of small metallic nanoislands - description of experimental setup and measuring protocol. The setup involves 2 normal metal reservoirs (e.g. Cu, Ag, Au) with a superconducting weak link in form of a Dayem nanobridge (Fig.1) in between them (Fig. 2). It allows to test the temperature of the reservoirs in the steady state (with a constant heating current applied) or in a transient (after heating has been switched off). The critical current of the bridge depends on temperature making junction perfectly suited for thermometry. By measuring changes in critical current I_c one can extract thermal dynamics of the reservoirs. Such an arrangement should be useful for studying electron-phonon thermal conductance G at a fixed temperature (steady state measurement), but more importantly, with the newly proposed protocol, addresses the nanosecond resolving measurement of electron-phonon thermal relaxation time τ_{e-p} in a thin normal metal film. Since τ_{e-p} is the ratio of heat capacity C and G, time-domain measurement allows to determine the heat capacity of the reservoir. Such a calorimeter can be considered a basic block for constructing very fast and sensitive bolometers – detectors of electromagnetic radiation, especially in the infrared and terahertz bands.

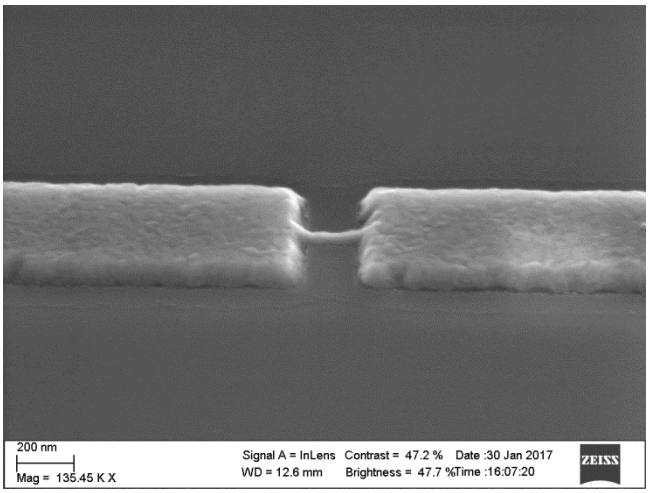

Fig 1. Dayem nanobridge obtaine with e-beam nanolithography

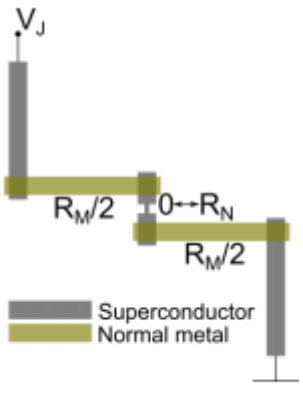

Fig. 2 Layout of calorimeter to be obtained with e-beam lithography

UPCONVERTING NANOPARTICLES FOR THERANOSTIC

Dovile Baziulyte-Paulaviciene[1], Ricardas Rotomskis[2], Vitalijus Karabanovas[2], Simas Sakirzanovas[1]

[1]Vilnius University, Faculty of Chemistry and Geoscience, Naugarduko 24, LT-03225, Vilnius, Lithuania
[2]Biomedical Physics Laboratory, National Cancer Institute, Baublio 3b, LT-08406, Vilnius, Lithuania
dbaziulyte@gmail.com

Lanthanide-doped upconverting nanoparticles (UCNPs) have the ability to convert lower energy radiation (NIR) into visible radiation with higher energy via a nonlinear optical process [1]. UCNPs created numerous opportunities for therapy and diagnostics due to the integration of the advantages of its suitable dimensions as well as its special optical properties. For example, the NIR excitation light not only allows for deeper light penetration and reduced photodamage effects, but also offers lower autofluorescence, reduced light scattering, and phototoxicity. Thus, ideal for image-guided therapy through which the tumor located deep inside a body can be seen and treated simultaneously [2]. UCNPs unique optical and chemical properties, such as non-blinking, non-photobleaching, absence of autofluorescence, low-toxicity, and low photodamage to the living system further strengthens their use in medical diagnostics, therapy and imaging. These nanomaterials provide a multifunctional platform, which now is known as theranostics (Fig. 1). Theranostics is the key for next generation personalized medicine, as opposed to adopting a 'one size fits all' approach. This can move the field of nanomedicine forward to an era of more effective and individual treatment approaches [3].

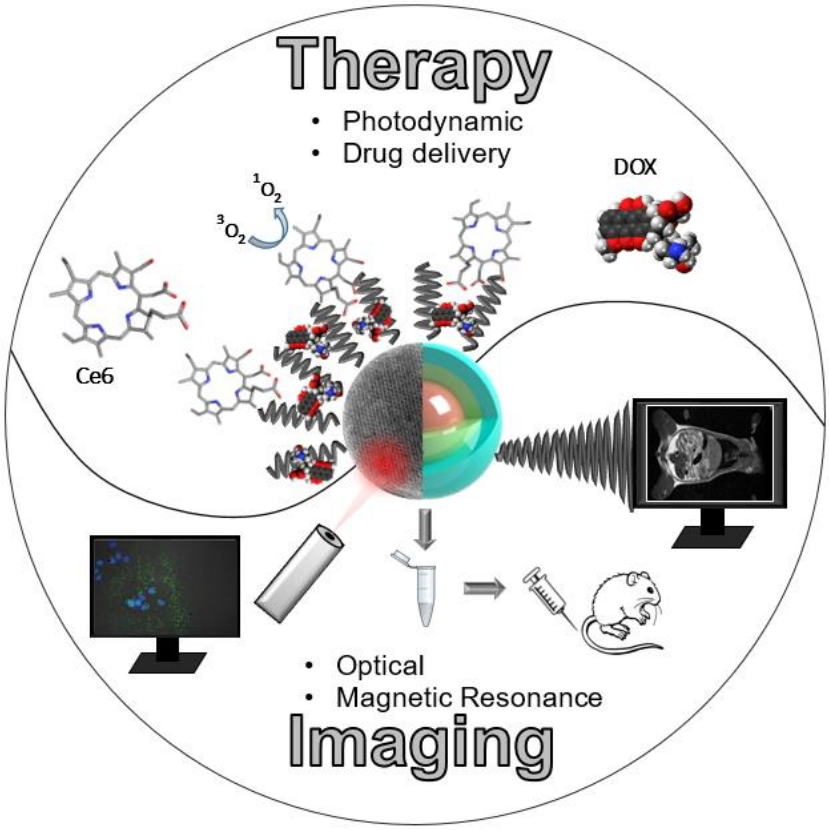

Fig. 1. Schematic illustration of upconverting nanoparticles application for theranostics.

In this work, we present synthesis, properties and uses of our prepared sodium gadolinium fluoride core/shell upconverting nanoparticles. By changing dopant ions, shell composition and surface ligands of these nanoparticles, we can achieve different properties for numerous application. Smart design of multifunctional nanocomposite should represent one of the future directions in theranostics. Further studies are still needed to generate sufficient data for better understand of long-term toxicity and safety of the UCNPs before introducing their wide applicability in medicine.

[1] L. Y. Ang, M. E. Lim, L. C. Ong, et al., Applications of upconversion nanoparticles in imaging, detection and therapy, Nanomedicine **6**, 1273–1288 (2011)
[2] G. Chen and G. Han, Theranostic Upconversion Nanoparticles (I),Theranostics **3**, 289–291 (2013)
[3] S. S. Kelkar, T. M. Reineke, Theranostics: Combining Imaging and Therapy, Bioconjugate Chem. **22**, 1879–1903 (2011)

DETERMINATION OF THE SIZE OF THE CORE OF MAGNETIC COBALT NANOPARTICLES USING THE FARADAY EFFECT

Arkadiusz Grempka[12], Mateusz Król[1], Michał Wójcik[2], Jacek Szczytko[1]

[1]*Institute of Experimental Physics, Faculty of Physics, University of Warsaw, Poland*
[2]*Faculty of Chemistry, University of Warsaw, Poland*
a.grempka@student.uw.edu.pl

Materials showing large magneto-optic effects have application in wide range of optical technology as fast shutters, switches, tunable phase retarders, etc [1]. Stable ferrofluids made of suspended cobalt nanoparticles are especially interesting due to their magnetic and magneto-optical properties. In this study we measure optical properties of suspension of such nanoparticles in toluene and cyclohexane in the presence of magnetic field and analyze the results with a theoretical model.

Cobalt magnetic nanoparticles were synthesized in o-dichlorobenzene via thermal decomposition of cobalt octacarbonyl under inert (Ar) atmosphere in a presence of oleic acid (OA), trioctylphosphine oxide (TOPO) and triphenylphosphine (TPP) [2]. Then the nanoparticles were precipitated using ethyl alcohol and dispersed in toluene and cyclohexane. The diameter of the nanoparticles was determined by SAXS (Small-angle X-ray scattering) while shape with TEM (Figure 1). The ratios of surfactants enabled to synthesize nanoparticles with different diameters.

The Faraday effect in the solution was observed. Polarized laser light was transmitted through the sample placed in magnetic field (from 0 to 0,4 T) and recorded using polarimeter. The analysis of the rotation angle compared with theoretical model provides the information about the effective size of the magnetic core [3], which corresponds with accuracy about 1 nm to the actual size of the nanoparticles.

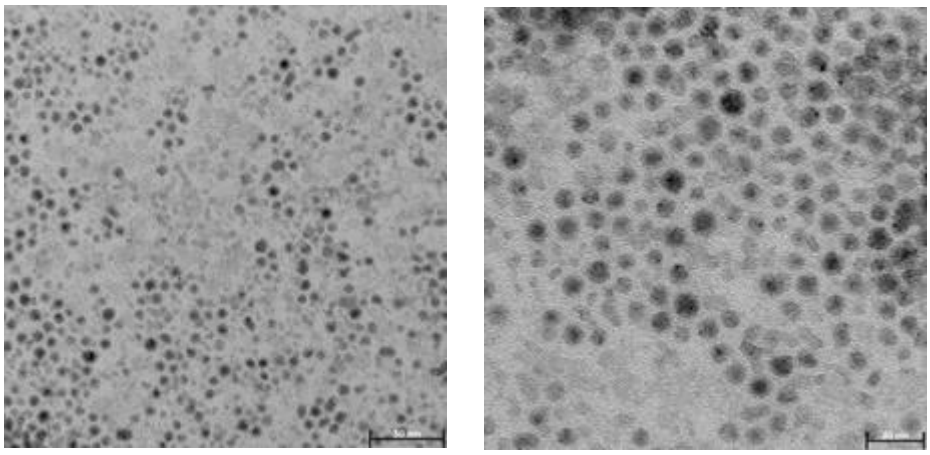

Fig. 1. Transmission Electron Microscopy of Co nanoparticles (mean size of 7.6±1.4 nm).

[1] W. Luo, T. Du, and J. Huang, Phys. Rev. Lett. **82**, 4134 (1999)
[2] H. T. Yang, C. M. Shen, Y. G. Wang, Y. K. Su, T. Z. Yang, H. J. Gao, Institute of Physics Publish., ,Nanotechnology, **15,** 70-74 (2004)
[3] J. Szczytko, N. Vaypotič, K. Madrak, P. Sznajder, Physical Review E, **87** (2013)

LOW TEMPERATURE RELOCATION OF ALIGNED SINGLE CRYSTAL SILICON NANOWIRES ONTO ALIEN SUBSTRATE.

Sakshum Khanna[1], Gauravi Xavier [2]
[1]Solar research and Development Centre, Pandit Deendayal Petroleum University, India
[2] Institute of Research and Development , Gujarat Forensic Science University, India
Sakshum.kphd16@sot.pdpu.ac.in

The fabrication of nanowire (NW) devices on alien substrates is necessary for applications such as flexible electronics, conformable sensors, and transparent solar cells. Although NWs have been fabricated on plastic and glass by lithographic methods, but these are limited by its temperature and the property of the alien substrate [1].

Here we demonstrate the method of relocation of aligned single crystal silicon nanowires (SiNWs) to alien substrate. The methods of transferring basically rely on the differences in adhesion of NWs, metal films, and devices from weakly adhesive donor substrates to more strongly adhesive receiver substrates. The Fig. 1(a) shows Metal assisted chemical etching (MACE) method used to fabricate vertically aligned SiNWs on Si substrates [2]. To detach SiNWs from Si substrates, the roots of the Si NWs were etched and became fragile by controlling direction of metal-assisted etching. Thus, every SiNW on the Si substrate can be easily transferred to alien substrates Fig. 1(b).

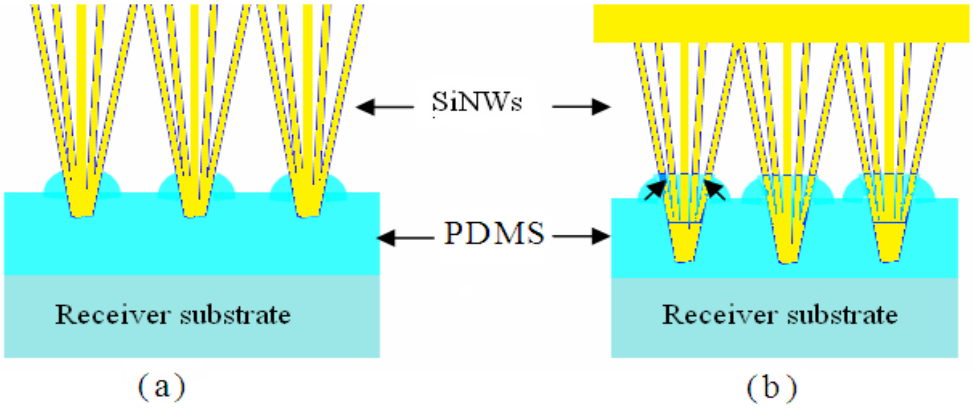

Fig.1. Vertically Aligned Nanowires and Transfer-Printing method.

The transmission coefficient below 10 % at a wide bandwidth, 400-1100 nm, was found in the transferred SiNWs and the alignment of the transferred nanowires was found to be almost same to the original. This high dense aligned SiNWs are promising for future photovoltaic applications [3]. At low temperature process, it enables a large variety of alien substrates to use.

[1] K Lu W, Lieber CM, Semiconductor nanowires. J Phys D Appl Phys 39(21):R387–R406 (2006).
[2] E. Katherine, A. Filler, M. Joshua, M. Kayes, S. Maldonado, S. Brunschwig, A. Atwater, S. Lewis, Flexible Polymer-Embedded Si Wire Arrays. Adv. Mater, 21, 325–328 (2009).
[3] Park W, Zheng GF, Jiang XC, Tian BZ, Lieber CM, Controlled synthesis of millimeter-long silicon nanowires with uniform electronic Properties. Nano Lett **8**(9):3004–3009 (2008).

ADSORPTION OF Y^{3+} IONS WITH NANOCOPOSITES BASED ON SINGLE-DOMAIN Fe_3O_4 MODIFIED WITH TiO_2

Andriy Kusyak[1,2], Natalia Kusyak[1], Katerina Sviriduk[1], Petro Gorbyk[2]

[1] Department of Chemistry, Ivan Franko Zhytomyr State University, Ukraine

[2] Chuiko Institute of Surface Chemistry, National Academy of Sciences of Ukraine, Ukraine

a_kusyak@ukr.net

Magnetosensitive nanocomposites with different surface types are the most promising materials produced for various branches of industry. These materials, taking into account their effectiveness and economic feasibility, are still used for solving numerous urgent problems like removing, separating and concentrating toxic compounds from natural and synthetic liquids, including the technogenic liquids. The nano-sized single-domain magnetite possesses an important place among other perspective materials used in creation of nanocomposites [1-3].

In this work, nano-sized single-domain magnetite was synthesized, its surface chemical modification was carried out, and adsorption properties of Fe_3O_4, Fe_3O_4/TiO_2 nanostructures were researched regarding Y^{3+} ions. Magnetite was synthesized according to the reaction: $Fe^{2+} + 2Fe^{3+} + 8NH_4OH \rightarrow Fe_3O_4 + 4H_2O + 8NH_4^+$. Magnetite particles with fraction size of 10-30 nm corresponding to single-domain state with optimum magnetic properties and specific surface area S = 105 m^2/g were used. To modify nanoparticles we used n-butylorthotitanates. The composites were obtained from samples of magnetite by adsorption modification (AM). So, we received the layered structure. Obtained composites were investigated by IR spectroscopy, DTGA, defined surface area.

Research in adsorption properties of Fe_3O_4, Fe_3O_4/TiO_2 (AM) nanocomposites with respect to Y^+ cations was carried out dynamically at pH = 6.5 and room temperature using standard solutions with 0.5 to 40 mg/l (m = 0.03g, V = 5 ml) concentrations. The composites were investigated IR spectroscopy (Fig.1, 2). To research into pH influence, acetate buffer (C_0 Y^{3+} = 25 mg/l) was used.

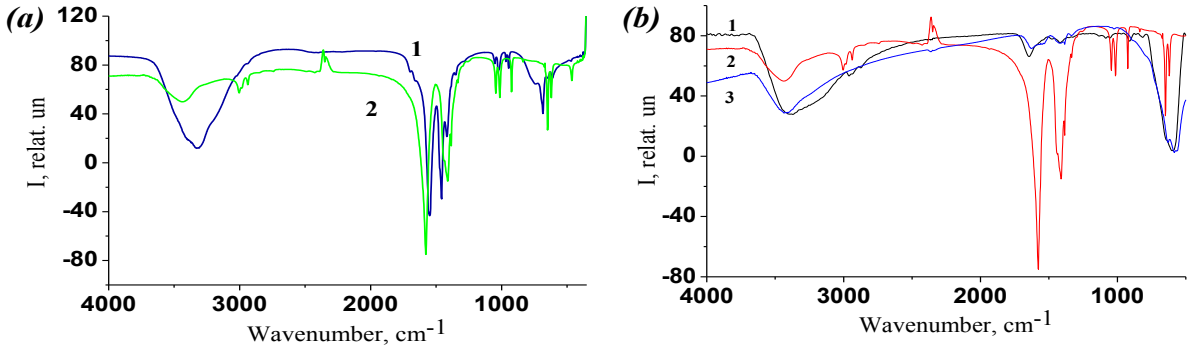

Fig. 1. IR-spectr $Y(Ac)_3$ (1), $Y(NO_3)_3$ (2) in acetate buffers solutions (***a***) and Fe_3O_4/TiO_2 (1), $Y(NO_3)_3$ in acetate buffers solutions (2) and after surface adsorption compounds Y^{3+} (3) (***b***)

Adsorption capacity on the surface of original and modified magnetite was determined by dynamic measuring of Y^{3+} concentration in solution with spectrophotometric method (λ = 645 nm). Adsorption capacity of magnetite after its surface modification with TiO_2 increases. Adsorption saturation is reached after 15-30 minutes for all the nanocomposites. The increase in Y^{3+} equilibrium concentration leads to adsorption saturation. The best Y^{3+} removal characteristics correspond to Fe_3O_4/TiO_2 (AM) surface. The calculated values of sorption capacity A mg/g (Fe_3O_4/TiO_2 - 7.23 mg /g), and extraction extent R% - 96%.

[1] Wen-Juan Li, Xian-Zhi Yao, Zheng Guo, Jin-Huai Liu, Xing-Jiu Huang. Fe_3O_4 with novel nanoplate-stacked structure: Surfactant-free hydrothermal synthesis and application in detection of heavy metal ions. Journal of Electroanalytical Chemistry,749 (15),75-82, (2015).

[2] A.P. Shpak, P.P. Gorbyk Nanomaterials and Supramolecular Structures. Physics Chemistry, and Applications (Springer, 2009).

[3] Emadi M., Shams E., Amini M.. Removal of Zinc from Aqueous Solutions by Magnetite Silica Core-Shell Nanoparticles. Journal of Chemistry, (2013).

THICKNESS OF THE EXFOLIATED $MoSe_2$ MEASURED BY REFLECTOMETRY AND RAMAN SCATTERING

Karolina Łempicka, Konrad Norowski, Magdalena Grzeszczyk, Barbara Piętka, Jacek Szczytko

Institute of Experimental Physics, Faculty of Physics, University of Warsaw, Pasteura 5, 02-093 Warsaw, Poland
k.lempicka@student.uw.edu.pl

Transition-metal dichalcogenide crystals (TMDCs) have emerged as a new class of materials that display exceptional physical and optical properties [1]. Thickness is one of the fundamental parameters that define their surprising and unique electronic properties. Monolayer of this materials have the direct bandgap which gives an advantage over the indirect bandgap in bulk TMDCs, thus makes them promising candidates for several interesting applications as light emitters, detectors, and photovoltaic devices [2].

One of the typical representative compound of the TMDCs family is molybdenum diselenide ($MoSe_2$), a synthetic crystal, which structure is characterized by strong intralayer covalent bonds within planes of hexagonally arranged between selenium and molybdenum atoms and by weak out-of-plane van der Waals interactions Se-Mo-Se layers [3].

It's important for applications and research purposes to have easy, quick and nondestructive method of determination of layer thickness. Optical microscopy can give inconclusive results, we propose using two different wavelengths in order to effectively determine number of layers of TMDCs and visualize defects. A confocal microscope was used for scanning the surface of $MoSe_2$ samples and for studying different defects formed during the exfoliation process. The measurements were carried out at room temperature using red (650 nm) and green (532 nm) laser light illumination. With increasing thickness of the sample the change of the relative reflection was observed. We use characteristic difference of relative reflections to determine the exact number of TMDC layers. This method provides also a quick method of visualization of the presence of defects of 2D materials.

We verified the experimental results by Raman spectroscopy. The energy difference between E^1_{2g} (active out-of plane vibrational mode), A_{1g} (active in-plane vibrational mode) and B^1_{2g} (inactive in-plane vibrational mode) allowed for independent measurement of the thickness of our sample. A key role is played by the intensity and shape of the peaks in the Raman scattering.

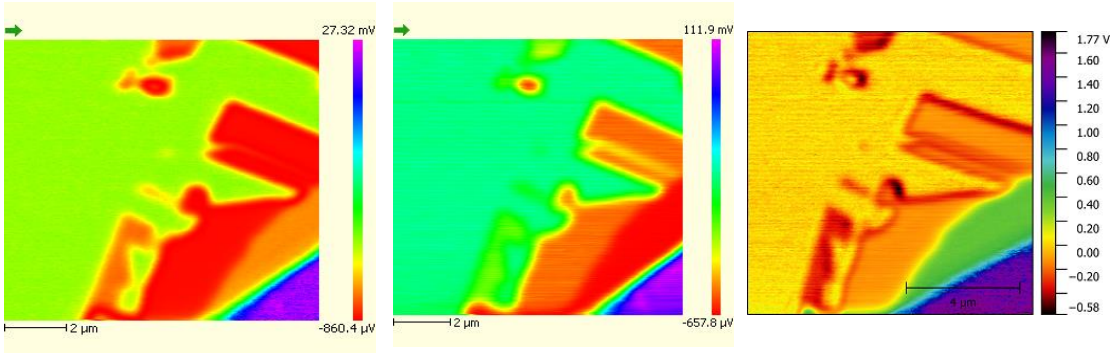

Fig. 1.The pictures from confocal microscope. They show the intensity form two types of lasers: from left: green, next: red and the last one picture is the difference of relative reflection.

The new method was checked by theoretical model. We used transfer matrix method to obtain dependence between the number of $MoSe_2$ layers and the intensity of reflected light. Main parameters of the model was thicknesses of materials, their indices of refraction at the given wavelength of light. Consistency of experiment and theoretical model was confirmed.

[1] Y. Li, A. Chernikov, T. F. Heinz et al., *Measurement of the optical dielectric function of monolayer transition-metal dichalcogenides: MoS_2, $MoSe_2$, WS_2, and WSe_2*, Physical Review B **90**, 205422 (2014).
[2] W. Zhao, Z. Ghorannevis, G. Eda et al., *Lattice dynamics in mono- and few-layer sheets of WS_2 and WSe_2*, Nanoscale **5**, 9677–9683 (2013).
[3] M. Grzeszczyk, K. Gołasa, A. Babiński et al., *Raman scattering of few-layers $MoTe_2$* 2D Materials **3**, 025010 (2016).

MATERIALS BASED ON SELF-ASSEMBLING BLOCK COPOLYMER AND LIQUID CRYSTAL HYBRIDS

Aneta Leniart, Pawel W. Majewski

Department of Chemistry, University of Warsaw, Poland
aneta.leniart@student.uw.edu.pl

Self-assembled soft materials such as liquid crystals (LC) and block copolymers (BCPs) thanks to their extraordinary ability to assemble into ordered periodic nanostructures are an elegant realization of Feynman's bottom-up fabrication strategy. The challenge we are facing now is to optimize the synthetic process and to investigate physicochemical properties of such materials.

We would like to create a BCPs-LC hybrid materials where each component has a different function. BCPs will play a static role (structure-directing template) while LC will be a dynamic part, which can give a response to external factors like temperature or light.

The presented project encompassed a few stages. An essential element of our strategy is to develop novel techniques for accelerated directed self-assembly (DSA) of block copolymers[1]. The properly structured BCP thin films are a start point to build a BCPs-LC hybrid materials.

The new synthetic strategy towards BCPs-LC materials opens the way to various applications, in particular in switchable membranes (for ion conduction or filtration) and synthetic templates for functional nanostructures (sensors, multi-functional catalytic materials).

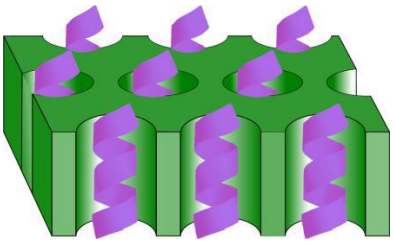

Fig. 1. Scheme of BCPs-LC hybrid material

[1] Majewski, P. W., & Yager, K. G. (2016). Rapid ordering of block copolymer thin films. Journal of Physics: Condensed Matter, 28(40), 403002. https://doi.org/10.1088/0953-8984/28/40/403002

STRUCTURE AND PROPERTIES OF EPOXY-SILICA AND EPOXY-TITANIA COMPOSITES OF CATIONIC POLYMERIZATION

Natalya Leonova, Svetlana Zhiltsova

Department of Biochemistry and Physical Chemistry, Faculty of Chemistry, Vasyl' Stus Donetsk National University, Ukraine
n.leonova@donnu.edu.ua

Epoxy polymers possess high mechanical, electrical, and adhesion properties. But one of the negative features of highly-crosslinked systems is their brittleness. The introduction of fillers obtained by the sol-gel method affords a decrease in the brittleness and increase in the operational characteristics.

Epoxy-silica composites of cationic polymerization based on epoxy resin Eponex 1510 (dicyclohexylolpropane diglycidyl ether) and tetraethoxysilane were synthesized. The catalyst for cationic polymerization was the complex of boron trifluoride with benzylamine (UP 605/3r). The epoxy-silica composites were obtained according to the procedure described in [1]. Highly dispersed TiO_2 nanoparticles were synthesized by hydrolytic polycondensation of titanium tetrabuthoxide (TBT) in the presence of epoxy resin, solvent and water at ambient temperature. Glacial acetic acid was added to TBT before mixing with other components to reduce the hydrolysis rate. Curing process of composites was 100 °C 1 h; 120 °C 2 h; 140 °C 2 h; 160 °C 2 h. All the received materials demonstrated high optical transparency.

The influence of the nano-sized filler on the structure and dynamic mechanical properties of the epoxy-silica systems of cationic polymerization were investigated. It was found that the effect of small additions in the composites takes place: at the concentrations of SiO_2 0.5–1.5 wt.% the high elasticity modulus and the concentration of internodal chains increase and the glass transition temperature reduces. Increase of concentration of silica particles' in the composites to 2.0–3.0 wt.% leads to imperfection of topological structure of epoxy resin and increasing of molecular weight of internodal chains of polymer network. Investigation of thermophysical characteristics of the epoxy-silica systems showed that filler introduction leads to decrease in crosslink density and glass-transition point owing to the changes in the topological structure of composites. The resulting polymers have heterogeneous structure that contains regions with increased molecular mobility showing their own values of the glass-transition point. Similar dependence was observed for the synthesized epoxy-titania nanocomposites. The higher the filler content the lower the glass transition point and sol-fraction yield. Despite decrease of network density of the composites compared to unmodified epoxy polymer, the received epoxy-silica and epoxy-titania materials demonstrate increased stability to thermal oxidation.

The obtained epoxy-inorganic composites can be used as adhesives and protecting coatings. It was established that the received epoxy-silica composites of cationic polymerization provide for the high adhesion of coatings to aluminum substrate already at low filler concentration in the system. The lattice-cut method was used to estimate the adhesion of the unmodified polymer and hybrid materials to D16 aluminum alloy surface. It was shown that an increase in the adhesion from three points to one is observed already at the introduction of 1 wt.% of SiO_2. The impact adhesion strength of the epoxy-silica films on D16 aluminum alloy was estimated. All the tested coatings possess the maximum impact strength (50 kgf cm). After tests with the D16 alloy plates coated with the composite, no mechanical damages, cracks, layering, and crumpling were observed. It was determined using potentiodynamic method that effectiveness of corrosion protection of surfaces of aluminum alloy D16 by epoxy-titania composite coatings is 96.2–99.6 % and for epoxy-silica composite coatings is 98.4–99,9 %.

[1] N. G. Leonova, V. M. Mikhal'chuk, L. A. Savenkova, and V. A. Beloshenko, Vopr. Khim. Khim. Tekhnol., No. 1, 48–53 (2009).

INFLUENCE OF THERMAL TREATMENT ON GRAPHENE – METAL CONTACT

Algimantas Lukša, Gvidas Astromskas, Viktorija Nargelienė, Andrius Sakavičius, Arūnas Šetkus

Center for Physical Sciences and Technology, Saulėtekio ave 3, Vilnius LT-10257, Lithuania
algimantas.luksa@ff.stud.vu.lt

The resistance of the contacts between graphene and metals is frequently the limiting factor in development of the graphene based electronic elements for practical applications. The characteristics of the contacts depend on the fundamental mechanisms of an interaction in the interface commonly identified as physisorbtion and chemisorbtion of metals on graphene. For the physisorbed metals, the outer shell *s* orbital interacts with graphene π orbital that results in weak interaction. For the chemisorbed metals the *d* orbital strongly interacts with graphene π orbital. The interaction mechanism allows to predict the minimal contact resistance [1]. However, there is still a great challenge to make the predictable contact.

This work focuses on the contact technology between graphene and metals, namely nickel and gold. An influence of thermal treatment on the resistance is studied. The contact resistance was measured for the samples adapted to the circular transfer length method (CTLM) [2]. For the contacts, the metal films were deposited by magnetron sputtering and shaped by photolithography. Then, a CVD grown graphene sheet was lifted from a copper foil and placed on the shaped metal film. We developed a wet transfer process for this. Polymethyl methacrylate (PMMA) was spin coated on the graphene. The copper substrtae was removed by etching and the PMMA with graphene was placed on the test sample. Then the PMMA was dissolved in chloroform. The I-V characteristics and the Raman spectra were obtained for the samples before and after annealing at 580 K. An influence of the annealing time on the experimental data was studied.

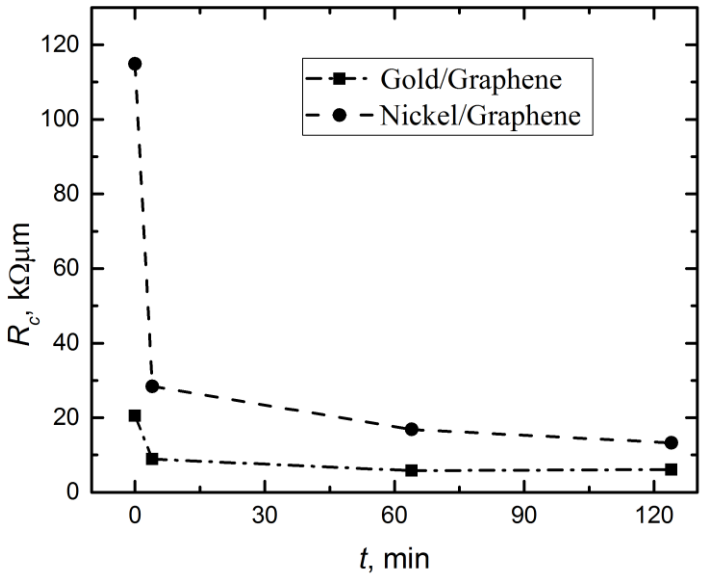

Fig. 1. Dependences of contact resistance on annealing time for samples with graphene on Au and Ni.

Extracted Gold/Graphene contact resistance before annealing was 20.63 kΩμm and after thermal treatment was reduced to 5.8 kΩμm. The largest reduction of contact resistance (80 % of total reduction) was achieved through first 4 minutes of thermal treatment. Nickel/Graphene resistance before annealing was 114.9 kΩμm and after annealing was reduced to 13.3 kΩμm. Contact resistance reduction of Nickel/Graphene structures was similar as Gold/Graphene. The largest drop of contact resistance (85 % of total reduction) was achieved through first 4 minutes also. Contact resistance dependence on annealing time for both structures presented in figure 1. Raman spectra of graphene on nickel showed, that after 4 minutes annealing nickel carbide begins to form. Wider investigation showed that carbide can be formed due to supporting polymer residues and contamination from photolithography resist during contact annealing.

[1] M. Politou, I. Asselberghs, I. Radu, T. Conard, O. Richard, C. S. Lee, K. Martens, S. Sayan, C. Huyghebaert, Z. Tokei, S. De Gendt, M. Heyns, Transition metal contacts to grapheme, Appl. Phys. Lett., **107** (2015).
[2] D. K. Schroder, *Semiconductor material and device characterization* (John Wiley & Sons Inc., Hoboken, New Jersey 2006).

MULTIMODAL NANOPROBE FOR GUIDED SURGERY OF OVARIAN PERITONEAL CARCINOMATOSIS

Mangeolle Tristan[1*], Pons Thomas[2], Marchal Frederic[1,3]

[1] Centre de Recherche en Automatique de Nancy, CNRS, Université de Lorraine, Nancy, France
[2] Ecole Supérieure de Physique et de Chimie Industrielles, Paris, France
[3] Institut de Cancérologie de Lorraine, Vandoeuvre-les-Nancy, France
* t.mangeolle@nancy.unicancer.fr

Ovarian and colo-rectal cancers are two of the most lethal malignancies, especially because of their natural progression from organ localized tumor to disseminated cancerous nodules around the whole abdominal cavity, namely peritoneal carcinomatosis [1].

Previously, this latest stage of cancer progression was considered as incurable. However, determined effort of surgeon, and practical approach of this pathology has led to the development of advanced surgical procedure. Nowadays, an effective cure, with high survival rates and acceptable life quality, is possible now by associating extensive surgery - to excise all tumor nodules, with advanced chemotherapy – to achieve residual cancerous cells.

Nevertheless, this achievement is still an awkward surgical challenge: if only one tumor, even the smallest, can escape from the surgeon's attention, survival rate is immediately decreased in two or more times, depending on the tumor size [2]. Moreover, surgeons still need effective techniques to detect tumors, in association with their only views and sense of touch.

To fulfill this request, fluorescence guided surgery (FGS) seems to be one of the most promising innovative technology. By using fluorescent dyes to stain cancerous tissues, and specific light sources and cameras, some research teams have improved the detection of tumors nodules, and even made visible the previously invisible smallest implants. These first steps of FGS are paving the way to better cure and easiest surgical operation [3]. However, many challenge remains, before using of this technology on humans.

In the present work, we used the quantum dot based nanoparticles for ovarian peritoneal carcinomatosis imaging by magnetic resonance imagery, and to guide surgery by fluorescence. For this purpose, we conceive and upgrade an advanced kind of nanoprobe for guided surgery: by associating the exceptional fluorescent properties of quantum dots, in a biocompatible shell of mesoporous silica, doped with magnetic particles, we are developing an effective multimodal (i.e. fluorescent and magnetic) nanoprobes (Fig. 1).

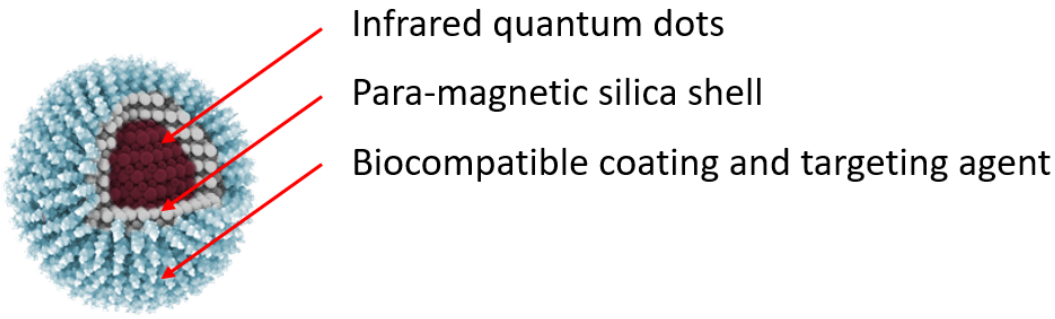

Fig. 1. The structure of NPs

After successful assessment of biocompatibility *in vitro*, we are now focused on chemical improvement to enhance *in vivo* biocompatibility of the probe. Also, we are developing murine model of ovarian peritoneal carcinomatosis, to assess imaging capability of our nanoparticles.

Acknowledgements. This study was supported by French Région Loraine and Institut de Cancérologie de Lorraine

[1] Tan, D., Agarwal, R. and Kaye, S. Mechanisms of transcoelomic metastasis in ovarian cancer. The Lancet Oncology, **7** (11), 925-934 (2006).
[2] Roviello, F., Pinto, E., Corso, G., Pedrazzani, C., Caruso, S., Filippeschi, M., Petrioli, R., Marsili, S., Mazzei, M. and Marrelli, D. Safety and potential benefit of hyperthermic intraperitoneal chemotherapy (HIPEC) in peritoneal carcinomatosis from primary or recurrent ovarian cancer. Journal of Surgical Oncology, **102**(6), 663-670 (2010).
[3] van Dam, G., Themelis, G., Crane, L., Harlaar, N., Pleijhuis, R., Kelder, W., Sarantopoulos, A., de Jong, J., Arts, H., van der Zee, A., Bart, J., Low, P. and Ntziachristos, V. Intraoperative tumor-specific fluorescence imaging in ovarian cancer by folate receptor-α targeting: first in-human results. Nature Medicine, **17**(10), 1315-1319 (2011).

TEMPLATE-FREE SYNTHESIS OF MAGNETITE NANORODS FOR THE IMPROVENMENT OF RHEOLOGICAL PERFORMANCE OF CARBONYL IRON OIL SUSPENSIONS

Valentin Natarov[1], Dzmitry Kotsikau[1], Eugenia Korobko[2], Anna Eroma[1], Zoya Novikova[2], Vladimir Pankov[1]

[1] Department of Physical Chemistry, Belarusian State University, Belarus
[2] A.V. Luikov Heat and Mass Transfer Institute of The National Academy of Sciences of Belarus
che.natarovVO@bsu.by

Magnetorheological fluids (MRF) based on micro-sized carbonyl iron particles (CI) and synthetic oil possesses a great interest due to the ability to control their properties, in particular viscosity, by using applied magnetic field. MRF can be easily changed within milliseconds from Newtonian liquid state to semisolid state due to formation of chain-like structures of CI particles which are self-arranged along the magnetic flux. Recently it was demonstrated that the addition of nanosized paramagnetic particles improves magnetorheological characteristics of MRF and their sedimentation stability [1]. Nanosized fraction fills microcavitys between CI particles within the chain (Fig. 1), thus increasing yield stress compared to the basic MRF. MRF are widely used for a number of engineering applications such as dampers and polishing systems.

Magnetite nanorods were obtained by modified template-free solution chemistry method [2]. On the first step $Fe(OH)_2$ was precipitated by the addition of ammonia to $FeSO_4$ aqueous solution. Then, goethite (α-FeOOH) nanorods were obtained via oxidation of $Fe(OH)_2$ by $KClO_3$. pH during oxidation was maintained lower than 8,0 to avoid formation of magnetite. After complete oxidation of $Fe(OH)_2$ goethite nanorods were washed with water via centrifugation and dried at 60° C. At the final step goethite nanorods were calcined in furnace under H_2 flow at 360° C for 2 hours.

According to electron microscopy and X-ray diffraction well-crystalline magnetite nanorods with 600 mn length and 90 nm thickness were synthesized. Magnetite nanorods possesses significantly higher saturation magnetization (112 emu/g) compared to magnetite nanoparticles (68 emu/g), obtained by the oxidation of $Fe(OH)_2$ at pH > 9. Magnitude of magnetorheological effect mainly depends of saturation magnetization of nanosized addition [1], thus using of nanostructures with shape anisotropy allow achieving a better results. Despite of shape anisotropy (aspect ratio ≈ 6) the nanorods demonstrate low coercivity (10 Oe), that makes them to be redisperced after removal of magnetic field.

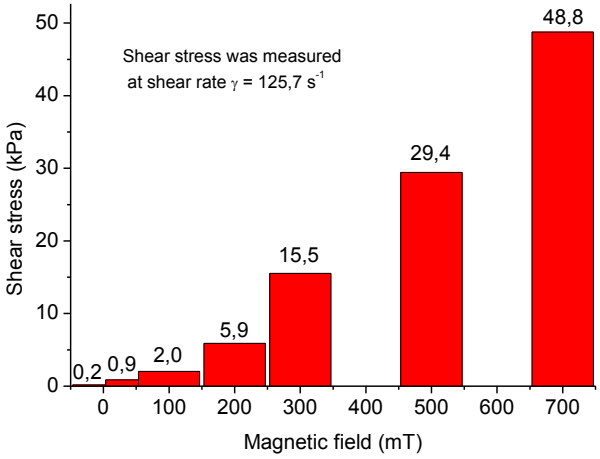

Fig. 2. Shear stress of MRF with addition of magnetite nanorods at different magnetic fields

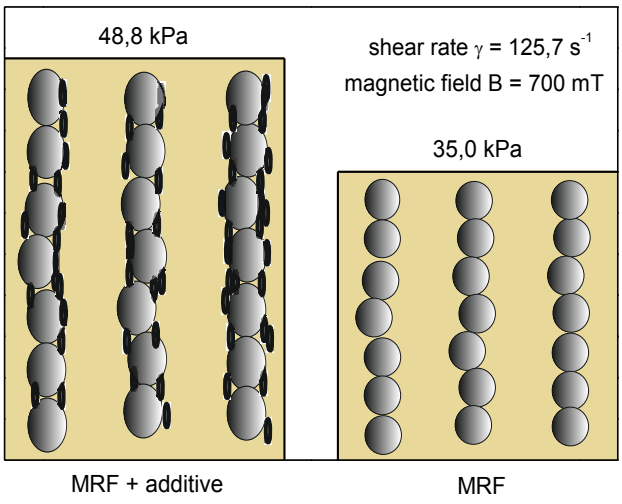

Fig. 1. Shear stress of basic MRF and MRF with additive. Scheme of chain formation under applied magnetic field

According to the data from fig. 2 the flow resistence at the cell of rotational rheometer increases by 244 times unedr aplying of applied magnetic field (B=700 mT). At the same time, the addition of magnetite nanorods lead to the increase of magnetorheological effectiveness of bicomponent MRF up to 28 % compared to basic MRF. Even small additions of nanosized component (1-2 Wt.%) allow to incerase MRF performance. Presented facile template-free synthesis can be used for large scale preparation of nanosized additives for MRF.

[1] A. Ghaffari, S.H. Hashemabadi, M. Ashtiani, A review on the simulation and modeling of magnetorheological fluids, J. Intel. Mat. Syst. Str. 26 881–904
[2] V.G. Melnyck at al. Rotue for the preparation of needle-like γ-iron oxide. USSR description for author's invention №385926. Date 29.10.1969

THE INFLUENCE OF ADDITION PURE AMINO ACIDS ON THE PROPERTIES OF LUMINESCENT GOLD CLUSTERS

Agnė Mikalauskaitė[1*], Renata Karpicz[2], Arūnas Jagminas[1].

[1] Department of Electrochemical Material Science, Center for Physical Sciences and Technology, Vilnius, Lithuania.
[2] Department of Molecular Compound Physics, Center for Physical Sciences and Technology, Vilnius, Lithuania.
agne.mikalauskaite@ftmc.lt

Recently, ultra-small gold nanoparticles and clusters have attracted considerable attention due to their unique catalytic, optical and electronic properties such as strong fluorescence, vis light absorption and as large as 1.77 eV energy gaps. Besides, due to biocompatibility and size as well as stabilizing shell-dependent fluorescence, gold clusters hold great potentials in biological applications and nanomedicine.

Among others, gold clusters, synthesized during past several years using proteins, such as bovine serum albumin [1], lactoferrin [2] and lysozyme [3] and possessing red-luminescence with lifetimes up to several micro seconds, good stability, non-toxicity and biocompatibility, can be used for cancer cells imagining and target detection.

Recently we have found a new class of protein-based cheap reducers, particular some food supplements, for formation of red-luminescent gold clusters under blue and green light excitation with a good quantum yield (7%), lifetime up to 2 μs and stability for month. These characteristics are close to Au nanoclusters (AuNCs) synthesized and stabilized with BSA (AuNCs@BSA). The first tests in Lithuania National Cancer Institute have shown that these clusters tend to accumulate in more tumorigenic breast cancer cells (line MDA-MB-213) and can be prospective for bio imagining. To full understanding the composition of our clusters as well as stabilizing shells, high-resolution mass spectrometry characterization is crucial.

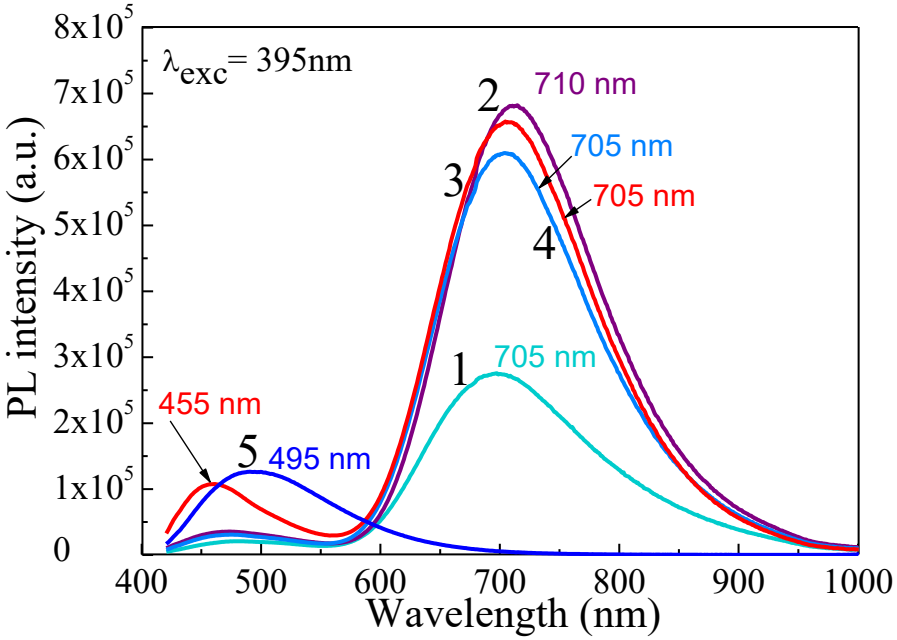

Fig. 1. PL spectra of gold clusters fabricated at 37 °C for 20 h in the solution containing 15 mg mL^{-1} BCAA'S and 3.0 μM/mL $HAuCl_4$ without (1) and with addition of 15 mM Leu (2), Ser (3), Glutamic acid (4) and Cis (5).

In this study that addition of some amino acids to the synthesis solution of BCAA'S and chloroauric acid can significantly increase or decrease the PL intensity of the synthesized NCs (Fig. 6) and the yield of red-luminescent gold clusters. The most effective influence was obtained using leucine, serine and glutamic acid whereas the addition of cysteine hindered the formation of red luminescent gold NCs. On the other hand, the addition of cysteine resulted in the formation of blue fluorescent gold clusters possessing emission peak at 495 nm (spectrum 5 in Fig. 6).

[1] J. Xie, Y.Zheng, J. Y. Ying, J. Am. Chem. Soc. **131** (2009) 888-889.
[2] C.-A. J. Lin, T.-Y. Yang, C.-H. Lee, S. H.; Huang, et al. ACS Nano **3** (2009) 395-401.
[3] W., H. and Wang, Z. and Y., L. and Tian, Shiliang and Hou, Changjun and Lu, Yi. The Royal Society of Chemistry (2010), **135**, 1406-1410.

FINITE DENSITY OF STATES FOR HYPERBOLIC METAMATERIALS WITHIN OPERATOR EFFECTIVE MEDIUM APPROXIMATION

Fyodor Morozko[1], Vladislav Popov[1], Andrey Novitsky[1,2]

[1]Department of Theoretical Physics and Astrophysics, Belarusian State University, Republic of Belarus
[2]DTU Fotonik, Technical University of Denmark, Denmark
fiz.morozko@bsu.by

Hyperbolic metamaterials (HMMs) are artificial subwavelength uniaxial media with principal effective dielectric (magnetic) constants of different signs. The name comes from hyperbolic dispersion law inside HMMs compared with "elliptic" one in ordinary media. This feature of a hyperbolic medium leads to numerous potential applications [1].

One of the consequences of hyperbolic dispersion and a promising application of HMMs we are interested in is the enhancement of spontaneous emission [2]. That is when one places a fluorescent molecule in the vicinity of a HMM its spontaneous emission rate strongly increases. This phenomenon occurs because photonic density of states (DoS) in a HMM is increased. Thus, one can control DoS (or the Purcell factor what is an equivalent) with different designs of HMMs. Hence, the calculation of the Purcell factor is of particular interest.

Abstract concept of a medium with hyperbolic dispersion law can be realized in practice as a set of alternating layers of metal and dielectric with subwavelength thickness. It can be very fruitful to homogenize initially non-uniform structure and describe it by means of an effective medium. However, a conventional effective medium approximation (provided by Maxwell Garnett approach) is poorly suitable for the purpose of DoS calculation as it leads to non-physical infinite value of DoS. The reason for breakdown of Maxwell-Garnett approach is that it does not take into account spatial dispersion of the corresponding layered structure. Recently operator effective medium approximation (OEMA) which allows accounting for spatial dispersion was developed in [3]. Hence, OEMA makes possible more accurate calculation of DoS.

In this work we investigate non-chiral three layer metal-dielectric-metal unit cell which has only ε and μ as nontrivial effective material tensors due to the presence of inversion center. We use the method, described in [4], to calculate the terms of Baker-Campbell-Hausdorff series and show that converging DoS is provided within the fourth order of OEMA. As a conclusion we discuss the convenience of the use of effective medium parameters for the Purcell factor engineering.

[1] A. Poddubny, I. Iorsh, P. Belov, and Y. Kivshar, "Hyperbolic metamaterials," *Nat Photon*, vol. 7, no. 12, pp. 948–957, 2013. [Online]. Available: http://dx.doi.org/10.1038/nphoton.2013.243

[2] Z. Jacob, I. I. Smolyaninov, and E. E. Narimanov, "Broadband Purcell effect: Radiative decay engineering with metamaterials," *Applied Physics Letters*, vol. 100, no. 18, p. 181105, 2012. [Online]. Available: http://dx.doi.org/10.1063/1.4710548

[3] V. Popov, A. V. Lavrinenko, and A. Novitsky, "Operator approach to effective medium theory to overcome a breakdown of Maxwell Garnett approximation," *Phys. Rev. B*, vol. 94, p. 085428, 2016. [Online]. Available: http://link.aps.org/doi/10.1103/PhysRevB.94.085428

[4] M. W. Reinsch, "A simple expression for the terms in the Baker–Campbell–Hausdorff series," *Journal of Mathematical Physics*, vol. 41, no. 4, pp. 2434–2442, 2000.

RAPID PROTOTYPING OF NANOELECTRODE AND METAMATERIAL ARRAYS BY LIPID DIP-PEN NANOLITHOGRAPHY

Vytautas Navikas, Martynas Gavutis, Ramūnas Valiokas

Department of Nanoengineering, Center for Physical Sciences and Technology, Vilnius, Lithuania
vytautas.navikas@ftmc.lt

Dip-pen nanolithography (DPN) is a scanning probe-based fabrication technique that allows direct writing/arraying of different molecules including lipids [1]. It is useful for nanoscale chemistry studies as well as for rapid prototyping of micro/nano devices. Despite numerous previous studies on a variety of bifunctional reactive compounds (DPN inks), the method is limited by the rather slow transport from the scanning probe onto the substrate. To address the problem of the low process efficiency, we have explored the molecular ink (eicosanethiol – ECT) transport in a liquid-like carrying medium (dioleoyl-phosphatidylcholine – DOPC lipid). Our aim was to increase the surface patterning speed for nanofabrication of metal nanostructures.

First, we have characterized the diffusion behavior of the ECT ink. Also, we studied molecular deposits on Au surfaces formed of pure DOPC and DOPC/ECT mixtures, respectively, by using imaging ellipsometry. As expected, the pure DOPC carrying medium was completely removed by treatment in chloroform, whereas the ECT-containing mixed inks yielded self-assembled monolayers (SAMs) of different quality, depending on the patterning speeds. Upon employing the ECT SAMs as resists for wet chemical etching of Au in aqueous etchant solutions, they acted as a sufficient barrier for etching. A more detailed ink transfer analysis indicated, that the DOPC carrying medium enabled us to boost up the DPN patterning speeds up to 30 times as compared to the pure ECT thiol. Moreover, the molecular writing in the carrying medium allowed us to increase the overall writing capacity up to 50 times and to obtain cm-sized patterned surface areas while using a single regular scanning probe inked only once. Finally, to demonstrate the applicability of this technique, we fabricated single cell electrode arrays and metamaterial-like structures, similar to the previously reported arrays that displayed strong second harmonic generation [2].

To summarize, we have characterized for the first time the molecular transport of chemically reactive compounds in lipid medium. We have shown that for the low molecular weight alkylthiol inks this process is governed by the highly efficient lipid transfer allowing to reach DPN patterning speeds up to 100 μm s^{-1}. The high versatility of this desktop fabrication technique makes it a competitive alternative to more expensive and complex electron beam lithography, especially for rapid prototyping of mesoscopic metal structures.

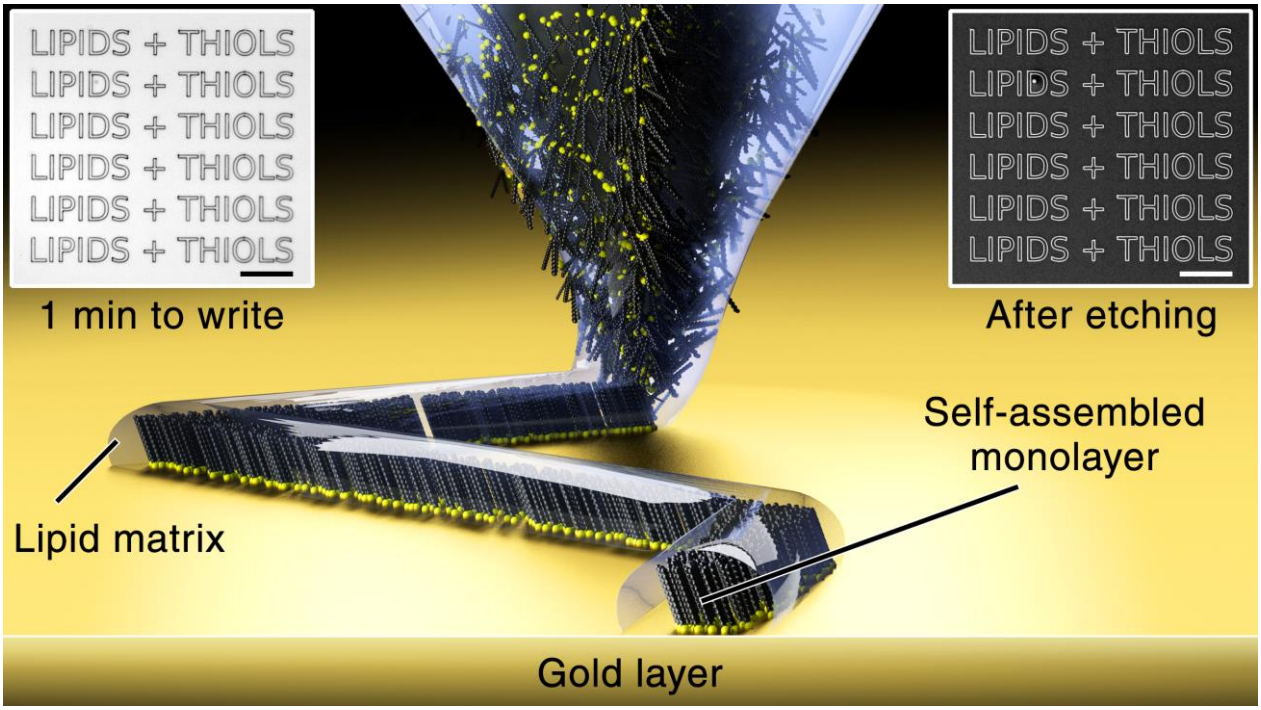

Fig.1 Schematic explanation of the lipid-mediated dip-pen nanolithography technique (not to scale). The insets show optical (left) and scanning electron microscopy (right) images of molecular and Au patterns, respectively. Scale bars are 20 μm.

[1] M. Gavutis, V. Navikas, T. Rakickas, Š. Vaitekonis and R. Valiokas, Lipid dip-pen nanolithography on self-assembled monolayers. J. Micromech. Microeng., **26** (2016).
[2] V. K. Valev et al., Nonlinear Superchiral Meta-Surfaces: Tuning Chirality and Disentangling Non-Reciprocity at the Nanoscale. Adv. Mater. **26**,

INVESTIGATION OF ELECTROCONDUCTIVITY AND LUMINESCENCE IN ORGANIC POLYMER THIN-LAYERS SYSTEM

Piotr Antoni Orłowski, Grzegorz Kołodziej, Bartłomiej Seredyński, Adam Wincukiewicz, Jakub Polaczyński, Arkadiusz Leniart, Maria Kamińska

Faculty of Physics, University of Warsaw, Poland
piotr.orlowski2@student.uw.edu.pl

Discovery of organic conductive polymers stimulated development of thin-layer, flexible electronic devices. For many years organic light emitting diodes (OLED) and organic photovoltaics (OPV) cells have been widely investigated because of unique properties which can be comparable with their non-organic semiconductor analogues. Simple fabrication and cheap depositing methods allowing to increase easily a range of production surpass disadvantages coming from typically lower efficiency of organic devices.

Nanotechnology is emerging field of natural sciences and it allows to improve parameters of many old-fashioned systems. Smaller crystallines allow not only to use less material, make devices smaller and, because of it, cheaper, but also often lead to better material parameters. Photoluminescence quantum efficiency of several zero-dimensional systems (so-called quantum dots (QD)) can surpass 50% [1]. Using them in hybrid QD-OLEDs can increase electroluminescence dozens times, for example ITO/TPD/QD/Alq_3/Mg:Ag QD-OLED structure surpasses luminescence efficiency of other similar devices 25 times [2]

Ease of controlling layer thickness by changing spin-coating speed (example of layer thickness control shown in Fig. 1) allows for a precise change of several parameters of a whole device. Solutions and liquid substances used in the spin-coating technique enable the smooth deposit of a single layer or even multilayer. Therefore, only a few fast and easy steps are required to achieve complexity of devices.

In this paper we present results of our initial work performed in aim to obtain cheap, efficient and flexible light source, based on QDs and organic thin layers. To construct QD-OLED with the following structure: ITO/PEDOT:PSS/CdSeQD/C_{60}/Al, we used spin coating deposition. Such prepared device was tested for luminescence efficiency and I-V characteristics. Similar system without QDs was also prepared by the same technique and used as a reference sample.

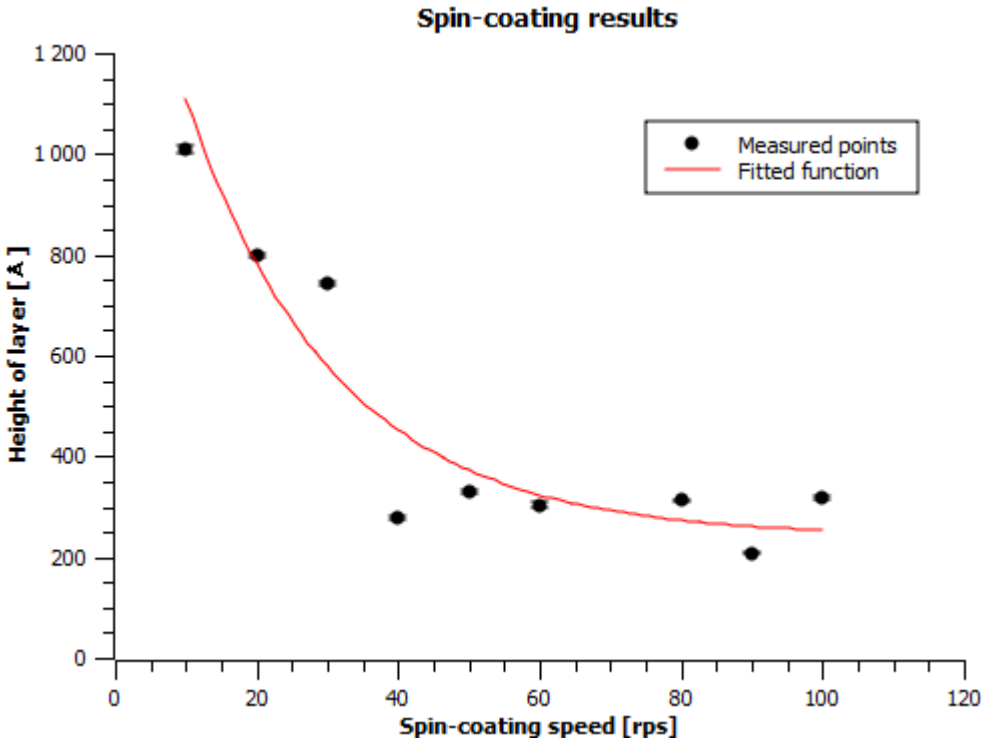

Fig. 1. Dependence of 0,5% P3HT $CHCl_3$ solution on spin-coating speed.

[1] Hines, M. A., \& Guyot-Sionnest, P. (1996). Synthesis and characterization of strongly luminescing ZnS-capped CdSe nanocrystals. The Journal of Physical Chemistry, 100(2), 468-471.

[2] Coe, S., Woo, W. K., Bawendi, M., \& Bulović, V. (2002). Electroluminescence from single monolayers of nanocrystals in molecular organic devices. Nature, 420(6917), 800-803.

NON-AGGLOMERATED $MgFe_2O_4$ NANOPARTICLES WITH INCREASED SATURATION MAGNETIZATION VALUE VIA ANNEALING IN NaCl MATRIX

Elena Petrova, Marina Roshchina, Vladimir Pankov

Department of Physical Chemistry, Belarusian State University, Belarus
petrovaeg@bsu.by

During last decades magnetic nanoparticles (MNPs) have attracted a lot of attention in different fields of industry, medicine and engineering [1]. Among them, MNPs based on magnetic iron oxides and ferrites are of great importance due to the possibility to tailor in a wide range the shape, size and magnetic characteristics of nanomaterials by varying synthesis conditions. Among other ferrites, magnesium ferrite ($MgFe_2O_4$) is of particular interest due to its high resistivity, photoelectrical properties and uniform characteristics [2]. However, the saturation magnetization of magnesium ferrite is quite low. One of the ways to increase ferrite magnetic properties, such as saturation magnetization, is thermal treatment of the nanoparticles. At higher temperatures a redistribution of metal ions in tetra- and octahedral sites occurs, which may result in the increase of magnetization.

For such applications as catalysts or adsorbents it is very important that nanoparticles have large surface area and saturation magnetization, so that the particles could be magnetically separated from the reaction media. One of the ways to produce ferrite nanoparticles with a high surface area to volume ratio and uniform size distribution is spray pyrolysis of inorganic metal salts solution. Further calcination of the produced MNPs results in the increase of crystallinity and magnetic properties. However, thermal treatment of the MNPs during both synthesis and calcination steps leads to the sintering of the particles and, therefore, to the decrease of the surface area.

In this work, magnesium ferrite nanoparticles were prepared via spray pyrolysis method in a nitrogen atmosphere at 700 ºC from a solution of magnesium and iron nitrates taken in stoichiometric ratio and then annealed at different temperatures (400, 600 and 800 ºC) to increase crystallinity and saturation magnetization of MNPs. Inert component of NaCl was added to precursor solution to prevent MNPs from agglomeration during pyrolysis and thermal treatment. After the annealing NaCl was removed by washing with deionized water. The morphology and phase composition of the MNPs was studied with XRD and SEM/TEM analysis, and magnetization curves were recorded at room temperature. The aim was to increase saturation magnetization of magnesium ferrite particles without a significant agglomeration of the MNPs during annealing.

Fig. 1. represents TEM images of the MNPs after annealing at different temperatures and removal of NaCl matrix. For the samples annealed at 400 and 600 ºC all the MNPs have a narrow size distribution with no significant increase in diameter as compared to as-prepared MNPs. For the MNPs annealed at 800 ºC the size distribution is less narrow and partial recrystallization leading to cutting of MNPs takes place. However, the number of inter-particle contacts is very low and NaCl matrix well prevents MNPs from sintering even at such a high temperature.

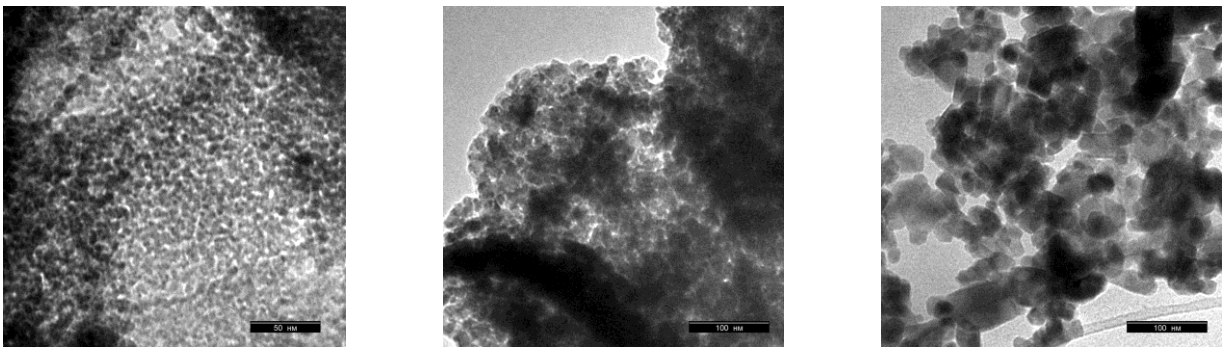

a b c

Fig. 1. TEM images of $MgFe_2O_4$ nanoparticles annealed at different temperatures:
a – 400 ºC, b – 600 ºC, c – 800 ºC.

The average nanoparticle size values for MNPs annealed at 400, 600 and 800 ºC were found to be around 10 nm, 20 nm and 30 nm (majority fraction), respectively. The saturation magnetization value of MNPs, however, increased significantly during annealing: from 14 emu/g in case of annealing at 400 ºC to 22 and 29 emu/g for 600 and 800 ºC, respectively. This proves the pyrolysis with sodium chloride and further annealing in NaCl matrix to be a good way to produce non-aggregated ferrite nanoparticles with high saturation magnetization value.

[1] J.W.M. Bulte, M.de Cuyper, D.Despres, J. A. Frank, Preparation, relaxometry, and biokinetics of PEGylated magnetoliposomes as MR contrast agent, Journal of Magnetism and Magnetic Materials **194**, Issues 1–3, 204-209 (1999).

[2] M. Sheykhan, H. Mohammadnejad, J. Akbari, A. Heydari, Superparamagnetic magnesium ferrite nanoparticles: a magnetically reusable and clean heterogeneous catalyst, Tetrahedron Letters **53**, Issue 24, 2959-2964(2012).

QUANTIFICATION OF AMPHIPHILIC POLYMER MOLECULES ON THE SURFACE OF HYBRID LUMINESCENT NANOCRYSTAL-POLYMER COMPOSITES FOR BIOMAGING

Aleksandra Fedosyuk[1], Aliaksandra Radchanka[1], Artsiom Antanovich[1], Anatol Prudnikau[1], Maksim V. Kvach[2], Vadim Shmanai[2], and Mikhail Artemyev[*,1]

[1] Institute for Physical Chemical Problems , Belarusian State University, Belarus
[2] Institute of Physical Organic Chemistry, National Academy of Sciences of Belarus, Belarus
aleksandraradchenko10@gmail.com

Highly luminescent nanocrystals (NCs) are considered to be attractive materials for a variety of applications in biological assays and detection platforms. Since, NCs are fabricated by using high-temperature methods, post-synthetic treatment is necessary to obtain water-soluble nanoparticles (NPs). The encapsulation of NCs with an amphiphilic polymer allows achieve high colloidal stability of NCs in aqueous solutions, while polymer side groups enables introduction of functional groups that can be further utilized for conjugation of NPs' with biomolecules and allows one to control hydrodynamic size and surface charge of NPs. The number and exact arrangement of polymer molecules on the surface of NPs, as well as the coverage density, are expected to be important parameters for regulatory requirements and quality control in clinical applications, and strongly influence the colloidal and chemical stability of NPs in a biological environment, their hydrodynamic size and zeta potential (ζ).

The aim of this work was to quantify the average amount of amphiphilic polymer molecules on the surface of colloidal semiconductor nanocrystals made of different materials, including CdSe, CdS, and ZnSe with ZnS shell, which have different size and shape (spherical (quantum dots) and elongated (nanorods)).

The idea of this experiment was to label amphiphilic polymer poly(maleic anhydride-alt-1-tetradecene) (PMAT) with a controlled amount of fluorescein-based dye as a marker for estimating the number of polymer chains on the surface of encapsulated NCs. The number of polymer chains per single NC was determined through optical absorption of the dye and NCs.

According to the obtained results, the number of polymer molecules attached to the surface of nanocrystals grows linearly with the surface area. At the same time, the surface area per single monomer (MAT) unit or equivalent average surface concentration of MAT units exhibits highly nonlinear character, because of the increased competition between PMAT molecules for surface binding sites. On the basis of experimental data we also proposed the model for the arrangement of PMAT-molecules on the surface of NCs of surface area (i.e. different size).

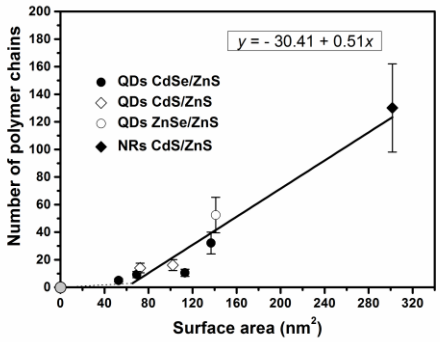

Fig.1. Average number of PMAT molecules per single NC versus the surface area of quantum dots (QDs) and nanorods (NRs). Black dots represent CdSe/ZnS QDs, white diamonds represent CdS/ZnS, white dot represents ZnSe/ZnS, and black diamond represents CdS/ZnS. The solid curve is a linear fitting to the equation y = −30.43 + 0.51x. Error bars represent 25% standard deviation, as determined from the statistical analysis of three different measurements.

Since zeta-potential (surface charge) of NCs is one of the key parameters that determines their colloidal stability, interaction with macromolecules, cell membranes, cell internalization and thus performance of NCs in a variety of biomedical assays, we also examined the influence of PMAT surface concentration on the zeta potential (ζ) of encapsulated NCs. The average value of zeta potential (ζ = - 35 mV) was found to be independent of the size, shape, and chemical composition of NCs at fixed buffer parameters (carbonate−bicarbonate buffer, pH 9.5 and 5 mM ionic strength). Since the surface charge density is proportional to the number of charged groups per unit area, the average value of zeta-potential at fixed buffer parameters can be further used as a reference point for the determination of the number of free carboxyl groups on the surface of PMAT-encapsulated NPs of different size and shape [1].

We acknowledge the financial support from Chemreagents Program. V.S. and M.K. acknowledge the financial support from the National Academy of Sciences of Belarus (3.1.03 "Convergence").

[1] Fedosyuk, A.; Radchanka, A.; Antanovich, A.; et al., Determination of Concentration of Amphiphilic Polymer Molecules on the Surface of Encapsulated Semiconductor Nanocrystals. Langmuir **32**, 1955–1961, (2016).

SOLVOTHERMAL SYNTHESIS OF COBALT FERRITE NANOPARTICLES

Simonas Ramanavičius[1,2], Arūnas Jagminas[1]

[1] State Research Institute Center for Physical Sciences and Technology of Physics, Lithuania
[2] Vilnius University, Faculty of Chemistry and Geosciences, Department of Physical Chemistry, Lithuania
simonas.ramanavicius@chf.stud.vu.lt

Superparamagnetic cobalt oxide nanoparticles are attractive candidates for magnetic resonance imaging of the body, magnetic field-assisted drug delivery and magnetothermal therapy. Thus it is important to obtain monodispersed particles with good magnetic characteristics. The size and stabilization shell of nanoparticles have high impact on these parameters [1,2].

This study is focused on the synthesis of cobalt ferrite ($CoFe_2O_4$) nanoparticles by high temperature solvothermal method seeking to better control their size, purity and magnetic properties. Solvothermal syntheses were performed using benzyl ether as solvent, Co(II) acetylacetonate and Fe(III) acetylacetonate as components of the reaction solution. Different additives, such as dodecylamine, oleylamine and oleic acid, were tested in order to obtain pure phase and monodisperse nanoparticles at a good yield. Scanning electron microscopy (SEM), Transmission electron microscopy (TEM) and X-ray diffraction (XRD) were employed in this study.

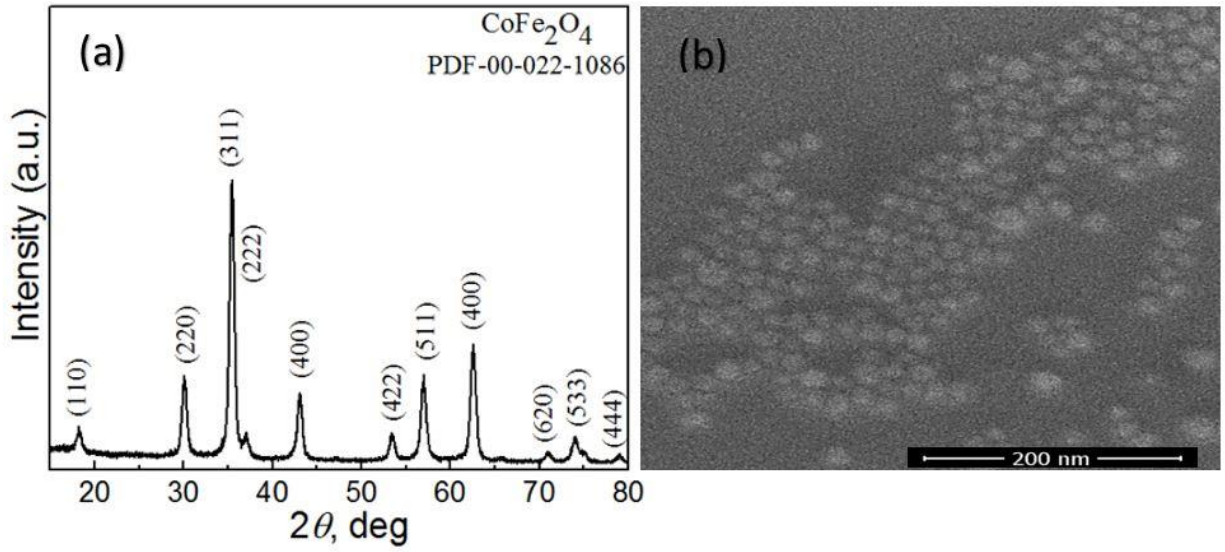

Fig. 1. Cobalt ferrite nanoparticles synthesized by solvothermal synthesis XRD pattern (a) and TEM image (b).

It was determined that high temperature solvothermal synthesis is good technique to obtain non-aggregated magnetic particles with low size distribution. As well, it was determined that it is possible to form 8-9 nm size cubic structure particles by adding oleic acid and removing water from the synthesis solution by evaporation before the synthesis begins (Fig. 1).

[1] G. F. Goya, T. S. Berquo, F. C. Fonseca, M.P. Morales. Static and dynamic magnetic properties of spherical magnetite nanoparticles. Journal of applied physics 2003;94(5): 3520-3528.. doi: 10.1063/1.1599959

[2] V. Pasukoniene, A. Mlynska, S. Steponkiene, V. Poderys, M. Matulionyte, V. Karabanovas, U. Statkute, R. Purviniene, J. Krasko., A. Jagminas, M. Kurtinaitiene, M. Strioga, R. Rotomskis. Accumulation and biological effects of cobalt ferrite nanoparticles in human pancreatic and ovarian cancer cells. Medicina. 2014;50(4):237-44. doi: 10.1016/j.medici.2014.09.009

ELEMENTAL AND PHASE ANALYSIS OF NANOSCALE STRUCTURES BY HRTEM

Martynas Skapas[12], Renata Butkutė[1], Arūnas Kadys[2], Valentina Plaušinaitienė[12]

[1] Center for Physical Research and Technology, Lithuania
[2]Vilnius University, Lithuania
Martynas.skapas@ftmc.lt

High Resolution Transmission electron microscopy (HRTEM) is the premier tool for understanding the internal microstructure of materials at the nanometer level. It allows one to obtain real-space images of materials with resolutions on the order of a few tenths to a few nanometers, depending on the imaging conditions, and simultaneously obtain diffraction information from specific regions in the images (e.g., nanoparticles)[1]. Variations in the intensity of electron scattering across a thin specimen can be used to image strain fields, defects such as dislocations and second-phase particles, and even atomic columns in materials under certain imaging conditions. In addition, the high-energy electrons (in Tecnai G2 F20 - 200 keV of kinetic energy) in TEM cause electronic excitations of the atoms in the specimen, thus allowing spectroscopic techniques make use of these excitations by incorporating suitable detector into the transmission electron microscope, such as energy-dispersive x-ray spectroscopy Nanometer-scale chemical compositional analysis can be performed by using a focused electron probe. Spatial distribution of elements can be obtained by scanning the probe over the specimen.

In this work, various TEM techniques are presented that were used for analysis of layered structures of GaAs, GaN and LSMO. Samples were prepared using Dual Beam Scanning microscope Helios Nanolab650. TEM images were obtained using 200kV TEM microscope FEI Tecnai G2 F20 equiped with Scaning module and High angle annular dark field detector for STEM mode, energy dispersive X-ray spectrometer EDAX, 11MPix ORIUS SC1000B (Gatan) CCD camera, single and double tilt specimen holders.

TEM allows making elemental analysis using energy dispersive X-ray spectrometer to be done in a very minute regions of sample. Features less than 10nm were be identified both by elemental and phase composition (fig. 1), compared with EDS resolution of SEM of around 1µm and XRD resolution of around 1mm.

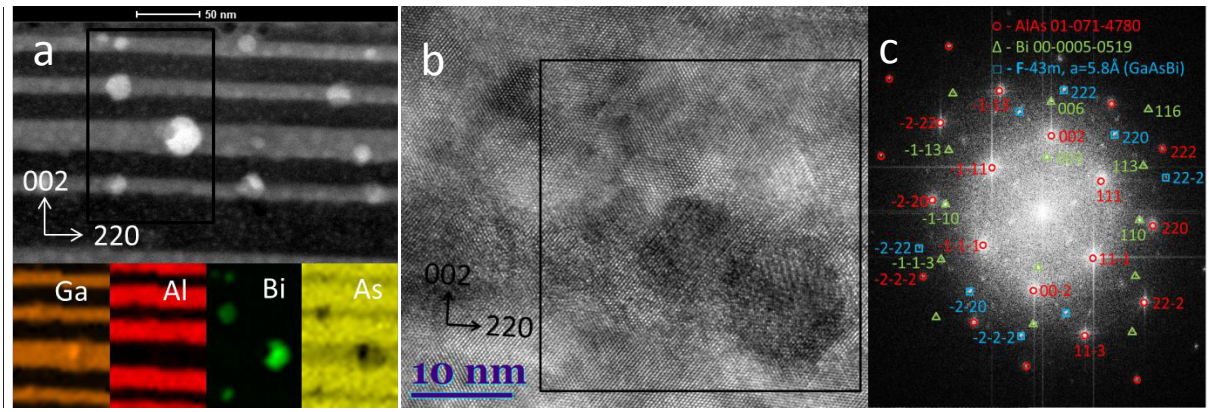

Fig. 1 a) STEM micrograph of GaAsBi-AlAs layered structure and corresponding elemental maps below, b) HRTEM micrograph of Bi nano-droplet and c) Fast-Fourier transform image of selected area in b) with assigned diffraction peaks

Other samples, such as GaN or LSMO thin layers were also investigated using Dark-Field imaging technique, that allowed analysis of polycrystalline films or crystal defects. Using this technique, image is formed from selected diffraction reflex only, so only desired orientation features are visible, while other parts of the sample remains in the dark-field.

[1] K. Melcher, L.-M. Ng, E. Zhou et al., Aberration corrected TEM: current status and future prospects, Journal of Physics: Conference Series **126** 012034 (2008)

RESISTIVITY AND LOW FREQUENCY NOISE CHARACTERISTICS OF EPOXY CARBON COMPOSITES

Marina Tretjak

Radiophysics Department, Vilnius University, Sauletekio 9, LT10022, Vilnius, Lithuania
marina.tretjak@ff.stud.vu.lt

Composite materials with carbon nano particles are potential candidates for being used in various nanostructures and nano-devices such as nano-sized transistors and bioelectronics devices, field effect transistors, nanoscale terahertz devices, inductors, sensors, etc. [1-4]. Those versatile applications are possible due to a unique combination of structural and physical properties presented by carbon nano particles composites, e.g. one-dimensional tubular structure, desired electrical, chemical and thermal properties, fast response, vapor adsorption, UV absorption, strength, durability and flame resistance.

It is worth mentioning an advantage of carbon nanotubes (CNTs): their presumed immunity to excess electrical noise that in general tends to increase dramatically as the dimensions of the devices decrease. Carbon nanotubes behaving as covalently bonded metallic wires might be less susceptible to such fluctuations. The strong carbon-carbon bonds that form the nanotube should indeed not be prone to electro-migration or defect propagation, which are two of the most important noise mechanisms in standard metal films and wires [5, 6].

Low frequency noise spectroscopy is an informative method for investigation of the charge carrier transport and conduction mechanisms in various materials [7, 8]. On the other hand, $1/f$ noise is an important consideration in assessing the potential of carbon nano particles composites for electronic and sensor applications. Therefore, aim of this work was to clear up noise and electrical transport properties of composites based on epoxy resin filled with various carbon nano inclusions.

Different nano carbon particles dispersed in epoxy resin were investigated: single-walled carbon nanotubes (SWCNTs), exfoliated graphite (EG), and high surface-area carbon black (CBH) [9]. EPIKOTE™ Resin 828 was used as composite matrix. It is a medium viscosity liquid epoxy produced from bisphenol A resin and epichlorhydrin. EPIKOTE 828 provides good pigment wetting and good resistance to filler settling and high mechanical and chemical resistance in the cured state. The concentration of fillers in all composites was 2 wt. % what is above the percolation threshold [9]. Resistance and low frequency (20 Hz – 20 kHz) noise characteristics have been carried out in temperature range from 73 K to 380 K.

Low frequency noise spectra of investigated materials comprises of $1/f^{\alpha}$ type components. $1/f^{\alpha}$ type fluctuations show that Mott's hopping and charge carrier capture and release processes in localized states dominate in the charge carrier transport in investigated materials. The temperature characteristic of the resistivity seconds this result: at low temperature, Mott's hopping and tunneling between conductive carbon particles dominate and percolation occurs at higher temperature. Above the polymer glass transition temperature (for SWCNT composites 292 K, for CBH composites 187 K, for EG composites 200 K) the resistivity of composites increases due to the rapid expansion of the polymer matrix what leads to the increase of the distance between conductive nanoparticles clusters and decreasing the electron tunneling current.

[1] T. Kawaharaa, S. Yamaguchia, Y. Ohnob, K. Maehashib, K. Matsumotob, S. Mizutanic, K. Itakad, Diameter dependence of 1/*f* noise in carbon nanotube field effect transistors using noise spectroscopy, Applied Surface Science 267, 101 (2013).
[2] B.S. Sreeja, Low-power CMOS LC QVCO using zero-biased transistor coupling of MWCNT network-based VCO structure, Microelectronics Journal 45, 196 (2014).
[3] T. Li, X. Liu, Ch. Dong, L. Yin, Single chip integration of MWCNTs/SiO_2 thin film humidity sensor based on standard CMOS IC process, Microelectronic Engineering 119, 155 (2014).
[4] B. Arash, Q. Wang, Detection of gas atoms with carbon nanotubes, Scientific reports 3, 1782 (2013).
[5] P. Dutta, P. M. Horn, Low-frequency fluctuations in solids: 1/*f* noise, Rev. of Modern Phys. 53, 497 (1981).
[6] J. W. Eberhard, P. M. Horn, Excess 1/*f* noise in metals, Phys. Rev. B 18, 6681 (1978).
[7] C. Barone, G. Landi, C. Mauro, H. C. Neitzert, and S. Pagano, Universal crossover of the charge carrier fluctuation mechanism in different polymer/carbon nanotubes composites, Appl. Phys. Lett. 107, 143106, (2015).
[8] M. Arjmand, M. Mahmoodi, G. A. Gelves, S. Park, U. Sundararaj, Electrical and electromagnetic interference shielding properties of flow induced oriented carbon nanotubes in polycarbonate, Carbon 49, 3430 (2011).
[9] A. Celzard, S. F. Mareche, G. Furdin, Modelling of exfoliated graphite, Prog. Mater. Sci. 50, 93 (2005).

STRUCTURE AND MECHANICAL PROPERTIES OF AlCuNiFeCr HIGH ENTROPY ALLOY REZULTED FROM MECHANICAL ALOYING, ANNEALING AND SINTERING

Chernyavsky Vadim, Kurasova Margarita, Gandzyuk Sergii, Yurkova Alexandra

National Technical University of Ukraine "Igor Sikorsky Kiev Polytechnic Institute",
vadikv13@gmail.com

As a new focus on materials research and a novel alloy design concept, high entropy alloys (HEAs) have been achieved successfully and have attracted great attentions of material researchers since it was proposed in 2004 [1,2]. HEAs exhibit promising future for engineering applications due to their good thermal stability, high hardness and high strength, excellent wear resistance, as well as many other outstanding properties [3,4]. Most of multi-component high entropy alloys were designed as equi-atomic or near equi-atomic and were mainly prepared by vacuum arc melting.

This study reports the structural evolution of equiatomic AlCuNiFeCr high-entropy alloy from elemental materials to solid solution during mechanical alloying (MA), and further, to equilibrium phases during subsequent thermal annealing and sintering. The effects of milling duration and subsequent annealing at temperatures ranging from 500 to 1000 °C on the structure and phase transformation were investigated by means of Rigaku Ultima IV X-ray diffractometer (XRD) with Cu Kα radiation. A scanning electron microscope with an energy dispersive spectrometer (EDS) was used to observe microstructures and measure the composition of powder alloy. The thermal analysis in the temperature range of 50–1430 °C was carried out in a STA449F1 differential scanning calorimeter (DSC) at a heating rate of 20 K/min under flowing purified argon atmosphere. It was justified experimentally that MA of Al-Cu-Ni-Fe-Cr powder mixture during 5 hours resulted in a single-phase nanocrystalline HEA with a structure of BCC-solid solution (Fig. 1). BCC solid solutions appear when the blended powder is ball milled more than 1h. The 5h ball milled alloy powder shows excellent chemical homogeneity and refined morphology with mean particle size of less than 10 μm. The microscaled particles are actually hard agglomerations of nanoscaled crystallites with crystal size of about 20 nm. During thermal annealing recovery and recrystallization of the BCC solid solution take place at temperatures ranging from 120 to 550 °C, and precipitation of second phase with FCC structure and grain growth of equilibrium phases occur at higher temperatures (Fig. 2). The phase composition transforms to BCC and FCC solid solutions when the mechanically alloyed powder was annealed at 500 °C for 1h. After annealing at 600 ºC, the XRD pattern exhibits small FCC1(α_1) peaks along with BCC and FCC peaks. The BCC and FCC solid solution structures can be maintained even after the alloy was annealed at 1000 °C. Simple equilibrium phases obtained in the annealed state of MA powders confirm that the high-entropy effect enhances the formation of simple solid solution phases instead of complex compound phases.

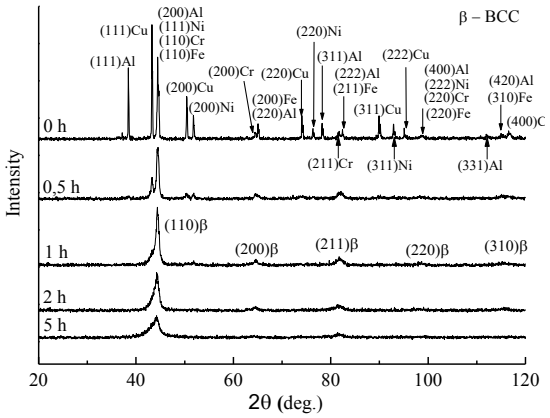

Fig. 1. XRD patterns of MA AlCuNiFeCr Powders with different milling times

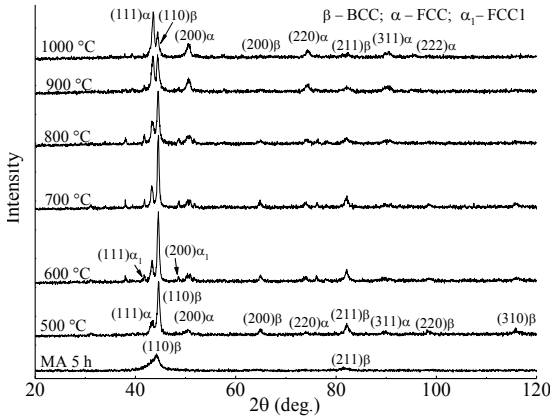

Fig. 2. XRD patterns of MA AlCuNiFeCr HEA powders after thermal annealing at different temperatures

The 5h milled alloy powder was subsequently consolidated by sintering under pressure 5 GPa and SPS at 800 °C for 30 and 15 min, respectively. The alloy with a density of 99 % after sintering exhibits excellent mechanical properties. The yield stress, Young modulus, and Vickers hardness of the alloy after sintering under pressure are 3.05, 148 and 9.2 GPa, and those after SPS are 2.8, 143 and 8.5 GPa, respectively.

[1] J.-W. Yeh, S.K. Chen, S.J. Lin, et. al., Nanostructured high-entropy alloys with multiple principal elements: novel alloy design concepts and outcomes, Adv. Eng. Mater. **6**, 299-303 (2004).

[2] B. Cantor, T.H. Chang, P. Knight et. al., Microstructural development in equiatomic multicomponent alloys, Mater. Sci. Eng. A. **375–377**, 213-218 (2004).

[3] C.Y. Hsu, J.-W Yeh, S.K. Chen et. al., Wear resistance and high temperature compression strength of FCC CuCoNiCrAl0.5Fe alloy with boron addition, Metall Mater. Trans. A. **35**, (1465–1469) 2004.

[4] S Varalakshmi, M. Kamaraj, B.S. Murty, Processing and properties of nanocrystalline CuNiCoZnAlTi high entropy alloys by mechanical alloying, Mater. Sci. Eng. A. **527** (1027–1030) 2010.

INFLUENCE OF MODIFIED DETONATION NANODIAMONDS ON ELECTRO-OPTICAL PROPERTIES OF NEMATIC LIQUID CRYSTALS

Vera Vashkevich[1], Valery Lapanik[2], Krystina Volk[1], Anatolij Minko[1]

[1] Department of Physical Optics, Belarusian State University, Belarus
[2] Institute of Applied Physics Problems, Belarusian State University, Belarus
vera-live93@mail.ru

Dispersion of different nanoparticles (NPs) has attracted attention of many researchers to improve electro-optical properties of liquid crystals (LCs) in recent years [1-4]. In the present study, we carried out a complex research of the effect of modified detonation nanodiamonds (DND) on electro-optical characteristics of NLC. Nanodiamonds are unique carbon NPs because of their intrinsic hydrophilic surface. The surface contains a complex array of chemical groups, including carboxylic acids, esters, ethers, lactones and amines. Alteration of DNDs surface can lead to a bunch of chemical properties, which can be compared with nanoscale diamond powders, since almost 15% of all atoms in the DND primary particle are located on the surface and, therefore, can dissolve. DNDs show potential for applications in energy storage, composites and catalysis. Besides, DNDs can be used in electroanalysis, electrochemical doublelayer capacitors and batteries. Other potential is biomedical applications including usage of nanodiamonds as supporters for solid-phase peptide synthesis and as sorbents for detoxification and separation.

To modify the structure of detonation nanodiamonds (DNDs) several carboxylate groups were added to DNDs. Activation of COOH-surface functionalized groups allowed attaching of various organic tails to molecules. It was investigated that dielectric and electro-optical properties of nematic liquid crystalline mixtures (LCMs) doped with modified DNDs (MDNDs). For the LC base two mixtures with different polar liquid crystalline compounds were prepared. M-1 is the mixture based on the compound with the NCS end group, M-2 is the mixture based on the compound with the CN end group (50%) and F atom (50%). The conglomerates based on 4-octylphenyl DNDs with a size of about 50 nm led to N-4. 0.5% of N-1, N-2, N-3, N-4 were added to the mixtures M-1 and M-2, leading to NLH-1, NLH-2, NLH-3, NLH-4 and NLH-5, NLH-6, NLH-7, NLH-8, respectively.

We demonstrated that the influence of DND on mesomorphic, dielectric and electro-optic properties of LC depends on the size of NPs and the type organic molecules grafted to DND. It was found that NPs of a small size (5–6 nm) do not significantly affect on the parameters of LCMs. At the same time conglomerates of a larger size (50 and 100 nm) depending on the tails polarity can increase or decrease the dielectric anisotropy and response time of LCMs in about 1.2–1.4 times.

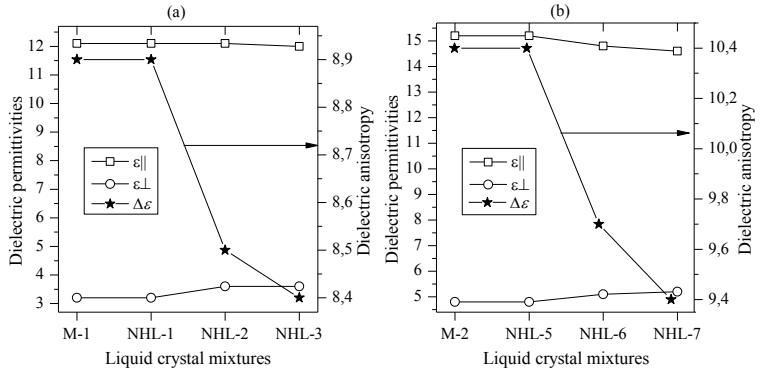

Fig. 1. Dependence of dielectric permittivity and dielectric anisotropy of M-1 (a) and M-2 (b) on the size of NPs.

To test the impact of such NPs on the parameters of compositions based on compounds with different polar groups compositions based on compounds with the isothiocyanate polar group (NCS) and with cyano group (CN) and F atoms were investigated. DNDs of various doping concentrations were dispersed in NLCs cells. The dependence of mesomorphic, dielectric and electro-optic properties of LCs on the NPs size and a type of organic molecules grafted to DNDs was shown. The grafting of polar fragment (dicyano-4-4'-biphenyl) to DND leads to increasing of dielectric anisotropy and switching time while non-polar fragment (4-octylphenyl) grafted to DNA leads to decreasing of listed properties. The change of the dielectric anisotropy and switching time is caused by the increase of the amount of DND particles.

[1] Neeraj, K.K. Raina. Nickel nanoparticles doped ferroelectric liquid crystal composites. Optical Materials 35 (3), 531–535 (2013).
[2] Al-Hazmi, F., Al-Ghamdi, A.A., Al-Senany, N., Alnowaiser, F., Yakuphanoglu, F. Dielectric anisotropy properties of nanostructure metal oxide semiconductor and 4-4′-n-pentylcyanobiphenyl based on nano-nematic composite systems. Journal of Molecular Liquids 190, 169–173 (2014).
[3] Avsec, M., Mertelj, A., Drevensek-Olenik, I., Mrzel, A., Copic, M. Visco-elastic properties of nematic- MoS_2 nanotubes mixtures. Molecular Crystals and Liquid Crystals 435 (1), 163-172 (2005).
[4] Ha, Y.-S., Kim, H.-J., Park, H.-G., Seo, D.-S. Enhancement of electro-optic properties in liquid crystal devices via titanium nanoparticle doping. Optics express 20 (6), 6448-6455.

TRANSFORMATION OF PHYSICAL PARAMETERS OF MICROWAVE DIODES ON THE BASE OF MODULATION DOPED SEMICONDUCTOR STRUCTURES UNDER LIGHT ILLUMINATION.

Maksimas Anbinderis

Department of Electronics, National Centre for Physical Sciences and Technology,
Saulėtekio av. 3, Vilnius LT-10257 Lithuania
maksimas.anbinderis@ftmc.lt

New techniques of detection of electromagnetic radiation in microwave and millimeter wave range, can be realized using microwave diodes on the base of modulation doped semiconductor structures. It was stated before, that microwave diodes on the base of semiconductor heterojunction are proper competitors for widely known sensitive Schottky diode detectors of microwave radiation in millimeter wavelength range [1]. In this paper, the results of investigation of the detection of microwave radiation under light illumination using microwave diodes on the base of modulation doped semiconductor structures are presented.

First experimental results show that measured diodes I-V characteristics and corresponding physical parameters can be transformed under light illumination. Figure 1 shows how measured microwave diode's I-V characteristics asymmetry can be changed by applying light illumination. Figure 2 shows how detected voltage depends on the illumination when applying electromagnetic radiation of 30 GHz frequency.

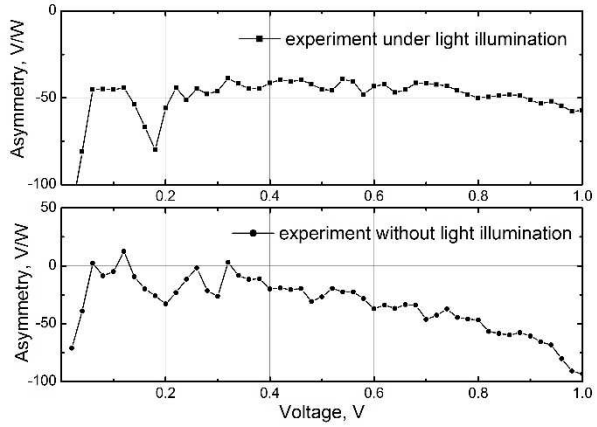

Fig. 1. The dependence of asymmetry of I-V characteristics of the microwave diodes on voltage under light illumination and without it.

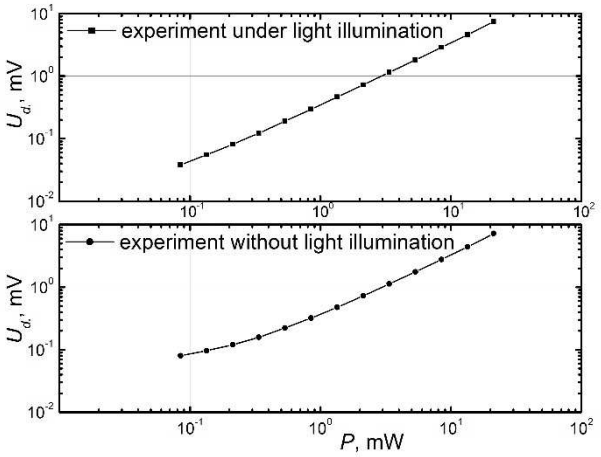

Fig. 2. The dependence of detected voltage of the microwave diodes on power under light illumination and without it.

A high frequency probe station for the detection measurements was used. Usual method to investigate high frequency parameters of the microwave diodes is to mount the single diode into microwave transmission line with following measurements of the detected voltage, for example. However, this is a time consumable process [2]. Using probe station is a modern and time saving technique for measuring the high frequency parameters of the microwave diodes.

[1] J. Gradauskas, A. Suziedelis, S. Asmontas, et al., Sensitive planar semiconductor detector from microwave to infrared applications, *IEEE Sensors Journal*, Vol. 10, No. 3, 662–667 (2010).
[2] A. Sužiedėlis, S. Ašmontas, J. Gradauskas, et al., Investigation of Microwave Properties of Planar Heterojunction Diodes in Ka Frequency Range Using Probe Station, in Proceedings of The Progress in Electromagnetics Research Symposium (PIERS 2016), Shanghai, China, 8–11 August, 3899-3903 (2016).

ANALYSIS OF InGaN STRUCTURES USING TIME–RESOLVED SPECTROSCOPIC TECHNIQUES

Milda Budreckaitė[1], Kazimieras Nomeika[2], Ramūnas Aleksiejūnas[3]

[1] Faculty of Physics, Vilnius University, Sauletekio ave. 9, LT–10222, Vilnius, Lithuania
[2, 3] Department of Semiconductor Optoelectronics, Institute of Applied Research, Sauletekio ave. 3, LT–10257, Vilnius, Lithuania
milda.budreckaite@ff.stud.vu.lt

InGaN has a direct band gap that covers the range from 0.65 to 3.4 eV, depending on indium content. Technically, InGaN is suitable for light emitting diodes (LED) emitting in the entire visible spectrum [1]; however, it is increasingly difficult to achieve an efficient yellow or red InGaN-based LED, a problem known as a green gap [2]. The green gap is caused mainly by decreasing material structural quality and increasing internal electric field, as indium content is increased [3]. Therefore, an improvement of growth techniques, allowing for higher quality InGaN layers, is in great demand. In this work, we study the impact of interrupted metalorganic chemical vapor deposition (MOCVD) growth method on InGaN electrical properties.

6 InGaN quantum well structures were grown by interrupted MOCVD method on c-plane sapphire substrates. The samples were grown by varying the duration of interruptions of metal precursor flow during the InGaN well growth; all samples are consisted of five InGaN quantum wells (QWs), separated by a several times thicker GaN quantum barrier (QB) [4]. For measurements, we used the differential transmission (DT) and photoluminescence (PL) techniques. For the evaluation of PL quantum efficiency (QE) we applied the three-measurement approach with an integrating sphere [5].

We demonstrate that the carrier lifetime increases with the increasing duration of metal precursor flow interruption (Fig. 1a). This can be a result of a more homogeneous distribution of indium atoms on the growth surface during the longer pause. We also show that longer lifetime results in higher quantum efficiency of the quantum well structure (Fig. 1b). This correlation points out to lower defect density in the samples grown with longer interruptions of metal precursor flow. On the negative side, a longer interruptions result in blue shift of PL spectra, probably due partial evaporation of indium atoms.

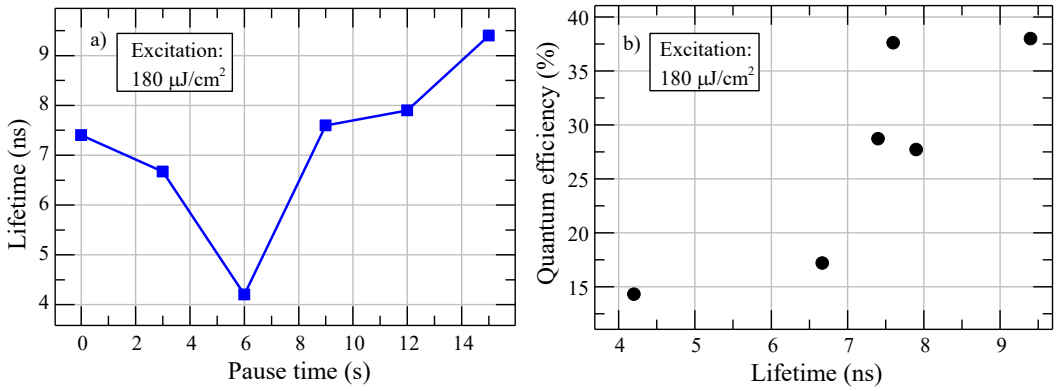

Fig. 1. Carrier lifetime dependence on pause time (a) and correlation between quantum efficiency and carrier lifetime (b).

[1] S. Saito, R. Hashimoto, J. Hwang, and S. Nunoue, "InGaN Light-Emitting Diodes on c -Face Sapphire Substrates in Green Gap Spectral Range," *Appl. Phys. Express*, vol. 6, no. 11, p. 111004, 2013.
[2] S. Pleasants, "LEDs: Overcoming the 'green gap,'" *Nat. Photonics*, vol. 7, no. 8, pp. 585–585, 2013.
[3] J. Xie, X. Ni, Q. Fan, R. Shimada, U. Özgür, and H. Morkoç, "On the efficiency droop in InGaN multiple quantum well blue light emitting diodes and its reduction with p-doped quantum well barriers," *Appl. Phys. Lett.*, vol. 93, no. 12, pp. 121103–121107, 2008.
[4] M. Dmukauskas, A. Kadys, T. Malinauskas, T. Grinys, I. Reklaitis, K. Badokas, M. Skapas, R. Tomašiūnas, D. Dobrovolskas, S. Stanionytė, I. Pietzonka, M. Strassburg, H-J Lugauer, "Influence of metalorganic precursors flow interruption timing on green InGaN multiple quantum wells."
[5] S. Leyre *et al.*, "Absolute determination of photoluminescence quantum efficiency using an integrating sphere setup Absolute determination of photoluminescence quantum efficiency using an integrating sphere setup," vol. 123115, pp. 1–10, 2014.

INVESTIGATION OF EXCITON DIFFUSION AND ANNIHILATION IN BIFLUORENE SINGLE CRYSTAL

Vladislavas Čerkasovas, Paulius Baronas, Gediminas Kreiza, Povilas Adomėnas, Ona Adomėnienė, Karolis Kazlauskas and Saulius Juršėnas

Institute of Applied Research, Vilnius University, Saulėtekio 3, LT-10222 Vilnius, Lithuania
vladislavas.cerkasovas@ff.stud.vu.lt

A majority of non-organic semiconductor devises have found organic substitution: organic light emitting devices (OLED), thin film transistors (OTFT), photovoltaics (OPV) and etc. However, an electrically pumped organic laser is still on demand [1]. One of the promising material families for organic laser applications are bifluorene compounds. These compounds have been investigated in previous researches and the promising properties such as low spontaneous emission threshold, low reabsorption and controllable intermolecular coupling have been found [2].

Without properties mentioned above organic laser operation strongly depends on excitonic processes such as exciton diffusion and annihilation. This reason encouraged to investigate these properties in bifluorene single crystal in more detail.

Exciton diffusion coefficient and diffusion length in current research were determined by measuring efficiency of exciton-exciton annihilation. This was realized by measuring and further theoretical modeling of transient absorption decay curves. One and three dimensional models were applied and compared. One dimensional model showed better compatibility with experimental data. This result indicates anisotropic behavior of exciton diffusion in bifluorene crystal.

The fits of one dimensional annihilation model (fig. 1) resulted in diffusion coefficient $D \approx 0.3$ cm^{2}s^{-1} and diffusion length $L_D \approx 120$ nm at relatively low exciton densities (below 1×10^{17}). At high exciton densities (4.5×10^{17}) increase of diffusion coefficient up to 0.7 cm^{2}s^{-1} can be observed (fig. 1). This can be an outcome of local heating which occurs at high excitation intensities [3]. To approve this assumption diffusion coefficient was measured at different sample temperatures. This research revealed that exciton diffusion in bifluorene single crystal is temperature dependent and increases at high temperatures.

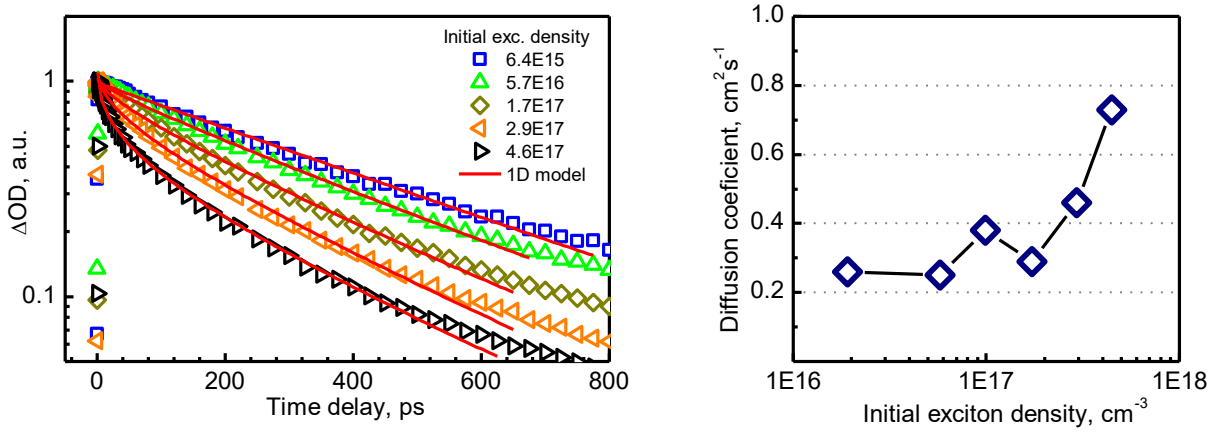

Fig. 1. On the left: transient absorption decay curves measured by pump-probe experiment at different initial exciton densities. Open dots represent experimental data and solid curves show appropriate theoretical fits. On the right: calculated values of diffusion coefficient at different excitation intensities.

[1] A. J. C. Kuehne, M. C. Gather, "Organic Lasers: Recent Developments on Materials, Device Geometries, and Fabrication Techniques" Chem. Rev. **116**, 13823-12864 (2016).

[2] G. Kreiza, P. Baronas, E. Radiunas, P. Adomėnas, O. Adomėnienė, K. Kazlauskas, J. C. Ribierre, C. Adachi, S. Juršėnas, "Bifluorene single crystals with extremely low-threshold amplified spontaneous emission", Adv. Opt. Mater. (2017).

[3] O. Mikhnenko, F. Cordella, A. Sieval, J. Hummelen, P. Blom, and M. Loi, "Temperature dependence of exciton diffusion in conjugated polymers", J. Phys. Chem. B. **112**, 11601–11604 (2008).

THE FOURIER MOBILITY SPECTRUM ANALYSIS APPLICATION TO BI-SN SUPERDILUTED ALLOYS

Alexander Fedotov[1], Sergey Perevoznikov[1,2], Uladzislau Humennik[1]

[1]Physics Faculty of Belarusian State University
[2]Research Institute for Physical Chemical Problems of the Belarusian State University
fedotov.alehandro@gmail.com

The Bi-Sn system is the promising basic compound for thermoelectrical *p*-type materials at low and medium temperatures [1].

The presence of several types of charge carriers (light electrons, light and heavy holes) encourages the researchers for the search of suitable galvanomagnetic methods for electronic properties characterization. Standard formulas for magnetoresistance and Hall coefficient are not applicable, so we propose the approach based on Fourier Mobility Spectrum Analysis (FMSA) technique.

We choose doping level of Bi_x-Sn_{1-x} small enough ($x \leq 0.08$ at. %) to keep dispersion law and electronic bands shape of Bi unchanged. The rapid solidification method allows the cheap synthesis of uniform polycrystalline samples (30 μm thickness, less than 1% surface roughness). We measured magnetoresistance and Hall coefficient (see Fig.1(a)) in temperature range 4−300 K tunder magnetic fields up to 8 T. Then, we determined magnetoconductivity tensor components from galvanomagnetic data for usage as the input to the FMSA code.

The FMSA code was implemented with Fourier-space fitting algorithm in addition to standard iterative fitting in direct-space and including derivatives to mean squared error [2]. Several versions of the code were made in different languages. The Fortran version of code proved itself to be the fastest, Fig.1(b).

The concentrations, mobilities and Fermi level temperature dependences were estimated for the studied range of Bi doped with Sn for the first time. For the He temperatures the comparison between our result and Fermi level found from the Shubnikov-de Haas oscillations [3] showed good coincidence (see Fig.1(c)).

The presented technique allowed us to extract not only low-temperature position of Fermi level but all the temperature range dependence of Fermi level. It was found that temperature dependences do not match with the Sommerfeld expansion due to significant relative changes in Fermi level values with temperature.

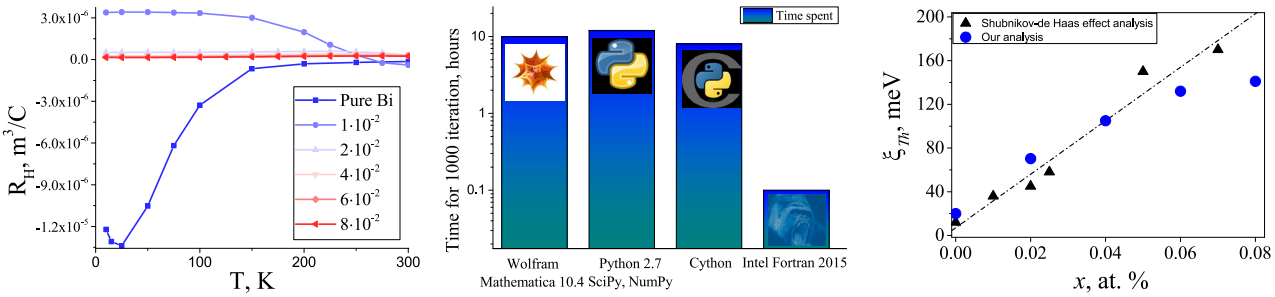

(a) (b) (c)

Fig. 1. (a) - temperature dependence of low-field Hall coefficient R_H ($B \approx 10^{-2}$ T) (b) - the comparison of time required for 1000 iteration on the same computational problem, (c) - the comparison of concentration dependences of Fermi level ξ_{Th} counted from the top of T-point for our analysis (round dots) and literature data (squared dots)

We thank the Belarusian Republican Foundation for Fundamental Research for the financial support given to project F16M-067 which made this research possible.

[1] Sung Hoon Park, Seungki Jo, Beomjin Kwon et al., High-performance shape-engineerable thermoelectric painting, Nature Communications **7**, 13403 (2016).

[2] I. Vurgaftman, J. R. Meyer, C. A. Hoffman et al., Improved quantitative mobility spectrum analysis for Hall characterization, Journal of Applied Physics **84** , 4966-4973 (1998).

[3] A. Nikolaeva, D. Gitsu, T. Huber et al., Thermoelectric properties of quantum Bi wire doped with Sn and electron topological transitions induced by stretch and doping, Reviews on Advanced Material Science **8**, 73-78 (2004).

PIEZOMAGNETISM IN FESE

Tatyana Gaydamak[1], Galyna Zvyagina[1], Konstantin Zhekov[1], Igor Bilich[1], Dmitriy Chareev[2]

[1] B. Verkin Institute for Low Temperature Physics and Engineering,
47 Lenin Ave., 61103 Kharkov, Ukraine
[2] Institute of Experimental Mineralogy, Chernogolovka, Moscow Region, 142432, Russia
gaydamak@ilt.kharkov.ua

The results of experiments on acoustic-electric transformation (AET) in high-quality single crystals $Fe_{0.963 \pm 0.005}Se$ indicating the existences of the piezomagnetic effect in them are presented.

Let us say a few words about the ideology of the AET experiment. A transverse elastic wave with the wave vector q = (0, 0, q) and the displacement vector u = (u, 0, 0) enters into the sample through a delay line. This wave produces an electromagnetic field (EMF) which forces free electrons to move to compensate the initial disturbance. The resultant current and the resultant electrical component of the EMF are aligned along the *x*-axis. In the magnetic field H = (0, 0, H) the Lorenz force applied to free electrons results in the appearance of the *y*-components of the current and the electrical field (the Hall components). So in the absence of magnetic order and the external magnetic field we can observe only *x*-component of the electrical field.

In spite of this in the absence of an external magnetic field were recorded signals of AET, in FeSe single crystals, observed in the Hall-polarization. The signals appear below the temperature of solidification of the silicon oil (T ~ 110K), used as bonded material.

Two effects may provide the Hall current in the absence of the magnetic field. They are the anomalous Hall effect (AHE) and piezomagnetic (PZM) effect and both of them are realized in magnetically ordered media. Our estimates indicate that the appearance of the signals can not be explained by AHE. As for PZM we obtained a quite reasonable estimate that is in one order less than the maximum know value for the PZM modulus which was measured in CoF_2 [1].

The explanation of our results in terms of the PZM effect immediately raises the question on the type of the magnetic structure in FeSe single crystals. It is obviously not an AFM in the common sense. It was shown in [1] that for the usual AFM the dependence of the PZM modulus on temperature reproduces the temperature dependence of the sublattice magnetization. But in our case the amplitude in the normal state increases almost linearly under decrease in temperature, and it does not show any tendency to the saturation. It is most likely that in case of FeSe we deal with a short range magnetic order. This conclusion correlates with an increase in AFM fluctuations in FeSe under approaching T_C [2]. But we note that in any case such fluctuations should have some preferable orientation of the antiferromagnetic vector.

The signal decreases below the temperature of the superconducting transition, but it does not disappear completely and saturates at the value easily accessible for the measurements. We believe the electromagnetic signal decreases with lowering of temperature due to the change in the London penetration depth. So we can measure the temperature dependence $\lambda^{-2}_L(T)$ and the value $\lambda_L(0) = 1.65$ μm. Our estimate for $\lambda_L(0)$ corresponds to the carrier density $n \sim 10^{19}$ cm^{-3}.

[1] A.S. Borovik-Romanov, G.L. Alexanjan, E.G. Rudashevskij, *Int. Conf. on Magnetism and Cryogenics,* Kyoto, (1961).
[2] T. Imai, K. Ahilan, F. L. Ning, T. M. McQueen, and R.J. Cava, Phys. Rev. Lett. **102**, 177005 (2009).

InN GROWTH ON GaN AND SAPPHIRE BY MOVPE AND CHARACTERIZATION

Marek Kolenda, Tadas Malinauskas, Darius Dobrovolskas, Arūnas Kadys

Institute of Applied Research and Semiconductor Physics Department, Vilnius University, Saulėtekio al. 9-III, Vilnius 10222, Lithuania
mkolendaus@gmail.com

The unique physical properties of indium nitride (InN) such as low effective mass, high electron mobility, saturation velocity and direct band gap make it a potential material for optoelectronic and microelectronic devices such as light emitters / detectors, high electron mobility transistor (HEMT) [1]. By changing the composition of In in gallium nitride (GaN), the band gap of $In_{1-x}Ga_xN$ can be tuned from 0.7 *eV* to 3.4 *eV* covering a broad range of spectrum from near infrared to ultraviolet regions [2]. However, the growth of high quality InN is a big challenge mainly due to low dissociation temperatures, high equilibrium vapor pressure of nitrogen and lack of lattice matched substrates [1, 3].

The main objective of this work was to perform technological growth experiments on a InN epilayers using MOVPE growth technology. Optimize growth parameters for InN layers on a GaN/sapphire templates. Carry out pilot growth experiments on the InN layers on a sapphire substrates to evaluate the possibilities of feasibility.

InN epilayers were grown on the GaN/sapphire templates and sapphire substrates by MOCVD (AIXTRON 3x2 FT reactor). Trimethylindium (TMIn) and ammonia (NH_3) have been used as precursors for indium (In) and nitrogen (N). During the growth of InN ammonia flux was flowing constantly, while TMIn flux was sent into reactor chamber in pulses of 7 *s* duration. A pause duration between metalorganic (MO) pulses was 20 *s.* This growth technique is called MO flow modulation or MO pulsed growth technique. Variable parameter was InN layers' thickness on the GaN/sapphire templates. InN layers on the sapphire substrates were gown by conventional method and variable parameter here was low temperature (LT) InN layers' thickness. Firstly, LT InN was grown on the sapphire. The growth process of LT InN was followed by baking process. At last, after the LT InN layers baking process high temperature (HT) InN layer was grown. Thickness of InN layers on the sapphire substrates was about 300 ÷ 400 *nm*.

The crystal quality of InN layers on the different substrates has been evaluated using high resolution X-ray diffraction measurements (HRXRD) (Fig. 1 a, b).

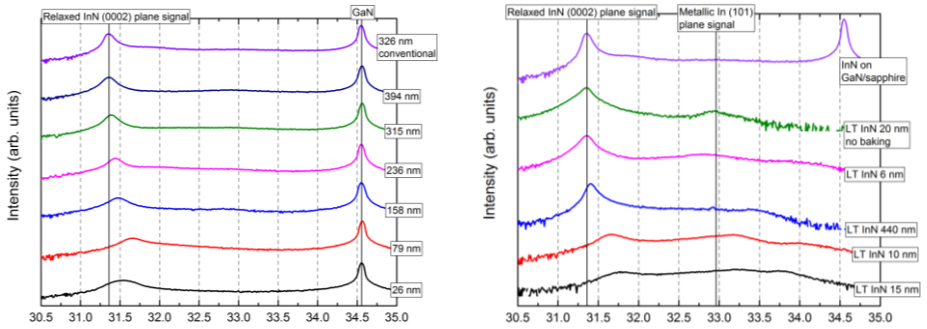

a) b)

Fig 1. XRD scans along (0002) direction for InN layers grown on GaN/sapphire (a) and sapphire (b) substrates.

From figure 1 (a) is seen, an increase of InN layer thickness to 79 *nm* results in a InN peak shift toward higher angles, indicating an increase in strain forces in those InN layers. Further increase in the InN layer thickness results in the InN peak shift to smaller angles, which means InN layers' relaxation. Black line shows an angle value of fully relaxed InN layer. The thinnest InN layer's XRD peak is quite broad compared to other InN peaks, which means that this layer is made of small, densely arranged InN islands. In the case of InN layers on the sapphire substrates (Fig. 1 (b)) two InN layers, which were grown on LT InN 15 *nm* and 10 *nm* have polycrystalline structure, because no clearly visible InN peak is seen in XRD scans.

In both cases the surface roughness of InN layers is quite high and are up to 55 *nm* and 85 *nm* for InN layers on the GaN/sapphire templates and sapphire substrates respectively. It could be due to different growth rates in *c* and *a* directions. InN layers on the GaN/sapphire templates grow in Stranski-Krastanov regime, because lattice mismatch between InN and GaN is ~11%. Between InN and sapphire lattice mismatch is ~25%, much higher than in the case of InN and GaN. In this case InN grows on the sapphire substrates in Volmer-Weber regime.

The optical properties of InN layers have been investigated by room temperature photoluminescence (PL). In both cases InN PL peaks were shifted toward higher photon energies from 0.7 *eV* due to Burstein-Moss effect. 70 *meV* shift was in the InN PL peak on the GaN/sapphire templates and 40 *meV* shift - in the InN on the sapphire substrates.

[1]. A. G. Bhuiyan, *et al*. J. Appl. Phys. 94, 2779 (2003)
[2]. L. H. Hsu, *et al*. Opt. Express 31150, 23, 24 (2015)
[3]. A. R. Acharya. Indium Nitride Surface Structure, Desorption Kinetics and Thermal Stability. Georgia State University. (2013)

HYDROGEN STATE TRANSFORMATION-DURING THE HEAT TREATMENT OF HYDROGENATED SILICON

Julia Kondratieva, Jury Pokotilo

Department of Physics, Belarusian State University, Belarus
julia_kondratieva@mail.ru

This study is aimed the investigation of the Si/P^+ structure, processed in hydrogen plasma. The processing was made at 150 ^{0}C during 10 hour. The spectra of Raman light scattering were recorded at room temperature using a Nanofinder High End (Lotis TII) – micro-Raman spectrometer, combined with 3D scanning confocal microscope. The spectra were recorded by the backscattering method, the resolution of the spectrometer was 0, 3 cm^{-1}. For the excitation, solid-state laser with a wavelength of 532 nm was used.

Figure 1(a) illustrates the spectra of Raman light scattering in the test samples after the 10 hours treatment in H-plasma (1) and after additional annealing at 275 ^{0}C for 20 minutes (2). In the first case, there are two intensive peaks detected at 2095 (Si-H) and 2129 cm^{-1} (1). Peak at 2095 cm^{-1} is related to silicon amorphization after the hydrogenation due to the formation of defects. The one peak at 2125 cm^{-1} with max indicator appear after an additional short annealing. This peak corresponds to the vibrations of bonds ($Si-H_2$) in platelets [1]. Additional heat treatment leads enhancement of the crystal structure and zone at 2095 cm^{-1} begins to disappear, because the annealing of main radiation donor -vacancy donor [2].

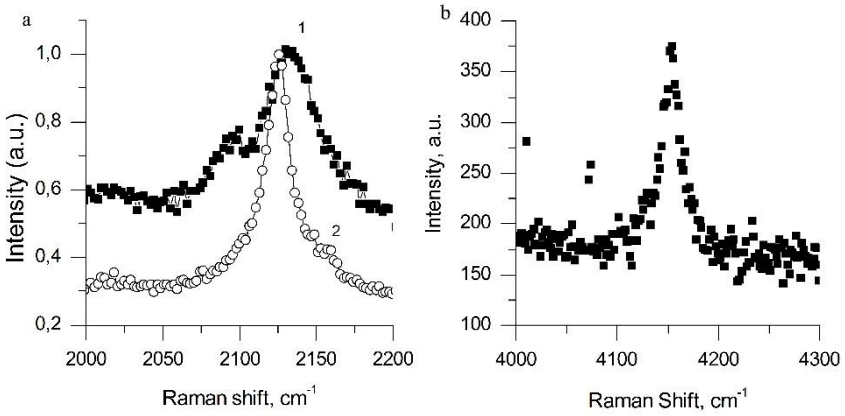

Fig.1. a. The spectrum of Raman scattering of light in the samples after treatment in a H -plasma (1) and after additional annealing at 275 ^{0}C for 20 minutes (2).
b. The spectrum of Raman scattering of light in the sample, which is processed in plasma and annealed at 275 ^{0}C for 20 minutes.

On the figure 1(b) one can see the spectra of Raman light scattering in the samples after the plasma treatment and further annealing. There is the peak at 4153 cm^{-1}, which is caused by the oscillations in hydrogen molecule. This frequency coincides with that of the hydrogen gas in [3]. Total energy of a hydrogen molecule is lower than the total energy of the two isolated neutral hydrogen atoms, and annealing of radiation defects leads to the restoration of broken bonds and the release of hydrogen released from the bound state. Indeed, the binding energy of the gap is about 1.8 eV, while the energy of diffusion of atomic hydrogen –is about 0.48 eV [3].

The work deals with the reasons for the origin of the H_2^* molecules and their interactions.

[1] E.I. Tyschenko, Crystallization in silicon-on-insulator films implanted with high doses of hydrogen ions, FTS **47**, 591-597 (2013).
[2] J.M.Pokotilo, A.N.Petuh, V.V.Litvinov, Hydrogen-containing donors formation in the epitaxial silicon implanted with protons. Inorganic materials. **45**, 1285-1287(2009).
[3] A.W.R. Leitch, J. Weber, V.Alex, Formation of hydrogen molecules in crystalline silicon, Mat.Science and Eng. B **58**, 6-10 (1999).

LUMINESCENCE IN YCAGG:Ce GLASS CERAMICS FOR WHITE LEDs

Vaida Marčiulionytė, Augustas Vaitkevičius[1], Yevgeny Tratsiak[2], Y. Bokshits[2], Andrei Borisevich[3], Mikhail Korjik[3], Gintautas Tamulaitis[1]

[1] Institute of Applied Research and Semiconductor Physics Department, Vilnius University, Lithuania
[2] Research Institute for Physical Chemical Problems, Belarusian State University, Belarus
[3] Research Institute for Nuclear Problems, Belarusian State University, Belarus
vaida.marciulionyte@ff.stud.vu.lt

Nowadays there is a high demand for energy efficient, high–power and high quality white light sources. The most promising device that satisfies all these requirements is the light–emitting diode (LED). However, several advances in LED technology still have to be made in order for them to be more widely used as light sources in household lighting. Currently blue-light LEDs and downconverting YAG:Ce phosphors encapsulated in silicon is the most commonly used method for producing white light. This approach suffers from a high thermal degradation rate and poor color rendering. Fortunately, color rendering properties can be improved by modifying the composition of the YAG host, while thermal degradation can be decreased by using glass ceramics.

We investigated heat–treated glass ceramics with composition $Y_2CaAlGe(AlO_4)_3$:Ce. After glass ceramics production two samples were further treated at 1300 °C and 1400 °C for 1 hour. An untreated sample was also investigated as a reference. The samples were produced in Belarusian State Technical University, Belarus.

The light–emitting properties of samples under study were investigated by measuring their photoluminescence (PL) spectra. The measurements were performed with a microscope system WITech Alpha 300 S in confocal mode. PL emission spectra was recorded using a spectrometer with a thermoelectrically cooled CCD camera. PL excitation was performed with a CW laser diode emitting at 405 nm (*ALPHALAS*) as well as a He-Cd laser emitting at 442 nm. Also photoluminescence at different excitation power densities was investigated. All measurements were performed at room temperature.

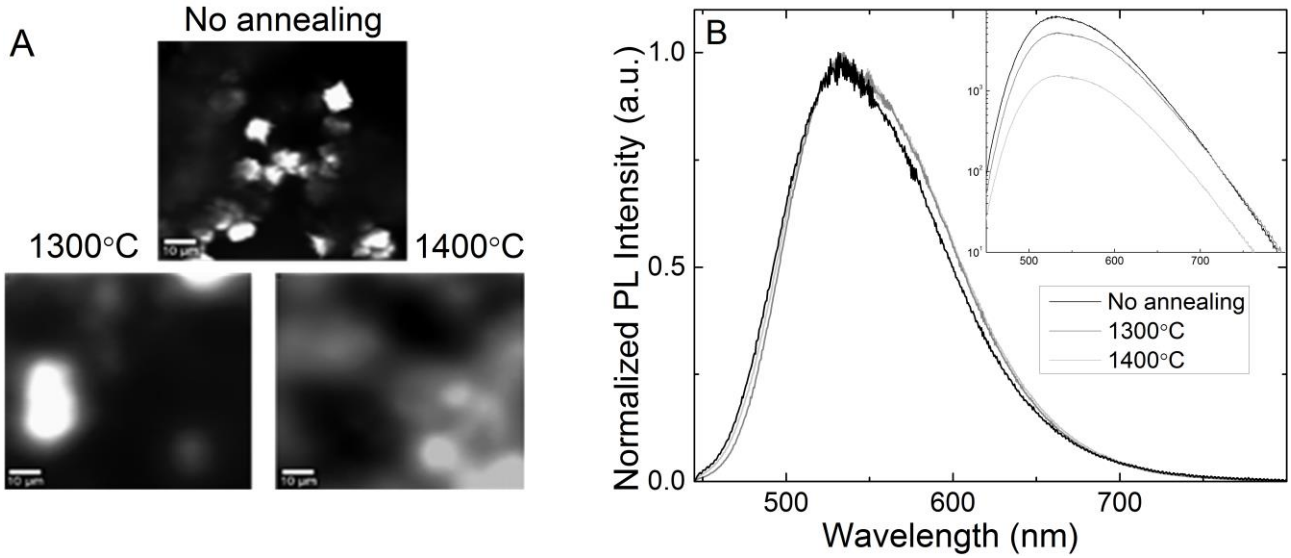

Fig. 1. Spectrally integrated PL Intensity distributions over 80×80 μm^2 area collected from samples after different thermal treatment, under 405 nm excitation (A). Normalized PL Intensity spectra collected from samples after different thermal treatment, under 405 nm excitation, inset shows spatially averaged PL Intensity spectra (B).

In the unannealed sample well defined, crystallite–like, structured areas are visible in the spectrally integrated PL Intensity distribution (Fig. 1 A). In comparison with other heat treated samples where there are no such defined areas. In the annealed samples only undefined, amorphous structures are visible. Comparison of spatially averaged spectra (Fig. 1 B) shows that average PL intensity of the annealed samples is lower than that of the unannealed sample. Additionally the FWHM of the PL spectra of annealed samples is larger, due to the longwave edge of the spectra being redshifted. The measurements performed with different excitation sources (405 nm and 442 nm) show that the spatial distributions of PL parameters are quite similar under different excitations. However, for the unannealed sample the bright PL areas are redshifted in comparison to the surrounding area when under 405 nm excitation. Under 442 nm excitation the bright areas are blueshifted relative to their surrounding area. Measurements over a wide range of excitation power densities reveal that the PL spectral shape is independent of excitation power and PL intensity increases linearly with increasing excitation density.

This widening and redshifting of the PL spectra is advantageous for producing warmer light sources, with better color rendering properties. As a result, the YCAGG:Ce ceramics are a promising candidate phosphor for white LEDs.

GROWTH OF THIN SILICON CARBIDE LAYERS ON SILICON-GERMANIUM BUFFERS

Andrei Novikau, Mikhail Lobanok, Stanislav Prokopyev, Peter Gaiduk

Department of Physical electronics and nanotechnology, Belarusian State University, Minsk
novikaua@bsu.by

Silicon carbide is very attractive material for microelectronic integrated circuits production due to chemical, electrical properties and also huge radiation and thermal durability. Silicon carbide substrates are expensive for serial production and it schould be found a method to growth defects free epitaxial silicon carbide layers on top of cheep silicon substrates. Silicon carbide layers grown directly on silicon are defect-riched due to significant lattice misfit and difference of thermal expansion coefficient [1]. Additionally, formation of porous layer under the silicon carbide results in decrease of elastic strain and consequently improves the structural quality of silicon carbide. One can suggest that additional growth of silicon-germanium (SiGe) buffer layer during SiC growth will leads to noticeable decrease of growth temperature as well as improvement of the quality of silicon carbide. The main goal of the present work is investigation of high temperature carbidization process of silicon wafers with epitaxial $Si_{1-x}Ge_x$ buffer layers.

(111) Si wafers were used as substrates. The $Si_{0,75}Ge_{0,25}$ (15 nm)/SiC layers were grown by molecular beam epitaxy (MBE) onto Si wafers. The structural properties were investigated by bright-field and dark-field transmission electron microscopy (TEM) and electron diffraction analysis. The Raman spectroscopy (NanofinderHighEnd) spectrometer, excitation at 532 nm) was used for comparison.

Fig. 1 shows the TEM image of Si/ $Si_{0,75}Ge_{0,25}$ /SiC sample grown by MBE at 950 °C. Well visible bright areas in Fig. 1 are pores in SiGe layer because of SiC epi-growth. The pores formation apparently takes place due to Kirkendall effect. The faceted boundaries of several grains (Fig. 1) reveal the microtwins formation due to specific reflection of crystalline matrix or due to matrix rotation around its crystallographic axis. Raman spectrum shows typical optical and acustical vibration pikes for cubic phase of silicon carbide layers[2].

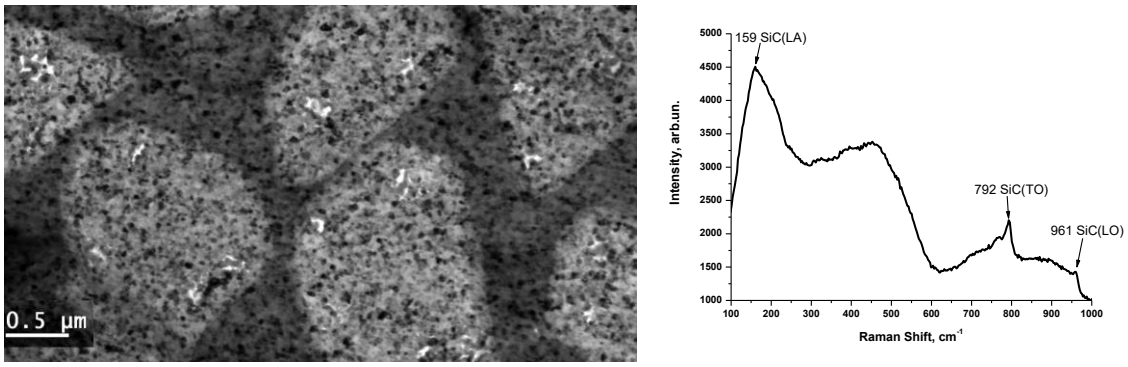

Fig. 1. Bright field TEM image and Raman spectrum of epitaxialy grown silicon carbide on top of SiGe\Si substrate.

Using electron microscopy, electron diffraction and raman spectroscopy it was shown, that thermal treatment of Si\SiGe buffer structure at 950 °C in carbon atmosphere is followed by epitaxial growth of thin layers of cubic silicon carbide with high density of microtwins.

[1] S.A. Kukushkin, A.V. Osipov FTT (2008) V. 50, P. 1188-1195.

[2] *I.G. Aksyanov, M.E. Kompan, I.V. Kulkova* FTT (2009) V. 52, P. 1724-1728.

FLUCTUATION CONDUCTIVITY AND PSEUDOGAP IN $Y_{1-x}Pr_xBa_2Cu_3O_{7-\delta}$ SINGLE CRYSTALS

Lyudmila Omelchenko[1], Andrei Solovjov[1], Ruslan Vovk[2]

[1]B.Verkin Institute for Low Temperature Physics and Engineering of NAS of Ukraine,
Nauky Ave., 47, Kharkiv 61103, Ukraine
[2]Physics Department, V. Karazin National University, 4 Svoboda Sq., 61077 Kharkiv, Ukraine
Omelchenko.ilt.kharkov@gmail.com

Pseudogap (PG), which is opening in the excitation spectrum at the characteristic temperature $T^* \gg T_c$, remains to be one of the most interesting and intriguing property of high- temperature superconductors (HTS's) with the active CuO_2 plane (cuprates) [1]. It is believed at present that the proper understanding of the PG physics has to give the possibility to decipher the basic pairing mechanism in the HTS's which is still uncertain. The conductivity characteristics of the HTS's compounds can be tailored through total or partial substitution of their components.

In this aspect, the $Y_{1-x}Ba_2Cu_3O_{7-\delta}$ compound has been studied more thoroughly and most rare-earth elements when substituted for yttrium (Y) yielded superconductors. Of particular interest in this aspect is the partial substitution of Y by praseodymium (Pr), which leads to the suppression of the superconductivity and allows the lattice parameters and oxygen stoichiometry of the compound to remain practically unaltered. The investigation of the impact of Pr impurities on the conditions and regimes of existence of the fluctuation conductivity state of such compounds plays an important role to elucidate the nature of HTS's but also for determining empirical ways of raising their critical parameters [2]. In the paper, effect of the Pr doping ($0.19<x<0.43$) on the magnitude and temperature dependence of the PG in $Y_{1-x}Pr_xB_2C_3O_{7-\delta}$ (YPrBCO) single crystals was studied for the first time over the temperature range from T* down to T_c.

Independently on effect of Pr, near T_c the excess conductivity $\sigma'(T)$ is well described by the Aslamasov - Larkin and Hikami-Larkin fluctuation theories demonstrating 3D-2D crossover with increase of temperature. The result points out the presence of the fluctuating Cooper pairs in the samples, which are believed to be responsible for the PG formation.

In the basic sample ($x = 0$ $T_c = 91.67$ K) the PG temperature dependence $\Delta^*(T)$, shows the maximum $\Delta^*(T_{max})$ ≈181 K at T≈110 K. With increasing of Pr concentration up to x=0.19, $\Delta^*(T_{max})$ increases and the maximum becomes wider. With further increase of the Pr concentration $\Delta^*(T_{max})$ decreases, and the maximum is noticeably smeared out and shift towards higher T. At the same time, Tc monotonically decreases down to about 38.5 K whereas T* greatly increases up to T*~ 236 K. According, for x = 0.43 the shape of the PG changes radically. Now the sharp peak of $\Delta^*(T)$ is observed at $\Delta^*_{max}(T) = 417$ K at $T_S \approx 226$ K, followed by a linear descanding region with a positive slope $\alpha \approx 7.2$ to $T_N = 210$K ($\Delta^*(T_N) \approx 292$K), below which the $\Delta^*(T)$ is a smooth curve with positive curvature down to $T_G = 40$K. Such dependence is typical for the magnetic superconductors of the $SmFeAsO_{0.85}$ type [3], $EuFeAsO_{0.85}F_{0.15}$ [4] and most likely is determined by the influence of the own magnetic moment of Pr ($\mu Pr = 4.6\mu B$). The magnetic superconductors T_S – corresponds to the structural transition and $T_N = T_{SDW}$ designates transition to the spin density wave mode (SDW) [3, 4], which in our case can occur most likely due to antiferromagnetic spin ordering of Pr.

[1] A. L. Solovjov, V.M. Dmitriev, Low Temp. Phys. **32,** N6, 576 (2006).
[2] R. V. Vovk, A. A. Zavgorodniy, M. A. Obolenskii, I. L. Goulatis, A. Chroneos, and V. M. Pinto Simoes, J. Mater Sci.: Mater. Electron. **22**, 20 (2011).
[3] A. L. Solovjov, et al., Low Temp. Phys. **37**, 557 (2011).
[4] A.L. Solovjov, L.V. Omelchenko, A.V. Terekhov, K. Rogacki, R.V. Vovk, E. P. Khlybov, and A. Chroneos, Mater. Res. Express, **3**, 076001(1-13) (2016).

EXCESS CONDUCTIVITY AND POSSIBLE PSEUDOGAP STATEIN $FeSe_{0.94}$ IRON-BASED SUPERCONDUCTORS

E. V. Petrenko[1], A. L. Solovjov[1],K. Buchkov[2], E. Nazarova[2],K. Rogacki[3]

[1] B. Verkin Institute for Low Temperature Physics andEngineering NAS of Ukraine, Kharkiv, Ukraine
[2] Institute of Solid State Physics, Bulgarian Academyof Sciences, Sofia, Bulgaria
[3]International Laboratory of High Magnetic Fields and Low Temperatures, PAS, Wroclaw, Poland
ilt@ilt.kharkov.ua

Pseudogap (PG), which opens at the T* >>T[1], where Tcis the superconducting (SC) transition temperature, is one of the most intriguing properties of cuprate high-Tcsuperconductors (HTSCs). However, the PG physics is still not completely clear. In resistivity measurements PG appears as a downturn of the longitudinal resistivity ρ(T) at T≤T* from its linear dependence ρN(T) at higher T. This leads to excess conductivity $\acute{\sigma}(T) = [1/\rho(T) - 1/\rho N(T)]$. Similar $\acute{\sigma}(T)$ is observed in the iron-based superconductors, for example, in FeSe. However, thequestion as for the PG presence in such compounds,which is associated with a decrease in the density of states at the Fermi level, remains highly controversial.

For the first time, temperature dependences of $\acute{\sigma}(T)$ measured on three FeSe0.94 samples has been studied in detail. It was shown that in the range from $T_c$up to T_{01}(~ 10 K above Tc) $\acute{\sigma}(T)$ obeys the classical fluctuation theories of Aslamazov-Larkin (AL) and Maki-Thompson (MT), pointing to the existence of fluctuating Cooper pairs (FCPs) in FeSe in this temperature range. Like in cuprates, AL-MT crossover at $T_0<T_{01}$is observed, which allows to determine the coherence length along the c-axis: $\xi_c(0)$ ~ 2.8 Å, in good agreement with results of Ref.[2].

PG parameter Δ*(T) was calculated within the local pair (LP) model [1]. For all samples studied, Δ*(T) shows a narrow peak corresponding to the firststructural transition at T ~ 247 K [3]. Then thereis a minimum at T_s~ 90-100 K corresponding to a structural transition from the tetragonal to orthorombic phase, which is followed by the transition to AF state of SDW-type typical for Fe-pnictides [3]. It was shown that the second structural transition is accompanied by the sharp decrease of magnetization at $T \leq T_s$, which can be considered as the evidence of the synchronous magnetic transition [2].

Nevertheless, the question about the role of the local pairs in the possible PG state formation in Fe-pnictides, still remains open.

[1] A. L. Solovjov, V. M. Dmitriev, Low Temp.Phys.35, 169 (2009).

[2] E. Nazarova, N. Balchev, K. Nenkov, K. Buchkov et al. Supercond. Sci. Technol. 28 025013 (8pp) (2015).

[3] V. Gnezdilov, Y. G. Pashkevich,P. Lemmens,D. Wulferding et al. Phys. Rev. B 87, 144508 (2013).

HIGH ASPECT RATIO DRY ETCHING METHOD FOR GaN BASED CAPACITOR TYPE DETECTOR FORMATION

Marius Pikčiūnas[1], Ignas Reklaitis[2], Domas Paipulas[2*]

[1]Semiconductor Physics Department, Vilnius University, Lithuania
[2]Laser Research Center, Vilnius University, Lithuania
marius.pikciunas@ff.stud.vu.lt

This work discusses the development of wide band gap semiconductor radiation detector formation method. Gallium nitride (GaN) was chosen as a suitable material for radiation damage resistant detector. The development of semiconductor detector with a higher radiation damage resistance is very important for many scientific applications, which can't rely on ordinary silicon detectors as they would decay faster than in few years. For example open space radiation can damage silicon detectors which are equipped in orbiting X-ray telescopes. GaN's wide band gap should result in detector with lower leakage currents than an equivalent Si detector. A further possible advantage of using GaN as a detector is that its displacement energy may be larger than Si resulting in it being more intrinsically resistant to radiation damage. In general there are several possible geometries in which semiconductor detectors could be made: p-n, Schottky or capacitor structures. It was decided to make capacitor detector, because the difficulties to growth p-doped GaN and complexity of ohmic contacts formation.

In order to fulfill detector in such geometry, extremely thick (~20 μm) GaN wafers are needed, which in this case were grown on a sapphire substrate using metalorganic chemical vapor deposition (MOCVD) reactor. Desirable aspect ratio of capacitor type mesa device is 1:10 or more and it could not been achieved using ordinary photolithography method. Instead femtosecond laser fabricated glass shadow masks were used for GaN mesa formation by dry etching process. However it resulted in formation of dry-etch resistant polymer structures around the inner features of the mask (see Fig. 1). It was shown that *ex-situ* sample treatment with 0,5 % KOH solution after every etching process effectively etch the polymer. Thus, polymer-free mesa structure is demonstrated, suitable for capacitor type GaN detector formation.

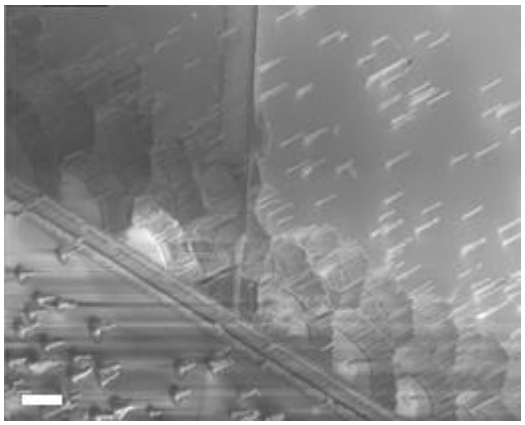

Fig 1. Mesa structure with an aspect ratio of 1:10 is seen in mid-top section of the SEM image. Honey comb like defect related structure prior KOH treatment is also visible in the center part. The bar is 15 μm.

STUDY OF PHOTORESPONSE CHARACTERISTICS IN NEUTRON IRRADIATED STRUCTURES OF AMMONO-THERMAL GALLIUM NITRIDE

Kornelijus Pūkas, Tomas Čeponis, Eugenijus Gaubas

Institute of Applied Research, Vilnius University, Lithuania
kornelijus.pukas@ff.stud.vu.lt

Gallium nitride (GaN) is a promising material for application to particle detectors in a harsh radiation environment at the Large Hadron Collider (LHC) and other particle accelerators [1]. In this study, the structures of capacitor-type detector have been fabricated on high crystalline quality semi-insulating bulk ammono-thermal GaN (AT GaN) materials. The operational characteristics of sensors have been investigated by pulsed current techniques. The measurements of photoconductivity and photoluminescence transients were also performed to estimate the variations of non-radiative and radiative recombination parameter, respectively.

In this study, fluences dependent variations of carrier recombination lifetime have been examined by means of microwave probed photoconductivity (MW-PC) transients. The time integrated and time resolved photoluminescence measurements were performed to study the dynamics of carriers related with radiative recombination processes in samples of the pristine and irradiated with different neutron fluences (10^{12} - 5×10^{16} cm^{-2}) GaN material. The charge collection efficiency (CCE) characteristics have been studied by inspection of current transients recorded on capacitor-type sensor.

The as-recorded and simulated MW-PC transients obtained at different excitation intensities are compared in Fig. 1a. Carrier recombination lifetime τ_R can be a measure for characterization of the non-radiative recombination defects It has been determined that a radiative recombination coefficient B= 2×10^{-8} cm^3/s should be assigned to the UV (band-to-band) recombination process. Study of the CCE characteristics dependent on neutron fluences revealed that efficiency decreases with increasing of neutron fluences as shown in Fig. 1b. Degradation of CCE can be explained by the increased density radiation of defects in GaN materials due to heavily neutron irradiation.

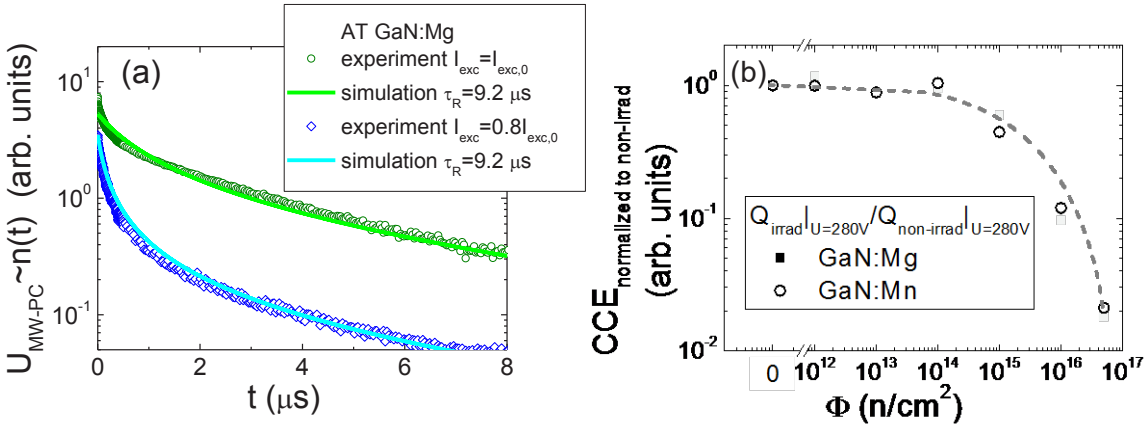

Fig. 1. As-recorded MW-PC transients (symbols) and simulated carrier decay transients (solid curves) at different excitation intensities of AT GaN:Mg material (a) and CCE normalized to pristine AT GaN samples (b).

The time-integrated photoluminescence (TI-PL) spectra, obtained for the neutron irradiated and pristine AT GaN:Mg by using integration time of 50 ns and 500 ns, consist of three bands: UV-PL assigned to excitonic or band-to-band luminescence, B-PL and YG-PL assigned to donor-acceptor pairs (DAP). Variations of the TI-PL transients exhibited the non-exponential two-componential PL relaxation. Such PL transients might be inherent for the radiative carrier recombination processes due to DAP [2]. The longest instantaneous PL decay times have been observed in YG-PL while the fastest decay appeared in UV-PL spectral range.

[1] M. Moll, Radiation tolerant semiconductor sensors for tracking detectors, Nucl. Instr. Meth. Phys. Res. A **565**, 202 (2006).
[2] D.G. Thomas, J.J. Hoizreld, M. Augustyniak, Kinetics of radiative recombination at randomly distributed donors and acceptors, Phys. Rev. A **202**, 140 (1965).

ELECTRICAL AND OPTICAL PROPERTIES OF ZnO LAYERS GROWN ON SiO_2/Si (111) SUBSTRATES BY ATOMIC LAYER DEPOSITION

Przemysław Puła[1*], Grzegorz Łuka[2], Elżbieta Guziewicz[2]

[1]Faculty of Physics, University of Warsaw, Warsaw, Poland
[2] Institute of Physics, Polish Academy of Sciences, Warsaw, Poland
[*] *pp358330@okwf.fuw.edu.pl*

Zinc oxide (ZnO) is a wide bandgap semiconductor that has drawn attention of the electronic and optoelectronic industry due to its unique properties such as large exciton binding energy at room temperature. Applications including thin film transistors (TFT) or transparent conductive oxides (TCO) require knowledge about the ways to obtain material with desirable electrical properties.

In our work, ZnO layers were grown by atomic layer deposition on Si(111) substrates covered with SiO_2 obtained by thermal oxidation. ZnO layers were grown at different growth temperatures (100-200 °C). The samples were then annealed in air at 300 – 500 °C. For the as-grown an annealed samples, electrical and optical measurements were performed. The influence of processing parameters on free electron concentrations and photoluminescence of ZnO films was investigated.

CARRIER DYNAMICS IN INN WITH DIFFERENT GROWTH PARAMETERS

Martynas Riauka, Kazimieras Nomeika, Saulius Nargelas, Ramūnas Aleksiejūnas

Department of Semiconductor Optoelectronics, Institute of Applied Research, Vilnius University, Saulėtekis Avenue 9-3, Vilnius 10222, Lithuania

martynas.riauka@ff.vu.lt

Solar cells are expected to be one of the key future technologies of environmentally friendly electric energy generation. For this purpose, group III-V element compounds are particularly favourable due to their flexible bandgap. It is especially important taking into account spectral energy distribution of solar radiation which extends to infrared regions – this is where narrow - gap semiconductors prove to be useful. InN with a band gap of about 0.7 eV is a promising material to be used in tandem solar cells to enhance their photovoltaic conversion efficiency. However, there is a large number of difficulties related to producing high quality InN films, with the most common being lattice mismatch between the semiconductor layer and the corresponding substrate, high thermal instability of InN and reactions with atomic hydrogen.

In this work we investigate InN samples grown by metalorganic chemical vapour deposition (MOCVD) on c-sapphire substrates under different conditions. Growth parameters such as growth temperature, growth pulse and pause duration as well as growth pulse count were varied. The samples were investigated at room temperature using pump-probe technique. Excitation was carried out with the 1st harmonic (1030 nm) of the Yb:KGW femtosecond laser (PHAROS), while for probing the wavelength was tuned to 2400 nm with optical parametric amplifier (ORPHEUS). The repetition rate of 250 fs laser pulses was set to 3 kHz.

Carrier lifetimes were used to evaluate the samples with the optimal growth conditions, as longer lifetimes usually indicate lower presence of defects in the crystal lattice, hence better overall quality. Direct relation between the sample thickness and non-equilibrium charge carrier lifetime was observed – higher number of growth cycles resulted in longer lifetimes (Fig. 1a). The increase of the thickness was confirmed with a higher initial pump-probe signal. The results also indicate that the optimal temperature for growing InN-based structures is around 600 K (Fig. 1b). Optimal growth pulse duration was found to be 7 s, with the pause duration being 20 s.

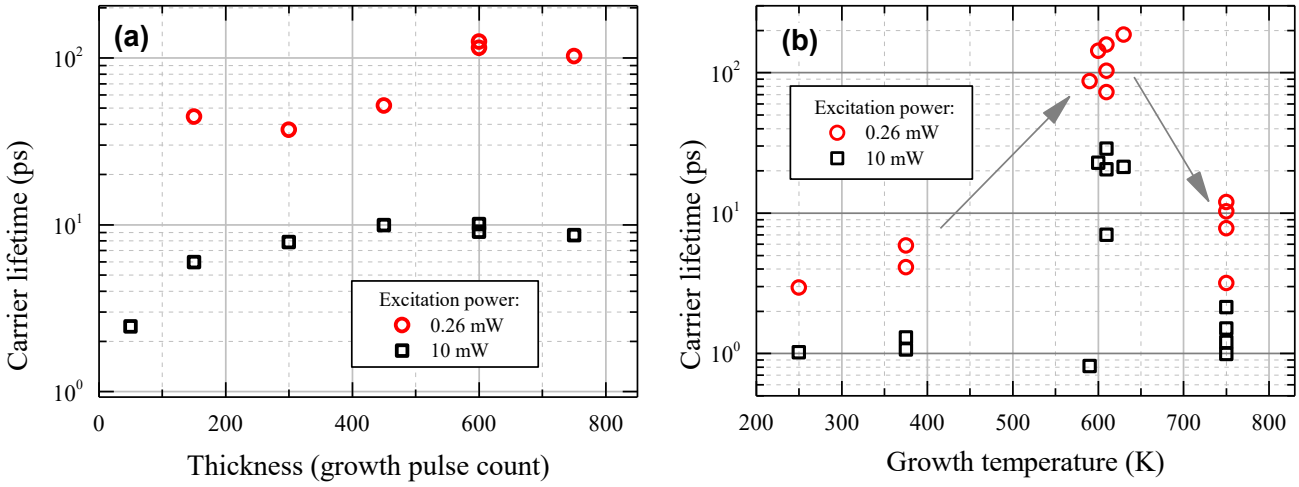

Fig. 1. Carrier lifetime dependence on sample thickness (expressed as the count of growth pulses) (a), carrier lifetime dependence on the growth temperature (b).

GROWTH OF GaInAsBi LAYERS ON InP FOR MID-INFRARED OPTICAL DEVICES

Sandra Stanionytė, Vaidas Pačebutas

Center for Physical Sciences and Technology, Saulėtekio ave. 3, LT-10257, Vilnius, Lithuania
sandra.stanionyte@ftmc.lt

Lattice-matched GaInAs/InP system is widely investigated and applied in optoelectronics for telecommunications and near-infrared applications up to ~1.7 µm wavelengths. Theoretically, it is possible to reach ~3.5 µm spectral range, but a development of high performance devices is limited by relatively large lattice-mismatch between GaInAs compound with high In content and InP substrate. The more prospective alternative for GaInAs could be GaInAsBi compound. Even low incorporation of Bi can considerably reduce bandgap (E_g). Proper selection of In and Bi content allows to grow latticed-matched GaInAsBi/InP systems working up to 6 µm [1].

The aim of this work was to growth quaternary GaInAsBi layers on semi-insulating InP:Fe (100) substrates using molecular-beam-epitaxy (MBE) reactor and characterize them. For characterization of crystallographic and optical properties of GaInAsBi layers, structural (HR-XRD, AFM, TEM) and optical (photoluminescence and transmittance) methods were selected.

Initially, GaInAs buffer layers for substrate smoothing were grown. The optimal In/Ga flux ratio for GaInAs layers lattice-matched to InP substrate was chosen. Afterwards GaInAsBi layers with same and smaller (to reduce strain caused by bismuth incorporation) In/Ga flux ratio and Bi/Ga flux ratio from 0,13 to 0,35 were grown on a buffer layer. Figure 1 shows the rocking curve dependence on Bi/Ga flux ratio. It is evidence that larger Bi flux shifts the peak related to the GaInAsBi layer to smaller angles keeping In/Ga flux ratio constant.

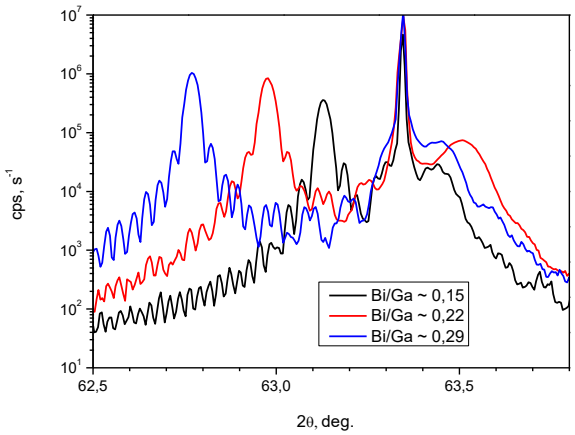

Fig. 1. ω-2θ XRD (004) rocking curves measured for the GaInAsBi layers (004) reflex grown under conditions of different Bi/Ga flux ratio

To avoid lattice distortion due to larger Bi atoms incorporation into InGaAs lattice, In concentration in buffer layer was increased to obtain the same lattice constant of buffer and bismide layer. AFM investigation revealed no significant difference in surface roughness for layers with different buffer composition. The elemental composition was optimized for lower E_g value, what was demonstrated in photoluminescence spectra, the emission peak was shifted to 0.52 eV (~2.4 µm).

GaInAsBi layers were successfully grown by MBE on InP substrates. The room temperature luminescence was observed. E_g values as small as 0.52 eV demonstrate that these layers are suitable to apply for mid-IR optoelectronics devices. Our future plans are to extend the bismide operation range by minimizing the lattice mismatch and shifting the characteristic emission to longer wavelengths.

[1] J. P. Petropoulos, Y. Zhong, J. M. O. Zide. Optical and electrical characterization of InGaBiAs for use as a mid-infrared optoelectronic material. Applied Physics Letters **99** 031110 (2011).

WAVELENGTH FILTERED CORRELATION FUNCTIONS IN ELECTRON MICROSCOPY-BASED CATHODOLUMINESCENCE FOR LIFETIME MEASUREMENTS

Henrikas Svidras[1,2], Luiz Galvao Tizei[2], Mathieu Kociak[2]

[1]Institute of Applied Research, Vilnius University, Saulėtekio al. 3, LT-10257 Vilnius, Lithuania
[2]Laboratoire de Physique des Solides, Université Paris-Sud, Orsay 91405, France
henrikas.svidras@ff.stud.vu.lt

Electron microscopy is one of the most rapidly advancing types of high-resolution microscopy, which has reached a resolving power close to 0.5 Å. Of particular interest now are scanning transmission electron microscopes (STEMs), that currently form the highest-available resolution images point by point. One of the main advantages of such microscope is the ability to acquire several different signals at the same time. Because of the high resolution achieved and an extremely small area of excitation (compared to optical microscopes), together with a light collection system they can be used to identify and monitor the emission of individual nano-sized emitters, for example, quantum wells. [1] However, even with a precisely controlled excitation area, one cannot guarantee that nearby structures will not be excited due to plasmon or electron-hole pair diffusion.

One paramater of particular interest to monitor is the electron-hole recombination lifetimes. It provides an insight to quantum-confined Stark effect (QCSE) that is often present in III-Nitride emitters due to internal electric field existing in structures made from these materials. Since electron-hole recombination lifetimes depend on the electron-hole wave function overlap, changes to the band structure induced by the mentioned effect can drastically increase this lifetime (by decreasing the overlap). [2]

In this study we present electron microscopy-based cathodoluminescence (CL) on AlN/GaN nanowires with quantum disks (QDisks). We show that by increasing the charge density in the QDisk (effectively screening the internal electric field), we can in turn reduce the QCSE, and observe a shift that is more evident in thick QDisks because the electrone-hole wavefunction overlap is smaller. Thus, the monitoring of lifetimes can give interesting insight to QCSE inside the confined GaN layer. We report the coupling of a CL system to an upgraded Hanbury-Brown Triss (HBT) interferometer (with an added spectrometer acting as a computer-controlled monochromator) shown in Figure 1. The setup was used for measuring the lifetimes of carriers in QDisks with non-larger than 15 nm separations. The lifetimes are extracted by observing a photon bunching effect, present in the QDisk emission. [3, 4]

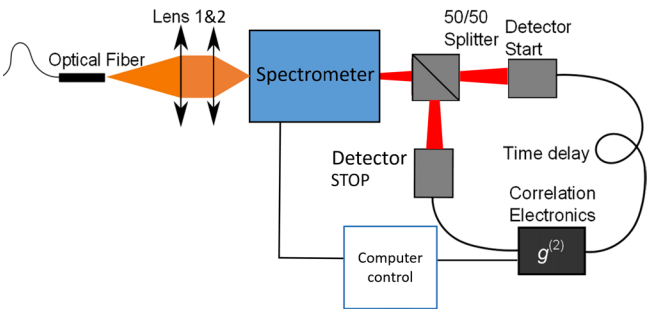

Fig. 1. Upgraded HBT interferometer with a spectrometer acting as a monochromator. An incoming beam is monochromated by a spectrometer and split into two detectors coupled to correlation electronics. The system was coupled to a STEM and worked with CL light.

The study is a continuation of prolonged measurements [1, 2, 3, 4] to fully model the QCSE in single emitters and possibly measure the internal electric field. It proves the model of carrier wave function separation and the compensation of it by a shielding effect, more evident in thick QDisks. The upgraded HBT interferometer provides further insight to QCSE and helps not only to establish a strong theory on the subject, but also to better understand and tackle this, usually, unwanted effect.

[1] Zagonel, L. F., et al. "Nanometer scale spectral imaging of quantum emitters in nanowires and its correlation to their atomically resolved structure." Nano letters 11.2 (2010): 568-573.
[2] Zagonel, L. F., et al. "Nanometer-scale monitoring of quantum-confined Stark effect and emission efficiency droop in multiple GaN/AlN quantum disks in nanowires." Physical Review B 93.20 (2016): 205410.
[3] Meuret, S., et al. "Photon bunching in cathodoluminescence." Physical review letters 114.19 (2015): 197401. APA
[4] Meuret, S., et al. "Lifetime measurements well below the optical diffraction limit." ACS Photonics 3.7 (2016): 1157-1163. APA

PHOTOELECTRIC PROPERTIES OF $Tl_{1-x}In_{1-x}IVA_xSn_2$ ALLOYS

Vilius Vertelis

Department of Semiconductor Physics, Vilnius University, Lithuania
Institute of Applied Research, Lithuania
viliusvertelis@gmail.com

$Tl_{1-x}In_{1-x}IVA_xSe_2$ compounds might be promising materials for the engineering of radiation detectors of different radiation types, ranging from neutron to gamma rays. Applications for solid state optical devices may also be considered. This group of alloys has not been extensively studied, so its properties are not fully analyzed and understood yet. The objective of this work was to study photoelectrical properties of these compounds.

Four samples with different composition were analyzed ($Tl_{0,75}In_{0,75}Sn_{0,25}Se_2$, $Tl_{0,9}In_{0,9}Sn_{0,1}Se_2$, $Tl_{0,8}In_{0,8}Si_{0,2}Se_2$, $Tl_{0,9}In_{0,9}Si_{0,1}Se_2$). We have concluded that the space charge limited currents with a notable influence of trapping states take place in all samples. The samples of $Tl_{0,9}In_{0,9}Sn_{0,1}Se_2$ and $Tl_{0,9}In_{0,9}Si_{0,1}Se_2$ were proved to be the single crystalline ones, meanwhile others were, most probably, two-phase materials with the "fingerprints" of both $SnSe_2$ and $SiSe_2$. We have determined that bandgap of $TlInSnSe_2$ increases linearly (Fig.1 and Eq.1):

$$E_g = 1.2eV + (1.2 \pm 0.1)eV \cdot x \quad (1)$$

depending on $SnSe_2$ concentration and that in $TlInSiSe_2$ it does not. Increase of $SiSe_2$ up to 20% results in a bend of the valence band thus resulting in an indirect bandgap. Our studies show that excess carriers recombine via several recombination channels, having different recombination time constants that depend on temperature and vary depending on material composition. From the analysis of the Thermally Stimulated Currents (TSC), we have shown that shallow traps are present in the crystals.

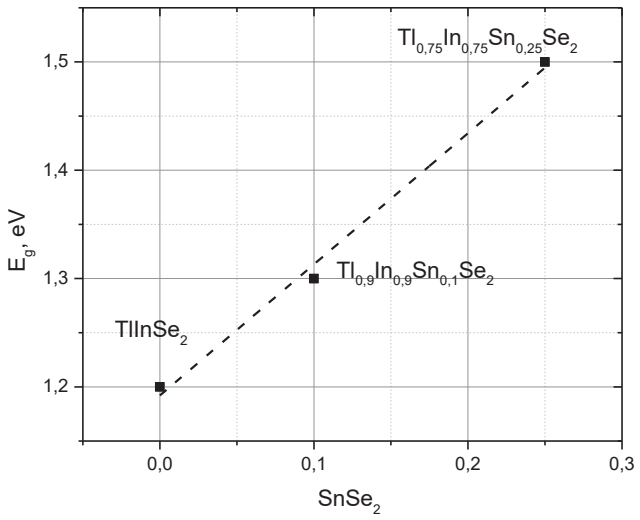

Fig. 1 Bandgap dependence on $SnSe_2$ concentration in $Tl_{1-x}In_{1-x}Sn_xSe_2$ alloys.

INVESTIGATION OF MAGNETORESISTANCE OF NANOSTRUCTURED $La_{1-x}Sr_xMn_{1+y}O_{3+\delta}$ FILMS WITH MANGANESE EXCESS

Martynas Vilkaitis[1,2], Nerija Žurauskienė[1]

[1] Department of Material Sciences and Electrical Engineering, Center for Physical Sciences and Technology, Lithuania
[2] Department of Semiconductor Physics, Vilnius University, Lithuania
martynas.vilkaitis@ftmc.lt

Polycrystalline manganite thin films exhibiting colossal magnetoresistance (CMR) phenomenon are promising materials for the fabrication of B-scalar sensors measuring high pulsed magnetic fields independently on field orientation [1, 2]. The demand of these sensors is increasing with the development of high pulsed magnetic field generation and application possibilities. Polycrystalline manganites with perovskite structure are good candidates for such applications.

The conductivity of $La_{1-x}Sr_xMn_{1+y}O_{3+\delta}$ (LSMO) films was investigated in a wide temperature range (5-310 K). The films were deposited at a temperature of 750 °C on a polycrystalline Al_2O_3 substrate using a Pulsed Injection Metal Organic Chemical Vapor Deposition (PI MOCVD) technique. The Sr content x was changed from 0.0545 to 0.2637, while keeping manganese excess constant (y=0.15). The magnetoresistance of the films was investigated in permanent magnetic field up to 0.7 T and pulsed magnetic fields up to 20 T in a temperature range (77-290 K).

It was demonstrated that these films having Mn excess of 15 % exhibit phase transition from paramagnetic to ferromagnetic state for all investigated Sr content x. The maximum of their resistivity decreases with increase of Sr content x, while it corresponding temperature T_m has a maximum at $x \approx 0.18$.

It was found that at room temperature the magnetoresistance at low magnetic fields (0.7 T) is largest for the films with x=0.1827. The magnetoresistance of the film with lowest x=0.0545 rapidly increases with decrease of temperature and becomes highest compared with other films at temperatures lower than 270 K (Fig. 1, *left*). The magnetoresistance in high magnetic fields (20 T) is largest for the films with x=0.0545 in the whole investigated temperature range.

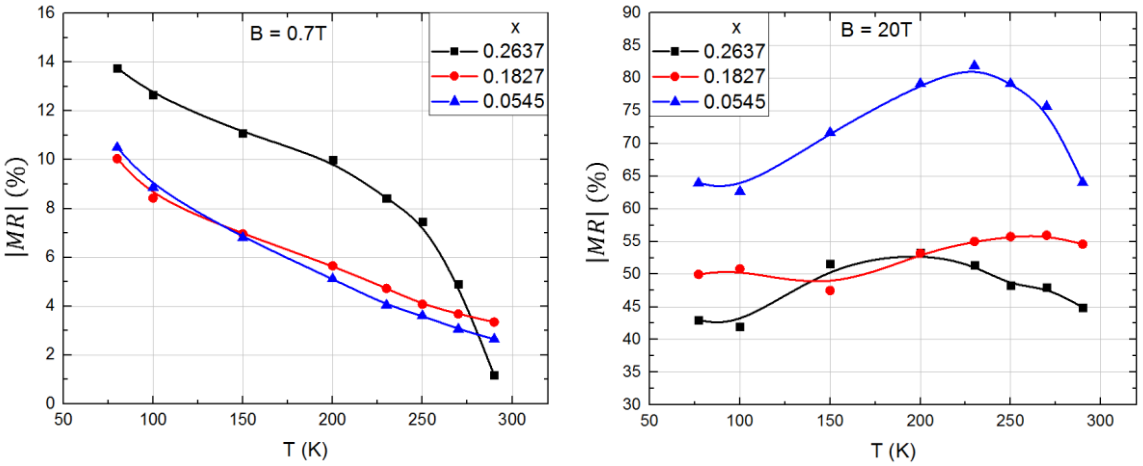

Fig. 1. Magnetoresistance *vs*. temperature dependences, when magnetic induction is 0.7 T (*left*) and 20 T (*right*).

[1] S. Balevičius, N. Žurauskienė, V. Stankevič, S. Keršulis, V. Plaušinaitienė „Nanostructured thin manganite films in megagauss magnetic field“, Appl. Phys. Lett. 101, 092407, 2012.

[2] T. Stankevič, L. Medišauskas, V. Stankevič, S. Balevičius, N. Žurauskienė, O. Liebfried, M. Scherider “Pulsed magnetic field measurement system based on colossal magnetoresistance-B-scalar sensors for railgun investigation”, Rev. Sci. Instrum. 85, 044704, 2014.

STRUCTURAL AND OPTICAL PROPERTIES OF $Cu_2ZnSnSe_4$ THIN FILMS FOR SOLAR CELLS

Vadim Zhivulko, Olga Borodavchenko

Scientific-Practical Material Research Centre of the National Academy of Science of Belarus,
P. Brovki 19, Minsk 220072, Belarus
vad.zhiv@gmail.com

Thin films of $Cu_2ZnSnSe_4$ (CZTSe) contains a low-cost non-toxic elements which are abundant in the Earth's crust and therefore are promising absorber semiconductor material for photovoltaic cells. The natural p-type doping of CZTSe is caused by intrinsic defects and therefore the determination of a nature such defects can help to accelerate progress in the solar cells performance. In the present study the photoluminescence (PL) and photoluminescence excitation (PLE) spectra were investigated at low temperature ~ 4.2 K to determine the nature of intrinsic defects and the mechanisms of a radiative recombination in CZTSe absorber layers. CZTSe thin films were prepared by selenisation of metallic Cu, Zn and Sn precursor deposited by magnetron sputtering on to Mo-coated glass substrates. The surface morphology and cross-section analyses were carry out by scanning electron microscopy (SEM). These experiments show a gradual increase of the grain size with the selenisation temperature rise in range of 450 – 550 °C. X-ray diffraction measurements were made by using a Siemens D-5000 diffractometer. These investigations are indicated on the formation of tetragonal CZTSe polycrystalline films for all range of selenisation temperatures. As an example the PL and PLE spectra taken at 4.2 K for the three samples (film 1 and film 2 ~ 500 °C, film 3 ~ 450 °C) at 532 nm laser excitation with power density of about ~ 0.01 $W \cdot cm^{-2}$ are shown in Fig. 1. In all the three case the PL bands at 0.77, 0.91 and 0.92 eV for films 1, 2 and 3, respectively, shows significant shifts to higher energies with increasing laser power.

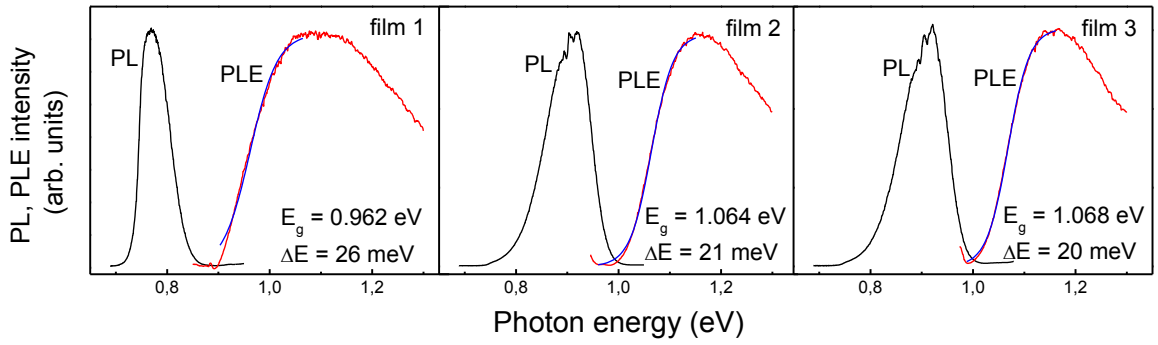

Fig. 1. Photoluminescence and photoluminescence excitation spectra of the CZTSe films at 4.2 K.

The blue shift increases from 11 to 14 meV per decade of excitation power as the selenisation temperature rises from 450 °C to 500 °C. Such j-shift PL bands with their asymmetric shape at 4.2 K imply that the radiative recombination is related with band to-tail optical transition that comprises free electrons and holes that are localized in the valence band tails formed by randomly distributed potential fluctuations in crystal lattice of CZTSe. The bandgap energy E_g of the thin films was determinate from PLE spectra, Fig. 1. The PLE spectra show broadening which suggests the presence of sub-bandgap absorption states associated with band tails. To take into account such broadening the low energy sides of the PLE spectra, representing absorptance α(E), are fitted with sigmoidal function: $\alpha(E) = \alpha_0/(1 + \exp(E_g - E)/\Delta E)$, where E_g is the bandgap, E is excitation energy at which the intensity of emission is recorded and ΔE is a broadening parameter (energy steepness). The Cu and Zn atoms in the kesterite structure of CZTSe can be either ordered or randomized on the cation sub-lattice. Such an ordering increases E_g and spectral energy of PL bands, Fig. 1. The change in the optical parameters is consistent with a reduction of the Cu_{Zn} and Zn_{Cu}-V_{Cu} as well as with increasing ordering of Cu and Zn atoms. It is proposed that the observed change of E_g are associated with the Cu–Zn ordering and are defined by the change in [Cu]/[Zn+Sn] ratio. This results demonstrate that [Cu]/[Zn+Sn] ratio can be used to control electronic characteristics of CZTSe thin films such as E_g and ΔE as well as solar cells fabricated using these films.

THE $Mn_{1-x}Gd_xSe$ SOLID SOLUTIONS AND THEIR STRUCTURAL CHARACTERISTICS

Sergey Aplesnin[1], Aliona Zhivulko[1,2], Olga Demidenko[2], Kazimir Yanushkevich[2]

[1]Siberian State Aerospace University named after academician M.F.Reshetnev, 660014 Krasnoyarsk, Russia
[2]Scientific-Practical Materials Research Centre of NAS of Belarus, P.Brovki Str.19, Minsk, Belarus
alyona_panasevich@mail.ru

The synthesis of new magnetic materials, the study of the crystal structure features and the establishment of the their relationship with the physical and chemical properties in a wide temperature range are the priority tendency of condensed matter physics because of the advantage over their use in the development of multi-functional instrumental matrix for solid-state electronics.

For fundamental research and application purpose the apparent interest introduce MnSe magnetic semiconductors and based on them solid solutions with cationic substitution of manganese by rare earth element – gadolinium [1].

The samples of $Mn_{1-x}Gd_xSe$ ($0 \le x \le 1,0$) system were obtained by a solid phase reaction method from initial chemical elements powders. X-ray diffraction analysis was carried out by "DRON-2" apparatus in the Cu-Kα - radiation. For example, on Fig. 1 is shown the X-ray pattern of the $Mn_{0,95}Gd_{0,05}Se$ sample.

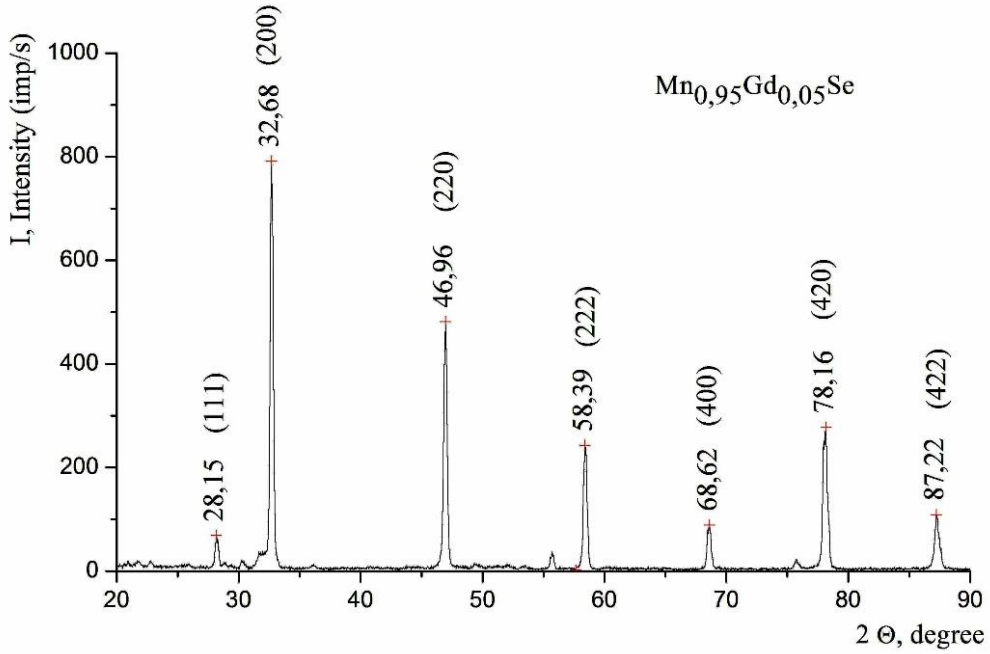

Fig.1. The X-Ray pattern of the $Mn_{0,95}Gd_{0,05}Se$ sample

All synthesized samples of the $Mn_{1-x}Gd_xSe$ systems have a NaCl type cubic lattice of the Fm3m space group. The unit cell parameter linearly increases with gadolinium content increasing in solid solutions: from 0.5468 nm (MnSe) to 0.5769 nm ($Mn_{0,1}Gd_{0,9}Se$).

[1]. S. S. Aplesnin, M. N. Sitnikov Magnetotransport effects in paramagnetic $Gd_xMn_{1-x}S$ // JETP Letters September 2014, Volume 100, Issue 2, pp 95–101

LASER DIODE INDUCED PHOTOLUMINESCENCE CHARACTERIZATION OF YAG:Ce^{3+} CERAMICS AND POWDER PHOSPHORS

Justina Aglinskaitė, Akvilė Zabiliūtė-Karaliūnė, Pranciškus Vitta

Institute of Applied Research, Vilnius University, Lithuania
justinaaglin@gmail.com

Laser diodes (LD) based lightning is becoming more promising as a future high power lightning technology. It is already used in automotive headlamps at BMW and Audi and it also has other applications such as white fiber light [1]. LDs exhibit greater output power at higher efficiency since they do not suffer efficiency droop which limits the brightness of light emitting diodes (LEDs). Although this brightness limit is not crucial for general lightning, higher light intensity per area is needed in some specific applications as mini projectors, car headlamps and narrow beam outdoor torches which require quasi-point source of light. For this case it is of interest to improve LDs based lightning technologies. As for LEDs, one of the ways to obtain white light is to use a blue LD and an inorganic phosphor which converts part of blue light to yellow. Even though the process of photoluminescence (PL) remains the same under the excitation of both LED and LD, the power density of LD is much higher. This causes the heating of a converter due to Stokes shift when energy is released as heat and therefore thermal phosphorescence quenching is induced. It results in a reduced output power and a shift of colour coordinates of phosphor conversion LD. For this reason it is important for a phosphor to have as good thermal conductivity as possible to avoid catastrophic rise of temperature.

YAG:Ce^{3+} phosphor is one of the most commonly used phosphors for lightning [2]. It has excellent mechanical and chemical properties. Broad emission spectrum that peaks at 550 nm together with a blue LD light create white light and therefore this phosphor is widely used in lightning industry. For the above mentioned reasons ceramics and powder YAG:Ce^{3+} phosphors were chosen to be investigated and compared under the LD.

In this work, photoluminescence decay time of powder and ceramics YAG:Ce^{3+} phosphors at different temperatures was estimated using the frequency-domain technique. This method is based on phase shift of the sinusoidal PL signal relative to that of the photoexcitation signal. As an excitation source Osram LD (450 nm, 1.6 W) was used. It was modulated by driving high-frequency (0.1 – 50 MHz) current. For calibration purposes ceramics and powder YAG:Ce^{3+} phosphors were embedded in cryostat and their PL decay times dependency on temperature were measured using low power LD light. Later phosphors were withdrawn from controlled temperature environment, and the PL decay time was measured as a function of excitation power. Temperature of YAG:Ce^{3+} nanoparticles in powder and ceramics phosphors were determined on the basis of calibration measurement described above.

During the investigation the temperatures of powder and ceramics phosphors as functions of excitation power were compared. The results have shown that ceramics phosphors have better thermal conductivity and are more stable under high excitation power density.

[1] Wierer, Jonathan J., Jeffrey Y. Tsao, and Dmitry S. Sizov. "Comparison between blue lasers and light-emitting diodes for future solid-state lighting." Laser & Photonics Reviews 7.6 (2013): 963-993.
[2] Setlur, A. "Phosphors for LED-based solid-state lighting." The Electrochemical Society Interface 16.4 (2009): 32.

INFLUENCE OF PERIPHERAL PHENYLS TO EXCITED STATE RELAXATION AND AGGREGATION INDUCED FLUORESCENCE IN NITRILE COMPOUNDS

Gintarė Kuksėnaitė[1], Karolis Kazlauskas[1], Gediminas Kreiza[1], Arūnas Miasojedovas[1], Paulius Baronas[1], Aurimas Bieliauskas[2], Vytautas Getautis[2], Algirdas Šačkus[2], Saulius Juršėnas[1]

[1]Institute of Applied Research, Vilnius University, Lithuania
[2]Faculty of Organic Chemistry, Kaunas University of Technology, Lithuania
gintare.kuksenaite@ff.stud.vu.lt

Fluorescent nanoparticles attract great interest in the field of technological applications. They were found to be suitable for constructing OLEDs, OFETs and other optoelectronic systems. They are also fit for tailoring biological probes for bio-sensing and bio-imaging. Fluorescent organic nanoparticles are usually composed of non-planar geometry molecules experiencing the aggregation induced emission (AIE) phenomenon. [1]

Three nitrile-based compounds with different number of peripheral phenyl moieties are studied in this work (Fig. 1). The compounds are designed to show AIE properties. The cyano-vinylene bridge is intentionally introduced into the core to provide a steric twist in the molecules. The pyrazole groups have the ability to deliver high fluorescence efficiency in addition to causing strong intermolecular hydrogen bonds and π-π interactions, which are important for supramolecular constructions. [2]

Nanoparticles based on the nitrile compounds have been formed using precipitation method. The compounds are non-fluorescent in diluted solutions, but demonstrate induced emission upon aggregate formation. The nitrile compound containing no peripheral phenyls demonstrated broad absorption and fluorescence spectra in aggregated state. It also exhibited an amorphous aggregate structure in the neat film and a moderate (10-fold) emission enhancement as compared to that in solution. The compound with two peripheral phenyl rings featured 100-fold emission enhancement in the solid phase, which was accompanied by vibronically-resolved spectrum of aggregates indicating their crystalline nature. The nitrile compound bearing four peripheral phenyls showed similar features as the compound with two phenyl moieties. Thus, the peripheral phenyl groups in turn affected the morphology of nitrile-based nanoaggregates formed by precipitation method.

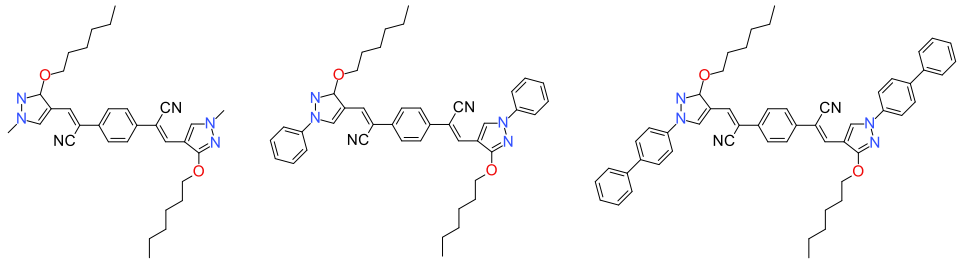

Fig. 1. The chemical structures of investigated compounds.

Optical properties of the compounds assessed in diluted solutions revealed that peripheral phenyl rings improve compound conjugation and significantly shortens excited state radiative decay time. Interestingly, the peripheral phenyls were found to not affect non-radiative decay time. It was also deduced that the central phenyl moiety is the main source of intramolecular vibrations/torsions, and therefore, is responsible for extremely weak fluorescence quantum yield in solutions.

[1] J. Mei, N. L. C. Leung, R. T. K. Kwok, J. W. Y. Lam, ir B. Z. Tang, „Aggregation-Induced Emission: Together We Shine, United We Soar!“, *Chem. Rev.*, t. 115, nr. 21, p. 11718–11940, 2015.
[2] K. Kazlauskas *et al.*, „Morphology and emission tuning in fluorescent nanoparticles based on phenylenediacetonitrile“, *J. Phys. Chem. C*, t. 118, nr. 43, p. 25261–25271, 2014.

GROWTH AND CHARACTERISATION OF NON-POLAR AND SEMI-POLAR GaN ON Si WITH Er_2O_3 INTERLAYER

Kazimieras Badokas[1], Tadas Malinauskas[1], Tomas Grinys[1], Rytis Dargis[2]

[1] Institute of Applied Research, Vilnius University, Saulėtekio Ave. 10, LT-10223 Vilnius, Lithuania
[2]IQE North Carolina, 494 Gallimore Dairy Rd, Greensboro, NC 27409, USA
badokas.k@gmail.com

Group-III nitrides are very promising materials for solid state lighting, high power electronics and even photovoltaics. It is preferred for nitride epitaxial layers to be grown on native substrates. However, native ones are still very expensive, thus nitrides are mostly grown on cheaper substrates such as silicon carbide and sapphire. Another problem is the lack of inversion symmetry in hexagonal crystal structure, giving rise to spontaneous and piezoelectric polarizations along c-direction leading to energy band bending and efficiency decrease of LEDs.

Integration of GaN to silicon technology is a promising way for cost reduction of a new device generation. A large difference in thermal expansion between Si and GaN, a mismatch in lattice constant and chemical reactivity must be solved to grow crack free, high quality epitaxial III-nitride films on Si substrates. Growth using rare-earth oxides as a buffer could solve these problems [1]. This study is aimed to develop growth technology of non-polar and semi-polar GaN on Si substrates using Er_2O_3 as the buffer layer.

In this work GaN growth was performed in a close-coupled showerhead metalorganic chemical vapor deposition reactor (MOCVD). Various parameters such as carrier gasses, temperature, growth starting conditions were varied. GaN annealing was also performed. Grown GaN layers were investigated using scanning electron microscopy (SEM), X-Ray diffraction (XRD) and photoluminescence (PL) techniques.

The XRD investigation showed the polycrystalline nature of GaN layers with dominant non-polar $(11\bar{2}0)$ and semi-polar $(10\bar{1}3)$ orientations. More detailed texture analysis revealed that both dominant GaN orientations are formed by growth of {0001} GaN planes parallel to the {111} facets of Si, thus causing the twinning in GaN layers. The domination of semi-polar or non-polar orientation is strongly dependent on Er_2O_3 (110) in-plane orientation respect to Si (100) wafer off-cut. XRD results also revealed how V/III ratio reduction leads to stronger semi-polar GaN orientation (Fig. 1). SEM investigation of the grown structures showed that nitrogen atmosphere helps to obtain smoother epitaxial layers, while in hydrogen atmosphere islands-like GaN growth was observed. The PL spectra of semi-polar and non-polar GaN showed a near band edge emission including luminescence from the stacking faults. A red shift was observed in spectra due to the expected thermal induced tensile strain in GaN.

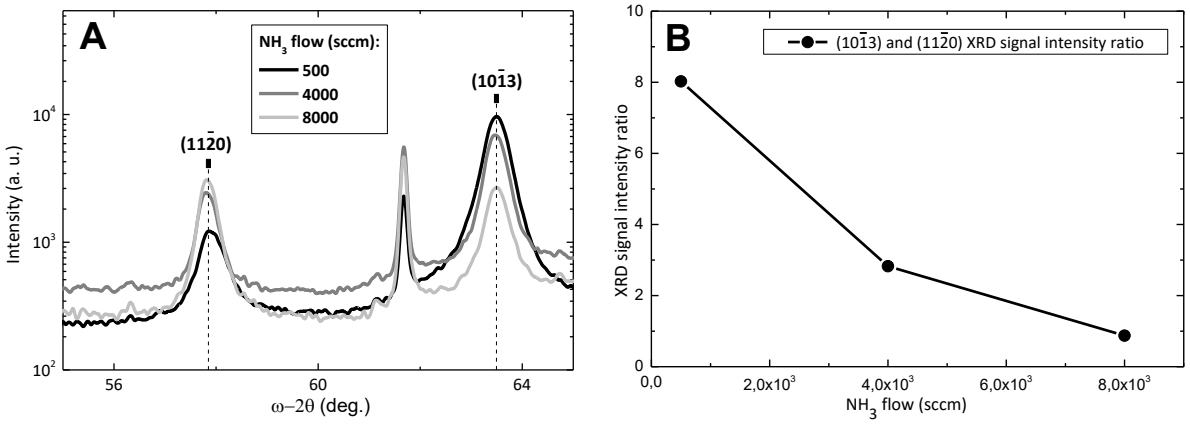

Fig. 1. XRD ω-2θ scans of GaN (A) and corresponding XRD signal ratios (B).

[1] T. Grinys, R. Dargis, M. Frentrup, A. Kalpakovaitė - Jucevičienė, K. Badokas, S. Stanionytė, A. Clark, T. Malinauskas, Facet analysis of truncated pyramid semi-polar GaN grown on Si (100) with rare-earth oxide interlayer, Journal of Applied Physics **120**, 105301 (2016).

Poster session 4

OXYGEN ELECTROREDUCTION CATALYSED BY LACCASE WIRED TO GOLD NANOPARTICLES *VIA* THE TRINUCLEAR COPPER CLUSTER

Marius Dagys[1], Audrius Laurynėnas[1,2], Dalius Ratautas[1,2], Juozas Kulys[1], Regina Vidžiūnaitė[1], Martynas Talaikis[1], Gediminas Niaura[1], Liucija Marcinkevičienė[1], Rolandas Meškys[1], Sergey Shleev[3,4]

[1] Life Sciences Center, Vilnius University, Lithuania
[2] Faculty of Fundamental Sciences, Vilnius Gediminas Technical University, Lithuania
[3] Malmö University, Sweden
[4] Kurchatov NBICS Centre, National Research Centre "Kurchatov Institute", Russian Federation
marius.dagys@bchi.vu.lt

Oxygen reduction directly to water is a reaction of utmost importance in aerobes as well as in artificial systems like fuel cells. Such cells are comprised of two electrodes (bioanode and biocathode) with their surface containing immobilized enzymes which catalyze oxidation or reduction of compounds present in working solutions, while the electrons are taken or given directly to electrode surface. The resultant electric current is sufficient to power micro devices, when the system is working in complex media such as blood. Oxidoreductases are the enzymes suitable for synthesis of effective, selective and rapid action biofuel cells. However, enzymatic cathodes currently suffer from low performance and rapid inhibition. One of the main reasons is a complex electron transfer mechanism during the biodevice operation, which involves heterogeneous and intramolecular electron transfer reactions. The latter is the rate-limiting step in oxygen bioelectroreduction under physiological conditions, where a biofuel cell is supposed to operate.

We have developed a unique high-redox-potential enzymatic cathode able to operate in electrolytes with a broad pH range and in the presence of high concentrations of halogen ions, as well as presented proofs for its reaction mechanism [1]. The efficiency of adsorbed enzymes is higher than that in homogeneous catalysis, because of the change of the reaction rate-limiting step achieved by specific orientation of a nanometer-size biocatalyst on a nanostructured surface. Specifically, the trinuclear copper cluster (T2/T3) of the low molecular weight, naturally deglycolysed laccase from *Didymocrea* sp. is able to receive electrons needed for oxygen reduction directly from gold nanoparticle surface (Fig. 1). Meanwhile, all the previously published and utilized laccase biocathode systems relied on direct electron transfer between the surface and intermediate T1 copper cluster with related shortcomings – poor operation in physiological pH and in presence of halogen ions.

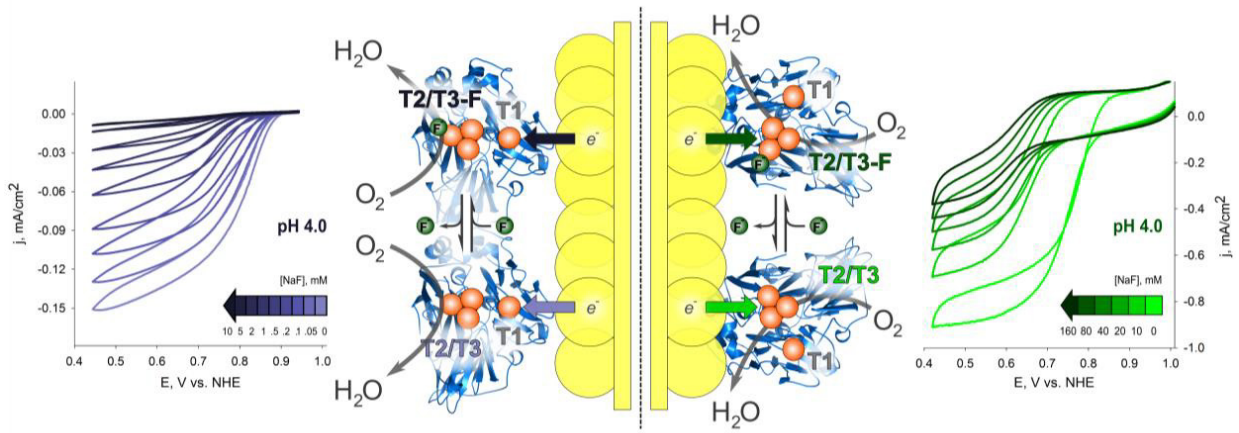

Fig. 1. Cyclic voltammograms of laccase-modified electrodes, synthesized by usual (*left*) and new enzyme adsorption method (*right*), recorded in working buffer solution at pH 4.0 and different NaF concentrations. Conditions: temperature – 23 °C, electrode spin rate – 1000 rpm, cathodic – anodic scan rate – 5 mV s^{-1}. The schemes show suggested electron transfer pathways for each electrode.

[1] M. Dagys, A. Laurynėnas, D. Ratautas, J. Kulys, R. Vidžiūnaitė, M. Talaikis, G. Niaura, L. Marcinkevičienė, R. Meškys, S. Shleev, Oxygen electroreduction catalysed by laccase wired to gold nanoparticles *via* the trinuclear copper cluster, Energy & Environmental Science, Advance Article, DOI: 10.1039/C6EE02232D, (2017).

CYTOGENOTOXIC EFFECTS IN COMMON ONION (*ALLIUM CEPA* L.) ROOT CELLS INDUCED BY TOPSOIL CONTAMINATED WITH ANTHROPOGENIC AND BIOGENIC BYPRODUCTS

Agnė Jurevičiūtė, Asta Stapulionytė

Institute of Biosciences, Life Sciences Center, University of Vilnius, Lithuania
agne.jureviciute@gf.stud.vu.lt

This study was conducted to examine harmful effects of the topsoil contaminated with anthropogenic and biogenic byproducts. 22 topsoil samples were collected from four sites with different anthropogenic pollution intensity (VITE secondary school stadium in Klaipėda, Fabijoniškės landfill in Vilnius, Verkšionys pit in Vilnius district, Vilnius city electrical substation No.1), and one site representing the topsoil contaminated with biogenic bird living activity byproducts (Cormorants colony in Neringa) and also a composite background sample of pooled topsoil samples from uncontaminated areas. 38 chemical elements were determined in all topsoil samples and 15 single potential harmful elements (PHE) were identified according to the Maximum Permissible Concentrations [1]. Overall topsoil contamination with multiple PHE was expressed as a total pollution index Zd. Topsoil samples with a hazardous level of total pollution were found in the stadium in Klaipėda city and their total contamination in decreasing order is as follows: VITE S (Zd = 40) > VITE W (Zd = 39) > VITE N (Zd = 18). All the rest sites had permissible levels of total contamination.

A standard model plant – common onion (*Allium cepa* L.) – was employed in our research for its broad and simple application in cytogenetic studies [2]. Onion root growth inhibition test was carried out in order to investigate the cytotoxic effects of contaminated topsoil on root growth capacity. *Allium* test was carried out to determine mitotic index (MI) and chromosome aberration (CA) frequency for the evaluation of genotoxic effects of topsoil on plant root cells [3]. Micronucleus (MN) test was carried out to evaluate mutagenic topsoil effects in onion root tip cells.

Onion root growth in Cormorants colony topsoil samples D, E and C was inhibited by 52, 50 and 34 %, in Vilnius city electrical substation topsoil – by 32 %, in pooled background samples – by 24 %, while root growth inhibition in Fabijoniškės landfill topsoil was only 9 % when compared to negative control.

Root tip cell MI was significantly lower ($P < 0.01$) in onions grown in topsoil from Fabijoniškės landfill, VITE S and N, Cormorants colony samples B, C and D, Verkšionys pit sample 3, Vilnius city electrical substation than in onions grown in negative control and background topsoil.

Estimation of CA frequency in onion root tip cells has revealed that genotoxic effects were induced by topsoil from Cormorants colony samples B, E and Verkšionys sample 1 as only in those the incidence of bridges, laggards and sticky chromosomes was significantly increased when compared to negative control and background topsoil ($P < 0.05$).

Screening of topsoil mutagenic effect has revealed a significant increase in MN frequency in root tip cells of onions grown in Verkšionys topsoil sample 4 and all VITE topsoil samples ($P < 0.01$). MN test results show that VITE stadium in Klaipėda is of real danger to pupils and the most probable reason is Cr anomaly because this element exceeds Maximum Permissible Concentration more than 10 times, while Verkšionys topsoil sample 4 has Cr, Cu, Hg, Mo and Zn exceeding Maximum Permissible Concentrations up to twice.

Determination of the relationships among cytogenetic indices and total pollution has revealed only one strong correlation between MN frequency and the total topsoil pollution level expressed as Zd ($P = 0.0033$; $r = 0.7262$), onion root length correlated with the MI as well ($P = 0.0058$; $r = 0.6749$), but other indices showed no significant relationships.

It is known that PHE may act differently in complex mixtures and influence the environment for extended periods as they do not decompose or degrade. When PHE exceed permissible concentrations in sites of high anthropogenic impact or due to geological anomalies we can see a negative mutagenic effect on living systems and our results confirm that most contaminated topsoil is the most dangerous. Low MI in root tip cells and strong onion growth inhibition in topsoil from Cormorants colony reflects the inability of the plant to pursue cell cycle at a normal rate under cytotoxic conditions of high amounts of biogenic byproducts. Nevertheless, Cormorants colony's topsoil has induced only genotoxic outcomes, which were not turned into mutagenic consequences later as in contrary in the case of VITE topsoil screening.

This research was funded by the Research Council of Lithuania, grant No. MIP-042/2015.

[1] Dėl Lietuvos higienos normos HN 60:2004 "Pavojingų cheminių medžiagų didžiausios leidžiamos koncentracijos dirvožemyje" patvirtinimo, Lietuvos Respublikos sveikatos apsaugos ministerija, Vilnius, 2004. https://www.e-tar.lt/portal/lt/legalAct/TAR.633ED152B54A.

[2] P.A. White, L.D. Claxton, Mutagens in contaminated soil: a review, Mutat. Res. **567,** 227-345 (2004). doi:10.1016/j.mrrev.2004.09.003.

[3] J. Rank, M.H. Nielsen, A modified Allium test as a tool in the screening of the genotoxicity of complex mixtures, Hereditas **118,** 49-53 (1993). doi:10.1111/j.1601-5223.1993.t01-3-00049.x.

INFLUENCE OF SIDERITIS TAURICA ON LIPID PEROXIDATION AND ANTIOXIDATIVE SYSTEMS IN ALLOXAN-INDUCED DIABETIC RATS

Diana Reznikova

Biology Department, Belarusian State University, Belarus
reznikova.dv@mail.ru

The present study was undertaken to investigate the antidiabetic capacity of Sideritis taurica's extract on lipid peroxidation and antioxidative systems of rats with alloxan-induced diabetes.

Sideritis taurica's extract was given to laboratory animals instead of water for 7 days with standard diet. 30 male rats were randomly divided into 3 groups: control, alloxan-induced diabetic and diabetic plus Sideritis extract treatment groups. Liver samples were taken from all animals and analyzed for superoxide dismutase and catalase activities and malondialdehyde levels. Blood samples were taken to analyze the level of lipids, in particularly, cholesterol and triacylglycerides.

Compared to the diabetic group, superoxide dismutase and catalase activities in the diabetic-treatment group were higher, whereas malondialdehyde level was the same as in the intact control group. The level of lipids, cholesterol and triacylglycerides in diabetic group were significantly higher than those in the intact group. These values were slightly higher than the values in the intact group.

These data demonstrated that the levels of lipid peroxidation of diabetic rats were high, whereas there was a slight increase in the basal antioxidant enzyme activities. However, extract of Sideritis taurica may attenuate oxidative stress by enhancing antioxidant enzyme activities and decreasing lipid peroxidation level in experimental rats with diabetes.

SUPEROXIDE DISMUTASES ACTIVITY IN MICE BRAIN UNDER SELENIUM AND/OR ALIUMINIUM IONS TREATMENT

Kristina Adomaitytė[1], Ilona Sadauskienė[2,3], Ingrida Stankevičienė[2,3], Arūnas Liekis[2], Rima Naginienė[2], Vaida Šimakauskienė[2], Dalė Baranauskienė[2,3]

[1] Department of Neurobiology and Biophysics, Faculty of Natural Sciences, Vilnius University
[2]Neuroscience Institute, Lithuanian University of Health Sciences
[3]Department of Biochemistry, Medical Academy, Lithuanian University of Health Sciences
kristinaad@gmail.com

Within a cell superoxide dismutases (SOD) are the first line of defence against reactive oxygen species. The present study was conducted to investigate the influence of Se and/or Al ions on the SOD activity in brain as well as distribution of these elements in the blood and the brain of laboratory mice.

Experiments were done on 4-6 weeks old outbreed mice. SOD activity was determined in brain after 24 h and 14 d. Al and/or Se solution i.p. injections. SOD activity was determined spectrofotometrically. The concentration of protein was measured by the Warburg-Christian method. Se and Al concentrations were determined by inductively coupled plasma mass spectrometer.

It was evaluated the effect of Al on SOD activity in mouse brain after a single i.p. Al injection. The results showed that SOD activity was the same value in control and experimental groups. After a single Se dose injection SOD activity decreased by 28.6% (compared to the control group). Subsequently, were evaluated changes in SOD activity following a single Se+Al mixture injection. It was observed a significant decrease in SOD activity (17.8%).

In further experiments, there was evaluated the effects of Al and/or Se on SOD activity after 14 d. i.p. injections. The results showed that injections of these elements alone did not cause changes of SOD activity. The data of the effect of both elements showed that SOD activity decreased by 41.5% (compared to the control group).

Estimation of the element distribution in brain homogenates showed that after 24 h and 14 d. concentrations did not differ from controls. While in blood: after 24 h exposure levels of Se increased in Se and Se+Al group (22% and 41% respectively) and after 14 d. increased Se and Al concentrations. It is also established in Se+Al group, but Al concentrations are significantly lower.

Our studies revealed that the Se and Al total effect in the mice brain reduce the enzymatic SOD activity after 24 h and 14 d. repeated exposure.

INVESTIGATION OF HYBRID MONTE CARLO ALGORITHM FOR RADIATION DOSE PREDICTION OF INTRABEAM® SPHERICAL APPLICATOR

Povilas Gabralevičius[1,2], dr. Sven Clausen[1], dr. Frank Schneider[1]

[1] Department of Radiation Oncology, University Medical Center Mannheim, Germany
[2] Department of Physics, Kaunas University of Technology, Lithuania
povilas.gabralevicius@ktu.edu

The Carl Zeiss INTRABEAM® system is a mobile x-ray unit for intraoperative radiotherapy (IORT). It has been clinically used for over fifteen years, however, up to now, the treatment prescription proceeded considering the patient as a large volume of water, neglecting the tissue inhomogeneities or backscatter. RADIANCE (GMV, Spain) is the only available treatment planning system (TPS) platform that has been designed for IORT devices, including INTRABEAM®. The engine of this TPS is a modified hybrid Monte Carlo algorithm. It is not clear, whether doses calculated by this algorithm agree with real doses produced by INTRABEAM®. The aim of this work is to investigate the behavior of hybrid Monte Carlo algorithm and accept or reject the feasibility of using the INTRABEAM-RADIANCE system in the clinical field.

Measured dose distribution from radiochromic Gafchromic EBT3 films were used as a reference in comparison with simulated dose distributions from RADIANCE TPS. PTW solid water (RW-1), solid muscle (RM-1) and solid fat (RF-1) slabs were used to examine the behavior of Hybrid Monte Carlo algorithm in homogeneous, as well as inhomogeneous medium for 4 cm spherical INTRABEAM applicator (Fig. 1). Comparisons were based on gamma index evaluation, 10%-1mm local pass criteria was considered a good agreement between measured and calculated dose distributions.

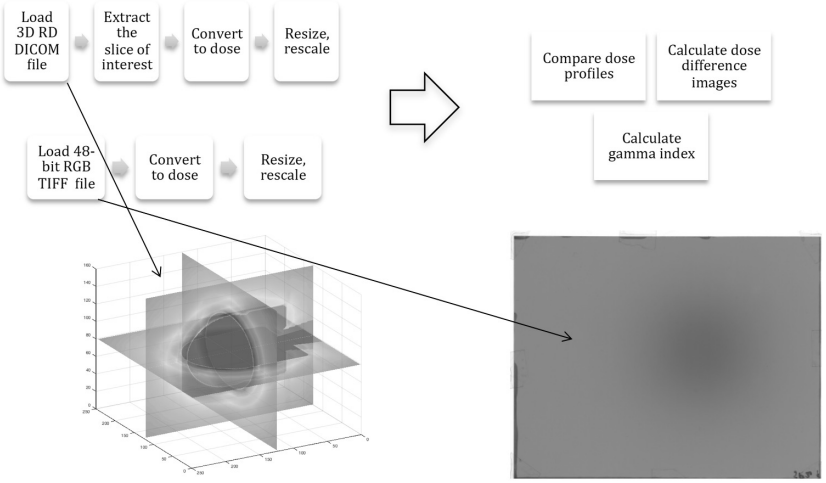

Fig. 1. Algorithm of simulated and measured radiation dose comparison.

Absolute dose distributions from RADIANCE TPS and Gafchromic EBT3 film were compared. Dose distributions calculated with hybrid Monte Carlo algorithm showed good agreement with the dose distribution measured on film in solid water medium, for 4 cm spherical applicator gamma (10%-1mm) passed with 98.26% pixels, however, in inhomogeneous materials, gamma passing rate was 91.87% in solid muscle and only 66.93% in solid fat.

To conclude, the hybrid MC algorithm in RADIANCE TPS simulates dose distributions in water material with high accuracy, nevertheless, the impact of inhomogeneities in media lead to failure in producing the equitable dose distributions. Therefore, to use the RADIANCE TPS in the clinical field for predicting the dose distributions in intraoperative radiotherapy for INTRABEAM® would be improper.

GENOTOXICITY ASSESSMENT OF HEAVY METAL MODEL MIXTURE IN SWAN MUSSEL, EUROPEAN PERCH AND COMMON ROACH GILLS

Greta Ašmenaitė, Gerda Petkutė, Milda Stankevičiūtė, Laura Butrimavičienė

The Nature Research Centre, Laboratory of Genotoxicology, Akademijos str. 2, 08412 Vilnius, Lithuania
g.asmenaite@yahoo.com

Aquatic pollution is a global environmental problem. One of the most hazardous and toxic pollutants are heavy metals which have been used by humans for centuries. Although heavy metals can occur in water naturally and some of them are essential nutrients that are required for various biochemical and physiological functions. Anthropogenic activities related to various industries also contribute to an increase of metals in the aquatic environment [1]. There is defined strict Maximum-Permissible-Concentrations of heavy metals (Zn-0.1; Cu-0.01; Ni-0.01; Cr-0.01; Pb-0.005 and Cd-0,005 mg/l) corresponding to Lithuanian inland water standards. However, there is a need to investigate the possible effect of these metals in mixtures aquatic individuals. To assess heavy metals contamination in the aquatic environment, different types of organisms must be used. Swan Mussel (*Anodonta cygnea*), European Perch (*Perca fluviatilis*) and Common Roach (*Rutilus rutilus*) were used as test-organisms. Bivalve mollusks have an ability to accumulate heavy metals to various orders of magnitude with respect to the levels found in their environment. Filter-feeding organisms can accumulate the contaminants at much higher levels than those found in the water column. Therefore, they are biological indicators of the pollution of aquatic ecosystem. Besides their widespread distribution, these species have additional criteria of ideal bioindicator as being sedentary and easy to sample [2]. Fishes are also described as perfect bioindicators in ecotoxicity studies,because of the ability to metabolise and accumulate xenobiotics. [3]. Perch and roach are valuable foodstuff therefore heavy metals in fishes can have a direct impact on human health [4].

The aim of this study was to evaluate genotoxicity responses in Swan Mussel (*Anodonta cygnea*), European Perch (*Perca fluviatilis*) and Common Roach (*Rutilus rutilus*) after 14 days of exposure to heavy metal model mixture (HMMM) at Maximum-Permissible-Concentration (Zn-0.1; Cu-0.01; Ni-0.01; Cr-0.01; Pb-0.005 and Cd-0.005 mg/l) corresponding to Lithuanian inland water standards. Micronucleus and two types of nuclear abnormalities were analysed in order to determine genotoxicity. This assay has been used increasingly to evaluate genotoxicity of various compounds in polluted aquatic ecosystems [5] Heavy metals, insecticides, pesticides, herbicides and other contaminants may be determined using this assay [6] [7]. In this study micronuclei (MN), nuclear buds (NB) and blebbed (BL) nuclei were analysed in gills of mussel, perch and roach. Gills were selected for genotoxicity assessment, because they are target tissue due to they direct contact with pollutants. Seven individuals were analysed in each treatment and control group. The results revealed that the levels of genotoxicity in mollusks, perch and roach have increased significantly after exposure to HMMM. The frequencies of nuclear buds and blebbed nuclei cells in mollusks were 15.94286 ‰ and 19.87143 ‰ respectively. The frequencies of micronucleus in roach were equal to 0.214286 ‰ and blebbed cells in perch - 0.041667 ‰ and these frequencies are significantly higher in comparison to control.

[1] Mustafa Türkmen, Aysun Tepe, Yalçın Ateş, Alpaslan Gökkuş, Kutalmı. Determination of metal contaminations in sea foods from Marmara, Aegean and Mediterranean seas: Twelve fish species, FOOD CHEM **108**, 794-800 (2008).

[2] Philip S Rainbow, Trace metal concentrations in aquatic invertebrates: Why and so what? ENVIRON POLLUT **120**, 497–507 (2002).

[3] Ahmed S.A. Harabawy, Yahia Y.I. Mosleh, The roleofvitaminsA,C,E and seleniumas antioxidants against genotoxicity and cytotoxicity of cadmium, copper, lead and zinc on erythrocytes of Nile tilapia, Oreochromis niloticus, ECOTOX ENVIRON SAFE **104**, 28–35 (2014).

[4] Yujun Yi, Zhaoyin Wang, Kang Zhang, Guoan Yu, Xuehua Duan. Sediment pollution and its effect on fish through food chain in the Yangtze river. INTERNATIONAL JOURNAL OF SEDIMENT RESEARCH **23**, 338–347 (2008).

[5] Toni P. Galindo, Lilia M. Moreira, Evaluation of genotoxicity using the micronucleus assay and nuclear abnormalities in the tropical sea fish Bathygobius soporator (Valenciennes, 1837) (Teleostei, Gobiidae), GENET MOL BIOL **32**, 394–398 (2009).

[6] Grisolia Cesar Koppe. A comparison between mouse and fish micronucleus test using cyclophosphamide, mitomycin C and various pesticides. MUTAT RES-GEN TOX EN **518**, 145-150 (2002).

[7] Ossana N.A, Salibian A. Micronucleus test for monitoring the genotoxic potential of the surface water of Luján River (Argentina) using erythrocytes of Lithobates catesbeianus tadpoles. ECOTOXICOL ENVIRON CONTAM **8**, 67-74 (2013).

ENVIRONMENTAL GENOTOXICITY STUDIES IN ERYTHROCYTES CELLS OF FISH COLLECTED IN THE EASTERN GOTLAND BASIN OF THE BALTIC SEA

Janina Greiciūnaitė, Roberta Valskienė, Laura Butrimavičienė, Janina Baršienė

Nature Research Centre, Akademijos str. 2, LT-08412 Vilnius, Lithuania
j.greiciunaite@gmail.com

Environmental genotoxicity was investigated in blood erythrocytes of flounder (*Platichthys flesus*), herring (*Clupea harengus*) and cod (*Gadus morhua*) specimens, which were collected at 20 stations located in the Eastern Gotland basin of the Baltic Sea, during 2011 – 2014 period (Fig. 1). The induction of micronuclei (MN), nuclear buds (NB), nuclear buds on filament (NBf), bi-nucleated erythrocytes with nucleoplasmic bridges (BNb) and blebbed (BL) nuclei in peripheral blood erythrocytes was evaluated as genotoxicity endpoints.

According to the results, the frequencies of analysed nuclear abnormalities have decreased during 2011–2013 period and increased in 2014. During the 2011-2014 period of the investigation, the highest frequency of MN (12.05 ‰) was detected in *C. harengus* from station 1e in 2014. This station is located in the centre of the chemical munitions dumpsite C (Fig. 1). In 2011, there were determined the highest frequencies of all other nuclear abnormalities. The frequency of NB reached 1.25 ‰, NBf – 1.80 ‰ level in blood erythrocytes of *C. harengus* collected from the station 19c. Meanwhile, nuclear abnormalities such as BL (1.65 ‰) and BNb (0.13 ‰) were detected in *P. flesus* caught at study stations 3c and 19c, respectively. Stations 3c and 19c are located approximately about 15 km from an official chemical munitions dumpsite C. There are known CW agent findings to west-south direction from the dumpsite C.

Induction of genotoxicity responses was higher in *C. harengus* than in *P. flesus*, while, the lowest responses were found in *G. morhua.* There were detected statistically significant interspecific differences between frequencies of the analysed endpoints NB (p=0.0481), NBf (p=0.005) in flounder and herring caught from the same station 19c. Statistically significant differences were found between these two species consider BL (p=0.0463) in station 3c, NB (p=0.0015) and BL (p=0.0232) frequencies in specimens caught at station 6k.

The analysis of MN induction revealed that fish sampled from 1e, 19c, 3c, 14e, 16e, 6k, 3y, 20k, 13k stations have attributed to extremely high genotoxicity risk levels. MN frequencies in 80–100 % of flounder specimens, collected inform the study stations (3c, 19c, 3y); were higher than the background level (P90). For herring, extremely high genotoxicity risk levels were determined in stations 1e and 14e. Low genotoxicity risk levels were assessed for all three fish species sampled only in two investigated stations (6v and 7v).

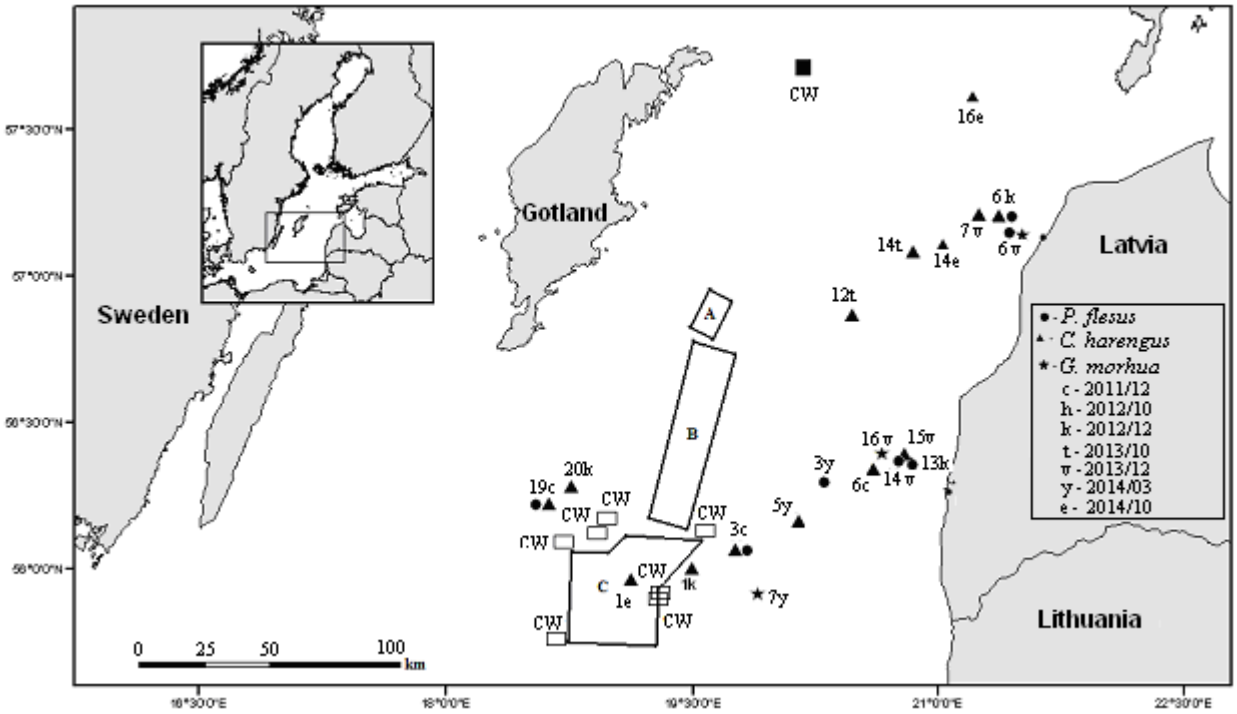

Fig. 1. Sampling stations of *Platichthys flesus*, *Clupea harengus*, *Gadus morhua* at the Eastern Gotland Basin of the Baltic Sea in 2011– 2014. A, B, C – chemical munitions dumpsites. CW – detected chemical warfare agents [1, 2].

[1] HELCOM, 2013. Chemical munitions dumped in the Baltic Sea. Report of the Ad Hoc Expert [2] Group to Update and Review the Existing Information on Dumped Chemical Munitions in the Baltic Sea (HELCOM MUNI). Baltic Sea Environment Proceeding (BSEP) 142, p. 128.
[2] CHEMSEA Findings, 2014. Beldowski, J., Fabisiak, J., Popiel, S., Östin, A., Olsson, U., Vanninen, P., Latsumaki, A., Lang, T., Fricke, N., Brenner, M., Berglind, R., Baršienė, J. et al., Gdansk, Institute of Oceanology, Polish Academy of Sciences, (86 pp.).

EFFECTS OF SEX HORMONES ON CELL DEATH IN CELLS WITH MUTATIONS RESPONSIBLE FOR LEBER'S HEREDITARY OPTIC NEUROPATHY

Elona Jankauskaitė[1], Agata Kodroń[1], Ewa Bartnik[1, 2]

[1] Institute of Genetics and Biotechnology, Faculty of Biology, University of Warsaw, 5a Pawińskiego Str., 02-106 Warsaw, Poland.
[2] Institute of Biochemistry and Biophysics, Polish Academy of Sciences, 5a Pawińskiego Str., 02-106 Warsaw, Poland.
elona.jankauskaite@gmail.com

Leber's hereditary optic neuropathy (LHON) is the most common mitochondrial disease resulting in central vision loss due to optic nerve atrophy. Most cases are caused by a mutation in mitochondrial genes encoding one of three subunits of mitochondrial complex I (ND1, ND4, and ND6). LHON is considered as a disease of young men because of its early onset between 20 and 30 years and male preponderance (50% men and only 10% women with mutations predisposing to LHON are affected). The mitochondrial DNA (mtDNA) usually is homoplasmic for the mutation in every cell, but for unknown reasons only retinal ganglion cells (RGC) are affected.

Changes in mitochondrial respiratory chain or ROS production can lead to induction of apoptosis. Most LHON mutations involve a decrease in Complex I activity and some data suggest that cells with these mutations are more prone to apoptosis. In females, estrogens are thought to modify the severity of mitochondrial dysfunction, including defective ATP synthesis, oxidative stress and apoptosis [1]. However, no increase of LHON in post-menopausal women is observed. It has been reported that high concentrations of testosterone initiate an apoptotic pathway and induce neurotoxicity in neuroblastoma cells [2]. So far not much data has been published regarding the role of testosterone in apoptosis in LHON affected men.

The aim of this research is to determine the effect of sex hormones on cell death in LHON patient and control cells. Human optic nerve cells are unavailable for testing, therefore a lymphoblast cell model was used. Lymphoblast cell lines were established from whole blood samples obtained from 3 LHON affected individuals with a confirmed m.11778G>A mutation and 3 healthy age-matched controls without the mutation. The effect of testosterone on initiation of apoptosis was investigated via the canonical apoptotic pathway which involves activation of aspartate-specific proteases (caspases). Apoptosis was confirmed by PARP cleavage. Autophagy was confirmed using the proportion of two isoforms of LC3 protein.

Here we present for the first time the influence of both sex hormones (estrogen and testosterone) on apoptosis and autophagy in LHON. Preliminary results indicate a higher level of apoptosis in LHON patient cells compared to controls. In addition, apoptosis in LHON cells was confirmed to occur via a caspase-independent pathway as previously reported in the literature using cybrids [3].

[1] C. Giordano, M. Montopoli, E. Perli et al., Oestrogens ameliorate mitochondrial dysfunction in Leber's hereditary optic neuropathy, Brain, 1-15 (2011)
[2] M. Estrada, A. Varshey, B. E. Erlich. Elevated Testosterone Induces Apoptosis in Neuronal Cells, The journal of biological chemistry 281, 25492–25501 (2006)
[3] C. Zanna, A. Ghelli, A.M. Porcelli, A. Martinuzzi et al., Caspase-independent death of Leber's hereditary optic neuropathy cybrids is driven by energetic failure and mediated by AIF and Endonuclease G, Apoptosis, 10 (5), 997-1007 (2005)

PROOFREADING DOMAIN FACILITATES SPACER INTEGRATION IN CRISPR-CAS – AN ADAPTIVE PROKARYOTIC IMMUNITY

Gediminas Drabavičius, Arūnas Šilanskas, Tomas Šinkūnas, Giedrius Gasiūnas

Institute of Biotechnology, Vilnius University, Lithuania
gdrabavicius@gmail.com

Bacteria and archaea are constantly assailed by viral pathogens. Like higher organisms, they have evolved defense systems, most of which could be likened to innate immunity. However, some microorganisms have an adaptive system called CRISPR-Cas (**C**lustered **R**egularly **I**nterspaced **S**hort **P**alindromic **R**epeats). This system works in three stages: (I) Adaptation, where pieces of destroyed viral DNA are incorporated into genomic CRISPR loci as spacers between identical repeats; (II) crRNA Maturation, where CRISPR locus and Cas genes are transcribed and effector complexes assemble; (III) Interference, where effector complexes, which patrol the cell find a pathogen which has complementary DNA to a spacer from CRISPR locus and destroys it.

Between different prokaryotes, a wide variety of CRISPR-Cas systems exist. They are subdivided into Classes 1 and 2. Class 1 is composed of CRISPR-Cas systems which has an effector complex composed of several proteins, whereas Class 2 exhibit effector complexes of a single protein, most famous of which is Cas9 [1, 2]. These Classes are further divided into Types and Subtypes. Despite this great variety, the adaptation (spacer acquisition) is achieved by similar means in all of them. All systems have highly conserved Cas1 and Cas2 proteins responsible for the immunization of bacteria or archaea.

In this study, we investigated Cas1 and Cas2 proteins from *Streptococcus thermophilus* strain DGCC7710. This bacterium has 4 different CRISPR-Cas systems and is very important for milk industry. Furthermore, it was the first microorganism in which the function of CRISPR-Cas systems, as an anti-viral defense mechanism, was demonstrated [3]. We chose CRISPR4-Cas system. It is unique in that its Cas2 protein is fused to DnaQ domain, which is an exonuclease domain homologous to ϵ subunit of *Escherichia coli* DNA polymerase. ϵ subunit is responsible for proofreading activity [4, 5]. Although several organisms exhibit Cas2-DnaQ fusion, its function in integration remained obscure. In this study, we set out to find out the function and a role of the DnaQ domain in CRISPR4-Cas adaptation.

[1] Makarova, Kira S., et al. "An updated evolutionary classification of CRISPR-Cas systems." *Nature Reviews Microbiology* (2015).
[2] Mohanraju, Prarthana, et al. "Diverse evolutionary roots and mechanistic variations of the CRISPR-Cas systems." *Science* 353.6299 (2016).
[3] Barrangou, Rodolphe, et al. "CRISPR provides acquired resistance against viruses in prokaryotes." *Science* 315.5819 (2007): 1709-1712.
[4] Huang, Yiping, Dan K. Braithwaite, and Junetsu Ito. "Evolution of dnaQ, the gene encoding the editing 3′ to 5′ exonuclease subunit of DNA polymerase III holoenzyme in Gram-negative bacteria." *FEBS letters* 400.1 (1997): 94-98.
[5] Hamdan, Samir, et al. "Hydrolysis of the 5 '-p-Nitrophenyl Ester of TMP by the Proofreading Exonuclease (ε) Subunit of *Escherichia coli* DNA Polymerase III." *Biochemistry* 41.16 (2002): 5266-5275.

REVIEW OF PACIENTS, DIAGNOSED WITH NON HODGINS LYMPHOMA, TREATED IN VILNIUS UNIVERSITY SANTARIŠKIŲ KLINIKOS CHILDRENS HOSPITAL IN YEARS 2010 TO 2015

Tomas Kairys[1],Vėtra Markevičiūtė[1], Dr. Gražina Kleinotienė[2], Gyd. Arijanda Neverauskienė[3]

[1] Department of Medicine, Vilnius univerisity, Lithuania
[2] Centre of Oncohematology, Children's Hospital, Affiliate of Vilnius University Hospital Santariškių klinikos, Vilnius, Lithuania
[3] Centre of Radiology, Children's Hospital, Affiliate of Vilnius University Hospital Santariškių klinikos, Vilnius, Lithuania
tomas.kairys@mf.stud.vu.lt

The term lymphoma describes a heterogeneous group of malignancies with different biology and prognosis. In general, lymphomas are divided into 2 large groups of neoplasms, namely non-Hodgkin lymphoma (NHL) and Hodgkin disease. About 85% of all malignant lymphomas are NHLs[1].
NHL includes many clinicopathologic subtypes, each with distinct epidemiologies; etiologies; morphologic, immunophenotypic, genetic, and clinical features; and responses to therapy. With respect to prognosis, NHLs can be divided into two groups: indolent and aggressive[2].
Although a variety of laboratory and imaging studies are used in the evaluation and staging of suspected NHL, a hematoxylin and eosin (H&E)–stained section of an excised lymph node is the mainstay of pathologic diagnosis. The treatment of non-Hodgkin lymphoma (NHL) varies greatly, depending on tumor stage, grade, and type and various patient factors[2]

Despite being one of the most common and well studied cancers,with both well documented diagnostic and treatment protocols, very little is know about epidemiological situation in Lithuania.Data for this study was collected in Vilnius university Santariškės Childrens hospital retrospectively, from case reports of pacients, treated from years 2010 to 2015.Out of 20 histories, 14 met our criteria: children, diagnosed with Non Hodgins lymphoma (NHL), currently juvenile, treated at VULSK Vaikų ligoninė.

20 pacient were diagnosed with NHL, 14 fully met our criteria.Four out of them were girls.(28,5%), 10 were boys (71.5%) Median age at the time of diagnosis 9.57 +- 4.9. Seven reached full remission 7 (50%). NHL was diagnosed in stages I to IV. NHL III st. – 8 (57%), IVst – 4 (29%), I and II st –1 (3.5%). Most common out of all histological subtipes was Burkitts lymphoma 6 (43%), followed by Anaplastic large cell limphoma 3 (22%).

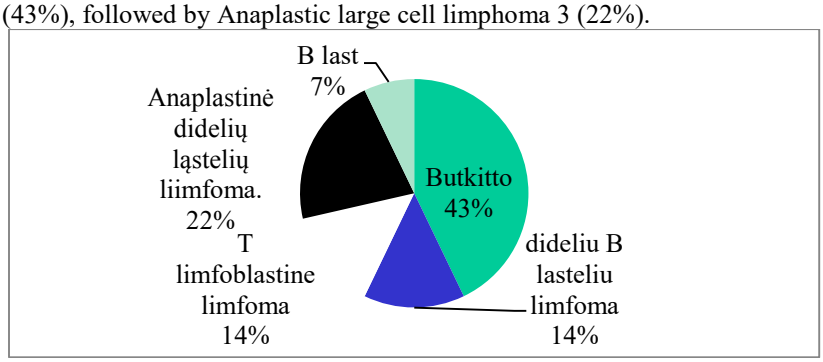

Fig. Distribution of diferent types of NHLs betwen pacients

Most common protocol of treatment used was B-NHL-BFM-04 7(50%). Most common symptoms were lymphadenopathy 5 (21proc.). Radiological diagnostic procedures performed 38 KT, 46Ro, 1 PET, 3 MRT, 3 scintigraphies. Most common out of these procedures were head and neck CT, Chest and abdominal CT and abdominal CT, all of which were performed 5 times (5,13%).

In conclusion, dominant first symptom for pacients, with NHL – enlarged lymph nodes. NHL most commonly diagnosed at stage III stadijos.Most common histological type- Burkitt limphoma .Main method of diagnostics-CT

1 Jaffe ES, Harris NL, Stein H, Vardiman JW, eds. World Health Organization Classification of Tumours: Pathology and Genetics of Tumours of Haematopoietic and Lymphoid Tissues. Lyon, France: IARC Press; 2001
2.Zhang QY, Foucar K. Bone marrow involvement by Hodgkin and non-Hodgkin lymphomas. *Hematol Oncol Clin North Am*. 2009 Aug. 23(4):873-902.
3.PDQ Adult Treatment Editorial Board. Adult Non-Hodgkin Lymphoma Treatment (PDQ®): Health Professional Version. June 1, 2016.

DEVELOPMENT OF MIXED-MODE POLYMERIC SORBENT ASSAY FOR A MULTI-RESIDUE ANALYSIS OF DRUGS IN BIOLOGICAL MATRICES BY FAST GAS CHROMATOGRAPHY TECHNIQUE

Nerijus Karlonas

The State Forensic Medicine Service, Toxicology Laboratory, Didlaukio 86E, LT-08303 Vilnius, Lithuania
nerijuskarlonas@yahoo.com

When developing a fast gas chromatography with negative-ion chemical ionization mass spectrometry (GC/NICI-MS) method matrix effects are a major issue. The effect of co-eluting compounds arising from the matrix can result in signal enhancement or suppression [1]. During the method development much attention should be paid to diminish matrix effects as much as possible. The present work evaluates matrix effects from whole blood and urine samples in the simultaneous analysis of fifteen benzodiazepines.

Therefore, the main aim of study was development of a new sensitive and specific method based on GC/NICI-MS using a mixed-mode solid phase extraction (SPE) for the identification and quantification of these drugs in biological samples. Moreover, the speed of the analytical separation was emphasized by modifying various GC/NICI-MS parameters. The fully validated method was applied for the quantification of several benzodiazepines in real whole blood and urine samples.

The proposed GC/NICI-MS method coupled with a mixed-mode SPE (a strong cation-exchange polymeric sorbent) and derivatization by N-(tert-butyldimethylsilyl)-N-methyltrifluoroacetamide:acetonitrile:ethyl acetate mixture (20:40:40 (v/v/v)) was shown to be useful for the analysis of benzodiazepines and their metabolites in biological samples. A derivatization step using different silylation reagents, duration, and temperature was investigated. This method is the fastest among the others reported up to now [1]. Under the optimized GC conditions derivatives of analytes were completely separated within 3.9 min, as shown in Fig. 1. Sensitive and specific NICI-MS detection combined with fast GC resulted in sharp and symmetric peak shape of the target analyte, while maintaining sufficient resolution (Fig. 1). Sample preparation conditions including selection of the solvent for washing and elution steps, pH values were also optimized. To the best of my knowledge, this method has been used for the first time for the optimization of sample preparation at pH 1.0.

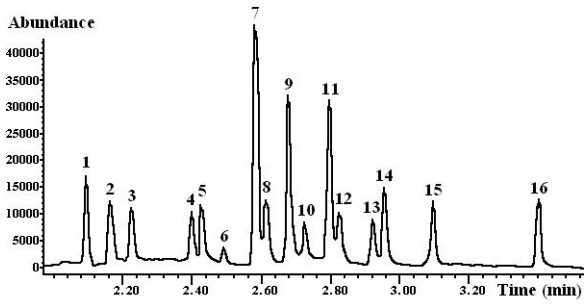

Fig. 1. Chromatogram of whole blood sample at pH 1.0 spiked with 20 ng mL^{-1} of 15 benzodiazepines. The peak numbering refers to: (1) internal standard; (2) diazepam; (3) nordiazepam; (4) midazolam; (5) flunitrazepam; (6) bromazepam; (7) oxazepam; (8) nitrazepam; (9) temazepam; (10) 7-aminoclonazepam; (11) lorazepam; (12) clonazepam; (13) alprazolam; (14) α-OH-midazolam; (15) triazolam; (16) α-OH-alprazolam.

The developed method for 15 benzodiazepines determination in biological samples was validated following the recommendation for new methods [1,2]. The linear relationships with the correlation coefficients (r2) better than 0.9960 was evaluated. It was determined that extraction efficiency ranged from 82.9 (±6.2) % to 94.6 (±3.4) %. The precision (RSD) for benzodiazepines was 4.08 - 9.52 %, while the accuracy was in the range of 93.0 - 106.3 %. The developed method provides significant advantages in comparison with other previously published methods [1]. It shows higher sensitivity (the limit of detection ≤ 0.62 ng mL^{-1}) in biological samples. Moreover, this method has several advantages: elimination of interferences (Fig. 1), low-volume of samples (0.2 mL) and a multi-residue analysis. According to the results, the developed GC/NICI-MS-SPE method is accurate, sensitive and specific enough to detect analytes after a long time use of a single oral administration of some drugs. Furthermore, this method enables to reach the highest specificity for major analytes and meets the requirements of good laboratory practice, especially when applied to pharmacodynamic investigations. Ultimately, the developed method has been applied in routine toxicological analysis during the investigation of both clinical and forensic cases.

[1] V. F. Samanidou, M. N. Uddin, et al., Benzodiazepines: sample preparation and HPLC methods for their determination in biological samples, Bioanalysis **1,** 755-784 (2009).

[2] N. Karlonas, et al., Mixed-mode SPE for a multi-residue analysis of benzodiazepines in whole blood using rapid GC with negative-ion chemical ionization MS, Journal of Separation Science **36**, 1437-1445 (2013).

ISOLATION AND IDENTIFICATION OF *PSEUDOMONAS SYRINGAE* PATHOVARS ON CEREALS IN LITHUANIA

Jurgita Kelpsienė, Skaidre Suproniene

Institute of Agriculture, Lithuanian Research Centre for Agriculture and Forestry, Instituto al. 1, LT–58344 Akademija, Kėdainiai dist., Lithuania.
jurgita.kelpsiene@lzi.lt

Based on DNA the homology, *Pseudomonas syringae* species is divided into more than fifty pathovars and at least nine different species; however, only two pathovars are clearly attributed to cereal diseases. Basal glume blotch and leaf blight caused by *P. syringae* pv. *atrofaciens* and P. *syringae* pv. *syringae* respectively, are the diseases of wheat, barley, rye, triticale and oats. These pathovars have been detected in Italy, Germany, Belgium, Mexico, Russia and other cereal-growing countries. Diagnosis of bacterial diseases based on expressed symptoms is difficult, because they can be confused with those caused by some fungi or other abiotic and biotic factors. It is therefore likely that these diseases could be more widespread and important than is commonly thought. *P. syringae* has not been studied on cereals in Lithuanian before; however, the atypical for fungal injuries leaf spots and glume discolorations have been frequently found recently. The aim of current study was to assess the presence of *P. syringae* pathovars on cereals in Lithuania.

The isolates of *P. syringae* used in this study originated from various regions of Lithuania. Samples of leaves, stems, heads and mature seeds of diseased winter and spring wheat, winter triticale, and spring barley plants were collected in 2013 - 2015. Pure cultures of the selected *P. syringae*-like isolates were recovered from accumulative onto selective media [1, 2]. The isolates were tested for production of blue-green fluorescent pigment on King's medium B and were used for LOPAT test (levan production from sucrose positive, oxidase reaction negative, pectolytic activity on potato slices negative, the presence of arginine dihydrolase negative, hypersensitivity to tobacco leaves positive) [1, 2]. Based on LOPAT test results to *P. syringae* assigned strains were evaluated for their pathogenicity to host plants using seedling spray and the leaf injection methods (fig. 1) [2, 3].

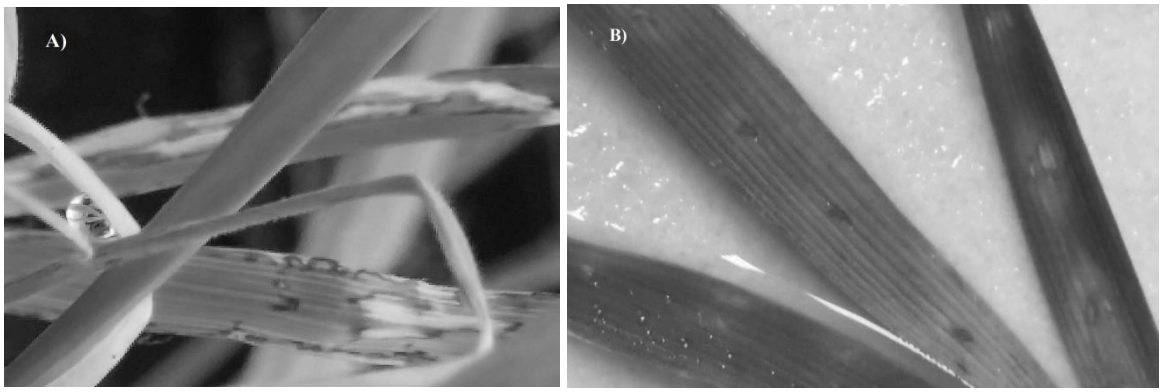

Fig. 1. Seedling test: A) leaf blight symptoms after spray inoculation of host plant seedlings in glasshouse B) according Toben et al. (1989) only *Pseudomonas syringae* pv. *atrofaciens* causes typical dark margins around the inoculation points on barley and wheat seedlings. (Photo: J. Kelpsiene.)

According to the above mentioned features, only 2.4% of all isolated bacteria were assigned to *P. syringae* [1, 2]. The leaf blight symptoms on seedlings sprayed with bacterial suspension were caused only by half of the selected strains. None of the strains caused dark margins around the injection point, therefore could not be attributed to *P. syringae* pv. *atrofaciens.* According to our results, *P. syringae* poses only minimal threat to Lithuania-grown cereals and it is likely that the environmental conditions in our country are more favourable for the occurrence of *P. syringae* pv. *syringae.*

References

[1] Lelliott, R. A. and Stead, D. E. (1987) Methods for the diagnosis of bacterial diseases of plants, Vol. II. Blackwell Scientific Publications, Oxford, Great Britain.

[2] Schaad, N. W., Jones, J. B., Chun, W. (2001) Laboratory Guide for Identification of Plant Pathogenic Bacteria, 3rd ed., American Phytopathological Society, Saint Paul, Minnesota, USA.

[3] Toben H., Mavridis A., Rudolph K.W.E. 1989. Basal glume rot (*Pseudomonas syringae* pv. *atrofaciens*) on wheat and barley in FRG and resistance screening of wheat. Bulletin OEPP/EPPO Bulletin 19, 119-125.

INTRAPERITONEAL VERSUS INTRAVENOUS CHEMOTHERAPY: TREATING OVARIAN CANCER

Emilija Kurlytė[1], Skaistė Tulytė[2]

[1] Faculty of Medicine, Vilnius University, Lithuania
[2] Vilnius University Hospital Santariskiu Klinikos, Centre of Hematology, Oncology and Transfusion Med.
kurlyte.emilija@gmail.com

Ovarian cancer is characterized as aggressive and usually asymptomatic disease therefore is diagnosed at late-stage, so it is important to look for the best treatment [1]. One promising way is intraperitoneal (IP) chemotherapy. Some studies have demonstrated its survival advantage in comparison to intravenous (IV), although more severe adverse effects have been noticed and it is unknown if it is long-term beneficial [2].

Our aim was to compare outcomes of IP and IV chemotherapy, progression-free survival (PFS) and side effects of drugs.

Methods we used: retrospective study of 36 patients with epithelial ovarian cancer at Vilnius University Hospital Santariskiu Klinikos. 15/36 patients were treated with IP chemotherapy and 21/36 – IV. Analyzed data: demography of patients, cytoreduction rate, tumor differentiation grade, existence of metastasis, influence of neoadjuvant chemotherapy, PFS and drugs' adverse effects. Associations between categorical variables were determined using Shapiro-Wilk test, t-test of independent samples; applications used – Microsoft Excel 2010, SPSS 17.0.

Results: average age of patients: IP – 47.5±7.9 years, IV – 52.8±12.4 years.

		IP (months)	IV (months)	p=
Statistically significant	Average PFS with neoadjuvant chemotherapy	13.3±2.5	21.5±10.7	0.001
No statistical significance	Average PFS	19.5±2.9	20.1±4.0	0.904
	PFS after radical debulking (R_0)	13,3±2,5	23,1±9,3	0.679
	PFS after G_3 differentiation grade	21.8±4.7	19.3±4.1	0.694
	PFS if metastatic disease	12	13.6±1.8	-
	PFS with no neoadjuvant chemotherapy	28.8±4.2	19.6±4.1	0.133

Table 1. Average PFS values in both groups, regarding different factors.

More often IP			More often IV			Similar frequency		
	IP (%)	IV (%)		IP (%)	IV (%)		IP (%)	IV (%)
Drug induced polyneuropathy	53.3	33.3	Anemia	46.7	71.4	Cardiotoxicity	26.7	23.8
Neutropenia	53.3	47.6	Thrombocytopenia	13.3	57.1	Nephrotoxicity	6.7	9.5
Obstipation	26.7	4.8	Hepatotoxicity	0	23.8	Postoperative adhesions	6.7	9.5
Dyspepsia	46.7	28.6	Arthralgia	0	14.3	Insomnia	6.5	9.5
Weakness	20.0	9.5	Rash	0	9.5			
Abdominal pain	13.3	0	Ototoxicity	0	4.8			
Infection at drain site	13.3	0	Anaphylaxis	0	4.8			
			Headache	0	4.8			

Table 2. Side effects of chemotherapeutic drugs.

To sum up: based on results, there were no statistical significance in both patient's groups average PFS, although treatment starting with neoadjuant chemotherapy is better with IV. Both ways are well tolerated, we did not observe extremely severe side effects.

[1] Chan JK, Cheung MK, Husain A, et al: Patterns and progress in ovarian cancer over 14 years. Obstet Gynecol 108:521-528 (2006)
[2] Tewari D, Java JJ, Salani R, Armstrong DK, Markman M, Herzog T,Bradley et al: Long-Term Survival Advantage and prognostic Factors Associated With Intraperitoneal Chemotherapy Treatment in Advanced Ovarian Cancer: A Gynecologic Oncology Group Study. Journal of Clinical Oncology 33: 1460 (2015)

REVIEW OF PACIENTS, DIAGNOSED WITH HODGKIN LYMPHOMA AND TREATED IN VUL S/K CHILDREN`S HOSPITAL IN 2010-2015

Vėtra Markevičiūtė[1], Tomas Kairys[1], Gražina Kleinotienė[2], Arijanda Neverauskienė[3]

[1] Department of Medicine, Vilnius univerisity, Lithuania
[2] Centre of Oncohematology, Children's Hospital, Affiliate of Vilnius University Hospital Santariškių klinikos, Vilnius, Lithuania
[3] Centre of Radiology, Children's Hospital, Affiliate of Vilnius University Hospital Santariškių klinikos, Vilnius, Lithuania
vetra.markeviciute@mf.stud.vu.lt

Hodgkin disease is a type of lymphoma. Lymphoma is a cancer of a part of the immune system called the lymph system. The first sign of Hodgkin disease is often an enlarged lymph node.[1] Hodgkin lymphoma accounts for 5% to 6% of all childhood cancer.[2] Hodgkin lymphoma is a potentially curable lymphoma. The World Health Organization classifies Hodgkin lymphoma into five gty: nodular sclerosing, mixed cellularity (see the image below), lymphocyte depleted, lymphocyte rich, and nodular lymphocyte-predominant.[3] The 5-year overall survival for Hodgkin lymphoma of all stages is very high, usually greater than 80%. Patients with stage I or II disease have overall survival rates greater than 90%, whereas those with stage III or IV disease have overall survival rates as low as 70%.[4]

Despite being one of the most common and well studied cancers, with both well documented diagnostic and treatment protocols, very little is know about epidemiological situation in Lithuania. Data for this study was collected in Vilnius university Santariškės Childrens hospital retrospectively, from case reports of pacients, treated from 2010 to 2015. Out of 27 histories, 8 met our criteria: children, diagnosed with Hodgkin's lymphoma (HL), currently juvenile, treated at Children`s Hospital, affiliate of Vilnius University Hospital Santariškių klinikos.

27 patients were diagnosed with HL in 2010-2015. 13 boys, 14 girls. Twelve are currently adults. 1 was treated in Kaunas. 1 refused biopsy, due to that, diagnosis could not be confirmed. 1 refused chemotherapy. 1 deceased. 1 patient was excluded due to receiving bone marrow transplant. No data on 2 patients.

Eight patients fully met our criteria. 4 boys (50%) and 4 girls (50%). Median age of diagnosis was 10,25+-5,1. Youngest patient was 4 years old. 5 patients were (62.5%) in full remission. Main symptom was enlarged lymph nodes 35%.

Stage at diagnosis: stage II to IV (II stage – 5 (62%), III stage – 2 (25%) ir IV stage – 1 (13%)). HL nodular sclerosis type– 6 (75%), HL mixed cellularity type – 2 (25%).

Chemotherapy applied in accordance with EuroNet-PHL-C1 protocol (2006). 2 patients, stage IIIA ir IIIB received radiotherapy. Relapses 2 (40%) out of 5, both boys. Both relapsed patientss reached remission again. Radiological diagnostic procedures performed: 36 CT, 4 Ro, 17 PET. Out of all radiological scans, most common were: Chest 13 (36%), neck and chest CTs 10 (28%). In average, one patient received 4,5 CT scans. Highest number of CT scans received - 10. First CT for all of the patients was either chest or lung CT scan.

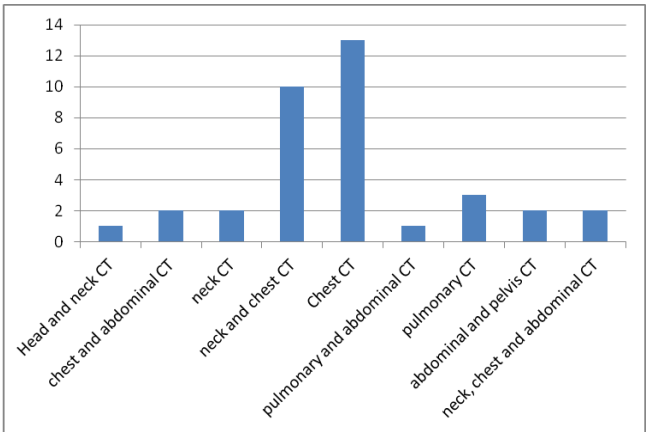

Fig. 1. CT, performed for children with HL, types and frequency

First symptom usually is lymphadenopathy for patients, diagnosed with HL. HL most commonly diagnosed at stage II, nodular sclerosis hystological type. Main method of diagnostics - CT scan.

[1] https://medlineplus.gov/hodgkindisease.htmll
[2] Hodgkin Lymphoma in Childhood. Laila M. Sherief, MD, Usama R. Elsafy, and etc. Medicine (Baltimore). 2015 Apr; 94(15): e670.
[3] Jaffe ES, Harris NL, Stein H, Vardiman JW, eds. World Health Organization Classification of Tumours: Pathology and Genetics of Tumours of Haematopoietic and Lymphoid Tissues. Lyon, France: IARC Press; 2001.
[4] Pediatric Hodgkin Lymphoma, Pedro A de Alarcon, MD William H Albers Professor and Chair. Updated: Apr 29, 2015 Medscape

USE OF DNA MARKERS IN THE DIFFERENTIATION OF RELATED PLANT SPECIES

Gediminas Misevičius, Jolanta Patamsytė, Donatas Žvingila

Institute of Biosciences, Life Sciences Center, Vilnius University, Lithuania
gediminas.misevicius@gf.stud.vu.lt

The development of molecular marker techniques is one of the most effective methods for marker-assisted selection and molecular breeding [1]. These techniques are also very promising in plant systematics and phylogenetic studies.

Identifying the correct plant species is the first step for a study, but sometimes related plant species are almost impossible to identify correctly using phenotypic characteristics as a guide. This is an issue in our research, and we found a method that helps us differentiate between such related plant species as *Stuckenia pectinata* and *Stuckenia* × *fennica*. By using DNA marker techniques, in particular inter-simple sequence repeats (ISSR), and agarose gel electrophoresis we were able to identify species-specific bands. Using molecular markers, it is possible to create a species profile that can later be used to identify the plant or differentiate it from other related plants. While we only used two species, we believe that the method can be generalized and should work as intended with any related plant species. With modern DNA extraction kits and laboratory equipment the whole process can be done in a single day and gives scientists a low-cost method of differentiating between otherwise indistinguishable plant species.

[1] Jo IH, et al., Applications of molecular markers in the discrimination of Panax species and Korean ginseng cultivars (Panax ginseng), Journal of Ginseng Research (2016).

BIOFILM PREVENTION OF *PSEUDOMONAS AERUGINOSA* AND *STAPHYLOCOCCUS EPIDERMIDIS* BY DICEPHALIC CATIONIC SURFACTANTS AND THEIR INTERACTIONS WITH DNA

Emil Paluch[1], Agata Piecuch[1], Ewa Obłąk[1], Łukasz Lamch[2], Kazimiera Wilk[2]

[1] University of Wrocław, Institute of Genetics and Microbiology, Poland
[2] Wroclaw University of Technology, Department of Organic and Pharmaceutical Technology, Poland
mikro.paluch.emil@gmail.com

The studies were aimed to contribute to the elucidation of the relationships between structure of the novel cationic surfactants- N,N-bis[3,3'-(dimethylamine)- propyl]alkylamide dihydrochlorides and N,N-bis[3,3'-(trimethylammonio)propyl]alkylamide dibromides (alkyl: n-C9H19, n-C11H23, n-C13H27, n-C15H31) (Fig.1) and their biological activity. The antibacterial activity of the compounds as well as their influence on the adhesion and biofilm formation of two bacterial strains - Pseudomonas aeruginosa PAO1 and Staphylococcus epidermidis ATCC 35984 was investigated. Tested surfactants exhibited antibacterial activity. All of the tested surfactants showed the ability to condense DNA. [1]

Formula	Abbreviation	R	MW (g mol^{-1})	CMC (mol l^{-1})
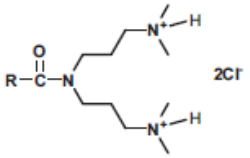	$C_{10}(DAPACl)_2$	n-C_9H_{19}	414·49	$7{\cdot}0 \times 10^{-2}$
	$C_{12}(DAPACl)_2$	n-$C_{11}H_{23}$	442·55	$2{\cdot}5 \times 10^{-2}$
	$C_{14}(DAPACl)_2$	n-$C_{13}H_{27}$	470·60	$9{\cdot}0 \times 10^{-3}$
	$C_{16}(DAPACl)_2$	n-$C_{15}H_{31}$	498·66	$3{\cdot}0 \times 10^{-3}$
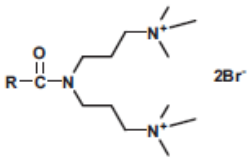	$C_{10}(TAPABr)_2$	n-C_9H_{19}	531·49	$8{\cdot}0 \times 10^{-2}$
	$C_{12}(TAPABr)_2$	n-$C_{11}H_{23}$	559·55	$3{\cdot}5 \times 10^{-2}$
	$C_{14}(TAPABr)_2$	n-$C_{13}H_{27}$	587·60	$1{\cdot}5 \times 10^{-2}$
	$C_{16}(TAPABr)_2$	n-$C_{15}H_{31}$	615·66	$4{\cdot}0 \times 10^{-3}$

*The values of Critical Micelle Concentration (CMC) come from ref. Frąckowiak *et al.* (2012a).
†The CMC values from ref. Skrzela *et al.* (2010).

Fig 1 Chemical structures and characteristics of dicephalic N,N-bis[3,30-(dimethylamine)- propyl]alkylamide dihydrochlorides (Cn(DAPACl)2)*and N,N-bis[3,30-(trimethylammonio)propyl]- alkylamide dibromides (Cn(TAPABr)2).[2]

[1] Piecuch A, Lamch Ł, Paluch E, Obłąk E, Wilk K. Biofilm prevention by dicephalic cationic surfactants and their interactions with DNA. J Appl Microbiol., 1-11, (2016).
[2] Skrzela, R., Para, G., Warszynski, P. and Wilk, K.A. Experimental and theoretical approach to nonequivalent adsorption of novel dicephalic ammonium surfactants at the air/solution interface. J Phys Chem B 114, 10471–10480, (2010).

CHARACTERISTICS OF GROUPING BY SIMILARITY IN CONJUNCTION VISUAL SEARCH

Tatjana Pladere[1*], Jurgis Skilters[2], Gunta Krumina[1]

[1] Department of Optometry and Vision Science, University of Latvia, Latvia
[2] Center for the Cognitive Sciences and Semantics, University of Latvia, Latvia
tatjana.pladere@gmail.com

In the very early stages of vision our perceptual processes attempt to organize sensory data into specific wholes, rather than separate parts. It is visual grouping that occurs automatically in lower visual processing areas of brain where input information is processed comparatively quickly. [1, 2]

It is characterized by strong Gestalt principles according to which definite physical properties of visual stimuli are preferred for grouping of information. However, it can be relatively influenced by top-down processes such as selective attention, interest, motivation and other. [1, 3]

Selective attention is a top-down controlled neuronal gain mechanism boosting relevant signals (information from targets), while at the same time actively ignoring irrelevant signals coming from so called distractors. It is proved to be highly involved in a successful accomplishment of conjunction visual search when more than one feature of visual stimuli differ a target from a distractor [4]. Findings prove that higher cognitive processes are resource limited and can be temporarily depleted, for instance, in the presence of mental fatigue [2].

Our study further explored the interaction of lower visual process with selective attention in different time of the day in order to determine characteristics of grouping by similarity. Within the study the computer program that generated sets of visual search and grouping tasks was created and implemented.

Results demonstrated that the longest reaction time that was required for finding the first target in conjunction visual search tasks was in the morning. Likewise grouping took longer time in the night group. Noticeably shorter reaction time was found in the day group and in the evening group. Our results showed that time for finding the first target was slightly longer when participants considered themselves being tired. Thus average reaction time per item varied from 3.11±0.27 to 3.84±0.79 seconds.

[1] Persson, J., Welsh, K. M., Jonides, J., & Reuter-Lorenz, P. A., "Cognitive fatigue of executive processes: Interaction between interference resolution tasks," *Neuropsychologia*, 45(7), 1571-1579 (2007).
[2] Palmer, S. E., [Vision science: photons to phenomenology], Cambridge, MIT Press (1999).
[3] Bundesen, C., "A theory of visual attention," *Psychological Review*, 97(4), 523-547 (1990).
[4] Wolfe, J. M., [Visual attention], In De Valois, K. K. (Ed.) Seeing, San Diego, Academic Press, 335-386 (2000).

F. GRAMINEARUM PRESENCE ON NON-GRAMINACEOUS PLANTS

Jurgita Kelpsiene, Neringa Rasiukeviciute, Skaidre Suproniene, Grazina Kadziene

Institute of Agriculture, Lithuanian Research Centre for Agriculture and Forestry, Instituto al. 1, LT-58344 Akademija, Kėdainiai distr., Lithuania

n.rasiukeviciute@lsdi.lt

Fusarium graminearum causing Fusarium head blight (FHB) is important cereal-pathogen rapidly spreading in Northern Europe, what most likely is promoted by changes in climate and farming practices. Besides of small grain cereals, *F. graminearum* is well known as causing ear and stalk rots in maize. In recent years, the host range has also expanded to non-graminaceous crops. In North America this pathogen is implicated as the cause tap roots and yellows of sugar beet, in the USA – soybean root and seedling rot and potato dry rot, in Canada – pea root rot. The observations of additional hosts of *F. graminearum* have epidemiological implications since all above-mentioned plants are frequently grown in close rotation. The aim of this study was to assess the presence of *F. graminearum* in non-cereal plants under field conditions and to evaluate the pathogenicity of this fungus to non-cereal plants *in vitro*.

The presence of *F. graminearum* was assessed in rapeseed, potato, sugar beet, and pea fields have grown in four conventional long-term cereal-based rotations in the Institute of Agriculture, Lithuanian Research Centre for Agriculture and Forestry in 2015-2016. For fifty healthy and symptomless plants per field were randomly collected. *Fusarium* isolated on potato dextrose agar (PDA), purified on Spezieller Nährstoffarmer agar medium and identified morphologically. Pathogenicity of *F. graminearum*, isolated from diseased wheats to non-graminaceous plants (pea, bean, rapeseed, potato, beet and sugar beet) seedlings was tested in a growth-camber under controlled conditions using agar plug method. Before use for inoculation, *F. graminearum* mycelium was grown for one week on PDA. In each experiment, 15 seedlings of each tested plant were inoculated with *F. graminearum* mycelium plugs in four replicates. Lesions of chlorosis and necrosis on leaves were evaluated according to the 0-5 rating scale.

During 2015-2016 403 of *Fusarium* isolates were isolated from non-cereal plants. *F. culmorum* (34.4%) dominated in all plant species. Prevalence of *F. equiseti, F. tricinctum, F. sporotrichioides, F. avenaceum, F. poae* and *F. graminearum* depended on year and plant species. The major FHB pathogen - *F. graminearum* composed only 5.2% of all isolates. *In vitro* tests showed that pathogenicity of *F. graminearum* differed depending on plant species. Least susceptible to *F. graminearum* were rape seedlings, most susceptible – pea and been.

Acknowledgement. The study was funded by the Lithuanian Research Council through the National Research Program “Sustainability of agro-, forest and water ecosystems” grant No. SIT-05/2015.

AN IMPORTANCE OF *PHYTOPHTHORA* SPECIES OF OAK DECLINE IN LITHUANIA

Karolis Sivickis[1], Dovile Cepukoit[2], Goda Norkute[1], Daiva Burokiene[1]

[1]Laboratory of Phytopathogenic Microorganisms, Institute of Botany at the Nature Research Centre, address: ZaliujuEzerustr. 49, LT-08406 Vilnius, Lithuania
[2]Vilnius University, Faculty of Nature Science, Department of Microbiology and Biotechnology, Vilnius, Lithuania
karolis.siv@gmail.com

Oaks, especially *Quercusrobur* has agreat importance to the forests of several European countries, including and Lithuania unfortunately decline is being observedsince the previouscentury.The rates and extent of the decline have dramatically increased during the last 25-30 years.In Western Europe and other world regions, a strong association has been observed between the presence of long drought and decline of *Phytophthora* spp. It has been proved that pathogenicity of *Phytophthora* spp. is one of the most important factors which determine the decline of treesin forests and nurseries. Until 2004 only one *P. infestans* was recognized in Lithuania. A few years ago, new *Phytophthora* species were recorded: *P. cinnamomi*, *P. cactorum* and *P. ramorum*.

In Lithuania, a disease of oak stands called “oak decline” was first described in 1976-1980.The last and the most severe wave of oak decline started in 2003-2004.In 2015 it was recorded that infectious diseases effected 4909 ha of forests, mostly ashes (2132 ha), asps(2038 ha) and declining oaks (352 ha). Mainly symptoms of a diseased tree are crown reduction in leaf discoloration and chlorosis, shoot death, bark damage.

The aim of this study was to investigate the impact of *Phytophthora* isolated from wood and soil of the declining oaks.

During summer of 2010, soils from 25 declining oaks in 5 locations in diseased stands have been collected for analysis. Subsequently, in 2016 samples from the soil of 5 oaks have been taken. Soil composition of sudden oak death places collected in 2010 and 2016 will be compared. Isolates were obtained using different bating techniques. 138 isolates assigned to oomycetes were characterized. Molecular identification of pathogens is in a process.

SYNTHESIS OPTIMISATION OF POLYVINYLPYRROLIDONE STABILIZED GOLD NANOPARTICLES

Sonata Adomaviciute, Akvile Slektaite-Kisone, Ricardas Rotomskis

Biomedical Physics Laboratory, National Cancer Institute, Vilnius, Lithuania
akvile.slektaite@nvi.lt

Cancer is the second leading cause of death (after heart diseases) in developed countries. Early and accurate detection of cancer using X-ray is valid, but complicated due to poor contrast of tissues. In order to enhance visibility of structures in body contrast agents were created. Water-soluble contrast agents made from iodinated molecules are clinically approved and widely used for X-ray imaging although sometimes can be insufficient. Different contrast agents were created and examined in order to overcome some limitations of iodinated contrast materials. Gold nanoparticles are considered to be one of the most reliable metal-based contrast agents which are expected to significantly improve X-ray imaging of soft tissues *in vivo* [1]. Gold nanoparticles (AuNP) have attracted intense interest as contrast agent over the past few years due to suitable properties for effective contrast material.

The aim of this study is to verify the best conditions of formation of polyvinylpyrrolidone (PVP) stabilised gold nanoparticles as well as to assess size distribution concentration and stability of AuNP dependence on reagents.

25 different synthesis products of AuNP were made by varying the concentrations of MES monohydrate and sodium hydroxide (NaOH) reagents. Synthesis was made at room temperature, by mixing MES and NaOH solutions, adding polyvinylpyrrolidone (PVPK30) and chloroauric acid ($HAuCl_4$) and vigorously stirring for 1 hour.

To determine properties and concentration of produced gold nanoparticles absorption spectra were measured (Fig. 1). The further stability and processes were monitored by measuring absorption spectra after 1, 2, 10 and 30 weeks.

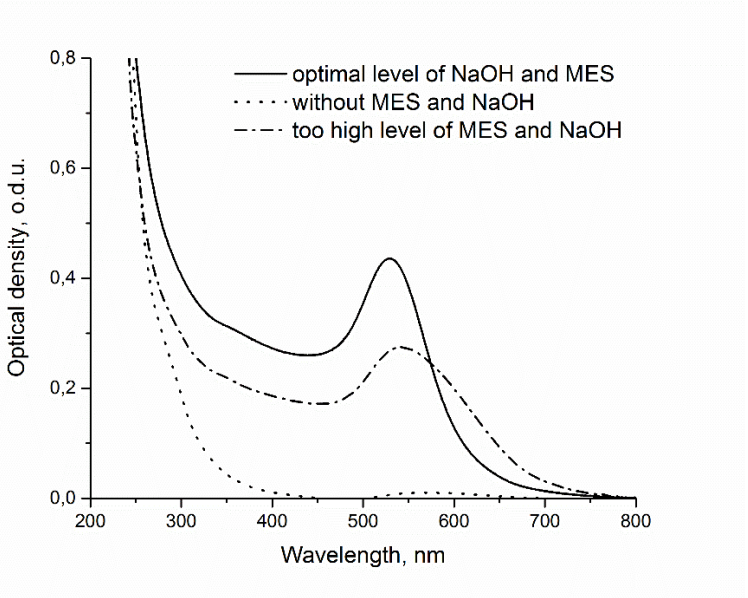

Fig. 1. Non-normalized absorption spectra of gold nanoparticles synthesized with different concentrations of reagents.

According to the absorption spectra (Fig. 1) the amount and size of produced AuNP depend on both concentration of reducing agent and pH. The sample without MES and NaOH had no significant absorption in comparison with other samples showing that synthesis did not occur. Nevertheless, when NaOH were added the absorbance appeared affirming that AuNP were produced. When NaOH and MES concentrations in primary solutions were optimal the concentration of uniformly sized nanoparticles was highest [2]. Although when concentrations of MES and NaOH exceeded these levels, synthesis of AuNP became not so efficient with higher distribution in size and decreased amount of formatted nanoparticles.

Results showed that concentration of reagents is critical for efficient synthesis of gold nanoparticles. Further investigation in conditions of AuNP synthesis will provide a more successful development of gold-based contrast agents and improvement in X-ray imaging.

[1] Laura Nebuloni, Gisela A. Kuhn, Ralph Muller, *A Comparative Analysis of Water-Soluble and Blood-Pool Contrast Agents for in vivo Vascular Imaging with Micro-CT* (Acad. Radiol. 2013, 20, 1247–1255)
[2] Wolfgang Haiss, Nguyen T. K. Thanh, Jenny Aveyard, and David G. Fernig, *Determination of Size and Concentration of Gold Nanoparticles from UV-Vis Spectra* (Anal. Chem. 2007, 79, 4215-4221)

COMBINED EFFECT OF HPV AND GENETIC POLYMORPHISMS IN *TP53*, *MDM2*, *MDM4*, *MTHFR*, *CCR5* AND *CASP8* IN LUNG CANCER

Agne Kunickaite[1], Ausra Stumbryte[2], Zivile Gudleviciene[2], Daiva Dabkeviciene[3], Regina Liudkeviciene[2], Genovefa Garmiene[2], Saulius Cicenas[4]

[1] Department of Human and Medical Genetics, Faculty of Medicine, *Vilnius University*
[2] Biobank, National Cancer Institute
[3] Institute of Biosciences, Vilnius University Life Sciences Center
[4] Department of Thoracic Surgery and Oncology, National Cancer Institute
agne.kunickaite@gmail.com

Non-small cell lung cancer (NSCLC) is one of the most common malignant tumors and the leading cause of all cancer related deaths worldwide. Aproximatelly 1.8 million people (1.240.600 men and 583.100 women) all over the world were newly diagnosed with lung cancer in 2012[2,3]. Epidemiological data in Lithuania reflects similar tendencies with 1421 new cases (8.0% of all cancers) and 1355 deaths (16.9%) in 2012[1].

Various studies showed that lung cancer is caused by both genetic and environmental factors and especially their interactions. Although exposure to carcinogens is considered to be the main cause, genetic variation and Human papillomavirus (HPV) may contribute to lung cancer risk. However, exact biomarkers for precise lung cancer prevention, diagnostics, treatment and prognosis still are under the investigations. Moreover, the functional polymorphisms in genes *TP53* Arg72Pro (rs1042522), *MDM2* T309G (rs2279744), *MDM4* (rs4245739), *MTHFR* (rs1801133), *CASP8* (rs3834129) and *CCR5* (rs333) alone or in combination, can affect survival (Fig.1).

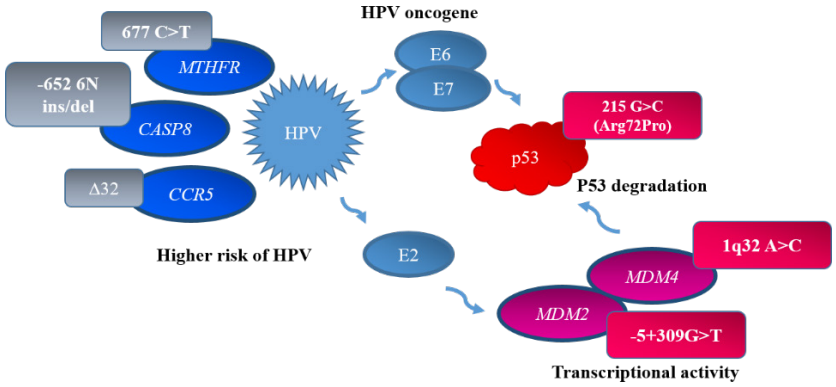

Fig. 1. Genes and HPV interactions.

The aim of our study was to evaluate the distribution of HPV and different SNPs involved in the carcinogenesis and its impact to the NSCLC patients survival.

Results: HPV infection was stated only in three patients with NSCLC. After genes polymorphisms analysis it was found that patients with *MDM2*c.-5+309G>T gene T/G polimorfic variant had a better survival rate over patients with G/G and T/T variants (P = 0,383). A/A polymorphic variant of the *MDM4*c.1q32A>C gene resulted in a better survival rate of the lung cancer patients than A/C polymorphic variant (P = 0,836). C/T and C/C polymorphic variants of the *MTHFR*c.677 C>T resulted in similar survival rates as the ones observed in the same test group. Del/del allelic variant of *CASP8*c.-652 6N ins/del gene SNP led to lower survival rates, when compared to the ins/del and ins/ins allelic variants. The analysis of the *CCR5*- Δ32 gene polymorphic wt/Δ32 and wt/wt variations observed in >10% survival difference, better survival rate was noted in the patients who were identified with wt/Δ32 polymorphic variant (P = 0.854). However all these differences were not statistically significant.

Conclusions: After cluster analysis, it was found that the best survival average median and better prognosis was noted in patients who were identified with *CASP8* ins/ins and *TP53* Arg/Pro polymorphic variants. Patients who were identified with *CASP8* ins/ins and *TP53* Arg/Pro gene polymorphic variants, survival rate was twice longer than those who were identified with *MDM4* A/A, *CCR5* wt/Δ32, *MTHFR* C/T, *MDM2* T/T genes polymorphisms.

[1] http://www.nvi.lt/wp-content/uploads/2016/04/Vezys_lietuvoje_2012.pdf.
[2] A.C. De Freitas, A.P. Gurgel, E.G. de Lima, B. de Franca Sao Marcos, C.M. Medeiros do Amaral, Human papillomavirus and lung carcinogenesis: an overview, Cancer Res Clin Oncol **142**, 2415-2427 (2016).
[3] L.A. Torre , F. Bray, R.L. Siegel, J. Ferlay, J. Lortet-Tieulent, A. Jemal. Global cancer statistics, CA Cancer J Clin **65**, 87–108 (2015).

EMOTION RECOGNITION ALGORITHM BASED ON INTEL REALSENSE TECHNOLOGY

Tarakanova Elizaveta, Kozlova Elena

Faculty of Radiophysics and Computer Technologies, Belarusian State University, Minsk, Belarus
l.tarakanowa@gmail.com

People communicate every day. Often there is a problem of misunderstanding that is closely connected to emotion recognition problem. The problem can be hard to solve for a human and is not easy to formulate. The solution of this problem may be applied in creating some useful programs from educational games to virtual psychologists and advertisement analyzers.

The idea of the present study is to create an emotion recognition algorithm using Intel RealSense technology. The algorithm can be used with other cameras, but Intel RealSense is used because it was originally made for recognition algorithms. Also it has a free software development kit [1].

The developed algorithm consists of six steps:

1. Getting image from the Intel RealSence camera.
2. Face detection.
3. Detection of 78 facial landmark points.
4. Counting key values using landmark points.
5. Analyzing key values.
6. Showing the result.

The picture is grabbed from the camera, then a face and facial landmark points are detected. As it is done the program counts the key values such as mouth and eyes being open in percents. Then the classification starts and the result is presented. Emotion classification for the algorithm was created using the Paul Ekman[2] studies and the mimic codes of emotional states. It was later improved according to the results of the algorithm testing.

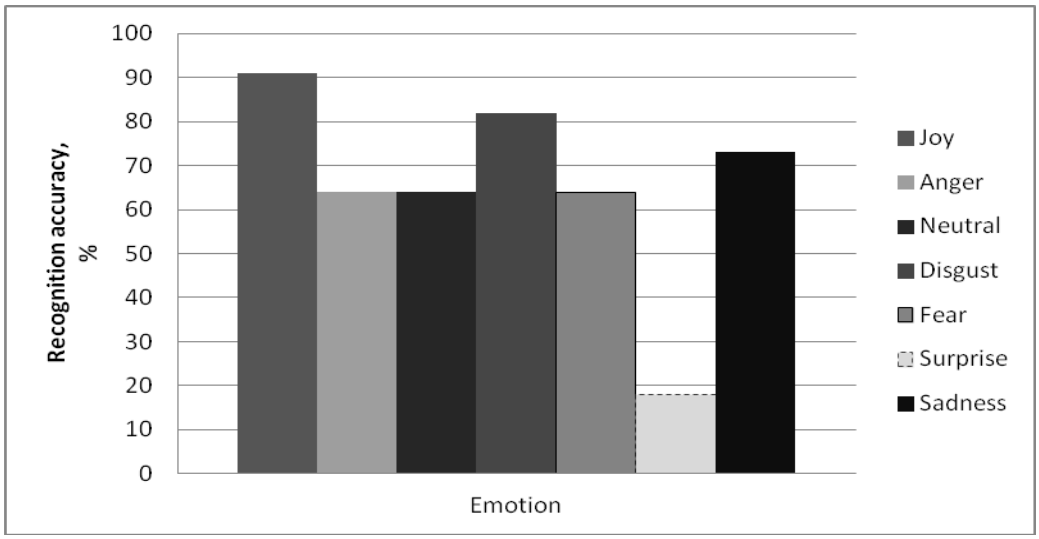

Fig. 1. Recognition accuracy of every emotion.

The algorithm was tested in the groups of people of different age and gender. Average accuracy of the algorithm is about 86% when it recognizes seven emotions with video frame rate about 30 fps.

[1] Internet address: http://click.intel.com/intelrrealsensetm-developer-kit-featuring-sr300.html.
[2] P. Ekman, W. Friesen, *Unmasking the Face: A Guide to Recognizing Emotions from Facial Clues* (Trans. Piter Publishing house, Russia, 2010).

THE COMPARISON OF CHONDROGENIC DIFFERENTIATION POTENTIALINHUMAN MESENCHYMAL STEM CELLS FROM MENSTRUAL BLOOD AND BONE MARROW USING ACTIVIN A AND TGF-β3

Ilona Uzielienė, prof. ZygmuntMackevič, dr. Daiva Bironaitė, JaroslavDenkovskij, Saulė Valiūnienė, Roma Grinienė, dr.Eiva Bernotienė

DepartmentforRegenerativemedicine, Centre forInnovativemedicine, Lithuania
i.uzieliene@imcentras.lt

Human mesenchymal stem cells (MSC) are multipotent cells found in many tissues. These cells generated a great deal of interest in regenerative medicine due to their high potential to differentiate into several lineages including osteoblasts,chondroblasts and adipocytes [1]. Articular cartilage due to its low capacity for self-repair is highly susceptible to degradative diseases such as osteoarthritis. Since cartilage is composed primarily of chondrocytes distributed in a specialized extracellular matrix, MSC with theirchondrogenic differentiation potential appear to be ideally suited for therapeutic use in cartilage regeneration [2]. Although the entire bond of molecular mechanisms that control chondrogenic differentiation in MSC is still unclear, some of the factors that help cell differentiation to occur have been developed. For instance,transforming growth factor β (TGF-β) was identified as a major cartilage-inducing factor and is always used for a qualitativechondrogenic response in cells [3]. Nowadays several literature sources suggest that a member of the TGF-β superfamily activin A also appears to play a pivotal role in the early stages of MSC chondrogenesis and osteogenesis, while inhibiting adipogenesis. It has been shown that activin A is necessary for the maintenance of self-renewal and pluripotency of MSC. Besides, activin A takes place in the regulation of women menstrual cycle and the uterus endodermis regeneration [4]. Since menstrual blood is enriched witheasy accessible MSC [5], wehypothesized that activin A may play a crucial role in chondrogenicdifferention of these MSC.

The aim of this study was to compare human mesenchymal stem cells isolated from two different tissues – menstrual blood (MenSCs) and bone marrow (BMSCs) and their potential to differentiate into chondrogenic lineage using two differentiation stimulation factors –activin A and TGF-β3. Firstly, we isolated the cells from 6 different healthy donors (3 – bone marrow donors; 3 – menstrual blood donors). Secondly, we compared these cells by different stem cell and chondrogenicdifferentiation surface markers (CD90, CD73, CD105, CD44, CD45, CD14, CD36, CD55, CD54, CD63, CD271, CD106, CD34, CD49a, CD49e, CD49c, CD338, ABCC1, CD10, Stro1, Notch1, CD221, CD133, Hla-DR) by flow cytometry and examined their proliferation capacity using proliferation kit CCK-8. Moreover, we analyzed the potential of MenSCs and BMSCs to differentiate into two MSC lineages – adipogenic and osteogenic. Adipogenic differentiation was assessed using Oil-Red staining, whereas osteogenic differentiation was assessed using alizarin red staining. Finally, chondrogenic differentiation was evaluated by histochemistry, staining cell pellets with safranin O and collagen II antibodies.

The results suggest that in contrast to BMSCs, MenSCs exhibited higher expression of CD10, CD49a and Notch1, and higher proliferative capacity. The potential ofadipogenic differentiation of MenSCs was weaker than BMSCs, and osteogenic differentiation capacity was positive and similar for both – MenSCs and BMSCs. Chondrogenic differentiation was also similar with TGF-β3 for both cell types, whileactivinAinduced chondrogenic differentiation was remarkably higher inMenSCsthan in BMSCs.

Even though several literature sources claimed that activin A is not a suitable alternative to TGF-β3 for chondrogenic differentiation of MSC [6], our results demonstrate that chondrogenic differentiation stimulated by activin A was positive for both tissue MSC, especially for MenSCs. In conclusion, to obtain stable cartilage formation, different cell types may require different growth factors inducing chondrogenic response in cells. Our comparative analysis implicates the significance of activin A as a functional growth factor for the induction of chondrogenic differentiation in MSC, suggesting MenSC as a perspective source for stimulation of cartilage repair and that activin A is implicated in their differentiation.

[1] Musumeci G, Castrogiovanni P, Leonardi R, et al. New perspectives for articular cartilage repair treatment through tissue engineering: Acontemporary review. World Journal of Orthopedics. 2014.

[2] Oldershaw RA. Cell sources for the regeneration of articular cartilage: the past, the horizon and the future. International Journal of Experimental Pathology. 2012; 93, 389–400.

[3] Tang J, Zhu X, Zhao J, Fung M, Li Y, Gao Z, Yan S, Li X, Ji X, Su F, Li1 Z. Tissue Transglutaminase-Regulated Transformed Growth Factor-β1 in the Parasite Links Schistosoma japonicum Infection with Liver Fibrosis. Mediators of Inflammation 2015; 11.

[4] Djouad F, Jackson WM, Bobick BE, Janjanin S, Song Y, Huang GTJ, Tuan RS. Activin A expression regulates multipotency of mesenchymal progenitor cells. Stem Cell Research & Therapy 2010; 1:11.

[5] Meng X, Ichim TE, Zhong J. Endometrial regenerative cells: A novel stem cell population. Journal of Translational Medicine. 2007; 5:57.

[6] Kroon LMG, Davidson ENB, Narcisi R. Activin and Nodal Are Not Suitable Alternatives to TGFβ for Chondrogenic Differentiation of Mesenchymal Stem Cells. Cartilage. 2016; 1-7.

EVALUATION OF ADIPOSE TISSUE FATTY ACID COMPOSITION IN PATIENTS WITH NEPHROLITHIASIS

Laima Vasiliauskaitė[1], Inga Bikulčienė[1], Zita Aušrelė Kučinskienė[1,2], Arvydas Kaminskas[1], Vaiva Hendrixson[1]

[1]Department of Physiology, Biochemistry, Microbiology and Laboratory Medicine, Faculty of Medicine, Vilnius University, M. K. Čiurlionio str. 21/27, LT-03101 Vilnius, Lithuania
[2]Center of Laboratory Medicine, Vilnius University Hospital Santariškių klinikos, Santariškių str. 2, LT-08861 Vilnius, Lithuania
Inga.bikulciene@mf.vu.lt

The aim of this study was to evaluate the relationship between abdomen adipose tissue fatty acid composition and type of kidney stones**.**

Abdominal adipose tissue fatty acid methyl esters of 71 patients with nephrolithiasis were identified by GC/MS while a type of kidney stones was identified using infrared spectroscopy. Individuals were divided into groups according to diagnosis of metabolic syndrome (MS) and type of kidney stones. Composition of adipose tissue fatty acids was compared within different groups of patients with nephrolithiasis and between 205 control individuals.

Our results showed that individuals with nephrolithiasis had significantly higher level of monounsaturated fatty acids (MUFAs) while values of polyunsaturated fatty acids (PUFAs) were lower *versus* control group and patients with kidney stones. Individuals with MS had a higher level of 18:1ω9 and a lower level of 16:1ω7 than patients without MS. Individuals with nephrolithiasis, but without MS, had a higher level of SFA compared to control. PUFAs level was ~2,4 times higher in control group compared to individuals with kidney stones, with or without MS. PUFAs, omega 6 PUFAs and 18:2ω6 were significantly higher in patients with calcium based kidney stones without MS *versus* patients with uric acid kidney stones with MS.

No statistically significant difference was found in abdominal adipose tissue fatty acid composition and individuals with kidney stones. MUFAs levels were significantly higher while PUFAs - lower in patients with nephrolithiasis compared to control.

.

ACCUMULATION OF SEVERAL HEAVY METALS AND CHANGES IN STABLE CARBON AND NITROGEN ISOTOPE RATIOS IN RED-CAPPED SCABER STALK (*LECCINUM AURANTIACUM)*

Lauma Busa[1], Kristine Zadvinska[1], Arta Bardule[1,2], Arturs Viksna[1]

[1] Faculty of Chemistry, University of Latvia, Latvia
[2] Latvian State Forest Research Institute "Silava", Latvia
lauma.busa@lu.lv

Red-capped scaber stalk is a mushroom of the *Boletaceae* family and genus *Leccinum*. It can be found fruiting during summer and autumn in forests of Europe and North America. The association between fungus and host tree is mycorrhizal. Although various studies have been carried out to evaluate the use of mycorrhizal fungi as bioremediators, only few researches have studied red-capped scaber stalk.

As Red-capped scaber stalks are edible mushrooms, the accumulation of heavy metals in the fruiting body must be considered as a potential harming factor to the consumers. Previous researches have shown that *Leccinum Aurantiacum* do accumulate rather high levels of copper and depends on the location of the sample site [1]. These mushrooms are between the most widely consumed ones in Latvia and therefore this research bears also importance of national level. Apart of being consumed as food, fungi can be named as some of the most vigorous agents for the decomposition of waste matter, and are an essential component of the soil food web [2]. While acting as decomposers of various waste and fertilizer matters, fungi accumulate not only heavy metals, but also other macro elements. To evaluate the capability of fungi to take up anthropological pollution and to follow the uptake patterns, stable isotope ratios can be used. Due to isotope fractionation and mixing, the heavier nitrogen isotope (^{15}N) can indicate higher levels of anthropological pollution.

In the research *Leccinum Aurantiacum* samples from hybrid aspen experimental plot (lat: 56.6919, lon: 25.1370) were analyzed. The plot was fertilized with biogas production residues or digestate (30 tonnes ha^{-1}), wastewater sludge (10 $tonnes_{DM}$ ha^{-1}) and wood ash (6 $tonnes_{DM}$ ha^{-1}) in the spring of 2011. After the fertilization an unexpected amount of red-capped scaber stalk mushrooms started to grow in the experimental plot and raised the interest of researchers. The samples were collected in the years 2014 and 2015.

In order to determine heavy metal content in *Leccinum aurantiacum* samples were digested, using microwave assisted sample digestion system and afterwards the elemental composition determined using PerkinElmer Sciex Elan 6000 DRC-e ICP-MS instrument. Total amount of Pb, Cd, Cu, Zn, Ni, Mg and Sr was determined. The determination of stable isotope ratios was carried out with Nu Horizon stable isotope mass spectrometer (SIRMS), using certified inorganic reference materials USGS-40 and USGS-41 (L-Glutamic acid). The $\delta^{13}C$ values were expressed relative to VPDB and the $\delta^{15}N$ values relative to AIR.

The obtained results have shown tendencies for the $\delta^{15}N$ values to increase in the *Leccinum Aurantiacum,* along with increasing amount of total nitrogen in the fertilizers used. This agrees with other researches that show enrichment in $\delta^{15}N$ values with nitrogen rich fertilizers [3]. The effect of fertilizers on the $\delta^{13}C$ values is not significant and therefore can't be used to identify the patterns of pollution uptake. Also four years after the fertilization the *Leccinum Aurantiacum* samples show slightly elevated content of heavier nitrogen isotope which suggests that the ^{15}N is not being taken up by other plants growing in the experimental plot.

The heavy metal amounts in the samples analyzed are higher than in the control samples, which suggests that *Leccinum Aurantiacum* do accumulate heavy metals and therefore can act as bioremediators. Along with the possible use as bioremediators, the consumption of the fruiting bodies should be evaluated, depending on the location of the mushroom growing places. The amounts of different elements vary for the samples from subplots that have been treated with different fertilizers and do not show clear tendencies for one of the fertilizers used to have impact on higher levels of all elements.

[1] Koroleva Y., Vakhranyova O., Okhrimenko M. Accumulation of trace elements by wild mushrooms in West part of Russia (South-Eastern Baltic), Pollution atmosphérique, climat, santé, société **226**, (2015).
[2] Rhodes C.J. Mycoremediation (bioremediation with fungi) – growing mushrooms to clean the earth, Chem. Spec. Bioavailab. **26**, 196-198 (2014).
[3] Lia Y., Zhanga H., Tua C., Fua C., Xueb Y., Luoa Y. Sources and fate of organic carbon and nitrogen from land to ocean: Identified by coupling stable isotopes with C/N ratio, Estuar. Coast. Shelf S. **181**, 114-122 (2016).

SUB-MICROSECOND PULSED ELECTRIC AND MAGNETIC FIELD GENERATION FACILITIES FOR TRANSIENT CELL MEMBRANE PERMEABILIZATION

Paulius Butkus[1], Gediminas Staigvila[1], Sonata Tolvaišienė[1], Vitalij Novickij[1,2]

[1] Faculty of Electronics, Department of Electrical Engineering, Vilnius Gediminas Technical University, Lithuania
[2] Institute of High Magnetic Fields, Vilnius Gediminas Technical University, Lithuania
paulius.butkus@vgtu.lt

Electroporation is a pulsed electric field (PEF) driven phenomenon, when the permeability of the cell membrane is increased due to polarization of cell, resulting in reorientation of lipids and formation of pores in the membrane [1,2]. The rationale of the sub-microsecond protocols is derived from the capability to bypass the plasma membrane of the cell and affect the inner organelles using energy efficient and non-thermal methodology [3,4]. As an alternative or an addition to the established PEF cell permeabilization technique, recently a contactless method based on pulsed magnetic fields (PMF) for both transient and non-reversible permeabilization of the membrane of biological cells has been proposed [5,6]. In both cases the methodologies require novel, flexible and high pulsed power setups, which are not available commercially. The majority of commercial pulsed power systems generate pulses with durations from microsecond to milliseconds, are limited by repetitive frequency, power and other pulse forming capabilities [7–9].

In this study, we overview two electroporation and magnetoporation setups, which enable investigation of the cell permeabilization phenomena in a significantly wider range of pulse parameters. We have developed a 0–30 kV/cm, 100 ns – 10 ms, PEF setup that is capable of generating burst of pulses with repetitive frequency in the range of several megahertz and a 0–4 Tesla pulsed magnetic field (PMF) setup (pulse width 450 ns) specifically adapted for permeabilization of biological cells.

We have determined that both setups have high applicability for investigation the biophysics of the electroporation and magnetoporation phenomena, while the high *dB/dt* sub-microsecond pulses show a synergistic effect with PEF methodology. The detailed structure of the generators and the applicators, resultant spatial magnetic and induced electric field distributions and other experimental data are reviewed.

Acknowledgements: This works was supported by Research Council of Lithuania Towards Future Technologies programme grant Reg. Nr. LAT-02/2016.

[1] Tsong T. Y. Y., Electroporation of cell membranes., Biophys. J. 60: 297–306 (1991).
[2] Bennett W. F. D., Sapay N., Tieleman D. P., Atomistic simulations of pore formation and closure in lipid bilayers, Biophys. J. 106: 210–219 (2014).
[3] Schoenbach K. H., Hargrave B., Joshi R. P., Kolb J. F., Nuccitelli R., Osgood C., Pakhomov A., Stacey M., Swanson R. J., White J. A., Xiao S., Zhang J., Beebe S. J., Blackmore P. F., Buescher E. S., Bioelectric effects of intense nanosecond pulses, IEEE Trans. Dielectr. Electr. Insul. 14: 1088–1107 (2007).
[4] Beebe S. J., Chen Y. J., Sain N.M., Schoenbach K.H., Xiao S., Transient Features in Nanosecond Pulsed Electric Fields Differentially Modulate Mitochondria and Viability, PLoS One. 7 (2012).
[5] Kardos T. J., Rabussay D. P., Contactless magneto-permeabilization for intracellular plasmid DNA delivery in-vivo, Human Vaccines Immunotherapeut., vol. 8, no. 11: 1707–1713 (2012).
[6] Towhidi L., Firoozabadi S. M. P., Mozdarani H., Miklavcic D., Lucifer Yellow uptake by CHO cells exposed to magnetic and electric pulses, Radiol. Oncol., vol. 46, no. 2: 119–125 (2012)
[7] Reberšek M., Miklavčič D., Bertacchini C., Sack M., Cell membrane electroporation-Part 3: The equipment. IEEE Electrical Insulation Magazine 30: 8–18 (2014).
[8] Novickij V., Grainys A., Kučinskaite-Kodze I., Žvirbliene A., Novickij J., Magneto-permeabilization of viable cell membrane using high pulsed magnetic field. IEEE Transactions on Magnetics 51 (2015).
[9] Matej R., Miklavčič D., Advantages and disadvantages of different concepts of electroporation pulse generation. Automatika–Journal for Control, Measurement, Electronics, Computing and Communications 52.1 (2011).

BIOCONVERSION OF GLYCEROL INTO GLYCERIC ACID CATALYZED BY PQQ-DEPENDENT ALCOHOL DEHYDROGENASE

Ana Chaleckaja[1], Lidija Tetianec[1,2], Juozas Kulys[1,2], Liucija Marcinkeviciene[1], Jonita Stankeviciute[1], Rolandas Meskys[1*]

[1] Institute of Biochemistry, Life Science Center, Vilnius University, Sauletekio al. 7, LT-10257, Vilnius, Lithuania
[2] Department of Chemistry and Bioengineering, Vilnius Gediminas Technical University, Faculty of Fundamental Sciences, Sauletekio al. 11, LT-10223, Vilnius, Lithuania
ana.chaleckaja@gmail.com

Glycerol is a major byproduct in the biodiesel manufacturing process. Biodiesel production generates about 10% of glycerol [1]. Very pure glycerol is an important stock material for the food products, pharmaceutical, tobacco or cosmetics industries, but obtained as biodiesel synthesis trash is shoddy, with impurities and its purification is expensive. Thus, the expansion of the biodiesel industry is confront with the problem of the lack of an economically favorable way in which glycerol is processed into higher value-added products [2,3]. Therefore the biodiesel producers must seek alternative methods for its conversion. One of the promising applications of glycerol is its bioconversion to glyceric acid, which is important compound as raw materials for chemical products, such as bioplastics, pharmaceuticals for acceleration of alcohol metabolism or liver disease treatment and cosmetics [4].

The task of our investigation is to create the prototype of a bioreactor for the oxidation of glycerol into glyceric acid. Electroenzymatic method was employed to achieve the goal, and the PQQ-dependent alcohol dehydrogenase (ADH IIG) was the key enzyme in conversion of the substrate along with the electrochemically oxidized mediator.

The reactivity of the enzyme with a compound defines the efficiency of the compound in the conversion scheme. The dependences of initial reaction rate on electron acceptor's (ferricyanide, *N*,*N*'-dimethyl-4,4'-azopyridinium methyl sulfate (MAZP) and -1-(NN'-dimethylamine)-4-(4-morpholine)benzene (AMB)) concentrations were analyzed and the bimolecular reactivity constant values were calculated by applying the ping-pong enzyme action scheme. For different electron acceptors the bimolecular ADH IIG and electron acceptor reactivity constant (k_{ox}) values varied from $(4.7\pm0.1)\cdot10^4$ $M^{-1}s^{-1}$ to $(2.8\pm1.0)\cdot10^5$ $M^{-1}s^{-1}$.

The MAZP was used as electron acceptor for reduced ADH IIG in order to assess the degree of conversion (R) of substrates - glycerol and glyceraldehyde. The decrease of the concentration of MAZP oxidized form in the presence of ADH IIG and substrates (glycerol, D,L-glyceraldehyde, D-glyceraldehyde or L- glyceraldehyde) was monitored spectrophotometrically. When glycerol was used as a substrate the obtained R-value was 2. This indicates that in the reaction mixture all glycerol was oxidized into glyceric acid. For racemic glyceraldehyde or its optically pure enantiomers the R equals to ~1, indicating that the oxidation of these substrates occurs via one stage to corresponding glyceric acid.

Ferricyanide, MAZP and AMB were used as an electrochemical oxidized mediators for ADH IIG catalyzed glycerol conversion. The formation of glyceric acid and glyceraldehyde, which are the products of glycerol oxidation, were revealed by monitoring their 2-nitrophenylhidrazine derivatives by HPLC. The larger glycerol conversion yields were obtained using the larger amounts of mediator MAZP and KOH to neutralize the glyceric acid. During the optimization of prototype of reactor the TTN's of up to 37 for MAZP and 2264 for enzyme were achieved.

[1] F. Yang, M.-A. Hanna and R., Sun, Value-added uses for crude glycerol-a byproduct of biodiesel production. Biotechnol Biofuels, **5 (13)**, 1-10 (2012).
[2] C. Santibáñez, M.-T. Varnero and M. Bustamante, Residual glycerol from biodiesel manufacturing, waste or potential source of bioenergy: A Review. Chilean journal of agricultural reseach **71(3)**, 469-475 (2011).
[3] N. Pachauri, B. He, Value-added Utilization of Crude Glycerol from Biodiesel Production: A Survey of Current Research Activities. ASABE Annual International Meeting Sponsored by ASABE Oregon Convention Center Portland, Oregon 9 - 12 July, 1-16 (2006).
[4] H. Habe, T. Fukuoka, D. Kitamoto, and K. Sakaki, Biotransformation of Glycerol to D-Glycericacid by Acetobacter tropicalis, Applied Microbiology and Biotechnology, **81,** 1033–1039 (2009).

CORRELATION AND CLASSIFICATION ANALYSIS OF HUMAN INTERVERTEBRAL DISC AUTO-FLUORESCENCE SPECTRA

Ignas Čiplys [1, 2], Vilmantas Gėgžna [1, 2], Darius Varanius [1, 2], Aurelija Vaitkuvienė [1], Gunaras Terbetas[3], Laura Neverauskienė[3], Jurgita Ušinskienė[4], Juozas Vidmantis Vaitkus[1]

[1] Institute of Applied Research, Vilnius University, Vilnius, Lithuania
[2] Institute of Biosciences, Life Sciences Center, Vilnius University, Vilnius, Lithuania
[3] Faculty of Medicine, Vilnius University, Vilnius, Lithuania
[4] National Cancer Institute, Vilnius University, Vilnius, Lithuania
Ignas.Ciplys@gf.stud.vu.lt

Medical conditions related to intervertebral disc (IVD) degeneration is a common disease in our society [1][2] and more in-depth investigations are needed to develop new and more effective treatment strategies. The aim of this study is to find possible links between age, sex and medical condition related changes in IVD and autofluorescence spectra of these samples. Thirty-seven specimens of this medical material were obtained in accordance with bioethical requirements. Its fluorescent properties were registered using 355nm excitation of laser (STA-01-TH, Standa Ltd.) and fiber-based optical system. The registered spectroscopic signals were preprocessed (Fig. 1) and analyzed by means of computational methods such as rank correlation as well as classificatory ROC (receiver operating characteristic) analyses. Two approaches to extract information from spectra were taken: (a) an at-every-wavelength based method in which comparisons were performed wavelength-wise and (b) a component-based method in which amount of similar spectroscopic information was reduced to so called components.

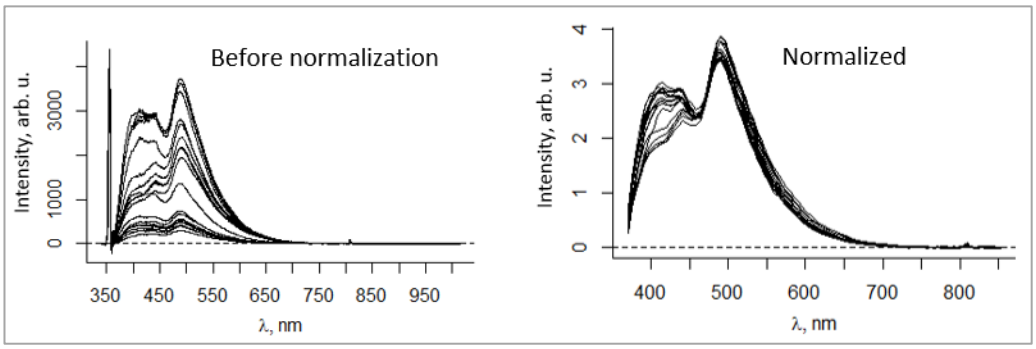

Fig. 1. An example of registered (left) and normalized (right) fluorescence spectra of IVD.

The results showed that method of normalization (in the stage of preprocessing) highly influences the accuracy of classification and value of correlation coefficient. Nevertheless, parameters of analysis algorithm that allow revealing correlation between age and spectroscopic properties (Fig. 2) were found. It was noticed that additional information, such as patient's age and gender, might lead to results that are more precise.

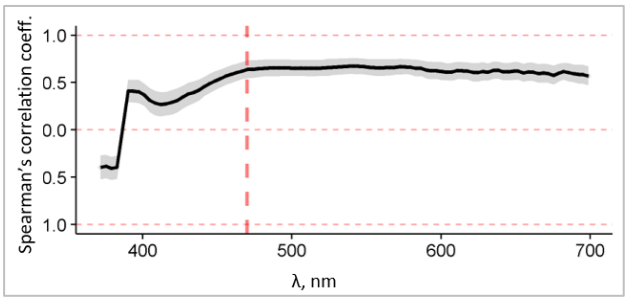

Fig. 2. Estimates of Spearman's rank correlation coefficient r_s (black curve) with 95% bootstrapped confidence interval (grey ribbon) between age and intensity of *normalized* spectra of IVD samples (subset of women only). Vertical dashed line indicates the wavelength at which the maximum point estimate of r_s was observed.

It can be concluded that autofluorescence spectra has information that may be valuable for medical diagnostics.

[1] J.L. Pinheiro-Franco, A.R. Vaccaro, E.C. Benzel, and H.M. Mayer, eds., Advanced Concepts in Lumbar Degenerative Disk Disease, (Springer Berlin Heidelberg, Berlin, Heidelberg, 2016).
[2] L.M. Benneker, P.F. Heini, S.E. Anderson, M. Alini, and K. Ito, *Eur. Spine J.*, **14**, 27–35 (2005).

DISTRIBUTION OF CHLORIN PHOTOSENSITIZERS IN MONOLAYER AND SPHEROID CELL CULTURES

Farrakhova Dina[1*], Yakavets Ilya[2,3,4], Loschenov Victor[1,5], Zorin Vladimir[2,6], Bolotine Lina[3,4]

[1] National Research Nuclear University «MEPHI», Moscow, Russia
[2] Department of Biophysics, Belarusian State University, Minsk, Belarus
[3] Centre de Recherche en Automatique de Nancy, CNRS, Université de Lorraine, Nancy, France
[4] Institut de Cancérologie de Lorraine, Vandoeuvre-lès-Nancy, France
[5] Prokhorov General Physics Institute Russian Academy of Science, Moscow, Russia.
[6] International Sakharov Environmental Institute, Minsk, Belarus.
*farrakhova.dina@mail.ru

Photodynamic therapy (PDT) efficiency primarily depends on light source and photosensitizer (PS) properties. Many conventional PSs are hydrophobic and have limited tissue distribution. The upgrading of conventional PSs by the chemical modification alters the drug pharmacokinetics and biodistribution in tumor tissues.

The aim of this study was to assess the distribution processes of chlorin type PSs in human adenocarcinoma HT29 monolayer and spheroid cell cultures. We used the second generation PS chlorin e6 (Ce6) which is already accepted for clinical use and its dimethyl ester (DME) (Minsk, Belarus) [1]. It was shown, that the difference in chemical structure didn't significantly influence spectroscopic characteristics of PS, while some physicochemical properties such as water solubility were changed.

In the present work we compared the interaction of Ce6 and DME with HT29 monolayer cells. DME accumulated faster than Ce6 with the 2.3 times increased equilibrium uptake level. Moreover, it was demonstrated, that the chemical modification of Ce6 molecules leads to the changes of the PS intracellular localization and enhanced photosensitizing activity. Indeed, two times higher photokilling ability was registered for DME-based PDT compared with that of Ce6.

Ce6 and DME biodistribution processes in tumor tissue were studied on multicellular tumor spheroids model. The PS concentration in spheroid cells treated for 6 hours was estimated by flow cytometry and fluorescence microscopy techniques. It was shown, that DME was accumulated better and more homogeneous in HT29 spheroids, while Ce6 had a heterogeneous distribution with bright spots on the surface of spheroids (Fig. 1).

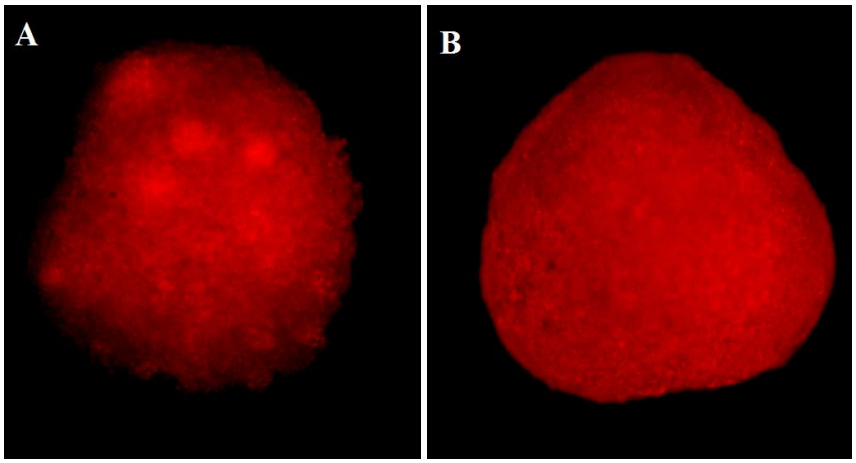

Fig. 1. Fluorescent images of spheroids after 6h incubation with (A) Ce6 and (B) DME

We suggest that improved accumulation, distribution and PDT efficacy of DME could be related to increased PS amphiphilicity and faster diffusion rate of DME molecules across biological membranes. Taken as a whole, we conclude that new chemically modified PS, based on Ce6, could be more efficient for the PDT of cancer, compared with conventional Ce6.

[1] Savitsky VP, Zorin VP, Potapnev MP. Accumulation of chlorine e6 derivatives in cells with different level of expression and function activity of multidrug resistance protein P-gp 170. Exp Oncol, Vol. 27, №1, p. 47-51, 2005.

INVESTIGATION OF LACCASE ADSORBTION ON MAGNETIC NANOPARTICLES AND KINETICS OF THE ADSORBED ENZYME

Justina Gruzauskaite[1], Ingrida Jurkeviciute[2], Lidija Tetianec[1,2], Regina Vidziunaite[1,2], Liucija Marcinkeviciene[1]

[1] Institute of Biochemistry, Life Sciences Center, Vilnius University, Sauletekio al. 7, Vilnius, Lithuania
justinagruzauskaite@gmail.com
[2] Vilnius Gediminas Technical University, Sauletekio al. 11, Vilnius, Lithuania

This study focuses on the direct binding of laccase from *Sclerotinia sclerotiorum* to magnetic nanoparticles (MNPs) and the investigation of adsorption characteristics, activity and kinetics of bound laccase (Fig. 1). The use of magnetic nanoparticles as a support for immobilized enzymes has advantages, such as high surface area for the binding of a large amount of enzymes and the selective separation of immobilized enzymes from a reaction mixture by the application of an external magnetic field [1, 2]. The laccase attachment to magnetic nanoparticles takes advantage of this enzyme in various biotechnological applications.

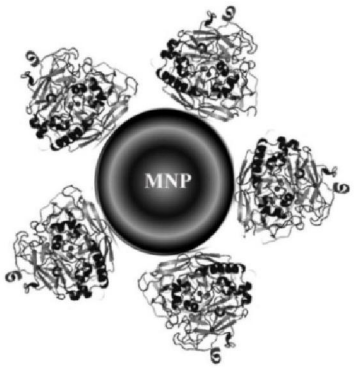

Fig. 1. The schematic representation of laccase adsorbed on MNPs.

Magnetic nanoparticles were preapared by following the procedures described in [3]. Atomic force microscope was used for nanoparticles characterization. The size distribution of synthesized magnetic nanoparticles is 30–48 nm with a mean size of 39 ± 5 nm.

The activity and kinetic parameters of bound and native laccase were determined spectrofotometically by measuring increase of absorption at 414 nm resulting from oxidation of 2,2'-azino-bis(3-ethylbenzothiazoline-6-sulphonic acid) (ABTS).

The adsorbtion was performed by incubating the laccase solution with magnetic nanoparticles for 10–110 minutes. After the incubation the MNPs with adsorbed laccase were separated by applying external magnetic field and the activity of the enzyme on the resuspended MNPs and in the supernatant was determined. During the incubation 6–27 % loss of activity of the enzyme was observed. The residual activity in the supernatant and the activity of the adsorbed enzyme depended on the ratio of the laccase and MNPs in the incubation mixture. The amount of adsorbed laccase on magnetic nanoparticles was from 0.41 μU/μg to 2 μU/μg if the ratio of enzyme and MNPs in incubation mixture was from 0.69 μU/μg to 3 μU/μg, respectively.

Desorption of laccase from the magnetic nanoparticles was investigated by seperating the MNPs with adsorbed laccase and resuspending them in DI water or buffer solution several times. The amount of desorbed laccase depends on the resuspending media and the number of repeated procedures. The residual activity of laccase after 10 times of desorption procedure in water or buffer solution was 58 % or 31 %, respectively.

The kinetics of ABTS oxidation with immobilized laccase were investigated and the parameters were calculated by applying the ping-pong scheme of the enzyme action [4]. The apparent values of Michaelis-Menten constant (K_m) were determined to be 14 ± 3 μM for the native enzyme and 51 ± 4 μM for the immobilized enzyme. The values of bimolecular constants of the enzyme reactivity with oxygen and ABTS decreased for the adsorbed enzyme in compare to native enzyme. The change of the values suggest the adverse orientation and restricted accessibility to substrates of the adsorbed enzyme.

[1] P. J. Halling, P. Dunnill, Magnetic supports for immobilized enzymes and bioaffinity adsorbents, Enzyme and Microbial Technology **2**, 2-10 (1980).
[2] S. H. Huang, M. H. Liao, D. H. Chen, Direct binding and characterization of lipase onto magnetic nanoparticles, Biotechnology Progress **19**, 1095-1100 (2003).
[3] M. Magro, D. Baratella, G. Salviulo et al., Core-shell hybrid nanomaterial based on prussian blue and surface active maghemite nanoparticles as stable electrocatalyst, Biosensors & Bioelectronics **52**, 159-165 (2014).
[4] L. Tetianec, J. Kulys, Kinetics of N-substituted phenothiazines and N- substituted phenoxazines oxidation catalyzed by fungal laccases, Central European Journal of Biology **4,** 62-67 (2009).

DIFFERENT PARTICIPATION OF CYTOSKELETON ELEMENTS IN REGULATION OF MECHANICAL PROPERTIES IN HUMAN BLOOD NEUTROPHILS AND ERYTHROCYTES

Elizaveta Kavalenka, Alena Kavalenka, Olga Hozyanin

Department of Biophysics, Belarusian State University
kovalenko.elizabeth@gmail.com

The functioning of blood cells in organism depends strongly on its geometrical and mechanical characteristics. Neutrophil activation processes (chemotaxis, adhesion, phagocytosis, formation of extracellular traps) and erythrocyte moving within the vascular system include cellular membrane deformation and change of the ratio of surface area to cell volume that can be accompanied by a change in surface mechanical tension. The aim of this work was to determine the parameters describing the geometrical and mechanical properties of red blood cells and neutrophils at various influences on the cells, in particular, when changing the osmolarity of the medium and the action of inflammatory mediators as well as to establish the role of cytoskeleton elements in mechanical properties regulation.

Erythrocytes and neutrophils were isolated from peripheral blood of healthy donors by standard methods [1]. The obtained cells were resuspended in Earle's balanced salt solution (pH 7.3, 300 mOsm/L). Then cells were placed in NaCl solutions (osmolarity 60-1000 mOsm/L). The geometrical parameters of cells were evaluated by light scattering methods with nephelometers developed at Belarusian State University [1]. Cell suspensions were used in nephelometric assay at a partial volume of less than 10^{-3}. Nephelometry results were verified by light microscopy.

It is found that in isotonic medium nonactivated neutrophils are spheroids with a diameter of (8.4 ± 0.2) microns, erythrocytes isolated from fresh blood are disks with a diameter of (7.6 ± 0.2) microns and a thickness of (2.5 ± 0.2) microns and erythrocytes from “old” blood (stored at minus 4 °C for more than 2 days) are deformed and can be approximated by a spheroid with a diameter (4.7 ± 0.2) microns.

It is revealed that neutrophils swollen in hypotonic medium could reach a maximum diameter of ~ 12.5 microns (at osmolarity of 120 mOsm/L), with that cellular surface area increases in 2 times and cell volume – in 3.5 times, then the cells are destroyed. The elastic modulus of neutrophil membrane is about 1 MPa and does not change substantially with a decrease in osmolarity to 120 mOsm/L. Action of microfilaments and microtubules assembly inhibitors (colchicine and cytochalasin B) and chemoattractant fMLP on neutrophils is accompanied by the significant increase of surface area and volume of the cells. If neutrophils are subjected to the action of cytochalasin B, colchicine or fMLP, that these cells can achieve more volume at osmotic swelling without rupture. The character of deformation differs from that of intact neutrophils, and the modulus of elasticity changes significantly.

Erythrocytes when swollen in hypotonic conditions reach a maximum diameter of 7-8 microns at ~ 160 mOsm/L, while the maximum extension of the membrane is less than 40% (relative to a normal disk erythrocyte membrane area). With further reduction of osmolarity erythrocytes are destroyed. The elastic modulus of erythrocytes from fresh blood is about 2 MPa, whereas for erythrocytes from “old” blood - about 1 MPa. Cytochalasin B has no effect on the volume of erythrocytes and the elastic properties of their membranes, which may be due to the lack of necessity of actin microfilament formation in maintaining of erythrocyte shape and deformability.

Thus, erythrocytes and neutrophils significantly differ in mechanical properties and deformation ability. Actin microfilaments and tubulin microtubules are important in providing the elastic properties of neutrophils, but not erythrocytes. The depletion of erythrocytes during the storage conditions *in vitro* and activation of neutrophils is accompanied by a change in cell geometry and mechanical properties.

[1] S.A. Kavalenka, A.I. Kavalenka, V.V. Popov, T.D.L. Nguyen, V.A. Loban, Investigation of blood cell properties using laser diffractometry and kinetic nephelometry, Journal of Physics – 2014.- Vol. 541.- 012043.-P.1-6

POLYPYRROLE-MODIFIED ASPERGILLUS NIGER CELLS FOR MICROBIAL FUEL CELL/BIOSENSOR ELECTROCHEMICAL SYSTEMS

Aura Kisieliūtė[1], Inga Morkvėnaitė-Vilkončienė[2], Jūratė Petronienė[1], Anton Popov[1], Almira Ramanavičienė[1], Aušra Valiūnienė[1], Roxana-Mihaela Apetrei[3], Geta Carac[3], Arūnas Ramanavičius[1]

[1] Faculty of Chemistry, Vilnius University, Lithuania
[2] Department of Mechatronics and Robotics, Vilnius Gediminas Technical University, Lithuania
[3]"Dunarea de Jos" University of Galati, Romania
aura.kisieliute@gmail.com

Microbial fuel cells (MFC) are bio-electrochemical systems that drive a current by using microorganisms which convert the chemical signal contained in organic matter into electricity by means of enzymatic catalysis [1]. For practical application the anode should be highly conductive, have high catalytic activity, biocompatibility, chemical stability and resistance to decomposition [2]. By using whole organisms in MFC we allow various enzymes and hence multiple substrates to be used also providing optimal conditions for each enzyme.

MFC have drawn attention because it is a promising technology for bio-electrochemical power source as they can recover electrical energy from organic matter. However, the power output from such MFC is too low for practical applications, which is mainly due to the difficult electron transfer between microbial cells and the extracellular electrode [3]. Typically, electron transfer is the rate-limiting reaction step during MFC operation. Facilitating electron transfer from bacteria to the anode can fundamentally improve the overall performance by overcoming the kinetic losses. Modification with a conductive polymer can enhance the biocompatibility of the anode. Furthermore, conductive polymers can increase the charge transfer to the anode and this effect may be the main reason for the performance improvement. Recently the electrodes have been modified with conducting polymers such as polypyrrole (Ppy) [4], polyaniline (PANI), multiwall carbon nanotubes and others with incorporated cells to form new composite materials possessing the properties of each component for a synergistic effect.

In our study we chose the conducting polymer Ppy, because it has been considered to have satisfying electric conductivity, stability, biocompatibility in mild conditions. We also chose a fungi strain *Aspergillus niger* which after modification was encapsulated with polypyrrole. To determine whether there was an electrochemical difference between the modified culture compared to the control group two electrochemical techniques were employed: Scanning electrochemical microscopy (SECM) and amperometric measurements for the evaluation in signal differences. Both methods showed several times enhanced signals for Ppy modified cells in comparison with the control group. This could be assigned to the better conductive cell wall or charge permeability. The improved electron transfer resulted in an increased sensitivity in biosensors which correlate to power density in microbial fuel cells because both are directly related to current density. This presents us that microorganism-assisted polypyrrole synthesis could be used for approaches in biosensor or microbial biofuel cell electrochemical systems.

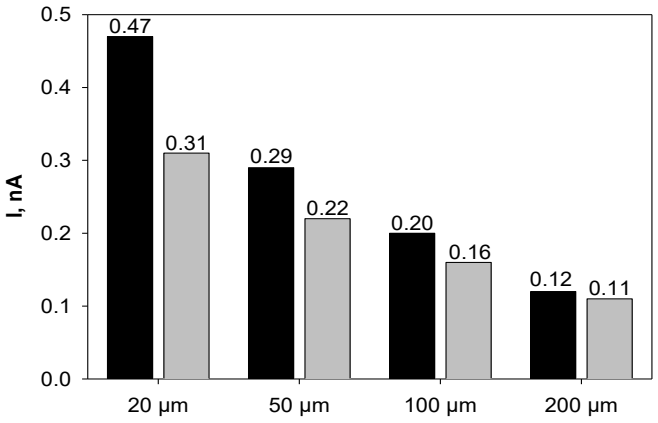

Fig. 1. histogram of registered maximum current values during x-direction scans at varying heights from the immobilized cell surface. Black columns represent the Ppy modified cell culture while the grey – the control group.

[1] A. Yazdia, L. D'Angeloa, N. Omera et al., Carbon nanotube modification of microbial fuel cell electrodes, Biosensors and Bioelectronics 85, 536-552 (2016)
[2] G.G. Kumar, V. G. S Sarathi, K.S.Nahm, Recent advances and challenges in the anode architecture and their modifications for the applications of microbial fuel cells, Biosensors and Bioelectronics, 43, 461-475 (2013)
[3] M. Kim, H.W.Kim, J-Y Nam et al., Recent Progress of Nanostructure Modified Anodes in Microbial Fuel Cells, Journal of Nanoscience and Nanotechnology, 15, 6891-6899 (2015)
[4] A. Zebda, S.Tingry, C. Innocent, et al., Hybrid layered double hydroxides-polypyrrole composites for construction of glucose/O2 biofuel cell, Electrochimica Acta 56, 10378-10384 (2011)

OPTIMIZING THE EFFECTIVENESS OF PHOTOSENSIBILISED TUMOR THERAPY BY USING 5 – AMINOLEVULINIC ACID, ITS ESTERS AND MIXTURES CONTAINING HYALURONIC ACID

Kristina Lupeikytė, Romualdas Rudys

Biomedical Physics Laboratory, National Cancer Institute, Vilnius, Lithuania
kristina.lupeikyte@gf.stud.vu.lt

Selective accumulation of endogenous sensitizer precursors, such as 5 – aminolevulinic acid (5 – ALA) and its derivatives in photodynamic therapy (PDT), entering cancer cells and disrupting the cell cycle of heme biosynthesis leads to photosensitized effect to tumor tissue. Cancer cells accumulate higher amount, concentration of photosensitizer protoporphyrin IX (PpIX) than healthy ones. However, several porphyrin precursor products, (e.g., Levulan, Metvix, that are approved and used in clinical practice for treating actinic keratosis and other superficial tissue precancerous and cancerous diseases) possess limited penetration in biological tissues. This quality based on chemical structure interferes with the control of selectivity of sensitization for deeper or larger volume of cancer affected tissue and limits the clinical application of the PDT method. In order to extend the application of the precursors to treat cancers of larger volume and to increase the efficacy of the selectivity of PDT, for transportation of the sensitizer precursor to the target cells different molecular weight polymeric compounds of hyaluronic acid (HA) are used, which are now being applied in cosmetics and rehabilitation medicine. HA agent facilitates drug delivery across the cell membranes [1]. It is also well-known, that HA is highly bound to the receptors CD44, CD168 found in cell membrane [2].

The study analyses HA product in cooperation with a 5 – ALA or its methyl ester (5 – ALA – Me), the influence of induction of endogenous PpIX in human breast adenocarcinoma (MDA-MB-231) cell populations. The MDA-MB-231 cells were incubated for 2, 4, 6, 24 hours with 0.5 mM 5 – ALA or 5 – ALA – Me, in the culture medium plus 0.1 mg/ml HA. The changes in the intensity of PpIX fluorescence in time were registered with the help of flow cytometry and florescence spectrometer.

The experiments revealed, that adding the HA into the media with 5 – ALA or 5 – ALA – Me, increases the intensity of the PpIX fluorescence. For PDT is very important to achieve more selective PpIX induction in cancer cells as fast as possible, in order to start an early radiation therapy. Thus, our results shows that after 4 hours of incubation with 5 – ALA – Me/ HA mixture the PpIX fluorescence intensity increases by 88.6% compared to 5 – ALA – Me, and in the case of 5 – ALA/HA mixture the intensity of PpIX fluorescence inreases by 24% (Fig.1).

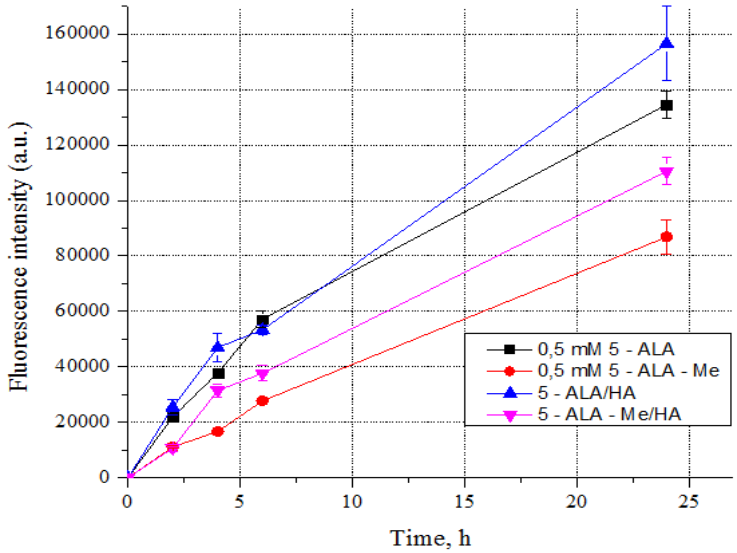

Fig.1. PpIX fluorescence intensivity kinetics in MDA- MB-231 cells incubated with 0.5 mM 5 – ALA and 5 – ALA – Me and HA medium.

[1] Schante CE, Zuber G, Herlin C, Vandamme TF. Chemical modifications of hyaluronic acid for the synthesis of derivatives for a broad range of biomedical applications. *Carbohydrate polymers.* 2011;85(3):469-489.
[2] Knudson W, Loeser RF. CD44 and integrin matrix receptors participate in cartilage homeostasis. *Cellular and molecular life sciences : CMLS.* Jan 2002;59(1):36-44.

OPTIMIZATION OF SOD1 AGGREGATION CONDITIONS *IN VITRO* AND IMPACT OF ENVIRONMENTAL FACTORS TO AGGREGATION KINETICS

Greta Musteikyte, Vytautas Smirnovas

Department of Thermodynamics and Drug Design, Institute of Biotechnology, Lithuania
gretamus@gmail.com

Amyotrophic lateral sclerosis (ALS) is a neurodegenerative disease that results in motor neuron death and has no approved treatment yet. Around 20% of ALS cases are caused by Cu, Zn human superoxide dismutase (SOD1) aggregation into amyloid-like fibrils. Wild type SOD1 is found to play the key role in the development of sporadic ALS (90% of ALS cases) [1], as well as co-aggregated with mutant SODs in familial ALS (fALS) [2]. However, most of research done in this field is based on fALS-associated mutant SODs, while inherited type of the disease comprises to only 10% of ALS cases.

We tested various aggregation conditions and found out that for aggregation into amyloid-like fibrils *in vitro*, SOD1 must first be reduced and partially denatured. The conditions were optimized to get rapid and repeatable aggregation kinetics. Following conditions were used for further studies: 0.2 mM concentration of monomeric SOD1, 0.5 M of GuHCl, 5 mM of DTT and 0.02 mM of SOD1 in amyloid-like form (seeds).

The effect of ethanol was the most exciting of further results. It was found to be an inhibitor of SOD1 aggregation *in vitro*. This trend agrees with the recent data [3], where inverse correlation between alcohol consumption disorders and risk of ALS was determined.

[1] Shibata, N. (1994). Cu, Zn superoxide dismutase-like immunoreactivity in Lewy body-like inclusions of sporadic amyotrophic lateral sclerosis, 179, 149152. https://doi.org/10.1016/0304-3940(94)90956-3

[2] Bruijn, L. I., Becher, M. W., Lee, M. K., Anderson, K. L., Jenkins, N. A., Copeland, N. G., Cleveland, D. W. (1997). ALS-Linked SOD1 Mutant G85R Mediates Damage to Astrocytes and Promotes Rapidly Progressive Disease with SOD1-Containing Inclusions, 18, 327338.

[3] Ji, J., Sundquist, J., & Sundquist, K. (2016). Association of alcohol use disorders with amyotrophic lateral sclerosis : a Swedish national cohort study, 270275. https://doi.org/10.1111/ene.12667

STUDY OF MESOPOROUS SILICA NANOWIRES AS POTENTIAL CONTRAST AGENT FOR CANCER DIAGNOSTICS

Marijus Plečkaitis[1], Vladimir Sivakov[2], Vitalijus Karabanovas[1,3]

[1] Biomedical Physics Laboratory, National Cancer Institute, Lithuania
[2] Leibniz Institute of Photonic Technology, Jena, Germany
[3] Department of Chemistry and Bioengineering, Vilnius Gediminas Technical University, Lithuania
marijus.pleckaitis@gf.stud.vu.lt

In the past years there has been a lack of contrast agents which would be able to emit light in near-infrared (NIR) diapason. Therefore mesoporous silica nanoparticles (MSN) have drawn up a lot of attention. With their tailored mesoporous structure and high surface area, MSNs as drug delivery systems (DDSs) show significant advantages over traditional drug nanocarriers.[1] They are widely studied and are promising biodegradable and biocompatible agents for potential applications in cancer diagnostics. This high interest is motivated by unique advantages of silica nanoparticles as multimodal labels for cancer diagnostics both in vitro and in vivo.[2] The aim of our study was to investigate optical properties and colloidal stability of fluorescent mesoporous silica nanoparticles.

Silicon nanowires (SNW) were synthesized by process called metal-assisted chemical etching (MACE) of low boron-doped single-crystalline wafers. After the synthesis, SNW were analyzed using scanning electron microscopy (SEM) Fig. 1 (a, b). The images of SEM show, that silica nanowires are porous and elongated form. It was also observed, that silicon nanowires have strong emission in VIS-NIR spectral range under ultraviolet (UV) irradiation. In order to get colloidal solution, SNW were mechanically removed from the substrate surface.

Aqueous suspensions of porous silica nanoparticles were prepared by using silica nanowires (SNW) which have been ultrasonicated for 3h in different solvents e.g. distilled water, ethanol,. Thereafter, the samples were centrifuged for 3 minutes at 2000 rpm. The resulting supernatant was used for further experiments. After centrifugation procedure supernatant was resuspended in distilled water for further investigations. Emission spectra of prepared silica nanoparticle were registered using “Cary 50”, Varian spectrophotometer. As it is presented in Fig. 1 (d), the obtained emission spectra had wide band with the peak at 655 nm. Such wide emission spectrum is associated with surface defects on silica nanoparticles and different porosity. Later on, optical stability of prepared colloidal solutions was studied. The graphs in Fig. 1 (d) show that silica nanoparticles emission intensity decay over time. It indicates that prepared colloidal silica nanoparticles are unstable in aqueous solution and require additional surface modification. As another results show, suspension made with ethanol had higher stability and bigger emission intensity than compared with the one made with distilled water.

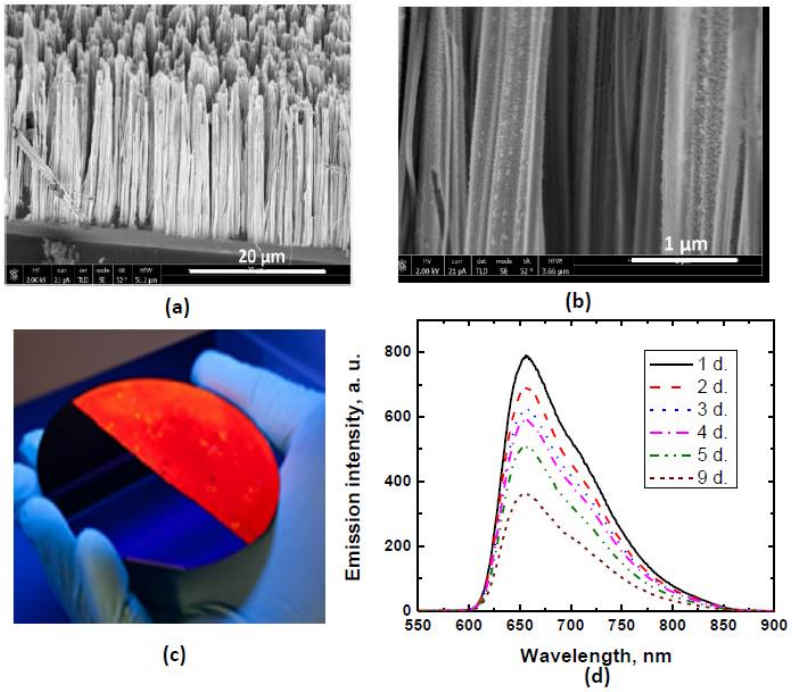

Fig. 1. (**a**) SEM image of silica nanowire array on crystalline silica substrate; (**b**) Magnified image of SNW; (**c**) Image of SNW array under UV light, left side is empty, right side has silica nanowires; (**d**) Emission spectra of prepared MSN solution.

[1] Tang, F., Li, L. and Chen, D. (2012), Mesoporous Silica Nanoparticles: Synthesis, Biocompatibility and Drug Delivery. Adv. Mater., 24: 1504–1534
[2] Li, Z.F.; Ruckenstein, E. Water-soluble poly(acrylic acid) grafted luminescent silicon nanoparticles and their use as fluorescent biological staining labels. Nano Lett. 2004, 4, 1463–1467.

ION CHANNEL ACTIVITY FOUND IN CYTOPLASMIC DROPLETS OF *NITELLOPSIS OBTUSA* USING PATCH CLAMP TECHNIQUE

Vilmantas Pupkis, Indrė Lapeikaitė, Vilma Kisnierienė

Life Sciences Center, Vilnius University, Lithuania
vilmantas.pupkis@gmail.com

Giant internodal cells of freshwater algae *Characeae* for many decades have provided an excellent experimental system expanding the knowledge in plant electrophysiology as well as offering some evolutionary insights. Experiments on Characeaen algae have significantly contributed to better understanding of the properties of plant signaling via analyzing action potentials as well as the characteristics of ion channels [1].

Patch clamp technique employs a microelectrode to seal an area of a chosen membrane to create a high resistance (usually larger than 1 GΩ) contact. Thus any electrical current passing through the sealed area can be easily detected in high resolution – activity of a single ion channel can be recorded. Since its development patch clamp technique has been an irreplaceable method for investigating ion channels in near physiological conditions in plants [2].

The cell wall of the Characeaen algae stands as an obstacle as it is very difficult to reach the plasma membrane without damaging it in order to observe the activity of ion channels. The cytoplasmic droplet (Fig. 1) technique overcomes this issue by taking advantage of the vacuolar membrane, the tonoplast. If a Characeaen cell is placed in a tube filled with a solution, approximately isotonic with the cell sap, and "decapitated", the cytoplasm may flow out of the cell to a drop of solution spontaneously forming cytoplasmic droplets [3]. The droplets consist of cytoplasm covered with the tonoplast and in the solution assume a spherical shape. The composition of ion channels in the tonoplast is not particularly diverse – K^+ and Cl^- channels of various conductivity have been previously described [4].

Glutamate is a neurochemical widely utilized in animal kingdom for signaling. Even though glutamate has some significance in the plant metabolism, its possible role as a signaling molecule in plants has not been investigated on a single channel level in Characeaen cells. The effect of another neurotransmitter acetylcholine has been already studied in *Chara corallina* tonoplast [5].

In our present experiments we attempted to adapt our equipment to suit the needs of making cytoplasmic droplets from Characeaen *Nitellopsis obtusa* and recording data via the patch clamp technique. Experimental conditions enabled us to record the activity of functional ion channels in the tonoplast.

Our goal is to characterize the found channels and determine whether glutamate has any effect on them.

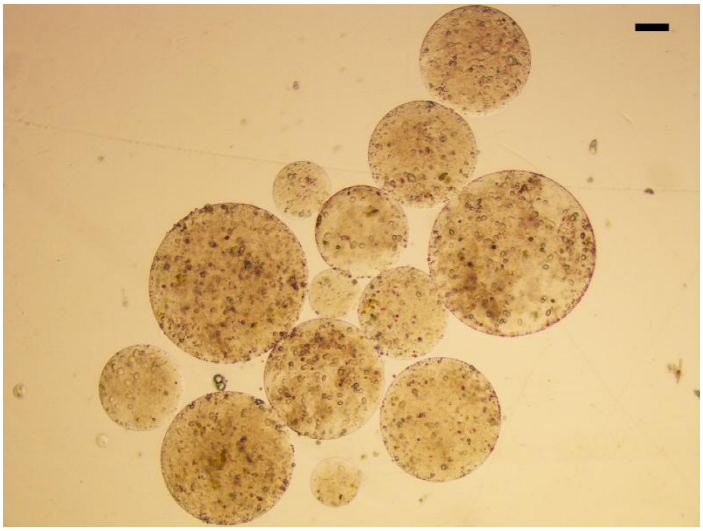

Fig. 1 A micrograph of cytoplasmic droplets isolated from internodal cells of *Nitellopsis obtusa*. Horizontal bar represents 100 µm.

[1] P.R. Andjus, Harvesting the Biophysical Field of the 'Green Axon', Iugoslav. Physiol. Pharmacol. Acta **34** (1), 1-9 (1998).
[2] B. Sakmann, E. Neher, *Single-channel recording* (Springer Science & Business Media, 2009).
[3] N. Kamiya, K. Kuroda. Cell Operation in Nitella: I. Cell Amputation and Effusion of the Endoplasm, Proceedings of the Japan Academy **33** (3), 149-152 (1957).
[4] M. J. Beilby, M. T. Casanova. *The physiology of characean cells* (Springer Science & Business Media, 2014).
[5] X-Q. Gong, M. A. Bisson. Acetylcholine-activated Cl^- Channel in the Chara Tonoplast, Journal of Membrane Biology **188** (2), 107-113. (2002).

AROMATIC FUNCTIONALLY SUBSTITUTED IMINES AND HYDRAZIDES–MYELOPEROXIDASE INHIBITORS

Shishkanova Polina, Sharshunovich Darya, Semenkova Galina, Sorokin Victor, Shadyro Oleg

Department of Radiation Chemistry and Chemical-Pharmaceutical Technology, Belarusian State University, Minsk
pavlina.shishkanova@gmail.com

Myeloperoxidase (MPO, EC 1.11.1.7) can be found in the azurophil granules of neutrophils, in monocytes and also in certain types of tissue macrophages. Generated by this enzyme reactive oxidants (HOCl, reactive oxygen species (ROS)) are involved in the microbicidal activity of neutrophils, contributing to innate host defenses. After the activation of phagocytes there is degranulation and MPO is secreted either inside the phagosome or to extracellular space [1]. Increased level of MPO in neutrophils and in blood may be accompanied by the hyperproduction of HOCl, which leads to the development of halogenating stress in the organism. This may become the cause to cardiovascular disease [2]. It is shown that an increasing level of the MPO in the blood increases the risk of myocardial infarction and sudden death of patients with chest pain and acute coronary syndrome. In the literature there are data that in the organism there are compounds that affect the output of hypochlorous acid, reducing its quantity(taurine) or inhibit the enzyme activity (ceruloplasmin) [5]. However, in the area of inflammation these endogenous compounds may not be in such quantity to prevent halogenating stress. In this case, you must use compounds aimed at reducing MPO activity. At the same time the ability of neutrophils to phagocytosis should be maintained. In this regard, is urgent to develop new approaches aimed at preventing the occurrence of halogenating stress in the organism.

The purpose of this study is to create new effective MPO inhibitors based on aromatic functionally substituted imines and hydrazides.

Neutrophils were allocated from blood of healthy people on the basis of a standard method. Cells were destroyed in three cycles of freezing and thawing. The resulting mixture was centrifuged. The supernatant containing free MPO was used for the analysis. The enzyme activity was determined by its ability to generate HOCl and ROS in peroxidase and halogenating cycles at pH 7.4 and 5.2 respectively. The formation of ROS and HOCl were registered by chemiluminescent method at the temperature of 37°C in Earl's solution, containing H_2O_2 and luminol. Measurements were conducted with using biochemiluminometer BHL-1 (BSU, Belarus).

We synthesized following compounds, which are derivations from aromatic functionally substituted imines and hydrazides: 4,6-di-tert-butyl-3-(((2-mercaptophenyl)imino)methyl)benzene-1,2-diol, 4,6-di-tert-butyl-3-(((2-mercaptoethyl)imino)methyl)benzene-1,2-diol, 4,6-di-tert-butyl-3-((2-phenylhydrazineylidene)methyl)benzene-1,2-diol, N'-(2,3-dihydroxybenzylidene)isonicotinohydrazide, 2-hydroxybenzohydrazide.

It was found that in the system «MPO - luminol - H_2O_2» at pH=5.2 degree of inhibition of halogenating activity of MPO in the presence of analyted substances in concentrations $4 \cdot 10^{-6}$ mol/l decreases from 96±3,9 to 29±5,5% in the following sequence: 4,6-di-tert-butyl-3-((2-phenylhydrazineylidene)methyl)benzene-1,2-diol > N'-(2,3-dihydroxybenzylidene)isonicotinohydrazide ≈ 4,6-di-tert-butyl-3-(((2-mercaptophenyl)imino)methyl)benzene-1,2-diol > 4,6-di-tert-butyl-3-(((2-mercaptoethyl)imino)methyl)benzene-1,2-diol > 2-hydroxybenzohydrazide.

The degree of inhibition of peroxidase activity of MPO (pH=7.4) in the presence of these compounds in a concentration $4 \cdot 10^{-6}$ mol/l decreases from 83±2,8 to 40±4,9% as follows: 4,6-di-tert-butyl-3-(((2-mercaptophenyl)imino)methyl)benzene-1,2-diol ≈ 4,6-di-tert-butyl-3-((2-phenylhydrazineylidene)methyl)benzene-1,2-diol > 4,6-di-tert-butyl-3-(((2-mercaptoethyl)imino)methyl)benzene-1,2-diol ≈ N'-(2,3-dihydroxybenzylidene)isonicotinohydrazide ≈ 2-hydroxybenzohydrazide.

These compounds do not have significant impact on the output of active products in the reactions of oxidation of luminol by hydrogen peroxide or HOCl.

Thus, the proposed substances, effectively inhibiting the formation of ROS and HOCl by myeloperoxidase, can be considered as potential medicine compounds for the prevention of halogenating and oxidative stress in the organism.

[1] Klebanoff S.J. // J. Leukoc. Biol. - 2005 - V. 77. P. 598.
[2] Zhang R., Brennan M.L., Fu X. // JAMA. - 2001 - V. 286. P. 2136.
[3] Baldus S., Heeschen C. et al // Circulation. - 2003 - V. 108. P. 1440.
[4] Brennan M.L., Penn M.S., Van Lente F. // N Engl J Med. - 2003 - V. 349. P. 1595.
[5] A.V. Sokolov, K.V. Ageeva et al // Chem. Phys. Lipids. – 2010. – V. 163. – P. 347–355.

ORGANIC COLORIMETRIC SENSORS FOR BIOLOGICAL APPLICATIONS BASED ON DIMETHYLAMINOBENZENE MOIETY

Rokas Skaisgiris[1], Arūnas Miasojedovas[1], Alytis Gruodis[2],
Dalius Gudeika[3], Juozas V. Gražulevičius[3], Saulius Juršėnas[1]

[1]Institute of Applied Research, Vilnius Univeristy, Saulėtekio 9-III, LT-10222 Vilnius, Lithuania
[2] Department of General Physics and Spectroscopy, Vilnius Univeristy, Saulėtekio 9-III, LT-10222 Vilnius, Lithuania
[3] Departament of Organic Technology, Kaunas University of Technology, Radvilenu pl. 19, LT-50254, Kaunas, Lithuania
rokas.skaisgiris@ff.stud.vu.lt

Detection of cations is of great importance to many scientist such as biologist, chemists and environmentalist. Fluorescent and colorimetric chemosensors receive much attention because of their advantages: high selectivity and sensitivity, cheap equipment, rapid response, nondestructive methodology and direct visual perception [1].

1,8-Naphthalimide derivatives are widely used for various applications such as anticancer agents, analgesics in medicine, fluorescent markers in biology, fluorescence switchers and sensors, etc. [2] Derivatives of 1,8-naphthalimide compounds generally have high electron affinity due to the existence of an electron-deficient center and can be easily functionalized. Meanwhile dimethylaniline (DMA) moieties are famous for they unusual dual fluorescence [3].

In this work we investigated photophysical sensing properties of 1-8-naphthalimide and dimethylaniline donor-aceptor compounds in different polarity and pH mediums as well as in aquas solutions. The naphthalimide derivatives were synthesized by D. Gudeika from prof. J. V. Gražulevičius group at Kaunas University of Technology (KTU).

The solvatochromic investigation of absorption and fluorescence spectra in medium of various polarity (0–3.96 D) approved a formation of charge transfer states. The color of fluorescence varies in the visible range of spectrum from 470 nm in non-polar solvent to 770 nm in the most polar solvent while the quantum yield is quenched from 82 % to 0.3 % respectively. Thus the molecules can be applied as polarity probe.

Investigation of metal ion sensing revealed that twisted internal charge transfer can be turned off on all molecules by adding of mercury(II) or iron(II) ions which leads to drastic changes in absorption and fluorescence spectra. Emmision enchantment of more than 1000 times is observed while ICT fluorescence is quenched up to 10 times. Moreover, naked eye visible color changes are seen under daylight or UV-light upon addition of Hg^{2+} or Fe^{2+}, thus the molecules can be easily used as fluorescnce probe for mercury(II) and iron(II) detection. The described detection of metal ions works in all tested organic solvents except non polar dimethyl-sulfoxide (DMSO) in which no absorbance or fluorescence changes are observed. The strongest photophysical effect due to metal ions is noticed in acetone solvent, which, in low concentrations, is not harmful to cells.

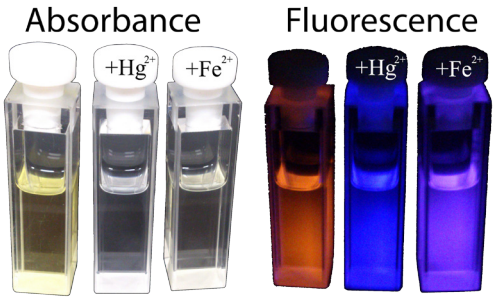

Fig. 1. Naked eye view of 4-(4-dimethylaminophenyl)-N-(2-(2-hydroxyethoxy)ethyl)-1,8-naphthalimide solution in acetone (10^{-3} mol L^{-1}) with added 10 equivalents of mercury(II) and iron(II) under normal light (absorbance) and under UV light (fluorescence).

4-(4-dimethylaminophenyl)-N-(2-(2-hydroxyethoxy)ethyl)-1,8-naphthalimide shows absorption response to Hg^{2+} in aqueous solution of acetonitrile/water (30 %:70 %, v/v) thus can be used as a colorimetric sensor for detection of mercury(II) ions in living organisms.

[1] Wei X, Yang X, Feng Y, Ning P, Yu H, Zhu M, et al., A TICT based two-photon fluorescent probe for cysteine and homocysteine in living cells. Sensors Actuators B Chemical **92**, 231-285 (2016).
[2] 1. Tang J, Ma S, Zhang D, Liu Y, Zhao Y, Ye Y, Highly sensitive and fast responsive ratiometric fluorescent probe for Cu2+ based on a naphthalimide-rhodamine dyad and its application in living cell imaging. Sensors Actuators B Chemical **15**, 236-109 (2016).
[3] A. Ito, S. Ishizaka, N. Kitamura, A ratiometric TICT-type dual fluorescent sensor for an amino acid, Physical Chemistry Chemical Physics **12**, 6641–6649 (2010).

FLUORESCENCE MICROSCOPY OF QUANTUM DOTS DISTRIBUTION IN RAINBOW TROUT EMBRYOS CHORION

Mantas Stankevičius[1], Živilė Cibulskaitė[1,2], Nijolė Kazlauskienė[2], Ričardas Rotomksis[1,3]

[1] Biomedical Physics Laboratory, National Cancer Institute, Baublio 3b, LT-08406, Vilnius, Lithuania
[2] Institute of Ecology of Nature Research Centre, Akademijos st.-2, LT-08412 Vilnius, Lithuania
[3] Biophotonics group of Laser Research center, Vilnius University, Sauletekio ave. 9, LT-10222, Vilnius, Lithuania
mantas.stankevicius@gf.stud.vu.lt

Environmental pollution is currently being raised by a rapid application of nanoparticles in various fields. However, toxicity properties of nanoparticles are little-known. Embryonic development is an important model for studying the toxicity, in vivo system damage, transport and biocompatibility of nanoparticles and drugs.

The aim of this study is to examine distribution of CdSe/ZnS-COOH quantum dots (QDs) in rainbow trout (*Oncorhynchus mykiss*) embryos chorion using confocal microscopy and 3D mathematical modeling.

Analysis was based on 3D imaging of autofluorescence signal of embryo chorion and CdSe, covered with an additional semiconductor layer (ZnS), carboxylate functionalized, negatively charged, water soluble QDs (CdSe/ZnS-COOH) photoluminescence using Nikon ECLIPSE TE2000-U confocal – fluorescence laser scanning microscope along with 3D reconstruction software (Fig. 1. A). QDs distribution in rainbow trout embryos chorion was estimated. The laboratory treatment was carried out in climatic camera under static conditions.

Light absorption and scattering, caused by embryo chorion tissues, allowed 3D reconstructions of external tissues with maximum thickness reaching up to 40 μm (Fig. 1. B). The autofluorescence of embryo membrane's surface is non-homogeneous (Fig. 1. C). This non-homogeneous autofluorescence can be seen as brighter spots with a diameter of 1.15 ± 0.29 μm and center to center distance of 2.27 ± 0.32 μm. TEM measurements of *Oncorhynchus mykiss* membrane pores has shown the same results [1]. Depending on the size of QDs conglomeration, photoluminescence of QDs can be seen directly in the area of brighter spots (Fig. 1. C – 1 and 2). As the size of QDs conglomeration increases, photoluminescence can be seen covering a wider area (Fig. 1. C – 3 and 4). A cross-section of 3D reconstruction shows a thin 3 – 4 μm external layer, composed of brighter cylindrical shaped autofluorescence structures, which coincide with the brighter spots on the surface. A part of QDs photoluminescence was observed in the area of these cylindrical shaped autofluorescence structures (Fig. 1. D – 1 and 2). As the size of QDs conglomeration increases, more dispersed QDs photoluminescence can be seen (Fig. 1. D – 3 and 4). Dispersion increases in lateral as well as vertical direction in respect to the surface of the chorion. In the case of small QDs conglomeration, QDs photoluminescence occurs up to 3 – 4 μm within the chorion. Concerning larger conglomeration, QDs photoluminescence up to 10 μm within chorion was registered.

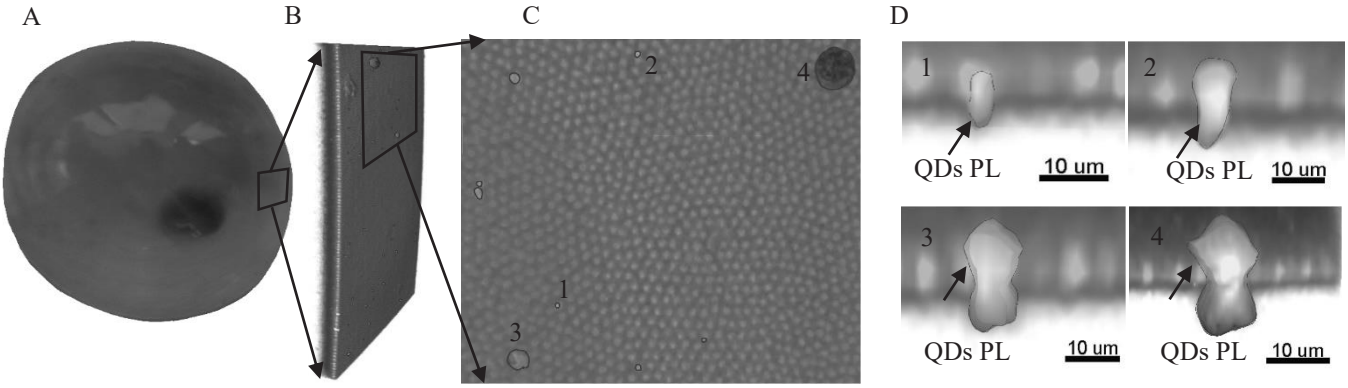

Fig. 1. *Oncorhynchus mykiss* caviar (A). A 3D reconstruction of embryo chorion with the maximum thickness of 40 μm (B). Non-homogeneous autofluorescence distribution is seen on the surface of membrane (C – brighter spots). Depending on the magnitude of QDs conglomeration, QDs photoluminescence (PL) can be seen covering: only the area of brighter autofluorescence spots as well as cylindrical shaped autofluorescence structures (C and D – 1, 2) or a much wider area (C and D – 3, 4).

[1] Kunz Y.W. 2004. Developmental biology of teleost fishes. Dordrecht, Netherlands:Springer;pp 636.

EFFICACY OF SELECTED *BACILLUS SUBTILIS* STRAINS AGAINST FUSARIUM HEAD BLIGHT OF WHEAT CAUSED BY ARTIFICIAL INFECTION

Karina Stumbriene[1], Skaidre Suproniene[1], Renata Gudiukaite[2], Roma Semaskiene[1]

[1]Institute of Agriculture, Lithuanian Research Centre for Agriculture and Forestry, Lithuania
[2]Vilnius university, Faculty of Natural Sciences, Department of Microbiology and Biotechnology, Lithuania
Karina_stumbriene@yahoo.com

Fusarium head blight (FHB) is a global problem. *F. graminearum* is the most prominent causal agent of head blight in the United States, Canada, and Europe. FHB reduces grain yield and quality and contaminates grain with mycotoxins; predominantly deoxynivalenol (DON). In Europe *Fusarium graminearum* and *Fusarium culmorum* are the most important and spread agents of FHB of wheat. FHB caused mainly by *Fusarium graminearum* is a devastating disease of wheat. Moisture appears to be the most important environmental factor influencing the severity of infection caused by *F. graminearum* in small grain cereals, given that FHB development can occur at temperatures that range from approximately 9 °C to 30 °C. Reliable wheat crop protection from pests, diseases and weeds are more important for yield and grain quality enhancement reserve. Proper use of biological and chemical measures can increase yields and improve quality.

Bacterial strains MBK-a3 and MBK-r4 identified as *Bacillus subtilis* were able to suppress *F. graminearum* growth *in vitro*, therefore the aim of this study was to investigate their ability to control FHB in artificially infected winter and spring wheat at field conditions.

The study was carried out in 2015 and 2016 years. Winter wheat "SW Magnifik", "Skagen" and one FHB susceptible breeding line, and spring wheat „Diskett" and „Tybalt" were sprayed at the middle of wheat flowering (BBCH 65) with the fungicide metconazole and cell-free supernatants of MBK-a3 and MBK-r4 bacteria. Artificial inoculation with *F. graminearum* (spore concentration 1.0×10^4) was done one day after application according to Haidukowski et al., 2005. FHB incidence and severity were evaluated at early dough (BBCH 77-83) stage. *Fusarium* damaged (visual assessment) and infected grain (agar plate method) and grain yield parameters were evaluated after harvest.

Bacteria was not able to control FHB in the fields at statistically significant levels, but the reduction in both incidence and severity of FHB was detected, and this indicates potential, which may be developed by further studies. Metconazole reduced FHB incidence, severity and amount of *Fusarium* damaged grain and resulted an increase in grain yield.

Acknowledgement. The study was funded by the long-term research program "Harmful Organisms in Agro and Forest Ecosystems (KOMAS)" implemented by Lithuanian Research Centre for Agriculture and Forestry.

[1] Haidukowski M., Pascale M., Perrone G., Pancaldi D., Campagna C., Visconti A. Effect of fungicides on the development of Fusarium head blight, yied and deoxinivalenol accumulation in wheat inoculated under field conditions with Fusarium graminearum and Fusarium culmorum // Journal of the Science of Food and Agriculture. – 2005, vol. 85, p. 191-198.

CASPASE DEPENDENT APOPTOSIS INDUCED IN YEAST CELLS BY NANOSECOND PULSED ELECTRIC FIELDS

Povilas Simonis[1], Skirmantas Kersulis[2], Voitech Stankevich[2], Vytautas Kaseta[3,1], Egle Lastauskiene[4,1] and Arunas Stirke[1, 4]

[1] Laboratory of Bio-Nanotechnology, State Research Institute, Center for Physical Sciences and Technology, Sauletekio ave. 3, LT-10257, Vilnius, Lithuania
[2] High Power Pulse Laboratory, State Research Institute, Center for Physical Sciences and Technology, Sauletekio ave. 3, LT-10257, Vilnius, Lithuania
[3] State Research Institute Center for Innovative Medicine, Santariškių 5, LT-08406, Vilnius, Lithuania
[4] BioScience Institute, Life Sciences Center, Vilnius University, Sauletekio ave. 7, LT-10257, Vilnius, Lithuania
simonis.povilas@gmail.lt

The effects that are induced by exposing biological tissues and cell suspensions to electric fields are intensively investigated. Pulsed electric fields are an effective method for improving conventional procedures such used in chemotherapy, gene transfer, microbiological inactivation in food preservation and the extraction of intracellular compounds. It has been previously shown that in mammalian cells, a nanosecond pulsed electric field (nsPEF) can improve the permeability of the plasma membrane, alter gene expression, cause phosphatidylserine translocation, affect the distribution of intracellular ions and even lead to the death of the cell [1].

Budding yeast (*Saccharomyces cerevisiae*) is one of the most well-studied and understood eukaryotic organisms. It is an irreplaceable component in the food industry, where it is used in the preparation of fermented foods and beverages and in the pharmaceutical and biotechnology sectors, where it is used for the production of recombinant proteins. In addition, it is also a highly useful organism for theoretical and practical modelling [2]. Yet there is still a lack of sufficient data related to the effects of nsPEF on yeast cells.

In our study *Saccharomyces cerevisiae* yeast cells were used as a model organism to investigate the effects of various pulsed electric fields on the programmed death of such cells. We analysed the effects of square shaped electrical pulses of different duration (τ = 10-90 ns) and pulse number (pn = 1-5) with electric field strength (E) up to 220 kV/cm and showed that nanosecond pulses can induce the cell death, which in turn is dependent on the electric field pulse parameters and increase with the rise in E, τ and pulse number (Fig. 1).

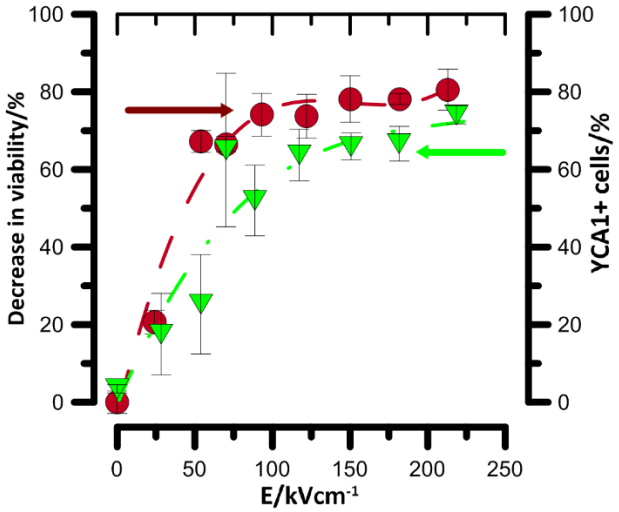

Fig. 1 Decrease in viability and YCA1+ activation dependence on the electric field strength after exposure to 5 pulses with durations of 90 ns.

Since nsPEFs which treated the electroporation buffer did not cause any reduction in the viability, we concluded that nsPEFs affects yeast cells directly. Exposure of yeast cells to nsPEFs was accompanied by metacaspase activation, membrane permeability to propidium iodide and the externalisation of phosphatidylserine. We conclude that square shaped electric field pulses with nanosecond durations induce caspase-dependent apoptosis in yeast cells, which in turn can be used as a model for more detailed analysis of the programmed cell death analysis induced by nsPEFs [3].

[1] T. B. Napotnik, M. Reberšek, P. T. Vernier, et al., Effects of high voltage nanosecond electric pulses on eucaryotic cells (in vitro): A systematic review, Bioelectrochemistry **110**, 1–12 (2016).
[2] F. Madeo, D. Carmona-Gutierrez, J. Ring, et al., Caspase-dependent and caspase-independent cell death pathways in yeast, Biochem. Biophys. Res. Commun. **382**, 227–231 (2009).
[3] P. Simonis, S. Kersulis, V. Stankevich et al., Caspase dependent apoptosis induced in yeast cells by nanosecond pulsed electric fields, Bioelectrochemistry (in press).

AGGREGATION AND STABILITY OF S100A9 PROTEIN

Darius Sulskis[1], Vytautas Smirnovas[1], Ludmilla Morozova-Roche[2]

[1]Institute of Biotechnlogy, Life Sciences Center, Vilnius University, Lithuania
[2]Department of Medical Biochemistry and Biophysics, Umea University, Sweden
sulskis.d@gmail.com

S100 family proteins are involved in different cell activities: proliferation, survival, movement, inflammatory signalling and reproduction [1]. Because of their wide range of functions, these proteins can be associated with many diseases, including cancer and neurodegenerative disorders. There are reports showing that S100A9 protein can aggregate into amyloid fibrils and is possibly involved in Alzheimers and Parkinsons diseases [2]. Similar to other members in S100 family, S100A9 stability can be regulated by calcium [3], however there is too little information on how calcium ions affect S100A9 protein stability and aggregation into amyloid-like structures. Therefore we decided to investigate these properties.

Thermal unfolding of the protein was monitored using ANS fluorescence assay. Calcium-protein binding events were studied using isothermal titration calorimetry (ITC). Aggregation kinetics of S100A9 were observed using Thioflavin-T (ThT) fluorescence assay (Fig.1). Formed amyloid-like fibrils were observed using atomic force microscopy and the nature of fibrils was confirmed using specific A11 and OC antibodies.

Our results show, that calcium exponentially increases protein thermal stability (Fig.1) and inhibits the rate of aggregation. ITC data suggests, that calcium binds to multiple sites and induces conformational changes of the protein structure, however more detailed research is needed to identify different protein states.

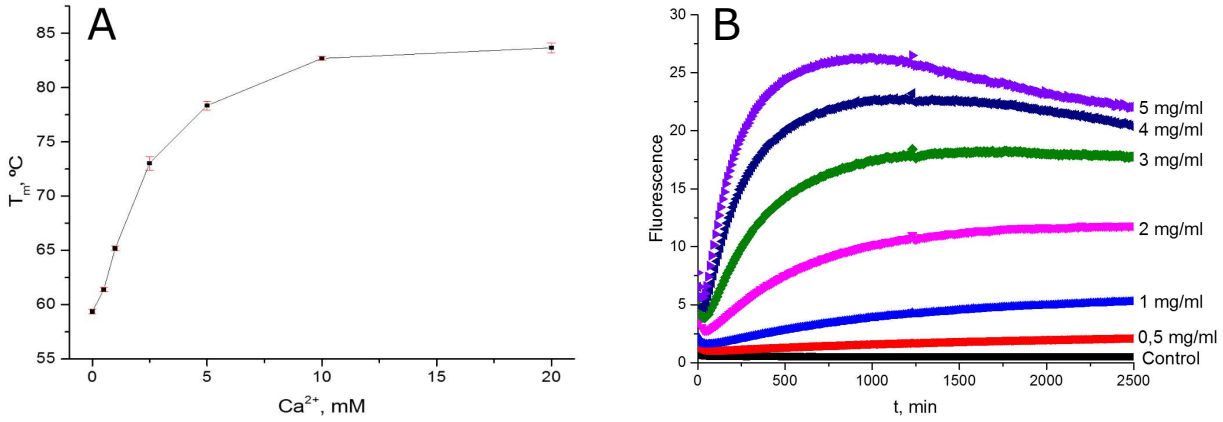

Fig. 1. (**A**) Dependence of S100A9 thermal unfolding on calcium concentration in HEPES 50 mM pH 7 buffer. (**B**) S100A9 aggregation kinetics in PBS, 42 °C.

[1] Donato, R., Cannon, B. R., Sorci, G., Riuzzi, F., Hsu, K., Weber, D. J., & Geczy, C. L. (2013). Functions of S100 proteins. Current Molecular Medicine, 13(1), 2457. http://doi.org/10.2174/1566524011307010024

[2] Wang, C., Klechikov, A. G., Gharibyan, A. L., Wrmlnder, S. K. T. S., Jarvet, J., Zhao, L., Morozova-Roche, L. A. (2014). The role of pro-inflammatory S100A9 in Alzheimers disease amyloid-neuroinflammatory cascade. Acta Neuropathologica, 127(4), 507522. http://doi.org/10.1007/s00401-013-1208-4

[3] Vogl, T., Leukert, N., Barczyk, K., Strupat, K., & Roth, J. (2006). Biophysical characterization of S100A8 and S100A9 in the absence and presence of bivalent cations. Biochimica et Biophysica Acta - Molecular Cell Research, 1763(11), 12981306. http://doi.org/10.1016/j.bbamcr.2006.08.028

UPCONVERTING NANOPARTICLES OPTICAL PROPERTIES DEPENDENCE ON SIZE AND SHELL

Aivaras Vilkas[1], Dovile Baziulyte-Paulaviciene[2], Simas Sakirzanovas[2], Vitalijus Karabanovas[1,3], Ricardas Rotomskis[1,4]

[1] Biomedical Physics Laboratory, National Cancer Institute, Baublio 3b, LT-08406, Vilnius, Lithuania
[2] Vilnius University, Faculty of Chemistry and Geoscience, Naugarduko 24, LT-03225, Vilnius, Lithuania
[3]Department of Chemistry and Bioengineering, Vilnius Gediminas Technical University, LT-10223 Vilnius, Lithuania
[4]Biophotonics group of Laser Research center, Vilnius University, Sauletekio ave. 9, LT-10222, Vilnius, Lithuania
aivaras.vilkas@ff.stud.vu.lt

Due to its special chemical-physical properties upconverting nanoparticles (UCNPs) can be applied in many fields such as bioimaging and drug delivery. UCNPs demonstrates many useful features such as narrow emission bands, large anti-Stokes shift, resistance to photobleaching, high chemical and physical stability, low chemical toxicity and long luminescence lifetimes. Upconversion of these nanoparticles is affected by the size of the particles as well as the size of its shell. Upconversion efficiency can be enhanced by using various core/shell combinations [1]. The aim of our study was to investigate how upconversion photoluminescence depends on nanoparticles shell, its thickness and the size of the particles.

In this work we investigated hexagonal upconverting nanoparticles with different core size, different shell thickness and different combinations of active and inert shells. Particles that were studied can convert near infrared light to visible light or ultraviolet light (UV) emissions. Photoluminescence emission spectra of the particles were measured by Edinburgh Instruments FLS980 spectrometer. For excitation 980 nm IR laser were used. We studied two groups of particles with different solvents: water and toluene.

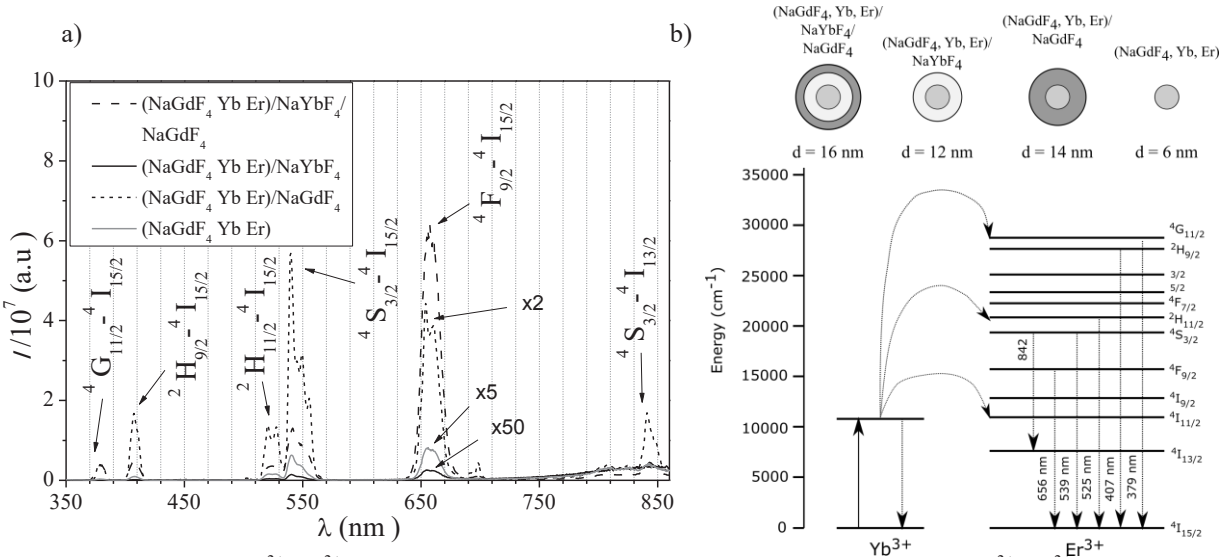

Fig. 1. a) ($NaGdF_4$: Yb^{3+} ,Er^{3+}) luminescence dependence on different particle shells, b) Yb^{3+} ,Er^{3+} ions energy diagram.

Firstly, upconversion photoluminescence spectra were used to determine differences between photoluminescence intensities of the UCNPs with different shells. These particles were soluble in water. Emission peaks were attributed to the energy transitions of Er^{3+} ions (Fig. 1). Measurement data shows that upconverting photoluminescence intensity of ($NaGdF_4$:Yb^{3+},Er^{3+})/$NaYbF_4$/$NaGdF_4$ is the highest while ($NaGdF_4$:Yb^{3+},Er^{3+})/$NaYbF_4$ is the lowest. Reason for this in the case of ($NaGdF_4$: Yb^{3+},Er^{3+})/$NaYbF_4$ might be surface defects that appears on the surface of the core due to lattice mismatch [2]. Upconverting photoluminescence emission intensity is highest for ($NaGdF_4$:Yb^{3+},Er^{3+})/$NaYbF_4$/$NaGdF_4$. The reason for this is that these particles have active core/active shell/inert shell structure. Active shell of the particle enhances photoluminescence while inert shell protects the particle from surface quenching effects. By using upconversion photoluminescence spectra of the particles that were soluble in toluene, photoluminescence intensity dependence on particle size and shell thickness were determined.

The results obtained show that active and inert shell combinations, shell thickness and core size affects photoluminescence intensity of upconverting nanoparticles.

[1] Anna Gnach and Artur Bednarkiewicz, Lanthanide-doped up-converting nanoparticles: Merits and challenges, Nano Today **7**, 532—563 (2012).
[2] Hailong Qiu, Chunhui Yang et al. Enhanced Upconversion Luminescence in Yb^{3+}/Tm^{3+}-Codoped Fluoride Active Core/Active Shell/Inert Shell Nanoparticlesthrough Directed Energy Migration", Nanomaterials **4**, 55-68 (2014).

SPECTROMETRIC ANALYSIS OF PHOTOTRANSFORMATIONS OF NATURAL PIGMENTS IN EXTRA VIRGIN OLIVE OIL

Povilas Zdanis, Saulius Bagdonas

Physics faculty, Vilnius University, Lithuania
Zdanis.povilas@gmail.com

Extra virgin olive oil's (EVOO) price is higher compared to most other vegetable oils because of the high content of natural antioxidants and other biologically active molecules. Therefore, there are known cases of its adulteration [1]. Sometimes, rapeseed oil with added colorants and flavors has been labeled as EVOO. Olive oil's quality depends on various factors: the region where olives were grown, fruit ripeness level, storage conditions, processing, etc. Because olive oil is processed from olive fruits, it contains natural photosensitizers such as chlorophylls or its derivatives. The sensitizers are the main initiators of the light-induced oxidation, while the presence of antioxidants creates a protective effect. Thus, pigments naturally degrade in oil during storage, and the factors affecting such transformations could be variations in temperature, oxygen level as well as accidental light exposure [2].

The purpose of this study was to investigate aging process and phototransformations of EVOO. Five commercially available products of extra virgin olive oil were chosen. According to the literature the main pigments in EVOO are lutein, β-carotene and pheophytin-a [3]. While measuring absorption, fluorescence and excitation spectra of specimens it has been found that there are two main types of pigments: carotenoids/xanthophylls and chorophylls, in all of studied EVOO's, but with different concentrations. Monitoring of the olive oil aging process has revealed that the intensities of the spectral bands of carotenoids and pheophytin-a decreased over time. Also, by irradiating the samples with a blue LED light, EVOO bleaching effect was studied with and without artificially added α-tocopherol. It has been found that the increased concentrations of added α-tocopherol had a stronger suppressive effect on the bleaching of EVOO absorption spectra. Irradiation of the specimen resulted in the formation of pheophytin's-a photoproduct spectral bands, which had disappeared over time.

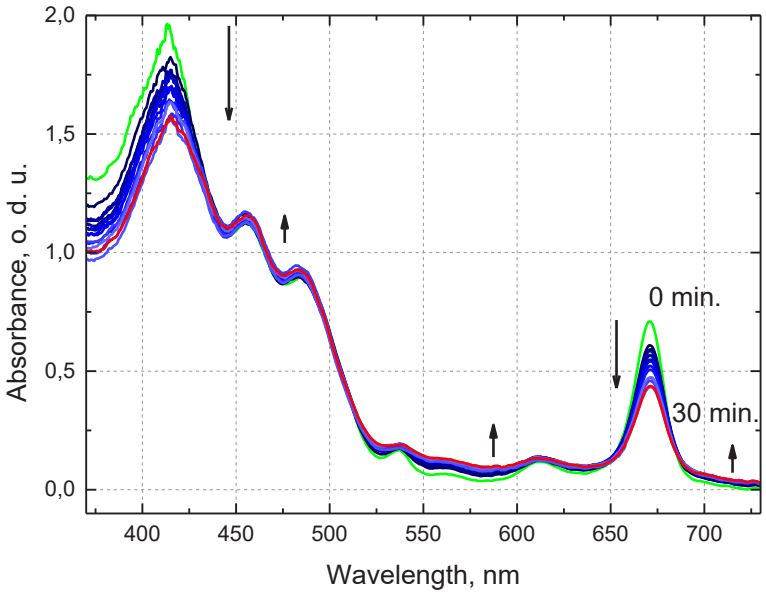

Fig. 1. Photoinduced changes in absorption spectra of EVOO specimen under irradiation applied repeatedly for two minutes.

Upon irradiation of EVOO with blue LED light, chlorophyll might undergo two reactions: oxidation and reduction. While there is enough oxygen in the medium, it will oxidize chlorophylls, but if amount of oxygen decreases and a reducing agent is in the neighborhood, chlorophyll might be reduced and a photoreduction product might form.

[1] M. Mowatt. In Search of Counterfeit Olive Oil Using the Spark Spectral Sensor, Applications Scientist. Ocean optics, 1-4, (2015).
[2] A. Giuliani, L. Cerretani, L. Cichelli. Chlorophylls in Olive and in Olive Oil: Chemistry and Occurrences. Food Science and Nutrition, 51:678 690, (2011).
[3] M. J. Moyano, F. J. Heredia, and A. J. Melendez-Martınez, The Color of Olive Oils: The Pigments and Their Likely Health Benefits and Visual and Instrumental Methods of Analysis. Comprehensive Reviews In Food Science And Food Safety,9:278-291, (2010).

IN SILICO ANALYSIS AND MOLECULAR DOCKING STUDIES OF RH1 DRUG WITH UPREGULATED KINASES IN RH1 RESISTANCE HUMAN BREAST CANCER CELL LINE MDA-MB231.

Pramodkumar P. Gupta[1, 2, 3], Dalius Kučiauskas[1], Shanker Lal Kothari[3], Virupaksha A. Bastikar[1,4], Mindaugas Valius[1].

[1]Institute of Biochemistry, Vilnius University, Vilnius, Lithuania
[2]School of Biotechnology and Bioinformatics, D Y Patil University, Navi Mumbai 400614, Maharastra, India.
[3]Amity Institute of Biotechnology, Amity University Rajasthan, Jaipur -303002, Rajasthan, India.
[4]Amity Institute of Biotechnology Amity University, Mumbai - Pune Expressway, Bhatan, Post – Somathne, Panvel, Mumbai, Maharashtra 410206, India.
pramodkumar785@gmail.com / mindaugas.valius@bchi.vu.lt

Identification of potential drug targets is a critical step towards the understanding of drug activity, improvement in the drug's therapeutic management and its therapeutic potential. In the last few years a pharmacological interest was developed on targeted therapies as a more specific and effective way for stopping cancer progression. Aziridinylquinone RH-1 is a potential anticancer agent which was developed to be activated by NAD (P) H: quinone oxidoreductase (NQO1) which reduces RH1 into DNA-alkylating hydroquinone and is overexpressed in many tumors. Another suggested mechanism of RH-1 toxicity is the formation of reactive oxygen species (ROS) arising from its redox cycling.

In this research we cultivated MDA-MB231 cell in the presence of RH1 to generate RH1 resistant cell line and used multiplexed kinase inhibitor beads (MIBs) and quantitative mass spectrometry analysis to compare kinase activity in parental and RH1 resistant MD-MDA-231 cell line of triple negative breast cancer. Using MIB/MS data, activity changes of over 150 kinases were quantitatively measured from various protein kinase families. We hypothesize that the observed change in kinase activity drives an off-target mechanism for RH1 activity. It is has been already shown that NQO1 can act as kinase inhibitors famitinib and 5-hydroxyl-defluorofamitinib (active form). NQO2 can be inhibited by serine-threonine kinase CK2 inhibitors and tyrosine kinase inhibitors Imatinib and Nilotinib.

Applying the rationale method of Computer Aided Drug Discovery (CADD), a comparative molecular docking study has been carried out between the kinase structures with their known, experimental inhibitors and RH1 drug.Our analysis show that casein kinase I isoform alpha (CSNK1A1), serine/threonine-protein kinase Chk1 (CHEK1), ribosomal protein S6 kinase alpha-3 (RPS6KA3), ephrin type-A receptor 3 (EPHA3), mast/stem cell growth factor receptor Kit (KIT) and dual specificity protein kinase TTK (TTK) show a highly similar and identical pharmacophoric interaction between RH1 and their indigenous inhibitors with comparable binding energies.

FLOOD FORECASTING SYSTEM UPGRADE BY ADDING ICE PHENOMENA

Janina Brastovickytė-Stankevič

Laboratory of Climate and Water Research, Geology and Geography Institute, Nature research centre, Lithuania
janina.brastovickyte@gmail.com

Modelling natural process is a very complex matter affected by many factors. In this study for water level forecast Mike Customised (MC) forecasting system is used. To get a good simulations, everyday on scheduled time system should get a new information from weather radar, numerical weather forecasting system, water gauging stations, and meteorological stations. After processing received data flood forecasting system can make water level forecast simulations.

Winter of 2015-2016 was the first one when the MC system was started to run. Forecasting system using all received data calculates and simulates some soil, snow and other parameters which are used to simulate reality and to make water level forecast. In this study, a decision was made to try and improve forecasting system by adding actual ice phenomena. Ice phenomena as a parameter is extremely difficult to value. Especially ice jams, that determines the sudden water level changes.

To understand the need of entering actual ice phenomena into the forecasting system, a few main characteristics has been chosen: ice coverage, slush/debacle, ice jam and ice (for other ice phenomena). For these parameters Manning roughness coefficient from 0,13 to 0,4 was assigned. For ice phenomena effect on water level forecast these water gauging stations have been selected: Nevėžis – Babtai, Neris – Jonava, Nemunas – Nemajūnai, Nemunas – Panemunė, Merkys – Puvočiai and Jūra – Tauragė. In these stations simulations with and without entered ice phenomena was compared.

The Study showed that entering ice phenomena didn't help to improve forecast, it makes forecast less accurate. Model is calibrated to give better forecasts, and for more accurate results Manning roughness coefficient should be changed.

ANXIETY AND DEPRESSION IN PEOPLE WITH EPILEPSY AND PATIENT WITH CORONARY ARTERY DISEASE: COMPARATIVE ANALYSIS

Austeja Juskaite[1], Karolis Kluonaitis[1], Jolita Badariene[2], Ruta Mameniskiene

[1]Faculty of Medicine, Vilnius University, M. K.Ciurlionio str. 21, LT-03101, Vilnius , Lithuania.
[2]Vilnius University, Department of Cardiology and Angiology, Center for Cardiology, Vilnius, Lithuania
[3]Vilnius University, Department of Neurology and Neurosurgery, Center for Neurology, Vilnius, Lithuania
austejajusk@gmail.com

Depression as well as anxiety is a serious and frequent problem among people with chronic somatic illnesses that has significant negative impact on their quality of life. The study aimed to analyze and compare levels of depression and anxiety in patients with epilepsy and compare findings to those with coronary artery disease.

This cross-sectional study was performed in Center of Epilepsy and Centre of Cardiology and Angiology of Vilnius University Hospital Santariskiu Klinikos. 530 (242 male) patients with epilepsy (PWE) and 276 (216 male) with coronary artery disease (CAD) were surveyed. The questionnaire included socio-demographic questions, Hospital Anxiety and Depression Scale (HADS) for anxiety and Beck Depression Inventory (BDI) for depression level evaluation. Data was analyzed using „SPSS 22“ program. Chi-square test and Pearson's correlation coefficient were used in the analysis. Statistical significance was defined by $p< 0.05$.

Patients with CAD were older than PWE (mean age 47.50±10.28 and 55.76±9.16 years respectively). 78.3% CAD patients and 45.7% PWE were male. Mean anxiety level was 8.74±4.79 in PWE and 6.20±3.33 in CAD group ($p< 0.05$); mean level of depression was 15.58±11.51 and 8.49±5.73 respectively ($p< 0.05$). PWE anxiety and depression levels were associated with residence ($p< 0.001$; $p=0.013$), education (both $p< 0.001$), marital status ($p=0.046$; $p< 0.001$), while CAD patients did not show significant differences. Alcohol and tabacco usage was not associated with anxiety or depression levels ($p>0.05$). Anxiety levels did not significantly correlate with age neither among PWE ($r=0.029$; $p>0.05$) nor CAD patients ($r=-0.006$; $p>0.05$); there was no significant correlation between depression levels and age: PWE — $r=0.079$; $p>0.05$; CAD patients — $r=0.132$; $p>0.05$. PWE more often had family history of mental illnesses than patients with CAD ($p< 0.05$).

There was no association between age and mood disorders among PWE and CAD patients. PWE had higher levels of anxiety and depression than CAD patients, which were associated with residence, education and marital status, while CAD patients showed no such association. PWE more often had family history of mental illnesses.

SELF-ESTEEM, ATTITUDE TOWARDS THE OWN BODY SIZE AND WEIGHT CONTROL OF WOMAN BEFORE AND DURING THE PREGNANCY

Justina Katinaite[1], Austeja Juskaite[1] and Janina Tutkuviene[1,2]

[1] Scientific Group of Human Biology and Evolutional Medicine, Faculty of Medicine, Vilnius University, M. K. Ciurlionio str. 21, LT-03101, Vilnius , Lithuania.
[2]Department of Anatomy, Histology and Anthropology, Faculty of Medicine, Vilnius University, M. K. Ciurlionio str. 21, LT-03101, Vilnius , Lithuania.
austejajusk@gmail.com

The pregnancy is a period in woman's life characterized by significant and rapid physiological and psychosocial changes. Given that many young women in Western culture have body image dissatisfaction, it is possible that pregnancy might trigger additional body image concerns. Moreover, body dissatisfaction during pregnancy is of particular importance because it might be related to weight loss behaviour, which in turn, may lead to serious health outcomes – both for infant and the mother. However, there is a lack of studies focusing on the changes of body image during the pregnancy. The objective of this study was to examine self-esteem, body image concerns and weight control of women before and during the pregnancy.

This cross-sectional study was conducted in Vilnius University hospital Santariskiu klinikos (VULSK), Center of Obstetrics and Gynecology. In total, 234 pregnant women (13 – at the first trimester of pregnancy, 80 – at the second, 141 – at the third) were investigated using specific questionnaire. Rosenberg's scale (1965) was used to evaluate self-esteem, and Stunkard's scale of figures (1983) – to estimate attitude towards own body. Height and weight were registered, and body mass index (BMI) was calculated. Research data set was processed using SPSS 22.0 – descriptive statistics and Pearson's correlation coefficients were analyzed, the differences between groups in terms of significance were evaluated by Student's t-test and Chi-square test.

BMI of pregnant women before the pregnancy varied from 15.57 to 39.79 (M±SD=23.19±5.01). From all the respondents, only 1.3% had low self-esteem, 64.4% – an average, and 34.3% had high self-esteem. When evaluating their opinion about their own body size prior to pregnancy using 9 figures, women chose figures from 1 to 7 (M±SD = 3.40±1.28), during the pregnancy – from 1 to 8 (M±SD = 4.38±1.30). When choosing the number of figure as the optimal one prior to pregnancy, on average most marked a slimmer figure (M±SD =2.93±0.98) than during the pregnancy (M±SD = 3.44±1.10; $p<0.05$). Figures chosen to estimate self-body size correlated with the desired figure prior to pregnancy stronger than during the pregnancy ($r=0.592$ and $r=0.505$, respectively). On the other hand, there was a strong correlation between depicted figure for own body size prior to pregnancy and during the pregnancy ($r=0.691$) and slightly weaker correlation between desired figure prior to and during the pregnancy ($r=0.620$). Women who rated themselves as slimmer or desired to be slimmer, were more satisfied with their own body size before the pregnancy ($p<0.05$), but their satisfaction with their own body was not dependant on the desired figure during the pregnancy ($p>0.05$). The women's efforts to not gain weight during the pregnancy were not dependant on the assessment of their own body size during the pregnancy ($p>0.05$; $r=0.141$). Pregnant women, regardless of how they rated their body size during the pregnancy, did not limit their diet ($p>0.05$; $r=-0.125$).

During the pregnancy women objectively rated themselves as having larger body size. However, during the pregnancy women's attitude towards the desired body size has been changing – respondents had chosen larger figures as the ideal body size. The satisfaction with the own body size before pregnancy did not correlate with the desired body size and shape during the pregnancy. Women's efforts to maintain their body weight during the pregnancy did not depend on the evaluation of the body size and shape during the pregnancy. Pregnant women, regardless of their body size evaluation during the pregnancy, did not restrict their diet. These findings suggest that most of women do adapt to body changes over the course of their pregnancy and shift to a more realistic ideal as their body grows larger.

SOURCE APPORTIONMENT OF SECONDARY ORGANIC AEROSOL IN CONIFEROUS FOREST AREA

Laurynas Krikščikas, Steigvilė Byčenkienė, Genrik Mordas, Vidmantas Ulevičius

Department of Environmental Research, SRI Center for Physical Sciences and Technology, Vilnius, LT-02300, Lithuania

laurynas.krikscikas@ftmc.lt

It is known that atmospheric aerosol particles have adverse effects on human health [1] and impact on climate change [2]. Recent studies show that organic aerosol constitutes a large fraction of total PM_1 (particles smaller than 1 μm) mass [3], furthermore, in some cases organic aerosol fraction is dominated by secondary organic aerosol particles [4,5].

In this study an ACSM (Aerosol Chemical Speciation Monitor, Aerodyne inc.) [6] was used to measure mass-spectral composition of organic non-refractory PM_1 (NR-PM_1) aerosol. Factor (aerosol source) mass spectra and factor concentration time series (Fig. 1) were reconstructed from measured data by using Positive Matrix Factorization (PMF) - a factor analysis method. ME-2 (Multilinear Engine 2 - a multilinear problem solver software [7]) and SoFi 6.0 (Source Finder, PSI - a graphical user interface for ME-2 data input and visualization [8]) were used to perform PMF analysis of measured data.

The composition of NR-PM_1 organic aerosol was measured from 1st to 23rd of June 2016 in Rūgšteliškis, Lithuania (55,46N; 26,00E). The measurement site is a forested area dominated by coniferous trees (>80%). Results of PMF analysis show that no primary organic aerosol (POA) sources had significant impact during measurement period and that NR-PM_1 composition were influenced by two secondary organic (SOA) aerosol sources – low volatility oxygenated organic aerosol (LV-OOA) and semi-volatile OOA (SV-OOA). The former factor (source) represents aged regional aerosol and the latter factor is interpreted as fresher, newly formed secondary aerosol particles [4,5]. The presence (59%) of SV-OOA factor indicates that a significant amount of organic aerosol is formed locally. These findings suggest that during the measurement period main precursor of SOA was plant-emitted biogenic volatile organic compounds.

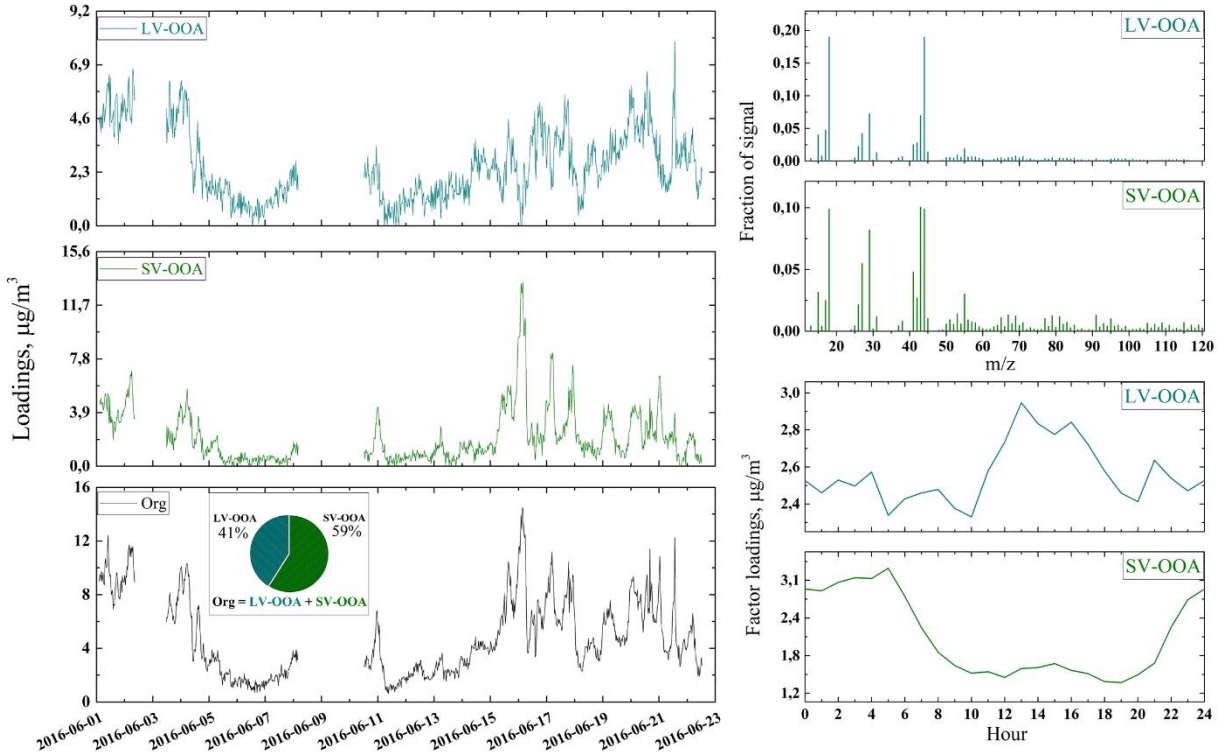

Fig. 1. Left: Time series of factor and total NR-PM_1 organic aerosol concentrations. Upper right: Factor mass spectra obtained in PMF analysis. Lower right: Average diurnal cycles of factor mass concentrations.

[1] D. K. Singh and T. Gupta, J. Hazard. Mater., vol. 306, pp. 257–268, 2016.
[2] J. Guo, Y. Yin, J. Wu, and D. Zhao, Atmos. Environ., vol. 106, pp. 110–119, 2015.
[3] C. Parworth, J. Fast, F. Mei, T. Shippert, C. Sivaraman, A. Tilp, T. Watson, Atmos. Environ., vol. 106, pp. 43–55, 2015.
[4] N. L. Ng et al., Atmos. Chem. Phys., vol. 10, no. 10, pp. 4625–4641, 2010.
[5] V. A. Lanz et al., Atmos. Chem. Phys., vol. 7, no. 6, pp. 1503–1522, 2007.
[6] N. L. Ng et al., Aerosol Sci. Technol., vol. 45, no. 7, pp. 780–794, 2011.
[7] P. Paatero, J. Comput. Graph. Stat., vol. 8, no. 4, pp. 854–888, 1999.
[8] F. Canonaco, M. Crippa, J. G. Slowik, U. Baltensperger, and A. S. H. Prévôt, Atmos. Meas. Tech., 6, pp. 3649–3661, 2013.

ENHANCEMENT OF RAT GLIOMA CELLS PROLIFERATION UNDER CHRONICAL ELECTRICAL STIMULATION AT 10 Hz

Yuliya Kunitskaya, Tatiana Kochetkova, Elizaveta Kavalenka, Elena Golubeva, Pavel Bulai

Department of Biophysics, Physics Faculty, Belarusian State University
yuliya.kunitskaya@gmail.com

Nowadays various methods to enhance the proliferative activity of the cells are being actively studied and developed. For this reason, more attention is paid to the use of cells electrical stimulation due to its obvious advantages. However, there is a lack of sufficient data in the literature on the influence of electric field on cells in culture. Because of the large number of variables of the electric field stimulation, there is currently the problem of choosing appropriate parameters of electrical stimulation as a result of the large number of variables of the electric field. Thus, the study of the effects of electrical stimulation on rat glioma cells proliferation in culture only by varying one parameter of the electrial stimulation is of great importance.

To study the effect of electrical stimulation the rat glioma cells C6 were used, cultured under standard conditions (in a humidified atmosphere of 5% CO_2 content at 37 ºC). Stimulation of cells in culture was performed with uniform alternating electric field during the 12 hours with the electric field strength of 6,6 V/m (1, 3 and 5 stimulation pulse in train). The electrical stimulation was started 8 hours after seeding the cells on the Petri dish, which corresponded – G1-S checkpoint or early S-phase. The proliferative activity was counted as the change in the number of cells after electrical stimulation relative to the control sample.

As a result of electrical stimulation the increase of proliferative activity of the rat glioma cells was revealed. It was shown that the initial increase in the number of pulses in the train (up to 3 stimulating pulses) leads to acceleration of proliferation, while a further increase in pacing pulses to 5 accompanied by a reduction in proliferative activity of the cells. It was found that maximum gain proliferative activity of rat glioma cell line C6 observed with three pacing pulses (statistical significance of differences> 95%).

The increase in proliferative activity may be due to the acceleration of the cell cycle S-phase cells due to depolarization of the plasma membrane. In turn, reduction of proliferative activity was due to hyperpolarization of the cell membrane, which caused a slowdown passage cell of the cell cycle [1].

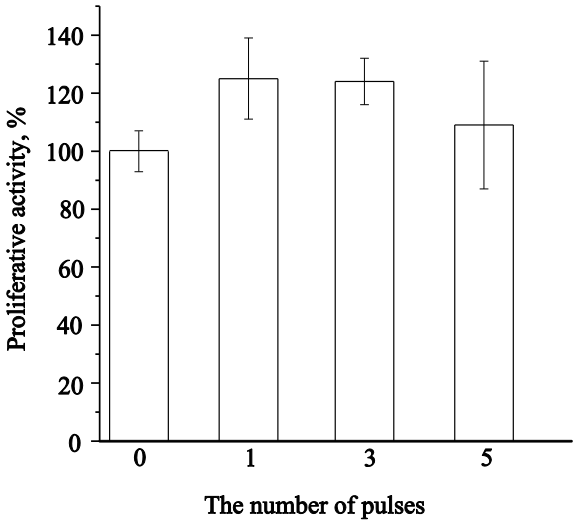

Fig. 1. Change of proliferative activity of the C6 cell line.

Thus, it was shown that the proliferative activity of C6 cells in culture can be regulated by selecting suitable parameters of electrical stimulation, in this case the number of stimulating pulses. The results of these studies can be used as a basis for the further development of effective methods for cell and tissue engineering.

[1] Kunitskaya Y.N., et al., The reorganization of the actin cytoskeleton and the change in the resting transmembrane potential of HeLa cell line under external electric field action, MMCFB **2**, 271-273 (2016).

COMBINING NEURON AND MCELL TO INVESTIGATE THE PROPERTIES OF CAV3-KV4 CHANNEL NANODOMAINS

Domas Linkevičius[1], Aušra Saudargienė[2]

[1] Faculty of Psychology, Vilnius University, Vilnius
[2] Neuroscience Institute, Lithuanian University of Health Sciences, Kaunas
dom.linkevicius@gmail.com

Mammalian nervous system is inherently constituted of multiple scales, including networks of neurons, various dendritic morphologies, membrane embedded ion channels, an abundance of cellular proteins, genes etc. All of these different scales and processes interact in a feedforward and feedback manner. This poses a monumental challenge, when trying to disentangle, model and understand how different levels of the brain interact. However, the multi-scale approach also offers novel solutions to existing problems.

It's been relatively well established that A-type potassium current (I_A) is responsible for attenuating the back – propagating action potentials (bAPs) in CA1 pyramidal cells [1]. Moreover, channels underlying I_A, primarily made up of K_{v4} subunits, have been inferred to increase 5-fold along the somato-dendritic axis, based on patch-clamp recordings. However, a recent imunogold labeling study by Kerti et al. recorded only a 1.7-fold increase in K_{v4} density [2]. In our study, using a multi-scale approach, combining two widely used simulators that simulate different levels of the cell, NEURON 7.4 and MCell 3.4, we reconcile these contradictory results. We accomplish that by including nanodomain interactions between K_{v4} and Ca_{v3} channels [3]. These interactions have been shown to make K_{v4} channel half-inactivation voltage (V_h) more positive, in turn increasing I_A [4]. An essential part of these nanodomain interactions is potassium channel interacting protein 3 (KChIP3). KChIP3 is a Ca^{2+} binding protein with three classical EF-hand motifs and binding kinetics varying by EF-hand [5].

Using this novel multi-scale model, we tried to estimate KChIP3 Ca^{2+} binding kinetics, investigated how increasing distance further than usual for nanodomains (<50nm) in conjunction with Ca^{2+} buffers affects bAP attenuation, simulated different effects to V_h per Ca^{2+} ion bound. Our model provides a variety of exploratory results in how microscopic phenomena, K_{v4} – Ca_{v3} nanodomains, can affect macroscopic processes, dendritic excitability via bAP attenuation.

[1] D. A. Hoffman, J. C. Magee, C. M. Colbert, D. Johnston, K^+ channel regulation of signal propagation in dendrites of hippocampal pyramidal neurons, Nature **387(26)**, 869 – 875 (1997).
[2] K. Kerti, A. Lorincz, Z. Nusser, Unique somato-dendritic distribution pattern of Kv4.2 channels on hippocampal CA1 pyramidal cells, European Journal of Neuroscience **35**, 66 – 75 (2012).
[3] R. W. Turner, G. W. Zamponi, T-type channels buddy up, European Journal of Physiology **466**, 661 – 675 (2014).
[4] D. Anderson, W. H. Mehaffey, M. Iftinca, R. Rehak, J. D. T. Engbers, S. Hameed, G. W. Zamponi, R. W Turner, Regulation of neuronal activity by Cav3-Kv4 channel signaling complexes, Nature Neuroscience **13(3)**, 333 – 340 (2010).
[5] M. Osawa, K. I. Tong, C. Lilliehook, W. Wasco, J. D. Buxbaum, H.-Y. M. Cheng, J. M. Penninger, M. Ikura, J. B. Ames, Calcium-regulated DNA Binding and Oligomerization of the Neuronal Calcium-sensing Protein, Calsenilin/DREAM/KChIP3, The Journal of Biological Chemistry **276(44)**, 41005 – 41013 (2001).

COMBINATION ALGORITHM OF LOW RESOLUTION MULTISPECTRAL IMAGE AND HIGH RESOLUTION PANCHROMATIC IMAGE FOR THE BELARUSIAN SATELLITE DATA

Aleksey Lomako[1], Leanid Katkouski[1]

[1] Research Institute of Applied Physical Problems named after A.N.Sevchecnko, Belarusian State University, Belarus
alekseylomako@gmail.com

The Belarusian Satellite (BS) was launched into orbit by «Sojuz-FG» launch vehicle from the «Baikonur» Cosmodrome in Kazakhstan on July 22, 2012. The BS has a Panchromatic Imaging System (PIS) that allows to capture black and white images with a ground resolution of 2.1 meters and a Multispectral Imaging System (MIS) to capture images with a resolution of 10.5 meters using four spectral bands [1].

There is an opportunity of combining the panchromatic band with high spatial resolution and low spatial resolution bands of the BS multispectral image for obtaining high spatial resolution color images. To tackle this task it is necessary to solve a number of such subtasks as spatial combination and alignment of images, interpolation of the multispectral image bands up to the panchromatic image resolution, a pansharpening and obtaining the RGB image. At the same time the solution has to be universal and suit not only BS multispectral images, but also any other both multispectral, and hyperspectral images. All subtasks can be understood, when looking at figure 1. Here area 1 is the panchromatic image, area 2 is any band of the multispectral image; N1 (black) is nodes and a net of multispectral image band, N2 (grey) is nodes and a net of panchromatic image.

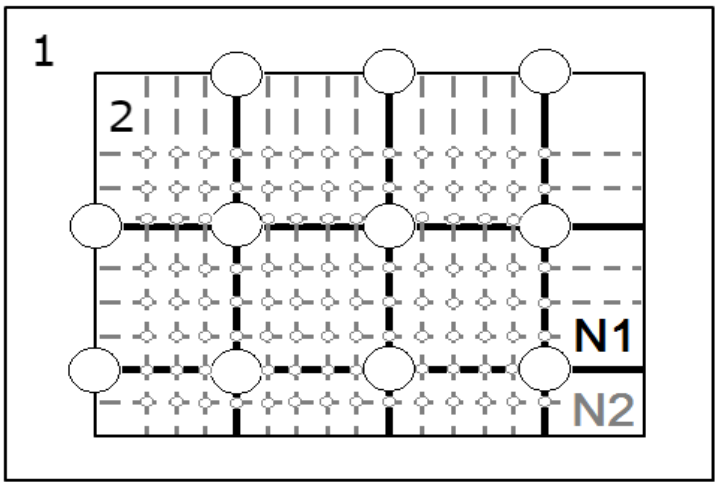

Fig. 1. Subtasks for combination.

Spatial combination of images (in fig. 1 is alignment of area 2 to area 1) can be reached by means of various algorithms. One way is to use preliminary interpolation of the multispectral image band with the subsequent binarization (using Otsu's method [2]) and segmentation. The next step on this way is to find area in previously binarized panchromatic image with the largest similarity to previously chosen segment using cross-correlation algorithm [3]. Another way is to find the same reference points on both images. Such reference points also can be found with using binarization and further segmentation techniques.

After combination of images, we have to interpolate a multispectral image band up to panchromatic image using imposing the interpolation grid (N2 onto N1). The nodes here are pixels in common sense. It is necessary for every pansharpening algorithm [4]. Then pansharpening using some a well-known algorithm (for example, HCS Resolution Merge [5]) takes place.

Thus, we can achieve the rise of the BS multispectral data resolution and, therefore, the rise of the RGB-image resolution.

Applying these algorithms to the BS data and its details will be shown in a presentation on the conference.

[1] S. Zolotoy, Belarusian Spacecraft (BS), gis.by, (2013).
[2] N. Otsu, A Threshold Selection Method from Gray-Level Histograms, IEEE Transactions on Systems, Man, and Cybernetics, Vol. 9, No. 1, 1979, pp. 62-66.
[3] J. P. Lewis, Fast Template Matching, Vision Interface, Vol. 15, №1, 1995, P. 120–123.
[4] I. Amro, J. Mateos, A survey of classical methods and new trends in pansharpening of multispectral images, EURASIP Journal on Advances in Signal Processing, Vol. 79, 2011.
[5] C. Padwick, M. Deskevich, Worldview-2 Pan-Sharpening, ASPRS Annual Conference, San Diego, California, April 26-30, 2010.

REMOTE SENSING OF VEGETATION CONDITIONS

Viktorija Mačiulytė[1,2], Edvinas Stonevičius[1]

[1] Institute of Geosciences, Vilnius University, Čiurlionio st. 21/27, LT-03101, Vilnius, Lithuania
[2] Climatology Division, Lithuanian Hydrometeorological Service, Rudnios st. 6, LT-09300, Vilnius, Lithuania
viktorija.maciulyte@meteo.lt

Drought is one of the natural hazards which impacts agriculture, crop production and water management. It become more relevant not only in arid, but also in humid areas like the Baltic Sea basin. Drought assessment and analysis reduces its devastating impact in vulnerable regions [1]**.** For this reason droughts receive more political attention. For its assessment, adaptation and decision-making, first of all objective information about droughts' frequency, spread in area and impact on the state of vegetation cover is needed. Vegetation cover quantity and quality depends on the surface temperature, soil moisture, water vapour content, accumulated rainfall and atmospheric pollution [2].

Nowadays the analysis of drought includes various indexes, based on meteorological parameters. Meteorological stations' data have poor spatial resolution of parameters. Satellite information could be powerful tool to improve the analysis of vegetation condition analysis and drought assessment.

Satellite information can help to identify vegetation conditions thought reflected red (R) and near-infrared (NIR) spectrum waves, used in the vegetation index, like NDVI (*Normalized Difference Vegetation Index*), calculations. NDVI shows vegetation colour (1) and vary from 0.1 (no vegetation) till 1.0 (perfect greenness vegetation):

$$NDVI = (NIR-R) / (NIR+R) \quad (1)$$

Also NDVI analysed by VCI (*Vegetation Condition Index*), which compares the current and previous years' NDVI values (2). VCI values vary from 0 to 100, where less than 40 could be an indication of drought [3].

$$VCI = ((NDVI - NDVI_{min}) / (NDVI - NDVI_{max})) \times 100 \quad (2)$$

In this study NDVI was used as detected by AVHRR (*Advanced Very High Resolution Radiometer*) onboard NOAA satellites in 1982-2014. The period of analysis is from May to September. Land cover data was identified using CORINE data sets. SPI (*Standard Precipitation Index*) from 1 to 24 months was used for moisture conditions. SPI values between -1 and +1 means normal, but less than -1 (more than +1) shows precipitation deficit (excess).

The best vegetation found in June and July and poorest – in September. Vegetation is most stable in summer but more varying in May and September because of a number of factors affecting start ant end of vegetation season.

Different land use has uneven NDVI distribution. In the middle of June maximum NDVI observed in arable lands, one week later in pastures and in coniferous, broad-leaved forests and wetlands in the beginning of July. It was found that date of maximum NDVI in arable land becomes 1.5 day earlier every 10 years, but in coniferous and pastures – 0.3 day.

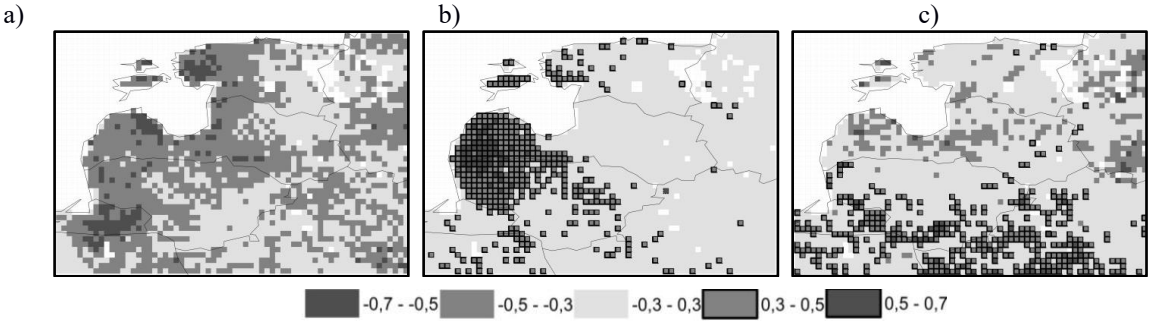

Fig. 1. Correlation between VCI and a) SPI1, b) SPI12 in May and c) SPI3 in August in eastern part of Baltic region.

Area is non-homogenous either in NDVI spatial distribution (vegetation depends on relief and distance from the sea), or in vegetation relation with SPI. It was found that VCI and SPI1 have a negative correlation in all areas. Strongest relation was found in May, when more precipitation determine worse vegetation, because soil still has enough moisture after spring snowmelt (Fig. 1a).

In other months, same monthly precipitation does not lead to better vegetation also. VCI and longer time SPI (SPI6, SPI9, SPI12, SPI24) have positive correlation in western Lithuania and Latvia, so these areas' vegetation depends on longer precipitation regime and is better with more moister conditions (Fig. 1b).

In summertime VCI and SPI1, SPI2 has negative correlation in northern part and positive – in southern (Fig. 1c). For this reason, area is divided into two parts, depending on main dominant parameter: northern (temperature and vegetation conditions are better when there are less precipitation) and southern (vegetation state is better when there is more moisture).

[1] K. Stahl, I. Kohn et al., Impacts of European drought events: insights from an international database of text-based reports. Nat. Hazards Earth Syst. Sci. Discuss. 3, 5453–5492 (2015).
[2] S. Kumar, D. Siingh et al., The influence of meteorological parameters and atmospheric pollutants on lightning, rainfall, and normalized difference vegetation index in the Indo-Gangetic Plain. Int J Remote Sens, 37:1, 57–77 (2016).
[3] F. N. Kogan, World Droughts in the New Millennium from AVHRR-based Vegetation Health Indices, Eos, Trans. Amer. Geophys. Union. 83, 562–563 (2002).

REMOVING SEASONALITY FROM FINANCIAL ASSETS (TIME SERIES) AS PART OF THE PRE-PROCESSING OF DATA

Tatsiana Mikhailava, Dmitry Shchehrykovich

Department of telecommunications and information technologies, Belarussian State university, Belarus
alluneeeeed@gmail.com

Relevance of the work related to the fact that the activities of any enterprise can`t exist without forecasting sales and production. Such processes are time series. On the prediction of time series affect the trend, seasonality and noise - three components of the time series. [1]

Purposes of the work is to explore the influence of methods of removing seasonal component on forecasting of time series different nature. Quality removing of seasonal effects allow to build more accurate forecast, detect failures that are disguised as seasonality, evaluate the actual number of sales for next few years or months, taking into account seasonality.

Removing seasonality from time series in theory most often solved by the methods of classical expansion for additive and multiplicative time series, ARIMA [2] methods and window functions.

Descriptions of such solutions are often found in the literature, but their practical implementation faces a number of problems.

For work was used the programming language R and a sample of the time series of the library «Datasets» for R [3] and open web resources such as "Daily data on the company's stock price of IBM." The study sample consisted of 18 time series.

To select and justify the selection of the optimal model of forecasting was analyzed few forecast models. Box-Jenkins model was selected. It allows to work with time series with a non-linear trend and changing the amplitude of seasonal fluctuations, while spending less resources than more complex models.

As a result, we`re received a computer program that allows to remove the effect of seasonal (seasonality) from time series depending on the nature of the time series and seasonality. Example of result of removing seasonality from time series after working the program is presented on figure 1.

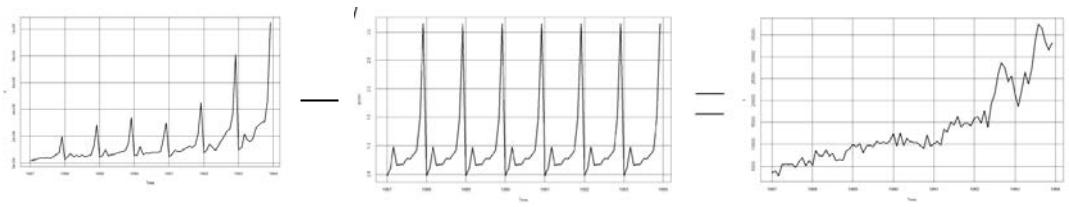

Fig. 1. The result of removing seasonality from time series.

[1] Rob J Hyndman Forecasting: principles and practice / Rob J Hyndman, George Athanasopoulos. — OTexts, 2013. — 292 p.;
[2] Gianluca Bontempi Statistical foundations of machine learning / Souhaib Ben Taieb, Gianluca Bontempi. — OTexts, 2013;
[3] “DataSets” package for R / CRAN Comprehensive R Archive Network [Electronic resource]. — Mode of access: http://cran.r-project.org/. — Date of access: 12.02.2016

COREALATION OF BOREHOLE HEAT EXCHANGER HEAT CONDUCTIVITY AND GEOLOGICAL CONDITIONS

Žygimantas Palaitis

Department of Hydrogeology and Engineering Geology, Vilnius University, M. K. Čiurlionio 21/23, LT-03101 Vilnius, Lithuania.
patvirtinta@gmail.com;

Shallow geothermal resources are widely utilized to meet a heat energy demands. Heat conductivity of geological structure is a paramount parameter to perform calculations of heat energy resource and draw up a design of the underground heat energy storage or extraction system before installation.

Estimation of heat conductivity of geological structure is time and cost requiring. The analysis of geological and geothermal data allows to perform a geothermal parameterisation of geological structure.

Complex of geological investigations were performed in 14 test fields. The depth of BHE varies from 14 to 180 m. The identification of the geological structure was performed by gathering the soil samples from the borehole during the drilling and the geophysical investigation logging data of the natural gamma and self-potential of the soils. The amount of sandy material varies from 11 to 64 %. Some of them contain separate marl, aleurite or dolomite layers Determination of the conductivity of geological structure was performed *in – situ* using a borehole heat exchanger (BHE). Estimated heat conductivity varies from 1.84 to 2.21 W/m*K [1].

After the statistical data processing it was found interdependences between the heat conductivity, lithological conditions and total depth of geological structure. Heat conductivity of sandy (more than 30 %) geological formations rises in average 0.94 present per each 10 m in the range of depth from 80 to 180 m. The interdependence between heat conductivity and lithological conditions is estimated with 89 % accuracy in investigated structures.

These results might be used for the predicting of the heat conductivity of geological structure by geological data. Allows us to create a conceptual model and calculate the amount of available underground heat energy resources.

---

[1] Palaitis Ž., Satkūnas J., 2016. Geologinių pjūvių sudėties ir šiluminio laidumo vertės korealiacija. Geologija. Geografija. 2(4): 182-194.

TEMPERATURE DEPENDING EMISSIONS OF BIOGENIC SECONDARY ORGANIC AEROSOL FROM FORESTS

J. Pauraitė, G. Mordas and V. Ulevičius

Center for Physical Sciences and Technology, Vilnius, Lithuania
julijapauraite@yahoo.com

Atmospheric aerosols have a substantial impact on the global climate and human health. Biogenic secondary organic aerosols (B-SAO) constitute a significant part of the atmospheric aerosols. B-SOA can be formed in the atmosphere upon oxidation of a number of biogenic volatile organic compounds (BVOC). Such ecosystem like forest is the main source of the BVOCs and in the global scale their emissions are higher than anthropogenic VOC (Misztal et al., 2015). In order to understand which B-SOA emissions from plants are related to the heat, the chemical composition of aerosol particles were investigated. The measurements were performed applying the Aerosol Chemical Speciation Monitor in the forested environment of Lithuania between 2013 and 2016.

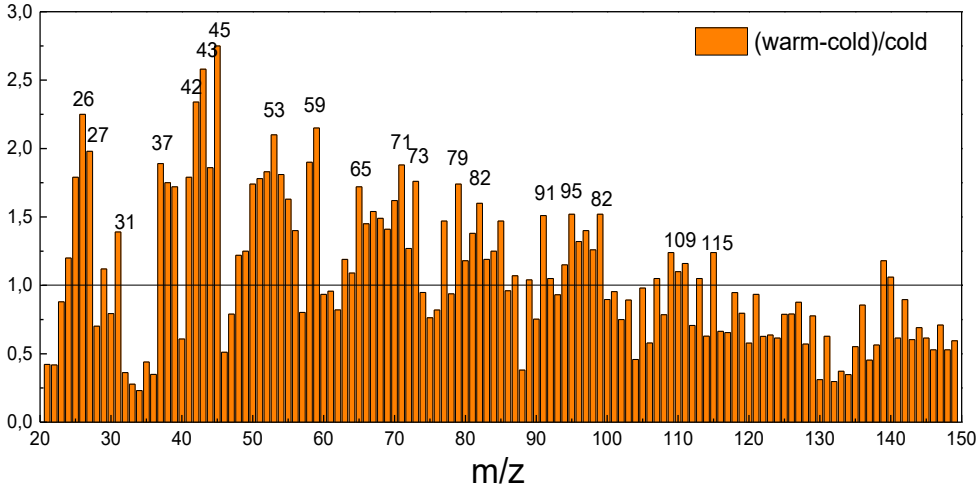

Fig. 1. The normalized distinction of average mass spectrum during warm and cold periods.

Days characterised by clean air masses and the domination of semi-volatile organic compounds were selected and divided into warm and cold periods (average daily temperature was 17.4 °C and 6.9 °C respectively). It should be noted that the distinction of average mass spectrum during warm and cold periods was normalized. As the result, a great temperature dependency was established – the signals of m/z 45 and 43 were more than 2.5 times higher during the warm period than during the cold one. Additionally, the normalized distinction of m/z 26, 27, 37, 42, 53, 59, 65, 71, 73 79, 82 was greater than 1.5. Moreover, for the selected days the submicronic forests organic aerosol mass (SFOM) analysis was performed. The SFOM concentration was 4 times greater during the warm period than during the cold one (4.7 and 1.2 μg/m^3 respectively). The average diurnal plot of SFOM concentration reached the maximum value during the night (from 20 to 8 h). Furthermore, the SFOM concentration dependency on temperature was found to be increasing exponentially. Thus, a clear temperature dependency was established for several m/z signals and SFOM concentration. All the above could lead to the expanded understanding of the forest ecosystem.

This work was supported by the National Research Programme "Sustainability of agro-, forest and water ecosystems" project FOREstRESS (No. SIT-3/2015)

[1] Misztal et al. (2015) Scientific reports 5, 1–10.

COMPRESSIVE PATTERN RECOGNITION USING PHASE-ONLY FILTERING

Michał Mikołajczyk[1], David Pastor-Calle[1], Anna Pastuszczak[1], Rafał Kotyński[1]

[1]University of Warsaw, Faculty of Physics, Warsaw, 02-093, Poland
michal.mikolajczyk@student.uw.edu.pl

In recent years compressive sensing [1] (CS) has been a rapidly growing field of information theory and signal processing. CS allowed measuring data at higher rates, using simpler imaging systems, especially in more exotic ranges of electromagnetic radiation, or measuring signal under strong influence of noise. In this work we study a possibility of employing these advantages to pattern recognition in highly compressed data.

Measurement $\mathbf{y}$ on a signal $\mathbf{x}$ in compressive sensing can be defined as $\mathbf{y} = \mathbf{M} \cdot \mathbf{x}$, where $\mathbf{M}$ is the measurement matrix. The vectors $\mathbf{y}$ and $\mathbf{x}$ have length m and n, respectively, and $m < n$. It is assumed that signal has sparse representation $\mathbf{s} = \mathbf{T}^{-1} \cdot \mathbf{x}$, where no more than $k < m$ elements are non-zero. This said, the recovery of the signal in CS can be defined as solving a following optimization problem [2]:

$$\tilde{\mathbf{s}} = \arg\min_{\mathbf{s}} \|\mathbf{A} \cdot \mathbf{s} - \mathbf{y}\|_2 \quad \text{subject to} \quad \|\mathbf{s}\|_1 \leq \tau, \tag{1}$$

where matrix $\mathbf{A}$ is defined as the product of the measurement and compression ($\mathbf{T}$) matrices. In our work we examine compression matrices of orthogonal (unitary) Toeplitz circulant form, which happen to correspond to phase-only filtering (POF). POF filter is one of the most used filters in optical correlation-based pattern recognition, for which the sparse representation is the correlation signal between the input scene and the target image. As one could assume, the correlation signal for such matched filter is strongly sparse.

To examine performance of the POF filter and the pure-phase correlation (PPC) filter we employ it in CS-based pattern recognition scheme using Walsh-Hadamard (WH), Discrete Fourier Transform (DFT) and noislet [3] measurement matrices. The measurements were constructed on synthetic image of ocean containing two ships: target and false-target, first as a computer simulation with different amounts of additive noise, and later on experimentally, using optical single-pixel detector [4].

The results are presented as a percentage of correct target detections in dependence on compression of measurements ($\rho = n/k$). For noise-free simulation we can observe near-perfect detection for compression as high as $\rho = 10^3 - 10^4$. The experimental results correspond to simulation with level of noise close to 0 dB.

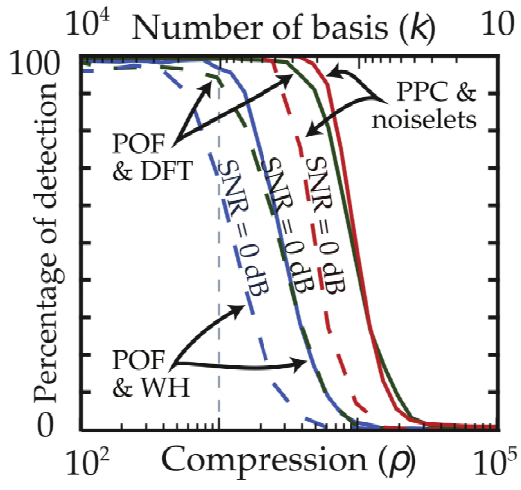

Fig. 1. Simulation results

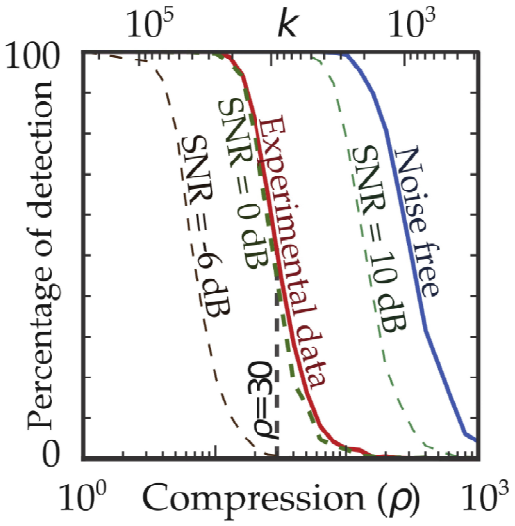

Fig. 2. Experimental results

Presented data shows that using phase-only filtering together with compressive sensing reconstruction can result in highly efficient pattern recognition on compressed measurements, when necessity of storing images is taken to account.

[1] Baraniuk, R. G. (2007). Compressive Sensing [Lecture Notes]. IEEE Signal Processing Magazine, 24(July), 118–121.
[2] Candès, E. J., Romberg, J. K., & Tao, T. (2006). Stable signal recovery from incomplete and inaccurate measurements. Communications on Pure and Applied Mathematics, 59(8), 1207–1223.
[3] Coifman, R., Geshwind, F., & Meyer, Y. (2001). Noiselets. Applied and Computational Harmonic Analysis, 10, 27–44.
[4] Duarte, M. F., Davenport, M. A., Takhar, D., Laska, J. N., Sun, T., Kelly, K. F., & Baraniuk, R. G. (2008). Single-Pixel Imaging via Compressive Sampling. IEEE Signal Processing Magazine, (March 2008), 83–91.

PREDICTION OF INTERNET TRAFFIC USING METHODS OF NONLINEAR DYNAMICS

Anželika Pavlova[1], Giedrius Tušinskis[2], Feliksas Kuliešius[1]

[1] Department of General Physics and Spectroscopy, Vilnius University, Lithuania
[2] Department of Theoretical Physics, Vilnius University, Lithuania
anzelika.pavlova@ff.stud.vu.lt

Internet traffic prediction is often required to ensure stable computer network functions. Traffic prediction is an irreplaceable tool for network optimization, prevention of malfunctions and attacks: it is necessary for adaptive applications [1], congestion control [2, 3, 4], planning of network infrastructure reconstruction [3] and attack detection [5].

The goal of this work is to achieve stable prediction of internet traffic by using nonlinear dynamics.

Internet traffic is quite unpredictable, is not periodic and cannot be described in a deterministic way. However, internet traffic is not completely stochastic: local self-similarity of the traffic flow [6, 7] helps to recognize a pattern, which allows the analysis of internet traffic by use of methods of nonlinear dynamics. By reconstructing a trajectory of the time series (the registered traffic) in a phase space it is possible to predict future values of the time series [8].

The main problem that occurs during such analysis is the determination of reconstruction parameters (delay τ and embedding dimension m). In this work delay is obtained using methods of autocorrelation, mutual information and time window and embedding dimension is obtained via false nearest neighbors and neural network methods.

A MATLAB code was written to determine the phase space reconstruction parameters (time delay and embedding dimension) and to predict the time series. In this work, common chaotic systems (Mackey Glass (Fig.1), Lorenz, Rössler) and internet traffic (Fig. 2) published by MIT (Massachusetts Institute of Technology) [9] were analyzed.

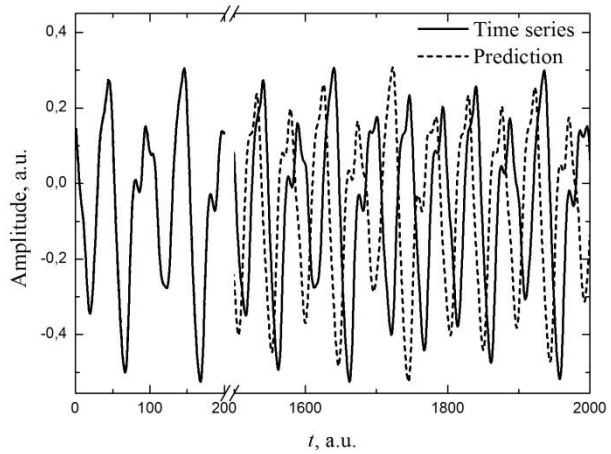

Fig 1. Prediction of Mackey Glass times series. $\tau = 17, m = 3$.

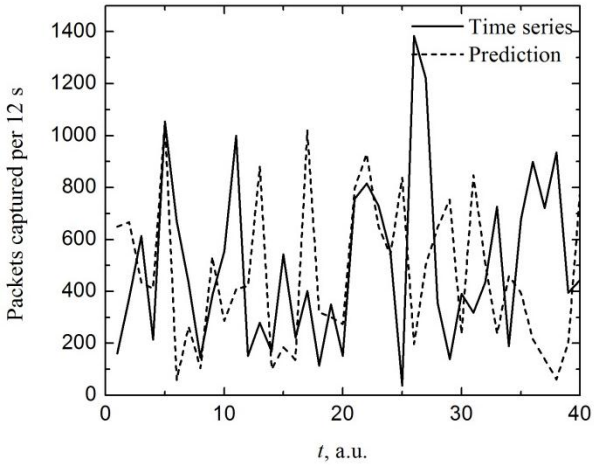

Fig 2. Prediction of internet traffic. $\tau = 3, m = 4$.

Main results and conclusions: 1) the analysis of the results of well-known chaotic systems has shown that with the optimal choice of phase space reconstruction parameters the prediction of up to 2000 points for chaotic time series is possible. The interval of maximum predictable amount of points (from a few to thousands) is mostly dependent on the choice of delay; 2) the analysis of different methods (autocorrelation, mutual information and time window) of obtaining the reconstruction parameter delay has shown that there is no single method of delay evaluation suitable for all chaotic systems; 3) only a short time prediction is available for internet traffic. Further investigation is needed in the determination of optimal and reasonable phase space reconstruction parameters.

[1] M. Stemm, S. Seshan, R. H. Katz, A Network Measurement Architecture For Adaptive Applications, Proceedings of INFOCOM 2000 1, 285–294 (2000).

[2] V. Jacobson, Congestion Avoidance And Control, Proceedings of the ACM SIGCOMM 1988 18 (4), 314–329 (1988).

[3] M. R. Joshi, T. H. Hadi. A Review of Network Traffic Analysis and Prediction Techniques, arXiv:1507.05722, 1-23 (2015). DOI: arXiv:1507.05722

[4] G. W. Lee, S. Y. Lee, E. N. Huh, Congestion Prediction Modeling for Quality of Service Improvement in Wireless Sensor Networks, Sensors (Basel) 14 (5), 7857-7880 (2014). DOI: 10.3390/s140507857

[5] J. Xue, Z. Shi, Short-Time Traffic Flow Prediction Based On Chaos Time Series Theory, Journal of Transportation Systems Engineering and Information Technology, 8 (5), 68-72 (2008). DOI: 10.1016/S1570-6672(08)60040-9

[6] W. E. Leland, , M. S. Taqqu, W. Willinger, D. V. Wilson, On the Self-Similar Nature of Ethernet Traffic, IEEE/ACM Transactions On Networking 2 (1), 1-15 (1994).

[7] K. Park, G. Kim, M. Crovella, On The Relationship Between File Sizes Transport Protocols And Self-Similar Network Traffic, Proc. International Conference on Network Protocols, 171-180 (1996). DOI.org/10.1109/ICNP.1996.564935

[8] Q. Meng, Y. Peng. A New Local Linear Prediction Model For Chaotic Time Series. Physics Letters A 370(5-6), 465-470 (2007). DOI: 10.1016/j.physleta.2007.06.010

[9] 1999 DARPA intrusion detection evaluation data set, https://www.ll.mit.edu/ideval/data/1999data.htm

THE INFORMATION MODEL OF EMOTION FOR FACIAL EXPRESSION COMPONENTS

Siarhei Sadau, Alena Kazlova

Department of Radio Physics and Computer Technologies, Belarusian State University, Belarus
seregasadov@gmail.com

Modeling of emotions in technical systems is a mathematical representation of properties and qualities of emotional conditions of the human for the purpose of the analysis of the proceeding processes in case of expression of emotions. For creation of effective system of the analysis of an emotional condition of the human it is necessary to formalize a concept of emotion – to determine its parameters and properties from the mathematical point of view.

According to Osgood, Suci and Tannenbaum's theory [1] and subsequent psychological research [2], the emotion computing can be conceptualized as three major dimensions of connotative meaning: tone, sensibilization and manifestation. Regarding the three dimensions as axes, a space of emotion can be modeled (Fig. 1).

During the development process of emotion model, the most important criteria were elaborated: completeness, high performance from the computing point of view, high adaptability under certain types of tasks. The structure of the developed formalized information emotion model is shown in the Figure 2 which essence consists in representation of emotional coloring of the analyzed video or the image as superpositions of the basic parametrized types of emotions for the further obtaining generalized characteristic of emotional coloring. Decomposition of emotional coloring of the analyzed image of a human face on the components from the allocated (basic) types of emotions is carried out by means of the qualifier of an emotional condition of the human on his face expressions.

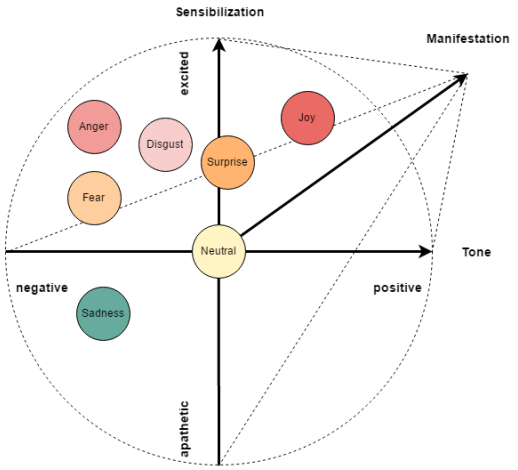

Fig. 1. Distribution of seven type of emotions in space of emotions

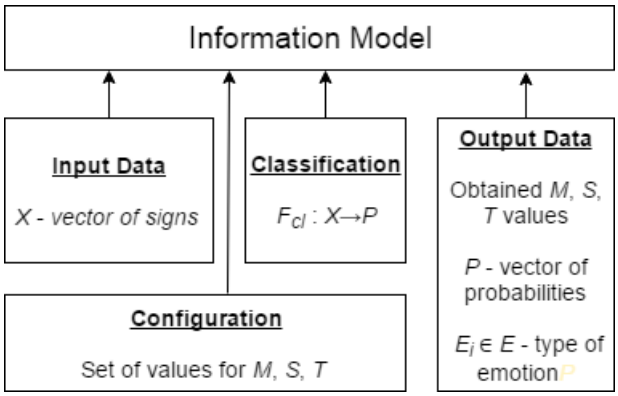

Fig. 2. Block diagram for information model of emotion

The key input parameter of the presented model is the vector of signs X, received on the basis of digital processing of the image of a human face in the analysis of change an arrangement of the defined points on him characterizing dynamics of reduction of the face muscles which are responsible for expression of this or that emotion. The key output parameter is the vector of P, which reflects information on probability of compliance of a facial expression to a certain type of emotion from the set of the considered emotions of E, and represents such vector that for his elements the following equality is carried out:

$$\sum_{i=1}^{E} p_i = 1,$$

where p_i – is an element of a vector of P, representing probability that the analyzed image corresponds to type of emotion $E_i \in E$. Elements of a vector of P represent coordinates of the analyzed emotion in multidimensional space where the single basic vector corresponds to the separate marked-out emotion. The $E_{res} \in E$ parameter corresponds to emotion type which is appropriated to emotional coloring of a face after its analysis Value of output parameters T (Tone), S (sensibilization) and M (manifistation) are proceeding from results of classification of emotion and can be used for additional informational content. Functional dependence of $F_{cl} : X \to P$ carries out display of values of a vector of signs of a facial expressions to a vector of probabilities of P. The qualifier, which is based on the training data is used for such functional display.

As a result, the similar theoretical base allows implementing process of the analysis of an emotional condition of the human on his face in the form of the sequence of methods of processing and the analysis of the entrance image of a human face.

[1] Osgood C.E., Suci J.G. and Tannenbaum P.H. : The Measurement of Meaning, University of Illinois Press, (1957) 31-75
[2] Davitz, Joel R.: Auditory correlates of vocal expression of emotional feeling, In The communication of emotional meaning, ed, (1964) 101-112

MECHATRONIC DESIGN OF AN ELECTROMECHANICAL PITCHING SYSTEM FOR MORE REALISTIC LOAD SIMULATIONS OF WIND TURBINES BY MEANS OF THE BOND GRAPH METHODOLOGY

Zakaria Khaouch[1*], Mustapha Zekraoui[1], Nourreeddine Kouider[1], Mustapha Mabrouki[1]

[1]Laboratory of Industrial Engineering, Department of Physics, FST, University Sultan Moulay Slimane, Beni Mellal, Morocco
zakariakh89i@gmail.com

The pitch system is the most safety subsystem of the wind turbine, at the same time; the pitch system is critical for optimizing the power production and serves as the actuator in the rotor speed control loop and as an emergency brake under failure conditions. To better understand the dynamic behaviors and enhance numerical simulation efficiency of electromechanical pitching system (EPS) in a wind turbine generator system (WTGS), a detailed mechatronic model is presented. By introducing the basic principle of all parts of EPS includes the subsystem models of actuator and its control strategy, driver train and blade. By means of the bond graph approach (BGA). For large wind turbines, control algorithms to enhance maximum and quality power are developed using the pitch system as an actuator, but these control loops are often designed without taking the real behavior of the pitch system into account. With the new model presented her, the real behavior of the pitch system is takes into consideration, as a result the final load simulation is more realistic and offering benefits and reliable system performance. First, a detailed bond graph model of an EPS is developed considering its dynamic characteristics. Thereafter, the control law is derived by using the concept of bicausality of the bond graph, and compared with a conventional PID controller. Finally, the dynamic characteristics of an EPS using the proposed model are analyzed and verified based on 20-sim program.

[1] Fernando D. Bianchi, Hernn De Battista and Ricardo J. Mantz. Wind Turbine Control Systems: Principles, Modelling and Gain Scheduling Design. 2007.
[2] T. Burton, N. Jenkins, D. Sharpe, et al., Wind Energy Handbook, John Wiley and Sons, 2011.
[3] Peter C. Breedveld, Port-based modeling of mechatronic systems, 2004.
[4] Hui Li, Chao Yang, Yaogang Hu, Xinglin Liao, Zheng Zeng, Chen Zhea. An improved reduced-order model of an electric pitch drive system for wind turbine control system design and simulation. Renewable Energy 93 (2016) 188-200.
[5] S. Morinaga, Y. Izumi, A.M. Howlader, et al., Output power control of a PMSG based wind turbine in strong wind conditions, in: Proceedings of the 2013 IEEE International Symposium on Industrial Electronics (ISIE), Taipei, Taiwan, May 2013, pp. 28-31.

TRANSCRIPTOME ANALYSIS OF BORRELIA AFZELII-INFECTED TICK IXODES RICINUS

Sazzad Mahmood[1,2], Ondřej Hajdušek[2]

[1] Department of Molecular Biology and Genetics, University of South Bohemia, Czech Republic
[2] Institute of Parasitology, Biology Centre CAS, Czech Republic
mahmood@paru.cas.cz

Ixodes ricinus is the most abundant tick species in Europe [1]. It transmits several serious human and animal diseases including Lyme disease (*Borrelia burgdorferi* sensu lato) [2]. There is no preventive solution to get rid completely of this Lyme disease.

Recent years spirochete *Borrelia afzelii* transmission to *I. ricinus* has been established as model where pathogen acquisition from mouse and transmission to mouse are managed. Hence, any target gene can be analysed by RNA interference in this model platform to observe their roles in pathogen acquisition and transmission.

Here a database of upregulated tick nymph midgut genes in the presence of *Borrelia afzelii* has been obtained using the method MACE (Massive Analysis of cDNA Ends) at different feeding time points (Unfed, Fed for 24h and Fully Fed). These quantitative transcriptomics are being analysed in-silico. Selected several upregulated genes are verified with technical and biological repeats by qPCR.

These genes will be silenced by RNA interference. That experiment will reveal the silencing effects of selected genes on pathogen acquisition by tick and transmission to mouse by feeding.

[1] Lindgren, E., & Jaenson, T. G. T. (2006). Lyme borreliosis in Europe: influences of climate and climate change, epidemiology, ecology and adaptation measures. *World Health Organization*, 35.
[2] Lewis, L. A., Radulović, Ž. M., Kim, T. K., Porter, L. M., & Mulenga, A. (2015). Identification of 24h *Ixodes scapularis* immunogenic tick saliva proteins. *Ticks and Tick-Borne Diseases*, *6*(3), 424–434.

PHOTOSTABILITY OF CORE AND CORE/SHELL QUANTUM DOTS IN THE PRESENCE OF ALBUMIN AND IN MOUSE FIBROBLAST CELLS

Agnė Kalnaitytė[1], Saulius Bagdonas[1], Ričardas Rotomskis[1, 2]

[1] Quantum Electronics Department, Faculty of Physics, Vilnius University, Lithuania
[2] Laboratory of Biomedical Physics, National Cancer Institute, Lithuania
agne.kalnaityte@gmail.com

Quantum dots (QDs) - semiconductor particles of nanometre size - are widely used as photoluminescent agents in material science, biology and medicine. Enhanced photostability, size-dependent absorption and bright tuneable photoluminescence (PL) as well as wide possibilities for surface modification of QDs are among the key properties stimulating their applicability in biological environment [1]. However, the spectral properties of QDs are determined by many internal and external factors. The structure of QDs, the nature of stabilizing surface ligands [2], the surrounding environment and an irradiation can affect the stability of the PL of QDs.

In this work the spectroscopy and microscopy methods were used to estimate the light-induced changes in the PL properties of several types of QDs terminated with a carboxyl group (COOH). These core and core/shell QDs were studied in aqueous suspensions, in the presence of bovine serum albumin (BSA) and in NIH 3T3 mouse embryo fibroblast cells. The presence of BSA (Albumin, V fraction, M = 69000 g/mol, Carl Roth GmbH, Germany) molecules increased the stability and the PL quantum yield (QY) of core structured CdTe QDs and core-shell structured CdSe/ZnS QDs capped with thioglycolic (TGA) acid. However, the interaction between BSA and these core/shell QDs capped with mercaptopropionic acid (MPA) had the opposite effect. Thus, the type of terminal ligands had a strong influence on the capacity of the albumin to stabilize the PL of hydrophilic QDs through the modification of the coating layer.

The exposure to the green laser light (532 nm, 35 mW/cm^2) instantly increased the PL intensity and the QY of TGA-capped core-shell QDs (Fig. 1a) irrespective of the presence or absence of BSA in solutions, but did not change the PL of MPA-capped QDs significantly. However, an instant decrease of the PL intensity and the QY, which were detected after the exposure of core QDs, mimicked the time-related changes occurring in unexposed control samples. Thus, the presence of the shell and the stability of the coating both play a role in whether their mutual effect on the PL intensity and the QY of the illuminated QDs will be suppressive or enhancing with respect to untreated samples.

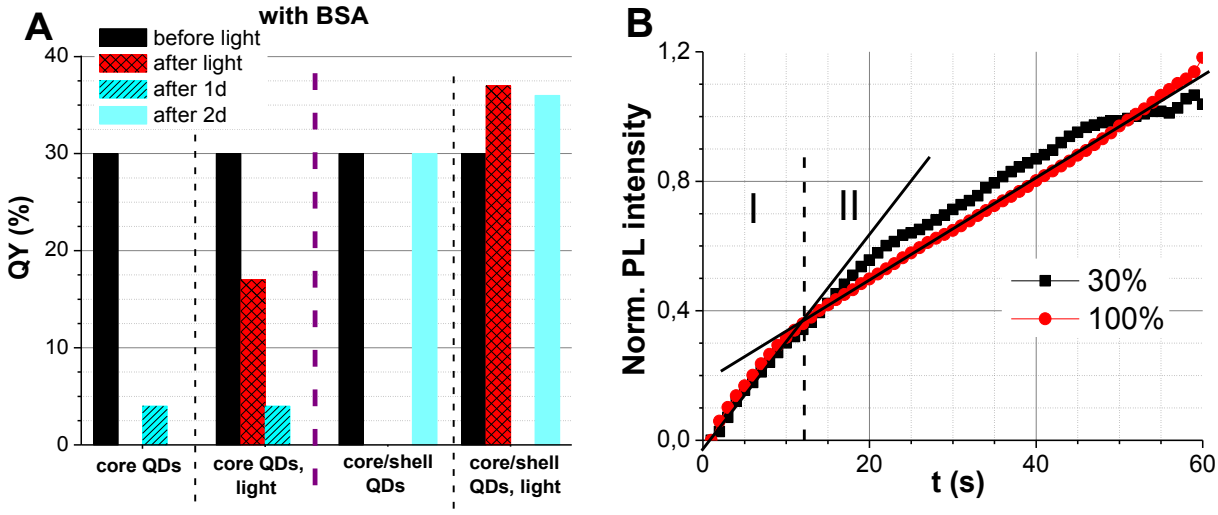

Fig. 1. (a) Time-related changes of the PL QY (λ_{exc} = 450 nm) for core CdTe-COOH QDs and core/shell CdSe/ZnS-TGA QDs in the presence of BSA and after exposure to the green laser radiation. (b) The dependence of normalized mean integral PL intensity of core/shell CdSe/ZnS-COOH QDs accumulated in NIH 3T3 cells on the exposure time; samples were exposed to the laser light (488 nm) with a relative intensity of 30% or 100%.

NIH 3T3 cells were incubated in a solution (c = 8 nmol/ml) with core/shell CdSe/ZnS-COOH quantum dots (Qdot 625 ITK carboxy, Invitrogen, USA) for 24 h. During subsequent exposure to the laser beam (488 nm) the PL intensity of QDs inside the cells was enhanced, and two stages were observed in the pattern of this enhancement (Fig. 1b). The increase was faster at the first stage, which lasted for initial 11-12 seconds of exposure; the increase at the second stage became slower. It has also been found that the mean PL intensity of core/shell QDs being accumulated in NIH 3T3 cells increased regardless of the excitation wavelength (488 nm or 405 nm), and during the second stage this increase of PL was directly proportional to the intensity of the excitation beam.

[1] T. Jamieson, R. Bakhshi, D. Petrova, R. Pocock, M. Imani, A. M. Seifalian, Biological applications of quantum dots, Biomaterials 28 (2007) 4717–4732.
[2] A. Kalnaitytė, S. Bagdonas, R. Rotomskis, Effect of light on stability of thiol-capped CdSe/ZnS quantum dots in the presence of albumin, Lithuanian Journal of Physics, Vol. 54, No. 4, pp. 256–265 (2014).

AMPLIFICATION OF HELA CELL PROLIFERATION BY PERIODIC PULSED ELECTRIC FIELD

Elizaveta Kavalenka, Tatiana Kochetkova, Yuliya Kunitskaya, Elena Golubeva, Pavel Bulai

Department of Biophysics, Belarusian State University
kovalenko.elizabeth@gmail.com

An important problem in cell technologies is to develop the methods of accumulation of cells with certain characteristics [1, 2]. The aim of this study was to choose the electrical stimulation modes which can provide a changing the cell proliferative activity. Epithelioid tumor cells of human cervix carcinoma (line HeLa) were used as object of the research. Cells were cultivated in DMEM 1152 supplemented with 25 mmol/L HEPES, 10% FBS at 37 ° C and 5% CO_2 content. Cell culture was stimulated by uniform periodic pulsed electric field using programmable electrical biological stimulator (BSU, Minsk, Belarus) with platinum electrodes. Electric stimulation modes differ in number of pulses in series (1, 3 or 5) and amplitude of the pulses (6.6 or 20 V/m). The frequency of pulse series was 10 Hz. The stimulation lasted for 12 h on the first or the second days after passaging.

It was revealed that in the absence of electric stimulation the cell doubling time of HeLa cells was 21-23 h. The stimulation of HeLa cells in the first culture growth day (from 8 to 20 h after passaging) led to significant amplification of cell proliferation at pulsed electric field intensity of 20 V/m (fig.1 A, modes 1 and 2). When the electric stimulation was carrying out on the second day of culturing (from 24 to 36 h after cell passaging) the proliferation enhancing effect was reduced (fig.1 B, modes 1 and 2). The changes in proliferative activity of HeLa cells were insignificant at lower electric pulse amplitude of 6.6 V/m under stimulation both the first and the second days (fig. 1 A and B, mode 3).

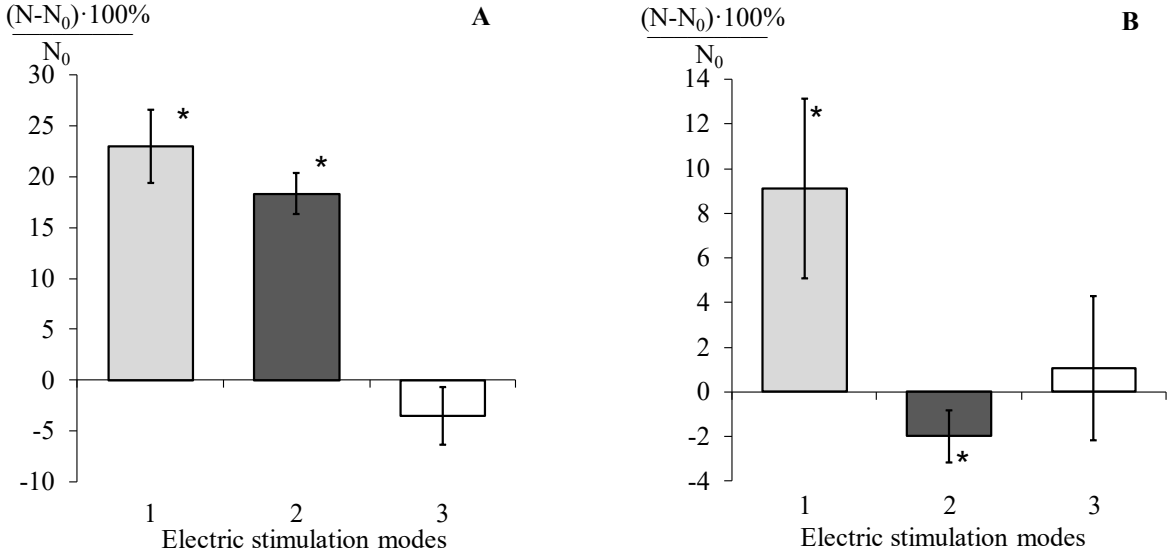

Fig. 1. The relative change in HeLa cell proliferative activity under stimulation the first (A) and the second (B) days by pulsed electric field. Electric stimulation modes: 1 – 20 V/m, 1 pulse; 2 – 20 V/m, 3 pulses, 3 – 6.6 V/m, 3 pulses. N – quantity of cells in the sample after electric stimulation, N_0 – quantity of cells in control. Values are shown as mean ± 95% confidence interval. *P<0.05 (compared to control).

The mechanism of electric field action on cells can include changes in ion channels activity, values of transmembrane electric potential, cell surface charge and as a consequence modulation of cell ability to adhesion and division [1-3]. The obtained data confirm the possibility of regulating cell proliferative activity by exposure to a periodic pulsed electric field. In particularly, HeLa cell proliferation is amplified under influence 20 V/m electric pulses with 10 Hz frequency during the first day of cultured growth.

[1] S. Koyama, Electrically modulated attachment and detachment of animal cells cultured on an optically transparent patterning electrode, Journal of Bioscience and Bioengineering – 2012. -V. 114. -I. 2. -P. 240-241

[2] M. Yamada et al., Electrical stimulation modulates fate determination of differentiating embryonic stem cells, J. Stem Cells – 2007. – V.25. – P.562–570

[3] DJ. Blackiston, KA. McLaughlin, M. Levin, Bioelectric controls of cell proliferation: ion channels, membrane voltage and the cell cycle, Cell Cycle. – 2009. – V.8, I.21.- P.3527-3536

MICROFABRICATED COLLAGENOUS HYDROGELS AS SCAFFOLDS FOR 3D CELL CULTURE

Airina Mazėtytė[1], Romual Eimont[2], Agnė Vailionytė[2], Gintarė Garbenčiūtė[2], Vytautas Cėpla[1], Rūta Aldonytė[2], Ramūnas Valiokas[1]

[1] Department of Nanoengineering, Center for Physical Sciences and Technology, Savanoriu ave 231, LT 02300 Vilnius, Lithuania
[2] UAB Ferentis, Savanoriu ave 235, LT 02300 Vilnius, Lithuania
airina.mazetyte@ftmc.lt

Grafting of artificial tissues and/or biomaterials into patients instead of transplantations from organ donors has become a vivid research field and a promising clinical strategy. Likewise the donated grafts, (bio)synthetic tissues can restore/replace the functions of lost organs, thus saving patients' lives or improving their quality of life. However, this strategy has been suffering from material-related issues such as toxicity, inflammations, rejection and other failures.

Artificial tissues that are nowadays produced in laboratories consist of cell networks that are grown within a 3D matrix. Biosynthetic collagen hydrogels [1] combined with micro/nanofabrication techniques create a new powerful platform for LEGO-like assembly of tissues and organs. Therefore, in the present work, we have explored fabrication of collagen-based, tissue microenvironments that enable proliferation and differentiation control and programing of different cell types. Namely, we have micromolded porcine collagen-based hydrogels to obtain groove/ridge textures, well, pyramid and other surface features, with a precision down to 50 nm. We have employed them as scaffolds that allowed us to control cell culture (e.g. human corneal epithelial cells, skin fibroblasts, skin epithelial cells, and mesenchymal stem cells) in 3D, as well as to combine different cell types. Our proof-of-principle study indicate that the developed toolbox is suitable for tissue-mimetic cell cultures, spatially defined co-cultures and as well as for artificial tissues in cell biology, high-throughput screening and regenerative medicine applications.

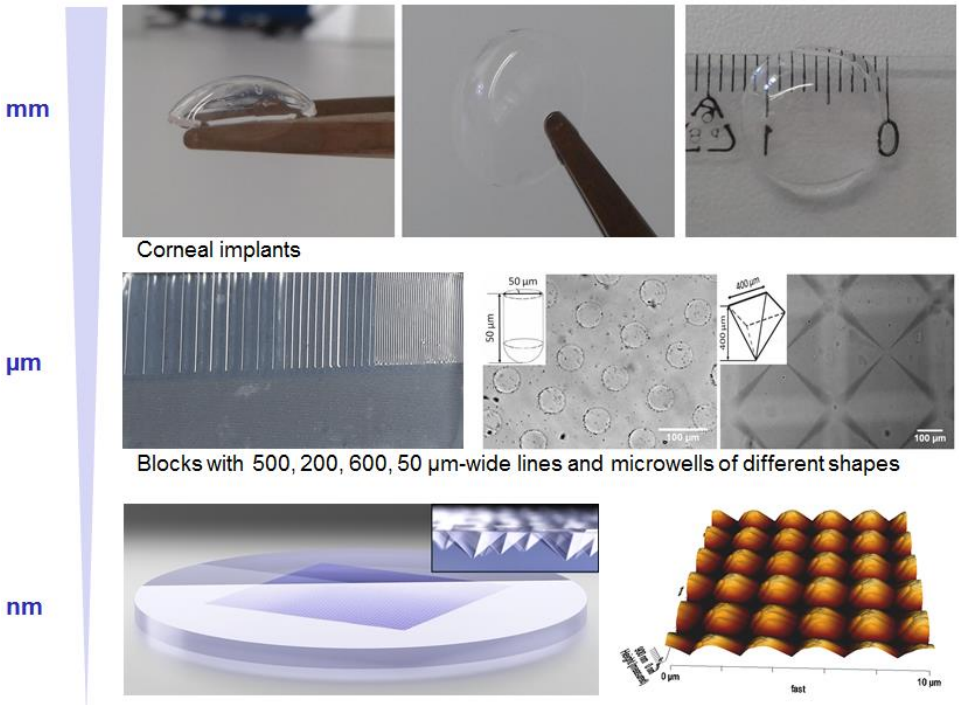

Fig. 1. Dimension range of various molded PC-MPC hydrogels.

[1] M. M. Islam, V. Cėpla, et al., Functional fabrication of recombinant human collagen-phosphorylcholine hydrogels for regenerative medicine applications, Acta Biomaterialia **12**, 70-80 (2015).

TRITIUM ACTIVITY DISTRIBUTION BY MONITORING DATA IN GROUNDWATER OF QUATERNARY AQUIFER SYSTEM, LITHUANIA

Vytautas Samalavičius, Robert Mokrik

Department of Hydrogeology and Engineering Geology, Vilnius University, Lithuania
vytautas.samalavicius@chgf.vu.lt

Tritium (3H or T) is a radioactive isotope of hydrogen with a nucleus containing two neutrons and one proton. Its concentration (or activity) in substance are expressed in tritium units (TU). The origin of 3H in environment could be natural or anthropogenic. Anthropogenic tritium occurredin the atmosphere during the detonation of thermonuclear bombs in 1954–1964 [2]. In the atmosphere, tritium reacts with oxygen forming tritium water (THO or 3HHO) [1]. As tritium becomes a part of water molecule, no chemical reactions can alter its amount and 3H could be used as a reliable traser. As anthropogenic tritium spreads globally, precipitation constantly recharges groundwater and 3H reach shallow freshwater aquifers. Due to processes in aquifers and nature of tritium itself – the amount and 3H activity constantly changes. Decrease of tritium activity through time depends on radioactive decay and water mixing in the aquifers.

This study includes one unconfined and five confined aquifers of active exchange zone in south-eastern Lithuania. These aquifers were formed during Quaternary period, between major glaciations: Waalian interglacial (Dzūkija–Dainava, *ag II dz-dn*), Holsteinian interglacial (Dainava–Žemaitija, *ag II dn-žm*), Drenthian-Warthian interglacial (Žemaitija–Medininkai,ag*II žm-md*), Eemian-Middle Weichselian interglacial/interstadial (Medininkai–Grūda,*ag II-III md-gr*), Upper Weichselian interstadial (Grūda–Baltija,*ag III gr-bl*). The number of aquifers were reduced to three because *ag III bl-gr* and *ag II dz-dn* are of limited occurrence and was combined with respectively, *ag II-III md-gr* and *ag II žm-dn* [4]. Using literature sources, previous research and databases, a graph of tritium activity change during the period 1980–2012 was made (Fig. 1). In addition to groundwater, 3H activity trends of precipitation in Ignalina (Lithuania),Vienna (Austria) and Ottawa (Canada) are included [2, 3, 5].

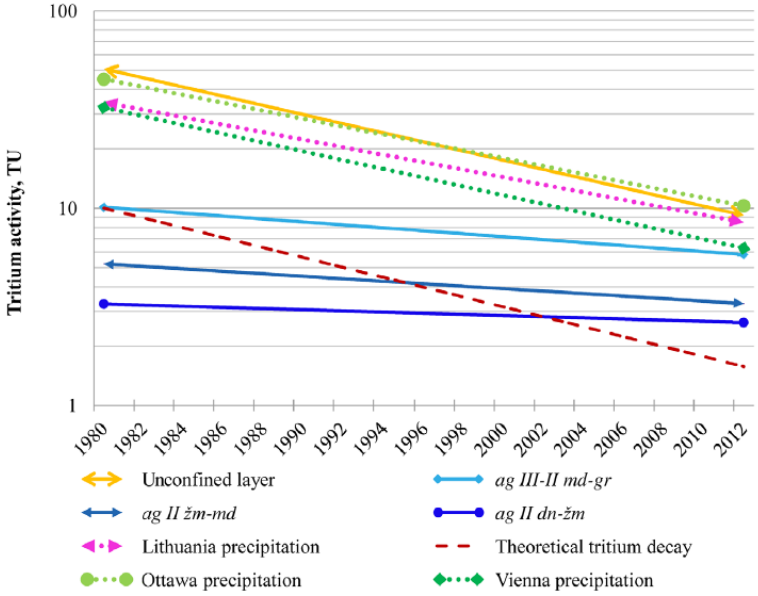

Fig. 1.Precipitation and groundwater 3H activity decrease in exponential trendlines (period of 1980–2012) [2, 3, 5]

In Figure 1an inclination of precipitation trends are similar comparing to the radioactive decay line.The 3H activity decrease rate is mainly determined by radioactive decay of tritium isotope. Absolute tritium values in Ottawa, Vienna and Lithuania precipitation vary, because of uneven 3H distribution in the atmosphere. It led to differences in precipitation water activity around the globe. Trend inclination in unconfined layer groundwater shows that decrease rate is determined by radioactive decay. Unconfined aquifer water absolute tritium values are greater than in precipitation recharging it. Accumulation of tritium in unconfined aquifer groundwater appeared because circulation rate in atmosphere is much rapid than in the aquifer. It means that equilibrium between unconfined layer groundwater and precipitation is reached. Confined aquifers 3H activity trend inclination is considerably smaller indicating that anthropogenic 3H reached the aquifers, but equilibrium with precipitation are not reached yet. The deeper aquifer is situated the smaller 3H values are observed.

[1]*Investigation of the Environmental Fate of Tritium in the Atmosphere*(Canadian Nuclear Safety Commission. Ottawa, Canada,2009).
[2]Clark I., Fritz P.,*Environmental Isotopes in Hydrogeology* (New York: Lewis Publishers, 1997).
[3]Juodkazis V., Mažeika J., Petrošius R., Radioisotopical methods in ecological hydrogeology. Geologija **18**, 1-132(1995). [In Lithuanian]
[4]Mokrik R., Mažeika J., Juodkazis V., Štuopis A., The Quaternary deposits cross-section study by groundwater flow modeling and chemistry-isotope data, eastern part of Lithuania,Hydrogeology Journal. **22**, 925-941(2014).
[5]Raidla V., Kern Z., Babre A., Erg K.., Ivask J., Kohan., Martma T., Mokrik R., Parn J., Vaikmae R. A δ18O isoscape for the shallow groundwater in the Baltic Artesian Basin .Journal of Hydrology.Vol. 542, 2016, p. 254-267 (2016).

TEMPERATURE DEPENDENT SPECTRAL CHANGES OF PROTEIN STABILIZED GOLD NANOCLUSTERS DISPERSED IN PHOTORESIST SOLUTION

Lukas Plastinkin[1], Marija Matulionytė[1], Vilius Poderys[1], Ričardas Rotomskis[1, 2]

[1]Biomedical Physics Laboratory of National Cancer Institute, Vilnius, Lithuania
[2]Biophotonics group of Laser Research Centre, Vilnius University, Vilnius, Lithuania
lukas.plastinkin@ff.stud.vu.lt

Three-dimensional (3D) laser micro/nano-structuring (LMNS) of polymers has improved dramatically in recent years. However, there is still very little concrete information in regards to the underlying processes. The two most plausible mechanisms for LMNS are as follows: purely chemical reactions based on two-photon absorption (2PA) where photoinitiator molecules are excited via 2PA and subsequently form radicals that initiate a polymerization reaction. This leads to the solidification of the photoresist [1]. The other plausible mechanism is a photo-thermal one where the rapid localized temperature changes initiate the polymerization reaction caused by laser irradiation.

For better understanding of the occurring processes one needs to be able to measure the local temperature changes in the photoresist during LMNS. In order to do that a suitable method must be applied. This work is dedicated to studying the suitability of bovine serum albumin stabilized gold nanoclusters (BSA-Au NCs) as photoluminescent temperature detectors dispersed in the photoresist solution. The photoresist we have chosen in this case was polyethylene glycol diacrylate (PEG-DA).

BSA-Au NCs were synthesized according to the modified Xie protocol [2]. The photoluminescence spectrum of BSA-Au NCs in aqueous solutions is dependent on temperature. By using spectroscopic methods we studied whether BSA-Au NCs retain these properties when dispersed in PEG-DA solution. The following results were obtained: the increase of the solution temperature caused the decrease of BSA-Au NC photoluminescence intensity and a bathochromic shift of the photoluminescence band (Fig. 1). The spectral changes in the PEG-DA solution are analogous to those in aqueous solutions. Therefore, BSA-Au NCs should be suitable for local temperature change monitoring in PEG-DA solutions during LMNS if no additional processes occur that cause the degradation of BSA-Au NCs.

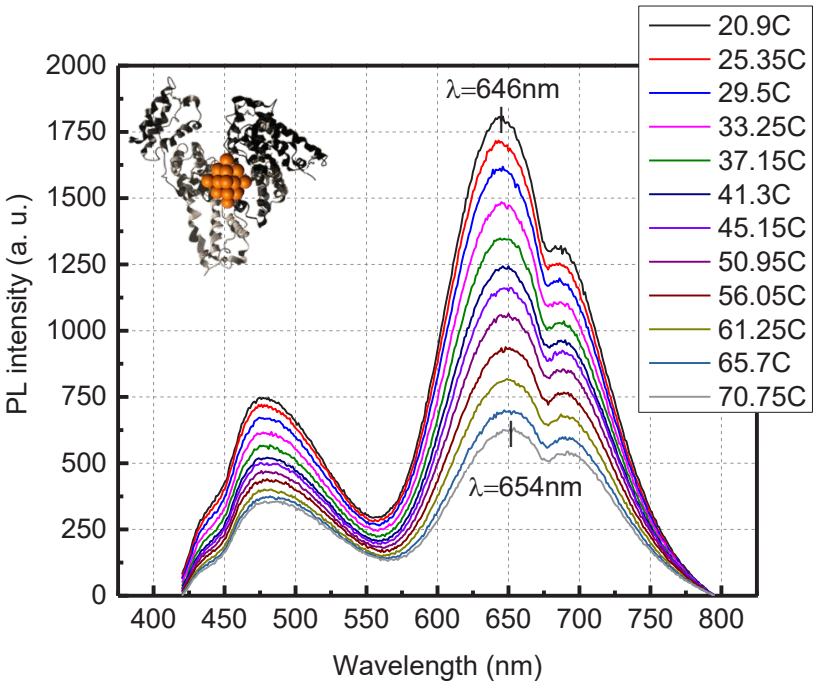

Fig. 1. Temperature dependent PL spectra changes of BSA-Au NCs dispersed in PEG-DA solution

[1] Mueller, J. B., Fischer, J., Mange, Y. J., Nann, T., & Wegener, M. (2013). In-situ local temperature measurement during three-dimensional direct laser writing. *Applied Physics Letters*, *103*(12). http://doi.org/10.1063/1.4821556
[2] Poderys, V., Matulionytė-safinė, M., Rupšys, D., & Rotomskis, R. (2016). Protein stabilized Au nanoclusters: spectral properties and photostability, 56(1), 55–65.

UPCONVERTING NANOPARTICLES OPTICAL PROPERTIES AND STABILITY DEPENDANCE ON PROTEIN COATING

Morta Marcinkutė[1], Vilius Poderys[1], Isabel Gessner[2], Sanjay Mathur[2], Eva Hemmer[3], Fiorenzo Vetrone[3], Ričardas Rotomskis[1, 4]

[1] Biomedical Physics Laboratory of National Cancer Institute, Vilnius, Lithuania
[2] Institute of Inorganic Chemistry, University of Cologne, Cologne, Germany
[3] Institut National de la Recherche Scientifique, Montreal, Canada
[4] Biophotonics group of Laser Research Centre, Vilnius University, Vilnius, Lithuania
morta.marcinkute@ff.stud.vu.lt

Lanthanide-doped upconverting nanoparticles exhibit unique luminescent properties based on an upconversion process. Because of this process, upconverting nanoparticles have an ability to push infrared long-wavelength radiation into shorter visible wavelengths [1]. This anti-Stoke shift property is extremely useful in research of various biological tissues, because the majority of biological tissues exhibit absorption peaks in the ultraviolet region while the excitation radiation of lanthanide-doped upconverting nanoparticles is in the near infrared range[2]. This allows reducing the autofluorescence background and reaching more efficient penetration into biological tissue.

The aim of this research was to investigate the optical properties of $NaGdF_4$: Er^{3+}, Yb^{3+} upconverting nanoparticles and discuss how protein coatings could affect luminescence intensity in different media.

All of the measurements were performed with *Edinburgh Instruments FL 920* spectrometer (*Edinburgh Ins.*, UK) and for $NaGdF_4$: Er^{3+}, Yb^{3+} upconverting nanoparticles excitation, a *MDL–III–980–2W* laser (*Changchun New Industries Optoelectronics Technology Co.*, China) with the wavelength of 980 nm and the excitation power of 1250 mW was used.

Investigation was executed in several stages. At first, five categories of $NaGdF_4$: Er^{3+}, Yb^{3+} upconverting nanoparticles with different surface coating were investigated to determine if human serum albumin (HSA) or polyallylamine hydrochloride (PAH) could have any effect on the luminescence intensity and stability of nanoparticles (Fig. 1). The reason why HSA was chosen is that in human blood nanoparticle is coated with naturally existing proteins forming a corona. This phenomenon usually leads to reduced stability of nanoparticle and artificial HSA coating could help to prevent this. The results of research showed that $NaGdF_4$: Er^{3+}, Yb^{3+} upconverting nanoparticles coated with one layer of HSA have the biggest luminescence intensity. This could be explained by the general increase of the nanoparticle's size. Finally, measurements with two different media – deionized water and Dulbecco's Modified Eagle's Medium (DMEM) – were made to reveal the change of $NaGdF_4$: Er^{3+}, Yb^{3+} upconverting nanoparticles stability depending on surrounding components. The results showed that $NaGdF_4$: Er^{3+}, Yb^{3+} upconverting nanoparticles in DMEM aggregated and lost the original optical properties while in deionized water stayed stable after more than 72 hours.

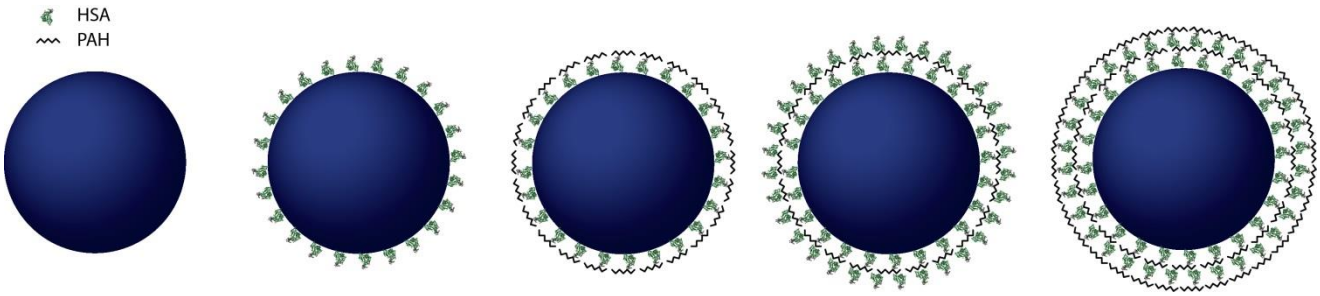

Fig. 1. Scheme of $NaGdF_4$: Er^{3+}, Yb^{3+} upconverting nanoparticles with different surface coatings, using human serum albumin (HSA) and polyallylamine hydrochloride (PAH).

[1] F. Wang and X. Liu, Recent advances in the chemistry of lanthanide-doped upconversion nanocrystals, Chemical Society Reviews, 8(4), p. 976, (2009).
[2] A. M. Smith, M. C. Mancini, and S. Nie, Bioimaging: Second window for in vivo imaging, Nature Nanotechnology, 4(11), pp. 710 – 711, (2009).

NANOSIZED INCLUSION COMPLEXES BETWEEN CYCLODEXTRINS AND PORPHYRINS

Yakavets Ilya[1,2,3*], Yankovsky Igor[1,2,3], Barysau Kiryl[1], Vorobyeu Maksim[1], Jukov Konstantin[1], Bezdetnaya Lina[2,3], Zorin Vladimir[1,4]

[1] Department of Biophysics, Belarussian State University, Minsk, Belarus
[2] Centre de Recherche en Automatique de Nancy, CNRS, Université de Lorraine, Nancy, France
[3] Institut de Cancérologie de Lorraine, Vandoeuvre-lès-Nancy, France
[4] International Sakharov Environmental Institute, 220070 Minsk, Belarus.
**viprorok@gmail.com*

Cyclodextrins (CDs) are macrocyclic oligosaccharides that combine a hydrophobic nanosized cavity with a hydrophilic surface [1]. The cavity enables the partial or total incorporation of lipophilic molecules by host-guest inclusion mechanism and formation and supramolecular water-soluble structures. Such structures may be used in various areas: pharmacology, molecular electronics, production of sensors, nanoscale chips, etc. Porphyrin–cyclodextrin complexes are supposed to be used for the purposes of photodynamic therapy. Generally, the formation of inclusion complexes enhance the solubility of the photosensitizer (PS) molecules and protect PS from aggregation.

The porphyrin used in the study is 5,10,15,20-tetra(*m*-hydroxyphenyl)chlorin (mTHPC). It is one of the most potent second-generation clinically approved photosensitizer [2]. The main limitation of its application in PDT is a low water-solubility. To prevent mTHPC aggregation several special formulations, such as liposomes, polymer solutions and bioconjugates were designed. An application of specialized pharmacological formulations supposes a development of new experimental techniques to control photosensitizer distribution in biological media. Cyclic oligosaccharides, cyclodextrins, are also considered as perspective formulation for tetrapyrrolic photosensitizers [3]. This study is aimed on the investigation of complexation mechanisms between mTHPC and β-CD derivatives: methyl-β-cyclodextrin (Me-β-CD) and trimethyl-β-cyclodextrin (TM-β-CD).

It has been shown, that the addition of β-CDs in aqueous solution of mTHPC results in the formation of stable inclusion complexes (Fig. 1) and monomerization of mTHPC. It results to the restoration spectral-fluorescence properties of mTHPC, including increase of fluorescence quantum yield compared to ethanolic solution.

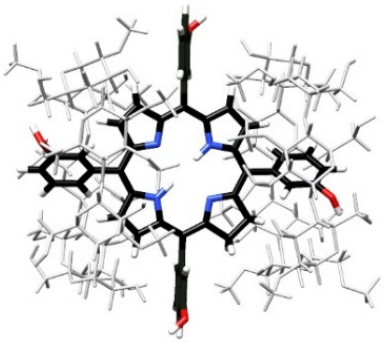

Fig. 1. The structure of mTHPC/β-CDs complex [4].

The kinetic and equilibrium processes of complexation between mTHPC and β-CDs were studied. It was demonstrated, that TM-β-CD possessed higher affinity to mTHPC as compared to Me-β-CD. The numerical values of mTHPC/m-β-CD association constants were determined from titration curves of mTHPC by β-CDs obtained by means of spectrofluorimetry and circular dichroism techniques. The estimation of association constants was performed by mathematical modeling with different complexation models. It was found, that value of apparent association constant is depends on concentration of mTHPC owing to PS aggregation. Moreover, the inclusion complexes may be realized with the both mTHPC: β-CD stoichiometry 1:2 and 1:1.

Acknowledgements. This study was supported by Belarussian Republican Foundation for Fundamental Research, the Ministry of Education of the Republic of Belarus. We thank Biolitec (Jena, Germany) for providing us with mTHPC.

[1] D. Duchêne Cyclodextrins and Their Inclusion Complexes. In Cyclodextrins in Pharmaceutics, Cosmetics, and Biomedicine, E. Bilensoy, ed. (Hoboken, NJ, USA: John Wiley & Sons, Inc.) 1–18 (2011).
[2] M. Senge mTHPC – A drug on its way from second to third generation photosensitizer? Photodiagnosis and Photodynamic Therapy **9**, 170-179 (2012).
[3] J. Mosinger, V. Kliment, J. Sejbal, P. Kubát and K. Lang Host-guest complexes of anionic porphyrin sensitizers with cyclodextrins. J. Porphyrins Phthalocyanines **6**, 514–526 (2002).
[4] I. Yakavets, I. Yankovsky, L. Bezdetnaya, and V. Zorin Soret band shape indicates mTHPC distribution between β-cyclodextrins and serum proteins. Dyes and Pigments **137**, 299–306 (2017).

3D PRINTING IMAGING PHANTOMS FOR GAMMA SCINTIGRAPHY

Jan Babiuch-Hall[1,2], Dr inż. Krzysztof Kacperski[3], Maciej Ustynowicz[4], Mgr Wojciech Adamczyk[1,2], Alexander Korneluk[1,2], Natalia Kuk[1,2], Kacper Ornat[1,2], Paweł Szczypkowski[1,2], Weronika Zdziarska[1,2], Dr hab. Jacek Szczytko[1]

[1] Faculty of Physics, University of Warsaw, Poland
[2] Faculty of Chemistry, University of Warsaw, Poland
[3] Department of Medical Physics, Maria Skłodowska-Curie Institute of Oncology, Poland
[4] Polish-Japanese Academy of Information Technology, Poland
j.babiuch-hall@student.uw.edu.pl

Positron Emission Tomography (PET) and Single-Photon Emission Computed Tomography (SPECT) are 3D nuclear medical imaging techniques which use radiopharmaceuticals administered to the patient and a gamma scintillation camera to produce functional images of metabolic activity in the patient's body. The radiopharmaceuticals emit gamma photons through radioactive decay (either directly in SPECT [1] or through positron-electron annihilation in PET [2]) and the signal is registered by a gamma scintillation camera, which is rotated around the patient's body to provide a set of projections, which in turn are processed using tomographic algorithms to create a 3D model of the distribution of the radiopharmaceutical in the patient's body. As the radiopharmaceutical is selected to accumulate in areas exhibiting metabolic activity of diagnostic interest, these techniques permit for noninvasive mapping of these types of metabolic activity.

Of particular interest for this research is the application of SPECT for imaging the heart. However, both PET and SPECT are prone to a few types of interference. Despite being selective, the radiopharmaceuticals used in these techniques accumulate in other organs in addition to the heart (particularly in the liver). In certain projections, the signal from those organs is difficult to distinguish from the signal from the heart. Moreover, due to their anatomy, the lungs have a non-uniform coefficient of attenuation of the gamma signal [3]. For these reasons, even the most advanced computationally-intensive iterative reconstruction algorithms used to stitch the individual projections into a 3D model have trouble providing precise images.

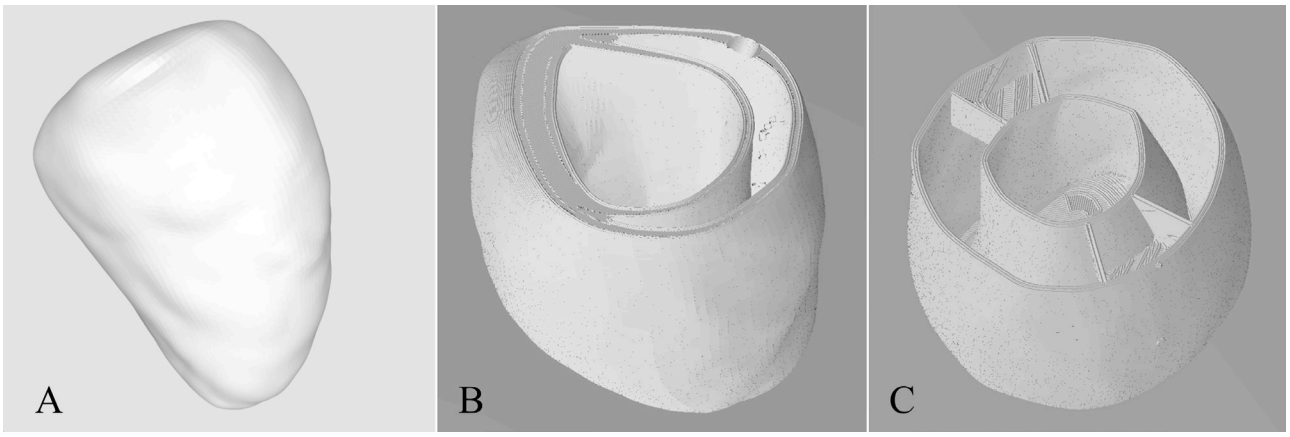

Fig. 1. 3D renderings of left atrium and left ventricle.
Inset A: normal heart, model; Inset B: normal heart, section; Inset C: heart with several defects, section

In order to improve PET and SPECT imaging technology, an accurate anthropomorphic phantom of the human chest is necessary so that modifications to the equipment and the processing algorithms can be tested in controlled settings. Commercially available phantoms suffer from several limitations, the most important ones being low detail, cost, and usability. We set out to create a highly accurate set of phantoms of the heart, representing both a healthy heart and hearts with various defects. Due to the internal complexity of the model, 3D printing was the obvious choice for the manufacturing technique. One of the challenges in 3D printing such a phantom is the fact that it must be watertight and reusable so that it may be repeatedly filled with solutions of the radiopharmaceuticals used in PET and SPECT. Working with a team of 3D design and 3D printing experts, we explored various materials, printing techniques, and processing techniques to produce these phantoms.

[1] Kuhler J. Single photon emission computed tomography (SPECT). *Magill's Medical Guide (Online Edition)* [serial online]. January 2016; Available from: Research Starters, Ipswich, MA. Accessed February 2, 2017.
[2] Rao D. Positron emission tomography (PET) scanning. *Magill's Medical Guide (Online Edition)* [serial online]. January 2016; Available from: Research Starters, Ipswich, MA. Accessed February 2, 2017.
[3] Kacperski K. Nuclear Medicine Imaging: Basic Technology, Recent Developments and Future Outlook. January 2017.

FROM STARDUST TO BLOOD STALLS: HOW INTERDISCIPLINARY CITIZEN SCIENCE IS CHANGING THE WAY WE DO RESEARCH

Eglė Marija Ramanauskaitė

Human Computation Institute
emramanauskaite@gmail.com

At the beginning of 2016 we started a project to breath new life into Alzheimer's research being done at Cornell University (US) – in an unconventional, but game changing way. One year later, we have an online game and more than 3000 volunteers catching blood stalls for science – that is logging week's worth of lab annotation in a day.

The first ever citizen science project to support Alzheimer's research – EyesOnALZ, was created at the Human Computation Institute, in collaboration with a network of researchers from the fields of physics, neuroscience, computer science and molecular biology [1]. Most importantly, we have built our first game – Stall Catchers, directly on another citizen science platform, Stardust@home. This project – one of the first "volunteer thinking" projects – was established in 2006 to solve the close-to impossible task to analyze almost a million stacks of aerogel images in search of just a few interstellar dust particles, brought back by the Stardust spacecraft [2]. Almost by accident, Stardust@home became inspiration for a seemingly entirely different kind of problem – the link between reduced blood flow in the brain and Alzheimer's disease.

EyesOnALZ now unites researchers from the Human Computation Institute, Schaffer-Nishimura Lab at Cornell University, where the ground-breaking data from live mouse brains that may help discover an Alzheimer's treatment is being generated, researchers behind Stardust@home from UC Berkley, neuroscience and machine learning experts from Princeton University, and crowdsourcing experts from the Human Computation Institute. In a trans-disciplinary effort, we adapted the same platform for an entirely different purpose, but a similar task. The virtual microscope first created to look through layers of aerogel, is now used to look through layers of a live mouse brain, to establish links between reduced blood flow in the brain and Alzheimer's disease.

Stall Catchers, an online citizen science game, is one of the many crowdsourcing efforts that are changing the way we do research completely [3,4]. Tasks that might be a challenge in the lab due to time or space constrains are now being crowdsourced to the public improving the speed – and sometimes quality – of that research by orders of magnitude.

---

[1] Schaffer, C. B. Funded R01 proposal to NIH provided to Guy Eakin (2015).
[2] Westphal, A. J. et al. Evidence for interstellar origin of seven dust particles collected by the Stardust spacecraft. *Science* **345**, 786–791 (2014).
[3] Khatib, F. et al. Crystal structure of a monomeric retroviral protease solved by protein folding game players. *Nat. Struct. Mol. Biol.* **18**, 1175–1177 (2011).http://stardustathome.ssl.berkeley.edu/about/stardusthome/
[4] Candido dos Reis, F. J. et al. Crowdsourcing the General Public for Large Scale Molecular Pathology Studies in Cancer. *EBioMedicine* **2**, 681–689 (2015).

Author index

A

Abate, Antonio....235
Abdulajev, Vladimir....223
Abe, Jiro....47
Abramavičius, Darius....125
Abrashitova, Ksenia....60
Abromavicius, Giedrius....210
Adachi, Chihaya....79
Adamczyk, Mgr Wojciech....398
Adomaitytė, K.....333
Adomaviciute, Sonata....349
Adomavičius, Karolis....63
Adomavičius, Ramūnas....84
Adomėnas, Povilas....79, 259, 306
Adomėnienė, Ona....79, 306
Aglinskaitė, Justina....325
Aidas, Kęstutis....126, 132, 134
Aldonytė, Rūta....393
Aleksa, Valdemaras....147
Aleksandra, Yurkova....242
Aleksandra, Kravchenko....242
Aleksiejūnas, Ramūnas....305, 318
Alkauskas, Audrius....122
Alnis, Janis....212
Ambroziak, Robert....141
Ambrulevičius, Filipas....162
Amirkhanov, Vladimir M.....272
Anbinderis, Maksimas....304
Anderson, Dovilė....158
Andzane, Jana....91
Andziukevičiūtė-Jankūnienė, Akvilė....243
Anilionytė, Danielė....256
Anisimovas, Egidijus....118
Antanovich, Artsiom....281, 298
Apetrei, Roxana-Mihaela...151, 361
Aplesnin, Sergey....324
Arlauskienė, Audronė....98
Armouzi, Naoual Al....280
Artemyev, Mikhail....281, 298
Arzamastseva, Tetiana O.....155
Asadauskas, Svajus....160
Asimov, Mustafo....205
Astashinski, Valentin....244
Astromskas, Gvidas....290
Ašmenaitė, Greta....335
Auffray, Etiennette....69
Auzinsh, Marcis....43
Avlasevich, Yuri....108

B

Babichev, Leonid....181
Babiuch-Hall, Jan....398
Badariene, Jolita....376
Badge, Robin Lovell....29
Badokas, Kazimieras....82, 327
Bagdonas, Saulius....373, 391
Balachninaitė, Ona....213
Balčiūnas, Evaldas....206
Balčiūnas, Sergejus....257
Balevicius, Vitas....130, 133, 170
Balevičius, Vytautas....159
Baltriukienė, Daiva....206
Baluschev, Stanislav....108
Banys, Jūras....257
Baranauskienė, D.....333
Baranowski, Piotr....258
Barauskas, Justas....109
Barcia, Monica Fernandez....239
Bardule, Arta....354
Barysau, Kiryl....397
Baronaitė, Sandra....98
Baronas, Paulius . 79, 149, 260, 306, 326
Baronas, Romas....180
Baršienė, Janina....336
Bartkiewicz, Anna....112
Bartmanski, Marcin....282
Bartnik, Ewa....337
Bartulevičius, Tadas... 188, 193, 194
Bastikar, Virupaksha A.....374
Bašinskaitė, Eglė....46
Baškevičius, Aurimas....213
Baumer, Vyacheslav N.....153
Baziulyte-Paulaviciene, Dovile..283, 372
Beleckaitė, Ieva....84
Bellucci, Stefano....92
Bereznev, Sergei....241
Bernotiene, Eiva....352
Berzins, Andris....43
Berzins, Jonas....204
Bessonov, Vladimir....60
Bezdetnaya, Lina....106, 397
Bhatt, Vishwa....70, 234
Bychanok, Dzmitry....92
Byčenkienė, Steigvilė....378
Bieliauskas, Aurimas....326
Bikulčienė, Inga....353
Bilich, Igor....308
Bilotas, Evaldas....231
Bironaite, Daiva....352
Bistarelli, Silvia....92
Bizdena, Erika....266
Bogomol, Gleb....124
Bokshits, Y.....311
Bomba, Jaroslaw....200
Borek, Karolina....42
Borisevich, Andrei....312
Borodavchenko, Olga....323
Borovkov, Victor....140
Brastovickytė-Stankevič, Janina.375
Braukyla, Titas....269
Brazevic, Sabina....47
Braziulis, Gediminas....175
Brice, Inga....212
Brycki, Bogumił....137
Brusatin, Giovanna....251
Bubilaitis, Vytautas....125
Bubnienė, Urtė....55
Bucevičius, Jonas....149
Bucevičius, Tadas....149
Buchkov, K.....314
Buciunas, Tadas....260
Bučinskas, Laurynas....222
Bučytė, Greta....259
Budreckaitė, Milda....305
Budriūnas, Miglius....233
Budriūnas, Rimantas....184
Bukauskytė, Austėja....142
Bukelskienė, Virginija....206
Bukowska, Jolanta....54
Bulai, Pavel....99, 379, 392
Burdzinski, Gotard....47
Burokiene, Daiva....348
Burokienė, Neringa....105
Busa, Lauma....354
Busaite, Laima....43
Butkus, Laurynas....222
Butkus, Paulius....355
Butkus, Simas....213
Butkutė, Renata....83, 300
Butrimavičienė, Laura....335, 336

C

Carac, Geta....361
Cedillo, Andrés....132
Celeda, Małgorzata....139
Cėpla, Vytautas....393
Ceponis, Tomas....220
Cepukoit, Dovile....348
Cepulis, Tadas....143
Cesiulis, Henrikas152, 172, 236, 248
Chaleckaja, Ana....356
Chareev, Dmitriy....308
Chauhan, Mihirsinh....70, 234, 277
Cherenda, Nikolai....244
Chernyavsky, Vadim....302
Cibulskaitė, Živilė....368
Cicenas, Saulius....350
Claeyssens, Frederik....30
Claramunt, Adrián Vicent....173
Clausen, Sven....334
Coccia, Eugenio....26
Correa-Baena, Juan-Pablo....235
Cukras, Janusz....54
Cvijetic, Ilija....126

Č

Čechavičius, Bronislovas....83
Čeponis, Tomas....316
Čerkasovas, Vladislavas....79, 306
Čikotienė, Inga....148, 169, 171
Čiplys, Ignas....357
Čižas, Vladislovas....232

D

Dabkeviciene, Daiva....350
Dagys, Marius....330
Dalgediene, Indre....100
Dapkus, Henrikas....72
Dargis, Rytis....327
Daskeviciene, Maryte...48, 235, 269
Daugnoraitė, Elena....226
Daukantiene, Virginija....245
Demchenko, Lesya....261, 278
Demidenko, Olga....324
Denkovskij, Jaroslav....352
Deuar, Piotr....42
Deveikis, Laimonas....220
Diana, Reznikova....332
Dina, Farrakhova....358
Dmitriy, Guschik....242
Dmukauskas, Mantas....82
Dobrovolskas, Darius....82, 309
Doliński, Jędrzej....262
Domanski, Konrad....235
Dormenev, Valera....249
Dosenovicova, Denisa....241
Drabavičius, Gediminas....338

Drazdys, Ramutis 210
Drunga, Tomas.....240
Druteikienė, Rūta.....222
Dubietis, Audrius.....186
Dūdėnas, Vytautas.....115
Dwivedi, U. K.....234

E

Eckardt, André 118
Edlund, Petra 46
Eimont, Romual 393
Elbaum, Danek.....95
Elek, Gábor Zoltán.....140
Ellis, John 22
Elvassore, Nicola 251
Eroma, Anna 292
Erts, Donats.....91
Ežerinskis, Žilvinas.....222

F

Fedyanin, Andrey.....60
Fedosyuk, Aleksandra 298
Fedotov, Alexander.....86, 307
Fedotov, Alexandr K.....61
Fedotov, Alexandr S.....61
Ferber, Ruvin 43
Feringa, Ben.....23
Foltyn, Marek.....282
Fornell, Jordina 248
Frąckiewicz, Justyna.....263
Frankinas, Saulius 193
Fronc, Krzysztof.....95

G

Gabralevičius, Povilas 334
Gahbauer, Florian 43
Gaydamak, Tatyana 308
Gaidamavičienė, Giedrė.....144, 175
Gaiduk, Peter 312
Gajauskaite, Ada 198
Gajdosik, Thomas.....115, 116
Gallego, Daniel.....57
Gandzyuk, Sergii 302
Gao, Peng.....76
Gaponenko, Sergey.....90
Garankin, Jevgenij.....223
Garbaras, Andrius 222, 223
Garbaras1, Andrius 223
Garbarczyk, Jerzy 258, 263, 279
Garbarczyk, Jerzy E. 77
Garbarczyk, Jerzy Edward .262, 264, 276
Garbenčiūtė, Gintarė 393
Gardias, Anita 95
Garejev, Nail 186
Garliauskas, Mantas.....227
Garmiene, Genovefa.....350
Gartman, Alexandra.....94
Gasiūnas, Giedrius 338
Gaubas, Eugenijus.....220, 316
Gavutis, Martynas.....295
Gawali, Sandeep 57
Gebert, Annett.....239
Gėgžna, Vilmantas 357
Genevicius, Kristijonas 76
Germanas, Darius 117
Gessner, Isabel.....396
Getauti, Vytautas .48, 235, 269, 326
Getautis, Vytautas 48, 269, 326
Ghoghoberidze, Vitali 178
Giomo, Monica.....251
Girskis, Justas 190
Gładysz, Piotr.....121
Glemžaitė, Monika 98
Globa, Pavel.....236
Gnilitskyi, Iaroslav.....61
Gołębiewska, Agata.....264
Golubeva, Elena..... 99, 379, 392
Goodfellow, Marc.....104
Gorbatsievich, Alexander 33
Gorbyk, Petro 286
Gorokhov, Gleb 92
Gotovski, Pavel 199
Grabusovas, Arturas 203
Grabusovas, Artūras 225
Graetzel, Michael 235
Gratia, Paul..... 48, 235
Grätzel, Michael 27
Grazulevicius, Juozas Vidas260, 267, 270
Gražulevičius, Juozas V. 256, 265, 274, 367
Gražulevičius, Juozas Vidas.....275
Gražulis, Saulius..... 51, 136
Greiciūnaitė, Janina 336
Grempka, Arkadiusz 284
Gribovskii, Gleb 73
Grigalevičiūtė, Giedrė.....206
Grigaravicius, Klaidas.....179
Grigelionis, Ignas 68
Grigoryev, Sergey 191
Grigorjevaitė, Julija.....78
Grinevičiūtė, Lina.....208
Griniene, Roma.....352
Grinys, Tomas..... 82, 240, 327
Griškevičius, Laimonas.....173
Grubisic, Sonja.....126
Gruodis, Alytis 142, 367
Gruzauskaite, Justina.....359
Grzaczkowska, Paulina.....95
Grzelak, Paulina.....145
Grzeszczyk, Magdalena.....287
Gudeika, Dalius. 143, 146, 157, 256, 274, 367
Gudelis, Arūnas 223
Gudeliūnaitė, Eglė 173
Gudiukaite, Renata.....369
Gudleviciene, Zivile.....350
Gulbinas, Vidmantas.....238
Gulkin, Dmitrii 60
Gupta, Pramodkumar P 374
Gustavsson, Emil 46
Guziewicz, Elzbieta 317

H

Habra, Naida El.....251
Hagfeldt, Anders.....235
Hajdusek, Ondrej.....390
Halas, Naomi 28
Hamedi, Hamid Reza 176
Hamera-Fałdyga, Róża.....139
Heintzmann, Rainer.....62
Hemmer, Eva.....396
Hendrixson, Vaiva.....353
Herring, Daniel.....104
Hysa, Azem.....35
Hoffmann, Volker 239, 248
Hozyanin, Olga.....360
Humennik, Uladzislau.....307

Y

Yadav, Alok Anand..... 213
Yadav, Pankaj 234
Yakavets, Ilya..... 106, 397
Yankovsky, Igor 106, 397
Yanushkevich, Kazimir..... 324
Yauhen, Tratsiak..... 166

I

Ignatjev, Ilja..... 168
Ilya, Yakavets..... 358
Imbrasas, Paulius..... 265
Ishchenko, Olena..... 268

Y

Yurkova, Alexandra 302

I

Ivanets, Andrei 50
Ivaniuk, Khrystyna 270
Ivanov, Maksim 257
Ivanova, Yuliya 154

J

Jagminas, Arūnas..... 293, 299
Jakštas, Vytautas 68, 229
Janarauskas, Algimantas 151
Jankauskaitė, Elona 337
Jankauskaitė, Virginija..... 243
Jankauskas, Vygintas 76, 269
Jankunaite, Dainora..... 146
Janonis, Vytautas..... 68, 229
Janulionienė, Aušra 105
Jarockytė, Greta 107
Jasiūnas, Rokas..... 238
Jasulaneca, Liga..... 91
Javorskis, Tomas..... 158
Jočys, Vytenis 147
Jokubauskis, Domas 230
Jonušauskas, Linas.....206, 207, 228
Jonušis, Mantas..... 148
Jovaišaitė, Justina..... 266
Jukov, Konstantin 397
Juodagalvis, Tomas..... 210
Juodėnas, Mindaugas..... 202
Jurevičiūtė, Agnė..... 331
Jurkeviciute, Ausrine 224
Jurkeviciute, Ingrida 359
Jursenas, Saulius 269
Jursenas, Saulius Antanas..... 260
Juršėnas, Alfonsas 196
Juršėnas, Saulius .79, 149, 216, 259, 265, 266, 273, 306, 326, 367
Juskaite, Austeja..... 376, 377
Juskowiak, Bernard 49
Jutas, Audrius..... 179
Juzeliunas, Gediminas 176
Juzeliūnas, Gediminas 118

K

Kacperski, Krzysztof..... 398
Kadys, Arūnas.....82, 300, 309
Kadziene, Grazina..... 347
Kairys, Tomas 339, 343
Kakulia, David..... 178
Kalinauskas, Ramutis Kazys 117

Kalnaitytė, Agnė.....391
Kamarauskas, Egidijus.....269
Kamińska, Maria 296
Kaminskas, Arvydas.....353
Kananovich, Dzmitry 140
Kancleris, Žilvinas.....231
Kapitanov, Illia V. 155
Karabanovas, Vitalijus107, 283, 364, 372
Karčiauskaitė, Dovilė.....105
Kareiva, Aivaras.....159, 250
Kariaka, Nataliia 271
Karlonas, Nerijus.....340
Karpichev, Yevgen.....155
Karpicz, Renata 293
Karpič, Renata.....55, 142
Kaseta, Vytautas 370
Kašalynas, Irmantas 68, 229
Kašėtaitė, Sigita.....228
Katelnikovas, Arturas 78, 163
Katinaite, Justina.....377
Katkouski, Leanid 221, 381
Katkovsky, Leonid 114
Kaur, Khushdeep.....70, 234
Kausteklis, Jonas 147
Kavalenka, Alena.....360
Kavalenka, Elizaveta....99, 360, 379, 392
Kavalenka, Sopfy.....215
Kazakevičius, Edvardas.....144
Kazakevičius, Rytis 41
Kazlauskas, Karolis 79, 216, 259, 265, 273, 306, 326
Kazlauskienė, Miglė 101
Kazlauskienė, Nijolė 368
Kazlova, Alena.....388
Kelpsiene, Jurgita 347
Kelpšienė, J. 341
Kerevičius, Gintaras 123
Kersulis, Skirmantas.....370
Keruckas, Jonas.....267
Keruckiene, Rasa.....267
Khanna, Sakshum.....285
Khaouch, Zakaria.....389
Khruschinsky, Arkadiy 181
Kiełczewska, Urszula 150
Kirsnyte, Monika 151
Kisielius, Girius.....148
Kisieliūtė, Aura.....361
Kisnierienė, Vilma 365
Kiverytė, Silvija.....173
Kleinotienė, Gražina.....339, 343
Klement, Uta.....246
Klemo, Marsida.....35
Klimavičius, Vytautas 159
Klinavičius, Tomas.....225
Kluonaitis, Karolis.....376
Kobayashi, Yoichi 47
Kocherbitov, Vitaly.....109
Kochetkova, Tatiana 99, 379, 392
Kociak, Mathieu 320
Kodroń, Agata 337
Kois, Julia 241
Kokareva, Natalia 60
Kolenda, Marek.....309
Koliada, Maksym.....268
Kolodziej, Grzegorz 93
Kołodziej, Grzegorz 296
Kolomzarov, Yu.V. 272
Komarov, Stanislav.....33
Komskis, Regimantas 269
Kondratieva, Julia.....310
Kontrimas, Tomas 64
Koreivaitė, Milda.....134
Korjik, Mikhail..... 69, 249, 312
Korneluk, Alexander 398
Kornienko, Tatiana 211
Korobko, Eugenia 292
Korza, Yauheniya 214
Kosmaca, Jelena 91
Kosman, Joanna.....49
Kothari, Shanker Lal.....374
Kotyński, Rafał 386
Kotsikau, Dzmitry..... 138, 292
Kouider, Nourreeddine..... 280, 389
Kowalczyk, Iwona 137
Kowalik, Przemyslaw 95
Kozhanovsky, Alex 133
Kozlova, Elena.....351
Kozlovskaya, Ekaterina 129, 130, 133, 170
Krasovskaja, Natalija.....98
Kreiza, Gediminas 79, 273, 306, 326
Krikščikas, Laurynas 378
Król, Mateusz.....284
Królikowska, Agata 54
Krotkus, Arūnas 83
Kruk, Paulina E.....77
Krumina, Gunta 346
Kubek, Monika.....127
Kučiauskas, Dalius.....374
Kučinskas, Dainius 184
Kučinskienė, Zita Aušrelė... 105, 353
Kudarauskas, Domas 192
Kuk, Natalia 398
Kukhta, Nadzeya A.....270
Kuksėnaitė, Gintarė 326
Kulakovich, O.....219
Kulakovich, Olga 90, 214
Kuliešaitė, Miglė 185
Kuliešius, Feliksas 387
Kulys, Juozas..... 330, 356
Kumar, Manoj..... 70, 234, 237, 277
Kuncinas, Anton.....116
Kunickaite, Agne.....350
Kunitskaya, Yuliya..... 99, 379, 392
Kuodis, Zenonas 168
Kurasova, Margarita 302
Kurlytė, Emilija.....342
Kusyak, Andriy 286
Kusyak, Natalia 286
Kuten, Semen 181
Kutuzau, Maksim 138
Kuzmitski, Anton.....244
Kvach, Maksim V. 298
Kvedaravičiūtė, Sonata 132

L

Laaksonen, Aatto.....126
Laanearu, Janek.....124
Labatsevich, Pavel 177
Lagzdina, Elena.....223
Lamch, Łukasz.....345
Lamela, Horacio.....57
Landfester, Katharina 108
Lapanik, Valery 303
Lapeikaitė, Indrė.....365
Lapinski, Mariusz 95
Lassalle, Henri-Pierre.....106
Lastauskiene, Egle 370
Latynis, Jekaterina 109
Laurynėnas, Audrius 330
Lavrova, Olga.....182
Lazda, Reinis 43
Ledinauskas, Eimantas.....32
Leggio, Luca.....57
Łempicka, Karolina 287
Lengvinaite, Dovilė..... 126
Leniart, Aneta..... 288
Leniart, Arkadiusz..... 296
Leonova, Natalya..... 289
Levchuk, Elena..... 182
Levinas, Ramūnas..... 152
Lewicki, Maciej 38
Liaudanskas, Mindaugas 243
Liebert, Karolina 200, 201
Liekis, A. 333
Lina, Bolotine 358
Lina, Lina Bezdetnaya..... 397
Lingis, Danielius..... 223
Linkevičius, Domas 380
Lisauskaitė, Aistė 243
Litsis, Olena 272
Liudkeviciene, Regina 350
Lo, Pok Man 120
Lobanok, Mikhail..... 312
Lomako, Aleksey..... 381
Lomia, Akaki..... 178
Lopp, Margus 140
Łotowski, Zenon 164
Lucchini, Marco 69
Luciunaite, Asta..... 100
Lugauer, Hans-Jürgen..... 82
Luka, Grzegorz..... 317
Lukošiūnas, Julius..... 186
Lukša, Algimantas..... 290
Lupeikytė, Kristina..... 362

M

Mabrouki, Mustapha..... 280, 389
Mackevic, Zygmunt 352
Mackoit, Mažena..... 122
Mačiulytė, Viktorija 382
Magomedov, Artiom 48
Mahilny, Uladzimir 62
Mahmood, Sazzad..... 390
Maydykovskiy, Anton 94
Majauskaitė, Greta..... 134
Majewski, Pawel W. 288
Makarova, Lyubov..... 154
Makauskas, Benas 63
Maksimovaitė, Eglė 104
Malakauskaitė, Justina 273
Malashevich, Alexander 244
Maleckaitė, Karolina..... 274
Malevich, Alex..... 128, 130
Malinauskas, Mangirdas... 206, 207, 228
Malinauskas, Tadas48, 82, 235, 269, 309, 327
Mameniskiene, Ruta 376
Mangeolle, Tristan 291
Marchal, Frédéric 291
Marcinkeviciene, Liucija 356, 359
Marcinkevičienė, Liucija 330
Marcinkutė, Morta..... 396
Marczenko, Michał..... 120
Marčiulionytė, Vaida 311
Maricheva, Jelena 241
Maryia, Bobkova 215
Mariichak, Oleksandra Yu.. 153, 155
Markevičius, Audrius..... 174
Markevičiūtė, Vėtra..... 339, 343
Marszalek, Tomasz 76
Martenov, Anton..... 221
Mathur, Sanjay..... 396
Matsui, Taisuke 235
Matsukovich, Anna.....90, 214, 218, 219
Matulaitienė, Ieva 168

Matulaitis, Tomas 260, 265, 275
Matulionytė, Marija 395
Matuzevičienė, Reda 105
Mazėtytė, Airina 393
Mazėtytė, Raminta 55
Mažeikienė, Asta 105
Mechinski, Vitaly 249
Meija, Raimonds 91
Meisak, Darya 92
Meniailava, Darya 131
Merkys, Andrius 51, 136
Meskys, Rolandas 356
Meškys, Rolandas 330
Miasojedovas, Arūnas 256, 274, 326, 367
Michailovas, Andrejus 193, 194
Michalski, Przemysław Piotr 262, 264, 276
Mickevičius, Saulius 117
Mikalauskaitė, Agnė 293
Mikalauskaite, Gerda 245
Mikhailava, Tatsiana 383
Mikołajczyk, Michał 386
Mikulski, Jakub 95
Mimaite, Viktorija 267
Minakova, I.E. 272
Mindarava, Yuliya 218
Minikayev, Roman 95
Minkevičius, Linas 230
Minko, Anatolij 303
Misevičius, Gediminas 344
Misiūnaitė, Indrė 148
Misztalewska-Turkowicz, Iwona 156
Mitetelo, Nikolai 94
Mlostoń, Grzegorz 139, 145
Mocci, Francesca 126
Mogila, Irmantas 101
Mokrik, Robert 394
Mordas, Genrik 378, 385
Morkvenaite-Vilkonciene, Inga .. 161
Morkvėnaitė-Vilkončienė, Inga .. 361
Morozko, Fyodor 294
Morozova-Roche, Ludmilla 371
Morzycki, Jacek W. 150, 164
Mulone, Antonio 246
Musteikyte, Greta 363

N

Naginienė, R. 333
Nargelas, Saulius 69, 318
Nargelienė, Viktorija 290
Narożnik, Mateusz 113
Nasan, Aleh 252, 253
Nasibulin, Albert 241
Naskręt, Michał 39
Natarov, Valentin 292
Naujalis, Evaldas 174
Navakauskienė, Rūta 98
Navikas, Vytautas 295
Nazarov, Sergey 62
Nazarova, E. 314
Nazarova, Nadzeya 108
Nazeeruddin, M. Khaja 48
Nazeeruddin, Mohammad Khaja 76, 235
Neagu, Alexandra 163
Nedilko, Sergiy A. 165
Nedilko, Sergiy G. 165
Nekrošius, Augustas 247
Neniškis, Algirdas 158
Neumüller, Alex 241
Neverauskienė, Arijanda 339, 343
Neverauskienė, Laura 357
Niaura, Gediminas 83, 109, 168, 330
Nicolenco, Aliona 248
Nicoleno, Aliona 246
Nomeika, Kazimieras 305, 318
Norkute, Goda 348
Norowski, Konrad 282, 287
Norvaisa, Karolis 157
Novickij, Vitalij 355
Novičkovas, Algirdas 71
Novikau, Andrei 312
Novikova, Zoya 292
Novitsky, Andrey 294

O

Obłąk, Ewa 345
Olefir, Andriy 278
Olyshevets, Iryna 271
Omelchenko, Lyudmila 313
Opeida, Iosyp 154

Ö

Öpik, Andres 241

O

Orazi, Leonardo 61
Orentas, Edvinas 158
Orlov, Sergej 197
Orlovas, Sergejus .. 64, 65, 196, 198, 199
Orłowski, Piotr Antoni 296
Ornat, Kacper 398
Orsich, Pavel 249
Ostrauskaitė, Jolita 228
Oswald, Steffen 239

P

P, Chandrakanth 277
Pabedinskas, Algirdas 222
Pacuski, Wojciech 87
Pačebutas, Vaidas 319
Paek, Sanghyun 76
Paipulas, Domas 315
Pakiet, Marta 137
Palaitis, Žygimantas 384
Paleček, David 46
Paltsev, Anton 130
Paluch, Emil 345
Pandey, Manoj Kumar 277
Pankov, Vladimir .. 50, 138, 292, 297
Pashkevich, Aliaksei 86
Pastor-Calle, David 386
Pastuszczak, Anna 386
Paškevičius, Algimantas 173
Patamsytė, Jolanta 344
Patel, Jessica 277
Pauraite, Julija 385
Pavasarytė, Lina 159
Pavlova, Anželika 387
Pellicer, Eva 248
Perepelitsa, Aleksey 90
Perevoznikov, Sergey 86, 307
Petkevičius, Linas 180
Petkutė, Gerda 335
Petrauskaitė, Roberta 173
Petrauskas, Karolis 160
Petrenko, E. V. 314
Petrikyte, Ieva 235
Petroniene, Jurate 161
Petronienė, Jūratė 361
Petronis, Laurynas 208
Petrova, Elena 50, 297
Petrulenas, Augustinas 187
Piasotski, Kiryl 40
Piecuch, Agata 345
Piętka, Barbara 287
Pietrzak, Tomasz 258, 263, 279
Pietrzak, Tomasz K. 77
Pietrzak, Tomasz Karol 262, 264, 276
Pietzonka, Ines 82
Pikčiūnas, Marius 315
Pilgun, Yuriy 195
Pisula, Wojciech 76
Pitsevich, George 128, 129, 130, 133, 170
Pladere, Tatjana 346
Plastinkin, Lukas 395
Plaušinaitienė, Valentina 300
Plavan, Viktoriia 268
Plečkaitis, Marijus 364
Plukienė, Rita 223
Plukis, Artūras 223
Pocevičius, Matas 222
Poderys, Vilius 395, 396
Pokotilo, Jury 310
Polaczynski, Jakub 85
Polaczyński, Jakub 296
Pons, Thomas 291
Popov, Anton 361
Popov, Vladislav 294
Pozingytė, Evelina 83
Pozza, Gianluca 251
Pribitoks, Antons 212
Prischepa, Serghej L. 224
Prystawko, Pawel 229
Prokopyev, Stanislav 312
Prozorovich, Vladimir 50
Prudnikau, Anatol 281, 298
Pūkas, Kornelijus 316
Pula, Przemyslaw 317
Pulmanas, Arūnas 162
Pupkis, Vilmantas 365
Purohit, Zeel 237

R

Rachon, Martyna 200, 201
Račiukaitis, Gediminas 226
Račiūnas, Mantas 118
Radchanka, Aliaksandra 298
Radio, Serhii V. 153, 155
Radiunas, Edvinas 216
Radiūnas, Edvinas 79
Radkiewicz, Artur 150
Radzevičius, Mantas 105
Radžvilaitė, Miglė 217
Ragulis, Paulius 231
Raišys, Steponas 259
Rakstys, Kasparas 76
Ramanauskaite, Egle Marija 399
Ramanaviciene, Almira 161
Ramanavicius, Arunas 161
Ramanavičienė, Almira 361
Ramanavičius, Arūnas 55, 361
Ramanavičius, Simonas 299
Rancova, Olga 125
Rao, Vaibhav 70, 234, 277
Rasiukeviciute, Neringa 347
Ratautas, Dalius 330
Raudonyte-Svirbutaviciene, Eva 163
Redlich, Krzysztof 120
Reklaitis, Ignas 82, 315
Rekštytė, Sima 206, 228
Remeikis, Vidmantas 222, 223

Reznikov, Ivan 135
Riauka, Martynas 318
Ribierre, Jean-Charles 79
Rybusinski, Jaroslaw 95
Rodin, Aleksej 188
Rodin, Aleksej M. 187, 189
Rodriguez, Sergio 57
Rogacki, K. 314
Roshchina, Marina 50, 297
Rotomksis, Ričardas 368
Rotomskis, Ricardas ... 283, 349, 372
Rotomskis, Ričardas .. 107, 391, 395, 396
Rozantsev, Georgii M. 153, 155
Rudys, Romualdas 362
Rudniewski, Rafal 95
Ruseckas, Julius 41
Russell, Philip 24
Rusteika, Nerijus 188, 193, 194

S

Sablinskas, Valdas 128, 129
Sadau, Siarhei 388
Sadaunykas, Audrius 174
Sadauskas, Aidas 34
Sadauskienė, I. 333
Safronov, Kirill 60
Sakai, Nobuya 269
Sakavičius, Andrius 290
Sakirzanovas, Simas 283, 372
Saliba, Michael 48
Samalavičius, Vytautas 394
Sanchez, Miguel 57
Sasaki, Chihiro 120
Saudargienė, Aušra 380
Savickienė, Jūratė 98
Scajev, Patrik 79
Schneider, Frank 334
Seliuta, Dalius 230
Selskis, Algirdas 83
Semaskiene, Roma 369
Semenkova, Galina 366
Seredyński, Bartłomiej 87, 296
Sergeev, Oleg 241
Sergienko, Yuliya 154
Seroka, Barbara 164
Shabunya-Klyachkovskaya, E. 219
Shabunya-Klyachkovskaya, Elena 214
Shabunya-Klyachkovskaya, Elena. 90
Shadyro, Oleg 366
Shalamberidze, Elena 128
Shapochkina, Irina 119
Sharshunovich, Darya 366
Shchehrykovich, Dmitry 383
Shemet, Liudmila 252, 253
Sherbakov, Sergei 252, 253
Shishkanova, Polina 366
Shkliaryk, Yury 182
Shleev, Sergey 330
Shmanai, Vadim 298
Shundalau, Maksim 131, 218
Siciński, Rafał R. 164
Sidletskiy, Oleg 69
Siergiejczyk, Leszek 150
Sikora, Bozena 95
Siliuk, Volha 114
Simatonis, Linas 203, 224
Simonis, Povilas 370
Sypek, Maciej 200, 201
Sirutkaitis, Valdas 213
Sivakov, Vladimir 364
Sivickis, Karolis 348
Skaisgiris, Rokas 367
Skapas, Martynas 82, 83, 300
Skilters, Jurgis 346
Skliutas, Edvinas 228
Skripka, Artiom 107
Skuodis, Eigirdas 143
Slektaite-Kisone, Akvile 349
Slepets, Alina 165
Slevas, Paulius 197
Sliva, Tatiana Yu. 272
Sliwa, Michel 47
Slowik, Karolina 127
Smilgevicius, Valerijus 197
Smirnov, Mikhail 90
Smirnovas, Vytautas 363, 371
Smola, Sergii 271
Snaith, Henry J. 269
Sobczyk, Artur 200
Solovjov, A. L. 314
Solovjov, Andrei 313
Sorokin, Victor 366
Sort, Jordi 248
Sosnovsky, Artem 129
Spielman, Ian B. 118
Staigvila, Gediminas 355
Stanchick, Valeriy 221
Stangret, Monika 112
Stanionytė, Sandra 82, 319
Stankevich, Voitech 370
Stankeviciute, Jonita 356
Stankeviciute, Zivile 250
Stankevičienė, I. 333
Stankevičius, Evaldas 226, 227
Stankevičius, Mantas 368
Stankevičiūtė, Milda 335
Stapulionytė, Asta 331
Starzyk, Piotr 87
Steponaitis, Matas 235
Stepšys, Augustinas 117
Stirke, Arunas 151, 370
Stocka, Joanna 167
Stolarczyk, Nikodem 56
Stonevičius, Edvinas 382
Story, Tomasz 85
Strassburg, Martin 82
Sträter, Christoph 118
Stumbriene, Karina 369
Stumbryte, Ausra 350
Supronienė, S. 341
Suproniene, Skaidre 347, 369
Suszek, Jaroslaw 200, 201
Svyakhovskiy, Sergey 94
Svidras, Henrikas 320
Sviriduk, Katerina 286
Szczypkowski, Paweł 398
Szczytko, Jacek 54, 95, 284, 287, 398
Szot, Michal 85

Š

Šablinskas, Valdas 217
Šačkus, Algirdas 326
Šapolaitė, Justina 222
Šerkšnytė, Laura 209
Šetkus, Arūnas 290
Šikšnys, Virginijus 101
Šilanskas, Arūnas 338
Šimakauskienė, V. 333
Šimatonis, Linas 202, 225
Šinkūnas, Tomas 338
Špandyreva, Marija 168
Šulgaitė, Justina 169
Šulskis, Darius 371
Šuminas, Rosvaldas 186
Švedienė, Jurgita 173

T

Tabolich, Anastasia 205
Tai, Cheuk-Wai 163
Talaikis, Martynas 330
Tamošauskas, Gintaras 186
Tamošiūnas, Vincas 71
Tamulaitis, Gintautas ... 69, 101, 312
Tamulevicius, Tomas 203, 224
Tamulevičius, Sigitas 202, 225
Tamulevičius, Tomas 202, 225
Tarakanova, Elizaveta 351
Tarasenko, Alexander 33
Tatsiana, Solomakha 166
Tavkhelidze, Avto 178
Terbetas, Gunaras 357
Tetianec, Lidija 356, 359
Titenko, Anatoliy 261, 278
Titenko, Yaroslav 261, 278
Tizei, Luiz Galvao 320
Tolenis, Tomas 208
Tolstik, Alexei 62, 211
Tolstik, Elen 62
Tolvaišienė, Sonata 355
Tomašiūnas, Roland 82
Tratsiak, Yevgeny 311
Tress, Wolfgang 235
Tretjak, Marina 301
Tretsiak, Yevgeny 69
Tripathi, Brijesh 70, 234, 237, 277
Trivedi, Maitrayee 277
Trofimova, Alexandra 62
Trotsiuk, Liudmila 214, 219
Tsimbrovsky, Nikita 170
Tsyntsaru, Natalia 172, 236, 248
Tsyntsaru, Natalija 152
Tulytė, Skaistė 342
Tumkevičius, Sigitas 149
Turks, Maris 149, 266
Tušinskis, Giedrius 387
Tutkuviene, Janina 377

U

Udovenko, Eduard 261
Uhlemann, Margitta 239
Ulevicius, Nortautas 187
Ulevicius, Vidmantas 385
Ulevičius, Vidmantas 378
Urbanaitė, Aurelija 171
Urbonas, Rytis Vincentas 169
Uścinowicz, Paulina 150
Usheva, Krystsina 181
Usinskas, Pranas 250
Ustynowicz, Maciej 398
Ušinskienė, Jurgita 357
Uzieliene, Ilona 352

V

Vailionytė, Agnė 393
Vainoris, Modestas 172
Vaitkevičius, Augustas 69, 311
Vaitkunas, Tomas 179
Vaitkus, Antanas 51, 136
Vaitkus, Juozas Vidmantis 357
Vaitkuvienė, Aurelija 357
Valiokas, Ramūnas 295, 393
Valiuniene, Ausra 161
Valiūnienė, Aušra 361
Valiuniene, Saule 352

Valius, Mindaugas 374
Valskienė, Roberta 336
Valušis, Gintaras 230
Varanavičius, Arūnas 184
Varanius, Darius 357
Varapnickas, Simonas 207
Vashkevich, Vera 303
Vasiliauskaitė, Laima 353
Velička, Martynas 217
Venckevičius, Rimvydas 230
Vengelis, Julius 185
Vengris, Mikas 209
Vernickaitė, Edita 236
Vertelis, Vilius 321
Veselis, Laurynas 188
Vetrone, Fiorenzo 396
Vyas, Jaishree 70
Victor, Loschenov 358
Vidziunaite, Regina 359
Vidžiūnaitė, Regina 330
Viksna, Arturs 354
Vilkaitis, Martynas 322
Vilkas, Aivaras 372
Visentin, Francesca 251
Vysotskaya, Ulada 119
Vitta, Pranciškus .. 72, 232, 233, 325
Vladimir, Zorin 358
Voitenko, Tetiana 165
Volyniuk, Dmytro 267, 270, 275
Volk, Krystina 303
Volobujeva, Olga 241
Vorobyeu, Maksim 397
Voronovič, Evelina 107
Vosylius, Vitalis 65
Vosylius, Žygimantas 71
Vovk, Ruslan 313

W

Wada, Satoshi 257
Wcisło, Piotr 56
Westenhoff, Sebastian 46
Wilczewska, Agnieszka Z. 156
Wilk, Kazimiera 345
Wincukiewicz, Adam 296
Witkowski, Marcin 54
Witowski, Andrzej 85
Wojciechowski, Tomasz 95
Wójcik, Michał 284
Wojcik, Michal M. 93
Wojtkielewicz, Agnieszka 150
Wolff, Ulrike 239

X

Xavier, Gauravi 285

Z

Zabiliūtė-Karaliūnė, Akvilė ... 72, 325
Zadvinska, Kristine 354
Zajkowska, Wiktoria 279
Zambon, Alessandro 251
Zanatta, Michele 251
Zaunick, Hans-Georg 249
Zdanis, Povilas 373
Zdziarska, Weronika 398
Zekraoui, Mustapha 389
Zentelytė, Aistė 98
Zgirski, Maciej 282
Zhang, Xi-Cheng 25
Zhekov, Konstantin 308
Zhiltsova, Svetlana 289
Zhiltsova, Svitlana 154
Zhivulko, Aliona 324
Zhivulko, Vadim 323
Zieba, Monika 85
Zigmantas, Donatas 46
Zolumskis, Audrius 174
Zopelis, Eimantas 189
Zorin, Vladimir 106, 397
Zubovas, Kastytis 32, 34
Zubritsky, Yaroslav 128
Żukowski, Krzysztof 49
Zvyagina, Galyna 308
Zvirbliene, Aurelija 100

Ž

Žalga, Artūras 144, 175
Žeimys, Ernestas 63
Žėkas, Vytautas 105
Žurauskienė, Nerija 322
Žvingila, Donatas 344